

PONTIFICIA UNIVERSIDAD
CATÓLICA DEL PERÚ

Escuela de Posgrado



FROM LIGHT NEUTRINO DECAY
PHENOMENOLOGY TO MUON NEUTRINO
CROSS-SECTION MEASUREMENT AT MINER_vA
EXPERIMENT

Tesis para obtener el grado académico de Doctor en
Física que presenta:

Marvin Vladimir Ascencio Sosa

Asesor:

Alberto Martin Gago Medina

Lima, 2022



© 2022

Marvin Vladimir Ascencio Sosa

ORCID: 0000-0001-5066-9675

All rights reserved except where otherwise noted

BIOGRAPHICAL SKETCH

The author was born in Puno, Perú in 1994. He attended *Universidad Nacional del Altiplano*, finishing his Bachelor's degree in Mathematics and Physics (*Ciencias Físico Matemáticas*) in January of 2015. In 2017 he finished the Master degree in Physics (*Magíster en Física*) at the *Pontificia Universidad Católica del Perú*. After that, he started at the *Pontificia Universidad Católica del Perú* as a Ph.D. student under the supervision of Alberto Gago. In 2016 he joined the MINERvA collaboration under the supervision of Minerba Betancourt, Richard Gran, and Jorge Morfin.

As a member of the MINERvA collaboration, the author contributed to UROC operations at PUCP, the production team, and data analysis. This ended up with the physics results shown in this thesis

ACKNOWLEDGEMENTS

I must mention a group of people without whom I would have never done this work.

In the first place, I want to express my special thanks and gratitude to my family: my mom Elvira, dad Oscar, and brother Arnold for their tremendous support and love.

Then, I would like to thank all my elementary, high school, and undergrad teachers. Without them, I would not have reached this point. Following this, I would like to thank my advisor, Dr. Alberto Gago, for his guidance in all this science path and for his friendship since my Master's degree. In addition, I would like to extend my thanks to all of the professors at PUCP, especially to HEP group mentors, Dr. Jose Bazo and Dr. Joel Jones.

I would like to communicate my huge thanks to my other warm family, the MINERvA Collaboration, especially to Dr. Minerba Betancourt, for her mentorship, patience even in hard times, and for constantly pushing this work. Subsequently, I would like to thank Dr. Richard Gran for teaching me his rigorous way of doing science, enjoyably explaining physics, and enriching

discussions. Then, I want to thank Dr. Jorge Morfin for his bet on the LAIF group; without this vision, none of this would succeed. For teaching me how to go from inspiration to approval in neutrino physics. In addition. I would like to thank all members of MINERvA: Dr. Deborah Appel Harris, Dr. Laura Fields, Dr. Daniel Ruterbories, Dr. Trung Le, Dr. Jiyeon Han, Dr. Xianguo Lu for always helping me in dispelling doubts, and thanks to all scientists, faculties, students, and postdocs.

I would like to thank Dr. Phil Rodrigues for building the MEC tool software based on which the current analysis is based.

I would like to thank my friends/colleagues from Puno, Lima, and Batavia: Yhony M., Mg. Andina A., Mg. Felix D., Mg. Jaime H., Mg. Anthony C., Mg. Sebastian S., Mg. Sandro H., Mg. Ernesto C., Mg. Jhonny R., Mg. Aransselly Q., Mg. Nhell C., Mg. Dante T., Mg. Jairo R., Dr. Faiza A., Maria M., Dr. Barbara Y., Adrian L., Dr. Gian C., Dr. Gilson C., Dr. Huma H., Mg. Diego A., Mg. Everardo G., Mg. Gonzalo D., Oscar M., Dr. Zubair A., Dr. Gabriela V., Nishat F., Dr. Anushree G., Mg. Miguel H., Dr. Sandeep K., Dr. Prianka P., Sarah H., Dr. Amy F., Dr. Amit B., Mg. Nafis F., Mg. Ishmam M., Abhilash D., Dr. Leonidas A. (and to all others who helped me in this path).

Finally, I would like to thank CienciActiva-CONCYTEC 2017 and FERMILAB for financing this work.

ABSTRACT

This thesis tackles two essential topics of neutrino physics: neutrino decay and neutrino cross-section measurement. First, the invisible and visible neutrino decay is analyzed through a phenomenological approach, considering future long-baseline neutrino experiments such as DUNE and a hypothetical neutrino beam toward the ANDES laboratory. The study takes into account the ν_μ and ν_e disappearance and appearance, respectively, for both FHC and RHC flux modes. The results showed a negligible matter effect for DUNE but significantly more notable at ANDES. At 90% C.L., the sensitivity to the decay parameter α_3 can be as small as $2 \times 10^{-6} \text{ eV}^2$ for a chosen coupling. The impact of neutrino decay in the determination of θ_{23} and δ_{CP} were also shown. Second, the double-differential cross-section measurement for ν_μ -carbon interactions with three-momentum transfer $|\vec{q}| < 1.2 \text{ GeV}$ obtained with medium energy exposures in the NuMI beam at MINERvA experiment are reported. The measurement is presented as a function of $|\vec{q}|$ and E_{avail} and reviews different interaction models and nuclear effects along quasi-elastic to resonance processes to define a new model for a better agreement. The double differential cross sections are compared to the MnvTunes, GENIE, and NuWro predictions.

RESUMEN

Esta tesis aborda dos temas esenciales de la física de neutrinos: el decaimiento de neutrinos y la sección transversal de neutrinos. En primer lugar, el decaimiento invisible y visible de neutrinos se analiza a través de un enfoque fenomenológico, considerando dos futuros experimentos de neutrinos de *long baseline* como DUNE y asumiendo un hipotético haz de neutrinos hacia el laboratorio ANDES. El estudio considera la desaparición y aparición de ν_μ y ν_e , respectivamente, para los modos de flujo neutrinos FHC y RHC. Los resultados mostraron un efecto de materia insignificante para DUNE, en contraste, más notable en ANDES. A 90% C.L., la sensibilidad al parámetro de decaimiento α_3 puede ser tan pequeña como $2 \times 10^6 \text{ eV}^2$ para un acoplamiento dado. También muestra el impacto de la desintegración de neutrinos en la determinación de θ_{23} y δ_{CP} . En segundo lugar, la medición de la sección transversal diferencial doble para las interacciones ν_μ -carbono con transferencia de momentum $|\vec{q}| < 1.2 \text{ GeV}$ obtenidos con una exposición a la energía media de neutrinos en el haz NuMI en el experimento MINERvA. La medida se presenta en función de $|\vec{q}|$ y E_{avail} , además se revisa diferentes modelos de interacción y efectos nucleares a lo largo de procesos cuasi-elásticos a resonantes para definir un

nuevo modelo para un mejor acuerdo con los datos. Las secciones transversales diferenciales dobles se comparan con las predicciones de MnvTunes, GENIE y NuWro.



PUBLISHED CONTENT AND CONTRIBUTIONS

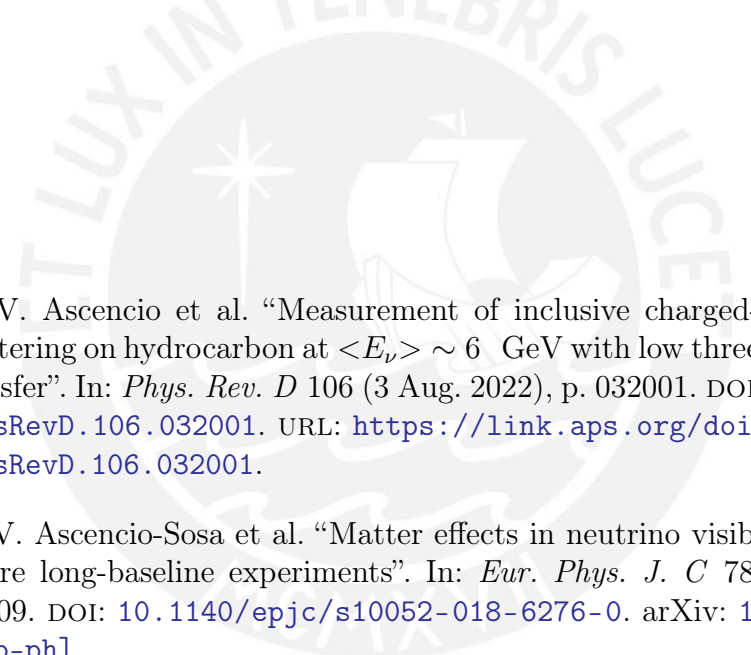
- 
- [1] M. V. Ascencio et al. “Measurement of inclusive charged-current ν_μ scattering on hydrocarbon at $\langle E_\nu \rangle \sim 6$ GeV with low three-momentum transfer”. In: *Phys. Rev. D* 106 (3 Aug. 2022), p. 032001. DOI: [10.1103/PhysRevD.106.032001](https://doi.org/10.1103/PhysRevD.106.032001). URL: <https://link.aps.org/doi/10.1103/PhysRevD.106.032001>.
- [2] M. V. Ascencio-Sosa et al. “Matter effects in neutrino visible decay at future long-baseline experiments”. In: *Eur. Phys. J. C* 78.10 (2018), p. 809. DOI: [10.1140/epjc/s10052-018-6276-0](https://doi.org/10.1140/epjc/s10052-018-6276-0). arXiv: [1805.03279](https://arxiv.org/abs/1805.03279) [hep-ph].

Table of Contents

Biographical Sketch	iii
Acknowledgements	iv
Abstract	vi
Published Content and Contributions	ix
Table of Contents	x
List of Illustrations	xiii
List of Tables	xxiv
I Introduction	1
0.1 From Beta Decay to Neutrinos Oscillation	2
II General theoretical Framework	7
Chapter I: Neutrino Oscillation and Neutrino Interaction with matter	8
1.1 Neutrino in the Standard Model	8
1.2 Beyond the Standard Model: Neutrino Oscillation	11
1.3 Neutrino Interaction with matter	20
1.4 Neutrino - Nucleon Interaction	21
1.5 Neutrino-Nuclei Interaction (Nuclear Models)	27
1.6 Neutrino-Nuclei Interaction (Nuclear Effects)	31
1.7 Neutrino-Nuclei Interaction (Final State Interactions)	34
III Neutrino Phenomenology	36
Chapter II: Perspective of neutrino decay effects at future long baseline experiments	37
2.1 Neutrino Decay	38
2.2 Matter effect with neutrino decay in DUNE and ANDES	44
2.3 Sensitivity and parameter fits at DUNE	55
2.4 Analysis, results and conclusions	59

IV Neutrino Cross Section Measurements at MINERvA	66
Chapter III: Neutrino Beam and Flux	67
3.1 Neutrino Beam	67
3.2 Neutrino at the Main Injector (NuMI)	68
3.3 Flux Simulation and Prediction	76
3.4 Nominal Flux and its error bands	81
3.5 Neutrino Flux Constraint	82
3.6 Flux, Low Hadronic Recoil, and Detector Energy Scale	85
Chapter IV: MINERvA Experiment	88
4.1 MINERvA Detector	90
4.2 Optical Arrangement of MINERvA Detector	97
4.3 MINOS Near Detector	101
Chapter V: ν_μ Low Recoil Analysis in Medium Energy	104
5.1 Kinematic Definition	105
5.2 Signal Definition	106
5.3 Data and MC Sample	106
5.4 Reconstruction Events with Nominal MC	109
Chapter VI: Model Study with Low Recoil Sample	111
6.1 Bodek-Ritchie Tail Enhancement	112
6.2 Super Scaling Approximations SuSA	120
6.3 Removal Energy in Resonant Events (RES)	126
6.4 Low Q^2 Pion Suppression JOINT fit	134
6.5 Pauli Blocking with Berger-Sehgal model	138
6.6 Minoo Kabirnezhad Single Pion Production Model	143
6.7 QERPA to RES events	156
6.8 Summary	160
Chapter VII: Measurement of Double Differential Cross-section	169
7.1 Event distribution	170
7.2 Background Subtraction	176
7.3 Efficiency	178
7.4 Migration Matrix	181
7.5 Unfolding	187
7.6 Flux and Target Normalization	191
7.7 Cross Section Extraction	191
7.8 Systematic Uncertainty	193
7.9 Covariance Matrix	223
7.10 Cross-section compared to neutrino generators	224
7.11 Interpretation of the chi-square and conclusions	231
Chapter VIII: Summary and Conclusions	238
Chapter A: Multi-Universe method	245
Chapter B: Derivation of iterative regularization: D'Agostini method	247
Chapter C: Hadronic tensor and W self-energy in nuclear matter in the context of neutrino-nucleus scattering	253
Chapter D: Particle Hole: $1p1h, 1p1h\pi, 2p2h$ and RPA	257

TABLE OF CONTENTS

D.1 1p1h	258
D.2 1p1h 1 π	259
D.3 2p2h	260
D.4 RPA	261
Chapter E: Cross-section uncertainty understanding	264
Chapter F: Removing the unphysical events of the extended 2p2h sample	267
Chapter G: Cross section comparison with GENIE 3 variations	270
Chapter H: Cross section χ^2 and Covariance Matrix	273
H.1 Cross-section χ^2 comparison diagonal/full covariance matrix . .	274
H.2 Cross-section χ^2 and covariance matrix (systematic)	277
H.3 Cross-section χ^2 (systematics Unc. combinations)	284
Chapter I: SuSAv2 QE	288
Chapter J: MINER ν A Collaboration	294
Bibliography	298



List of Illustrations

<i>Number</i>	<i>Page</i>
1.1 Model BP04 of solar neutrino prediction.	12
1.2 Data comparison with the solar model.	13
1.3 The zenith-angle data events compared with MC.	14
1.4 Parameters of the PMNS matrix.	20
1.5 Neutrino interaction with free nucleon/nuclei including nuclear effects and FSI.	21
1.6 Feynman diagram for CCQE process.	22
1.7 Feynman diagram for CCRES process	24
1.8 Feynman diagram for CCDIS process.	26
1.9 Scheme of Fermi Gas Model.	28
1.10 Local Fermi Gas compared with Global Fermi Gas.	29
1.11 Spectral function for oxygen in terms of momentum and energy.	32
1.12 Global/Local Fermi gas compared with Spectral Function.	32
1.13 Illustration of Short Range Correlation.	33
1.14 Electron scattering with carbon data.	34
1.15 FSI illustration.	35
2.1 Neutrino decay couplings (pseudoscalar and scalar).	39
2.2 Visible decay functions for scalar/pseudoscalar coupling.	44
2.3 Scheme of DUNE experiment.	45

LIST OF ILLUSTRATIONS

2.4	Scheme of LBNF for DUNE	45
2.5	Scheme of LarTPC proposed for FD of DUNE.	46
2.6	Density profile of the Earth based on PREM.	47
2.7	Matter/vacuum ν_e appearance in FHC, $m_{\text{lightest}} = 10^{-10}$ eV. . .	49
2.8	Matter/vacuum ν_μ disappearance in FHC, $m_{\text{lightest}} = 10^{-10}$ eV. . .	50
2.9	Matter/vacuum ν_e appearance in RHC, $m_{\text{lightest}} = 10^{-10}$ eV. . .	50
2.10	Matter/vacuum ν_μ disappearance in RHC, $m_{\text{lightest}} = 10^{-10}$ eV. . .	51
2.11	Matter/vacuum ν_e appearance in FHC, $m_{\text{lightest}} = 0.07$ eV, PS. . .	51
2.12	Matter/vacuum ν_μ disappearance in FHC, $m_{\text{lightest}} = 0.07$ eV, PS. . .	52
2.13	Matter/vacuum ν_e appearance in RHC, $m_{\text{lightest}} = 0.07$ eV, PS. . .	52
2.14	Matter/vacuum ν_μ disappearance in RHC, $m_{\text{lightest}} = 0.07$ eV, PS. . .	53
2.15	Matter/vacuum ν_e appearance in FHC, $m_{\text{lightest}} = 0.07$ eV, S. . .	53
2.16	Matter/vacuum ν_μ disappearance in FHC, $m_{\text{lightest}} = 0.07$ eV, S. . .	54
2.17	Matter/vacuum ν_e appearance in RHC, $m_{\text{lightest}} = 0.07$ eV, S. . .	54
2.18	Matter/vacuum ν_μ disappearance in RHC, $m_{\text{lightest}} = 0.07$ eV, S. . .	54
2.19	Visible decay only plots for PS,S, and $x_{31} \rightarrow \infty$	55
2.20	θ_{23} 38° vs 52° : pseudoscalar events ($(x_{31} \rightarrow 1)$), FHC/RHC. . .	57
2.21	θ_{23} 38° vs 52° : scalar events ($(x_{31} \rightarrow 1)$), FHC/RHC.	57
2.22	θ_{23} 38° vs 52° : $(x_{31} \rightarrow \infty)$ events, FHC/RHC.	58
2.23	δ_{CP} 90° vs -90° : pseudoscalar events, $((x_{31} \rightarrow 1))$, FHC/RHC. . .	58
2.24	δ_{CP} 90° vs -90° : scalar events, ($(x_{31} \rightarrow 1)$), FHC/RHC.	59
2.25	δ_{CP} 90° vs -90° : $(x_{31} \rightarrow \infty)$ events, FHC/RHC.	59
2.26	Sensitivity to θ_{23} as a function of $\theta_{23}^{\text{true}}$	60
2.27	Sensitivity to δ_{CP} as a function of $\delta_{\text{CP}}^{\text{true}}$	62
2.28	Sensitivity to α_3 , by combining ν_μ disappearance and ν_e appearance FHC/RHC.	63
2.29	Allowed regions as function of θ_{23} and δ_{CP}	64
3.1	Low and Medium NuMI fluxes at MINERvA.	69
3.2	Scheme of LINAC, Booster, Main Injector, and Tevatron.	70

LIST OF ILLUSTRATIONS

3.3	Big picture of neutrino production.	71
3.4	Fin target configuration and dimensions.	72
3.5	Scheme of the Target fin and its surrounding components.	73
3.6	Scheme of the magnetic horns to focus the mesons.	74
3.7	Horn 1 and 2 description.	75
3.8	Horn displacements for LE and ME neutrino.	75
3.9	Average Number of hadronic interactions per ν_μ	77
3.10	Flux distribution with hadron production wight in ME.	79
3.11	Fractional Uncertainties for flux distribution with hadron production.	79
3.12	Ratio of predicted ν flux with beam parameters shifted by 1σ deviation to the nominal ν flux.	81
3.13	Toy example of multi-universe approach.	82
3.14	Neutrino flux at MINERvA versus the ME ν mode of the NuMI beam.	82
3.15	Neutrino flux constraint in ME and flux uncertainty effect.	84
3.16	Neutrino flux constrain with Inverse Muon Decay	85
3.17	Horn model comparison in LE and ME.	86
3.18	Ratio of low- ν events of data over simulation.	87
4.1	Scheme of the whole experiment MINERvA/MINOS ND.	89
4.2	MINERvA coordinates.	90
4.3	Size comparison of the MINERvA detector.	92
4.4	Scheme of MINERvA detector.	93
4.5	Nuclear targets scheme.	94
4.6	Water target configuration.	95
4.7	MINERvA Plane orientation.	97
4.8	Scintillator strips used in MINERvA.	98
4.9	Basic working principle of photo-multiplier tube (PMT).	99

LIST OF ILLUSTRATIONS

4.10	Multi-anode photo-multiplier tube (PMT), similar one used in MINERvA.	99
4.11	Scheme of the scintillator strips, fiber optic and PMT used in MINERvA experiment.	100
4.12	Event in MINERvA detector.	101
4.13	Schematic description of MINOS ND detector.	102
4.14	Schematic description of MINOS ND detector.	102
4.15	MINOS ND magnetic field distribution.	103
5.1	Event selection with MnvTune-v1.2 MC breakdown and systematic errors.	110
6.1	Nucleon momentum distributions in a ^{12}C nucleus.	112
6.2	Nucleon momentum distributions in a ^{12}C (historical plot).	113
6.3	Nucleon momentum distributions for LFG, RFG and CFG from GENIE3.	113
6.4	Bodek-Ritchie Tail Enhancement proposal setups.	114
6.5	Reconstructed E_{avail} and BR tail enhancement effect.	117
6.6	Ratio nominal MC over BR tail enhancement MC for reconstructed E_{avail}	118
6.7	Ratio of data over BR tail enhancement MC for reconstructed E_{avail}	119
6.8	SuSAv2 and Valencia 2p2h cross-section.	122
6.9	Reconstructed E_{avail} and the effect of SuSAv2 2p2h effect.	123
6.10	Ratio of nominal MC over SuSAv2 2p2h MC for reconstructed E_{avail}	124
6.11	Ratio of data over SuSAv2 2p2h MC for reconstructed E_{avail}	125
6.12	Electron cross-section versus energy loss for inelastic scattering.	127
6.13	Electron cross-section versus energy loss for inelastic scattering.	128
6.14	E_{avail} in pads of q_3 for different removal energies values.	129

LIST OF ILLUSTRATIONS

6.15	Ratio of data over MC for E_{avail} in pads of q_3 for different removal energies.	130
6.16	Reconstructed E_{avail} and effect of RE.	131
6.17	Ratio of nominal MC over MC RE for reconstructed E_{avail} . . .	132
6.18	Ratio of data over MC RE for reconstructed E_{avail}	133
6.19	Extracted low- Q^2 suppression factors from the FrAbs+low- Q^2 tuning to each channel.	134
6.20	Reconstructed E_{avail} and effect of Low Q^2 Pion Supp.	135
6.21	Ratio of nominal MC over MC Low Q^2 pion suppression for reconstructed E_{avail}	136
6.22	Ratio of data over MC Low Q^2 pion suppression for reconstructed E_{avail}	137
6.23	Cross-section with Rein-Seghan and Berger-Sehgal Pion production model in GENIE.	139
6.24	Parametrization weight to implement in the low recoil sample. .	139
6.25	Reconstructed E_{avail} and effect of auli Blocking with Berger Sehgal.	140
6.26	Ratio of nominal MC over MC Pauli Blocking with Berger-Sehgal.	141
6.27	Ratio of data over MC Pauli Blocking with Berger-Sehgal for reconstructed E_{avail}	142
6.28	Born Diagrams.	143
6.29	Non-resonant diagrams.	143
6.30	GENIE cut at $W_{\text{cut}} = 1.7$ GeV the resonate and the DIS region.	144
6.31	MK and GENIE resonant model cross-section, charge current $\nu_{\mu}p \rightarrow \mu^{-}p\pi^{+}$ channel.	145
6.32	BEBC/ANL data compared to MK-SPP model.	146
6.33	Ratio MK/GENIE cross-section, $\nu_{\mu}p \rightarrow \mu^{-}p\pi^{+}$ channel.	146
6.34	MK and GENIE resonat cross-section, $\nu_{\mu}n \rightarrow \mu^{-}p\pi^0$ channel. .	147
6.35	BEBC/ANL data compared with MK-SPP model, $\nu_{\mu}n \rightarrow \mu^{-}p\pi^0$ channel	147
6.36	Ratio MK/GENIE resonant cross-section, $\nu_{\mu}n \rightarrow \mu^{-}p\pi^0$ channel	148

LIST OF ILLUSTRATIONS

6.37	MK and GENIE cross-section, $\nu_\mu n \rightarrow \mu^- n\pi^+$ channel	148
6.38	BEBC and ANLdata compared with MK-SPP, $\nu_\mu n \rightarrow \mu^- n\pi^+$ channel.	149
6.39	Ratio MK/GENIE cross-section, $\nu_\mu n \rightarrow \mu^- n\pi^+$ channel	149
6.40	True W distributions of low recoil sample.	150
6.41	True W distributions of low recoil sample (different channels.) .	151
6.42	Reconstructed W distributions of low recoil sample.	152
6.43	Reconstructed W distributions of low recoil sample (resonant events only).	152
6.44	Reconstructed E_{avail} and MK effect.	153
6.45	Ratio of nominal MC over MC MK for reconstructed E_{avail} . .	154
6.46	Ratio of data over MC MK for reconstructed E_{avail}	155
6.47	Quasi-elastic RPA weight.	156
6.48	Reconstructed E_{avail} and QERPA to RES effect.	157
6.49	Ratio of nominal MC over MC QERPA-RES for reconstructed E_{avail}	158
6.50	Ratio of data over MC QERPA-RES for reconstructed E_{avail} . .	159
6.51	Reconstructed E_{avail} data and MC (QE and 2p2h models). . . .	163
6.52	Ratio of data over MC RE for reconstructed E_{avail} in projections of reconstructed q_3 regions, the dashed lines are nominal MC, and continuous lines are the QE-RPA to RES effect. In red the Total MC and in purple RES event types.	164
6.53	Reconstructed E_{avail} data and MC (RES models).	165
6.54	Ratio of reconstructed E_{avail} data and MC (RES models). . . .	166
6.55	χ^2 at reconstructed level for QE and 2p2h models.	168
6.56	χ^2 at reconstructed level for RES models.	168
7.1	Low q_3 reconstructed distribution comparison.	171
7.2	Low q_3 reconstructed ratio distribution comparison.	172
7.3	Medium q_3 reconstructed distribution comparison.	173

LIST OF ILLUSTRATIONS

7.4	Medium q_3 reconstructed ratio distribution comparison.	174
7.5	High q_3 reconstructed distribution comparison.	175
7.6	High q_3 reconstructed ratio distribution comparison.	176
7.7	Reconstructed E_{avail} and background distributions.	177
7.8	2D efficiency distribution.	179
7.9	Efficiency breakdown in E_{avail} and projections of q_3 regions. . .	180
7.10	Row normalized migration matrix.	181
7.11	Total projected migration matrix.	182
7.12	QE projected migration matrix.	183
7.13	2p2h projected migration matrix.	184
7.14	Delta migration matrices of E_{avail} in panel of reconstructed q_3 , which corresponds to diagonal big boxes of Figure 7.10.	185
7.15	Other projected migration matrix.	186
7.16	Number of iterations vs χ^2 of “truth fake data” and unfolded distribution.	188
7.17	Unfolding matrix with row normalized.	189
7.18	Unfolded background subtracted data and MC distributions. . .	190
7.19	Data double differential cross-section as function of E_{avail} and q_3 . .	192
7.20	Fractional uncertainties in projections of reconstructed q_3	199
7.21	Legend used in Figure 7.22.	200
7.22	Fractional uncertainties of Final State Interaction in projections of reconstructed q_3	201
7.23	Legend of Interaction fractional uncertainty of Figure 7.24. . .	202
7.24	Fractional Interaction breakdown uncertainties.	203
7.25	Differential cross-section with neutrino energy of 3 GeV. Left plot is neutrino, where the white lines are $W = \{0.938, 1232, 15220\}$ GeV. The right side plot is anti-neutrino, where the white lines represents Q^2 from 0.2 to 1.0 GeV ² . Figure taken from [235]. . .	204
7.26	Legend of fractional RPA uncertainty of Figure 7.27.	205
7.27	Fractional RPA uncertainty.	206

LIST OF ILLUSTRATIONS

7.28	Legend of fractional Detector uncertainty of Figure 7.29.	207
7.29	Fractional detector uncertainty.	208
7.30	Legend of fractional Detector uncertainty of Figure 7.31.	209
7.31	Fractional detector (breakdown) uncertainty.	210
7.32	Legend of fractional Detector uncertainty of Figure 7.33.	211
7.33	Fractional detector (breakdown) uncertainty.	212
7.34	Legend of fractional Detector uncertainty of Figure 7.35.	213
7.35	Fractional detector (breakdown) uncertainty.	214
7.36	Legend of grouped fraction uncertainties background subtracted data (see Figure 7.37).	215
7.37	Fractional Uncertainty of Background Subtracted Data. Y-axis zoomed.	216
7.38	Legend of grouped fraction uncertainties background subtracted data (see Figure 7.39).	217
7.39	Fractional Uncertainty of Unfolded Background Subtracted Data.	218
7.40	Fractional Uncertainty of Data Cross-Section.	220
7.41	Legend of grouped absolute uncertainties background subtracted data (see Figure 7.42).	221
7.42	Absolute Uncertainty of Data Cross-Section.	222
7.43	Covariance matrix in q_0 and q_3 bin index mapping (V)	223
7.44	Data double differential cross-section compared with different generators.	225
7.45	Ratio of data double differential cross-section compared with different generators.	226
7.46	χ^2 calculated with only the diagonal elements of the covariance matrix V	232
7.47	χ^2 calculated with full elements of the covariance matrix V	233
7.48	$\Delta\chi^2$ for with all cross-section models	234
7.49	$\Delta\chi^2$ comparison with full and diagonal only covariance and matrix.	235

LIST OF ILLUSTRATIONS

7.50	$\Delta\chi^2$ with full covariance matrix with/without signal models uncertainty.	235
C.1	Diagram of W -boson self-energy in a nuclear matter.	254
D.1	Diagram of W -boson self-energy in a nuclear matter, 1p1h and 1p1h π	259
D.2	Diagram of W -boson self-energy in a nuclear matter, 2p2h. . .	260
D.3	Diagram of W -boson self-energy in a nuclear matter. Figure based on [94].	262
E.1	Comparison of different signal model uncertainties.	265
E.2	Reconstructed 2p2h and truth 2p2h for SuSA2p2h, default MEC and default MEC withlow recoil tune.	266
E.3	Ratio of double differential cross-section with SuSA over Valencia default MEC.	266
F.1	Extended 2p2h distribution in truth variables (q_3, q_0) with unphysical events at high q_3 region.	268
F.2	Right side, truth W and q_0 before weight to remove the unphysical events. Left side, same distribution with the removing weight. 268	
F.3	The weight function in the truth q_0 and q_3 distribution designed by Richard Gran.	269
F.4	Extended 2p2h distribution in truth variables (q_3, q_0) without unphysical events at high q_3 region.	269
G.1	Data double differential cross-section as function of E_{avail} and q_3 , compared with MnvTune.v3, MnvTune.v1.2, and GENIE3 (variations).	271
G.2	Data double differential cross-section as function of E_{avail} and q_3 , compared with MnvTune.v3, MnvTune.v1.2, and GENIE3 (variations) Ratios.	272

LIST OF ILLUSTRATIONS

H.1	χ^2 comparison mc:MnvTune-v3	274
H.2	χ^2 comparison mc:MnvTune-v1.2	274
H.3	χ^2 comparison mc:NuWro SF	275
H.4	χ^2 comparison mc:NuWro LFG	275
H.5	χ^2 comparison mc:GENIE3-10a	276
H.6	covariance matrix with only flux uncertainty	277
H.7	χ^2 full covariance matrix with only flux uncertainty	277
H.8	covariance matrix with only hadronic energy uncertainty	278
H.9	χ^2 full covariance matrix with only hadronic energy uncertainty	278
H.10	covariance matrix with only Muon reconstruction uncertainty .	279
H.11	χ^2 full covariance matrix with only muon energy and angle un- certainties	279
H.12	covariance matrix with only RPA uncertainty	280
H.13	χ^2 full covariance matrix with only RPA uncertainty	280
H.14	covariance matrix with only FSI uncertainty	281
H.15	χ^2 full covariance matrix with only FSI uncertainties	281
H.16	covariance matrix with only Interaction model uncertainty . . .	282
H.17	χ^2 full covariance matrix with only interaction models uncertainties	282
H.18	covariance matrix with only Signal Model uncertainty	283
H.19	χ^2 full covariance matrix with only Signal model uncertainty .	283
H.20	χ^2 full covariance matrix with only FSI and Interaction model uncertainties	284
H.21	χ^2 full covariance matrix with only flux and hadronic uncertainties	285
H.22	χ^2 full covariance matrix with only flux, hadronic energy, muon energy+angle uncertainties	286
H.23	χ^2 full covariance matrix with only hadronic energy, muon en- ergy+angle uncertainties	287
I.1	SuSAv2 QE cross-section in function of q_0 and q_3	289

LIST OF ILLUSTRATIONS

I.2	Ratio plot from SuSAv2 QE cross-section over GENIE with GFG cross-section in terms of q_0 and q_3	289
I.3	Reconstructed E_{avail} in projections of reconstructed q_3 regions, SuSAv2 QE effect	291
I.4	Reconstructed E_{avail} in projections of reconstructed q_3 regions, SuSAv2 QE effect. MC/MC ratio	292
I.5	Reconstructed E_{avail} in projections of reconstructed q_3 regions, SuSAv2 QE effect. Data/MC ratio	293
J.1	MINERvA Collaboration meeting Pittsburgh, USA 2019	294

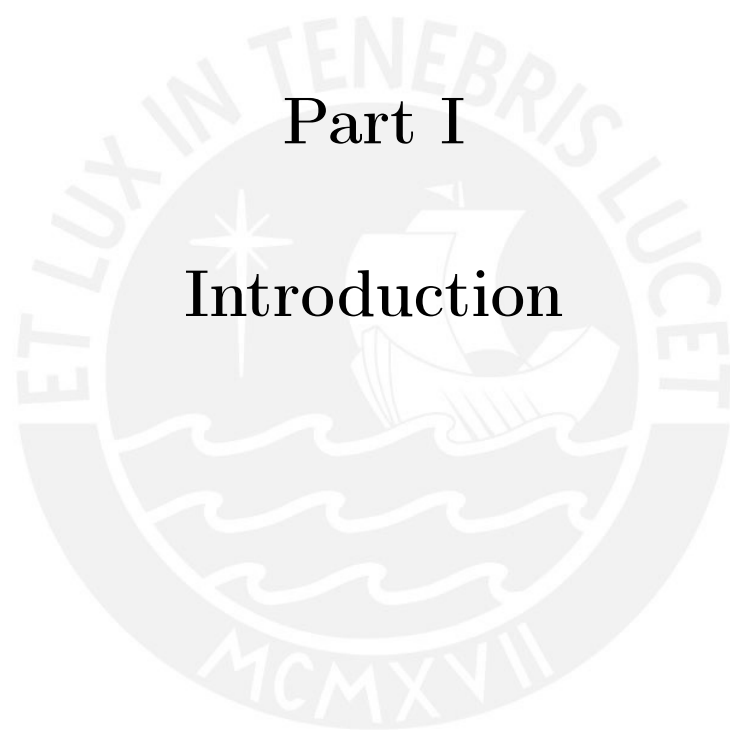


List of Tables

<i>Number</i>	<i>Page</i>
2.1 $\nu_e/\bar{\nu}_e$ appearance AEDL rules for FHC/RHC flux.	48
2.2 $\nu_\mu/\bar{\nu}_\mu$ disappearance AEDL rules for FHC/RHC flux.	48
2.3 α_3 sensitivity as function of $\theta_{23}^{\text{true}}$, ν_e appearance only.	61
2.4 α_3 sensitivity marginalized on $\theta_{23}^{\text{true}}$ and $\delta_{\text{CP}}^{\text{true}}$	62
2.5 DUNE α_3 sensitivity at 90% C.L.	65
3.1 POCO ZXF-5Q graphite target composition.	72
3.2 Hadron production contributions in the neutrino flux.	78
3.3 Nominal and 1σ shift of the NuMI ME beam parameters configuration.	80
4.1 Target z-location, thickness, fiducial area, fiducial mass, and total mass.	94
4.2 Material density and percentage of chemical composition.	96
4.3 Component of strip and plane.	96
5.1 Protons on target for different data sets.	108
6.1 Summary of models component used in GENIE and MINERvA tunes.	162

LIST OF TABLES

6.2	χ^2 of reconstructed distributions in bins of q_3 (1D) and total (2D). The degree of freedom of q_3 bins are 8, 10, 12, 15, 19, and 24. The total degree of freedom is 88. The $i < q_3 < j$ intervals refers the q_3 binning region limits in GeV.	167
7.1	Detector uncertainty description.	194
7.2	FSI uncertainties I. Table taken from [290].	194
7.3	FSI uncertainties II. Table taken from [290]	195
7.4	Interaction uncertainties I. Table taken from [290] except the MaCCQE 1σ uncertainty.	196
7.5	Interaction uncertainties II. Table taken from [290].	197
7.6	RPA and Low Recoil Fit uncertainties.	198
7.7	χ^2 of the data with MC at cross section level. Here the NDF is 44. Only Diagonal elements of covariance matrix.	233
7.8	χ^2 of the data with MC at cross section level. Here the NDF is 44. Only diagonal elements of the covariance matrix	233
7.9	χ^2 of the data with MC at cross section level. Here the NDF is 44. Full covariance matrix	234
7.10	χ^2 of the data with MC at cross section level. Here the NDF is 44. Full covariance matrix	234



Part I

Introduction

INTRODUCTION

0.1 From Beta Decay to Neutrinos Oscillation

The history of neutrino started in 1930, at least theoretically, when Wolfgang Pauli proposed a desperate remedy to save the "exchange theorem" of statistics and the law of conservation of energy [1]. In the letter written by W. Pauli to the Tübingen conference, W. Pauli proposed the possibility of the existence in the nuclei of new electrically neutral particles, which he called neutrons, that particle had to have spin $1/2$ and obey the exclusion principle [1]. The reason for such a hypothesis was the problem of the theoretical interpretation of J. Chadwick's demonstration in 1914, in which the beta spectrum was continuous [2], later also confirmed in 1927 by Ellis and Wooster [3]. The other reason was the unknown spin-statistics relation for ^{14}N and ^6Li nuclei.

After J. Chadwick discovered the neutrons in 1932, [4] there were two particles named neutrons. The name **neutrino** came up later (October 1933) in the Solvay Conference, where W. Pauli offered his hypothesis for publication adopting E. Fermi's notation. [5].

In 1933 E. Fermi [6] and F. Perrin [7] described the theoretical model

that gives us the interpretation of the beta decay, where the neutrino emission occurs just like electrons in the context of a proton-neutron model. Another important outcome of their independent work was the massless behavior of neutrinos. The formulation of β -decay of E. Fermi today is known as Fermi theory [8]. Later on, in 1936, the extension of Fermi theory by adding axial-vector currents was introduced by G. Gamow and E. Teller [9] to describe the beta decay when there is no change in parity of the nuclear state and the total angular momentum of the electron-neutrino is one. At the time, the parity violation was not discovered, and therefore coupling such as scalar, axial-axial vector, pseudoscalar, and tensor could be involved in the weak interaction¹.

From the experimental side, the history of neutrinos started 26 years after the letter of W. Pauli. The group led by F. Reines and C. L. Cowan [10] observed anti-neutrinos from the nuclear reactor using a liquid scintillator detector based on triethylbenzene, terphenyl, and 1,4-di(2(5-phenyloxazole))-benzene (POPOP) loaded with a cadmium compound (cadmium octoate) at the Savannah River Plant reactor [11]. In reaction ($\bar{\nu}_e + p \rightarrow e^+ + n$), they observed a clear signature coming from the two-gamma sources. The first source comes from the annihilation radiation of two gammas of 0.5 MeV ($e^- + e^+ \rightarrow \gamma + \gamma$) and the second source comes from the neutron capture by the cadmium. The capture ($n + {}^{108}\text{Cd} \rightarrow {}^{109}\text{Cd} + \gamma$) produces another gamma which occurs a few microseconds after first source. The resulting cross-section is $\sigma = (11 \pm 2.6) \times 10^{-44} \text{cm}^2/\text{nucleon}$ [12].

After 32 years of W. Pauli's hypothesis, another kind of neutrino, today known as **muon neutrino**, was discovered at Brookhaven National Laboratory (lead by L. M. Lederman, M. Schwartz, and J. Steinberger [13]).

The introduction of the lepton number by E. J. Konopinski and H. M. Mahmoud [14] primarily focuses on explaining the missing decay modes. This

¹Relevant later to understand the long-range correlation in the neutrino cross-section in the nuclei.

new conservation law in general allowed reactions like ($\mu \rightarrow e + \gamma$). However, that process was far from the experimental observations (currently forbidden), suggesting that this new conservation law assigns different numbers to each lepton. [15] [16].

Suggested by B. Pontecorvo and M. Schwartz [17] the muon neutrino was detected primary produced as the result of the decay of a meson called pion ($\pi^\pm \rightarrow \mu^\pm + (\nu/\bar{\nu})$), the pions were produced by 15-GeV proton striking a beryllium target. They used a 10-ton aluminum spark chamber to observe the neutrino interaction. To complete the entire lepton generation or family, the DONuT Collaboration discovered the third neutral lepton [18] configuring what today we call **active neutrinos** settled down by Z boson decay [19].

After about 40 years after Pauli's letter, another mystery pops up. R. Davis and J. Bahcall at Homestake Experiment measured the flux of solar neutrinos with a chlorine-based detector, and they notice a deficit which would again need an explanation [20]. The deficit was confirmed by different detector technologies, including other international collaborations such as Kamioka Observatory [21] and Sudbury Neutrino Observatory [22].

The context of that mystery later called as "solar neutrino problem", starts nine years after Pauli's letter, in which H. A. Bethe explains the thermonuclear reaction mechanisms of how the stars produce their energy [23]. The general description is that there are groups of reactions in which, on the one hand, carbon, nitrogen, and oxygen play the role of catalysts in a cycle while hydrogen lasts. That cycle is known as CNO. On the other hand, there is a cycle where there is a proton intervention, and it is called the p-p cycle. Nowadays, all are under the so-called Standard Solar Model (SSM). In each cycle, we can determine the neutrino production, such as whether they originate from ${}^7\text{Be}$, ${}^8\text{B}$, or other elements of the p-p cycle, as well as their energies. A clear demonstration of the discrepancy between theory and experiments has

been discussed in Figure 2 of J. N. Bahcall's paper [24].

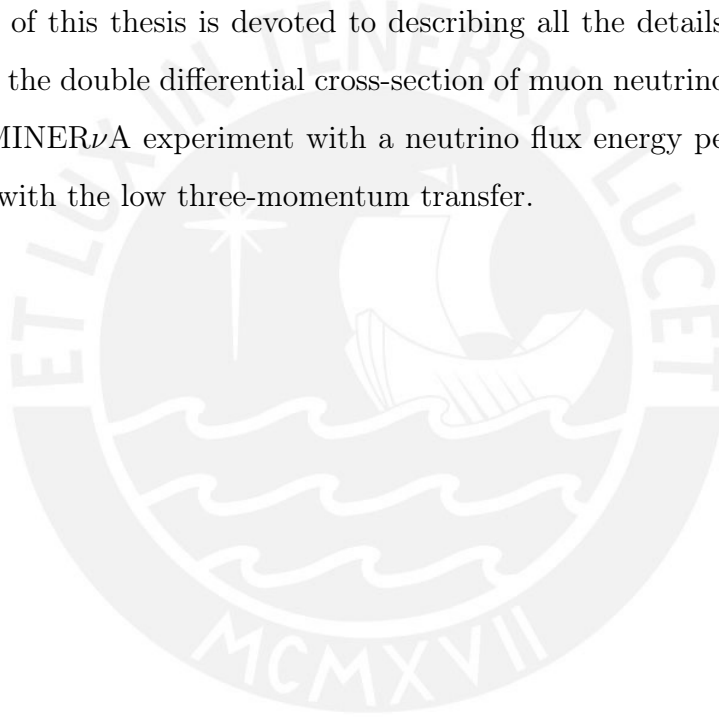
Another problem arose in the late 1980s, the atmospheric neutrinos that the Kamiokande-II Collaboration measured, showed a discrepancy between the electron-like events compared with muon-like events [25]. The ratio of muon neutrino and electron neutrino should follow the pion decay in which a single positive charged pion can decay with a high probability to muon neutrino and anti-muon. Then, the outgoing anti-muon will decay in a positron, electron neutrino, and anti-muon neutrino. Therefore there is a 2 to 1 relation between muon neutrinos and electron neutrinos for the case of positive pion, similarly for the negative one. The experiments [[26], [27], [28]] were reporting this low ratio, and the problem was the so-called "atmospheric neutrino problem" .

Many theoretical explanations like neutrino decay [29], neutrino oscillations [30], and others have been proposed to solve those problems. Motivated on kaon oscillation [31], the neutrino oscillation [32], [33] was finally confirmed by the experiments. It was one of the first pieces of evidence of physics beyond the Standard Model. So that neutrinos oscillate, their mass must be different from zero, meaning that at least two neutrinos must be massive.

Neutrino oscillation also could help us in solving a long-lasting puzzle problem: the asymmetry between matter and antimatter in the universe, by measuring the CP-violation oscillation phase. Because of that, the current neutrino oscillation experimental effort is aimed to perform precision measurements of the oscillation parameters, being the major goal for near-future experiments to measure with high accuracy the CP-violation phase δ_{CP} . However, there is still plenty of room for exploring in neutrino physics such as the test of the existence of a fourth sterile neutrino [34]. In the same line, there is not forbidden that new physics, other than oscillation induced by non-zero neutrino masses, can contribute to the neutrino flavor phenomenon. The hy-

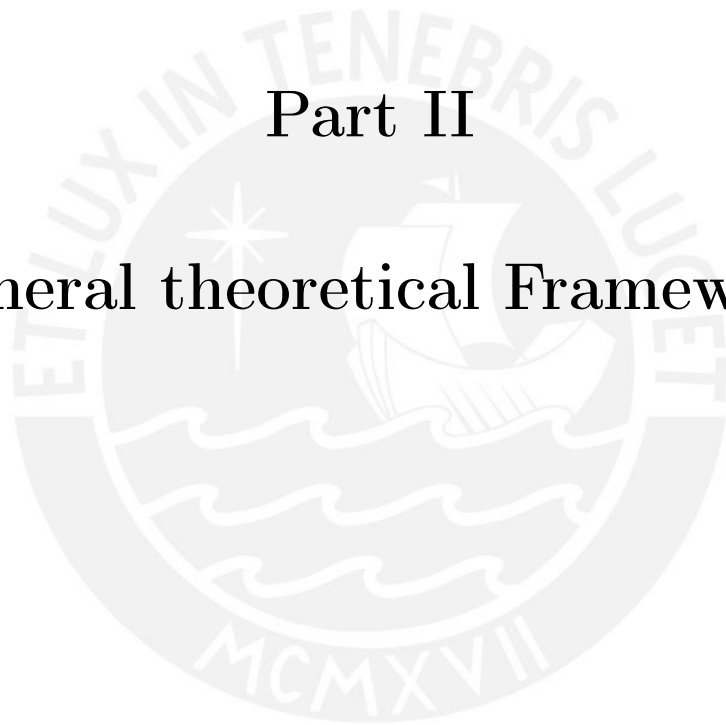
pothesis of neutrino decay is one of these new physics alternatives. In the first part of this thesis, we discuss the matter effects that affect the visible and invisible neutrino decay framework within the context of future long-baseline experiments.

On the other hand, a basic ingredient to achieving a precision measurement of the oscillation parameters is to have a detailed knowledge of the neutrino interaction with matter, i.e. the neutrino-nucleon cross-section, which is vital to reduce the uncertainties of the aforementioned measurements. The second part of this thesis is devoted to describing all the details of the measurement of the double differential cross-section of muon neutrino with hydrocarbon at MINER ν A experiment with a neutrino flux energy peaked around 6 GeV and with the low three-momentum transfer.



Part II

General theoretical Framework



CHAPTER 1

NEUTRINO OSCILLATION AND NEUTRINO INTERACTION WITH MATTER

1.1 Neutrino in the Standard Model

The Standard Model (SM) is a model based on quantum field theory formulated by S. Weinberg [35] and A. Salam [36] based on the gauge symmetry groups $SU(2) \times U(1)$ proposed by S.L. Glashow [37]. To explain the mass of the particles, the SM has the Higgs mechanism [38, 39, 40, 41, 42, 43].

The SM describes the matter particles¹ (fermions) and force carrier particles (bosons) and their interactions. The matter particles are grouped in a subset of quarks and leptons in three generations or families. On the other

¹We are referring by particles to both particles and antiparticles

hand, the force carrier particles carry the electromagnetic force, the nuclear strong force, and the nuclear weak force. The mass of the particles in the context of SM is coming from the interaction with the Higgs field.

To understand the nature of SM, let's start with the groups,

$$SU(3)_C \times SU(2)_L \times U(1)_Y \quad (1.1)$$

the first part of the equation 1.1 represents the world of the quantum chromodynamics describing the (C) colors charge of quarks and the fields of gluons. The part ($SU(2)_L \times U(1)_Y$) represents the left handed fields (L) and weak hyper-charge (Y). The left handed fields side has massless bosons A_μ^a (where $a = 1, 2, 3$) associated to $SU(2)_L$ and hyper-charge side has massless boson B_μ associated to $U(1)_Y$.

Because our interest is the neutrino side, let focus in the electroweak part ($SU(2)_L \times U(1)_Y$), and start with the Lagrangian density before Spontaneous Symmetry Breaking (SSB),

$$\mathcal{L}_{SU(2) \times U(1)} = \mathcal{L}_f + \mathcal{L}_{gauge} + \mathcal{L}_\varphi, \quad (1.2)$$

where f is the fermionic field, φ is the scalar field and $gauge$ the vectorial field. Now, zooming in the vectorial and scalar part of the Lagrangian density,

$$\mathcal{L}_{gauge} + \mathcal{L}_\varphi = -\frac{1}{4}F_{\mu\nu}^a F_a^{\mu\nu} - \frac{1}{4}B_{\mu\nu}B^{\mu\nu} + (D_\mu\varphi)^\dagger D^\mu\varphi - \lambda\left(\varphi^\dagger\varphi - \frac{v^2}{2}\right)^2, \quad (1.3)$$

$F_{\mu\nu}^a$ and $B_{\mu\nu}$ have the fields A_μ^a and B_μ in them. The v is defined as $v \equiv \sqrt{-\mu^2/\lambda}$, where the λ interaction constant and μ is a mass-like coefficient. The scalar-field doublet in the ground state or *vacuum expectation values* (VEV) is,

$$\varphi = \begin{pmatrix} 0 \\ v/\sqrt{2} \end{pmatrix} \equiv \langle \Phi \rangle. \quad (1.4)$$

Introducing a small perturbation $(v/\sqrt{2} + \chi)$ on φ in Equation 1.4 and calculating the covariant derivative of the Lagrangian, we will end up Lagrangian which describes a massive real vector field Z_μ with mass m_Z (Z^0 boson), the massive complex vectors W_μ^\pm with mass m_W (W^\pm bosons), a massless vector field A_μ (γ photon), and a massive real scalar field χ (Higgs boson field)².

A similar mechanism determines the mass of fermions described previously, although additional work is required before breaking the symmetry. The reason is that the left and right-handed chiral states do not have the same transformation properties. Those properties came from low-energy studies involving parity violation discovery [45] and V-A theory development³ [47, 48, 49, 50]. So, the $SU(2)$ gauge boson only couples to left-handed fermion. In other words, a fermion mass term in the lagrangian has the following structure,

$$-m\bar{\psi}\psi = -m(\bar{\psi}_R\psi_L + \bar{\psi}_L\psi_R), \quad (1.5)$$

which does not respect the symmetry before SSB, so it does not appear in the SM lagrangian. Consequently, a new coupling between the fermion field (ψ) and the Higgs double was required; this coupling is called *Yukawa coupling*.

One of the take-out messages from the lagrangian after the SSB is the type of interactions. Specifically, we have the charge current (CC) for the neutrino case,

$$\mathcal{L}_{\text{int CC}} = -\frac{g}{\sqrt{2}}\bar{\nu}_\alpha\gamma^\mu\frac{(1-\gamma^5)}{2}l^\alpha W_\mu + \text{H.c} \quad (1.6)$$

and neutral current (NC),

$$\mathcal{L}_{\text{int NC}} = -\frac{g}{2\cos\theta_W}\bar{\nu}_\alpha\gamma^\mu\frac{(1-\gamma^5)}{2}\nu^\alpha Z_\mu + \text{H.c}, \quad (1.7)$$

α stands for the different e, μ and τ charged lepton types.

²The reader can find more detailed description on [44].

³An excellent book about Fermi theory, V-A and SM transition is [46](chapter 5)

1.2 Beyond the Standard Model: Neutrino Oscillation

The neutrino oscillation is a quantum phenomenon associated with the interference between non-zero neutrino mass-eigenstates (ν_1, ν_2 and ν_3). This translates into the neutrino flavor conversion after its travel a distance, recalling that the neutrino flavor-eigenstates (ν_e, ν_μ and ν_τ) are a linear superposition of the three neutrino mass-eigenstate.

The Solar Standard Model (SSM) built by John Bahcall predicts that the different nuclear reactions that take place in the Sun must produce electron neutrinos within a broad range of energies. With the aim of probing the SSM, several experiments were developed to be able to carry out the measurements of electron-neutrinos coming from the Sun. A pioneering experiment was Homestake proposed by D. Raymond [51] in the 1960s. This experiment observed a deficit of electron neutrinos. Similar observations (deficit) were later confirmed by Kamiokande experiment [52, 53], as well as other experiments [54, 55]. The conflict between the SSM prediction of electron-neutrinos (see Figure 1.1) and their experimental observations (see Figure 1.1) was known as the “Solar Neutrino Problem”.

On the other hand, there are also neutrinos produced as a consequence of the interaction between cosmic rays and nuclei in the upper atmosphere. This interaction produces a pion meson (+/-), then the pion (+/-) decays into a muon (+/-) and a muon neutrino ($\nu/\bar{\nu}$). Then, finally, that muon (+/-) decays in an electron (+/-), neutrino electron ($\nu/\bar{\nu}$), and a muon neutrino ($\bar{\nu}/\nu$). One can then expect that the two-to-one relation of the ratio of muon neutrinos over electron neutrinos holds, regardless of the location of the detector (due to the isotropy of the cosmic rays). However, it did not happen to have that several experiments observed a deficit of muon neutrinos. In particular, the Super-Kamiokande experiment observed a zenith-angle dependence of the muon neutrinos [56] (See Figure 1.3). This inconsistency between data and expectations, which resembles the Solar Neutrino Problem,

was known as the Atmospheric Neutrino Anomaly.

There were several theoretical explanations for the solar and atmospheric neutrino data [57, 58, 59]. One of them and the current theoretical description was suggested in the 1950s by B. Pontecorvo. Motivated in kaon oscillations [31], he proposed a neutrino-antineutrino oscillation, which resulted in a neutrino flavor oscillation in his later papers [30, 60, 61, 62, 63]. As we will see in the next section with further detail, the neutrino oscillations phenomenon is induced by non-zero neutrino masses squared differences.

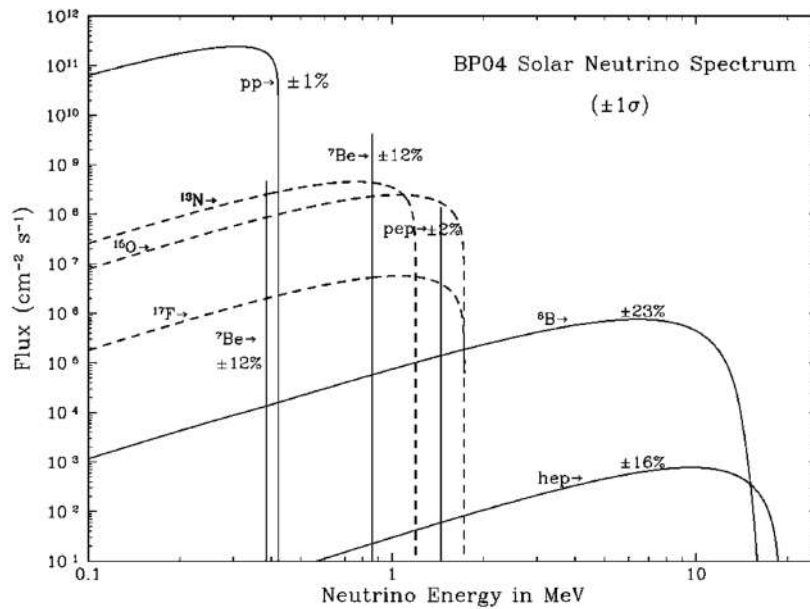


Figure 1.1: Model BP04 of solar neutrino prediction, figure taken from [24].

1.2. BEYOND THE STANDARD MODEL: NEUTRINO OSCILLATION

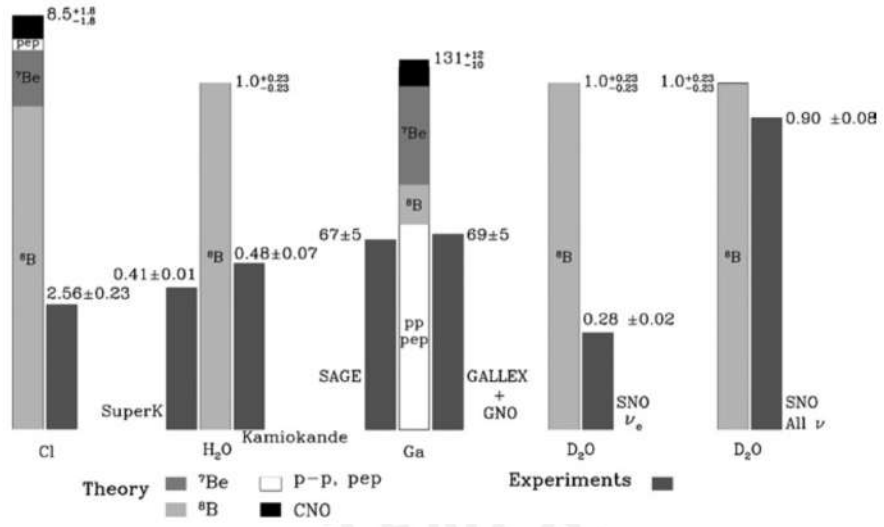
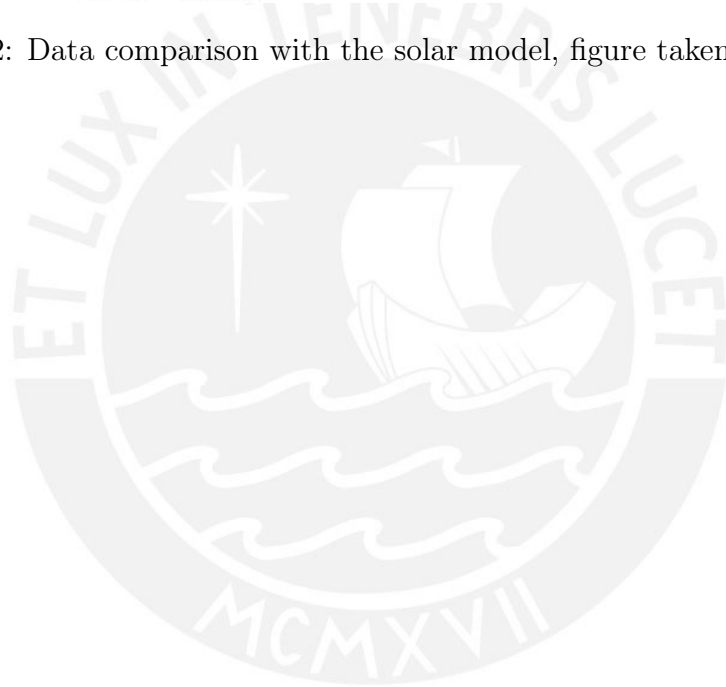


Figure 1.2: Data comparison with the solar model, figure taken from [24].



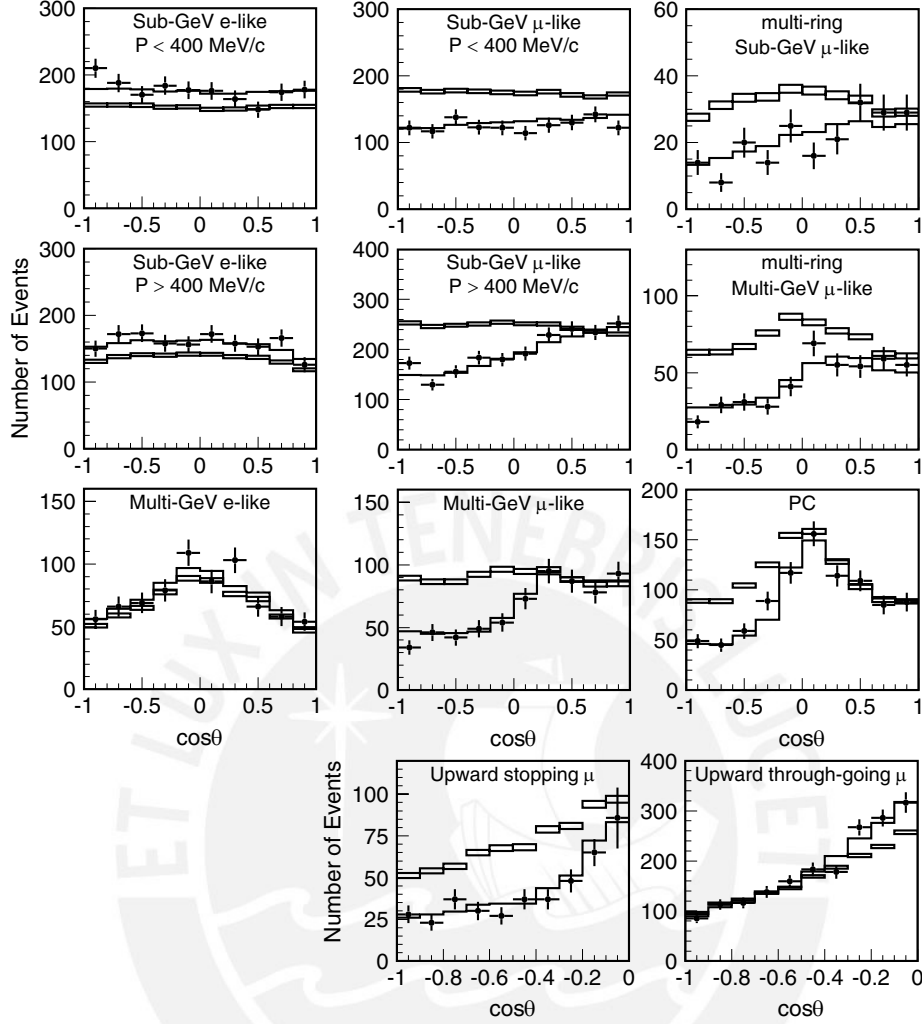


Figure 1.3: The zenith-angle distribution data events compared with non-oscillated Monte Carlo events in boxes and oscillation hypothesis in continue line, figure taken from [56].

Neutrino Oscillation

As mentioned earlier, the neutrino flavor or interaction eigenstates ($|\nu_\alpha\rangle$) are a linear superposition of the mass eigenstates ($|\nu_i\rangle$) with mass m_i or, in other words, the flavor eigenstates represents a rotation with respect to neutrino mass eigenstates. Thus, mathematically it is represented as,

$$|\nu_\alpha\rangle = \sum_i U_{\alpha i}^* |\nu_i\rangle, \quad (1.8)$$

where $U_{\alpha i}^*$ is the rotation matrix that relates the neutrino eigenstates. The $U_{\alpha i}^*$ is a unitary complex matrix. It has the following properties,

$$\sum_i U_{i\alpha}^* U_{i\beta} = \delta_{\alpha\beta}, \quad \sum_\alpha U_{\alpha i}^* U_{\alpha j} = \delta_{ij}. \quad (1.9)$$

The U matrix is called Pontecorvo-Maki-Nakagawa-Sakata (PMNS)[64], and it has three mixing angles and one complex phase, is represented below,

$$U_{\text{PMNS}} = \underbrace{\begin{pmatrix} 1 & 0 & 0 \\ 0 & c_{23} & s_{23} \\ 0 & -s_{23} & c_{23} \end{pmatrix}}_{\text{Atmospheric and LBL}} \underbrace{\begin{pmatrix} c_{13} & 0 & e^{-i\delta_{\text{CP}}} s_{13} \\ 0 & 1 & 0 \\ -e^{i\delta_{\text{CP}}} s_{13} & 0 & c_{13} \end{pmatrix}}_{\text{Mixed}} \underbrace{\begin{pmatrix} c_{12} & s_{12} & 0 \\ -s_{12} & c_{12} & 0 \\ 0 & 0 & 1 \end{pmatrix}}_{\text{Solar and Reactors}}, \quad (1.10)$$

where s_{ij} and c_{ij} are $\sin \theta_{ij}$ and $\cos \theta_{ij}$. Before seeing the propagation, we have to consider an approximation of the energy,

$$E_i = \sqrt{p_i^2 + m_i^2} \approx p_i + \frac{m_i^2}{2p_i} = E + \frac{m_i^2}{2E}, \quad (1.11)$$

which is possible because we consider a small mass and ultrarelativistic neutrino behavior. From the equation 1.11 we can obtain a useful relation,

$$E_k - E_j = \frac{\Delta m_{kj}^2}{2E}, \quad (1.12)$$

Where Δm_{kj}^2 represents $m_k^2 - m_j^2$. Now, let's consider the equation of the evolution of the quantum state,

$$\hat{H} |\nu\rangle = i\hbar \frac{\partial}{\partial t} |\nu\rangle, \quad (1.13)$$

where \hat{H} is the Hamiltonian operator, and as is expected, it is diagonal in the mass vacuum basis,

$$H_{ij} = E \begin{pmatrix} 1 & 0 & 0 \\ 0 & 1 & 0 \\ 0 & 0 & 1 \end{pmatrix} + \frac{1}{2E} \begin{pmatrix} m_1^2 & 0 & 0 \\ 0 & m_2^2 & 0 \\ 0 & 0 & m_3^2 \end{pmatrix}, \quad (1.14)$$

which written in the interaction basis is,

$$H_{\alpha\beta} = U_{\alpha i} \begin{pmatrix} E + \frac{m_1^2}{2E} & 0 & 0 \\ 0 & E + \frac{m_2^2}{2E} & 0 \\ 0 & 0 & E + \frac{m_3^2}{2E} \end{pmatrix} (U^\dagger)_{\alpha i}. \quad (1.15)$$

The $\hat{S} = \exp(-i\hat{H}x)$ operator in the mass basis is introduced to solve the equation 1.13. We are considering the ultrarelativistic approximation in order to have $t = x$. The amplitude therefore is,

$$S_{ij} = \langle \nu_i | \hat{S} | \nu_j \rangle = \delta_{ij} \exp\left(-i \frac{m_j^2}{2E} x\right), \quad (1.16)$$

where we consider only the right-hand side of the equation 1.14. The S matrix for interaction basis is given by

$$S_{\alpha\beta} = \langle \nu_\alpha | \hat{S} | \nu_\beta \rangle = \sum_i U_{\alpha i} U_{\beta i}^* \exp\left(-i \frac{m_i^2}{2E} x\right). \quad (1.17)$$

Thus, we can calculate the probability of the amplitude using the equation 1.17, 1.12 and $x = L$,

$$\begin{aligned} P_{\nu_\beta \rightarrow \nu_\alpha} &= |S_{\alpha\beta}|^2 \\ &= \left| \sum_i U_{\beta i}^* U_{\alpha i} \exp\left(-i \frac{m_i^2}{2E} x\right) \right|^2 \\ &= \sum_{j,k} U_{\alpha k} U_{\beta k}^* U_{\alpha j}^* U_{\beta j} \exp\left(-i \frac{\Delta m_{kj}^2}{2E} L\right), \end{aligned} \quad (1.18)$$

that probability is valid for the vacuum. We can also make decomposition of the equation 1.18 in such a way that can have real and imaginary parts split given by,

$$\begin{aligned} P_{\nu_\alpha \rightarrow \nu_\beta} &= \delta_{\alpha\beta} - 4 \sum_{k>j} \sin^2\left(\frac{\Delta m_{kj}^2 L}{4E}\right) \text{Re} [U_{\alpha k} U_{\beta k}^* U_{\alpha j}^* U_{\beta j}] \\ &\quad - 2 \sum_{kj} \underbrace{\text{Im} [U_{\alpha k} U_{\beta k}^* U_{\alpha j}^* U_{\beta j}]}_J \sin\left(\frac{\Delta m_{kj}^2 L}{2E}\right), \end{aligned} \quad (1.19)$$

where J is the Jarlskog invariant [65].

From the neutrino oscillation probability in equation 1.19, we can only determine the mass squared differences Δm_{ij}^2 , but not the absolute neutrino mass. The actual best fit of the neutrino oscillation parameters, the PMNS neutrino mixing angles and neutrino mass squared differences, are summarized in Figure 1.4. Currently, it is known that the ν_2 mass eigenstate is heavier than the ν_1 mass eigenstate. However, it is still uncertain whether the ν_3 neutrino mass eigenstate is heavier or lighter than the ν_1 and ν_2 mass eigenstate [66], called normal and inverted ordering, respectively.

It is convenient to point out that the hierarchy between masses only can be determined when the neutrino oscillation probability is affected by matter effects. These effects are especially notorious when neutrinos go through high matter densities such as the stars' core. However, the matter effect in neutrino oscillation is not negligible for the Earth's density matter. This is because ordinary matter contains electrons, protons, and neutrons but not muons or taus. So, only electron neutrinos will be affected by the interaction of charged and neutral currents. The other neutrino types will only take into account neutral current interaction.

The effect can be understood as a change in the effective mass of a particle as it moves through a medium. The effect in neutrino oscillation probability is due to the coherent forward scattering on electrons [67, 68, 69].

The interaction Hamiltonian for Charged Current and Neutral Current is written as:

$$H_{\text{eff}}^{CC}(x) = \frac{G_F}{\sqrt{2}} [\bar{e}(x)\gamma^\mu(1 - \gamma^5)\nu_e(x)] [\bar{\nu}_e(x)\gamma_\mu(1 - \gamma^5)e(x)], \quad (1.20)$$

$$H_{\text{eff}}^{NC}(x) = \frac{G_F}{\sqrt{2}} \sum_{\alpha=e,\mu,\tau} [\bar{\nu}_\alpha(x)\gamma^\rho(1 - \gamma^5)\nu_\alpha] \sum_f [\bar{f}(x)\gamma_\rho(g_V^f - g_A^f\gamma^5)f(x)], \quad (1.21)$$

the CC is typically defined for the electron neutrino case due to its abundance

in our universe and NC for the three flavours. The potential for CC is,

$$V_{CC} = \langle \nu_e | \int d^3x H_{\nu_e e}^{CC} | \nu_e \rangle = \sqrt{2} G_F N_e \approx 7.6 Y_e \frac{\rho}{10^{14} \text{g/cm}^3} \text{eV}, \quad (1.22)$$

where ρ is the density, $Y_e = \frac{N_e}{N_p + N_n}$ is the number of relative density of electron, proton, and neutron (N_e , N_p , and N_n). The NC potential is,

$$V_{NC}^f = \sqrt{2} G_F N_f g_V^f, \quad (1.23)$$

where g_V^f are the related with the coupling constant in the equation 1.7 for the leptonic weak neutral-current and it can be found in the Table 3.6 of [70] as well as a discussion of the potential with more details. The G_F the Fermi constant and N_f is similar that N_e but for all charge leptons.

To get the neutrino oscillation probability, we have to modify the Hamiltonian,

$$H = H_0 + H_I \quad (1.24)$$

where H_0 is the vacuum Hamiltonian and H_I has the part that contains the matter potential matrix (right matrix in Equation 1.25), in general,

$$H = U \begin{pmatrix} 0 & 0 & 0 \\ 0 & \frac{\Delta m_{21}^2}{2E} & 0 \\ 0 & 0 & \frac{\Delta m_{31}^2}{2E} \end{pmatrix} U^\dagger + \begin{pmatrix} V_{CC} & 0 & 0 \\ 0 & 0 & 0 \\ 0 & 0 & 0 \end{pmatrix}, \quad (1.25)$$

Now, the evolution equation is given by,

$$i \frac{d}{dx} \begin{pmatrix} |\nu_e\rangle \\ |\nu_\mu\rangle \\ |\nu_\tau\rangle \end{pmatrix} = \left(U \begin{pmatrix} 0 & 0 & 0 \\ 0 & \frac{\Delta m_{21}^2}{2E} & 0 \\ 0 & 0 & \frac{\Delta m_{31}^2}{2E} \end{pmatrix} U^\dagger + \frac{1}{2E} \underbrace{\begin{pmatrix} 2EV_{CC} & 0 & 0 \\ 0 & 0 & 0 \\ 0 & 0 & 0 \end{pmatrix}}_A \right) \begin{pmatrix} |\nu_e\rangle \\ |\nu_\mu\rangle \\ |\nu_\tau\rangle \end{pmatrix}, \quad (1.26)$$

$$= \frac{1}{2E} [UM^2U^\dagger + A] \begin{pmatrix} |\nu_e\rangle \\ |\nu_\mu\rangle \\ |\nu_\tau\rangle \end{pmatrix}, \quad (1.27)$$

where $A = 2EV_{CC}$, V is the potential. In this case, we can consider only the CC potential because NC affects the global phase and it can be absorbed. We introduce the matrix (U^m) which turn out the evolution equation above into:

$$i \frac{d}{dx} \begin{pmatrix} |\nu_1^m\rangle \\ |\nu_2^m\rangle \\ |\nu_3^m\rangle \end{pmatrix} = \left[\frac{1}{2E} \underbrace{\begin{pmatrix} \mathcal{M}_1^2 & 0 & 0 \\ 0 & \mathcal{M}_2^2 & 0 \\ 0 & 0 & \mathcal{M}_3^2 \end{pmatrix}}_{\text{After diagonalization}} \right] \begin{pmatrix} |\nu_1^m\rangle \\ |\nu_2^m\rangle \\ |\nu_3^m\rangle \end{pmatrix}, \quad (1.28)$$

where $(U^m)^\dagger [UM^2U^\dagger + A](U^m) = \text{Diag}(\mathcal{M}_1^2, \mathcal{M}_2^2, \mathcal{M}_3^2)$ and $|\nu_i^m\rangle = (U^m)^\dagger |\nu_\alpha\rangle$ is the mass diagonal basis in matter. Therefore, the neutrino oscillation probability for constant matter density, which have similar structure than the neutrino oscillation probability for vacuum (see equation 1.19), is given by [71],

$$P_{\nu_\alpha \rightarrow \nu_\beta} = \delta_{\alpha\beta} - 2\text{Re} \sum_{j=1}^2 \sum_{k=j+1}^3 U_{\beta j}^m U_{\alpha j}^{m*} U_{\beta k}^{m*} U_{\alpha k}^m (1 - e^{-i\Delta_{ij}^m}), \quad (1.29)$$

where $\Delta_{jk}^m = \frac{\Delta\mathcal{M}_{jk}^2 L}{2E}$ and $\Delta\mathcal{M}_{jk}^2 = \mathcal{M}_k^2 - \mathcal{M}_j^2$.

		Normal Ordering (best fit)		Inverted Ordering ($\Delta\chi^2 = 2.7$)	
		bfp $\pm 1\sigma$	3σ range	bfp $\pm 1\sigma$	3σ range
without SK atmospheric data	$\sin^2 \theta_{12}$	$0.304^{+0.013}_{-0.012}$	$0.269 \rightarrow 0.343$	$0.304^{+0.013}_{-0.012}$	$0.269 \rightarrow 0.343$
	$\theta_{12}/^\circ$	$33.44^{+0.78}_{-0.75}$	$31.27 \rightarrow 35.86$	$33.45^{+0.78}_{-0.75}$	$31.27 \rightarrow 35.87$
	$\sin^2 \theta_{23}$	$0.570^{+0.018}_{-0.024}$	$0.407 \rightarrow 0.618$	$0.575^{+0.017}_{-0.021}$	$0.411 \rightarrow 0.621$
	$\theta_{23}/^\circ$	$49.0^{+1.1}_{-1.4}$	$39.6 \rightarrow 51.8$	$49.3^{+1.0}_{-1.2}$	$39.9 \rightarrow 52.0$
	$\sin^2 \theta_{13}$	$0.02221^{+0.00068}_{-0.00062}$	$0.02034 \rightarrow 0.02430$	$0.02240^{+0.00062}_{-0.00062}$	$0.02053 \rightarrow 0.02436$
	$\theta_{13}/^\circ$	$8.57^{+0.13}_{-0.12}$	$8.20 \rightarrow 8.97$	$8.61^{+0.12}_{-0.12}$	$8.24 \rightarrow 8.98$
	$\delta_{\text{CP}}/^\circ$	195^{+51}_{-25}	$107 \rightarrow 403$	286^{+27}_{-32}	$192 \rightarrow 360$
	$\frac{\Delta m_{21}^2}{10^{-5} \text{ eV}^2}$	$7.42^{+0.21}_{-0.20}$	$6.82 \rightarrow 8.04$	$7.42^{+0.21}_{-0.20}$	$6.82 \rightarrow 8.04$
	$\frac{\Delta m_{3\ell}^2}{10^{-3} \text{ eV}^2}$	$+2.514^{+0.028}_{-0.027}$	$+2.431 \rightarrow +2.598$	$-2.497^{+0.028}_{-0.028}$	$-2.583 \rightarrow -2.412$
	with SK atmospheric data	$\sin^2 \theta_{12}$	$0.304^{+0.012}_{-0.012}$	$0.269 \rightarrow 0.343$	$0.304^{+0.013}_{-0.012}$
$\theta_{12}/^\circ$		$33.44^{+0.77}_{-0.74}$	$31.27 \rightarrow 35.86$	$33.45^{+0.78}_{-0.75}$	$31.27 \rightarrow 35.87$
$\sin^2 \theta_{23}$		$0.573^{+0.016}_{-0.020}$	$0.415 \rightarrow 0.616$	$0.575^{+0.016}_{-0.019}$	$0.419 \rightarrow 0.617$
$\theta_{23}/^\circ$		$49.2^{+0.9}_{-1.2}$	$40.1 \rightarrow 51.7$	$49.3^{+0.9}_{-1.1}$	$40.3 \rightarrow 51.8$
$\sin^2 \theta_{13}$		$0.02219^{+0.00062}_{-0.00063}$	$0.02032 \rightarrow 0.02410$	$0.02238^{+0.00063}_{-0.00062}$	$0.02052 \rightarrow 0.02428$
$\theta_{13}/^\circ$		$8.57^{+0.12}_{-0.12}$	$8.20 \rightarrow 8.93$	$8.60^{+0.12}_{-0.12}$	$8.24 \rightarrow 8.96$
$\delta_{\text{CP}}/^\circ$		197^{+27}_{-24}	$120 \rightarrow 369$	282^{+26}_{-30}	$193 \rightarrow 352$
$\frac{\Delta m_{21}^2}{10^{-5} \text{ eV}^2}$		$7.42^{+0.21}_{-0.20}$	$6.82 \rightarrow 8.04$	$7.42^{+0.21}_{-0.20}$	$6.82 \rightarrow 8.04$
$\frac{\Delta m_{3\ell}^2}{10^{-3} \text{ eV}^2}$		$+2.517^{+0.026}_{-0.028}$	$+2.435 \rightarrow +2.598$	$-2.498^{+0.028}_{-0.028}$	$-2.581 \rightarrow -2.414$

Figure 1.4: Neutrino mixing angles and squared mass differences, table taken from [72].

1.3 Neutrino Interaction with matter

In order to achieve precision measurements of the neutrino oscillation parameters are needed to understand well the neutrino interaction with matter, a cornerstone piece of identifying correctly the neutrino events.

Our approach for describing/studying the scattering of neutrinos with the nucleons of the target's nuclei will be to divide it into four different stages. These stages are: the neutrino interaction with a single nucleon ((1) of Figure (1.5)). The second is to perform the neutrino interaction in an environment,

in this case, the nuclear domain (represented in (2) of Figure (1.5)), which is entailed with the review of some of the existing nuclear models. After that, we will discuss the nuclear effect inside the nuclei (represented in (3) of Figure (1.5)). The fourth is to describe the possible reinteraction/absorption of the resultant particle of the neutrino interaction before leaving the nuclei. The last process is known as Final State Interaction (FSI) (represented in (4) of Figure (1.5)).

The upcoming section reviews each of these four stages illustrated in Figure (1.5).

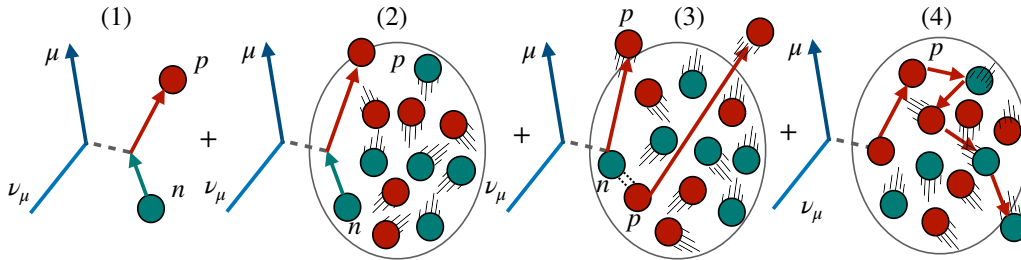


Figure 1.5: Sub-Figure (1) represents the free nucleon interaction, Sub-Figure (2) the interaction inside of nuclei, Sub-Figure (3), the nuclear effects in the neutrino-nuclei interaction, and the Sub-Figure (4) the represents the Final State Interactions (FSI). Figures based on C. Wilkinson's representation.

1.4 Neutrino - Nucleon Interaction

The characteristics of the neutrino interaction with a single nucleon change depending on the energy of the former. The latter translates into the classification of different regimes. Quasi-elastic, Resonant production, or Deep Inelastic Interaction. For the purpose of part II of this thesis, we will only review the relevant ones.

Charge Current Quasi-elastic (QE)

The quasi-elastic charge current interaction of neutrino (ν_l) and antineutrino ($\bar{\nu}_l$) with a single nucleon (n or p) are,

$$\nu_l + n \rightarrow p + l^- \quad (1.30)$$

$$\bar{\nu}_l + p \rightarrow n + l^+ \quad (1.31)$$

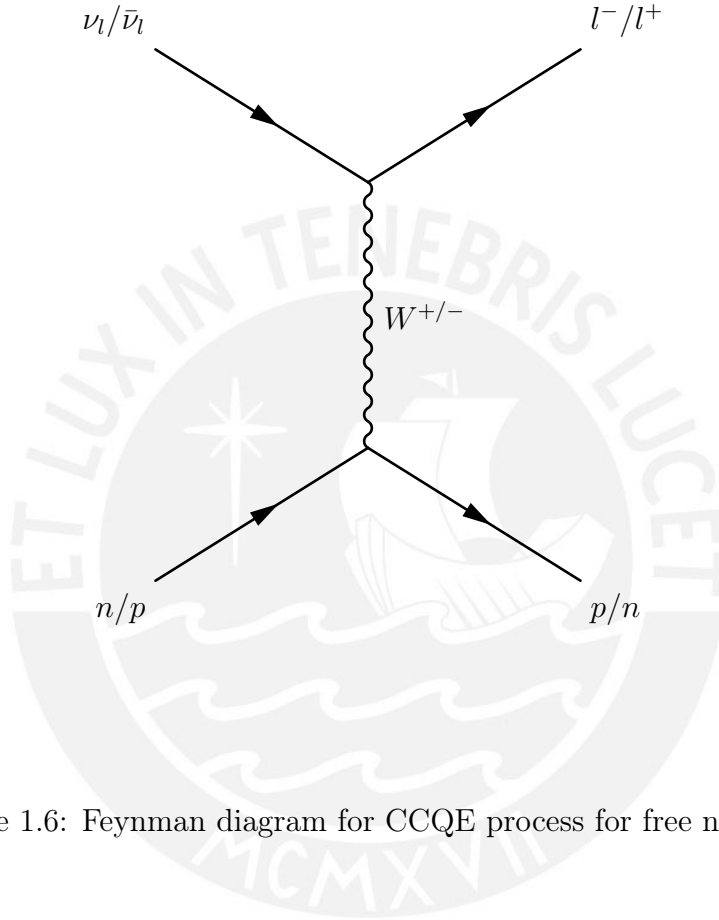


Figure 1.6: Feynman diagram for CCQE process for free nucleon.

where $l = e, \mu, \tau$. The amplitude of the neutrino-nucleon scattering for instance for a channel,

$$\nu_l(k) + n(p) \rightarrow p(p') + l^-(k'), \quad (1.32)$$

where k, p, p', k' are momentum, and $q = p' - p$ is the four-momentum trans-

ferred is,

$$\begin{aligned}
 \mathcal{A}_{\nu_l n \rightarrow pl^-} &= \langle l^-(k'), p(p') | H_{weak} | \nu_l(k), n(p) \rangle \\
 &= -i \frac{G_F}{\sqrt{2}} V_{ud} \bar{u}_l(p) \gamma_\mu (1 - \gamma^5) u_{\nu_l}(k) \\
 &\quad \times \left\{ \bar{u}_p(p') \left[\gamma^\mu F_1(Q^2) + \frac{i}{2m_N} \sigma^{\mu\eta} q_\eta F_2(Q^2) \right. \right. \\
 &\quad \left. \left. - \gamma^\mu \gamma^5 G_A(Q^2) - \frac{q^\mu}{m_N} \gamma^5 G_P(Q^2) \right] u_n(p) \right\}, \quad (1.33)
 \end{aligned}$$

where V_{ud} is a elements of CKM matrix, m_N the mass of nucleon, and $Q^2 = -q \cdot q$. $F_1(Q^2)$, $F_2(Q^2)$, $G_A(Q^2)$, and $G_P(Q^2)$ are, respectively, Dirac, Pauli, axial and pseudo-scalar weak charge current form factor. The $\sigma^{\mu\eta} q_\eta$ is the commutation of gamma matrix, with q_η as momentum transfer. The differential cross-section for $\nu_l/\bar{\nu}_l$ channels are given by⁴

$$\frac{d\sigma_{CC}^{\nu/\bar{\nu}}}{dQ^2} = \frac{G_F^2 |V_{ud}|^2 m_N^4}{8\pi(k \cdot p)^2} \left[A(Q^2) \pm B(Q^2) \frac{s-u}{m_N^2} + C(Q^2) \frac{(s-u)^2}{m_N^4} \right], \quad (1.34)$$

where u, s are the Mandestram variables. The A, B and C are functions in term Q^2 given by

$$\begin{aligned}
 A(Q^2) &= \frac{m_l^2 + Q^2}{m_N^2} \left\{ \left(1 + \frac{Q^2}{4m_N^2} \right) G_A^2 - \left(1 - \frac{Q^2}{4m_N^2} \right) \left(F_1^2 - \frac{Q^2}{4m_N^2} F_2^2 \right) \right. \\
 &\quad \left. + \frac{Q^2}{m_N^2} F_1 F_2 - \frac{m_l^2}{4m_N^2} \left[(F_1 + F_2)^2 + (G_A + 2G_P)^2 - \frac{1}{2} \left(1 + \frac{Q^2}{4m_N^2} \right) G_P^2 \right] \right\}, \quad (1.35)
 \end{aligned}$$

$$B(Q^2) = \frac{Q^2}{m_N^2} G_A (F_1 + F_2), \quad (1.36)$$

$$C(Q^2) = \frac{1}{4} \left(G_A^2 + F_1^2 + \frac{Q^2}{4m_N^2} F_2^2 \right), \quad (1.37)$$

where m_l is the lepton mass.

Charge Current Resonances (RES)

The resonant charge current neutrino scattering happens because the interaction of a neutrino with a nucleon has high energy, which excited the nucleon.

⁴See [73, 74, 75] for the deduction.

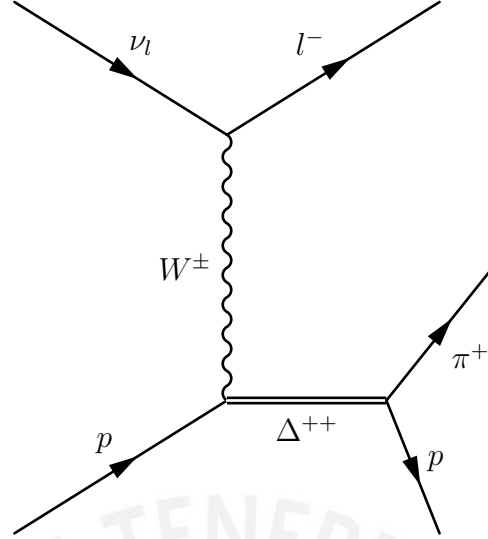


Figure 1.7: Feynman diagram for CCRES process for free nucleon. The nucleon N in this case is a proton and the resonance R in this case is a Δ^{++} .

So, instead of getting a nucleon after the process, like in the CCQE, we have a unstable state so-called resonance. We can describe that process by

$$\nu(k) + N(p) \rightarrow l^-(k') + N^*(p') + R(p_R), \quad (1.38)$$

$$\bar{\nu}(k) + N(p) \rightarrow l^+(k') + N^*(p') + R(p_R), \quad (1.39)$$

where N represents the nucleon, R the resonance particle and N^* the nucleon from the resonant decay (as shown in Figure 1.7). The neutrino generator, as will be presented in the Part III of this thesis, typically use the Rein-Sehgal calculation [76] to describe that cross-section,

$$\frac{d^2\sigma_{CC}^{\nu/\bar{\nu}}}{dQ^2 dq_0} = \frac{G_F^2 Q^2}{4\pi^2 q_3^2} \left(\frac{M_{res}^2 - m_N^2}{2m_N} \right) \left\{ \left(\frac{E_\nu + E_l + q_3}{2E_\nu} \right)^2 \sigma_R^\pm + \left(\frac{E_\nu + E_l - q_3}{2E_\nu} \right)^2 \sigma_L^\pm + \right. \quad (1.40)$$

$$\left. 2 \left(\frac{E_\nu + E_l + q_3}{2E_\nu} \right) \left(\frac{E_\nu + E_l - q_3}{2E_\nu} \right) \sigma_s^\pm \right\} \quad (1.41)$$

where

$$\sigma_R^\pm = \frac{\pi M_{res}}{M_{res}^2 - m_N^2} \mathcal{F}^- \delta(W - M_{res}), \quad (1.42)$$

$$\sigma_L^\pm = \frac{\pi M_{res}}{M_{res}^2 - m_N^2} \mathcal{F}^+ \delta(W - M_{res}), \quad (1.43)$$

$$\sigma_s^\pm = \frac{m_N^2 \pi}{M_{res}(M_{res}^2 - m_N^2)} \frac{q_3^2}{Q^2} \mathcal{F}^0 \delta(W - M_{res}), \quad (1.44)$$

and \mathcal{F}^- , \mathcal{F}^+ and \mathcal{F}^0 are the helicity amplitudes and they are provided by the dynamical model, q_0 is the energy momentum transfer and q_3 is norm of the three momentum transfer or \vec{q} of Q^2 . The W and M_{res} in $\delta(W - M_{res})$ are observed mass or invariant mass of the final state and resonant particle mass respectively. The W^2 can be define as $W^2 = (p + q)^2$, where q is the four-momentum transfer. The cross section in the equation (1.40) describes a single resonance in narrow-width approximation. Suppose we want to go for resonances over finite width. In that case, the $\delta(W - M_{res})$ needs to be replaced by the Breit-Wigner factor,

$$\frac{1}{2\pi} \frac{\Gamma}{(W - M_{res})^2 + \Gamma^2/4}$$

due to in general, the cross-section that involves resonances obeys the Breit-Wigner distribution [77]. The Γ is the resonance width. Although the article (original article [76]) indeed considers the non-resonant part, these are calculated via linear sigma models, which are currently discarded. Some models nowadays consider the lepton's mass and calculations of the non-resonant part with non-linear sigma models, which in the present work are studied in Part II.

Charge Current Deep Inelastic (DIS)

When the neutrino interacts with the nucleon at higher energy, the neutrino stops seeing the nucleon as a point object. Instead, as we saw in the previous subsection, at higher energy, the processes become inelastic. In this case, the neutrino interacts with the components of the nucleon, the quarks. Processes like this are called deep inelastic scattering

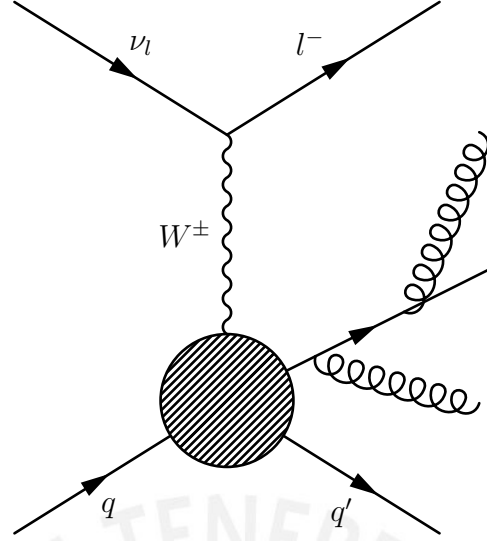


Figure 1.8: Feynman diagram for CCDIS process for free nucleon.

$$\nu_l(k) + N(p) \rightarrow l^-(k') + X(p') \quad (1.45)$$

$$\bar{\nu}_l(k) + N(p) \rightarrow l^+(k') + X(p') \quad (1.46)$$

where N refers to neutron or proton and X to any set of outgoing hadrons.

The matrix element is

$$|\mathcal{M}|^2 = \left(\frac{4G_F}{\sqrt{2}} \right)^2 L_{\mu\nu} W^{\mu\nu} \quad (1.47)$$

where $L_{\mu\nu}$ is the leptonic tensor and $W^{\mu\nu}$ is the hadronic tensor. $W^{\mu\nu}$ is a mix of nucleon mass m_N and six form factors $W_i, i = 1, \dots, 6$. The differential cross-section is usually presented in terms of Bjorken scaling variables,

$$x \equiv \frac{Q^2}{2m_N q_0}, \quad (1.48)$$

$$y \equiv \frac{p \cdot q}{p \cdot k}, \quad (1.49)$$

where $q_0 = \frac{p \cdot q}{m_N}$, m_N is the nucleon mass, and $Q^2 = -q^2$. In the lab frame the $p^\mu = (m_N, 0, 0, 0)$ and $k^\mu = (\omega, 0, 0, \omega)$. The cross-section for neutrino and antineutrino without the charged mass lepton is given by, [78, 46, 79]

$$\frac{d\sigma_{CC}^{\nu/\bar{\nu}}}{dx dy} = \frac{G_F^2 m_N \omega}{(1 + Q^2/M_W^2)\pi} \times \left[xy^2 m_N W_1 + \left(1 - y - \frac{m_N xy}{2\omega}\right) q_0 W_2 + y \left(1 - \frac{y}{2}\right) x q_0 W_3 \right]. \quad (1.50)$$

The W_i with $i = 4, 5,$ and 6 are neglected due to they are proportional to the charged lepton mass. The W_i in the DIS context is called as structure functions and the nature of them are obtained from experimental cross-section measurements [80].

1.5 Neutrino-Nuclei Interaction (Nuclear Models)

In the previous section, we have reviewed the interaction of a neutrino with a nucleon. However, nature is not so merciful. We have to deal with the nuclei and the nuclear environment, and this complicates the cross-section measurements. In this section, we will review some nuclear models and their influence on neutrino scattering.

Fermi Gas Model (FGM)

The Fermi gas model is a nuclear model where we can distinguish between neutrons and protons. These nucleons are almost free or do not interact with each other within a potential (Fermi motion). Due to their distinguishability, they are placed in separate potential wells. The potential for these nucleons is spherical with the same radius. The only rule that applies to them is the Pauli exclusion principle because of its fermionic nature. On the other hand, it is considered “gas” since these nucleons are in thermal equilibrium.

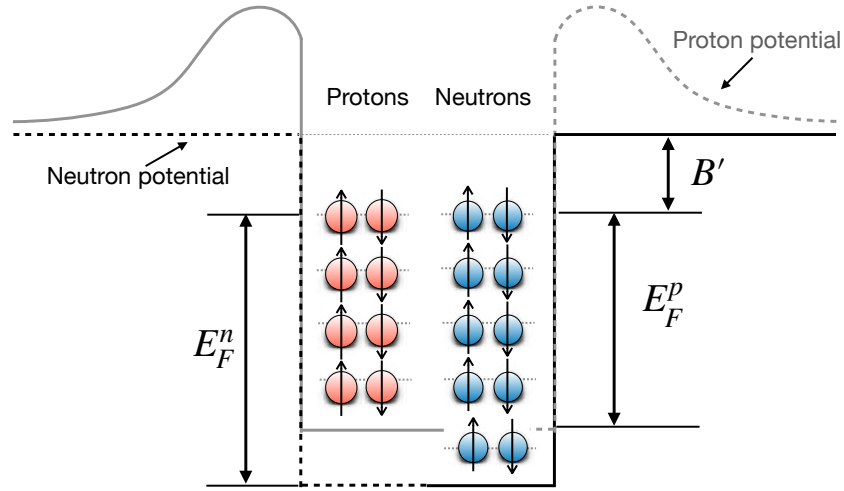


Figure 1.9: Scheme of Fermi Gas Model, where E_F^n , E_F^p and B' represent the Fermi energy of neutron, Fermi energy of proton and binding energy.

Figure 1.9 represents both potentials (in different shapes and colors to distinguish). That potential is generated by all nucleons.

The maximum available energy state that the nucleon can occupy is the Fermi energy ($E_F^{p/n}$). The binding energy (B') is proportional to the energy that the nucleon has to pay to escape the nuclei. It is represented in Figure 1.9 as the difference between the top potential and Fermi level. In the neutrino context, the Fermi gas model has been very popular since the incorporation of [81]. Neutrino generators use the relativistic Fermi model. Generator like GENIE[82], used in this work, incorporates an additional effect called Short Range Correlation SRC, which is studied in detail in part III and the role of Pauli blocking in resonant inelastic events.

Local Fermi Gas Model (LFG)

The Fermi local gas model is an alternative way of understanding the nuclei given the Fermi gas formalism. It is based on the local density approximation (LDA) developed initially by [83], where the dependence of the nucleon position within the nucleus becomes relevant because the density distribution depends on the radius $\rho(r)$ [84, 85].

Figure (1.10) shows the comparison with Global Fermi Gas as a function of Fermi momentum⁵ and distance from the center of the nucleus. The GFG has a constant field for the entire nucleus. On the other side, the momentum distribution in LFG depends on the nucleon's position inside the nucleus.

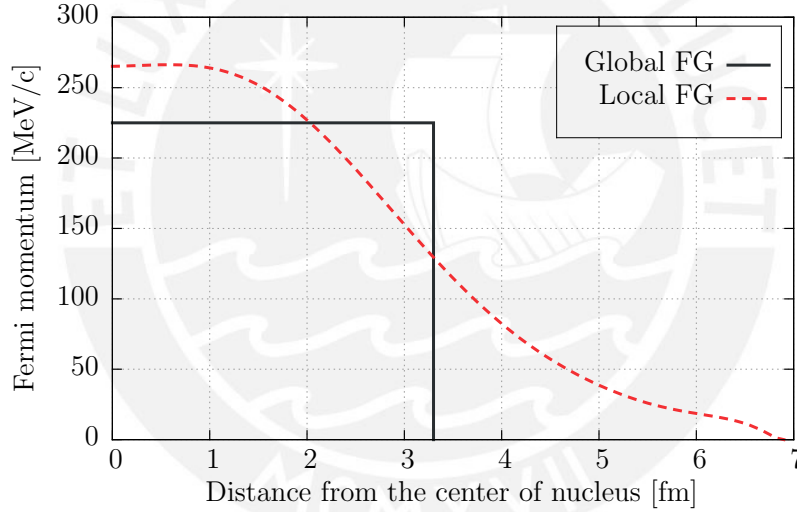


Figure 1.10: Local Fermi Gas compared with Global Fermi Gas. Figure taken from [86]

Impulse Approximation and Spectral Function

The Impulse Approximation (IA) is an approximation scheme in the GeV regime (~ 1 GeV of momentum transfer) of the lepton-nucleus interaction, where it is assumed that in this regime, the dominant process is the lepton-nucleon (single nucleon interaction [87]). This means that the lepton sees the

⁵In Fermi Gas the momentum \vec{p} of the nucleons in the nucleus has a maximum momentum p_F denominated *Fermi momentum*.

nucleus as a set of individual nucleons. After the interaction, the resulting hadrons are not affected by Pauli Blocking or Final State Interaction (FSI) of the other nucleons (they remain as spectator nucleons). The validity of this approximation depends on how large the transferred momentum is (the lepton scans a region of extension $\sim 1/|q_3|$ of the nucleus [87, 88]).

Other Models

Another way to describe the nucleus is based on the atomic shell model, where the electrons are in specific orbits that depend on some quantum numbers. A prediction of such an atomic model is the energy necessary to remove the electrons of the last layer. Similar to the atomic model, the protons and neutrons are described as being in layers within the nucleus. It was observed that the energy necessary to remove them also follows a pattern denominated by magic numbers [89]. So, that model is called a nuclear shell model.

Another nuclear model, called Spectral Function, based on the nuclear shell model and short-range correlation (SRC), which we will see in the next section, gives the probability distribution as a function of removal energy and momentum [86, 90],

$$P(\vec{p}, E) = \sum_n |\langle N_0^A | a_p^\dagger | N_n^{A-1} \rangle|^2 \delta(E - E_N^{A-1} + E_0^A), \quad (1.51)$$

where \vec{p} is the nucleon momentum, a_p^\dagger creator operator, $|N_0^A\rangle$ is the A nucleons initial state with E_0^A energy, $|N^{A-1}\rangle$ is the final state of the (A-1) nucleons with E_N^{A-1} energy, and E represents the removal energy.

The $P(\vec{p}, E)$ can be split in first, mean-field spectral function part, led by $(e, e'p)$ reaction [91] and the single-particle momentum distribution [92], and second, the correlated part, based on local density approximation [83] and short range correlation (SRC),

$$P(\vec{p}, E) = P_{\text{MF}}(\vec{p}, E) + P_{\text{Corr}}(\vec{p}, E). \quad (1.52)$$

An example of the spectral function for oxygen is given in Figure 1.11. The comparison with the global and local fermi gas is given in Figure 1.12, where the tail in the spectral function is coming for the short-range correlation contribution.

1.6 Neutrino-Nuclei Interaction (Nuclear Effects)

So far, we have described in the previous sections the interaction of neutrinos with a single nucleon, then some nuclear models. In this section, we will see some of the nuclear effects of the neutrino-nuclei interaction.

Long Range Correlation: RPA

In the previous section, we described that nuclear models include removal energy; this means that the nucleons in the nucleus are bound. When the neutrino hits the nucleus by electroweak interactions, the coupling (axial-vector coupling mostly, see Appendix D) is affected by the correlated nucleon. This effect is calculated via Random Phase Approximation (RPA) [94].

The RPA comes from the description of electron interactions [95, 96] (see Appendix C and D). This RPA response is used as a substitute for the nuclear response (medium polarization effects) obtained when considering a single particle-hole excitation (1p-1h) to the W boson self-energy in the context of many body framework [94, 97].

Short Range Correlation

In the nuclei, nucleons (N) (protons (p) and neutrons (n)) are bounded as we saw before. When nucleons momentum are opposite (back-to-back), higher than Fermi momentum (k_F) and lower in the mass center a correlation between nucleon pairs occurs. Such a phenomenon is known as short-range correlation (SRC) pairs [98, 99]. To illustrate it, we can suppose the Sub-figure 3 of Figure 1.5 where n and p are correlated under the condition mentioned above (momentum back-to-back, higher than Fermi momentum, etc.). The effect in

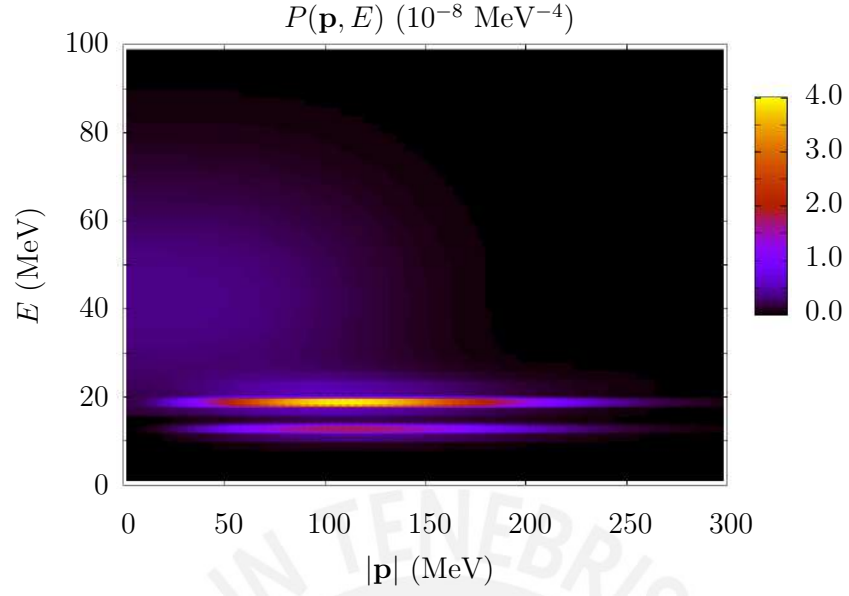


Figure 1.11: Spectral function for oxygen in terms of momentum and energy. The figure is taken from [93]

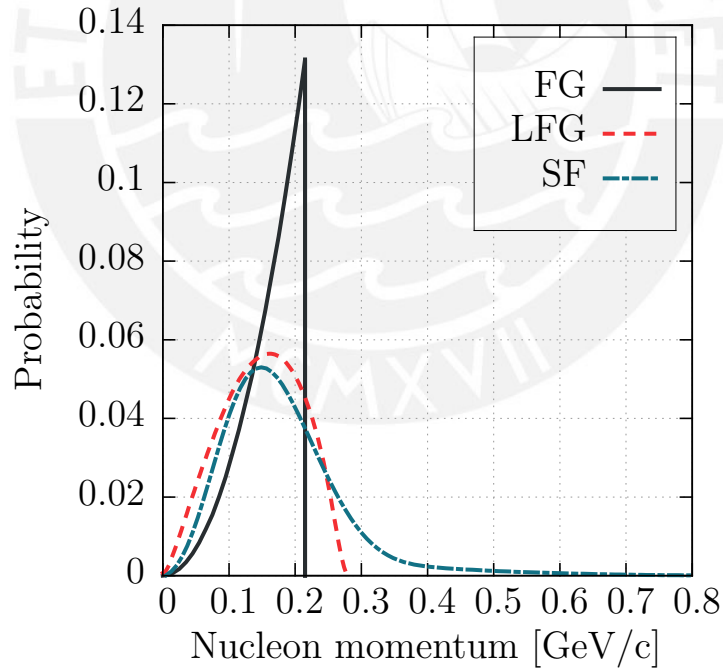


Figure 1.12: Fermi Gas, Local Fermi Gas compared with a projection in momentum of spectral function. Figure taken from [86]

the momentum distribution is illustrated in Figure 1.13, where the SRC is represented in the tail of the distribution.

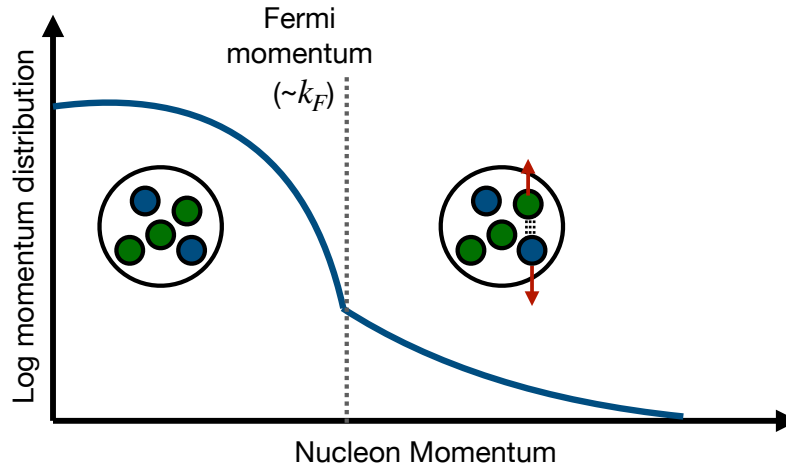


Figure 1.13: Illustration of Short Range Correlation (SRC). Figure based on [100]

The SRC preferentially leads to two nucleon knockout, including the 2p2h process (described later). At one extreme, the neutrino may transfer most of its momentum to just one correlated nucleon. At the other extreme, it can deliver the momentum and energy to one, both nucleons, or with the strong force-carrying exchange pion, given more freedom than regular QE or Δ reaction (Resonant interaction).

The SRC pair has a preference for proton-neutron instead of neutron-neutron or proton-proton, in Carbon target the pn pair occurs around 20 times than nn or pp [101], that imbalance is due to NN tensor force [102, 101, 103, 104]. One of the theoretical model approaches is the Generalized Contact Formalism (GCF) [105]. Since the SRC influences higher nucleon momentum, it has implications for the “slow” quark movement in the nucleus, known as the “EMC” effect, in the DIS region [106].

Meson Exchange Current (MEC)

The 2p-2h process (2-particles 2-holes) was initially studied in interactions of charged leptons with nuclei. The interaction involved two nucleons, such as neutron-proton pairs, as shown in Figure 1.14, plotted as a function of the transferred energy. These events constitute extra events in the region between QE and resonant, called the "dip" region. A detailed description of the 2p2h process is in Appendix C and D.

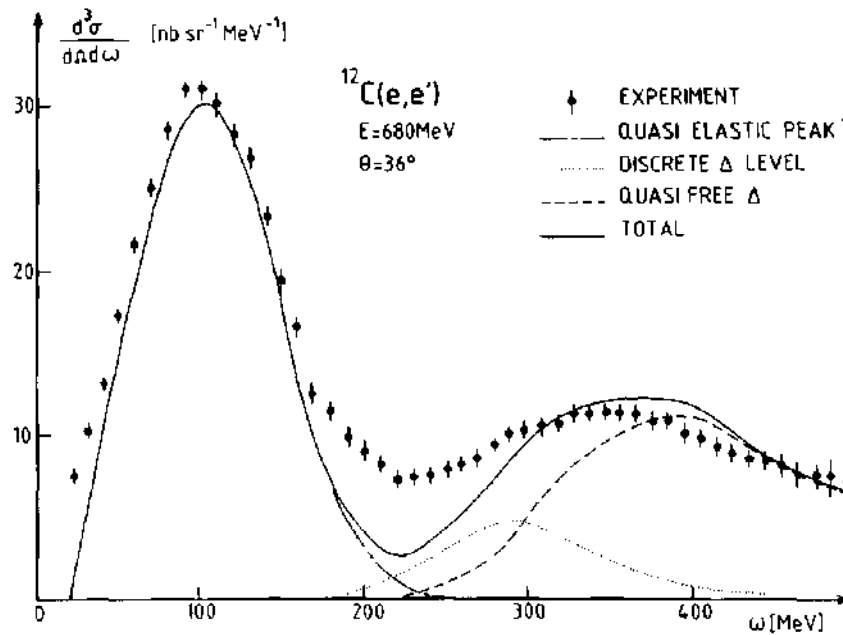


Figure 1.14: Electron scattering with carbon data ($C(e, e')$), the two peaks represent QE and Δ resonance. Figure taken from [107, 108]

1.7 Neutrino-Nuclei Interaction (Final State Interactions)

After the neutrino-nucleon interaction, the outgoing particle can re-interact, be absorbed, or be scattered before leaving the nuclei. The Final State Interaction, handed this propagation through several methods. Neutrino generator like NuWro and GENIE uses intranuclear cascade, and intranuclear hadron transport [109].

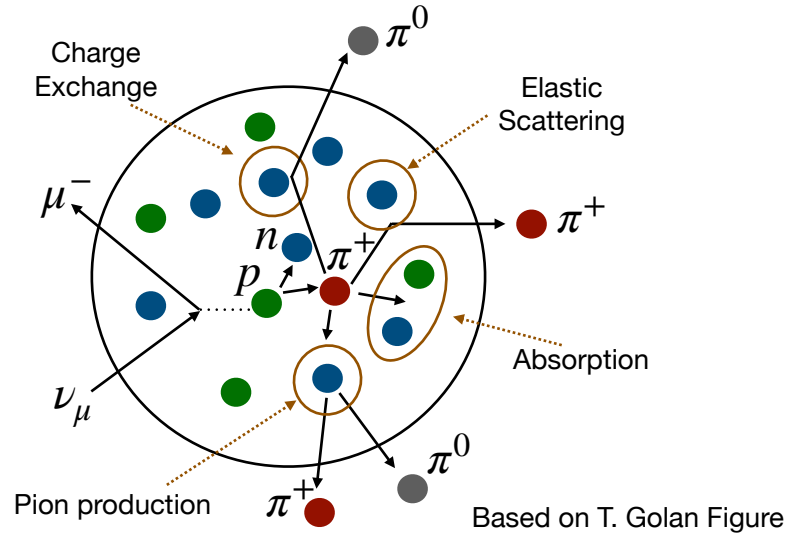
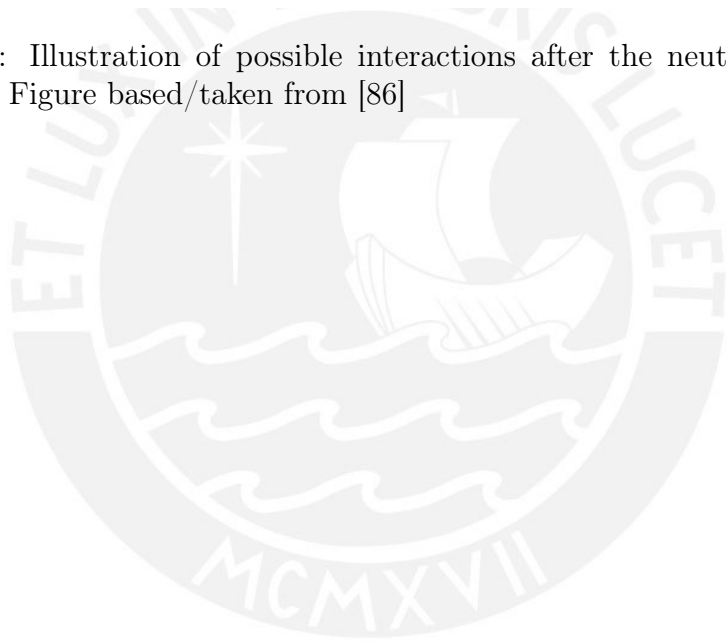
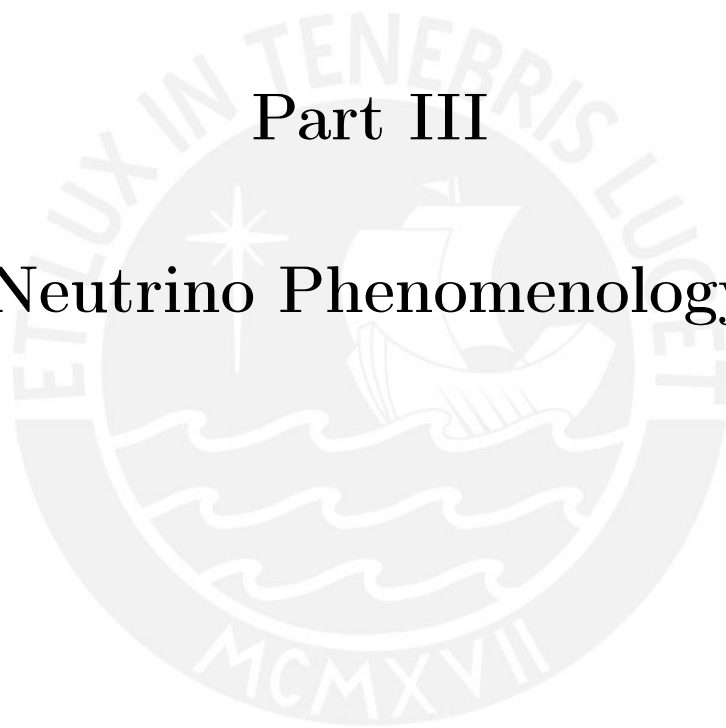


Figure 1.15: Illustration of possible interactions after the neutrino-nucleon interaction. Figure based/taken from [86]



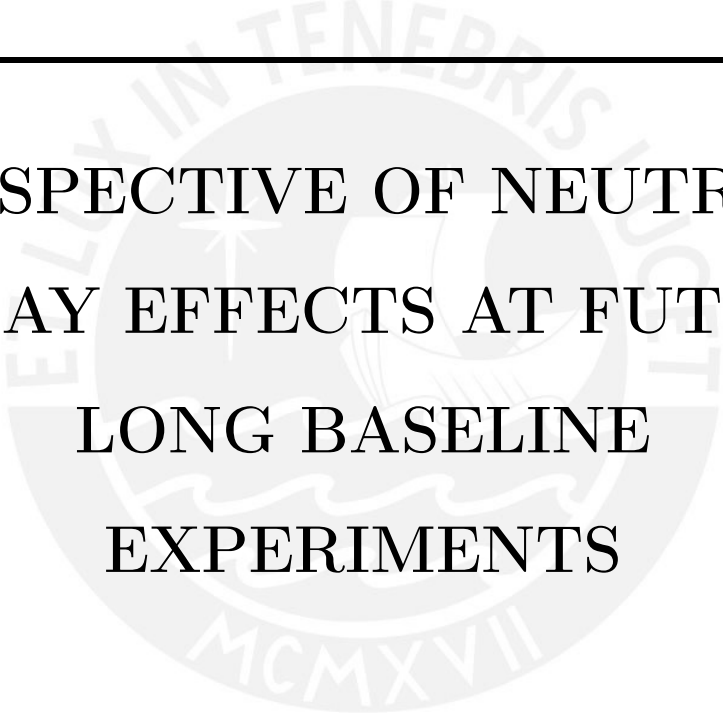
Part III

Neutrino Phenomenology



CHAPTER 2

PERSPECTIVE OF NEUTRINO DECAY EFFECTS AT FUTURE LONG BASELINE EXPERIMENTS



With its experimental confirmation, the neutrino oscillation phenomenon is a warning that new physics beyond the Standard Model is needed, as shown in the introductory chapter. A deep understanding of that phenomenon could give knowledge moreover concerning a bigger picture of Nature. In this case, in this precision era, the experimental results could ultimately differ from the standard neutrino oscillation paradigm. Numerous studies have been conducted over the years, such as the decoherence effect and non-standard interactions in neutrino oscillation [110, 111, 112, 113, 114, 115, 116, 117, 118,

119, 120, 121, 122, 123, 124, 125, 126, 127, 128, 129, 130], regardless of the standard paradigm deviation. Another approach to producing changes in the experimental results, perhaps hidden behind the neutrino oscillation, is the light neutrino decay. In this part, we will study that effect in the context of two future long-baseline experiments focusing on the impact of the matter on visible and invisible light neutrino decays¹. The experiments are Deep Underground Neutrino Experiment (DUNE) and a hypothetical beam pointed towards Agua Negra Deep Experiment Site (ANDES).

2.1 Neutrino Decay

The earliest work about neutrino decay was given in the context of the solar neutrino problem [132], and the introduction of the Majoron like the Goldstone boson in the spontaneous breaking of lepton number symmetry [133, 134, 135, 136]. The approach within the neutrino oscillation context are described in [137, 138, 139, 140, 141, 142, 143, 144]. The model of neutrino decay considers two types Majorana neutrino interaction with Majoron by Yukawa-type couplings,

$$\mathcal{L}_{\text{int}} = \left(\frac{(g_s)_{ij}}{2} \bar{\nu}_i \nu_j + i \frac{(g_p)_{ij}}{2} \bar{\nu}_i \gamma_5 \nu_j \right) J, \quad (2.1)$$

these couplings are scalar and pseudoscalar, the ν_i are the Majorana neutrinos and J is the Majoron (see an illustration in Figure 2.1). The neutrino decay process can be split into two types; the **invisible decay** (ID), which refers to the decay product, can not be detected. The second type is the **visible decay** (VD), where the decay products are detectable particles. We refer to **full decay** (FD) to the sum of ID and VD.

¹Based on work made in [131].

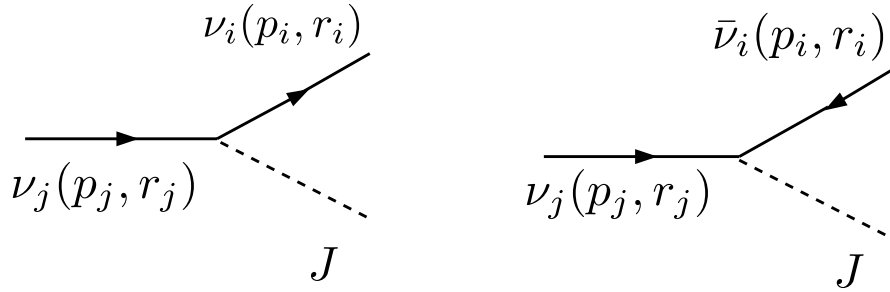


Figure 2.1: Diagrams of neutrino decay for pseudoscalar and scalar coupling. The p_k is the 4-momentum and r_k the spin, which can be $(+, -)$.

The square amplitude of the neutrino decay ($\nu_j \rightarrow \nu_i + J$) with four-momentum and spin (p_j, r_j) is [144]:

$$\begin{aligned}
 |\mathcal{M}|^2 &= \frac{g_s^2}{4m_i m_j} [(p_i \cdot p_j + m_i m_j)(1 - r_i \cdot r_j) + (p_i \cdot r_j)(p_j \cdot r_i)] \\
 &\quad + \frac{g_p^2}{4m_i m_j} [(p_i \cdot p_j - m_i m_j)(1 + r_i \cdot r_j) - (p_i \cdot r_j)(p_j \cdot r_i)] \quad (2.2)
 \end{aligned}$$

Equation 2.2 can be separated in pure helicity change components and it is given by [144, 142],

$$|\mathcal{M}(\nu_j \rightarrow \nu_i)|^2 = \frac{g_s^2}{4}(A + 2) + \frac{g_p^2}{4}(A - 2), \quad (2.3)$$

$$|\mathcal{M}(\nu_j \rightarrow \bar{\nu}_i)|^2 = \frac{g_s^2 + g_p^2}{4} \left(\frac{1}{x} + x - A \right) \quad (2.4)$$

where $x = m_j/m_i$, $x > 1$ with $m_j > m_i$,

$$A = \frac{E_j}{xE_i} + x \frac{E_i}{E_j}, \quad (2.5)$$

$r_j = s_L$, $r_i = \pm r_L$, and $r_L^\mu = (c/mv)p^\mu - (\sqrt{c^2 - v^2}/v)g^{\mu 0}$ [144].

With Equations 2.3 and 2.4, the decay rates of a neutrino with energy E are [144, 142, 145],

$$\Gamma(\nu_j \rightarrow \nu_i J) = \frac{m_j^2}{16\pi x E_j} \left[g_s^2 \left(k_+(x) + f_+(x) \right) + g_p^2 \left(k_+(x) + f_-(x) \right) \right], \quad (2.6)$$

$$\Gamma(\nu_j \rightarrow \bar{\nu}_i J) = \frac{m_j^2}{16\pi x E_j} \left(g_s^2 + g_p^2 \right) k_-(x), \quad (2.7)$$

where

$$k_{\pm}(x) = \frac{x}{2} \pm \frac{2}{x} \log x - \frac{1}{2x^3}, \quad (2.8)$$

$$f_{\pm}(x) = \pm \left(2 - \frac{2}{x^2} \right), \quad (2.9)$$

the differential decay width is [145]:

$$\frac{d}{dE_i} \Gamma(\nu_j \rightarrow \nu_i) = \frac{m_i m_j}{4\pi E_j^2} \left(\sqrt{1 - \frac{m_j^2}{E_j^2}} \right)^{-1} |\mathcal{M}(\nu_j \rightarrow \nu_i)|^2 \Theta(E_j, E_i), \quad (2.10)$$

where $\Theta(E_j, E_i) = \Theta_H(E_j - E_i) \Theta_H(x^2 E_i - E_j)$, Θ_H is the Heaviside function. Similar procedure can be followed for $\frac{d}{dE_i} \Gamma(\nu_j \rightarrow \bar{\nu}_i)$. Let's now define the decay parameter as:

$$\alpha_{ij} = E_j (\Gamma(\nu_j \rightarrow \nu_i J) + \Gamma(\nu_j \rightarrow \bar{\nu}_i J)), \quad (2.11)$$

in such a way that,

$$\alpha_i = E_j \Gamma_j \quad (2.12)$$

$$= \sum_j \alpha_{ij}. \quad (2.13)$$

Before introducing the decay width in the oscillation probabilities. We must remember that the Hamiltonian in the matter is not diagonal, as we saw in Equation 1.25, now further adding the decay parameter. The resulting Hamiltonian is:

$$H = \frac{1}{2E} U_0 \begin{pmatrix} m_1^2 & & \\ & m_2^2 - i\alpha_2 & \\ & & m_3^2 - i\alpha_3 \end{pmatrix} U_0^\dagger + \begin{pmatrix} \sqrt{2} G_F N_e & & \\ & 0 & \\ & & 0 \end{pmatrix}, \quad (2.14)$$

in this case the normal ordering is considered with the lightest neutrino stable. As we saw in the previous chapter, the Hamiltonian must be diagonalized [67, 68], since it is not diagonal in either the flavor base or the mass base. Because of that we must introduce a new basis in which the Hamiltonian of Equation 2.14 is diagonal, and it is refer here like **matter** basis. The diagonalization is made by non-unitary matrices defines as $\tilde{U}_{\alpha I}$ with $I = \tilde{1}, \tilde{2}, \tilde{3}$, thus the diagonalized Hamiltonian is:

$$\tilde{U}^{-1} H \tilde{U} = H^{\text{diag}} \quad (2.15)$$

where the complex eigenvalues of the new Hamiltonian is:

$$\tilde{m}_I^2 - i\tilde{\alpha}_I = 2E(H^{\text{diag}})_{II}. \quad (2.16)$$

The next step is to evolve the Hamiltonian 2.14 and obtain the probability, where a neutrino $\nu_{\alpha}^{(r)}$ is subjected to oscillation and decay to a neutrino $\nu_{\beta}^{(s)}$, where r and s in this case represent the helicity². The function which accounts for that is calculated [146, 142, 145] by

$$P_{\text{dec}} \left(\nu_{\alpha}^{(r)} \rightarrow \nu_{\beta}^{(s)} \right) = \left| \sum_{I=1}^3 \left(\tilde{U}^{(r)} \right)_{I\alpha}^{-1} e^{\left[-i \frac{\tilde{m}_I^2 L}{2E_{\alpha}} \right]} e^{\left[-\frac{\tilde{\alpha}_I L}{2E_{\alpha}} \right]} \tilde{U}_{\beta I}^{(s)} \right|^2 \delta_{rs} \delta(E_{\alpha} - E_{\beta}) + P_{\text{vis}}(E_{\alpha}, E_{\beta}), \quad (2.17)$$

where the first term represents the oscillation and ID. The terms δ_{rs} and $\delta(E_{\alpha} - E_{\beta})$ are included because they describe the neutrinos that have not decayed. The second part of Equation 2.17 refers to the VD part in which the neutrino can have different energy and helicity.

In order to describe the $P_{\text{vis}}(E_{\alpha}, E_{\beta})$ of Equation 2.17, let's define matrices which can allow us to connect the matter basis with mass basis as follow:

$$\tilde{C}_{Ij}^{(r)} = \sum_{\rho=e,\mu,\tau} \tilde{U}_{\rho I}^{(r)} (U_0)_{\rho j}^{(r)*} \quad (2.18)$$

$$\hat{C}_{Ij}^{(s)} = \sum_{\rho=e,\mu,\tau} \hat{U}_{\rho I}^{(s)} (U_0)_{\rho j}^{(s)*} \quad (2.19)$$

²By helicity, we refer to ν or $\bar{\nu}$ state.

where \tilde{U} relates the flavor/interaction basis (α, β) to matter basis (I, J) before the decay. Therefore \tilde{C} relates matter basis with mass basis. We use \hat{U} to refer the rotation after the decay. Considering Equations 2.18 and 2.19 we can determine the visible component [142] by

$$\begin{aligned}
 P_{\text{vis}}(E_\alpha, E_\beta) &= \int d\ell \left| \sum_{I=\hat{1}}^{\hat{3}} \left(\tilde{U}^{(r)} \right)_{I\alpha}^{-1} \exp \left[-i \frac{\tilde{m}_I^2 \ell}{2E_\alpha} \right] \exp \left[-\frac{\tilde{\alpha}_I \ell}{2E_\alpha} \right] \sum_{i=2}^3 \sum_{j=1}^{i-1} \tilde{C}_{Ii}^{(r)} \right. \\
 &\quad \times \sqrt{\frac{d}{dE_\beta} \Gamma_{\nu_i^r \rightarrow \nu_j^s}(E_\alpha)} \sum_{J=\hat{1}}^{\hat{3}} \left(\hat{C}^{(s)} \right)_{jJ}^{-1} \exp \left[-i \frac{\hat{m}_J^2 (L - \ell)}{2E_\beta} \right] \\
 &\quad \left. \times \exp \left[-\frac{\hat{\alpha}_J (L - \ell)}{2E_\beta} \right] \hat{U}_{\beta J}^{(s)} \right|^2, \tag{2.20}
 \end{aligned}$$

Which can be interpreted as the neutrino from the flux is in the interaction eigenstate (ν_α^r) . However, the propagation occurs in the matter eigenstate, which requires rotating with \tilde{U}^{-1} . After propagation of distance ℓ , the neutrino in matter eigenstate $(\nu_I^{(r)})$ decays. Nevertheless, the decay occurs in the mass eigenstate in vacuum, and using Equation 2.18 we can rotate $\nu_i^{(r)}$. After the decay, the neutrino must propagate an $(l - \ell)$ distance, and to do that, Equation 2.19 is used to rotate back to the matter eigenstate. Finally, to detect the neutrino $(\nu_\beta^{(s)})$, we rotate with \hat{U} .

Equation 2.20 can be rewritten considering a constant N_e , defining $\alpha_{<IJ>} = \alpha_I + \alpha_J$, using Equation 2.10, taking into account one decay channel

like ($\nu_3^r \rightarrow \nu_1^s J$) and one non-vanishing coupling [142, 145]

$$\begin{aligned}
 & P_{\text{vis}}(E_\alpha, E_\beta) \\
 &= 2 \sum_{I=1}^3 \sum_{J=1}^3 \sum_{M=1}^3 \sum_{N=1}^3 \left(\tilde{U}^{(r)} \right)_{I\alpha}^{-1} \left(\tilde{U}^{(r)} \right)_{M\alpha}^{-1*} \hat{U}_{\beta J}^{(s)} \hat{U}_{\beta N}^{(s)*} \\
 & \times \frac{[(E_\beta/E_\alpha)\tilde{\alpha}_{<IM>} - \hat{\alpha}_{<JN>}] - i[(E_\beta/E_\alpha)\Delta\tilde{m}_{IM}^2 - \Delta\hat{m}_{JN}^2]}{[(E_\beta/E_\alpha)\tilde{\alpha}_{<IM>} - \hat{\alpha}_{<JN>}]^2 + [(E_\beta/E_\alpha)\Delta\tilde{m}_{IM}^2 - \Delta\hat{m}_{JN}^2]^2} \\
 & \times \left\{ \exp\left[-i\frac{\Delta\hat{m}_{JN}^2 L}{2E_\beta}\right] \exp\left[-\frac{\hat{\alpha}_{<JN>L}}{2E_\beta}\right] \right. \\
 & \left. - \exp\left[-i\frac{\Delta\tilde{m}_{IM}^2 L}{2E_\alpha}\right] \exp\left[-\frac{\tilde{\alpha}_{<IM>L}}{2E_\alpha}\right] \right\} \\
 & \times \tilde{C}_{I3}^{(r)} \tilde{C}_{M3}^{(r)*} \left(\hat{C}^{(s)} \right)_{1J}^{-1} \left(\hat{C}^{(s)} \right)_{1N}^{-1*} \\
 & \times \left(\frac{(E_\beta/E_\alpha)\alpha_3}{E_\alpha} \right) \left(1 - \frac{m_3^2}{E_\alpha^2} \right)^{-1/2} F_g'^{rs}(E_\alpha, E_\beta)
 \end{aligned} \tag{2.21}$$

where α_3 is mass basis in vacuum which represents the neutrino-Majoron coupling, $x = x_{ji} = x_{31}$, $g = \{g_s, g_p\}$, and

$$F_g'^{rs}(E_\alpha, E_\beta) = \frac{x_{31}^2}{(x_{31}^2 - 1)} F_g^{rs}(E_\alpha, E_\beta) \Theta_H(E_\alpha - E_\beta) \Theta_H(x_{31}^2 E_\beta - E_\alpha), \tag{2.22}$$

where,

$$\begin{aligned}
 F_{g_s}^{\pm\pm}(E_\alpha, E_\beta) &= \frac{1}{E_\alpha E_\beta} \frac{(E_\alpha + x_{ji} E_\beta)^2}{(x_{ji} + 1)^2} \\
 F_{g_s}^{\pm\mp}(E_\alpha, E_\beta) &= \frac{(E_\alpha - E_\beta)(x_{ji}^2 E_\beta - E_\alpha)}{E_\alpha E_\beta (x_{ji} + 1)^2}
 \end{aligned} \tag{2.23}$$

$$\begin{aligned}
 F_{g_p}^{\pm\pm}(E_\alpha, E_\beta) &= \frac{1}{E_\alpha E_\beta} \frac{(E_\alpha - x_{ji} E_\beta)^2}{(x_{ji} - 1)^2} \\
 F_{g_p}^{\pm\mp}(E_\alpha, E_\beta) &= \frac{(E_\alpha - E_\beta)(x_{ji}^2 E_\beta - E_\alpha)}{E_\alpha E_\beta (x_{ji} - 1)^2}.
 \end{aligned} \tag{2.24}$$

There is indistinguishable effect of scalar and pseudoscalar when the ν_1 mass ($m_{\text{lightest}} = 0$, $x_{31} \rightarrow \infty$) as it is shown in the Figure 2.2, see the purple line [145]. The largest value allowed by cosmology for the ν_1 mass is ($m_{\text{lightest}} = 0.07$ eV, $x_{31} \rightarrow 1$) [147].

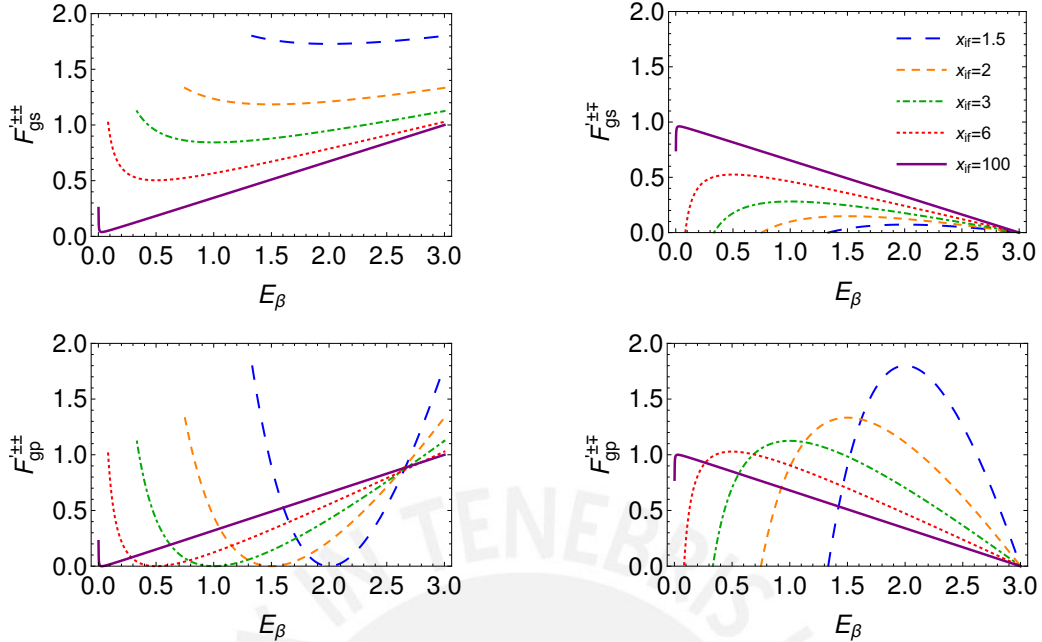


Figure 2.2: Visible decay function from equation 2.22, E_{β} is the final energy and $E_{\alpha} = 3$ GeV (DUNE’s average energy) the initial energy. Top (bottom) is scalar (pseudoscalar) coupling and left (right) is chirality conserving (changing) processes. Figure taken from [145].

2.2 Matter effect with neutrino decay in DUNE and ANDES

Deep Underground Neutrino Experiment (DUNE)

DUNE is a Long-Baseline next-generation neutrino oscillation experiment [148] (see Figure 2.3). The near detector (ND) will be located at the Long-Baseline Neutrino Facility (LBNF) at Fermilab, 574 m from the neutrino source. The far detector (FD) will be sited 1300 km far from ND at Sanford Underground Research Facility (SURF). The neutrinos will be produced at the Main Injector by hitting a primary proton of 1.07 MW to a target (first-year [149]), then passing through the Earth with an average matter density of $\rho_{DUNE} = 2.96\text{g/cm}^3$. The different setups of technology will perform near and far detectors. The ND will consist of several components like a highly modular LArTPC, a magnetized gaseous argon time projection chamber (TPC), and a magnetized beam monitor [150] (see Figure 2.4). The FD will use a massive modular liquid argon time projection chamber (LArTPC) of 70 kt and a fiducial mass of

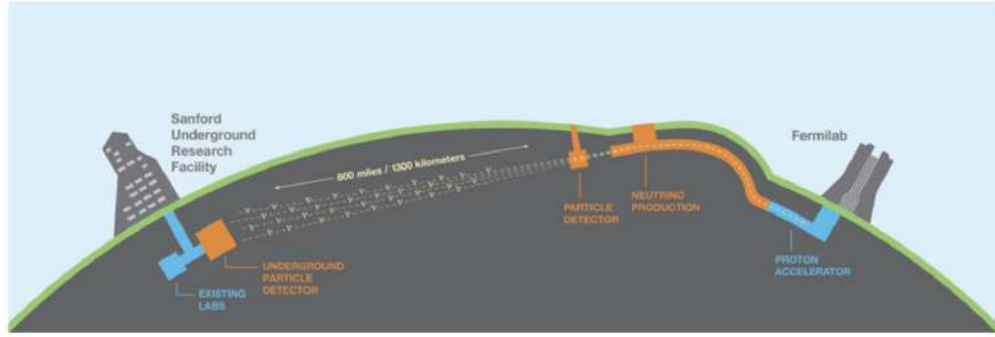


Figure 2.3: Scheme of DUNE experiment. Figure taken form [152].

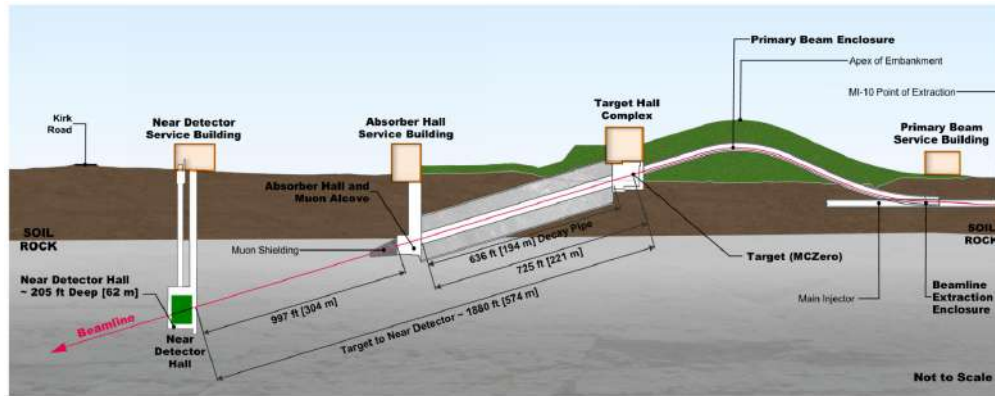


Figure 2.4: Scheme of LBNF. Figure taken form [152].

approximately 40 kt [151] (see Figure 2.5).

The main goals of DUNE are: The study of the preponderance of matter over antimatter in the early universe (by measuring the CP violation phase δ_{CP} and determining the neutrino mass ordering, resolving the octant for the atmospheric mixing angle as shown in equation 1.10), the dynamics of the supernova neutrino bursts (SNBs) that produced the heavy elements needed to exist life (by measuring the ν_e flux from a core-collapse supernova within our galaxy), and proton decay [152].

To study the effect of neutrino decay, we use the simulation provided by [153], where there are both flux modes, Forward Horn Current (FHC) and Reverse Horn Current (RHC), the proton on target (1.47×10^{21} POT) per year, for 3.5 years on neutrino and 3.5 for antineutrino run, and the cross-sections

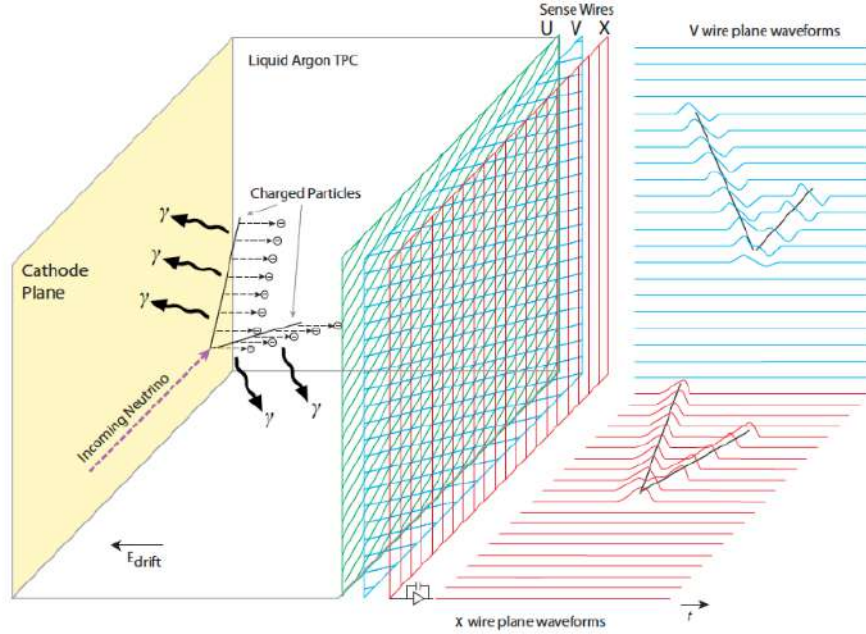


Figure 2.5: Scheme of LarTPC proposed for FD of DUNE. Figure taken from [152].

for Charge Current (CC) and Neutral Current (NC).

Agua Negra Deep Experiment Site (ANDES)

ANDES is a proposed underground facility in the Southern Hemisphere [154]. It will be located in the deepest part (~ 1750 m) of the road tunnel (14 km long) in the Andes, between San Juan, Argentina, and Coquimbo, Chile. ANDES's goal is broad, including dark matter, geophysics, neutrino, biology, and others [155].

In the context of the present study, we assume a hypothetical neutrino beam originating from Fermilab. The flux used is the one provided by the DUNE collaboration. The baseline (Fermilab to ANDES) and matter density (computed using profile [157]) were properly adjusted to 7650 km and $\rho_{ANDES} = 4.7\text{g/cm}^3$ respectively. The constant matter density for DUNE and ANDES as a function of Radius is shown in Figure 2.6.

To see the impact of matter effect with neutrino decay we will use the

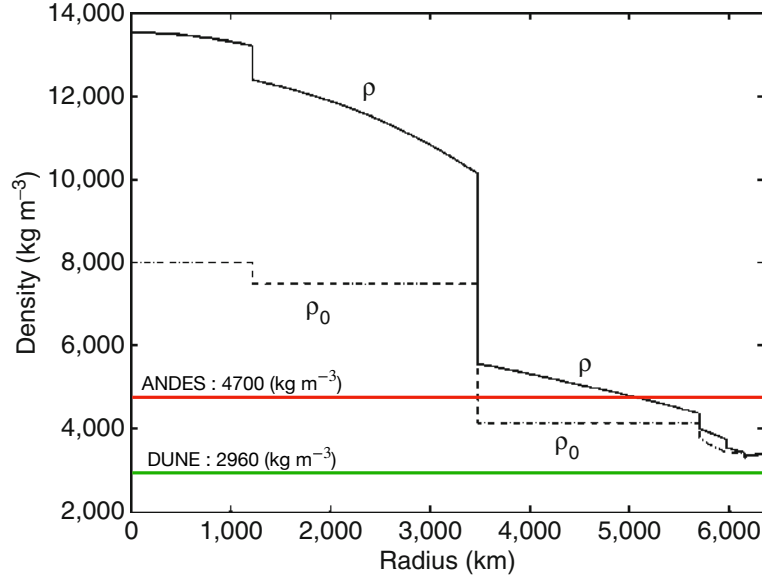


Figure 2.6: Density profile of the Earth based on PREM (continuous line) and the profile of $\rho_{0,0}$ (dashed line) [156].

flux and cross-section ($\Phi \times \sigma$). The cross-section correspond to charge-current for a neutrino with flavor β and helicity s as follows:

$$(\Phi \times \sigma)_\beta \equiv \sum_s \sigma_\beta^{s, CC}(E_\beta) \frac{d\Phi_\beta^{(s)}}{dE_\beta}, \quad (2.25)$$

where

$$\frac{d\Phi_\beta^{(s)}}{dE_\beta} = \int P_{\text{dec}}(\nu_\alpha^{(r)} \rightarrow \nu_\beta^{(s)}) \frac{d\Phi_\alpha^{(r)}}{dE_\alpha} dE_\alpha. \quad (2.26)$$

In order to properly study the impact of the neutrino decay, let's define the following channels: ν_e appearance for FHC Flux, $\bar{\nu}_e$ appearance for RHC Flux, ν_μ disappearance for FHC Flux, and $\bar{\nu}_\mu$ disappearance for RHC Flux. The channels will be introduced as rule in the Abstract Experiment Definition Language (AEDL) needed in the GloBES package. The channels are defined in the Table 2.1 and Table 2.2.

Once the channels have been defined, the next step is to define the oscillation parameters of the PMNS matrix. For this, we will follow the [158],

2.2. MATTER EFFECT WITH NEUTRINO DECAY IN DUNE AND ANDES

where $\sin^2 \theta_{12} = 0.306$, $\sin^2 \theta_{13} = 0.02166$, $\sin^2 \theta_{23} = 0.441$ $\Delta m_{21}^2 = 7.5 \times 10^{-5}$ eV², $\Delta m_{31}^2 = 2.524 \times 10^{-3}$ eV², for normal ordering, and $\delta_{\text{CP}} = -\pi/2$.

We will split the effects of neutrino decay when neutrino m_{lightest} is vanishing (Case I), that is $x_{31} \rightarrow \infty$, and as we shown previously, in that case, we do not have coupling dependence (see Figure 2.2). The other two-part is pseudoscalar (Case II) and scalar (Case III) couplings, both with neutrino $m_{\text{lightest}} = 0.07$ eV, that is, $x_{31} \rightarrow 1$.

	ν_e appearance, FHC Flux	$\bar{\nu}_e$ appearance, RHC Flux
Signal		
CC:	$(\nu_\mu \rightarrow \nu_e)_{ID} + (\nu_\mu \rightarrow \nu_e)_{VD}$ $+ (\bar{\nu}_\mu \rightarrow \nu_e)_{VD}$	$(\nu_\mu \rightarrow \nu_e)_{ID} + (\bar{\nu}_\mu \rightarrow \nu_e)_{VD}$ $+ (\nu_\mu \rightarrow \nu_e)_{VD}$
CC:	$(\bar{\nu}_\mu \rightarrow \bar{\nu}_e)_{ID} + (\nu_\mu \rightarrow \bar{\nu}_e)_{VD}$ $+ (\bar{\nu}_\mu \rightarrow \bar{\nu}_e)_{VD}$	$(\bar{\nu}_\mu \rightarrow \bar{\nu}_e)_{ID} + (\bar{\nu}_\mu \rightarrow \bar{\nu}_e)_{VD}$ $+ (\nu_\mu \rightarrow \bar{\nu}_e)_{VD}$
Background		
CC:	$(\nu_e \rightarrow \nu_e)_{ID}$	$(\nu_e \rightarrow \nu_e)_{ID}$
CC:	$(\bar{\nu}_e \rightarrow \bar{\nu}_e)_{ID}$	$(\bar{\nu}_e \rightarrow \bar{\nu}_e)_{ID}$
CC:	$(\nu_\mu \rightarrow \nu_\mu)_{ID} + (\nu_\mu \rightarrow \nu_\mu)_{VD}$	$(\nu_\mu \rightarrow \nu_\mu)_{ID} + (\bar{\nu}_\mu \rightarrow \nu_\mu)_{VD}$
CC:	$(\nu_\mu \rightarrow \nu_\tau)_{ID} + (\nu_\mu \rightarrow \nu_\tau)_{VD}$	$(\nu_\mu \rightarrow \nu_\tau)_{ID} + (\bar{\nu}_\mu \rightarrow \nu_\tau)_{VD}$
CC:	$(\bar{\nu}_\mu \rightarrow \bar{\nu}_\tau)_{ID} + (\nu_\mu \rightarrow \bar{\nu}_\tau)_{VD}$	$(\bar{\nu}_\mu \rightarrow \bar{\nu}_\tau)_{ID} + (\bar{\nu}_\mu \rightarrow \bar{\nu}_\tau)_{VD}$
NC:	$(\nu_\mu \rightarrow \nu_\alpha)_{ID} + (\nu_\mu \rightarrow \nu_\alpha)_{VD}$	$(\nu_\mu \rightarrow \nu_\alpha)_{ID} + (\bar{\nu}_\mu \rightarrow \nu_\alpha)_{VD}$
NC:	$(\bar{\nu}_\mu \rightarrow \bar{\nu}_\alpha)_{ID} + (\nu_\mu \rightarrow \bar{\nu}_\alpha)_{VD}$	$(\bar{\nu}_\mu \rightarrow \bar{\nu}_\alpha)_{ID} + (\bar{\nu}_\mu \rightarrow \bar{\nu}_\alpha)_{VD}$

Table 2.1: ν_e appearance AEDL rules for FHC flux and $\bar{\nu}_e$ appearance rules for RHC flux.

	ν_μ disappearance, FHC Flux	$\bar{\nu}_\mu$ disappearance, RHC Flux
Signal		
CC:	$(\nu_\mu \rightarrow \nu_\mu)_{ID} + (\nu_\mu \rightarrow \nu_\mu)_{VD}$	$(\nu_\mu \rightarrow \nu_\mu)_{ID} + (\bar{\nu}_\mu \rightarrow \nu_\mu)_{VD}$
CC:	$(\bar{\nu}_\mu \rightarrow \bar{\nu}_\mu)_{ID} + (\nu_\mu \rightarrow \bar{\nu}_\mu)_{VD}$	$(\bar{\nu}_\mu \rightarrow \bar{\nu}_\mu)_{ID} + (\bar{\nu}_\mu \rightarrow \bar{\nu}_\mu)_{VD}$
Background		
CC:	$(\nu_\mu \rightarrow \nu_\tau)_{ID} + (\nu_\mu \rightarrow \nu_\tau)_{VD}$	$(\nu_\mu \rightarrow \nu_\tau)_{ID} + (\bar{\nu}_\mu \rightarrow \nu_\tau)_{VD}$
CC:	$(\bar{\nu}_\mu \rightarrow \bar{\nu}_\tau)_{ID} + (\nu_\mu \rightarrow \bar{\nu}_\tau)_{VD}$	$(\bar{\nu}_\mu \rightarrow \bar{\nu}_\tau)_{ID} + (\bar{\nu}_\mu \rightarrow \bar{\nu}_\tau)_{VD}$
NC:	$(\nu_\mu \rightarrow \nu_\alpha)_{ID} + (\nu_\mu \rightarrow \nu_\alpha)_{VD}$	$(\nu_\mu \rightarrow \nu_\alpha)_{ID} + (\bar{\nu}_\mu \rightarrow \nu_\alpha)_{VD}$
NC:	$(\bar{\nu}_\mu \rightarrow \bar{\nu}_\alpha)_{ID} + (\nu_\mu \rightarrow \bar{\nu}_\alpha)_{VD}$	$(\bar{\nu}_\mu \rightarrow \bar{\nu}_\alpha)_{ID} + (\bar{\nu}_\mu \rightarrow \bar{\nu}_\alpha)_{VD}$

Table 2.2: ν_μ disappearance AEDL rules for FHC flux and $\bar{\nu}_\mu$ disappearance rules for RHC flux.

In DUNE , we will use the decay parameter $\alpha_3 = 4 \times 10^{-5} \text{ eV}^2$, which corresponds to approximately 10% of $\langle E_\alpha \rangle / L$, and for ANDES, $\alpha_3 = 8 \times 10^{-6} \text{ eV}^2$, which reaches $\sim 10\%$ of $\langle E_\alpha \rangle / L$. The following cases are presented: DUNE on the left and ANDES on the right, with VD and ID separate, the ID contents also the standard oscillation (SO) hypothesis. All three cases show the difference between decay+matter and decay+vacuum effect.

Case I: $x_{31} \rightarrow \infty$

As we saw before, for this particular case the coupling are irrelevant, so we will show just as one case. They are presented for the FHC mode (Figure 2.7 and Figure 2.8), and then RHC (Figure 2.9 and Figure 2.10). As we pointed out, the main difference between DUNE and ANDES is the baseline and the matter density. The effect of those differences is shown in the comparison of left and right side plots of Figure 2.7 and Figure 2.8 and all other $(\Phi \times \sigma)$ figures.

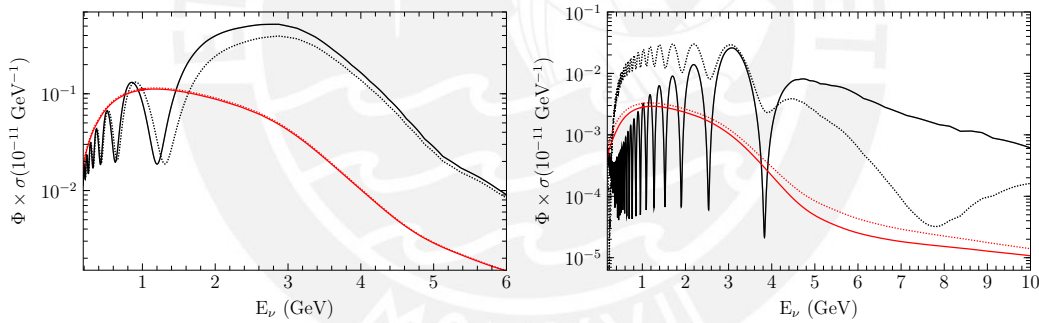


Figure 2.7: Matter (continuous line) and vacuum (dashed line) difference for ν_e appearance in **FHC** mode, with $m_{\text{lightest}} = 10^{-10} \text{ eV}$. Red lines are VD and black ID+SO. Left plot corresponds to DUNE and right plot to ANDES.

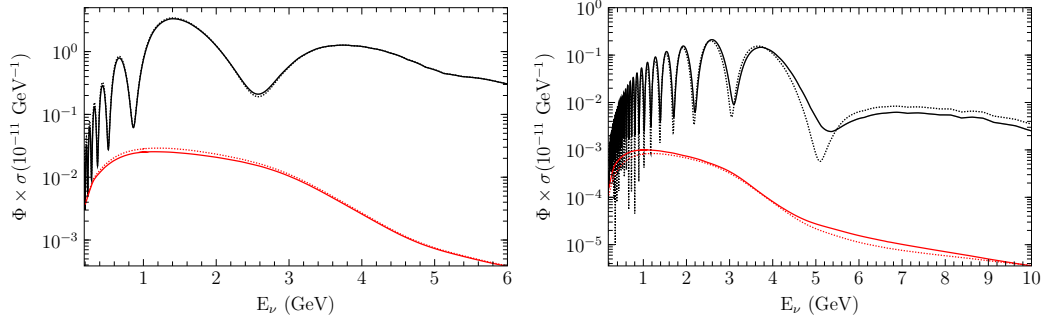


Figure 2.8: Matter (continuous line) and vacuum (dashed line) difference for ν_μ **disappearance** in **FHC** mode, with $m_{\text{lightest}} = 10^{-10}$ eV. Red lines are VD and black ID+SO. Left plot corresponds to DUNE and right plot to ANDES.

From the FHC plots, we can observe that the matter effect in the ID and VD can be neglected for the ν_μ disappearance channel (see DUNE plot). However, the ν_e appearance channel has a noticeable impact, the reason, first, the ID is following the SO, and second, as we saw in Equation 1.22 the CC matter potential affects almost only ν_e . That effect is prominent in the ANDES case due to large matter density (except in DUNE case, see Figure 2.9). Another observation is that, in all the cases, the magnitude of the VD contribution is low. But, the difference between VD-ID differs for FHC and RHC (Figure 2.9 and Figure 2.10).

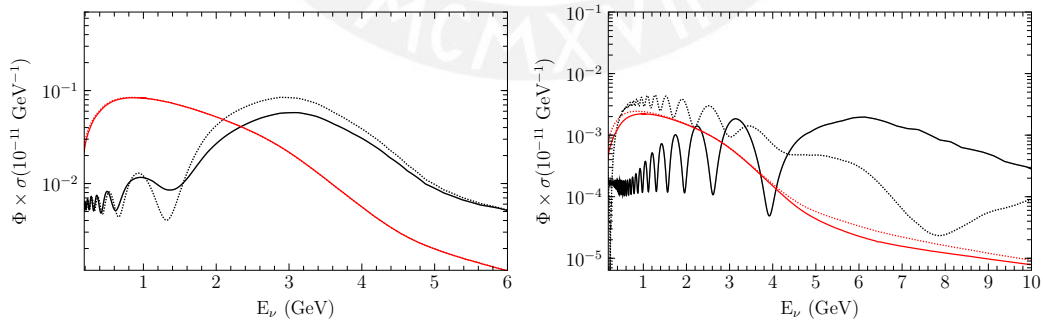


Figure 2.9: Matter (continuous line) and vacuum (dashed line) difference for ν_e **appearance** in **RHC** mode, with $m_{\text{lightest}} = 10^{-10}$ eV. Red lines are VD and black ID+SO. Left plot corresponds to DUNE and right plot to ANDES.

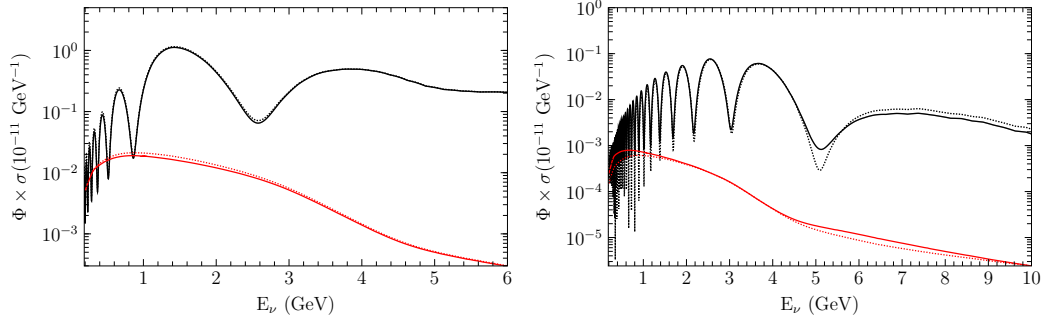


Figure 2.10: Matter (continuous line) and vacuum (dashed line) difference for ν_μ **disappearance** in **RHC** mode, with $m_{\text{lightest}} = 10^{-10}$ eV. Red lines are VD and black ID+SO. Left plot corresponds to DUNE and right plot to ANDES.

We can understand the small VD-ID in RHC focusing on the helicity changing channel. In the FHC case, part of the incoming neutrino changes the helicity to antineutrino. In opposition, RHC has a portion of antineutrinos, which will transform into neutrinos. Since particles have a bigger cross-section than antiparticles, the VD-ID differences for RHC become small.

Case II: Pseudoscalar coupling for $x_{31} \rightarrow 1$

The plots are described as FHC (Figure 2.11 and 2.12) and RHC (Figure 2.13 and 2.14) for DUNE and ANDES. The ID keeps the same for this and scalar cases (new subsection) because the coupling affects only the VD part.

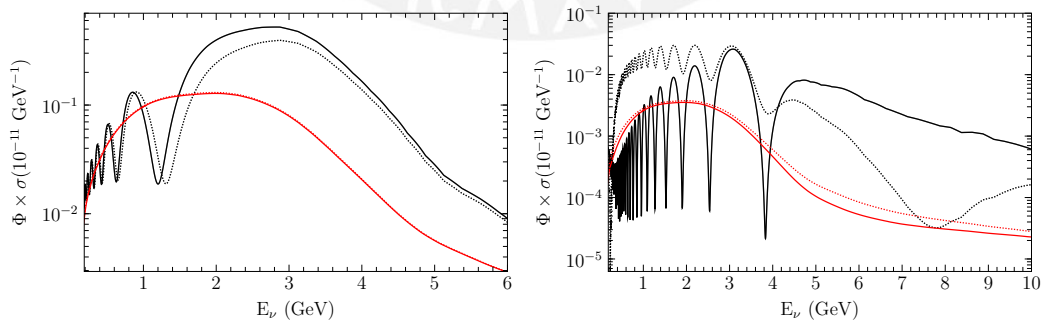


Figure 2.11: Matter (continuous line) and vacuum (dashed line) difference for ν_e **appearance** in **FHC** mode, with $m_{\text{lightest}} = 0.07$ eV, and **pseudoscalar** coupling. Red lines are VD and black ID+SO. Left plot corresponds to DUNE and right plot to ANDES.

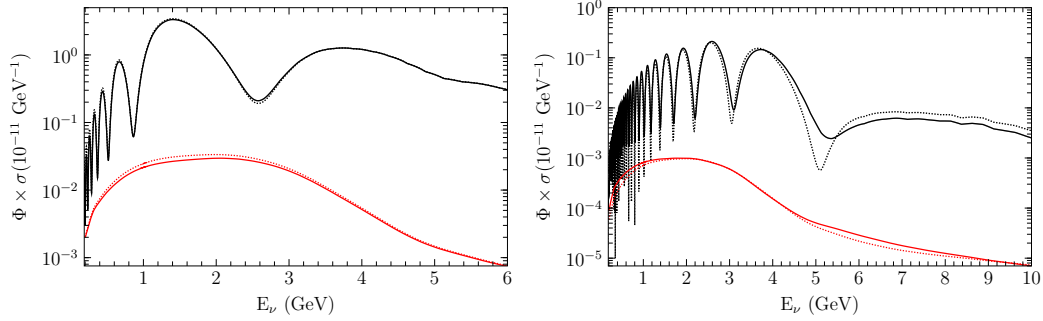


Figure 2.12: Matter (continuous line) and vacuum (dashed line) difference for ν_μ **disappearance** in **FHC** mode, with $m_{\text{lightest}} = 0.07$ eV, and **pseudoscalar** coupling. Red lines are VD and black ID+SO. Left plot corresponds to DUNE and right plot to ANDES.

We observed that the general effect is higher in low energy region. Compared with $(x_{31} \rightarrow \infty)$, the VD effect with large mass and pseudoscalar coupling is notable, with a slight enhancement.

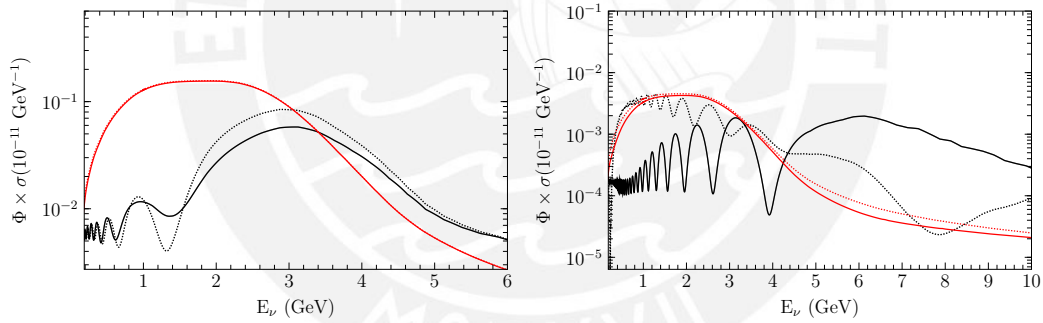


Figure 2.13: Matter (continuous line) and vacuum (dashed line) difference for ν_e **appearance** in **RHC** mode, with $m_{\text{lightest}} = 0.07$ eV, and **pseudoscalar** coupling. Red lines are VD and black ID+SO. Left plot corresponds to DUNE and right plot to ANDES.

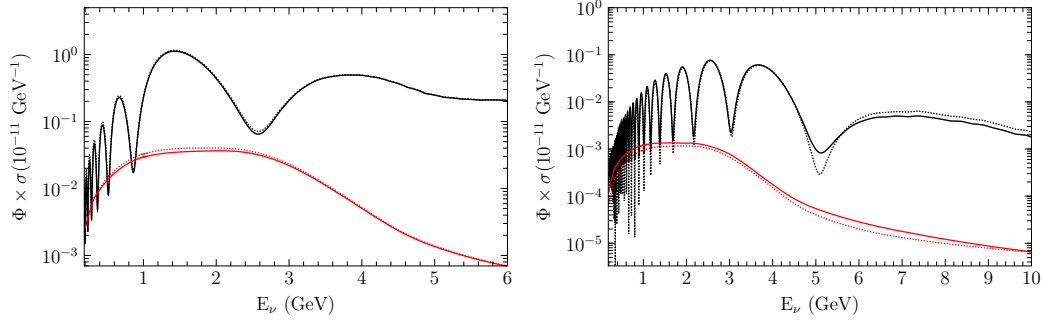


Figure 2.14: Matter (continuous line) and vacuum (dashed line) difference for ν_μ **disappearance** in **RHC** mode, with $m_{\text{lightest}} = 0.07$ eV, and **pseudoscalar** coupling. Red lines are VD and black ID+SO. Left plot corresponds to DUNE and right plot to ANDES.

Case III: Scalar coupling for $x_{31} \rightarrow 1$

Similar to previous two subsections, the cases are presented for the FHC mode (Figure 2.15 and Figure 2.16), and then RHC (Figure 2.17 and Figure 2.18). In this case, a reduction of the VD contribution is shown for RHC flux compared to Case I, but with an increase for the FHC flux of neutrinos. In all three cases, the most remarkable difference between matter and vacuum is shown in ANDES. Finally, there is a notorious difference at low energy (< 1 GeV) for the VD in ANDES (see Figure 2.15). A summary with all the comparisons of only the VD components is shown in Figure 2.19.

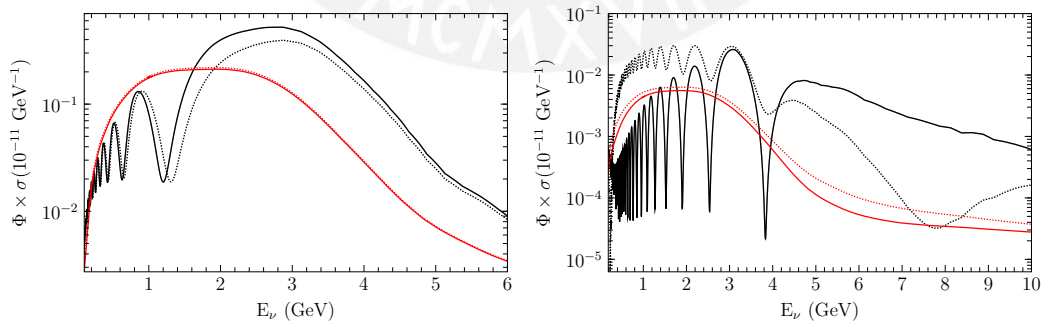


Figure 2.15: Matter (continuous line) and vacuum (dashed line) difference for ν_e **appearance** in **FHC** mode, with $m_{\text{lightest}} = 0.07$ eV, and **scalar** coupling. Red lines are VD and black ID+SO. Left plot corresponds to DUNE and right plot to ANDES.

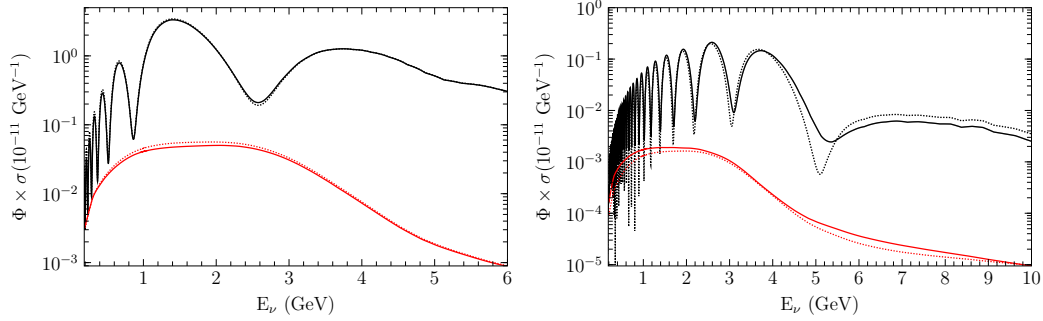


Figure 2.16: Matter (continuous line) and vacuum (dashed line) difference for ν_μ **disappearance** in **FHC** mode, with $m_{\text{lightest}} = 0.07$ eV, and **scalar** coupling. Red lines are VD and black ID+SO. Left plot corresponds to DUNE and right plot to ANDES.

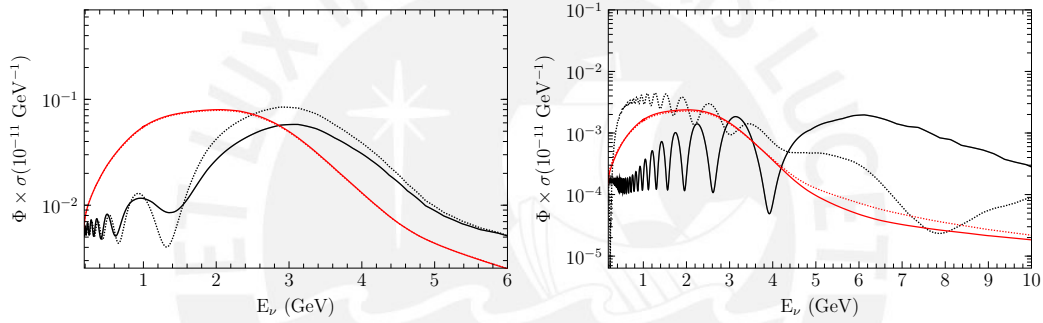


Figure 2.17: Matter (continuous line) and vacuum (dashed line) difference for ν_e **appearance** in **RHC** mode, with $m_{\text{lightest}} = 0.07$ eV, and **scalar** coupling. Red lines are VD and black ID+SO. Left plot corresponds to DUNE and right plot to ANDES.

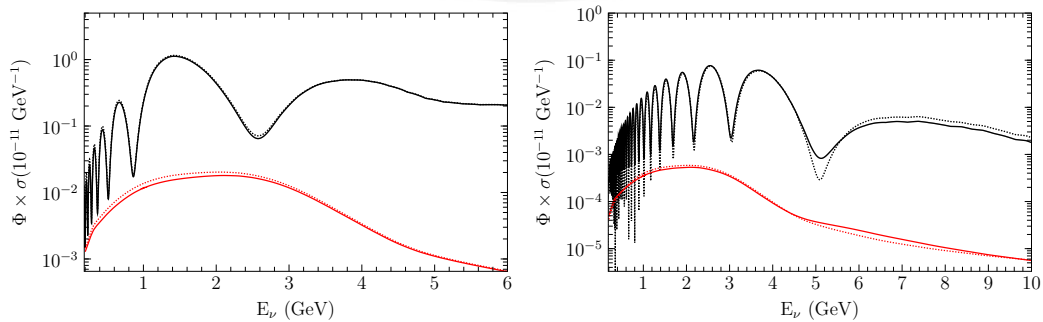


Figure 2.18: Matter (continuous line) and vacuum (dashed line) difference for ν_μ **disappearance** in **RHC** mode, with $m_{\text{lightest}} = 0.07$ eV, and **scalar** coupling. Red lines are VD and black ID+SO. Left plot corresponds to DUNE and right plot to ANDES.

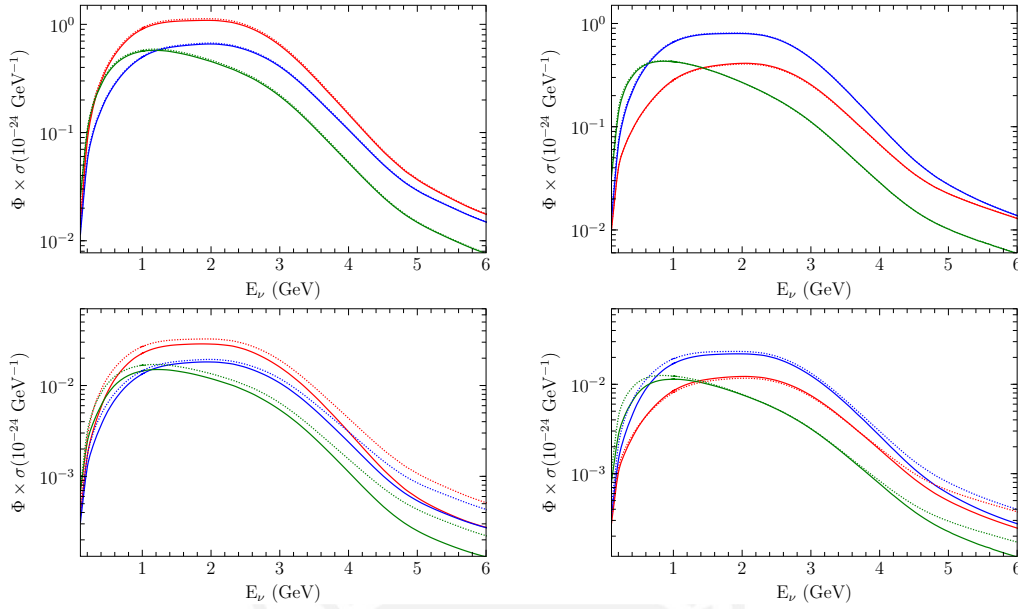


Figure 2.19: Visible decay only, red lines are scalar coupling, blues lines are pseudoscalar coupling, and green line is $(x_{31} \rightarrow \infty)$. Top plots are DUNE and bottom ANDES. Right plots are FHC and left RHC for matter (continues lines) and vacuum (dashed lines).

2.3 Sensitivity and parameter fits at DUNE

In this section we study the DUNE sensitivity to decay parameter α_3 . Similar studies were performed in [159] and [160]. In order to generate the channel, the General Long Baseline Experiment Simulator package (GLOBES) [161, 162] is used. The channel is defined in the AEDL as shown before.

Event generation

The number of event distributions are getting by convolution of cross-section, flux, and detector effect functions. For instance, for incoming neutrino $\nu_\beta^{(s)}$ the number of event in i bin and type of interaction $int = \{CC, NC\}$ is:

$$N_{i,\beta}^{(s),int} = \int dE_\beta K_i^{int}(E_\beta) \sigma_\beta^{s,int}(E_\beta) \frac{d\Phi_\beta^{(s)}}{dE_\beta}, \quad (2.27)$$

where

$$K_i^{int}(E_\beta) = \int_{E_{i,\min}}^{E_{i,\max}} dE_{\text{bin}} \epsilon_\beta^{int}(E_{\text{bin}}) R^{int}(E_{\text{bin}} - E_\beta), \quad (2.28)$$

which $K_i^{\text{int}}(E_\beta)$ takes into account the detector efficiency $\epsilon_\beta^{\text{int}}(E_{\text{bin}})$, and resolution function $R^{\text{int}}(E_{\text{bin}} - E_\beta)$. All the information used in this simulation are provided by [153].

Before moving to χ^2 analysis lets see the effect of the couplings in $(x_{31} \rightarrow 1)$, and $(x_{31} \rightarrow \infty)$ in the number of event distributions for ν_e appearance. To do that, we added a variation in θ_{23} with 38° and 52° (Comparison I). The second variation changes the δ_{CP} in 90° and -90° (Comparison II).

The general behavior from Figure 2.20 to 2.25 is: First, the ID compared with SO (no decay) is always small because the decay products are not detectable; therefore, the distribution is suppressed. Second, the FD (full decay) is always large than the SO because the decay products can be detectable. Third, as we say in the previous section, the $(x_{31} \rightarrow \infty)$ case has a significant enhancement at low energy, more visible in the RHC channels, confirmed at the event rate level. Fourth, the VD in pseudoscalar coupling, with no vanishing light neutrino mass, is significant due to large helicity changes. Finally, there is a high enhancement in the number of events for $\delta_{\text{CP}} = -90^\circ$ and $\theta_{23} = 52^\circ$ (see section Comparison I and II) because the dominant component is the VD for RHC. This is consistent with the left plot of Figure 2.13.

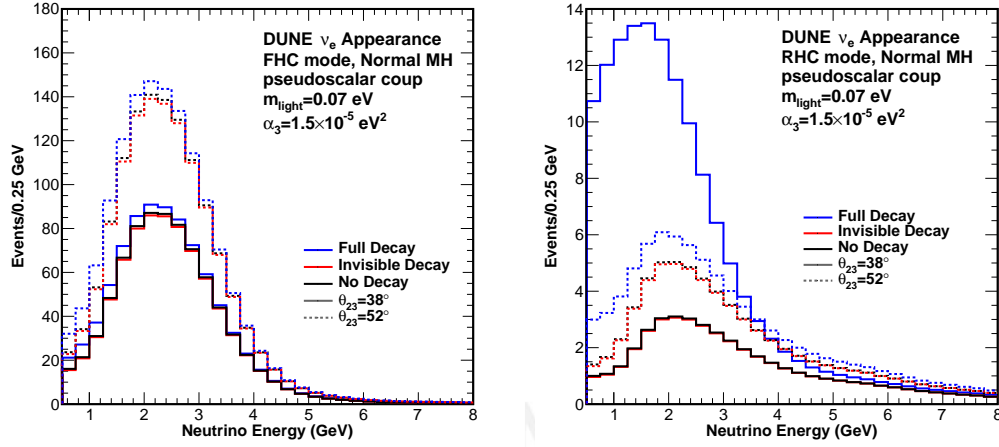
Comparison I: θ_{23} 38° vs 52°


Figure 2.20: Event rate distribution for **pseudoscalar** coupling (for $(x_{31} \rightarrow 1)$), dashed lines are $\theta_{23} = 52^\circ$ and continuous line are $\theta_{23} = 38^\circ$. Right side plot is FHC and left side is RHC.

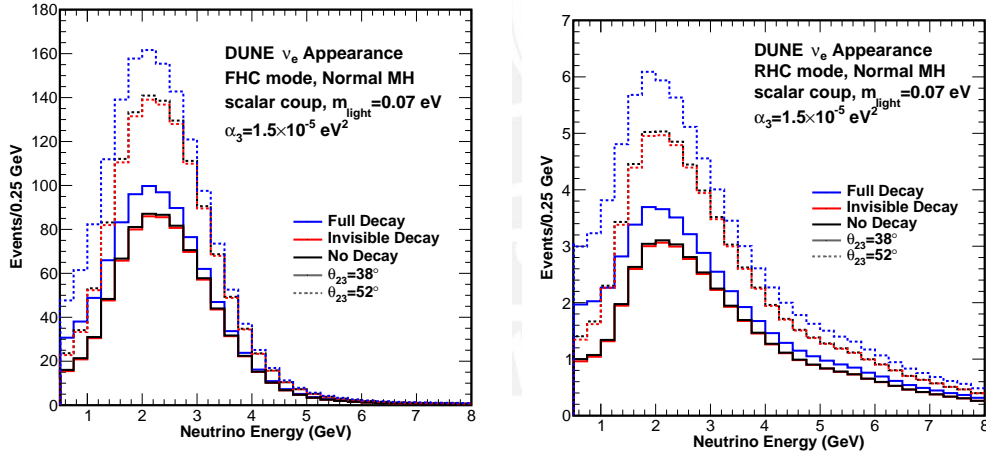


Figure 2.21: Event rate distribution for **scalar** coupling (for $(x_{31} \rightarrow 1)$), dashed lines are $\theta_{23} = 52^\circ$ and continuous line are $\theta_{23} = 38^\circ$. Right side plot is FHC and left side is RHC.

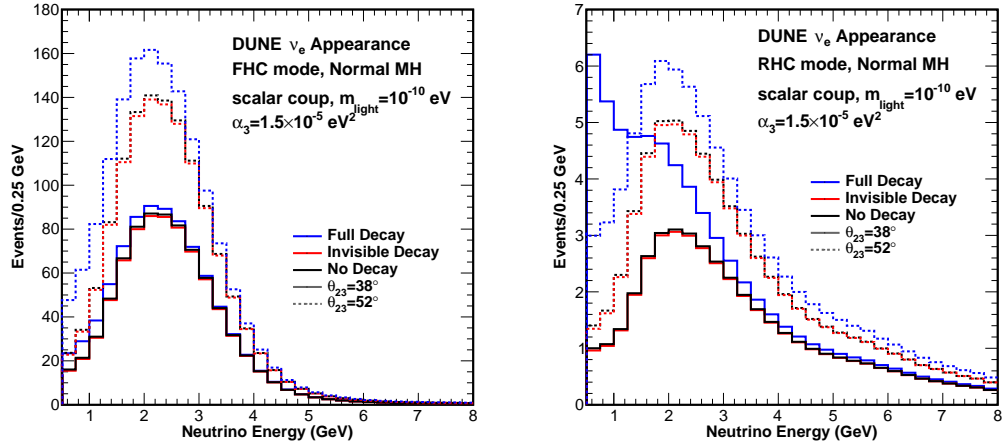


Figure 2.22: Event rate distribution for $(x_{31} \rightarrow \infty)$, dashed lines are $\theta_{23} = 52^\circ$ and continuous line are $\theta_{23} = 38^\circ$. Right side plot is FHC and left side is RHC.

Comparison II: $\delta_{CP} 90^\circ$ vs -90°

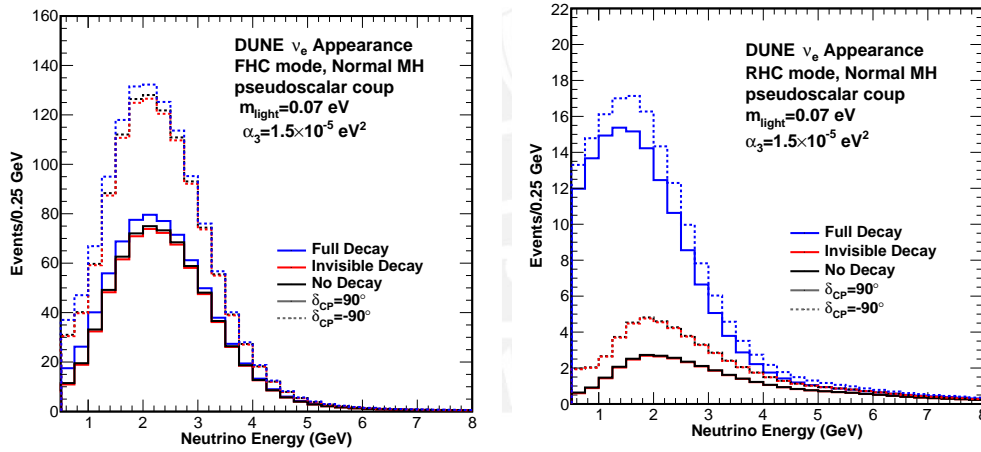


Figure 2.23: Event rate distribution for **pseudoscalar** coupling (for $(x_{31} \rightarrow 1)$), dashed lines are $\delta_{CP} = -90^\circ$ and continuous line are $\delta_{CP} = 90^\circ$. Right side plot is FHC and left side is RHC.

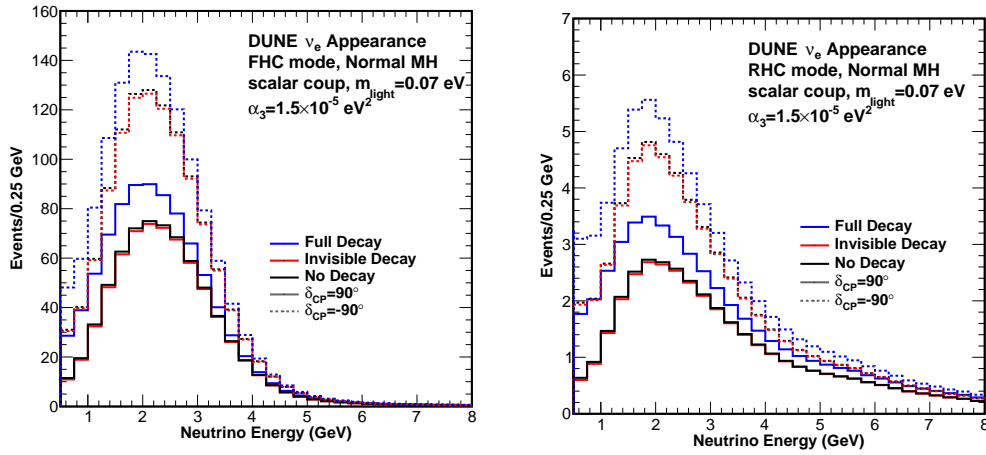


Figure 2.24: Event rate distribution for **scalar** coupling (for $(x_{31} \rightarrow 1)$), dashed lines are $\delta_{CP} = -90^\circ$ and continuous line are $\delta_{CP} = 90^\circ$. Right side plot is FHC and left side is RHC.

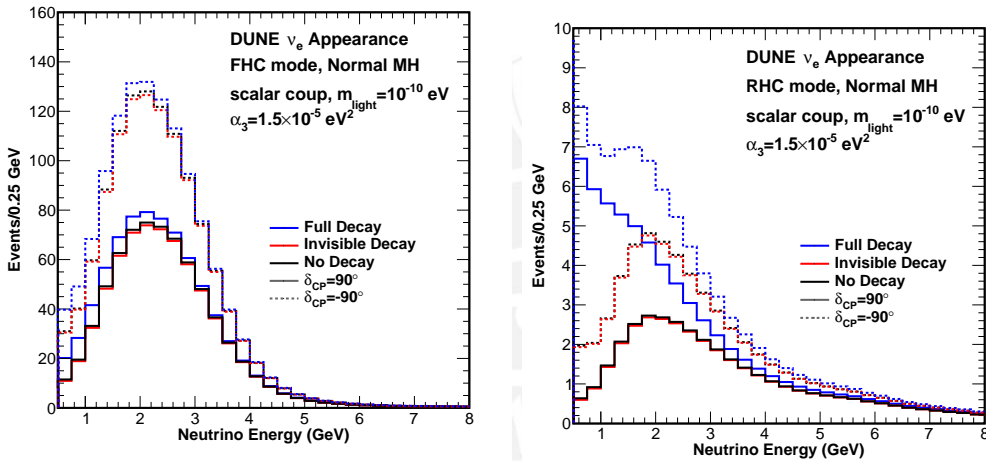


Figure 2.25: Event rate distribution for $(x_{31} \rightarrow \infty)$, dashed lines are $\delta_{CP} = -90^\circ$ and continuous line are $\delta_{CP} = 90^\circ$. Right side plot is FHC and left side is RHC.

2.4 Analysis, results and conclusions

For the analysis only θ_{23} and δ_{CP} are considered, θ_{13} is fixed by reactor measurements [163]. The other parameters are fixed on their best fit. We will consider the $x_{31} \rightarrow \infty$ case and the combination of ν_e appearance and ν_μ disappearance channels.

The χ^2 is defined on θ_{23} , δ_{CP} , and α_3 as follows:

$$\chi^2(\theta_{23}, \delta_{\text{CP}}, \alpha_3, \theta_{23}^{\text{true}}, \delta_{\text{CP}}^{\text{true}}, \alpha_3^{\text{true}}) = \sum_i^{\text{bins}} \frac{(N_i(\theta_{23}, \delta_{\text{CP}}, \alpha_3) - N_i(\theta_{23}^{\text{true}}, \delta_{\text{CP}}^{\text{true}}, \alpha_3^{\text{true}}))^2}{N_i(\theta_{23}^{\text{true}}, \delta_{\text{CP}}^{\text{true}}, \alpha_3^{\text{true}})} \quad (2.29)$$

where the *true* refers to default SO best fit values. To get the sensitivity of α_3 as a function of $\theta_{23}^{\text{true}}$ we have to marginalize $\delta_{\text{CP}}^{\text{true}}$, and set $\alpha_3^{\text{true}} = 0 \text{ eV}^2$. The χ^2 is given by:

$$\chi^2(\theta_{23}^{\text{true}}, \delta_{\text{CP}}^{\text{true}}, \alpha_3, \theta_{23}^{\text{true}}, \delta_{\text{CP}}^{\text{true}}, 0) \Big|_{\min \delta_{\text{CP}}^{\text{true}}} \quad (2.30)$$

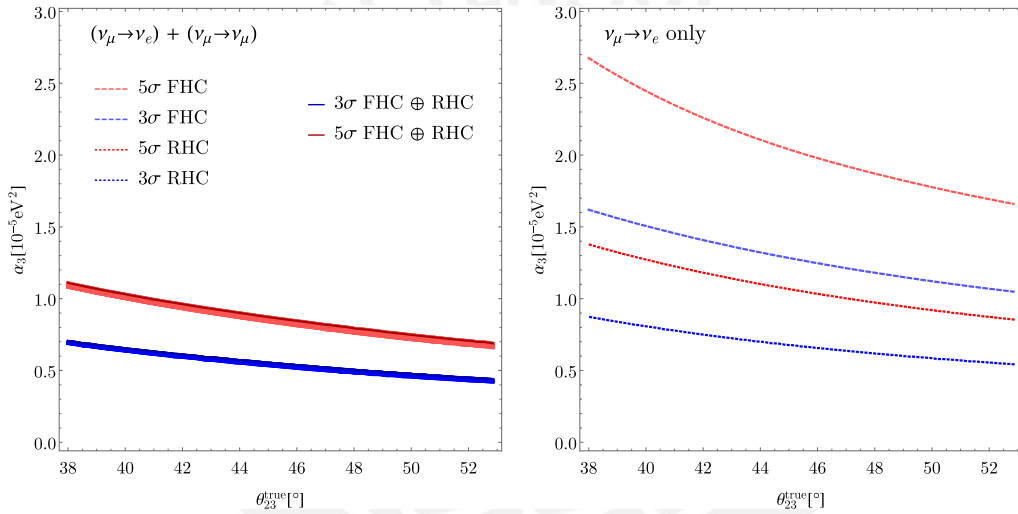


Figure 2.26: Sensitivity to θ_{23} as a function of $\theta_{23}^{\text{true}}$. On the left the sensitivity using both channels, with the shaded area below giving the sensitivity for fixed values of the phase. The right side plot is the sensitivity of ν_e appearance only with FHC or RHC.

The Figure 2.26 shows the sensitivity to α_3 in terms of $\theta_{23}^{\text{true}}$. The left plot combines both appearance and disappearance channels for FHC and RHC. The α_3 sensitivity with whole channels are: $(4 - 7) \times 10^{-6} \text{ eV}^2$ for 3σ and $(0.7 - 1.1) \times 10^{-5} \text{ eV}^2$ for 5σ . While, the right plot only accounts for appearance channel since we saw how sensitive is to VD before (see Table 2.3).

	FHC	RHC
3σ	$(1.0 - 1.6) \times 10^{-5} \text{ eV}^2$	$(5 - 9) \times 10^{-6} \text{ eV}^2$
5σ	$(1.6 - 2.7) \times 10^{-5} \text{ eV}^2$	$(0.8 - 1.4) \times 10^{-5} \text{ eV}^2$

Table 2.3: α_3 sensitivity as function of $\theta_{23}^{\text{true}}$ for ν_e appearance channel only. Right side plot of Figure 2.26.

The α_3 sensitivity as function of $\delta_{\text{CP}}^{\text{true}}$ is calculated marginalizing $\theta_{23}^{\text{true}}$, and fixing $\alpha_3^{\text{true}} = 0 \text{ eV}^2$,

$$\chi^2(\theta_{23}^{\text{true}}, \delta_{\text{CP}}^{\text{true}}, \alpha_3, \theta_{23}^{\text{true}}, \delta_{\text{CP}}^{\text{true}}, 0) \Big|_{\min \theta_{23}^{\text{true}}}. \quad (2.31)$$

Similar to the previous α_3 sensitivity, the left side plot of Figure 2.27 shows the sensitivity as a function of $\delta_{\text{CP}}^{\text{true}}$ for both channel combinations as well as FHC and RHC. Compared with Figure 2.26, the curves are flat, which seems to say that the values of $\delta_{\text{CP}}^{\text{true}}$ is not relevant for determine the α_3 . However, the right plot of Figure 2.27 shows a very strong $\delta_{\text{CP}}^{\text{true}}$ dependence, with large impact on FHC. The reason is the influence of $\delta_{\text{CP}}^{\text{true}}$ on the total number of events. For instance, let's consider the FHC mode, so, a positive $\delta_{\text{CP}}^{\text{true}}$ would reduce the events coming from ID, which has a stronger dependence on $\delta_{\text{CP}}^{\text{true}}$ than VD. As a consequence of this suppression, a small α_3 is enough to generate a VD contribution that can be comparable to the ID. In opposite, a negative $\delta_{\text{CP}}^{\text{true}}$ implies a larger number of events expected from ID, in that case, a larger α is required to reach the same level of sensitivity compared to positive $\delta_{\text{CP}}^{\text{true}}$.

Now, let's compare the sensitivity of α with $x_{31} \rightarrow 1$ and $x_{31} \rightarrow \infty$. To do that, we must marginalize in both $\delta_{\text{CP}}^{\text{true}}$ and $\theta_{23}^{\text{true}}$, and the result of that is shown in the Figure 2.28. The values on the α_3 are in the Table 2.5.

2.4. ANALYSIS, RESULTS AND CONCLUSIONS

	Pseudoscalar	Scalar
$x_{31} \rightarrow 1$		
3σ	$3.8 \times 10^{-6} \text{ eV}^2$	$5.2 \times 10^{-6} \text{ eV}^2$
5σ	$6.4 \times 10^{-6} \text{ eV}^2$	$8.8 \times 10^{-6} \text{ eV}^2$
$x_{31} \rightarrow \infty$		
3σ	$6.1 \times 10^{-6} \text{ eV}^2$	6.1×10^{-6}
5σ	$1.0 \times 10^{-5} \text{ eV}^2$	1.0×10^{-5}

Table 2.4: α_3 sensitivity marginalized on $\theta_{23}^{\text{true}}$ and $\delta_{\text{CP}}^{\text{true}}$, from Figure 2.28.

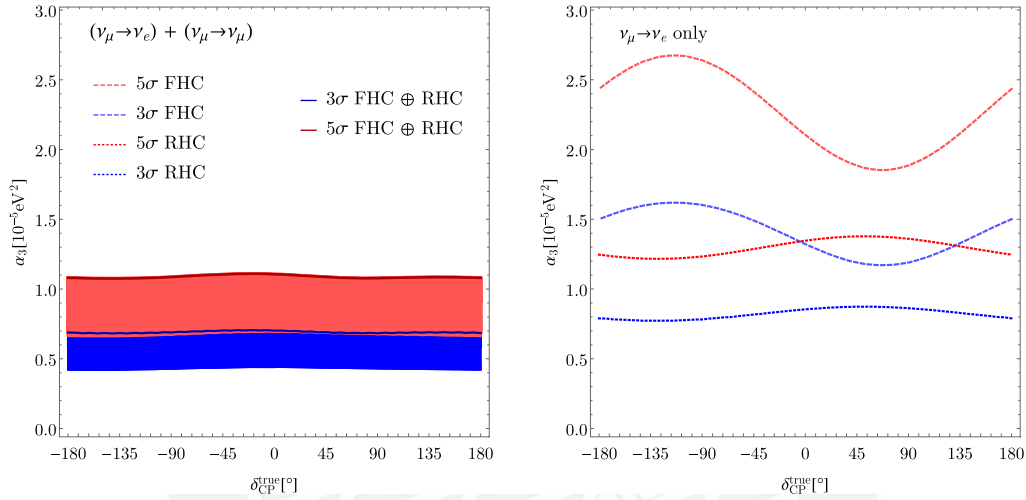


Figure 2.27: Sensitivity to δ_{CP} as a function of $\delta_{\text{CP}}^{\text{true}}$. On the left the sensitivity using both channels, with the shaded area below giving the sensitivity for fixed values of the phase. The right side plot is the sensitivity of ν_e appearance only with FHC or RHC.

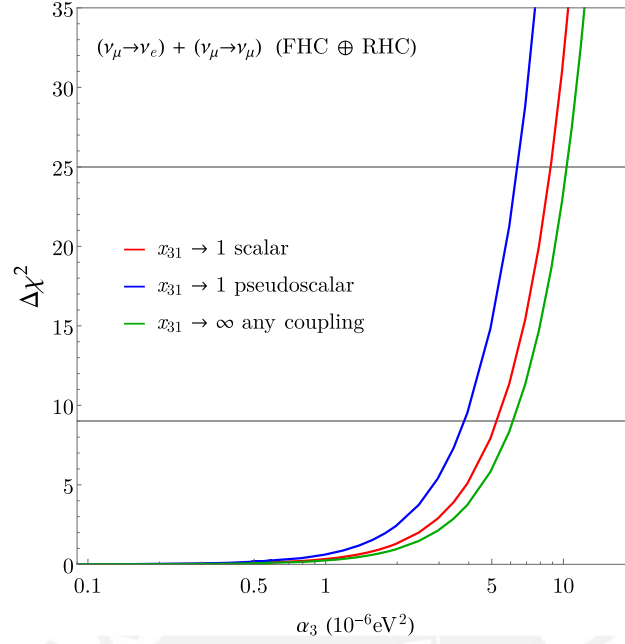


Figure 2.28: Sensitivity to α_3 , by combining ν_{μ} disappearance and ν_e appearance, with FHC and RHC modes. For this sensitivity, $\theta_{23}^{\text{truth}}$ and $\delta_{\text{CP}}^{\text{true}}$ were marginalized. The horizontal lines indicate the 3σ and 5σ confidence levels.

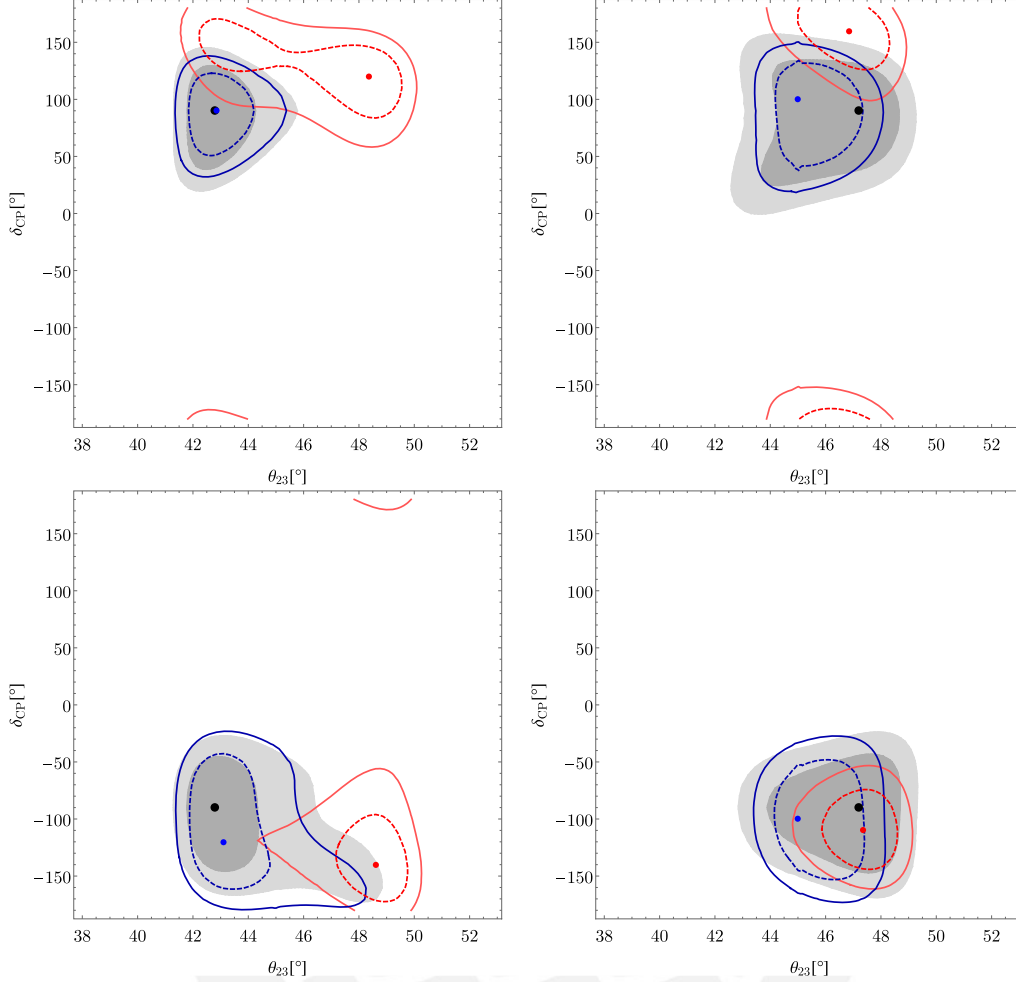


Figure 2.29: Allowed regions as function of θ_{23} and δ_{CP} . The gray region represents the SO, blue ID and red FD. The upper (lower) row has $\delta_{\text{CP}}^{\text{true}} = 90^\circ (-90^\circ)$, while the left (right) column has $\theta_{23}^{\text{true}} = 42.8^\circ (47.2^\circ)$. The $\alpha_3^{\text{true}} = 4 \times 10^{-5} \text{ eV}^2$. Dashed and solid lines (dark and light regions) correspond to 3σ and 5σ confidence levels, respectively, with the dots indicating the best-fit points.

The final part of the analysis is shown in the Figure 2.29, where the SO, ID, and FD is evaluated in different $\delta_{\text{CP}}^{\text{true}}$, and $\theta_{23}^{\text{true}}$ scenarios with $\alpha_3^{\text{true}} = 4 \times 10^{-5} \text{ eV}^2$. Using the χ^2 give by the following equation:

$$\chi^2(\theta_{23}, \delta_{\text{CP}}, 0, \theta_{23}^{\text{true}}, \delta_{\text{CP}}^{\text{true}}, \alpha_3^{\text{true}}), \quad (2.32)$$

where $\alpha_3^{\text{true}} = 0 \text{ eV}^2$ for SO case. Just like Figure 2.28, includes all channel and neutrino, flux models. Figure 2.29 shows a slight difference between SO

	Pseudoscalar	Scalar
$x_{31} \rightarrow 1$	$< 2.0 \times 10^{-6} \text{ eV}^2$	$< 2.8 \times 10^{-6} \text{ eV}^2$
$x_{31} \rightarrow \infty$	$< 3.2 \times 10^{-6} \text{ eV}^2$	$< 3.2 \times 10^{-6} \text{ eV}^2$

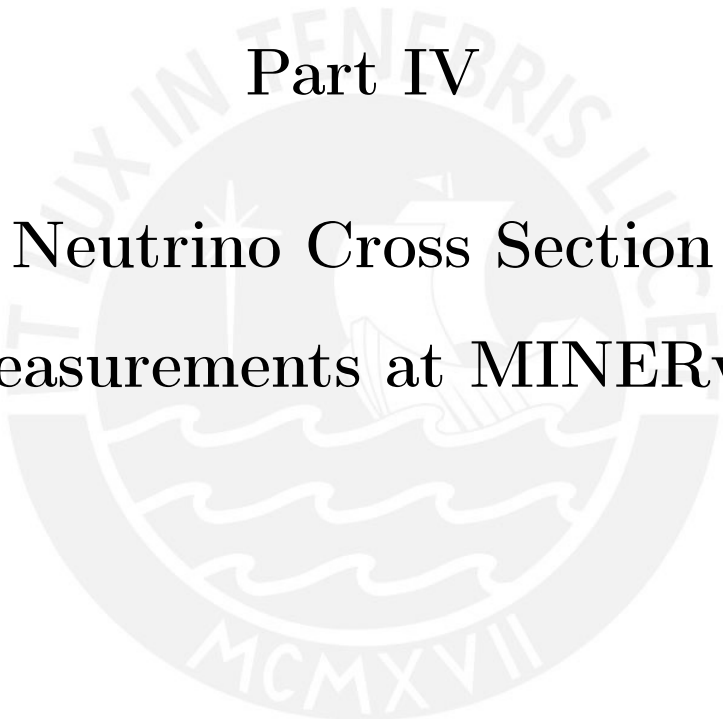
Table 2.5: DUNE α_3 sensitivity at 90% C.L

and ID, and it is due to α not being big enough to have any relevant influence, as reported by [159]. On the other hand, FD has more susceptibility to α_3 values, as shown in $(\sigma \times \Phi)$ plots.

We started from a decay scenario [144, 142, 145], where we studied the matter effect in visible neutrino decay. To comprehend that effect, we conducted a study in two distinct circumstances. On the first, we use the flux and baseline for DUNE, while on the second, we use the same flux but take into account the baseline for ANDES. Only the ID component of ν_e appearance is affected by matter in DUNE; the effect on all other components, like VD ν_e appearance, can be neglected.

In the case of ANDES, however, we not only see an enhanced effect on the ID component due to matter, but we also see a relevant modification in the VD component. That is important for ν_e appearance, but it also has an impact on ν_μ disappearance.

In addition, the sensibility of decay α parameter study was performed for DUNE. The values found at 90% of confidence level are shown in Table 2.5. Finally, we observed that the permitted regions would shift toward larger values of θ_{23} and CP-conserving values of CP.



Part IV

Neutrino Cross Section
Measurements at MINERvA

CHAPTER 3

NEUTRINO BEAM AND FLUX

In this chapter, we will describe, in a general way, the accelerator neutrino production, focusing mostly on the neutrino flux production at NuMI (Neutrino at the Main Injector), which is the starting point for the measurement of the double differential cross-section presented in chapter VIII. We will also describe the primary sources of errors associated with the flux. For more details, the reader can find some information about neutrino production and history in [164, 165, 166, 167, 168]. Finally, to use the neutrino flux in the MINERvA experiment, we adjust the flux simulation. Flux adjustment can be made through constraints and scaling the muon momentum. Those studies will be discussed in the last two sections of this chapter.

3.1 Neutrino Beam

Typically, a neutrino beam production follows the next steps: First, we need to have a source of accelerated protons that then hits a target, which is thick and

narrow enough to avoid a lot of re-interactions. Of which short-lived mesons are produced. Second, the mesons produced are aligned by parabolic magnetic horns to decay [169, 170], among other particles, into neutrinos. The decay occurs usually in a vacuum or low density or gas-filled pipe [171, 167]. Third, the decay product is filtered to have an aligned neutrino beam. The neutrino energy can be inferred from the mesons' decay which follows the usual two-body decay—for example, the meson π^\pm , which decays in μ^\pm and $\nu_\mu^{(h)}$ ¹ with a probability of 99.9877% [172]. The relation between π decay kinematics with neutrino energy is [173, 174, 175]:

$$E_\nu = \frac{0.427E_\pi}{1 + \gamma^2\theta^2}, \quad (3.1)$$

where γ is the Lorentz boost of the pion, and θ is the angle between the π and neutrino direction. The 0.427 is a factor that involves the μ and π masses.

All these steps are similar to producing atmospheric neutrinos. However, instead of a controlled accelerator, you have charged particles (cosmic rays) colliding with molecules in the atmosphere to produce mesons and neutrinos. This similarity is not an accident. In fact, the production of neutrinos has its origin in the atmospheric neutrinos or at least their motivation [15, 17, 176].

3.2 Neutrino at the Main Injector (NuMI)

NuMI [174] is a Fermilab facility that provides an intense neutrino (antineutrino) beam to NoVA [177] and in the past to MINOS [178] and MINERvA. The neutrino generation follows that described in the previous section. The proton beam used in the first step hits a carbon target with 120 GeV. The neutrino energy distribution goes up to 120 GeV, with a peak of the neutrino distribution at around 3 GeV and 6 GeV called Low Energy (LE) and Medium Energy (ME), respectively. A comparison between LE and ME in MINERvA and off-axis ME NoVA is shown in Figure 3.1.

¹Here s can be “+” for neutrino or “−” for antineutrino

From hydrogen to proton beam

There are four different instruments used to produce the 120 GeV proton beam, and they are [179]: Pre-accelerator (RIL), LINAC, Booster, and Main Injector. Those are shown in Figure 3.2.

The process begins in RIL (Radio Frequency Quadrupole Injection Line) or pre-accelerator, a set of instruments² that takes negative hydrogen ions (H^-) to accelerate from 35 keV to 750 KeV [180].

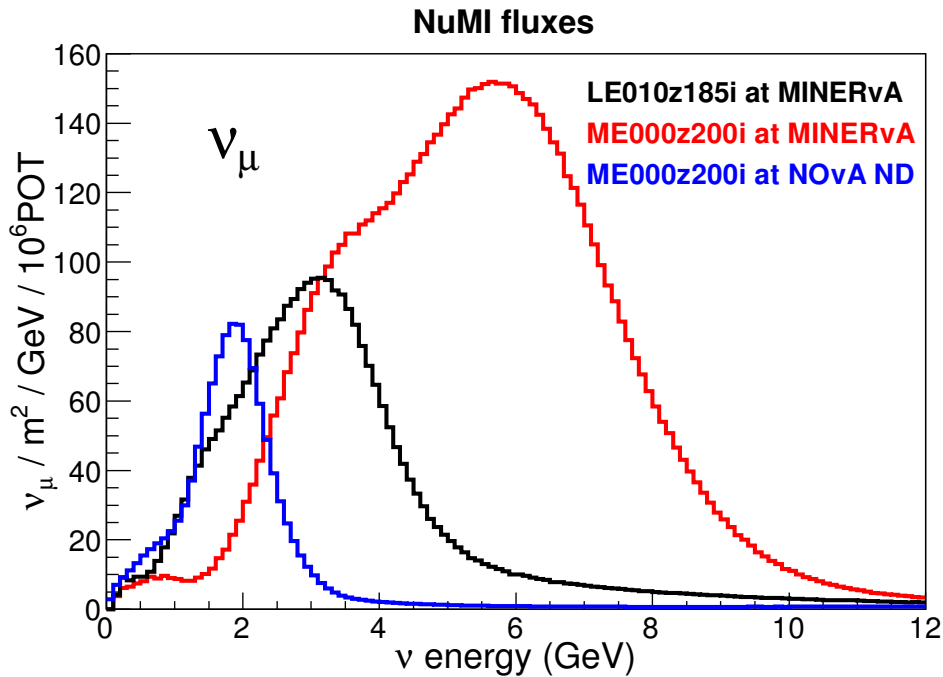


Figure 3.1: Low Energy (LE) and Medium Energy (ME) neutrino fluxes distributions in MINERvA, and off-axis ME in NoVA. Figure taken from [181].

The second part is handled by LINAC (LINear ACcelerator), a linear accelerator with 150 m of length, operating for more than 50 years [182, 183], which went through several updates, where the last one³ is under construction;

²The RIL consists in four parts, the Ion source, Low Energy Beam Transport line (LEBT), Radio Frequency Quadrupole (RFQ), and Medium Energy Beam Transport (MEBT).

³The PIP-II will replace the LINAC. It will increase the energy up to 800 MeV.

3.2. NEUTRINO AT THE MAIN INJECTOR (NUMI)

the PIP-II [184]. The LINAC ⁴ is injected with the ions coming from the pre-accelerator, in the quadrupole radio-frequency [185], and then enter the radiofrequency (RF) cavity that oscillates at 201 MHz, increasing the ions' energy to from 750 KeV to 116.5 MeV. Finally, before leaving the LINAC, the ions pass through other side-coupled RF cavities that oscillate at a frequency of 805 MHz, increasing the energy of the ions to 400 MeV [186].

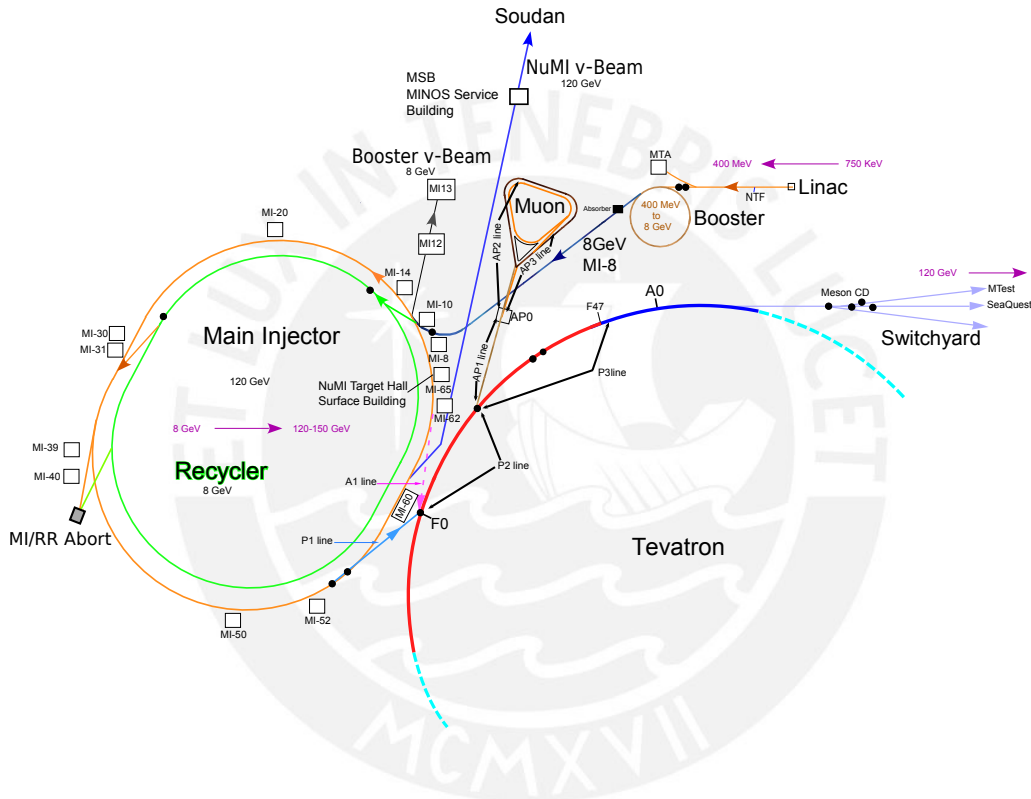


Figure 3.2: Scheme of LINAC, Booster, Main Injector, and Tevatron. Figure taken from [167].

The third part of the acceleration process passes through the Booster accelerator, which is a synchrotron accelerator with a circumference of 474.2 m, RF from 37.77 MHz to 52.8 MHz. The booster gets LINAC's ions with 400 MeV and removes the electrons through a stripping foil to have a proton

⁴LINAC has two main components: Drift Tube Linac (Low Energy Linac) and Side-Coupled Cavity Linac (High Energy Linac).

source. The new source is accelerated with an initial revolution period of $2.2\mu\text{s}$ (400 MeV) to $1.6\mu\text{s}$, which gives us proton energy of 8 GeV [187].

The last part of the proton acceleration process involves the Main Injector; A proton synchrotron accelerator with 3319.4 m of circumference, a revolution period of $11.1\mu\text{s}$, and RF from 52.8 MHz to 53.1 MHz.[188]. The protons at 8 GeV coming from the booster are delivered by MI-8 Line⁵ to the Main Injector, which with its dipoles, quadrupoles, and RF cavities, end up in a pulsed proton beam with 120 GeV of energy, 1.1 mm of Gaussian beam sigma, 1.87s of cycle time, and $10\mu\text{s}$ beam spill duration [179].

From proton to neutrino beam

The general description from proton source to neutrino source is summarized in Figure 3.3 and discussed briefly previously. Now, in this subsection, we will discuss it a bit in detail.

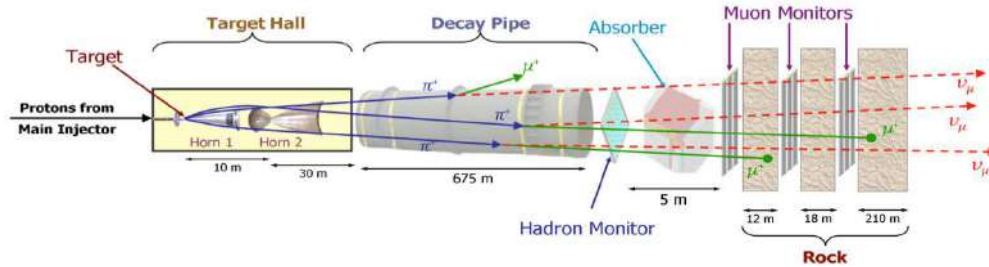


Figure 3.3: Big picture of neutrino production. Figure taken from [167].

The target that the proton beam hits is an isotropic POCO ZXF-5Q graphite with an apparent density of 1.78 g/cm^3 [167]. The chemical composition is shown in Table 3.1, and it consists (see Figure 3.4) of 47 fins, where each fin has $6.6\text{mm} \times 15\text{mm} \times 20\text{mm}$ with 0.3 mm of space between fin to fin. The total length is 95.38 cm. The proton is directed at the target through a collimating baffle. As is pointed out in Figure 3.5, the fins are

⁵MI-8 Line is composed by mostly magnet [179].

3.2. NEUTRINO AT THE MAIN INJECTOR (NUMI)

Element	Concentration (ppm wt)
C	Matrix
Cl	0.38
Cr	0.18
B	0.7
S	0.18
Ta	<5
F	0.07
Al	0.09
Si	0.05
Fe	0.03
P	0.02
Zn	<0.05

Table 3.1: POCO ZXF-5Q graphite target composition. Table taken from [189]

brazed in a vacuum to two stainless steel tubes that carry the water coolant. Finally, there is one more fin mounted upstream in the target canister at 15.73 cm from the main target.

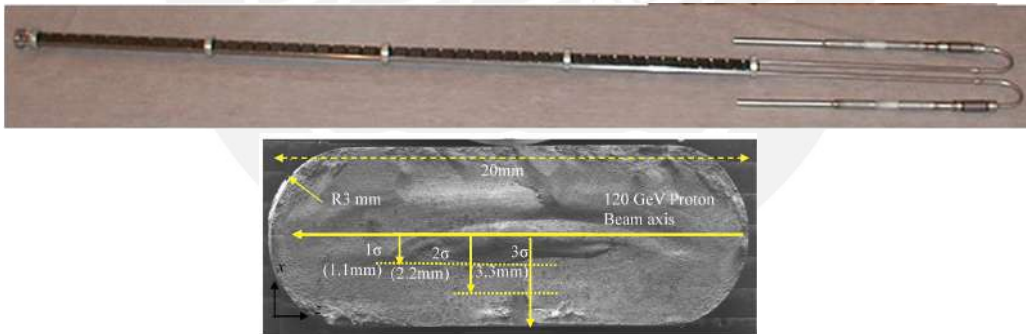


Figure 3.4: Fin target configuration (top plot) and dimension of individual fin (bottom). Figure top taken from [190] and bottom from [189].

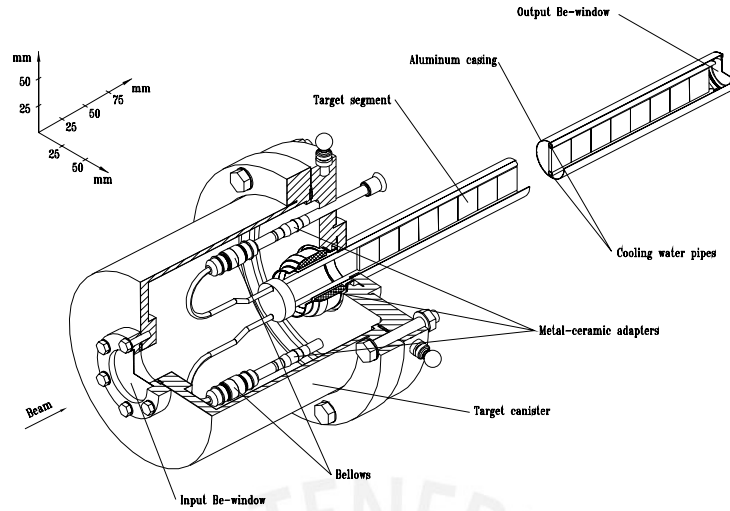


Figure 3.5: Scheme of the Target fin and its surrounding components. Figure taken from [191].

From the bombarded graphite with the proton beam, secondary particles are produced. Those particles, mostly mesons, are focused by two magnetic horns. The focusing process works similarly to optic lenses, in which, instead of photons and lenses, we have mesons and magnetic fields. The illustration of the horns is shown in Figure 3.6.

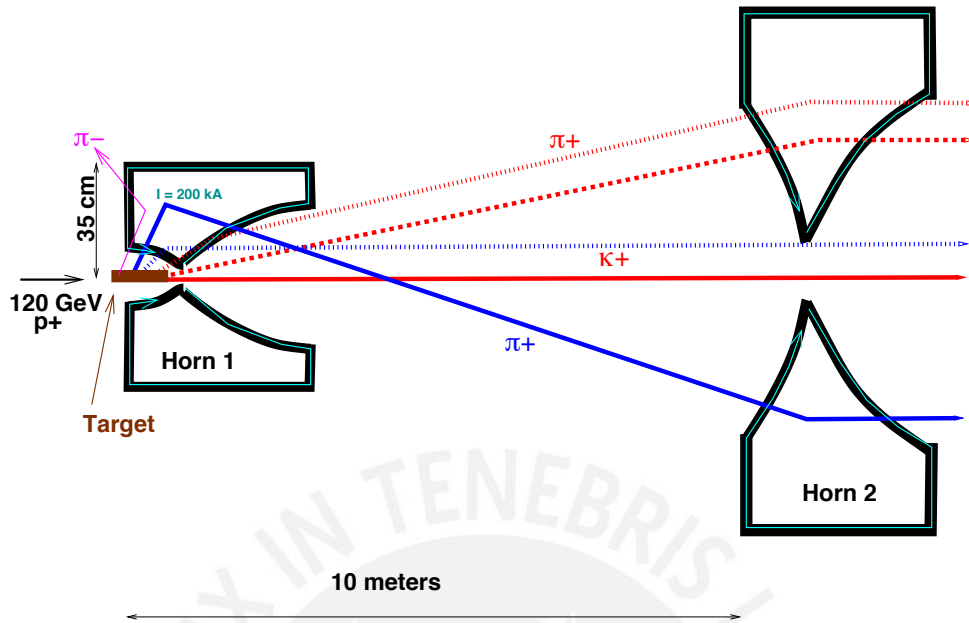


Figure 3.6: Scheme of the magnetic horns to focus the mesons. Figure taken from [167].

Horn 1 and Horn 2 have a double parabolic shape with an inner conductor of nickel-plated aluminum and anodized aluminum for the outer conductor (the geometric dimensions for both horns are showed in Figure 3.7). Both horns operate at 200 kA of current, producing a 3 T. The horn's length has a 300 cm (focus region). The minimum aperture field-free neck is 9 mm and 3.9 cm of radius for Horn 1 and 2, respectively. The distance from Horn 1 to Horn 2 is 10 m, and its variation allows us to have less or more neutrino average energy (see Figure 3.8).

After aligning the mesons, the next part is to pass through a space where the mesons can decay into neutrinos. That place is the decay pipe. The vacuum (<1 Torr) pipe has a 1.98 m inner diameter x 677.1 m long. The pipe's upstream and downstream vacuum windows have 1.57 mm of aluminum and 6.35 mm of steel, respectively.

3.2. NEUTRINO AT THE MAIN INJECTOR (NUMI)

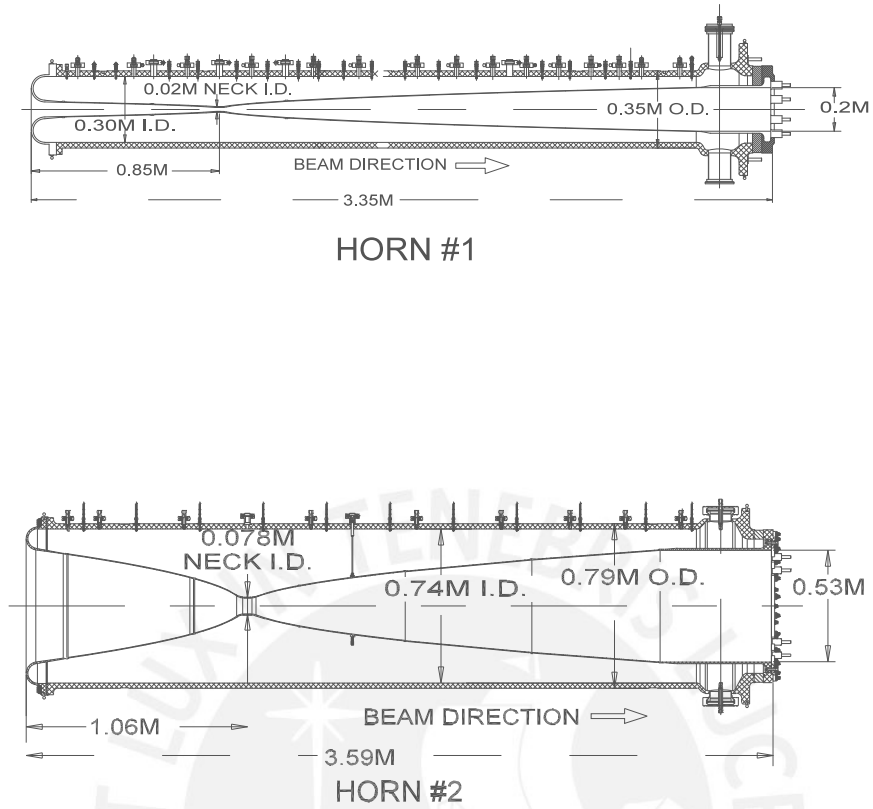


Figure 3.7: Horn 1 and 2 description. Figure taken from [167].

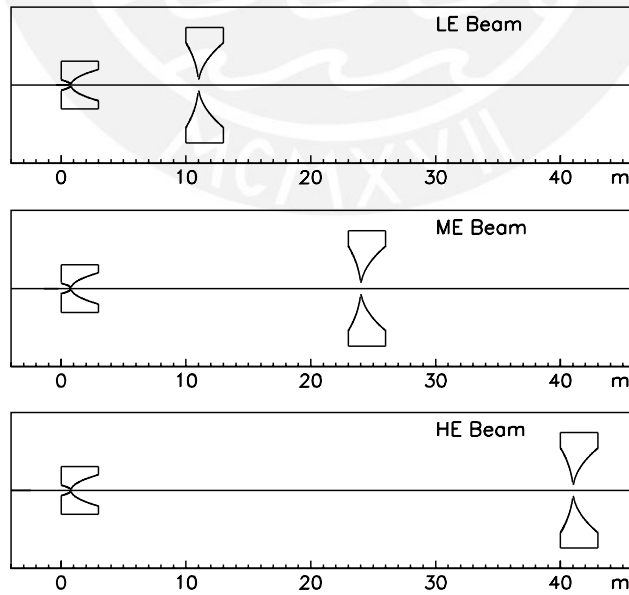


Figure 3.8: Horn displacements for LE and ME neutrino. Figure taken from [191].

Finally, after the mesons decay in the pipe, they must be filtered to have a pure neutrino beam. Downstream of the decay pipe, there is a hadron absorber which consists of massive aluminum, steel, and concrete structure.

3.3 Flux Simulation and Prediction

The flux simulation, which will lead to the prediction, is performed in GEANT4-based MC[192], denominated g4numi. Every step of the description above is simulated. For our measurement purpose, we will focus on two main parts of the simulation, the hadron production, and the focusing. The first part concentrates on the hadrons produced due to the proton interaction with the target and the meson reinteractions. The second part of our interest is the correct simulation of the geometry around the target and horns. A detailed description of the simulation can be found in [181].

Hadron production

The mesons produced from the proton interaction do not decay cleanly. They can re-interact, and from the product of those re-interactions, we can also have neutrinos also. However, re-interaction belongs to nonperturbative QCD. Furthermore, the simulation becomes complicated due to different models. Figure 3.9 shows the simulation of the average number of hadrons interactions per neutrino as a function of the produced neutrino energy. The main contribution in the peak of the neutrino energy spectrum comes from proton-carbon ($pC \rightarrow \pi X$), nucleon-A⁶, and meson inc⁷. In the tail of the spectrum, the contributions are nucleon-A and ($pC \rightarrow KX$).

The solution (followed by MINERvA) is to use existing data to constraint the models. The data from NA49[194] is take into account. To get the pion yield per inelastic interaction we have [193],

$$\mathcal{F}_{\text{Data}} = \alpha E_{\pi}, \quad (3.2)$$

⁶nucleon-A refers to nucleons interacting in material that is not C.

⁷meson inc means meson interacting on any material.[193]

where E_π is the pion energy and α is:

$$\alpha = \frac{1}{\sigma_{\text{Inel}}} \frac{d^3\sigma}{dp^3}, \quad (3.3)$$

the σ_{Inel} is a factor to have the yield. In order to correct with this data, we have the same calculation for MC, the weight is [193]:

$$\mathcal{W}(x_F, p_T, p) = \frac{\mathcal{F}_{\text{Data}}(x_F, p_T, p_0 = 158 \text{ GeV})}{\mathcal{F}_{\text{MC}}(x_F, p_T, p_0 = 158 \text{ GeV})} s(x_F, p_T, p), \quad (3.4)$$

where x_F is the Feynman variable, p the proton momentum, p_T the transverse momentum, and $s(x_F, p_T, p)$ a scale in FLUKA⁸ to turn from 158 GeV to proton momenta.

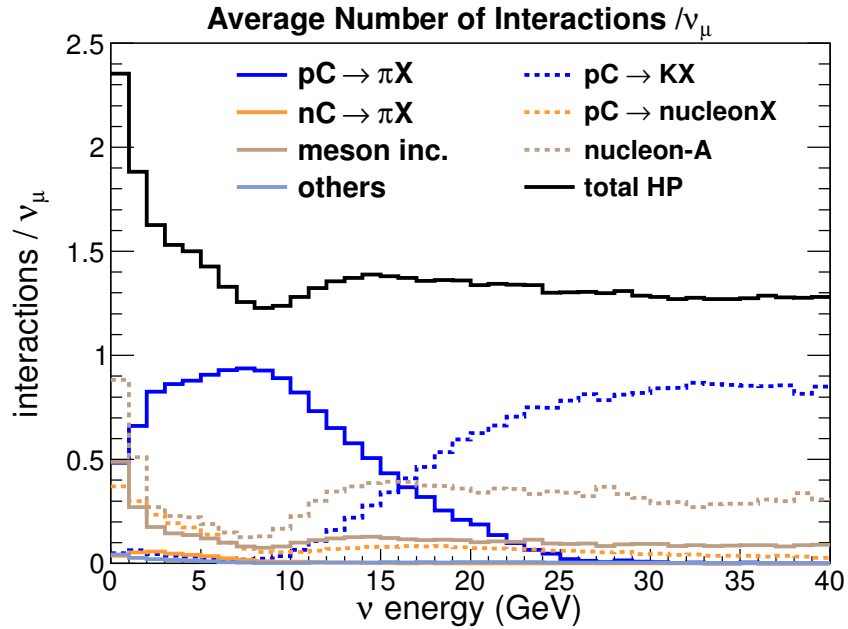


Figure 3.9: Average number of hadronic interactions per neutrino as a function of the neutrino energy ME in MINERvA. Figure taken from [181].

Table 3.2 shows the description of the components of the hadronic production presented in Figure 3.9. Finally, we have the flux reweighted (see Figure 3.10). The uncertainties associated with each channel are shown in Figure 3.11.

⁸FLUKA [195, 196] is also used for hadron production simulation.

Contribution Description	
pC→πX	The thin target data from NA49[194] is used to reweight the π production on pC in order to corresponds to their measured π^\pm yield per incident p (α from eq. 3.3), and Feynman scales in FLUKA. The NA49's energy used 158 GeV for $x_F < 0.5$ and Barton [197] data for $x_F > 0.5$.
pC→KX	The reweight is applied with NA49 data[194] to $pC \rightarrow K^\pm X$ channel in the $x_F < 0.2$ range. For high values $0.2 < x_F < 0.5$, the K/π yield ratios on a thin C target is used.
pC→NX	Similar to K and π the NA49 data[194] is used to correct the nucleon (N) production in the region $x_F < 0.95$.
nC→πX	This channel is reweighted same like pC→ π X, with NA49 [194] and Barton[197] data. That is because the isoscalar symmetry of carbon.
nucleon-A	Refers to Nucleon-nuclei interaction, where the nuclei (A) can be He, Fe, Al and not carbon. A-dependence scaling as a function of momentum and angle is used from [198].
Meson incident	These are neutrinos from the 10–40 GeV meson interaction in the beamline, where 40% uncertainty is applied from the data-MC discrepancies in pC and pA (from Geant4-FTFP model [192]).
Target attenuation	This contribution corresponds to an uncertainty dependent on nucleon and meson inclusive cross-section modeling. The uncertainty can be around 10%, taking from the probability that a particle interacts inside the target or exits the target.
Absorption	Similar that target attenuation, this contribution focuses on the absorption of nucleon and meson for Al, He, and Fe.
Others	The category represents any other channel not included above, and it has a 40% uncertainty assigned (similar to Meson incident with FTFP model [192]).

Table 3.2: Hadron production contributions in the neutrino flux. Table based on [199, 200]

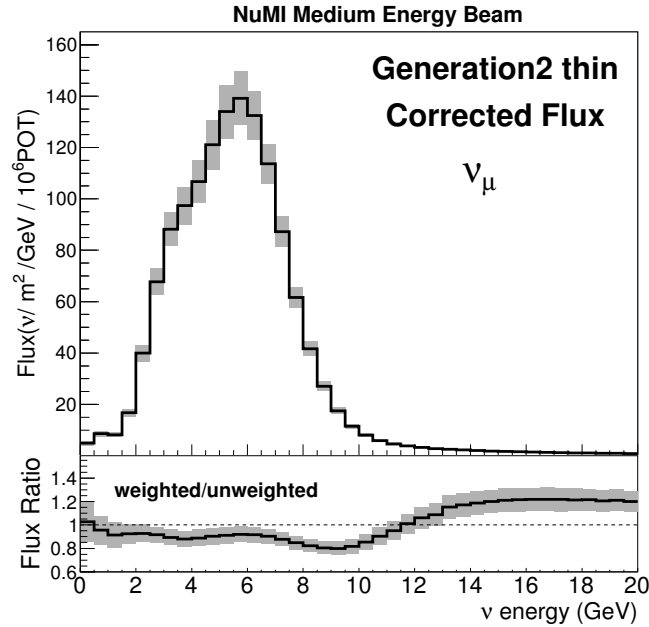


Figure 3.10: Flux distribution with hadron production weight in ME. Figure taken from [181].

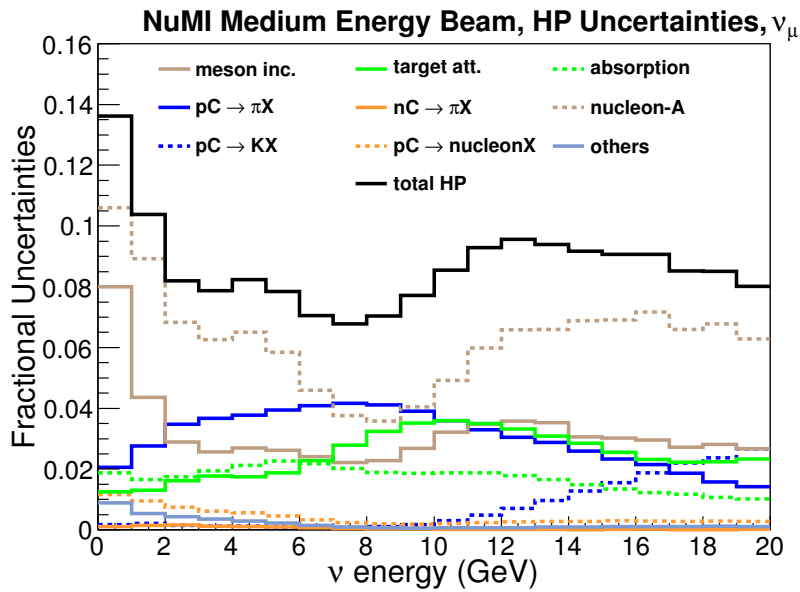


Figure 3.11: Fractional Uncertainties for flux distribution with hadron production weight in ME. The figure is taken from [181].

Beam focusing

The beam focusing is simulated based on the beamline geometry and all component information that involves the neutrino production, like the target, the device surrounding the target, the horns, the pipe, and others. The nominal parameters values are shown in Table 3.3. Even though we have all that information, the values compared with the real experiment are slightly different. So we do not know exactly those values, for instance, the magnetic field of the horns or the horn current. For that reason, it is implemented with one sigma deviation associated with all these parameters (see the focusing uncertainty in Figure 3.12).

Some parameters are more sensitive at 1σ shift in the flux focusing uncertainty. The significant uncertainties at the peak of the distribution are the proton beam spot size and horn water layer. The tail of the distribution is more sensitive to the horn position and the horn water layer.

Parameter	Nominal Value	Final 1σ shifts
Beam Position (X)	0 mm	0.4 mm
Beam Position (Y)	0 mm	0.4 mm
Beam Spot Size	1.5 mm	0.3 mm
Horn Water Layer	1.0 mm	0.5 mm
Horn Current	200 kA	1 kA
Horn 1 Position (X)	0 mm	1 mm
Horn 1 Position (Y)	0 mm	1 mm
Horn 1 Position (Z)	30 mm	2 mm
Horn 2 Position (X)	0 mm	1 mm
Horn 2 Position (Y)	0 mm	1 mm
Target Position (X)	0 mm	1 mm
Target Position (Y)	0 mm	1 mm
Target Position (Z)	-1433 mm	1 mm
POT Counting	0	2% of Total POT
Baffle Scraping	0	0.25% of POT

Table 3.3: Nominal and 1σ shift of the NuMI ME beam parameters configuration. Used for flux focusing uncertainty (see Figure 3.12). Table taken from [201].

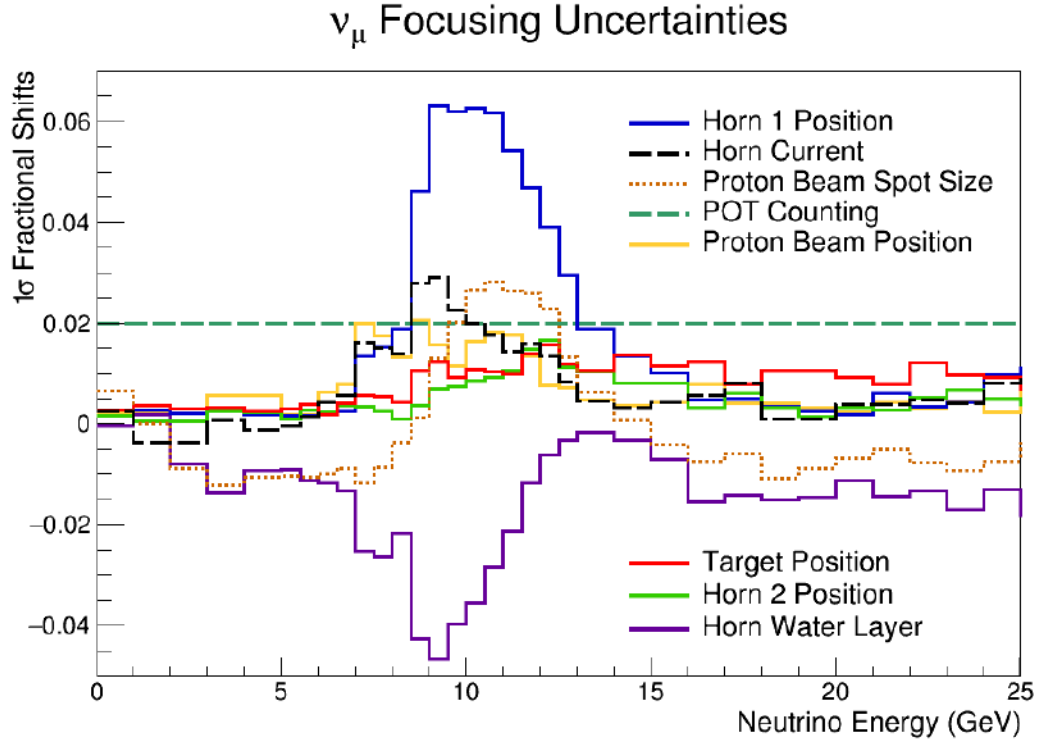


Figure 3.12: Ratio of predicted ν flux with beam parameters shifted by 1σ deviation to the nominal ν flux. Figure taken from [201].

3.4 Nominal Flux and its error bands

The uncertainties coming from the hadronic production and the focusing are propagated to the neutrino energy distribution through a “multi-universe method” technique, which follows the multivariate normal distribution⁹ (MV-G) introduced to MINERvA by [204] and used in flux uncertainty propagation by [181]. The mathematical description is in the appendix A.

This method aims to make a shift to an uncertainty parameter given a known covariance matrix (V). We get the shift value (R) randomly from MV-G with the mean in the central value (default parameter denoted in the appendix A by μ).

⁹Known also as Normal many-dimensional or multivariable Gaussian (Ref [202], ch. 4.2.2 and Eq. 3.36 of [203])

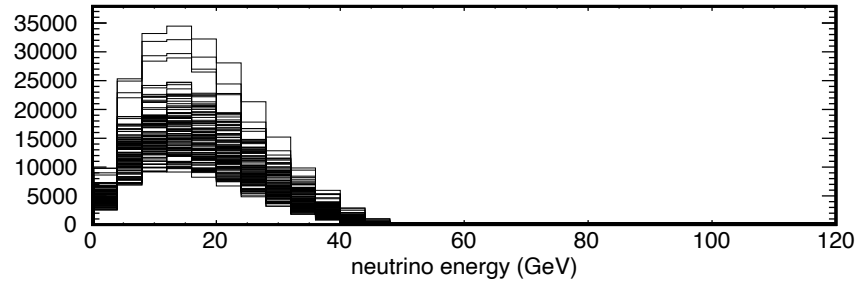


Figure 3.13: Toy example of multi-universe approach, where all universes are stored in different histograms. Figure taken from [204].

3.5 Neutrino Flux Constraint

The Flux simulated in FHC mode for Medium Energy (ME) after the hadron production and focusing uncertainty corrections are shown in Figure 3.14, wherein the dominant contribution is the muon neutrinos, followed by $\bar{\nu}_\mu$, ν_e , and $\bar{\nu}_e$. The peak of the distribution sits around 6 GeV, and it is used in the coming double differential cross-section measurement.

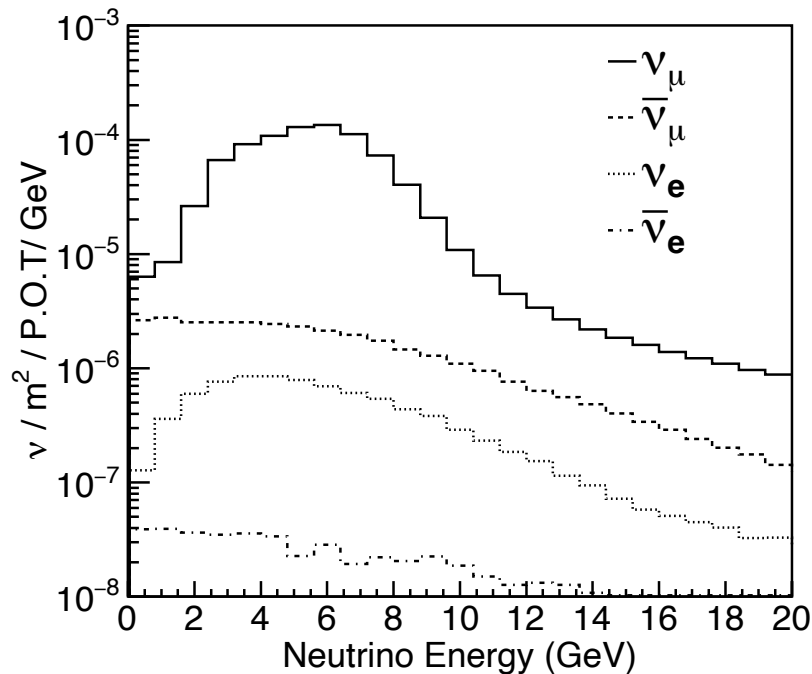


Figure 3.14: Neutrino flux at MINERvA versus the ME ν mode of the NuMI beam. Figure taken from [205].

In the previous section, we saw the rule that the hadron production and focusing play. Therefore, we can conclude that we need other dedicated experiments for hadron production to reduce part of the flux uncertainty for coming or future experiments. However, we can still mitigate or reduce the flux uncertainties using a standard candle, which means processes we handle with high precision, such as neutrino scattering on electrons[206]. That process is well understood in the standard electroweak theory¹⁰, and it can be precisely predicted due to the lepton-only process. Thus, MINERvA does that study for LE[207] and ME[205]. The signal of that process is a single forward-going electron; however, it is limited by the statistics.

In this subsection, we will describe the flux using the neutrino scattering on electrons. The number of events¹¹ measured (N_e) is:

$$N_{\nu_e \rightarrow \nu_e} = \sigma \times D_m \times \Phi, \quad (3.5)$$

where σ is the neutrino-electron scattering cross section, D_m mass of the detector, and Φ the flux. We can consider the measurement of an energy-weighted flux integral equivalent to the total uncertainty of the number of signal events[207].

Now, in order to constrain the flux with the neutrino scattering on electrons measurement, let us consider the rewritten Bayes' theorem [208],

$$P(\text{theory}|\text{data}) \propto P(\text{data}|\text{theory})P(\text{theory}) \quad (3.6)$$

where “theory” represents the *a-priori* model of the flux; our hypothesis, “data” is the $N_{\nu_e \rightarrow \nu_e}$. The $P(\text{theory})$ is $P(M)$ which is the prior probability of the *a-priori* model, and $P(\text{data}|\text{theory})$ is the probability to have gotten the $N_{\nu_e \rightarrow \nu_e}$ measured, given the *a-priori* model, which is now also as likelihood ($\mathcal{L}(N_{\nu_e \rightarrow \nu_e}|M)$).

¹⁰Neutrino scattering on electrons is mediated by the Z boson.

¹¹In this case, the number of the events is also corrected by the efficiency.

On the other hand, we know that the uncertainties of the flux parameters (focusing and hadron production) in each bin are multivariable Gaussian-distributed and follow the form presented in equation A.2 of appendix A. We can approximate our likelihood, given by,

$$\mathcal{L}(N_{\nu_e \rightarrow \nu_e} | M) = \frac{1}{(2\pi)^{n/2}} \frac{1}{\det(V_N)^{1/2}} \exp\left(-\frac{1}{2}(N - M)^T V_N^{-1} (N - M)\right), \quad (3.7)$$

where n is the number of bins of the distribution, N is the vector of the bins of the measured data ($N_{\nu_e \rightarrow \nu_e}$), M the vector of bins of predicted by model M , V_N is the total data uncertainty covariance matrix.

The constrained and unconstrained (from *a priori*) flux are shown in Figure 3.15, where the **mean** constraint the weighted Probability Distribution Function (PDF) is down by 9.6%, and the root mean square **RMS** is lowered by 53% in ME, the number for LE are **mean** (9% down) and **RMS** (40% lower), the reason is because in ME we have more statistics than LE. In addition (right plot in Figure 3.15), we can see the lower flux uncertainty compared with the unconstrained flux.

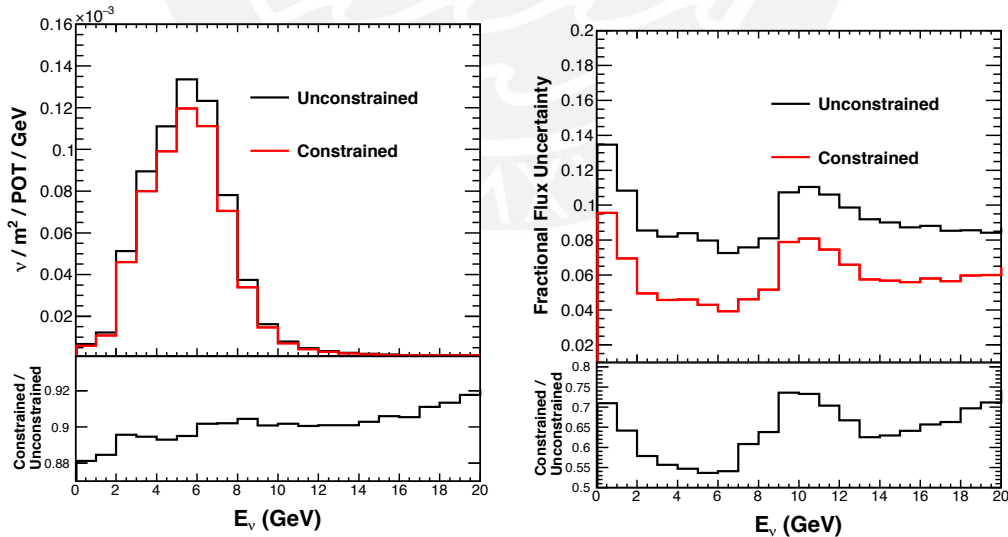


Figure 3.15: Neutrino flux constraint in ME (left plot), effect of the neutrino scattering on electrons constraint in the flux uncertainty (right plot). Figure taken from [205].

Another observation that we can make is that the flux uncertainty reduction is more prominent, on average, in the neutrino energy region $E_\nu < 10$ GeV. We will only consider the constraint described above for the double differential cross-section measurement presented in this thesis. However, the region greater than 10 GeV can be constrained with another standard candle[209]. The recent analysis uses the Inverse Muon Decay (IMD), which constrains higher neutrino energy by following less neutrino-electron scattering analysis. The IMD results are shown in Figure 3.16.

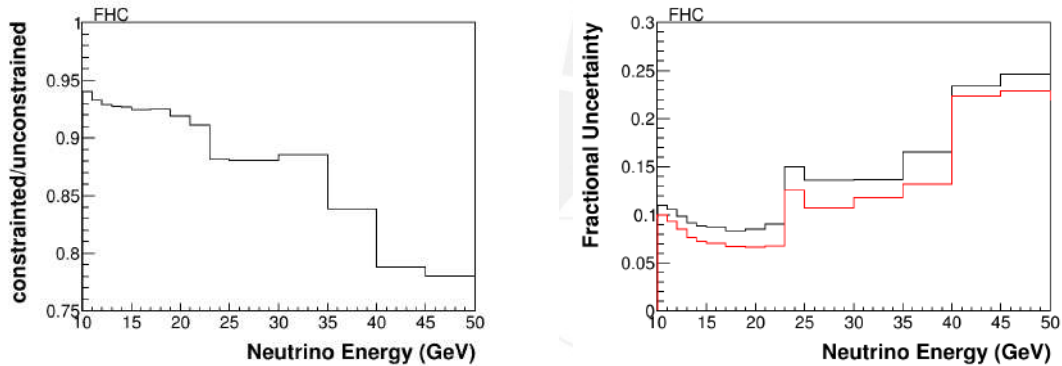


Figure 3.16: Neutrino mode flux ratio of constrained over unconstrained (left) and the uncertainties constraint (right), before constraint in black, and after constraint in red for Inverse Muon Decay. Figure taken from [209].

3.6 Flux, Low Hadronic Recoil, and Detector Energy Scale

Another method to handle the flux is denominated “low- ν ”, which is studied in detail by [210] in LE and extended to high energy in [211]. This “low- ν ”, is another standard candle, which is a low hadronic recoil CC interaction with cross-section approximately constant versus neutrino energy. Low- ν have been used to measure the shape of neutrino fluxes as a function of neutrino energy. A demonstration of measurement of the parameters of neutrino flux is studied in [201].

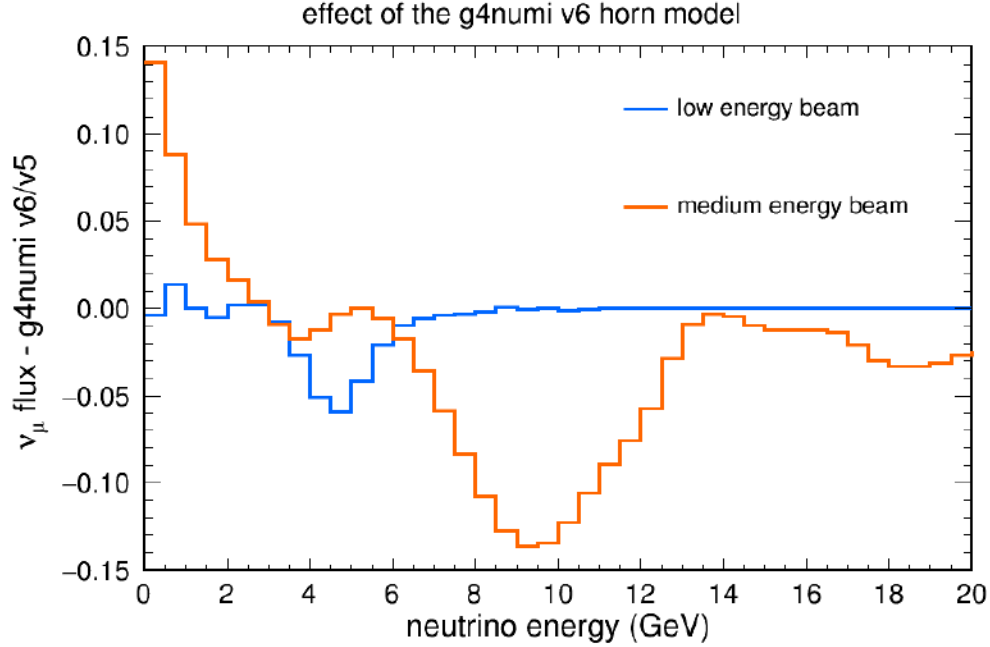


Figure 3.17: Horn model comparison in LE and ME. Figure taken from [181]

In the previous studies of the flux [181], ME flux showed sensitivity to alignment parameters as shown in Figure 3.17. Similar behavior was found with “low- ν ” analysis (see back ratio histogram in [201]), and that discrepancy can also be due to the detector energy scale. The study concluded that the discrepancy is more consistent with a 3.6% shift to the MINOS muons energy scale (see blue ratio histogram in Figure 3.18).

Finally, as the conclusion of this chapter, the neutrino flux used to measure the double differential cross-section (see Chapter 7) has the improvements developed by MINERvA. First, it has the corrections with external data for the hadron production and one sigma shift in the focusing uncertainties [200]¹². Second, the flux is constrained by the neutrino electron scattering analysis [205]. Third, a 3.6% shift in the MINOS muons energy scale is added thanks to the low- ν study[201]. On the other hand, the IMD[209] is not taken into account for the coming measurement.

¹²All improvements are in a package called PPF (Package to Predict the FluX)

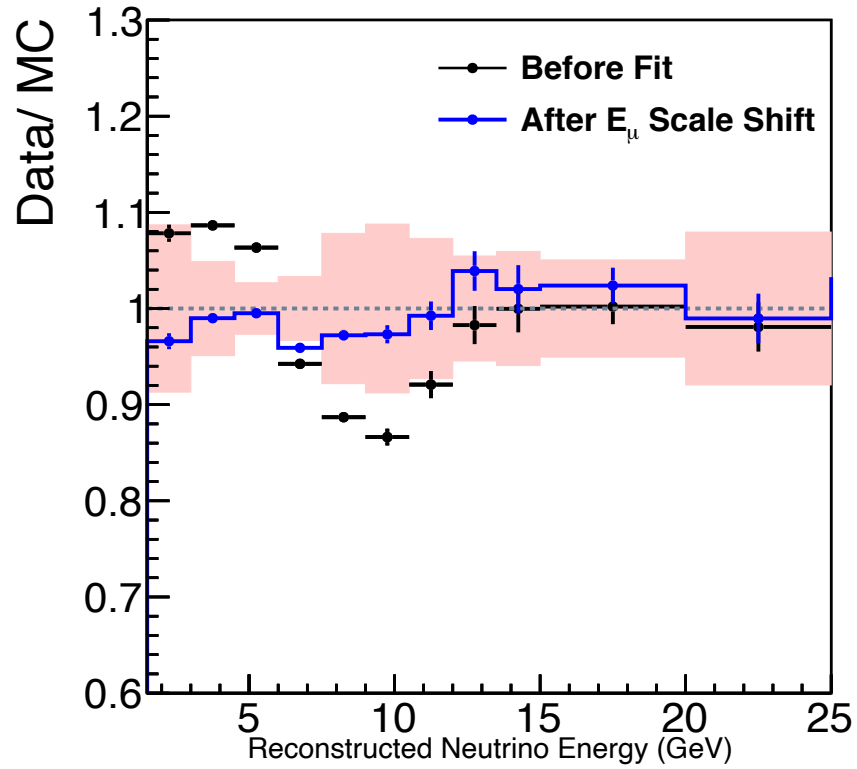


Figure 3.18: Ratio of low- ν events of data over simulation. With before and after of the muon energy scale correction (shifted by 3.6% from its nominal value). Figure taken from [201].

CHAPTER 4

MINER ν A EXPERIMENT

MINER ν A (Main Injector Experiment for ν -A) is a neutrino-nucleus scattering experiment proposed 75 years after Pauli's letter [212]. The detector is located on-axis in the NuMI underground hall¹ at Fermilab, Batavia, IL, USA. The MINER ν A goal is to perform precision studies of neutrino-nucleus scattering with high statistics in both channels, FHC and RHC, with different nuclei in a few-GeV region². The variety of target elements in MINER ν A allows exploring the nuclear effects. As we mentioned in the introduction, oscillation experiments require a good understanding of the neutrino cross-section to determine, mass hierarchy, probe CP violation, or other new physics that can be hidden behind neutrinos.

The neutrinos from the beam interact with MINER ν A's fine-grained

¹100 m below the surface.

²Started with LE with peak of neutrino energy distribution around 3 GeV (2010-2012) and the ME in ~ 6 GeV (2012-2019).

detector [213], which consists of hexagonal modules situated longitudinally of the beam into several regions like nuclear targets, the scintillator tracker, and downstream electromagnetic and hadronic calorimeters. The support structure is composed of an outer detector and a frame of steel with an embedded scintillator. The nuclear target region contains five solid passive targets of carbon (C), iron (Fe), and lead (Pb), separated from each other by 4 and 8 scintillator planes for vertex and particle reconstruction. The tracker is made solely of scintillator planes. Each hexagonal plane of the tracker is composed of 127 nested polystyrene scintillator strips of length 2.45 m and a triangular cross-section of base of 3.3 cm and height of 1.7 cm.

In addition, MINERvA uses MINOS Near Detector as a magnetized muon spectrometer [214], and it is located two meters downstream of the MINERvA detector. The design of the experiment is represented in Figure 4.1, where the beam comes from the MINERvA side.

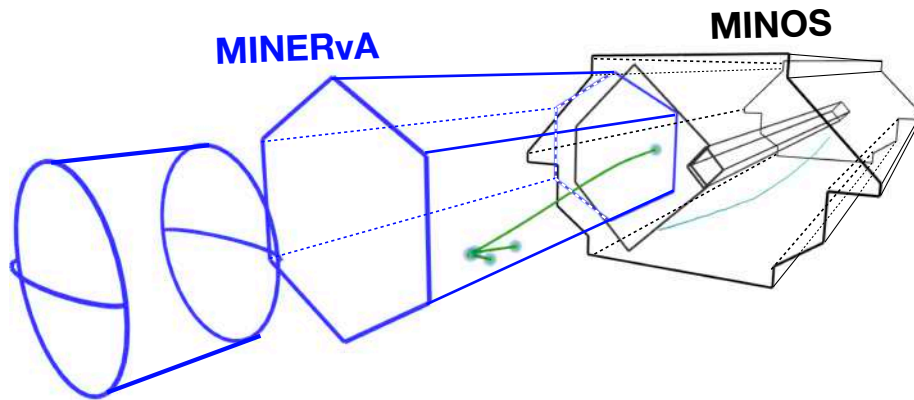


Figure 4.1: Scheme of the whole experiment, in blue represents MINERvA detector and in black MINOS magnetized Near Detector. In the example there is a neutrino event in MINERvA and curved track in MINOS. Figure based on [215].

4.1 MINERvA Detector

The MINERvA detector is composed of the veto wall, the helium target, and the main detector. The latter is subdivided into the nuclear region, tracker region, downstream electromagnetic, and hadronic calorimeter (ECAL and HCAL). Those four detectors compound the so-called inner detector (ID). The outer detector (OD) is a support structure made by the hadronic calorimeter (see the top sub-figure of Figure 4.4). The detector size comparison and the details mentioned above are shown in Figure 4.3.

The MINERvA coordinate system is shown in Figure 4.2, where the z-axis is defined as the horizontal central axis of the detector and points downstream to the MINOS detector. The y-axis points upward, and the x-axis leads to the left of the beam. The angle of the beam with respect to the z-axis in the y-z plane is 3.34° . MINOS, in this system, is located 1200 cm downstream of the MINERvA center.

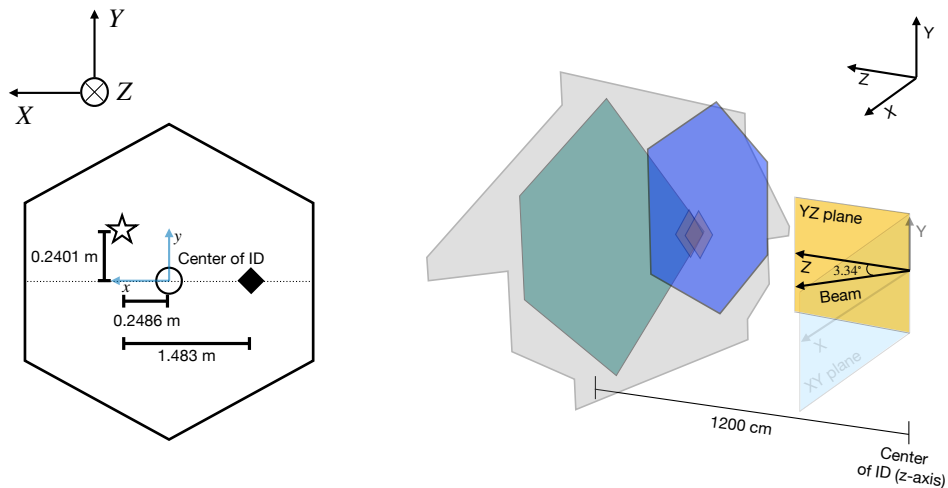
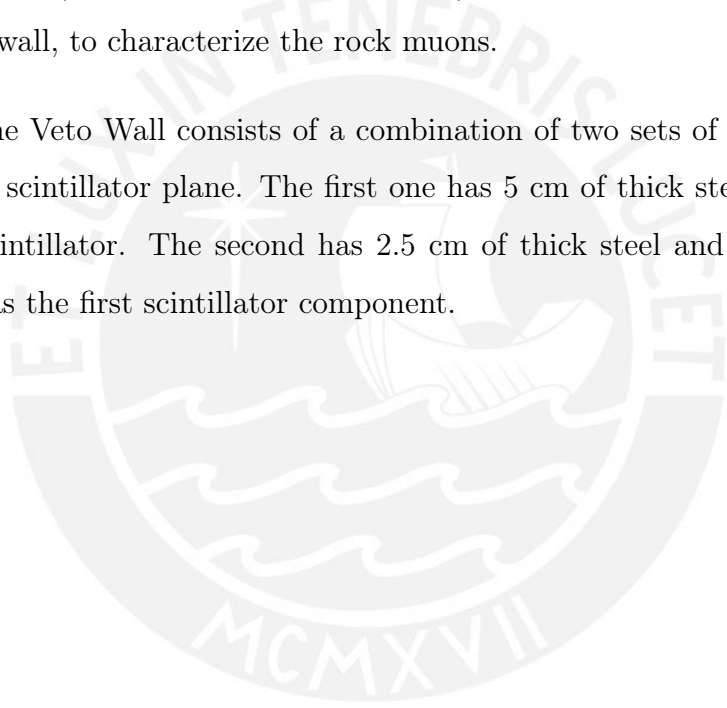


Figure 4.2: MINERvA coordinates. Left figure shows the ID center or MINERvA center (circle), the MINOS coil (black filled diamond), and the beam centroid (star). Figure based on [215, 213, 216]

Veto Wall

In the neutrino beam production chapter, we saw that the last stage to produce the neutrino flux is filtering the charged leptons; as we can see in Figure 3.3, filters are rock, and they are upstream of the MINERvA detector. However, the neutrino can see the same rocks as though target and therefore interact and produce hadron and charged leptons or the so-called “rock muons”. We have to characterize them because they will contaminate our signal, especially for more upstream targets such as the helium target. So, MINERvA employs a plane structure (green structure in Figure 4.3) upstream of the helium target, called veto wall, to characterize the rock muons.

The Veto Wall consists of a combination of two sets of a thick steel plate and a scintillator plane. The first one has 5 cm of thick steel and a 1.9 cm thick scintillator. The second has 2.5 cm of thick steel and is the same dimension as the first scintillator component.



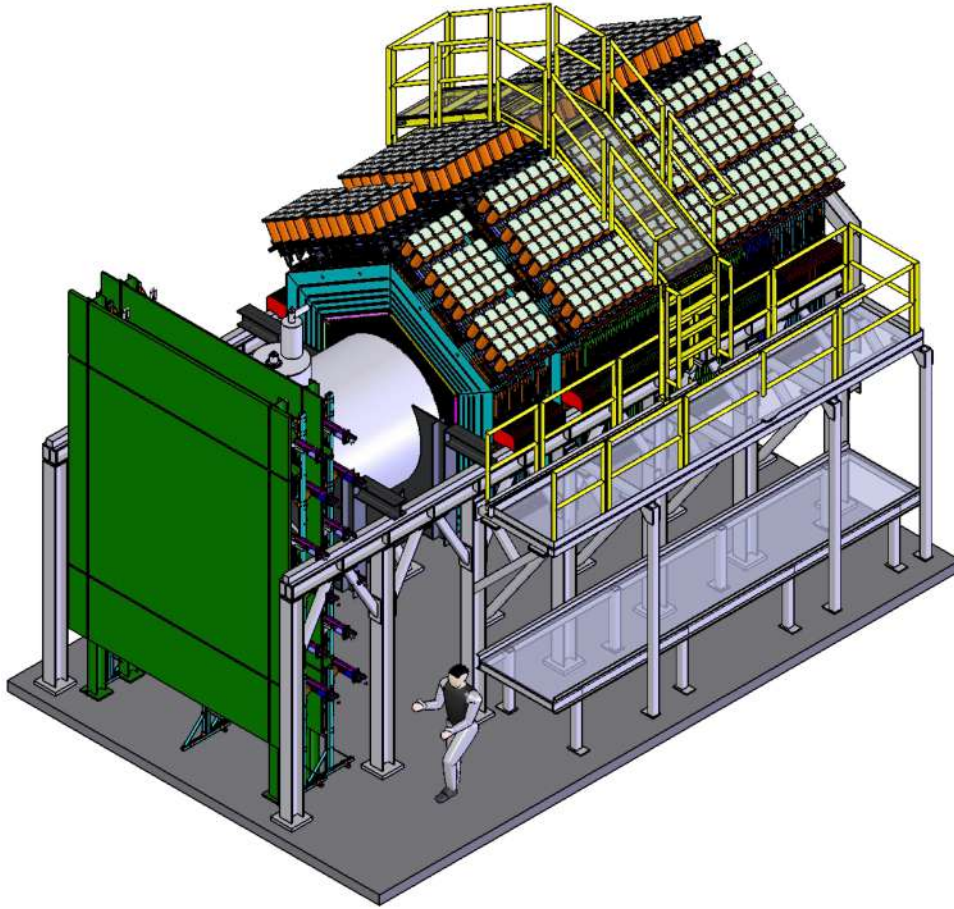


Figure 4.3: Size comparison of the MINERvA detector shown in from the veto wall (green plane in front), followed by the helion target and the main detector. Figure taken from [217]

Nuclear Target Region

After the Veto Wall, still upstream, we have the nuclear targets. The first target is helium, which is filled in a cryogenic vessel. And it uses several instruments to maintain the helium, such as pressure, temperature and others (see details in section 2.5. of [213]). The helium target is represented as a green tank in Figure 4.4.

The next part, after the helium target, is a set of different targets. MINERvA experiment is the only multi-nuclear target experiment; in total, five layers of passive material are interspersed with four tracking modules, and

4.1. MINERVA DETECTOR

each module is made of eight scintillator planes. As can be appreciated in the lower subfigure of Figure 4.4, the bluish region is labeled the nuclear targets region. In addition to that, between targets 3 and 4, there is a water target (see Figure 4.5).

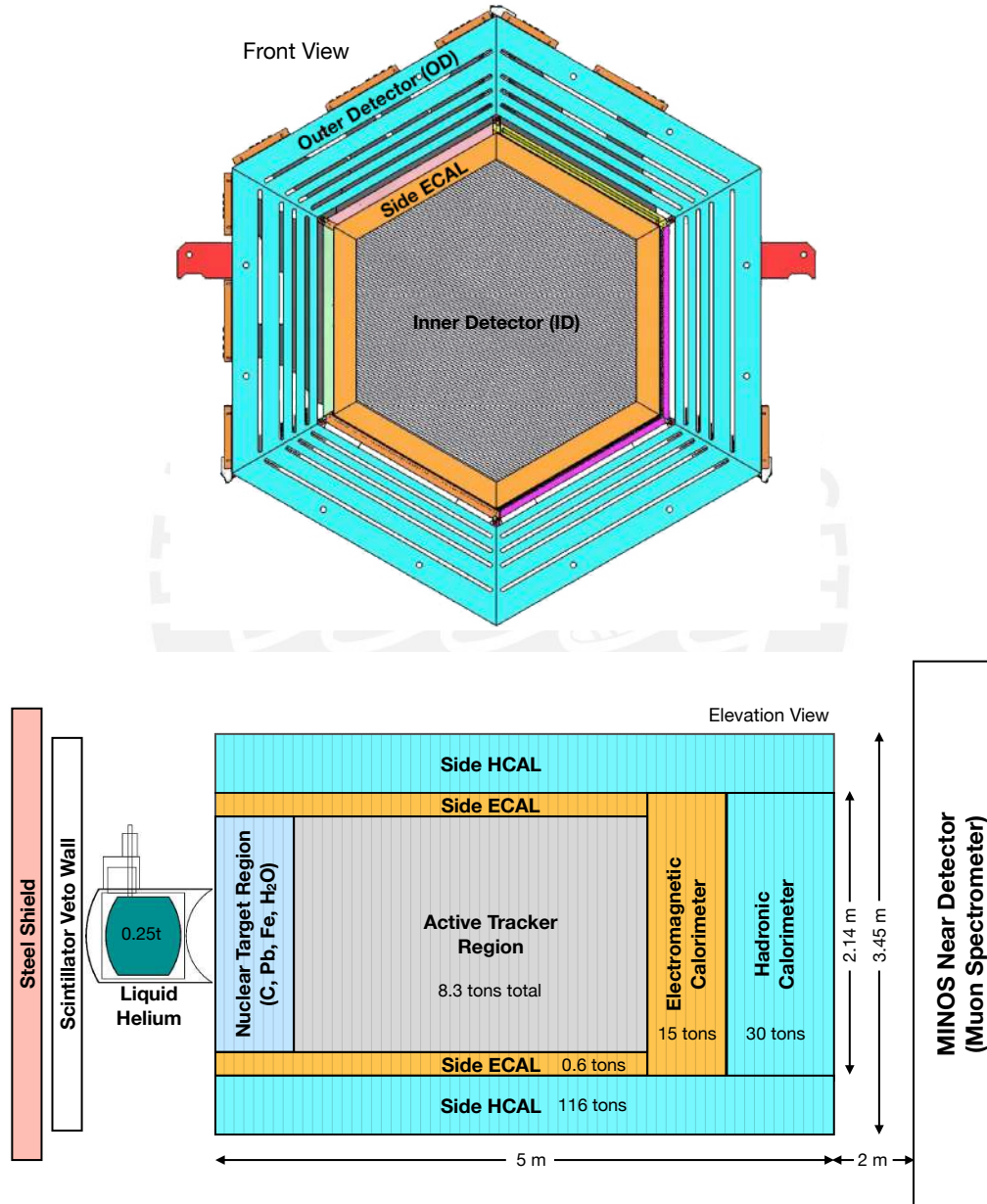


Figure 4.4: Scheme of MINERvA detector [213].

The targets are constructed by combining pieces of Graphite, Steel,

4.1. MINERVA DETECTOR

and Lead. The density of the pieces is $1.74 \pm 0.01 \text{ g/cm}^3$ for Graphite, $11.29 \pm 0.03 \text{ g/cm}^3$ for Lead, and $7.83 \pm 0.03 \text{ g/cm}^3$ for Steel. The Graphite is compounded by more than 99.5% of Carbon (C); the Steel is compounded by 98.7% of Iron (Fe), 0.2% of Silicon (Si), 0.13% of Carbon (C), and 0.1% of Manganese (Mn); and the Lead is compound by 99.95% of Lead (Pb) and Copper 0.05% (Cu).

Target	z-location (cm)	Thickness (cm)	Fiducial Area (cm ²)	Fiducial Mass (kg)	Total Mass (kg)
1-Fe	452.5	2.567 ± 0.006	15999	322	492
1-Pb	452.5	2.578 ± 0.012	9029	263	437
2-Fe	470.2	2.563 ± 0.006	15999	321	492
2-Pb	470.2	2.581 ± 0.016	9029	263	437
3-Fe	492.3	2.573 ± 0.004	7858	158	238
3-Pb	492.3	2.563 ± 0.004	3694	107	170
3-C	492.3	7.620 ± 0.005	12027	160	258
Water	528.4	17-24	25028	452	627
4-Pb	564.5	0.795 ± 0.005	25028	225	340
5-Fe	577.8	1.289 ± 0.006	15999	162	227
5-Pb	577.8	1.317 ± 0.007	9029	134	204

Table 4.1: Target z-location, thickness, fiducial area, fiducial mass, and total mass. The location follows the MINERvA coordinate system shown in Figure 4.2. Table taken from [213].

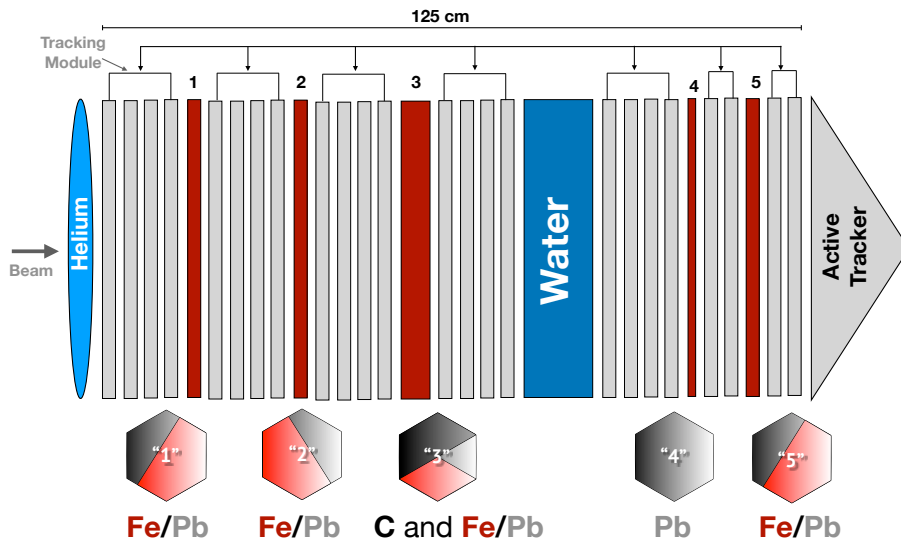


Figure 4.5: Nuclear targets scheme. Figure based on [213] and [217].

Other parameters of the targets, such as the z-position, thickness, fiducial area, fiducial mass, and total mass, are summarized in Table 4.1. The scheme of the targets is illustrated in Figure 4.5 and follows the color scheme of the target column of Table 4.1, as well as the orientation of the nuclear targets (lower part of the figure).

Finally, the water target consists of a circular steel frame between targets 3 and 4. The diameter of the circular structure is larger than the ID, as can be appreciated in Figure 4.6. A detailed description of this target can be found in section 2.4 of [213].

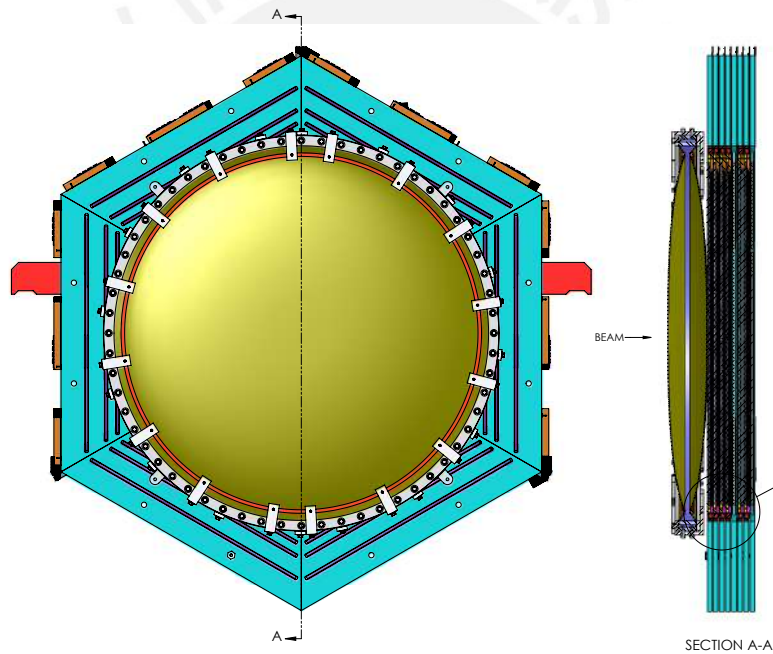


Figure 4.6: Water target configuration. Figure taken from [213]

Tracker Region

The next region after the nuclear region downstream is the tracker region. It consists of hexagonal scintillator modules where each is made of two planes. The scintillators plane is built by 127 nested polystyrene scintillator strips of length 2.45 m and a triangular cross-section of base of 3.358 cm and height

4.1. MINERVA DETECTOR

of 1.7 cm (see left sub-figure of Figure 4.8). The strips are glued with 3M-DP190 translucent epoxy. On top of that, the planes are covered by a sheet of Lexan, attached with 3M-DP190 gray epoxy. Finally, black PVC electrical tape surrounds the plane to avoid any light leak.

The density and chemical composition of the plane are summarized in Tables 4.2 and 4.3.

Material	Density (g/cm ³)	H	C	N	O	Al	Si	Cl	Ti
Scintillator	1.043 ±0.002	7.6%	92.2%	0.06%	0.07%	-	-	-	-
Coating	1.52	6.5%	78.5%	-	6.0%	-	-	-	9.0%
Lexan	1.2	6.7%	66.7%	-	26.7%	-	-	-	-
PVC tape	1.2	4.8%	38.7%	-	-	-	-	56.5%	-
DP190	1.32	10.0%	69.0%	2.6%	17.0%	-	-	0.5%	-
transl. DP190	1.70	5.0%	47.0%	1.7%	27.0%	6.0%	6.0%	0.05%	-
gray									

Table 4.2: Material density and percentage of chemical composition. Table taken from [213].

Component	H	C	O	Al	Si	Cl	Ti
Strip	7.59%	91.9%	0.51%	-	-	-	0.77%
Plane	7.42%	87.6%	3.18%	0.26%	0.27%	0.55%	0.69%

Table 4.3: Component of strip and plane. As well as the percentage of chemical composition. Table taken from [213].

The planes alternate between three orientations, 0° and $\pm 60^\circ$ around the beam axis, allowing an accurate three-dimensional reconstruction. The 0° is denominated “X” plane, the “U” is rotated 60° with respect to the X plane, and the “V” rotated counterclockwise from the X plane. An illustration of the plane rotations and “VX” and “UX” can be found in Figure 4.7.

In order to perform the measurement the target mass used in the

fiducial volume is carbon (88.51%), hydrogen (8.18%), oxygen (2.5%), titanium (0.47%), chlorine (0.2%), aluminum (0.07%), and silicon (0.07%).

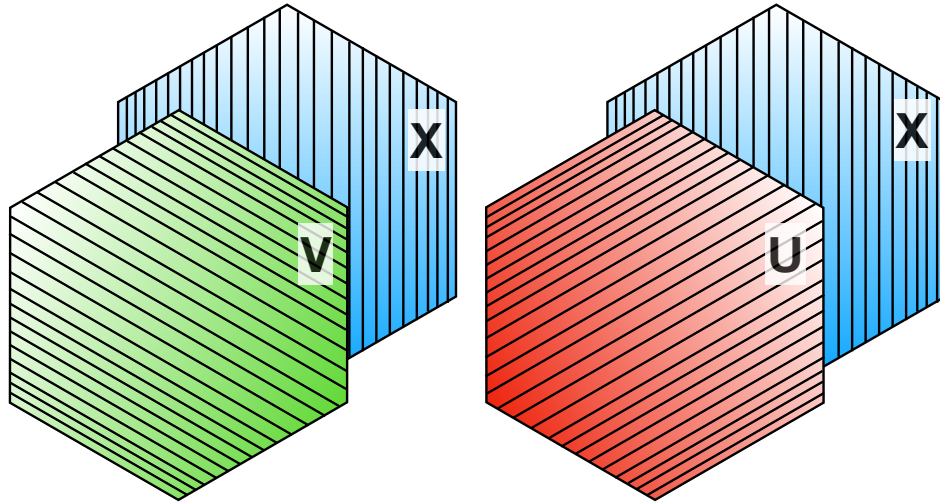


Figure 4.7: Plane orientation, “VX” view on left and “UX” on the right side.

Electromagnetic Calorimeter

The Electromagnetic Calorimeter (ECAL) is located downstream of the tracker region and is built by ten modules. Each module of the ECAL configuration follows pretty much the tracker region. The difference is in the 0.2 cm thick sheet of lead shielding the whole scintillator plane. As it is shown in Figure 4.4, it extends to sides, but it does not extend to OD.

Hadronic Calorimeter

The Hadronic Calorimeter (HCAL) region is located downstream of ECAL, and it has 20 modules. The HCAL configuration is similar to the tracker and ECAL region; the difference is the 2.54 cm thick hexagonal steel. The scintillator planes that alternate the HCAL have the VXU view. In contrast to ECAL, it extends to OD.

4.2 Optical Arrangement of MINERvA Detector

The MINERvA detection system is based on scintillation. We saw in the tracker part that strip scintillators make the planes; also, we saw its dimen-

4.2. OPTICAL ARRANGEMENT OF MINERVA DETECTOR

sions and materials (see Table 4.3). This section will be focused on how the light of charged particles produced by the neutrino interaction that passes through the scintillator strip is collected. In the middle of each scintillator bar, a wavelength-shifting fiber sends light through an optical cable to photomultiplier tubes (PMT) (see right side sub-figure of Figure 4.8). The PMT is fixed on top of the detector inside of a container.

The scintillators are made from polystyrene pellets doped with 1% of 2,5-diphenyloxazole (PPO) and 0.03% of 1,4-bis (5-phenyloxazol-2-yl) benzene (POPOP) [213]. On the other hand, the wavelength shifting (WLS) fiber has mirrored the unread end (the mirrored procedure is described in [213]).

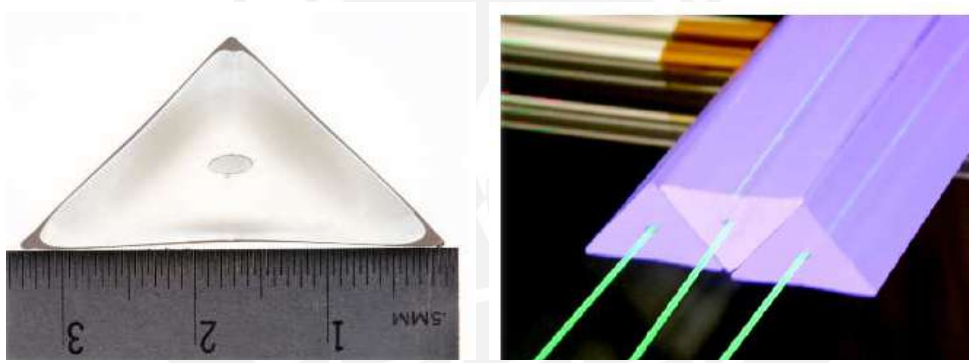


Figure 4.8: Scintillator strips used in MINERvA. Figure taken from [213]

The basic description of the PMT could be a device that collects the photon, which converts with photocathode into an electron by the photoelectric effect. Then this electron is amplified many times before detecting the signal. Figure 4.9 shows the incoming photon hitting the photocathode, and an electron is created. After that, the electron is focused by the focusing electrode to hit the dynode, by which it will generate more electrons. Finally, at the anode, we end up with a large number of electrons. The device which houses the dynodes is a vacuum tube to avoid any air molecules.

The MINERvA detector uses a 64-anode (8×8 array of pixels laid

4.2. OPTICAL ARRANGEMENT OF MINERVA DETECTOR

out) H8804MOD-2 Hamamatsu photo-multiplier tube, which is represented in a scheme in Figure 4.10. The similar PMT is used in MINOS experiment. In total there are 32,000 scintillator strips and 507 PMTs used in MINERvA experiment [213].

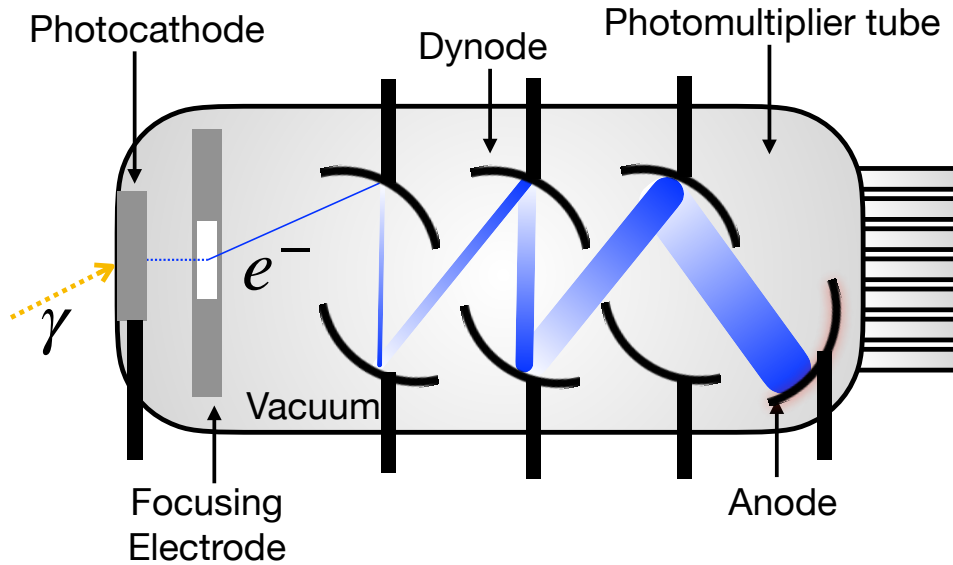


Figure 4.9: Basic working principle of photo-multiplier tube (PMT).

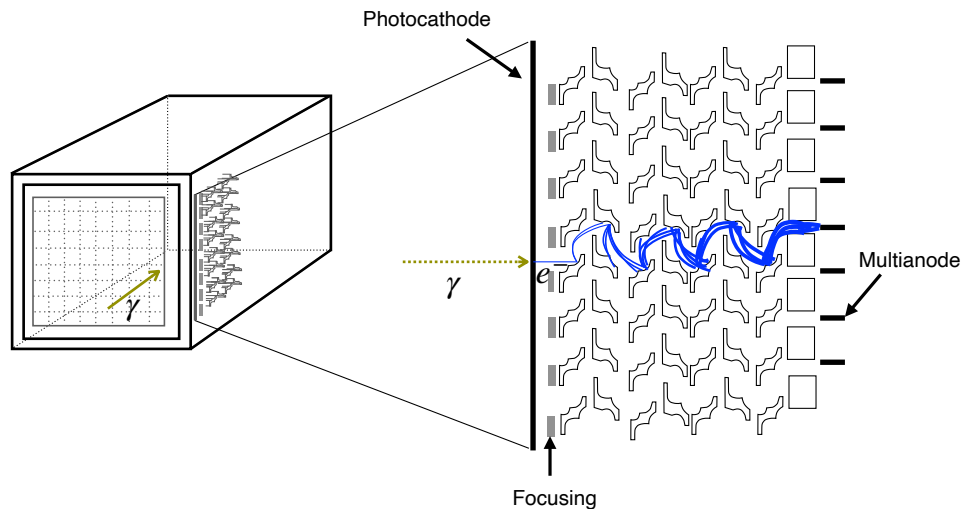


Figure 4.10: Multi-anode photo-multiplier tube (PMT), similar one used in MINERvA. Figure based on [218].

4.2. OPTICAL ARRANGEMENT OF MINERVA DETECTOR

A schematic description of the scintillator strips using the Wavelength Shifting Fibers and PMT coverage is shown in Figure 4.11. The raw signals from the PMTs are fed to a board placed at the end of each PMTs. The board is called a front-end board (FEB) and it digitizes the coming pulse height and timing of the analog signal. In addition, it provides a high voltage (HV) to PMT. The main components of FEB are 4 TriP-ts for high and medium gain, and 2 TriP-ts for low gain. The TripP-ts are chips developed for DØ experiment [219]

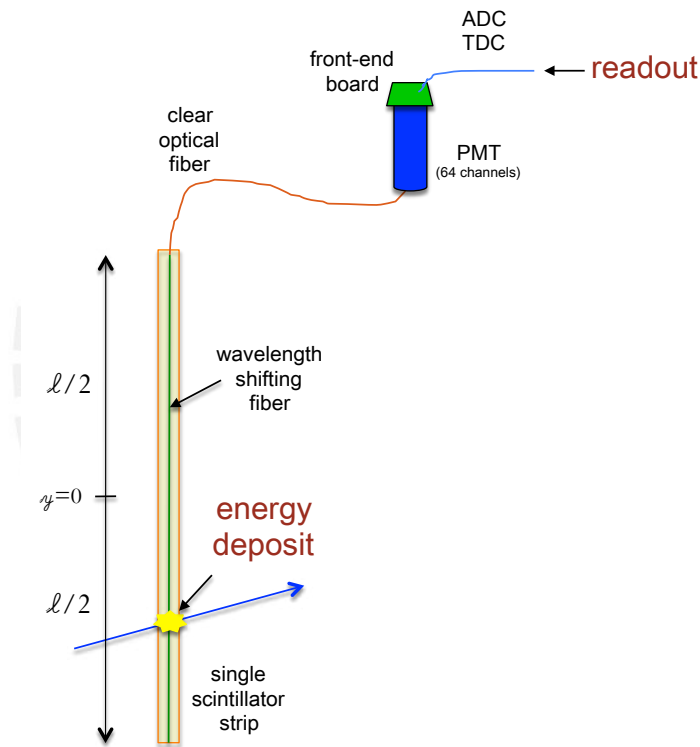


Figure 4.11: Scheme of the scintillator strips, fiber optic and PMT used in MINERvA experiment. Figure taken from [213]

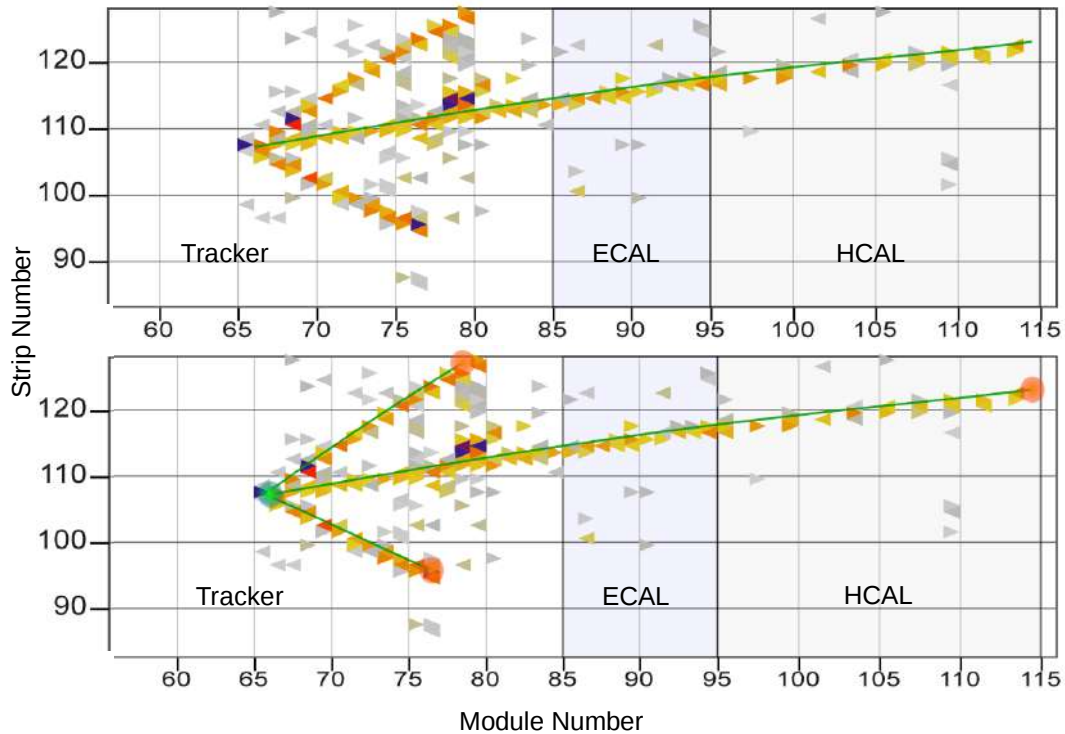


Figure 4.12: Event in MINOSvA detector. Figure taken from [213]

4.3 MINOS Near Detector

In order to determine the helicity of the neutrino by determining the curvature in a magnetized detector MINOSvA uses MINOS near detector (ND). MINOS is located downstream of MINOSvA at 2.1 m, as is shown in Figure 4.1. Similar to MINOSvA, MINOS is also in an on-axis experiment. The total mass of MINOS is 1kTon, and it is composed of a tracker calorimeter that has planes of magnetized iron and a scintillator (see Figure 4.13 and 4.14). The curvature discussed above helps determine the sign of the charged particle, in this case, the muon sign, to determine the helicity of the neutrino in MINOSvA. The magnetic field in a usual operation keeps the same as NuMI focusing system.

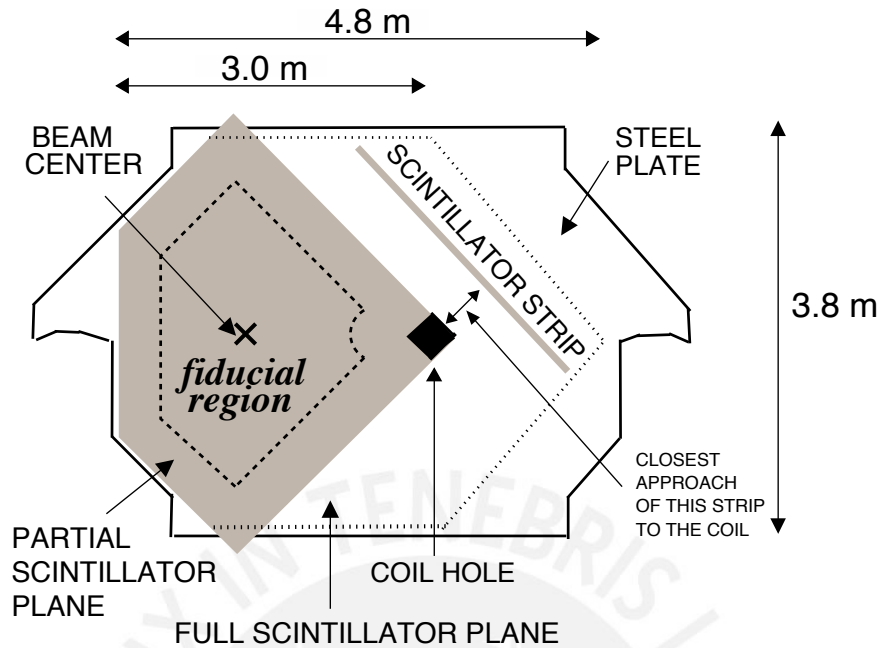


Figure 4.13: Schematic description of MINOS ND detector. Figure taken from [213]

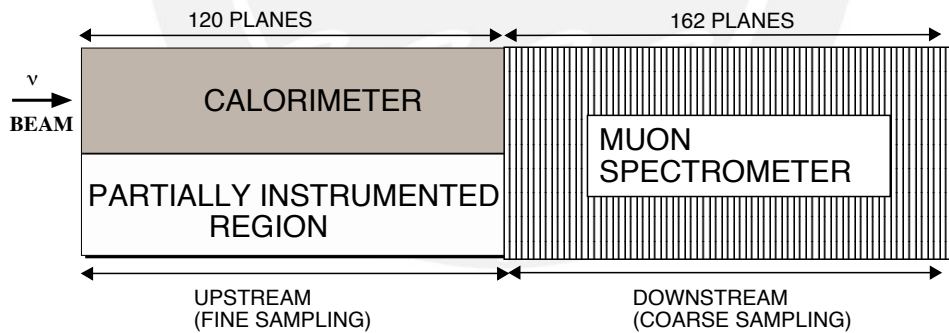


Figure 4.14: Schematic description of MINOS ND detector. Figure taken from [213]

MINOS ND has in total 282 steel plates with 2.54 cm of thickness each. Of the total plates, 152 are instrumented with scintillator planes like MINERvA, where each plane is 1cm thick. Comparable to MINERVA, the planes are made of 4.1 wide strip scintillator oriented $\pm 45^\circ$ with respect to

4.3. MINOS NEAR DETECTOR

the vertical. They are alternated with other planes with $\pm 90^\circ$ orientations. MINOS calorimeter region has 120 planes with scintillators planes with the partial instrumented area. The Muon spectrometer has 162 planes, and it does not have a partial instrumented region. The magnetic field distributions along the MINOS detector are shown in Figure 4.15.

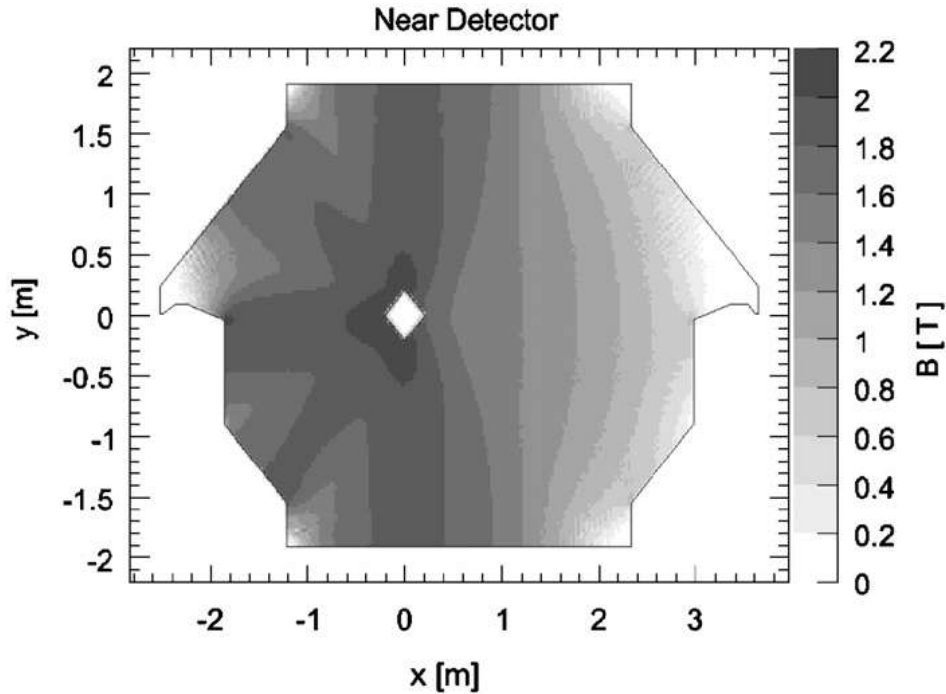


Figure 4.15: MINOS ND magnetic field distribution. Figure taken from [214].

A detailed description of the MINOS detector is found in [214]. On the other hand, the description of the on-site calibration (Hit Calibration Chain, Ex-situ and In situ Calibrations) of the MINERvA detector is fully described in chapters 5 and 6 of [213].

CHAPTER 5

ν_μ LOW RECOIL ANALYSIS IN MEDIUM ENERGY

The muon neutrino Low Recoil analysis refers to an inclusive charged current analysis sample at a low three momentum transfer¹. The analysis is performed mainly in the tracker region and part of the ECAL of the MINERvA detector and uses the Medium Energy neutrino flux from NuMI. The Low Energy version for neutrino and antineutrino were presented by the MINERvA collaboration [220, 221]. The low recoil analysis is developed in 2D. It comes from the following reason, in Q^2 -only kinematic, for instance, the RPA and 2p2h (MEC) effects are hard to distinguish [222]; those first effects are studied in the neutrino mode at Low Energy [220].

The primary motivation of this analysis, and the previous analysis,

¹We are considering the three-momentum transfer (q_3) up to 1.2 GeV.

is to study the nuclear effects in neutrino-nucleus interactions. At low three-momentum transfer, reach regions are overlapping, which we can explore with a proper kinematic definition using the flux—such regions like between QE and Delta ($\Delta(1232)$), the so-called “dip” region.

5.1 Kinematic Definition

The kinematic variable used in the Low Recoil analysis is the magnitude of three-momentum $q_3 = \vec{q}$ and hadronic available energy E_{avail} . The reason comes from the first studies of nuclear effect in charged lepton scattering in which it was needed to separate the QE and Delta contributions. One way to differentiate them is using the energy transfer q_0 and q_3 to the nucleus. On the other hand, the reconstruction of q_0 needs model-dependent corrections and involves other problems². Because of that, the E_{avail} is defined, and it is around similar to q_0 but less model-dependent.

To have q_3 and E_{avail} first, we need to reconstruct neutrino energy (E_ν). The E_ν uses the hadronic energy and muon kinematics,

$$E_\nu = E_\mu + q_0, \quad (5.1)$$

and given the equation 5.1, the Q^2 is defined by,

$$Q^2 = 2E_\nu(E_\mu - p_\mu \cos \theta_\mu) - M_\mu^2, \quad (5.2)$$

where E_μ , p_μ , θ_μ , and M_μ , are the muon energy, muon momentum, muon scattering angle and muon mass respectively. Finally with the equation 5.2, the q_3 is defined,

$$q_3 = \sqrt{Q^2 + q_0^2}. \quad (5.3)$$

On the other hand, the hadronic available energy is defined by

$$E_{\text{avail}} = \sum T_p + \sum T_{\pi^\pm} + \sum E_{\text{particles}}, \quad (5.4)$$

²The q_0 also involves neutrons which are almost invisible in the detector, and the other problem similar to mass invariant variable W is at the time to unfold to true distributions.

where $\sum T_p$ is the proton kinetic energy, $\sum T_{\pi^\pm}$ is the pion kinetic energy, and

$$\sum E_{\text{particles}} = \sum E_{K^\pm} + \sum E_{e^\pm} + \sum E_{\pi^0} + \sum E_\gamma + \sum E_{\text{other}} \quad (5.5)$$

where E_{other} is primary eta mesons. In summary $\sum E_{\text{particles}}$ is the total energy of other particles except neutrons.

5.2 Signal Definition

The signal cuts applied to the analysis are:

1. The events should be charged current (CC)³.
2. The muon scattering angle should be $\theta_\mu < 20^\circ$.
3. The muon momentum is $1.5 < p_\mu < 20.0$ GeV.

The cuts guarantee that the event matches with MINOS ND.

5.3 Data and MC Sample

The MINERvA medium energy (ME) data is analyzed with the ME Monte Carlo (MC) production. In addition, the total MC has a sub-sample of extended Meson Exchange Current (MEC) of the Valencia model, which is extended to $q_3 = 2.0$ GeV from the default production ($q_3 = 1.2$ GeV). The Protons on Target (POT) for total data is $1.06081\text{e}+21$, MC $4.97942\text{e}+21$, MC (2p2h extended) $2.16016\text{e}+22$. The MC and data process is divided into subsets called “playlists” due to intensity dependence in the ME run [223]. The playlists POT are described in Table 5.1.

The default MC is GENIE v.2.12.6 [224], in addition, has some weights to form the MnvTune.v1.2⁴.

³We select events with muon track in MINERvA and MINOS ND.

⁴The MnvTune.v1.2 is based on MnvTune.v1 introduced in the ME era [225] plus the suppression of LE pion coherent production

- A Central Values (CV) is adjusted with flux corrections coming from PPFX package [200], then a neutrino-electron constraint is applied to the CV and to the flux uncertainty [205]. In addition, the simulation has the muon kludge correction or muon scale [201].
- The Valencia RPA suppression [226, 227] applied as a weight to QE events [227].
- The non-resonant pion weight [228, 229] based on reanalysis of bubble chamber data [230, 231].
- The suppression of coherent production of pions with kinetic energy below 450 MeV based on MINERvA data [232].
- The simulate 2p2h events using the Valencia 2p2h model [233, 234, 235]. These were already part of the model used in [220]. To better describe these data compared to the previous result, the 2p2h event rate is enhanced in the kinematic region between QE and Δ reactions, first described in [221]. In addition, an extended sample ($q_3 < 2.0$ GeV) was added to remove the unphysical events at high q_3 (see Appendix F).
- Finally, two more weights are added to correct errors in the GENIE FSI elastic scattering and pion absorption models [236].

5.3. DATA AND MC SAMPLE

Playlist	Data	MC Generic	MC(2p2h ext.)
minervaME1A	8.98778e+19	4.07556e+20	1.88529e+21
minervaME1B	1.86922e+19	1.09583e+20	4.97236e+20
minervaME1C	4.29215e+19	2.05467e+20	8.99785e+20
minervaME1D	1.44357e+20	6.08278e+20	2.49546e+21
minervaME1E	1.03145e+20	5.09476e+20	2.49236e+21
minervaME1F	1.67465e+20	7.07948e+20	2.9936e+21
minervaME1G	1.38121e+20	5.92289e+20	2.41426e+21
minervaME1L	1.3399e+19	5.80679e+19	4.76996e+20
minervaME1M	1.58635e+20	8.99976e+20	3.99735e+21
minervaME1N	1.07385e+20	5.13728e+20	1.47458e+21
minervaME1O	2.98369e+19	1.5843e+20	9.86482e+20
minervaME1P	4.69792e+19	2.08622e+20	9.8819e+20

Table 5.1: Protons on target for different data sets.

In the current study, there are two different binning for E_{avail} . Binning I is constructed to study the different neutrino interaction models (coming chapter) and Binning II, in which the double differential cross-section measurement is presented. To define Binning II, we guarantee three critical things. First, the distribution resolution is around 1σ in the diagonal in the majority of the bins (migration matrix). Second, the dip region is distinguishable as well as the other contribution in which we are interested. Finally, binning does not present problems at the unfolding stage like Binning I does.

The q_3 binning in both Binning I and Binning II are same, and they are 6 bins. The total E_{avail} in Binning I is 17, and 11 for Binning II. The binning definition is given by:

Binning I

$$q_3[6] = \{0.0, 0.2, 0.3, 0.4, 0.6, 0.9, 1.2\} \text{ [GeV]}$$

$$E_{\text{avail}}[17] = \{0, 0.02, 0.04, 0.06, 0.08, 0.1, 0.12, 0.14, 0.16, 0.2, 0.25, 0.299, 0.35, 0.399, 0.499, 0.599, 0.799, 0.999\} \text{ [GeV]}$$

Binning II

$$q_3[6] = \{0.0, 0.2, 0.3, 0.4, 0.6, 0.9, 1.2\}[\text{GeV}]$$

$$E_{\text{avail}}[11] = \{0.0, 0.04, 0.08, 0.12, 0.16, 0.24, 0.32, 0.4, 0.6, 0.8, 1.0, 1.2\}[\text{GeV}]$$

5.4 Reconstruction Events with Nominal MC

The events that past the cuts are shown in Figure 5.1 as projections of q_3 pads. The MC breakdown used the true MC information.

The panels are distributed in such a way that the first two panels represent the low region of q_3 (from 0 to 0.3 GeV), the next panel represents the medium q_3 region (from 0.3 to 0.6 GeV), and the high q_3 region (from 0.6 to 1.2 GeV). The red histogram in Figure 5.1 is the total MC with the error band, which has statistical and systematic uncertainty. The blue, magenta, green, and orange histograms, are QE, $\Delta(1231)$, 2p2h with enhancement, and Other, which has mostly the other resonances, DIS, and a small sample of coherent events.

In Figure 5.1, we observe that the low q_3 region is dominated by QE and Delta dominates the following q_3 regions. Another important observation is that most of the low and medium regions do not match the data well. Therefore, new studies in those areas need to be done, and it is covered with detailed studies in the next chapter.

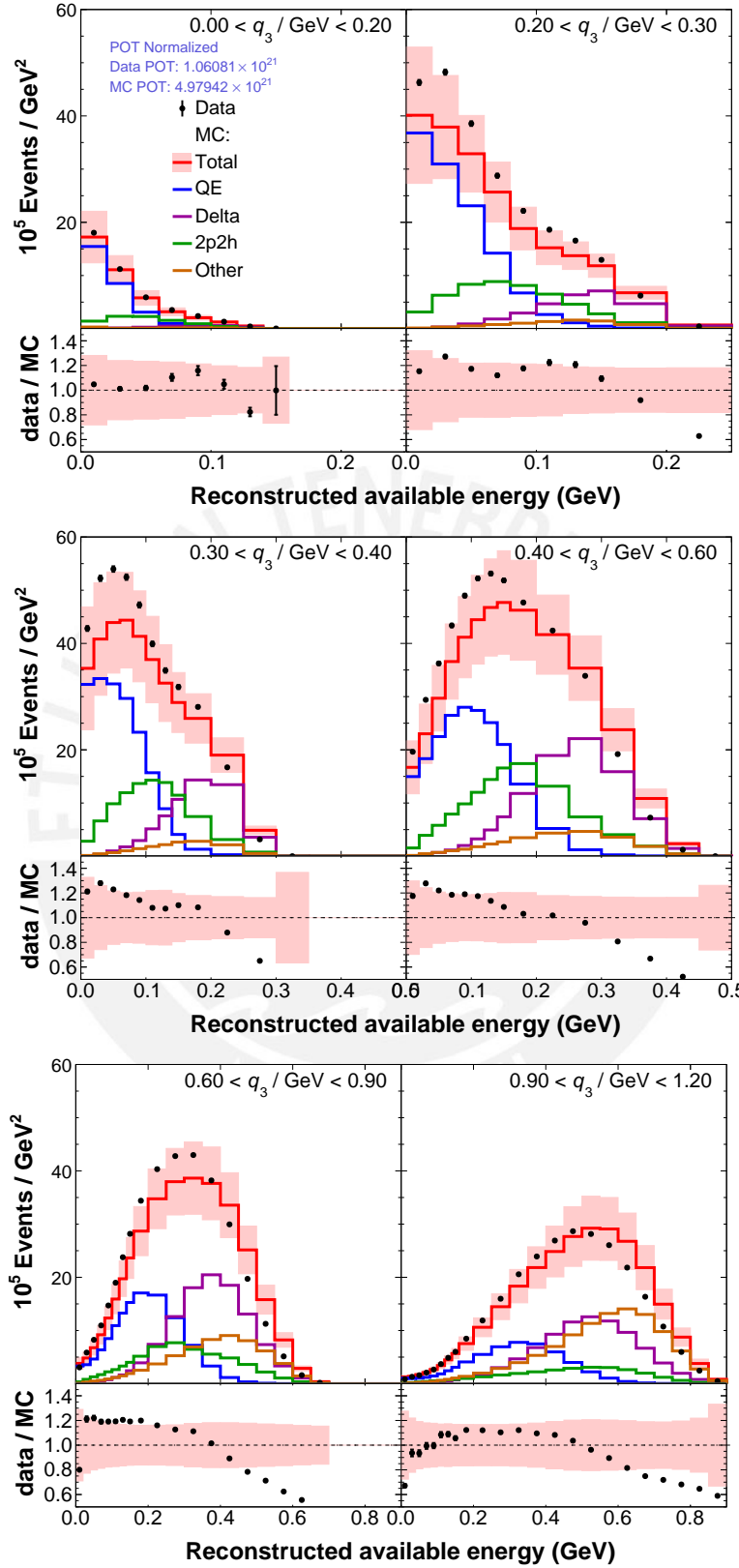


Figure 5.1: Event selection with MnvTune-v1.2 with the band coming from the MC systematic errors, the blue lines represent the QE MC events, green the MEC+2p2h fit, magenta the first resonance ($\Delta(1231)$) and in orange others which mostly are DIS event a small sample of coherent events. Page 110

CHAPTER 6

MODEL STUDY WITH LOW RECOIL SAMPLE

This chapter aims to study the different interactions from QE, and MEC, to the Resonant (RES) region. The QE region is studied with Bodek-Ritchie tail enhancement applied to QE events. The MEC region was studied with SuSA 2p2h which replaces the default MEC. Finally, the RES region is studied with the RES Removal energy, low Q^2 π suppression, the Berger-Sehgal SPP with RES Pauli-Blocking, the MK (Minoo Kabirnezhad) single pion production (SPP) model, and QE-RPA on RES events. There is one more study performed in the QE region (SuSA QE) which has been made available in GENIE 3.0.6 [237], but is not included in the main model's studies because we can only use muon kinematics in the reweight ¹.

¹An approximation version can be found in Appendix I. However, this must be used only for warping studies.

6.1 Bodek-Ritchie Tail Enhancement

GENIE's generation of neutrino event starts with picking a neutrino from flux distribution and a target with which the picked neutrino will interact. That scattering occurs with a single nucleon, then the effects of the bounded nuclei are added. There are several models for the motion of nucleons in the nucleus, which can depend on momentum distributions and removal energy, as shown in Figure 6.1. These momentum distributions or spectral functions are compared with Global Fermi Gas (GFG) [238]. GENIE uses GFG with extra incorporation of Short Range Correlation (SRC). The effect of this addition is the tail above Fermi Momentum (k_F) and it is appreciated in Figure 6.2 (the upper left plot for carbon) and the tail of Figure 6.4. The specific implementation of this tail in GENIE is known as Bodek-Ritchie tail [239]. Another well known version of this effect is the Benhar-Fantoni spectral function [90, 240, 241, 242, 243], used in other neutrino event generators [244].

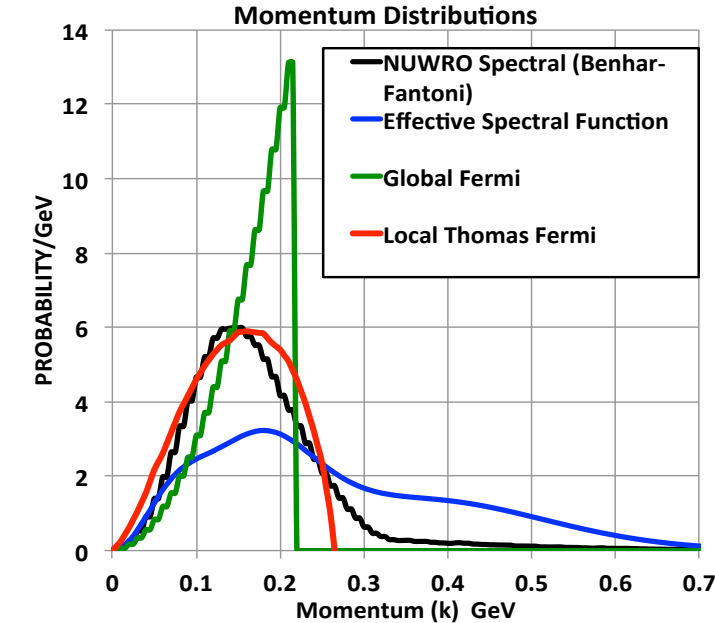


Figure 6.1: Nucleon momentum distributions in a ^{12}C nucleus for several spectral functions from [238].

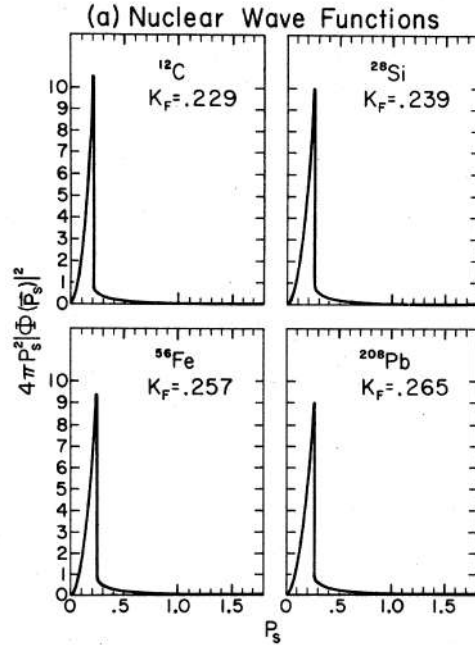


Figure 6.2: Nucleon momentum distributions in a ^{12}C nucleus (top left plot) for RFG with Short Range Correlation added by Bodek-Ritchie [245].

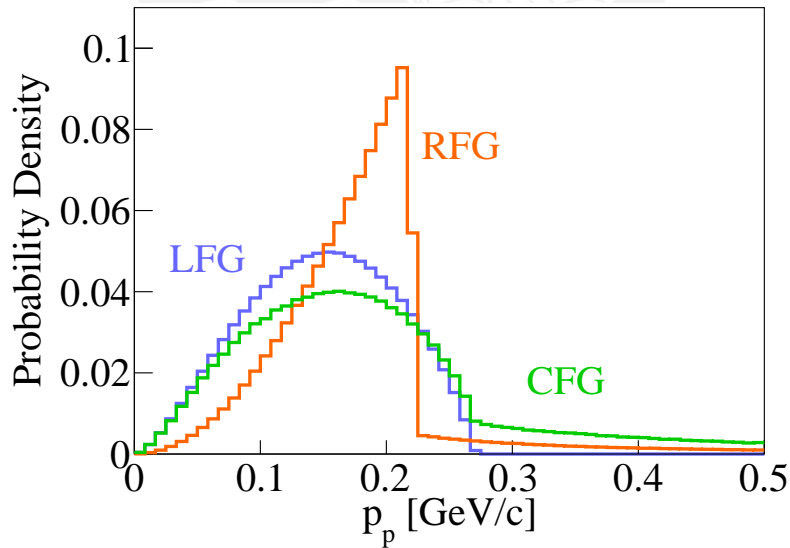


Figure 6.3: Nucleon momentum distributions for Local Fermi Gas, Relativistic Fermi Gas and Correlated Fermi Gas (CFG) [246], figure taken from GENIE [247].

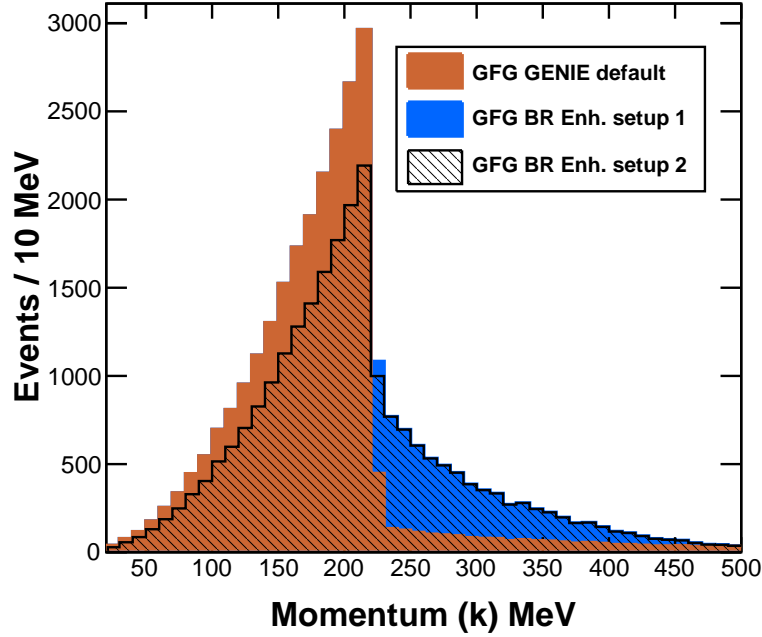


Figure 6.4: Bodek-Ritchie Tail Enhancement proposal in blue and black. Orange are the default GENIE GFG with Bodek-Ritchie tail. The result are presented with setup 1.

Bodek-Ritchie Tail Enhancement

Unlike the original Bodek-Ritchie work, we now know 20 to 25% of the reaction rate is on nuclei in this tail, as GENIE added in the new GENIE 3 release (see the relevant plot in Figure 6.3) [247], where the enhancement is in LFG. Since they are not fully simulated in GENIE 2, we can apply weight to enhance this component. One option is to reduce the QE global Fermi gas peak by the same amount as we enhanced the tail, thus preserving the total QE event rate, and one option in our implementation does exactly this (black histogram in Figure 6.4 labeled as setup 2). This option can be turned off, thus equivalent to increasing the overall scale by around 25%. This second option better describes the MINERvA ME data and is what we are using. The study here enhances the Bodek-Ritchie tail weighting up the QE events by a factor of 6 at 221 MeV and reduces the weight to a factor of 1 (i.e. no enhancement) at

0.5 GeV or below 221 MeV.

The enhancement in the total MC is placed in the middle of the Effective Spectral Function and Benhar-Fontoni spectral function [238] as shown in Figure 6.4, blue distribution.

Effect in Low recoil sample

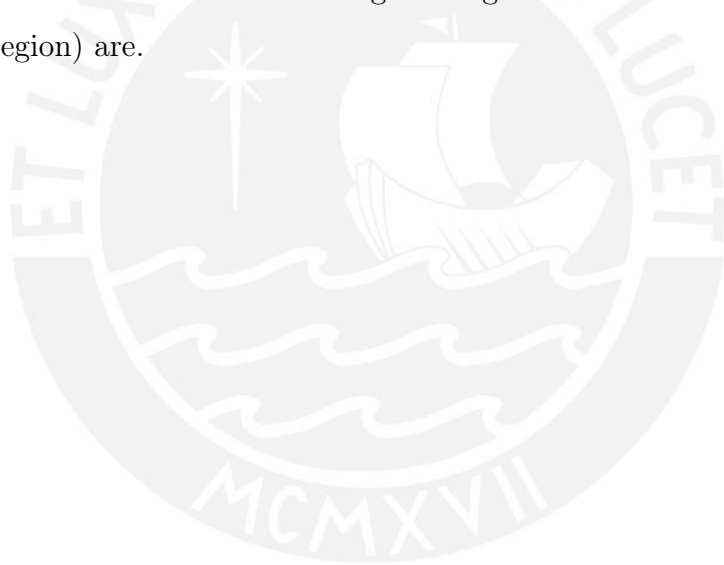
The plots regarding the effects of the variation in the MC in the low recoil analysis presented here follow an order, first an event rate, then the ratio between MC upon MC, and finally the ratio of data over MC. In the event rate plots, the continuous lines represent the MC with the model variation, and the dashed lines the nominal MC. In the same plots, the red histograms are always Total MC, and blue, green, and magenta are QE, 2p2h, and Delta, following the Figure 5.1 color scheme. The black dots are MINERvA ME data. The ratio plots MC upon MC are nominal MC upon MC with the model variation. Between total over total and event type nominal MC over event model variation type MC. Finally, the last ratio plots are data over MC. The type of lines and color follow the event rate type plots.

The initial momentum of the struck nucleon is responsible for much of the smearing of QE reaction in energy and momentum transfer. Stationary nucleons would simply produce a delta-function thin line at the invariant mass of a nucleon. Therefore these highest momentum nucleons will produce energy and momentum transfers furthest from and broaden the QE peak.

As shown in Figure 5.1 and 6.5, the QE dominance decreases as one goes a long higher q_3 region. Another feature of the QE component is, at higher q_3 , the shape of the QE spectrum is separated from other details and is easier to appreciate. Let's understand the enhancement splitting the q_3 into three regions, low q_3 from 0.0 to 0.3 GeV, the medium region from 0.3 to 0.6 GeV, and higher q_3 part from 0.6 to 1.2 GeV. The low q_3 dominated by QE shows an enhancement of around 25% in the total. It goes higher than 50% in the region

of 0.1 to 0.16 of E_{avail} in QE. In addition, a higher enhancement appears in the tail of the QE distribution. The better appreciation is shown in the ratio plots (Figure 6.6) comparing both MCs. The feature of tail enhancement is much more appreciated in the medium and higher q_3 region, where one can see the whole QE spectrum. In both tails, the enhancement is more significant than the peak.

On the other hand, the implication compared with the data is shown in Figure 6.7. It seems that the enhancement is more substantial than the nominal QE MC for the lower region q_3 between 0.0 to 0.2 GeV. However, it agrees with data in the following q_3 range, similarly in the medium and higher q_3 . The enhancement is more affecting the region where also has RES and MEC (dip region) are.



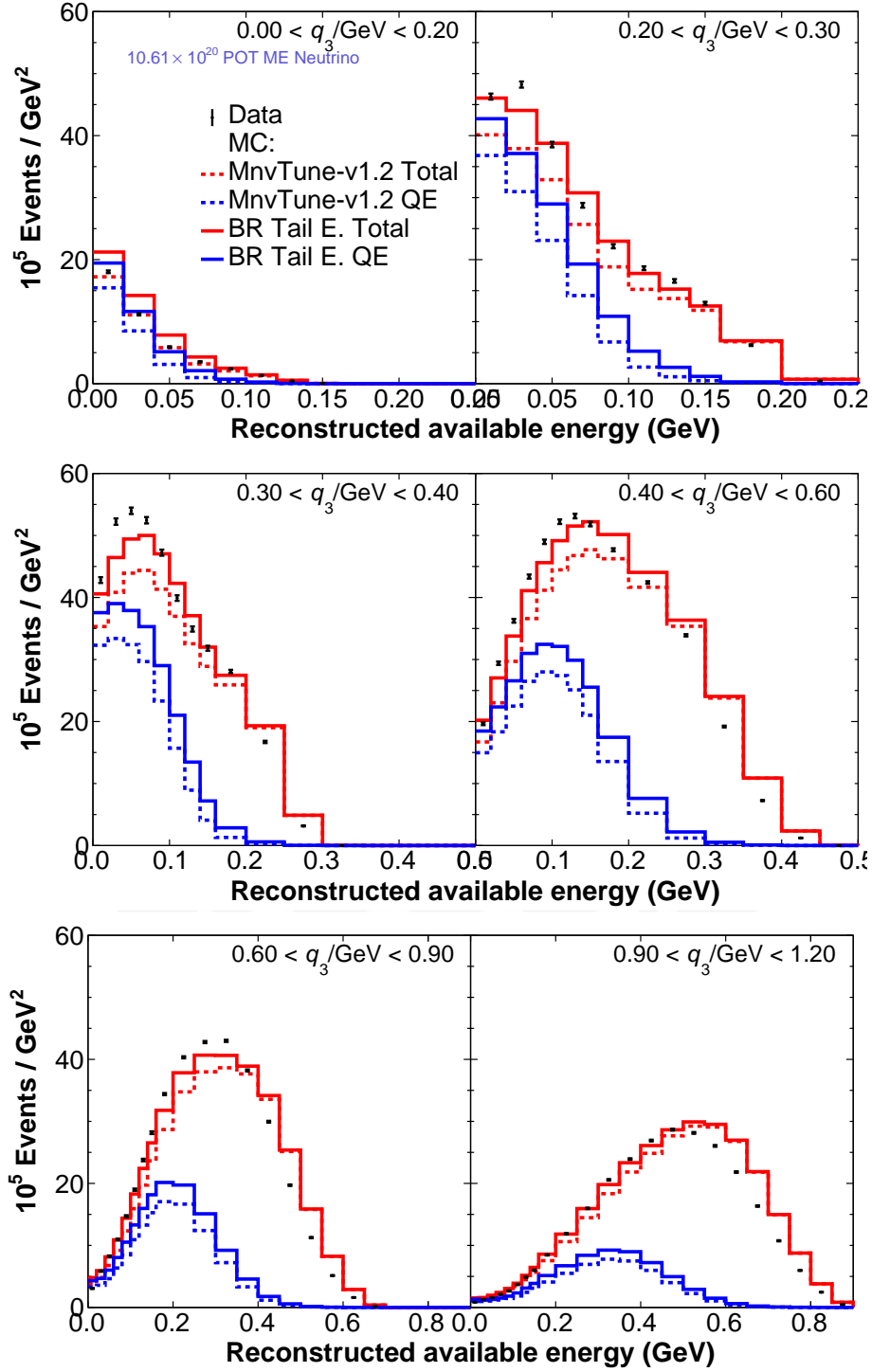


Figure 6.5: Reconstructed E_{avail} in projections of reconstructed q_3 regions, the dashed lines are nominal MC, and continuous lines are the BR tail enhancement effect. In red the Total MC and in blue QE event types.

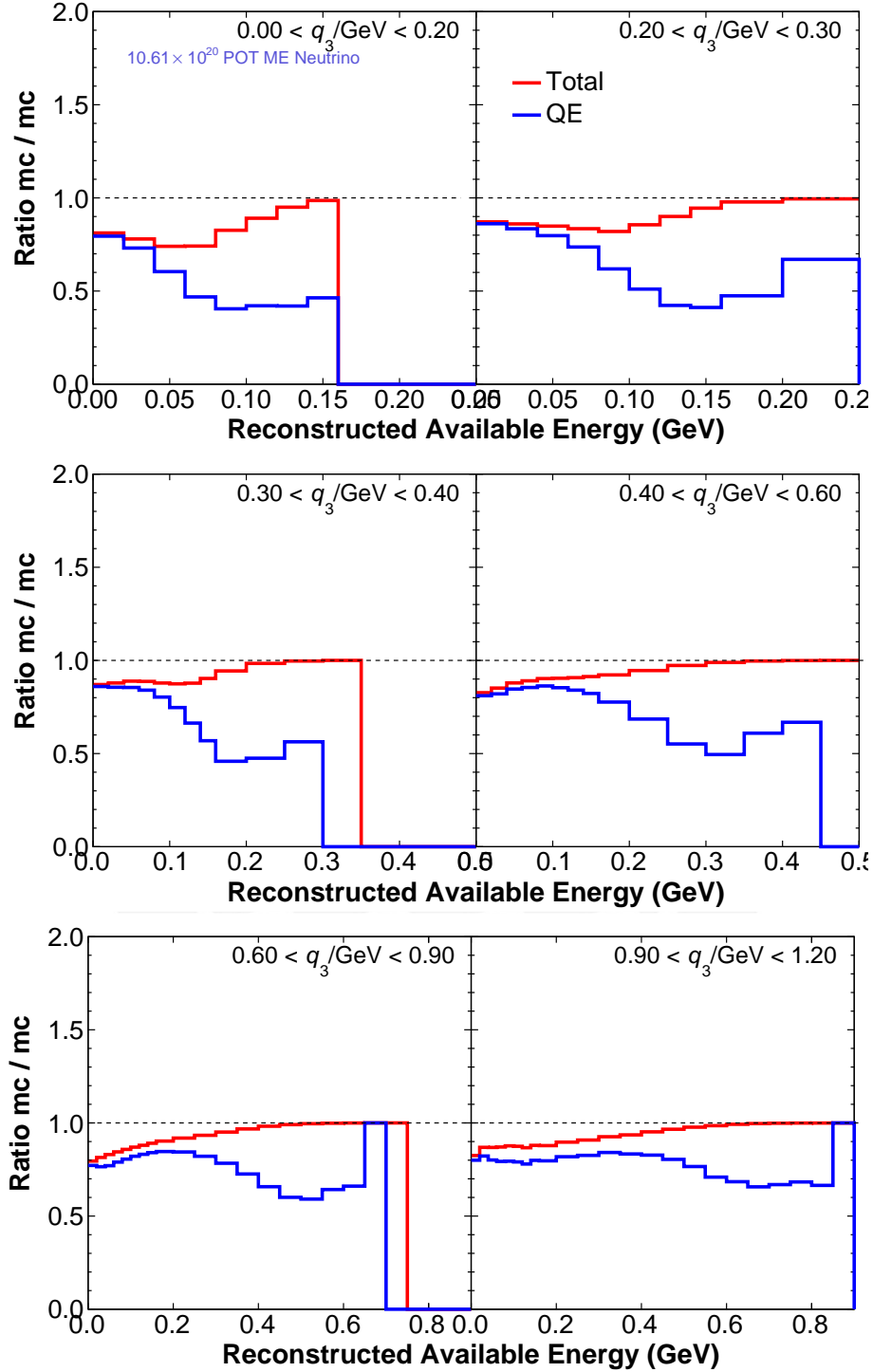


Figure 6.6: Ratio of nominal MC over BR tail enhancement MC for reconstructed E_{avail} in projections of reconstructed q_3 regions, the dashed lines are nominal MC, and continuous lines are the BR tail enhancement effect. In red the Total MC and in blue QE event types.

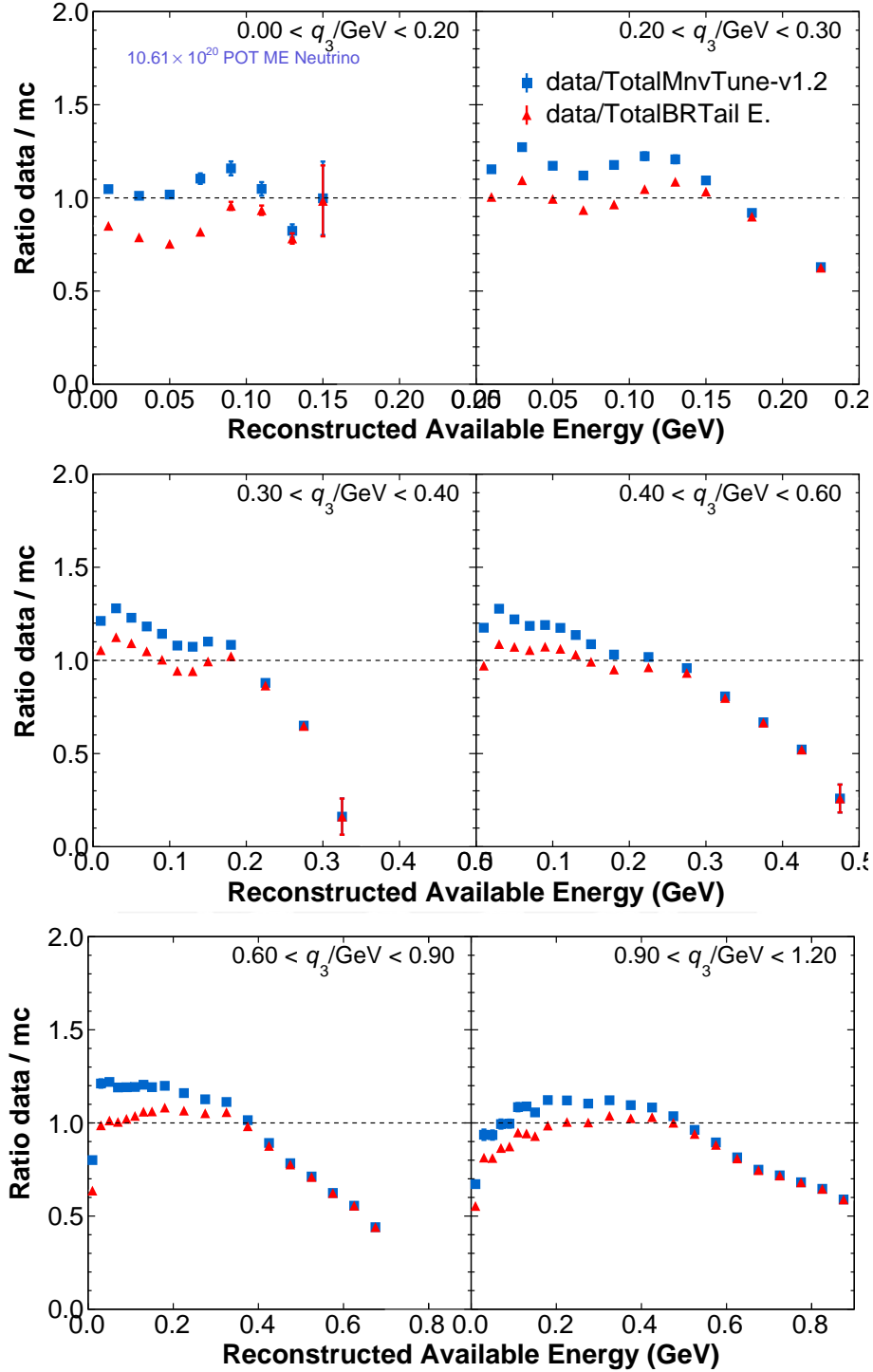


Figure 6.7: Ratio of data over BR tail enhancement MC for reconstructed E_{avail} in projections of reconstructed q_3 regions, the dashed lines are nominal MC, and continuous lines are the BR tail enhancement effect. In red the Total MC and in blue QE event types.

6.2 Super Scaling Approximations SuSA

Super Scaling Approximations

In this subsection we will introduce general concepts of Super Scaling Approximation (SuSA). The “superscaling” concept was first introduced by Alberico *et al.* [248] when studying a scaling behavior of nuclear response² in electron scattering on top of existent non-relativistic “ y ” scaling in nuclear physics; analogous to “ x ”³ scaling [249]. The superscaling is a formalism that describes the charge lepton scattering. When valid, scaling behavior can be very powerful, allowing a small amount of data or calculation to describe a wide range of situations. To be called superscaling, the scaling variable ψ has two requirements; first, the scaling variable does not depend on momentum transfer q (*scaling of first the kind*), and is independent of Fermi Momentum (k_F) (*scaling of second the kind*). In other words, let’s take a CC neutrino reaction ($\nu_l + A \rightarrow l^- + B$) with \mathbf{p} and \mathbf{p}' lepton momenta. The four-momentum transfer defined like $Q^2 = \mathbf{p}' - \mathbf{p}$. We can define a dimensionless variables as follows $\lambda = \frac{q_0}{2m_N}$, $\kappa = \frac{q_3}{2m_N}$, and $\tau = \kappa^2 - \lambda^2$. The Fermi kinematic is defined as $\xi_F = \sqrt{1 + \eta_F^2} - 1$, where $\eta_F = k_F/m_N$. A superscaling function could be, $f_{RFG}(\psi)$ for Relativistic Fermi Gas (RFG) for example, where ψ is defined as:

$$\psi = \frac{1}{\sqrt{\xi_F}} \frac{\lambda - \tau}{\sqrt{(1 + \lambda)\tau + \kappa\sqrt{\tau(1 + \tau)}}}. \quad (6.1)$$

The equation 6.1 does not explicitly depend on momentum transfer or Fermi Momentum. In addition, ψ also has a shift of energy binding Es (empirical parameter) becoming a ψ' which has been found in the literature, and a detailed discussion can be found in the references [250, 251, 252, 253, 254, 255, 256, 257]. In the QE electron scattering studies, the “universal” scaling function is obtained based on the available separation of the scattering data into longitudinal and transverse contributions. When the longitudinal and transverse scaling functions are equal is called *scaling of zeroth kind* [258], by determin-

²A nuclear response function is a function that takes into account nuclear medium effects.

³Bjorken (x) scaling for quarks in the nucleon.

ing this scaling function from a collection of data, the result is effectively an empirical parameterization and interpolation of the input data.

SuSAv2 is an extension of super scaling approximation incorporating the formalism information of the Relativistic Mean Field (RMF) theory by merging the strong q dependence of RMF and SuSA with scaling of the zeroth kind [258]. The implementation in GENIE that this work follows can be found in [237]. If the application of a weighted theoretical calculation also superscales and reproduces the empirical scaling function, like this one, then it is an excellent model for these reactions. As good as the original empirical function, and possibly able to make additional predictions about the hadron system. The implementation in MINERvA is described in [259].

SuSAv2 2p2h

The 2p2h events do not obey superscaling. But the SuSA collaboration wanted a 2p2h prediction so they could compare their model to pionless reaction neutrino data. Led by Guillermo Megias, their calculation takes a similar approach to the Valencia 2p2h and so does the GENIE implementation of it [237].

Compared to the Valencia version, it makes the calculation fully relativistic. In addition to accuracy, it also means the calculation is applicable at higher momentum transfer. And the calculation includes some additional diagrams and the resulting interference terms [237]. One additional comment is that the super scaling approximation for MEC first takes out the QE peak. The GENIE re-weighting comes from [260]. The main effect of SuSA is in the dip region compared with Valencia 2p2h, which brings the Δ part down to lower energy transfers and into the dip region. In the low recoil sample, SuSAv2 2p2h is compared with Valencia 2p2h plus low recoil fit (enhancement of Valencia 2p2h). The maximum difference with total nominal MC is around 25% (Figure 6.9), with shifts of MEC peak is some q_3 regions (medium) (Figures 6.10 and 6.11). The comparison of SuSAv2 2p2h with the data shows

a larger disagreement than the nominal MC. However, that can be solved by adding other effects in the dip region.

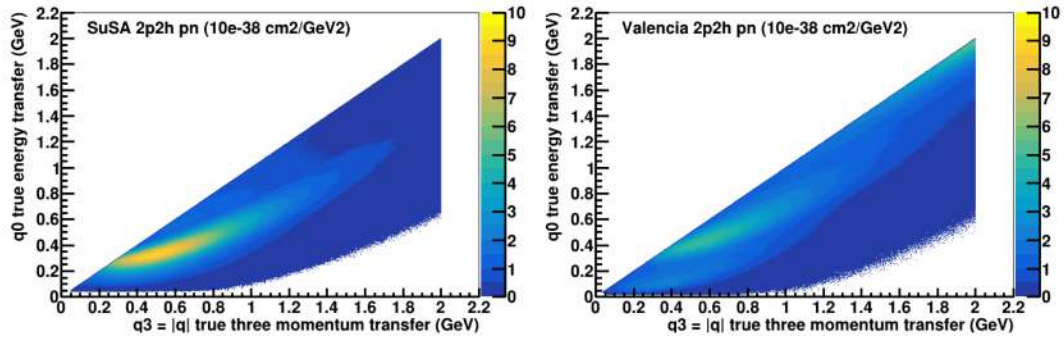
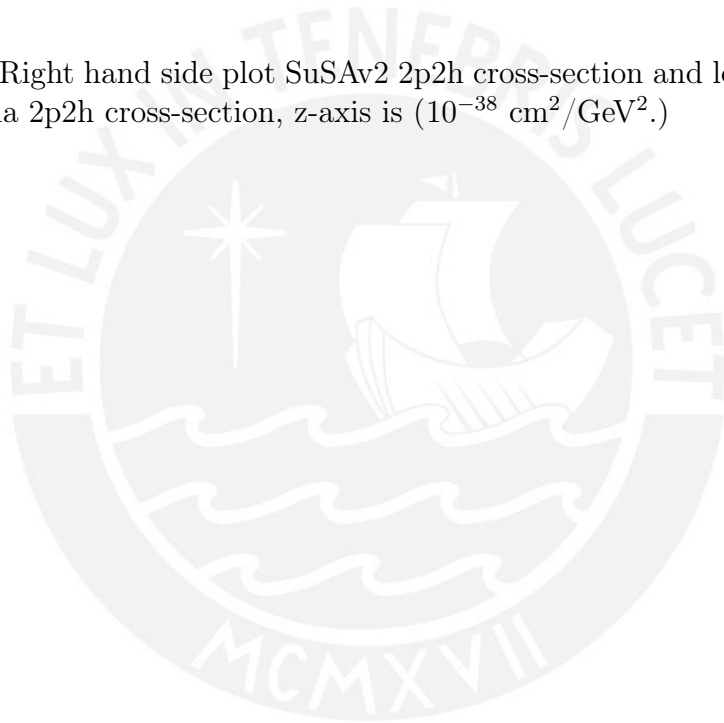


Figure 6.8: Right hand side plot SuSAv2 2p2h cross-section and left hand side plot Valencia 2p2h cross-section, z-axis is ($10^{-38} \text{ cm}^2/\text{GeV}^2$.)



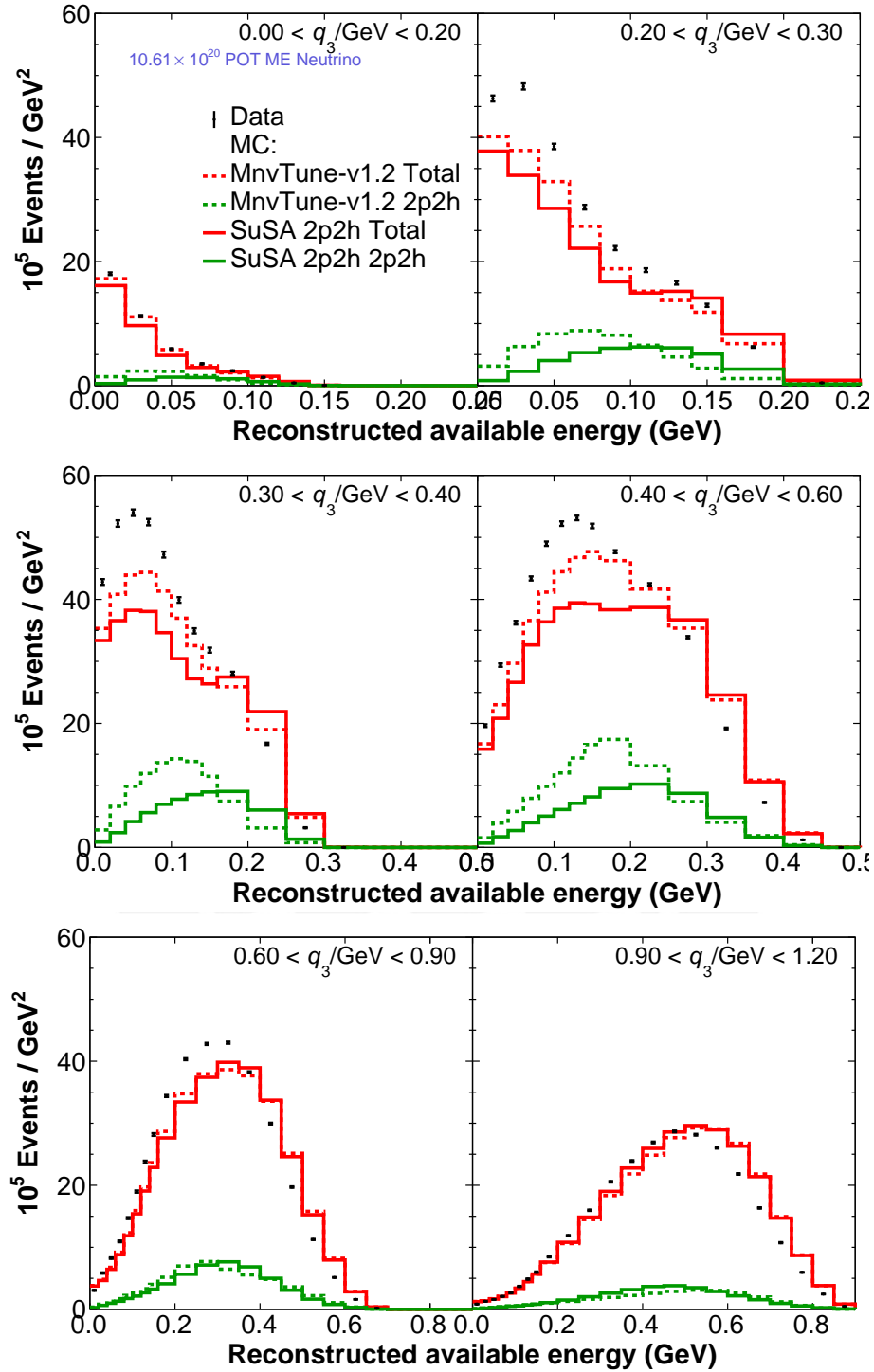


Figure 6.9: Reconstructed E_{avail} in projections of reconstructed q_3 regions, the dashed lines are nominal MC, and continuous lines are the SuSAv2 2p2h effect. In red the Total MC and in green 2p2h event types.

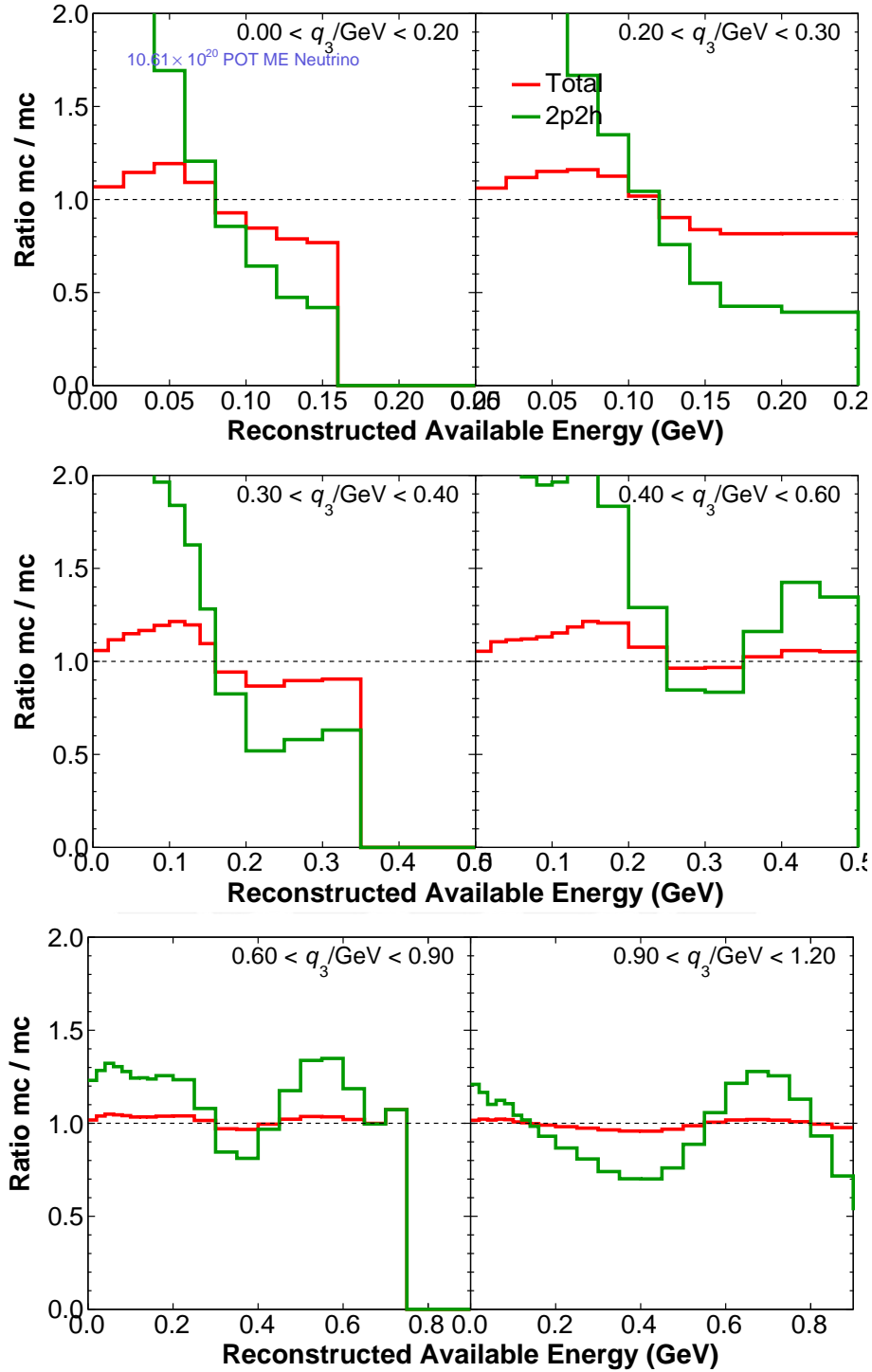


Figure 6.10: Ratio of nominal MC over SuSAv2 2p2h MC for reconstructed E_{avail} in projections of reconstructed q_3 regions, the dashed lines are nominal MC, and continuous lines are the SuSAv2 2p2h effect. In red the Total MC and in blue green 2p2h types.

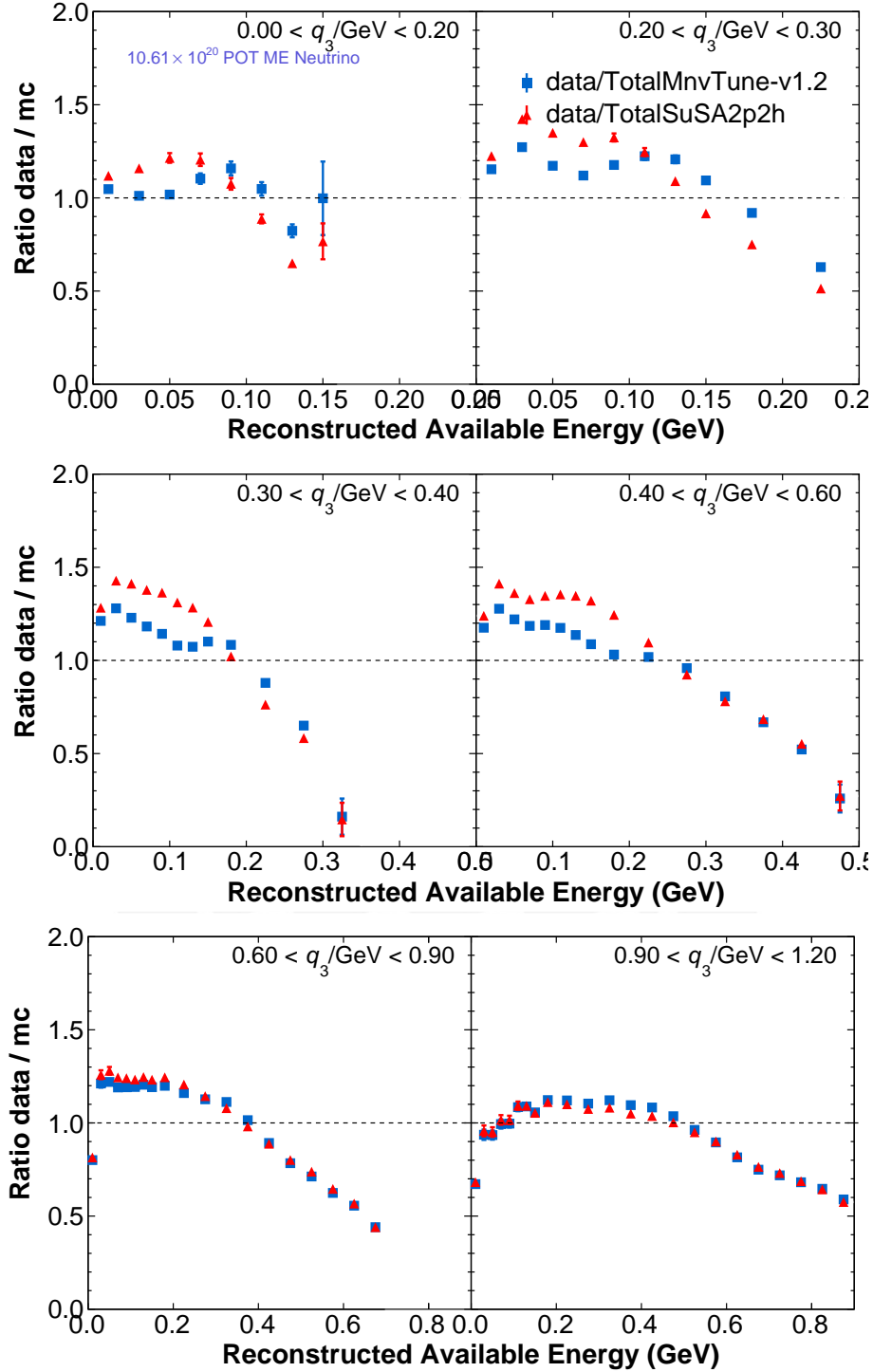


Figure 6.11: Ratio of data over SuSAv2 2p2h MC for reconstructed E_{avail} in projections of reconstructed q_3 regions, the dashed lines are nominal MC, and continuous lines are the SuSAv2 2p2h effect. In red the Total MC and in blue green 2p2h types.

6.3 Removal Energy in Resonant Events (RES)

In the early days of electron scattering, to explain the data in the quasi-elastic region, it was necessary to introduce removal energy $\bar{\epsilon}$ (called nuclear parameter at that time [261]) for each target.

To understand the reason, let's start with an elastic scattering on a free nucleon, where the part of the kinetic energy is transferred to the nucleon without losing kinetic energy in the process. In these cases, we expect a delta function ideally. In other words, the kinetic energy is conserved in the center-of-the mass but not the case in the lab frame. In the quasi-elastic scattering process, there is a small energy exchange. In this context, a shift represents an average cost that must be paid to remove a nucleon from the nuclear potential, as is described in the Figure 6.12 for Ca^{40} target, and Figure 6.13 for carbon, nickel and lead after the shift correction.

The removal energy treatment is handled in different ways by the generators. For example, generators with spectral functions like NuWro, calculated in two variables, missing energy and nucleon momentum, describes the removal energy directly from probability distribution functions when picking a nucleon [235]. On the other hand, one-dimensional Relativistic Fermi Gas (RFG) models, like those used in Figure 6.13 and 6.12 need constant removal energy, which is also the GENIE's approach. The Local Fermi Gas (LFG) accounts for the correlation between removal energy and local nuclear density [235]. However, all the models described above do not consider the Optical and Coulomb potentials of the nucleus. Also, they do not consider the final state interaction (FSI) of the final state lepton to estimate the amount of energy to be removed. Those approaches are described in detail in [262] which can be added to the generators.

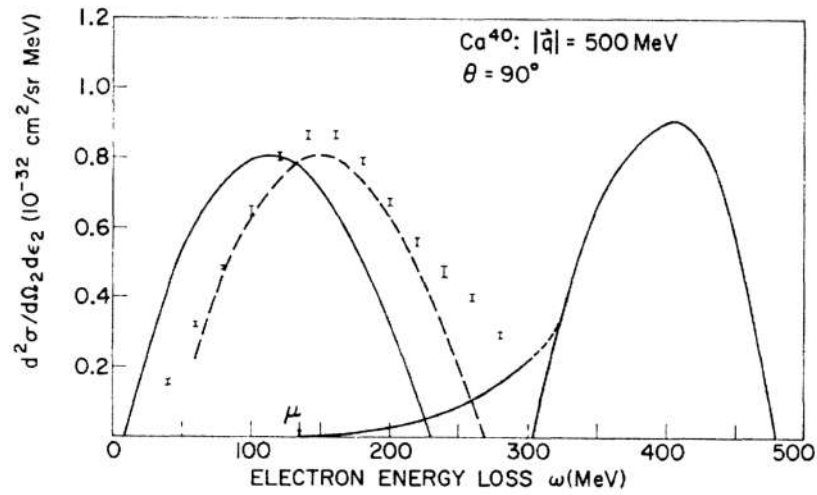
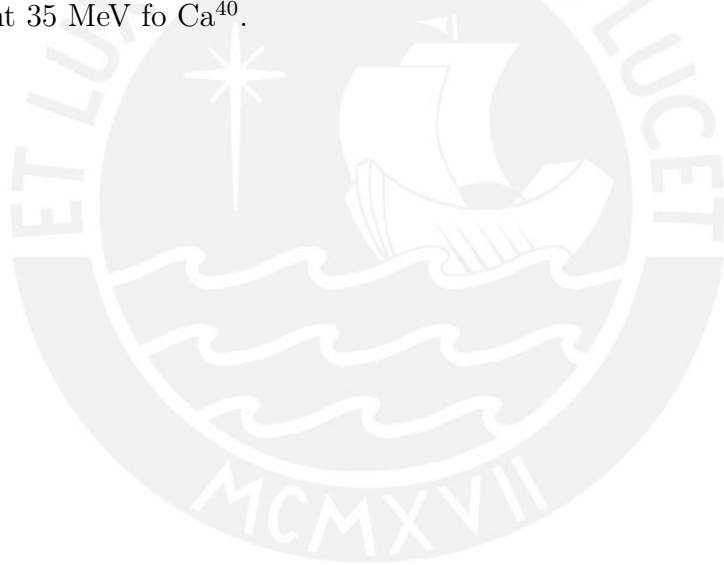


Figure 6.12: Cross-section versus energy loss for inelastic scattering taken from [263]. Solid line is the Fermi-gas and dashed line is Fermi-gas with a displacement 35 MeV for Ca^{40} .



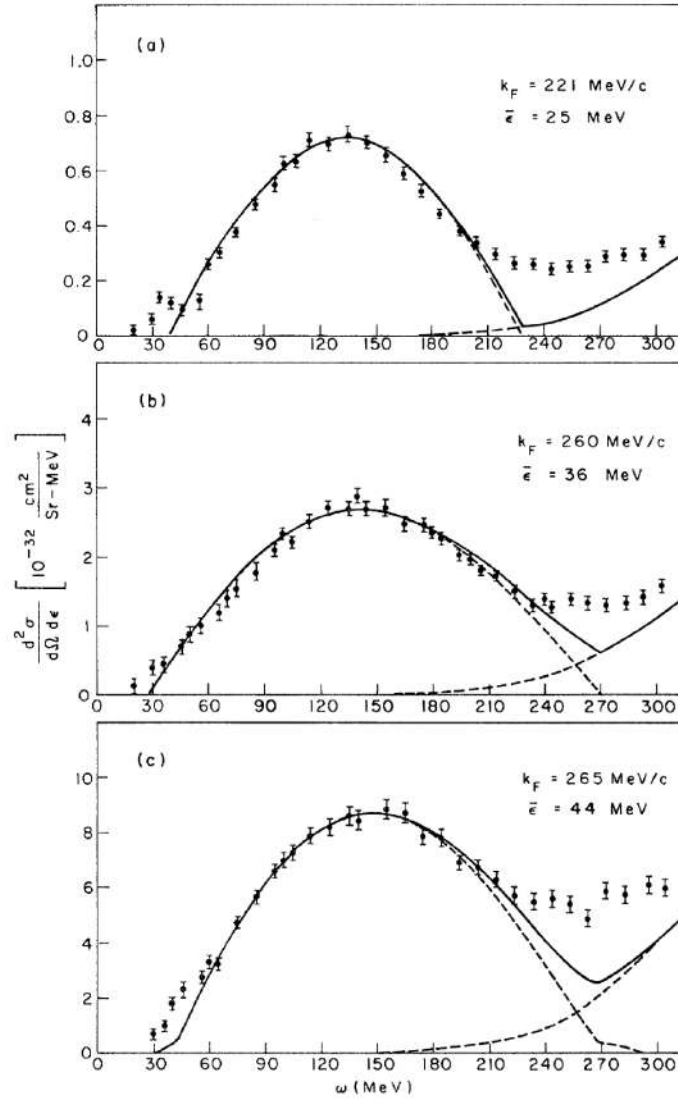


Fig. 1. Cross sections $d^2\sigma/d\Omega d\epsilon$ versus electron energy loss $\omega = \epsilon_1 - \epsilon_2$ for inelastic scattering of 500-MeV electrons at 60° from (a) carbon, (b) nickel, and (c) lead. Solid lines are the results of the Fermi-gas calculation with the nuclear parameters indicated on the figure.

Figure 6.13: Cross-section versus energy loss for inelastic scattering taken from [261]

The same concept is used to introduce the removal of energy in resonant events. We are proposing a 25 MeV Removal Energy (RE) that will be subtracted from the E_{avail} for resonant events. There were tested with many

6.3. REMOVAL ENERGY IN RESONANT EVENTS (RES)

other values of RE (Figure 6.14) and the data has a preference for 25 MeV, which is also appreciated in the ratio plots (Figure 6.15). Given that the E_{avail} contains all the kinematic energy pion and proton and total energy of all other particles except neutron, the amount is paid from the whole summed energy.

The implementation in the MC requires that in all charge current resonant processes, after FSI, a 25 MeV is removed if there is at least a proton. With this requirement, we guaranty that at least there is a nucleon going out of the nucleus.

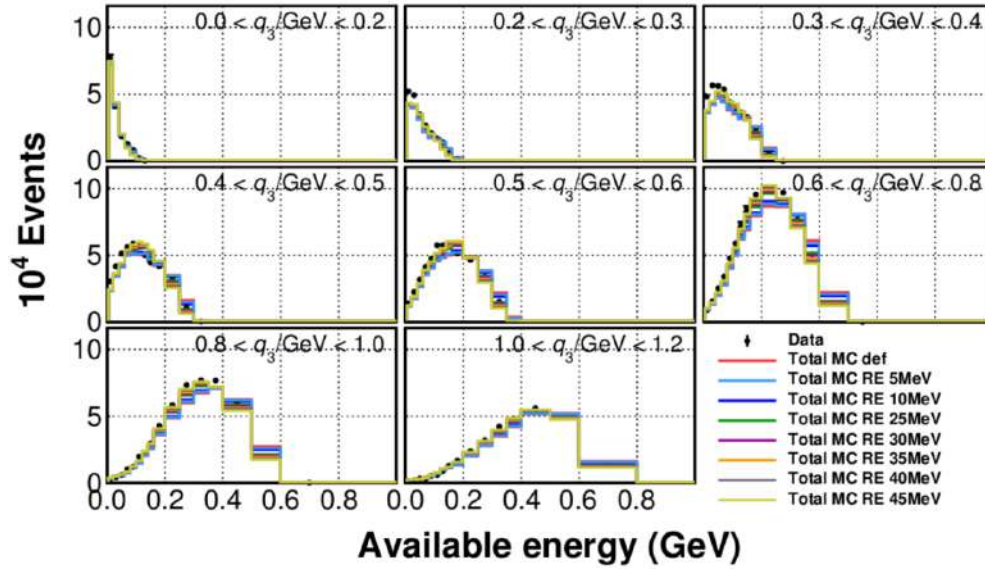


Figure 6.14: E_{avail} in pads of q_3 for different removal energies applied to the resonant events, MC def means nominal MC.

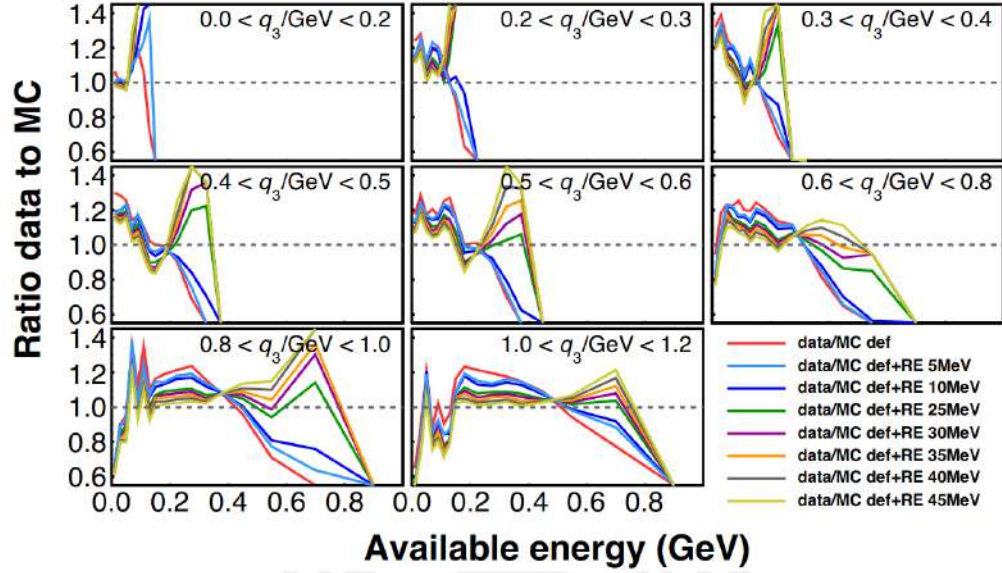


Figure 6.15: Ratio of data over MC for E_{avail} in pads of q_3 for different removal energies applied to the resonant events, MC def means nominal MC.

The main feature of removal energy is a shift to the left of Δ peak; a characteristic observed in the crossing line of ratio plots (Figure 6.16 and 6.17), the medium and higher region of q_3 the effect is much more substantial. The more significant change occurred at high E_{avail} (Figure 6.18), where the dramatic overestimation of the tail is much reduced because the excess in the MC is migrated to the left.

6.3. REMOVAL ENERGY IN RESONANT EVENTS (RES)

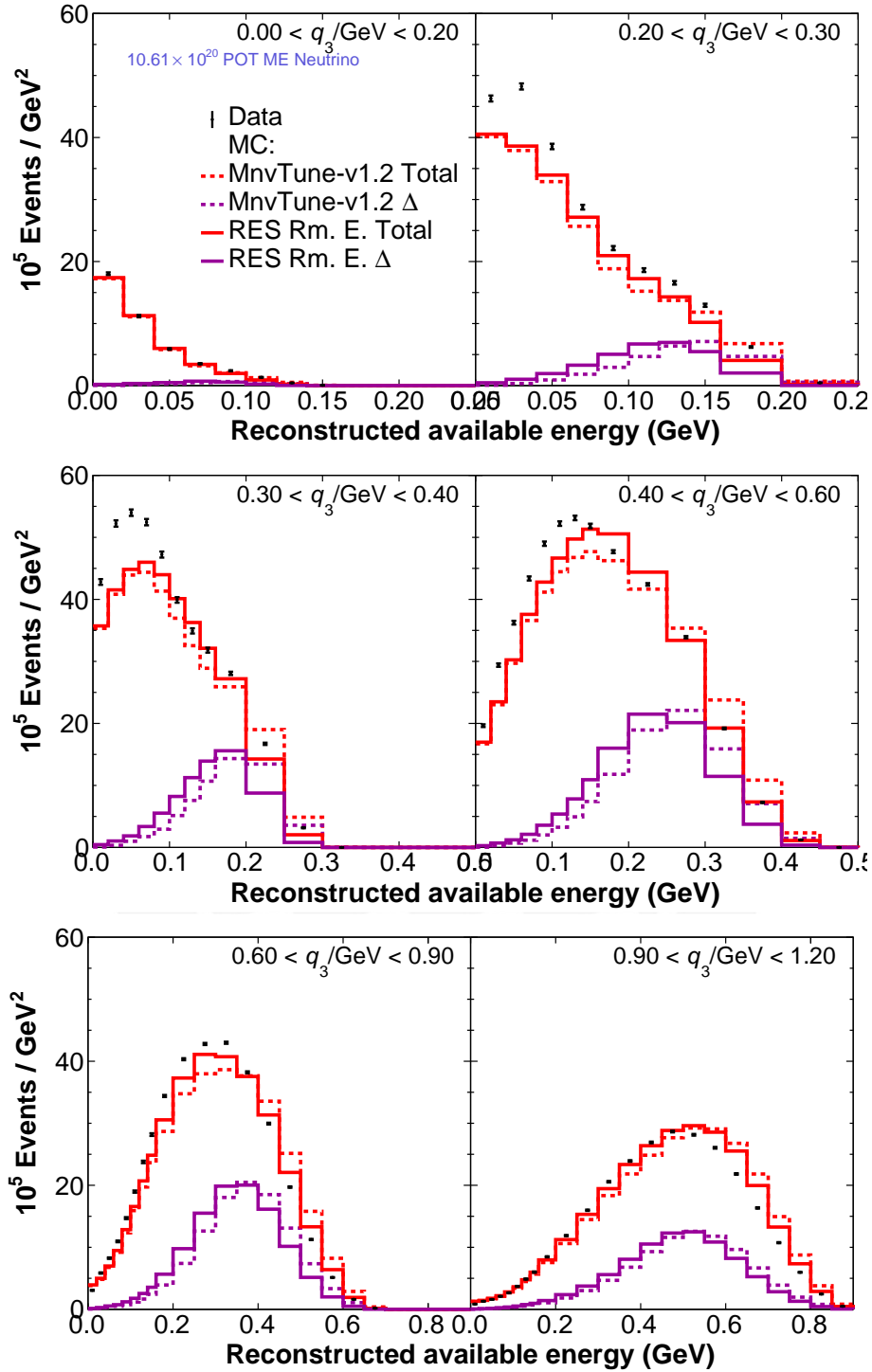


Figure 6.16: Reconstructed E_{avail} in projections of reconstructed q_3 regions, the dashed lines are nominal MC, and continuous lines are the purple RES effect of Removal Energy. In red the Total MC and in purple RES event types.

6.3. REMOVAL ENERGY IN RESONANT EVENTS (RES)

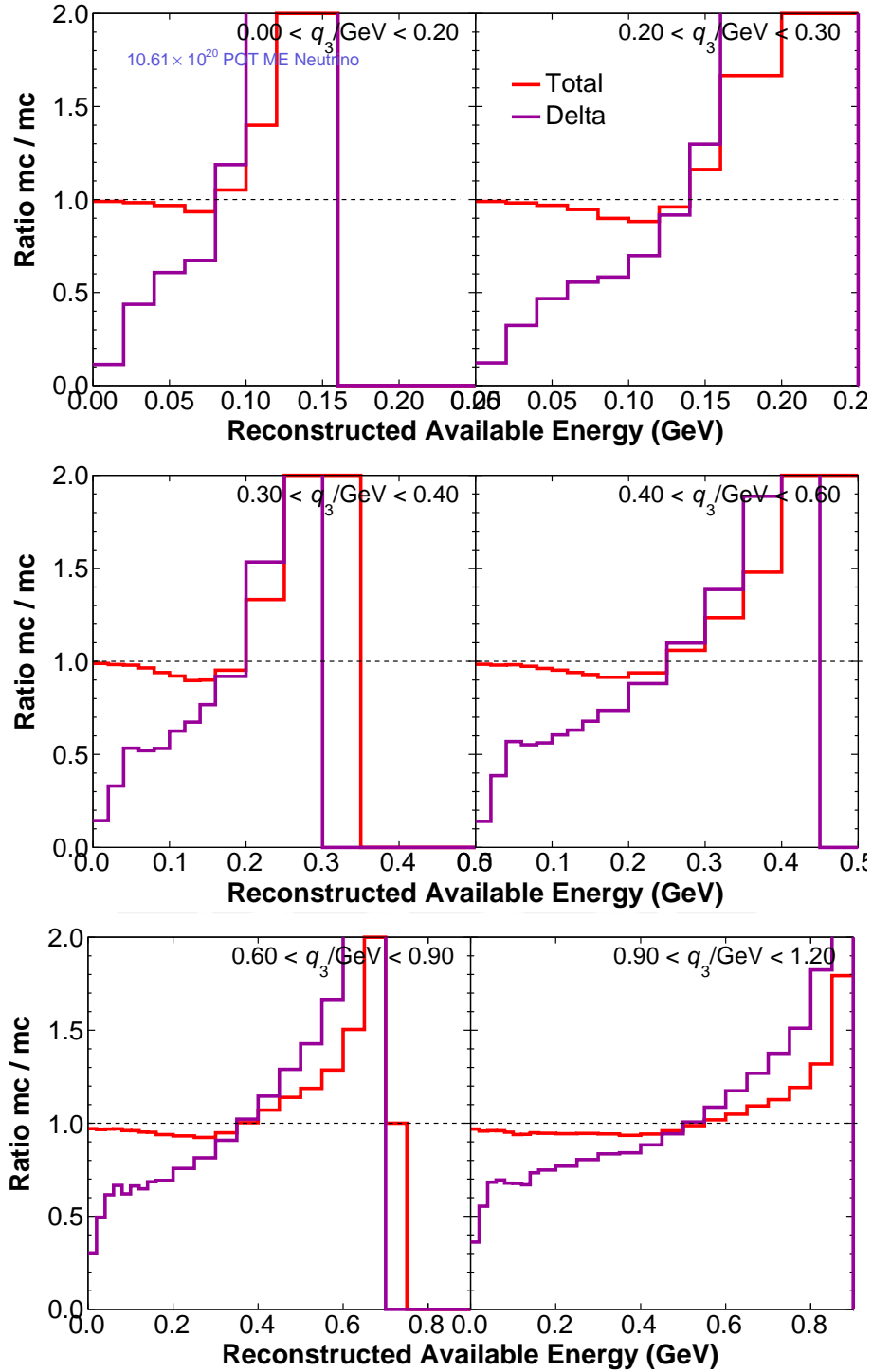


Figure 6.17: Ratio of nominal MC over MC RE for reconstructed E_{avail} in projections of reconstructed q_3 regions, the dashed lines are nominal MC, and continuous lines are the RE effect. In red the Total MC and in purple RES event types.

6.3. REMOVAL ENERGY IN RESONANT EVENTS (RES)

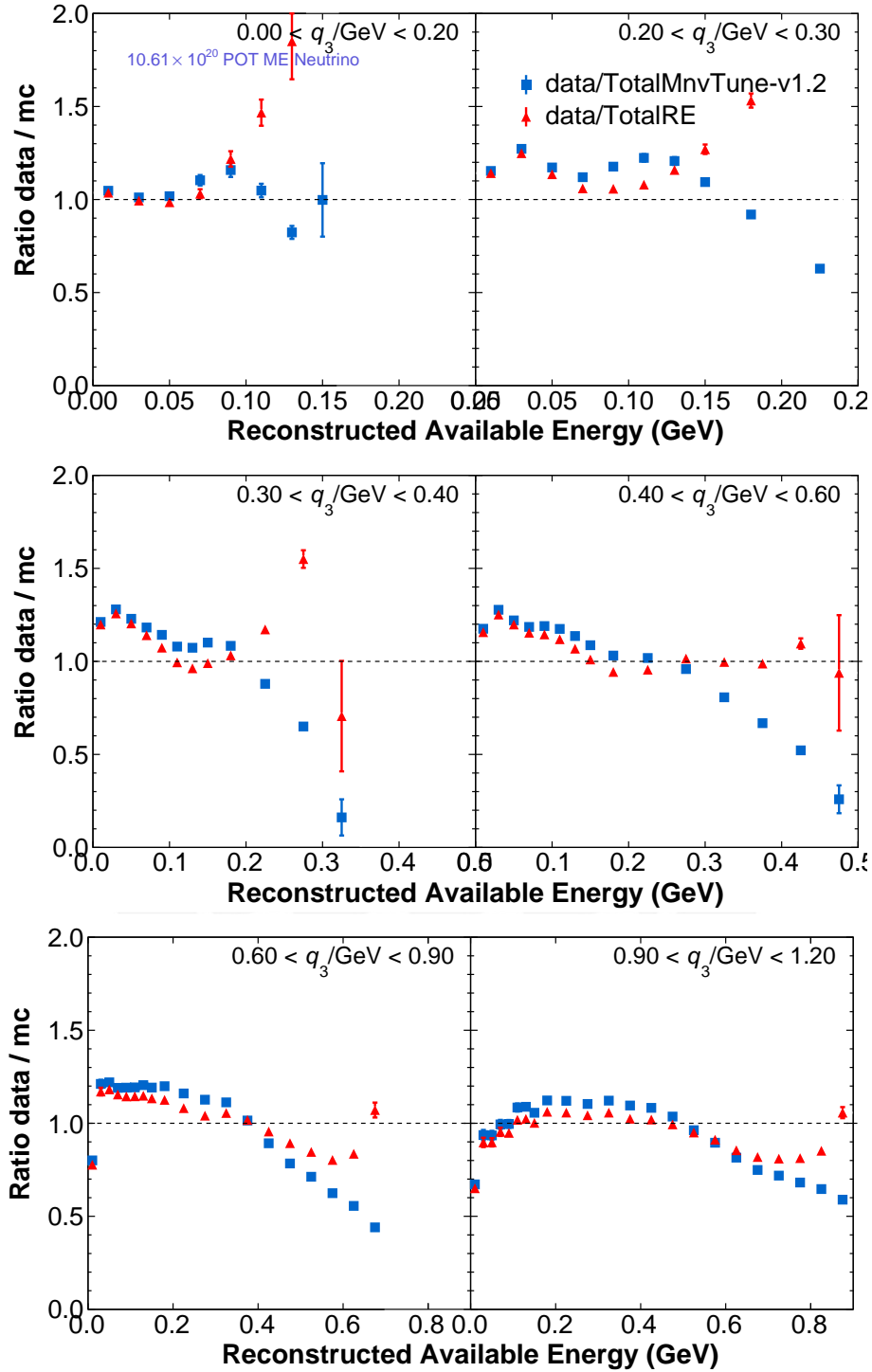


Figure 6.18: Ratio of data over MC RE for reconstructed E_{avail} in projections of reconstructed q_3 regions, the dashed lines are nominal MC, and continuous lines are the RE effect. In red the Total MC and in purple RES event types.

6.4 Low Q^2 Pion Suppression JOINT fit

MINERvA tuned the existent pion measurements partly inspired by MINOS experiment parametrization [264] (hereafter Low Q^2 Pion Supp. or Low Q^2 π Supp.). A Q^2 dependence was found. At lower Q^2 there is a suppression shown in the iron (MINOS data [265]), less strong than the MINERvA parametrization. MINERvA has added this prominent effect to its MC and called it MnvTune.v2. A detailed and extended study can be found in [266].

This particular tune affects the medium and higher available energy, impacting the high q_3 region primarily (See Figure 6.20). The suppression in the MC in some available energy bins reaches around 80% of the total MC (see Figure 6.21). That reminds one of the features of Resonant Removal Energy; the improvement at a higher E_{avail} . But in this case, the small improvement is only for higher available bins. The underlying physics effect, in this case, is not a peak shift, it is just a suppression and that is why the worst description of the data using this tune is in the medium region of available energy. That makes us think that it is possible that the effect is part suppression and part removal of energy cost.

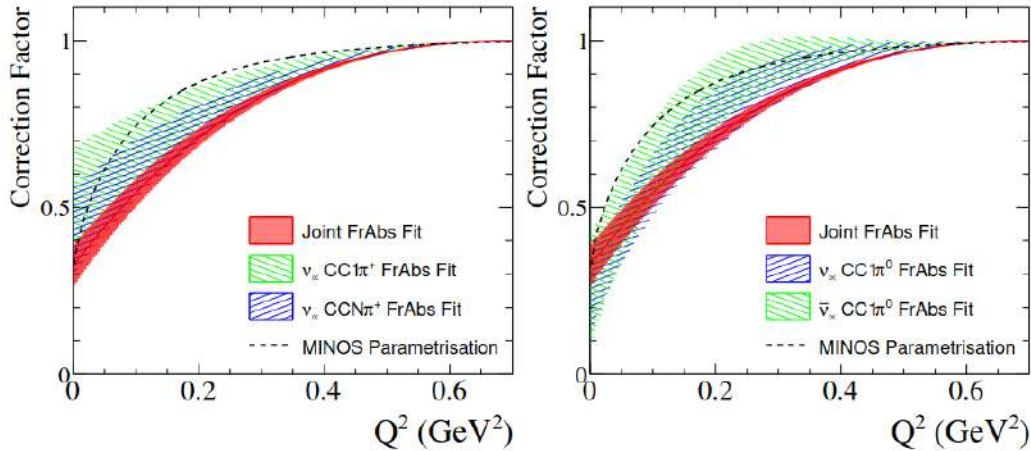


Figure 6.19: Extracted low- Q^2 suppression factors from the FrAbs+low- Q^2 tuning to each channel. The fits compared with MINOS parametrization. The Joint FrAbs Fit is applied in this work. Figure taken from [266].

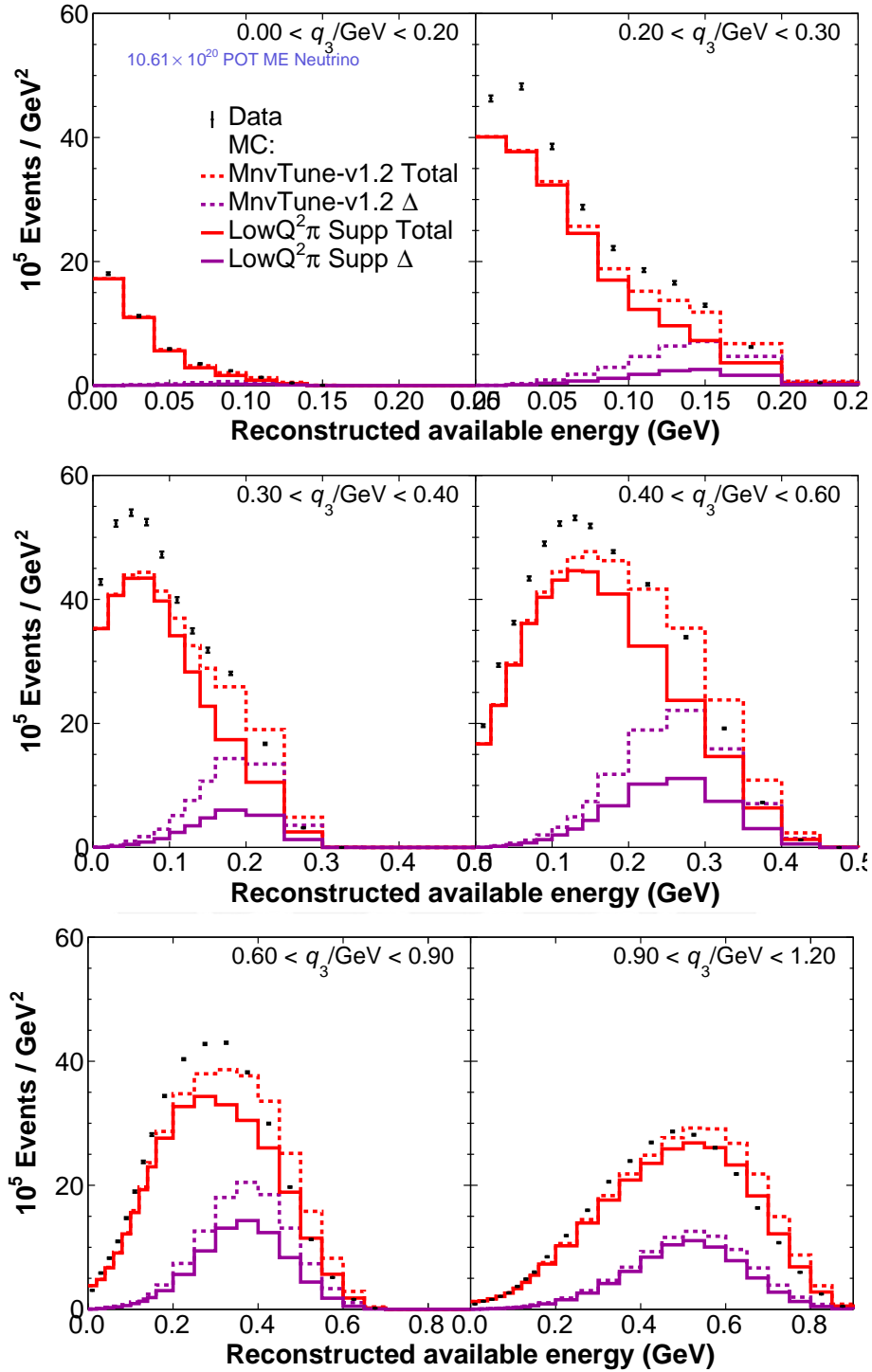


Figure 6.20: Reconstructed E_{avail} in projections of reconstructed q_3 regions, the dashed lines are nominal MC, and continuous lines are the purple Low Q^2 Pion Supp. effect. In red the Total MC and in purple RES event types.

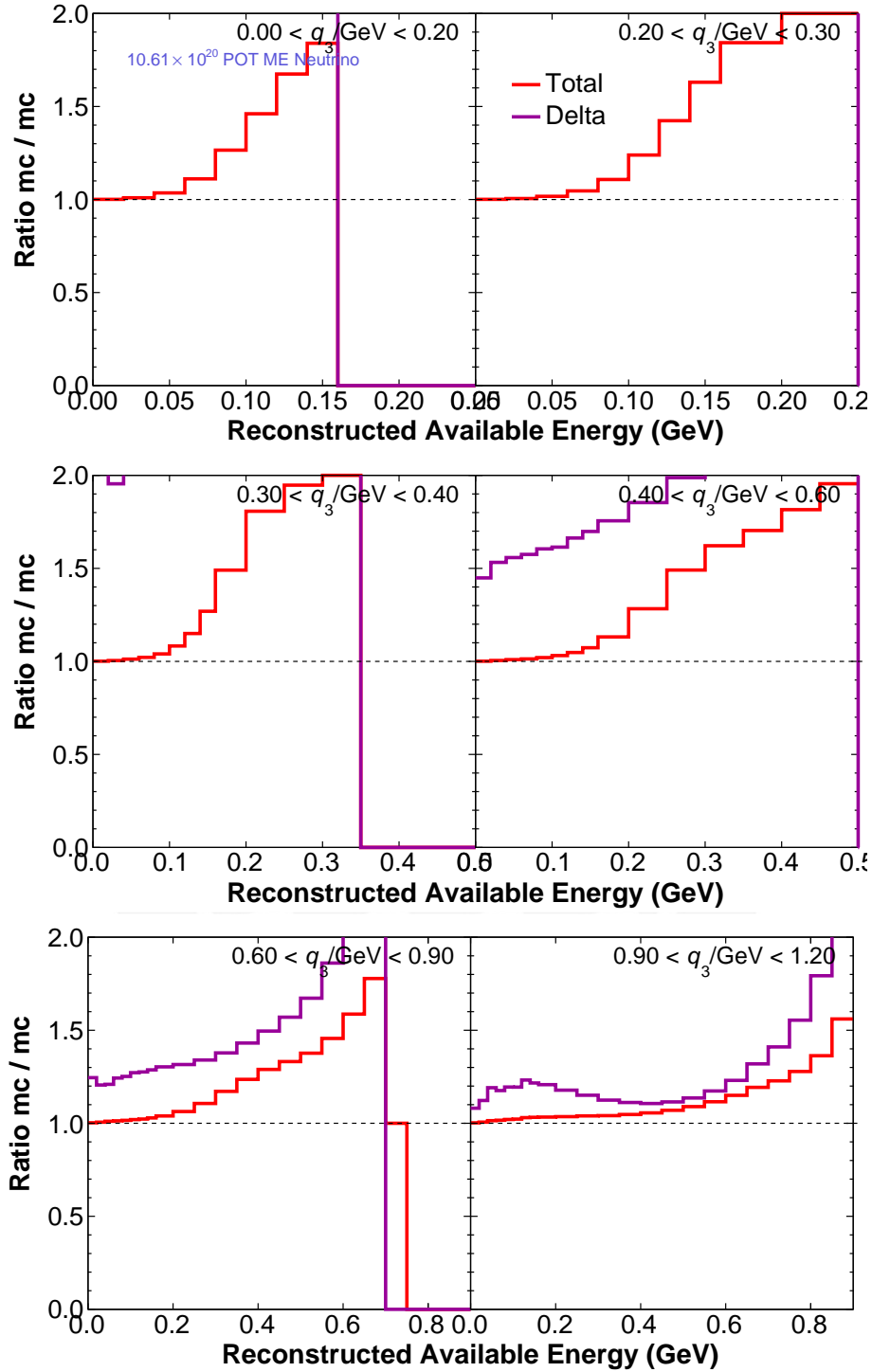


Figure 6.21: Ratio of nominal MC over MC LowQ2 pion suppression for reconstructed E_{avail} in projections of reconstructed q_3 regions, the dashed lines are nominal MC, and continuous lines are the LowQ2 pion suppression effect. In red the Total MC and in purple RES event types.

6.4. LOW Q^2 PION SUPPRESSION JOINT FIT

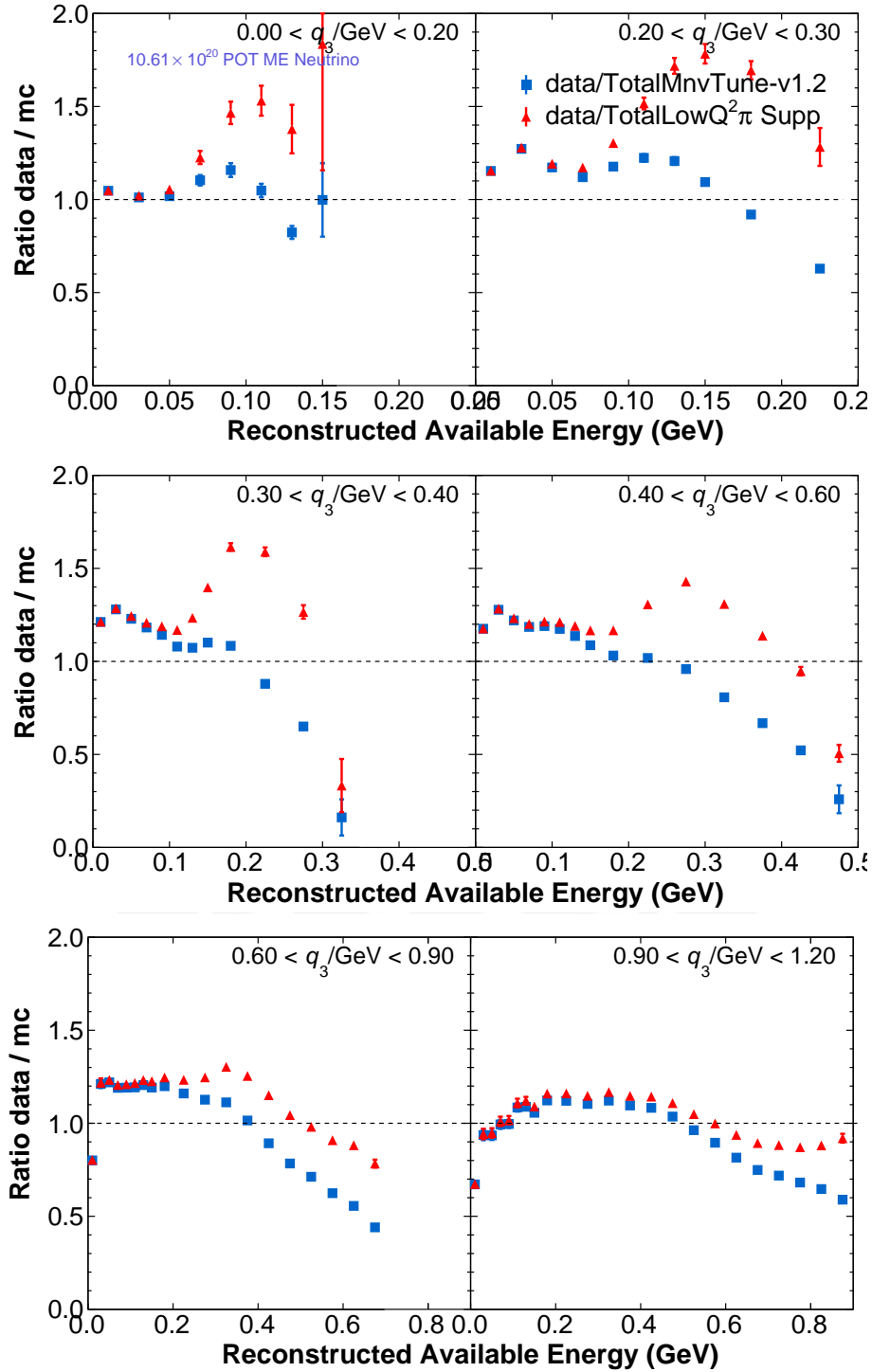


Figure 6.22: Ratio of data over MC LowQ2 pion suppression for reconstructed E_{avail} in projections of reconstructed q_3 regions, the dashed lines are nominal MC, and continuous lines are the RE effect. In red the Total MC and in purple RES event types.

6.5 Pauli Blocking with Berger-Sehgal model

Important points to consider, the Berger-Sehgal (B-S) pion production model [267] adds the mass charge lepton, which is not the case on the Rein-Sehgal (R-S) model. Second, the B-S has an additional upgrade, it incorporates the Jarek Nowak's MiniBoone GA, and GV tune Modify *ModelConfiguration.xml* and *BergerSehgalRESPXSec2014.xml* [268], the detail of B-S can be found in the technical presentation in [269]. To re-weight, [270] used a monochromatic neutrino beam of 5 GeV, and B-S has integrated suppression of around 20% at $Q^2 < 0.1$ GeV [270].

The implementation we are testing against the MINERvA data also adds Pauli blocking, which modifies the RES MC by weighting to zero resonant events if the Δ reaction produces a proton or neutron with momentum less than Fermi level (~ 211 MeV) in carbon. The Pauli blocking addition suppresses the low Q^2 part of the resonance spectrum furthermore. Compared with the Low Q^2 suppression tune (MnvTune.v2) the overall suppression is around half of the MnvTune.v2 and the main impact is in the medium region of q_3 .

The effect of that combined modification on low recoil sample are showed in the Figure 6.25, 6.26 and 6.27. Significant change compared with nominal MC, there is a suppression in the Δ peak in medium q_3 range by about 60% in the lower tail and lower E_{avail} . Second, the total change in the resonant dominant region is less than 30%, mainly similar to nominal MC when compared with the data and slight improvement at high E_{avail} regions. The different changes are motivated theoretically. However, it is difficult to separate, but this modification is the closest to what a neutrino experiment using GENIE.v3 will get from the model.

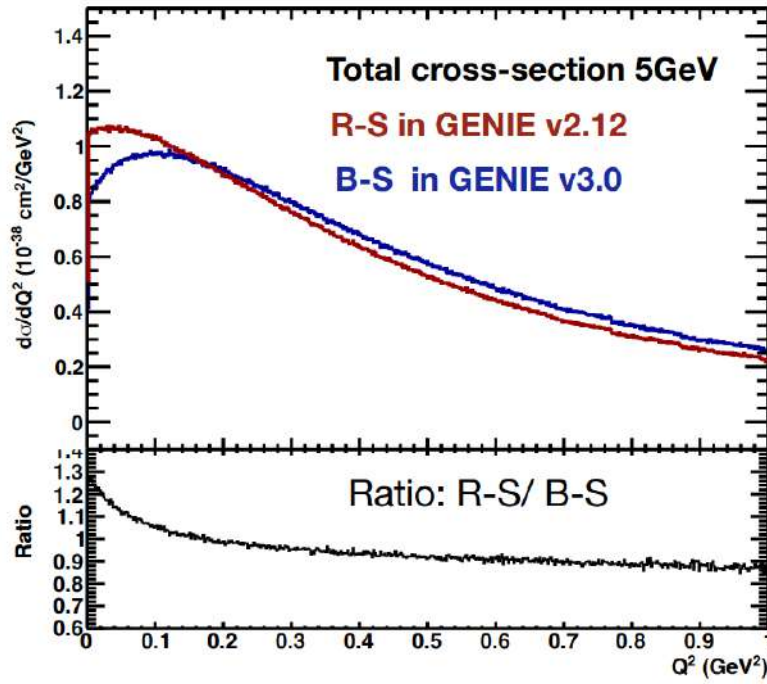


Figure 6.23: Cross-section with Rein-Sehgan and Berger-Sehgal Pion production model in GENIE, plot taken from [270]

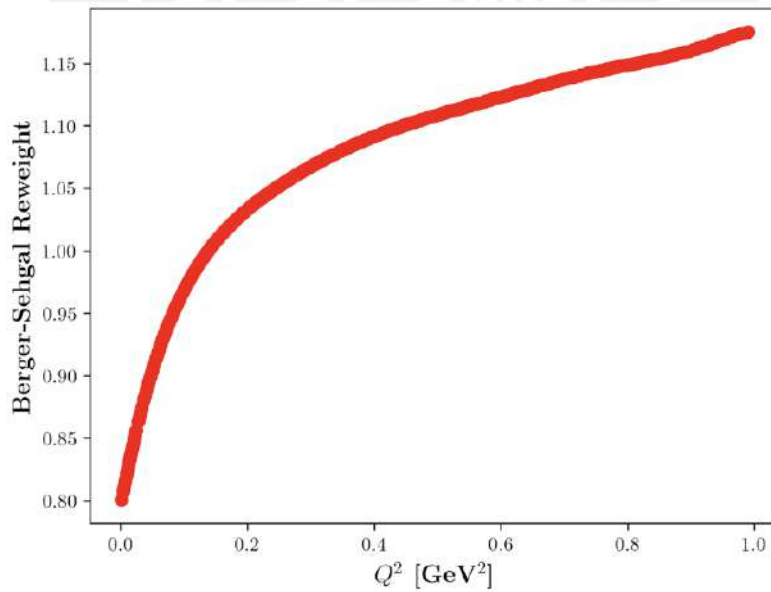


Figure 6.24: Parametrization weight to implement in the low recoil sample, parametrization provided by [270].

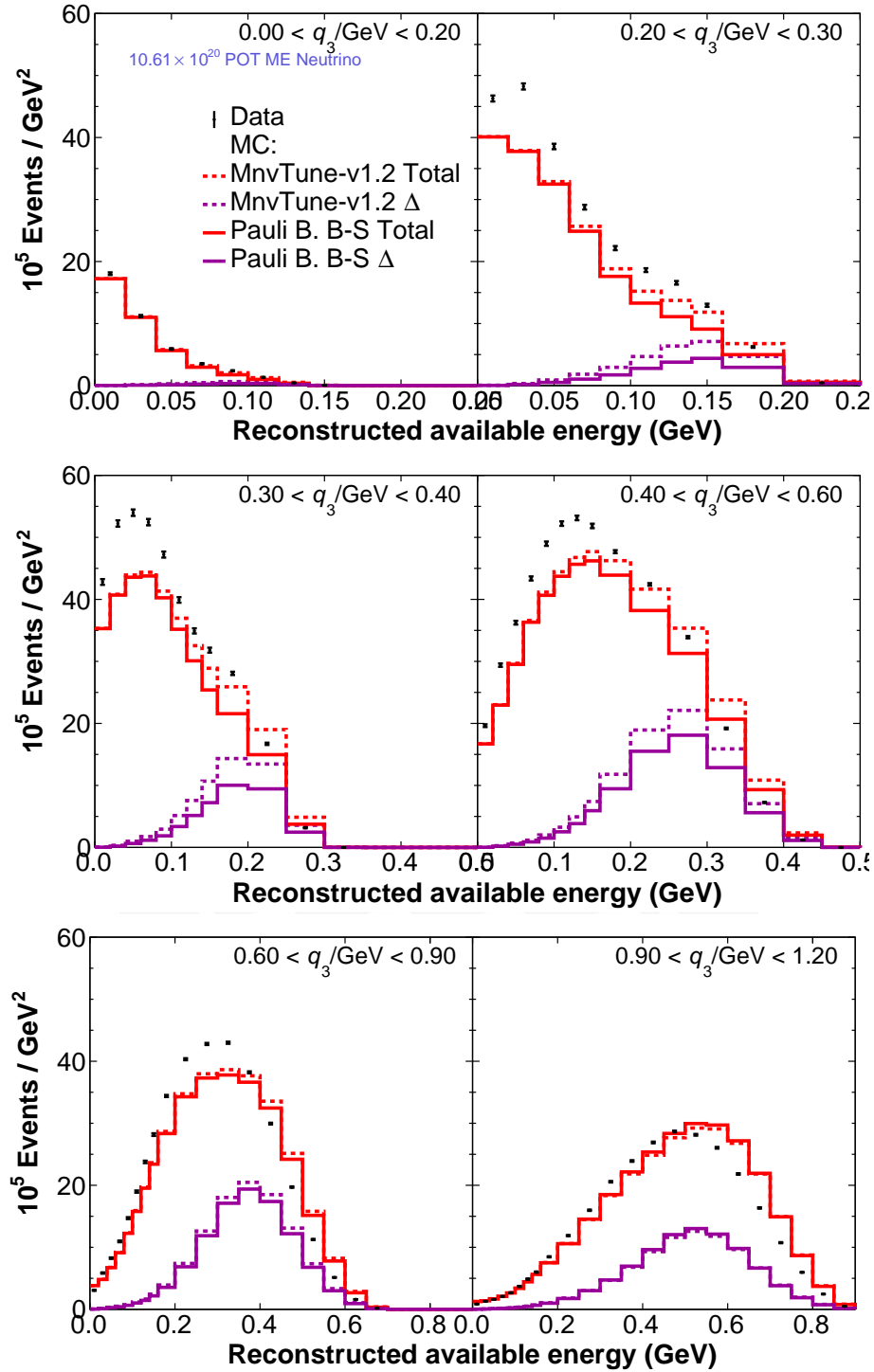


Figure 6.25: Reconstructed E_{avail} in projections of reconstructed q_3 regions, the dashed lines are nominal MC, and continuous lines are the purple Pauli Blocking with Berger Sehgal effect. In red the Total MC and in purple RES event types.

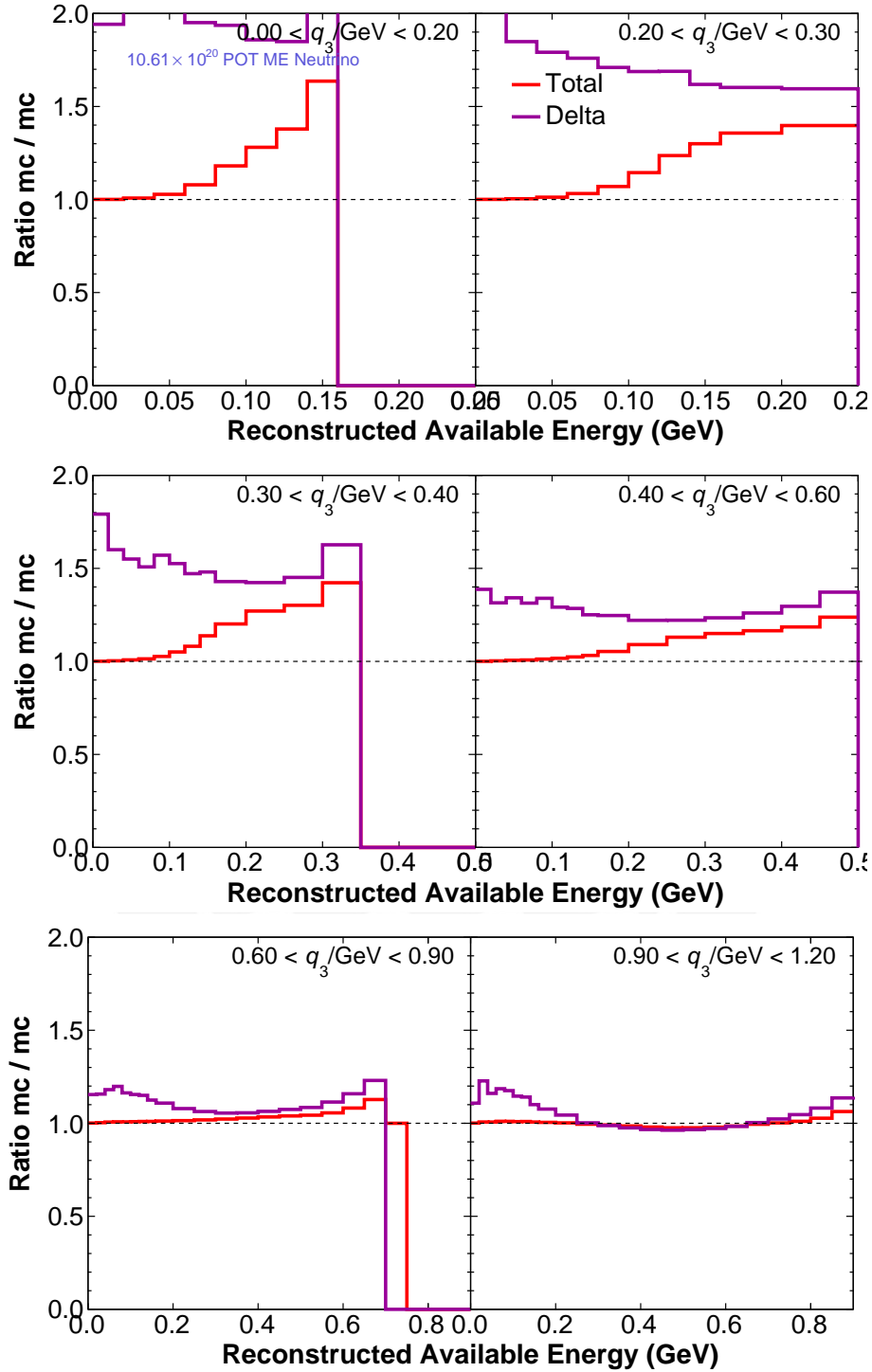


Figure 6.26: Ratio of nominal MC over MC Pauli Blocking with Berger-Sehgal for reconstructed E_{avail} in projections of reconstructed q_3 regions, the dashed lines are nominal MC, and continuous lines are the Pauli Blocking with Berger-Sehgal effect. In red the Total MC and in purple RES event types.

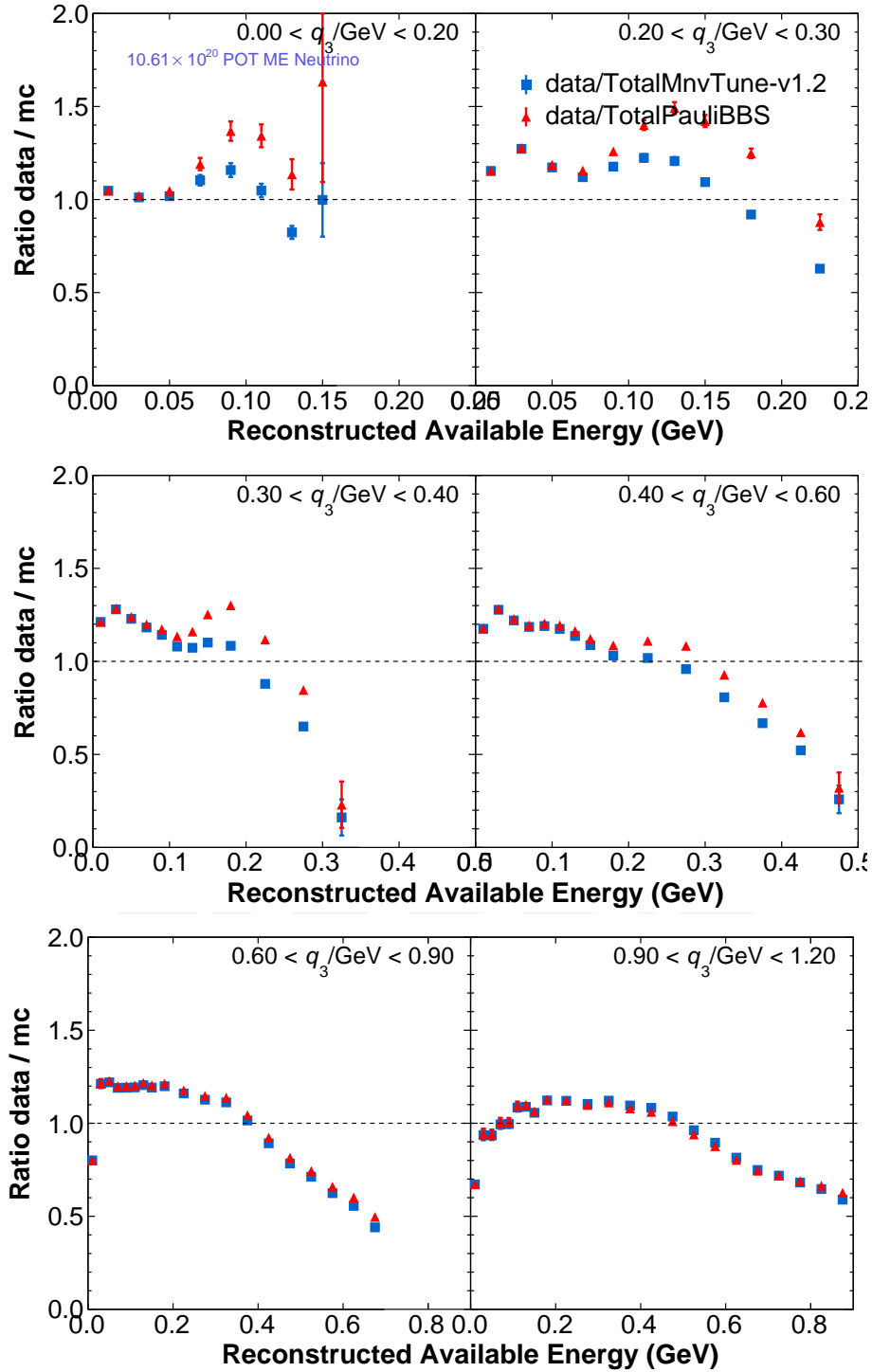


Figure 6.27: Ratio of data over MC Pauli Blocking with Berger-Sehgal for reconstructed E_{avail} in projections of reconstructed q_3 regions, the dashed lines are nominal MC, and continuous lines are the Pauli Blocking with Berger-Sehgal effect. In red the Total MC and in purple RES event types.

6.6 Minoo Kabirnezhad Single Pion Production Model

A extended version of Rein [271] Single Pion Production M. Kabirnezhad (MK-SPP) model is applied [272]. The MK-SPP model includes the lepton mass effect, resonant, and non-resonant background pion production.

The non-resonant background is calculated on piN center-of-mass frame (helicity basis) with 5 diagrams (Figure 6.29) instead of three Born diagram (Figure 6.28), exactly the part in which GENIE was replaced by DIS background. The main contribution at the time to compare with the default resonant production with GENIE is this Non-resonant and interference characterized of MK-SPP model.

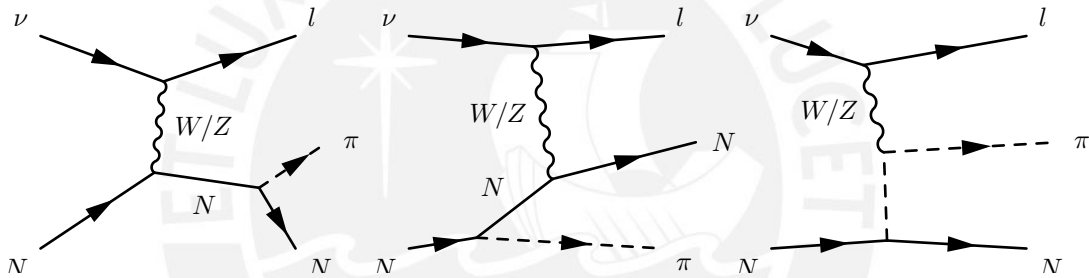


Figure 6.28: Born Diagrams from [272].

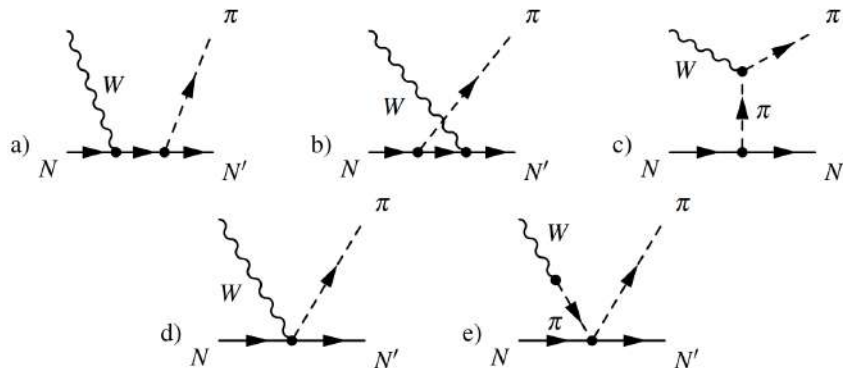


Figure 6.29: Five non-resonant diagrams taken from [272] and used in [273].

The MK-SSP model is implemented in NEUT [274], and to re-weight

GENIE, the first step was to generate events in both generators with the MINERvA flux and with invariant mass up to 2.0 GeV. The events were for free nucleon in both cases. However, in GENIE, the DIS event was generated in addition to Reigh-Sehgal resonant model. The reason is instead of calculating the non-resonant amplitudes and the interferences directly, GENIE takes the DIS model to propagate in the lower region (invariant mass lower than 1.7 GeV) as the background of RES, see Figure 6.30.

The total (RES and DIS for this case) inelastic cross section,

$$\frac{d^2\sigma^{\text{inel}}}{dQ^2dW} = \frac{d^2\sigma^{\text{RES}}}{dQ^2dW} + \frac{d^2\sigma^{\text{DIS}}}{dQ^2dW}, \quad (6.2)$$

where RES and DIS are,

$$\frac{d^2\sigma^{\text{RES}}}{dQ^2dW} = \sum_k \left(\frac{d^2\sigma^{\text{R/S}}}{dQ^2dW} \right)_k \cdot \Theta(W_{\text{cut}} - W), \quad (6.3)$$

$$\frac{d^2\sigma^{\text{DIS}}}{dQ^2dW} = \frac{d^2\sigma^{\text{DIS,BY}}}{dQ^2dW} \Theta(W_{\text{cut}} - W) + \frac{d^2\sigma^{\text{DIS,BY}}}{dQ^2dW} \Theta(W_{\text{cut}} - W) \cdot \sum_m f_m. \quad (6.4)$$

where the second part of the sum in the equation 6.4 affects the RES region.

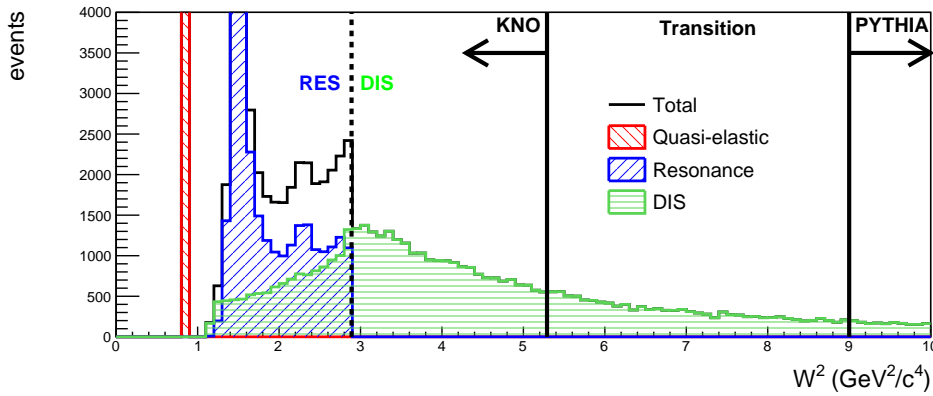


Figure 6.30: GENIE cut at $W_{\text{cut}} = 1.7$ GeV the resonate and the DIS region. Figure taken from [275].

The re-weight was develop in two dimensional free nucleon cross

section⁴, W and Q^2 . Because the GENIE W cuts the re-weight region is $0.0 < Q^2 < 1.5 (\text{GeV}/c^2)^2$ and $1.08 < W < 1.7\text{GeV}/c^2$. The events were generating for charge current neutrino channel, CC $\nu_\mu p \rightarrow \mu^- p\pi^+$, CC $\nu_\mu n \rightarrow \mu^- p\pi^0$ and CC $\nu_\mu n \rightarrow \mu^- n\pi^+$.

CC $\nu_\mu p \rightarrow \mu^- p\pi^+$ Channel

The neutrino interaction in this channel is dominated by $\Delta(1232)$ resonance with principal decay mode (Γ_1) of 99.4% to proton and positive charge pion [172]. In the Figure 6.31, we can observe for MK-SSP model (left) and RS model (right) with high contributions in the high Q^2 region and high tail in the invariant mass with a visible cut in $W = 1.7 \text{ GeV}$, more visible in the Figure 6.33.

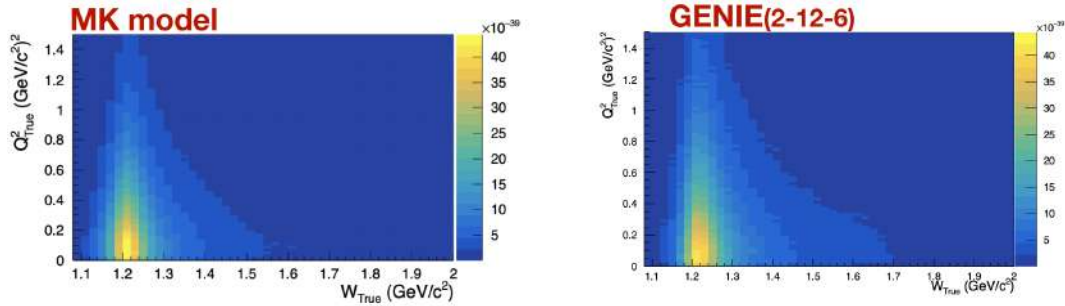


Figure 6.31: The z axis is $d\sigma^2/dQ_{\text{True}}^2 dW_{\text{True}}$ ($\text{cm}^2/(\text{GeV}/c^2)^2/(\text{GeV}/c^2)^2/\text{nucleon}$) and corresponds to charge current $\nu_\mu p \rightarrow \mu^- p\pi^+$ channel.

In the lower corner of Q^2 and W , for $W < 1.2 \text{ GeV}/c^2$ there is an enhance of around ~ 1.5 (Figure 6.33) with in general means a shift to the left of the Δ tail. The small shift is coming from the contribution of background part of MK-SPP model, which is appraised in the plots compared with BEBC 90 and ANL data for $\nu_\mu p \rightarrow \mu^- p\pi^+$ channel (Figure 6.32). Once applied the re-weight to low recoil sample that channel contributes more see grenn histogram

⁴The re-weight was implemented with the help of Clarence Wret from University of Rochester

of Figure 6.41 to total, see Figure 6.40, both are showing the contributions in truth distributions. Same behavior is appreciated in the reconstructed total (see Figure 6.42) and only resonant distributions (see Figure 6.43).

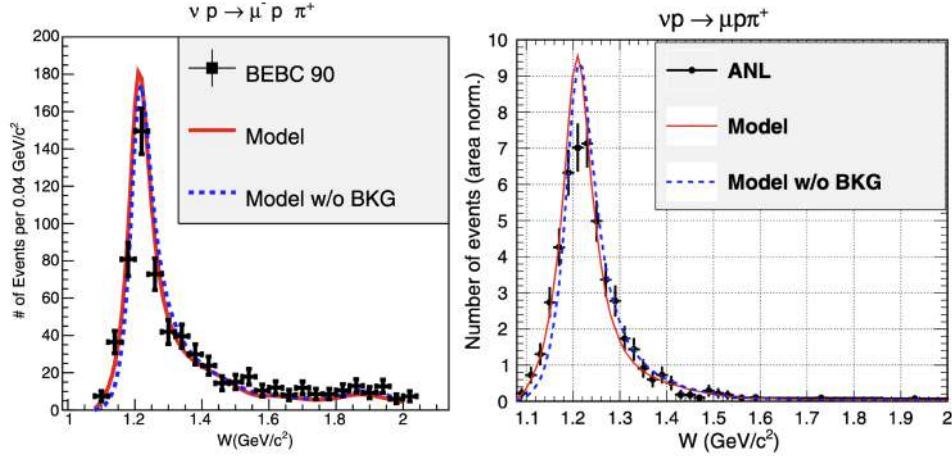


Figure 6.32: Data of BEBC [276] (left) and data of ANL [277] compared against MK-SPP model with (red) / without (dashed blue) background. Plots taken from Figure 10 and 11 from [272] and M. Kabirnezhad's thesis [278].

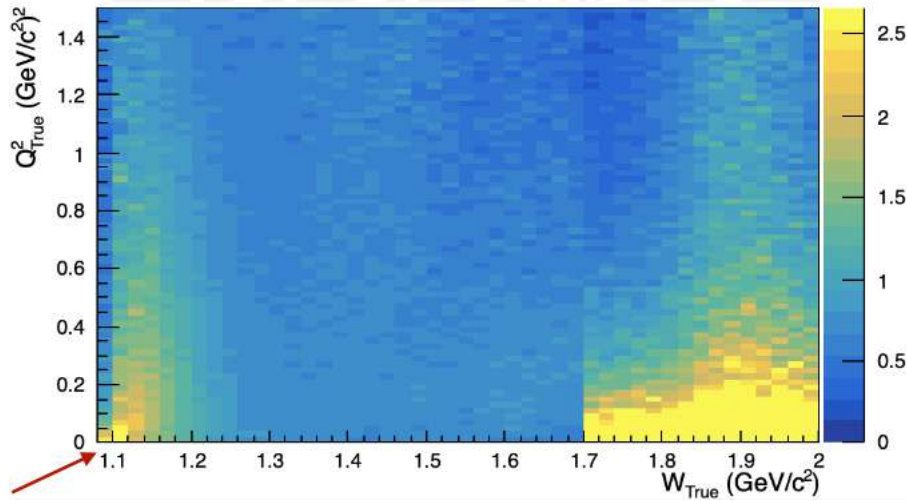


Figure 6.33: Ratio of left (MK model) plot over right plot (GENIE) of Figure 6.31, the region of interest is $1.08 < W < 1.7(\text{GeV}/c^2)$ and $0. < Q^2 < 1.5 (\text{GeV}/c^2)^2$.

CC $\nu_\mu n \rightarrow \mu^- p \pi^0$ Channel

The same trend that Δ channel follows the $\nu_\mu n \rightarrow \mu^- p \pi^0$ channel. The Figure 6.35 show different model behaviour for ANL and BEBC 90 data, and that is because they are in different energy regions, ANL goes from around 0,5 GeV to 6 GeV and BEBC 90 for high energies that 6 GeV, that changes the Q^2 and therefore W (see ratio plot in Figure 6.36).

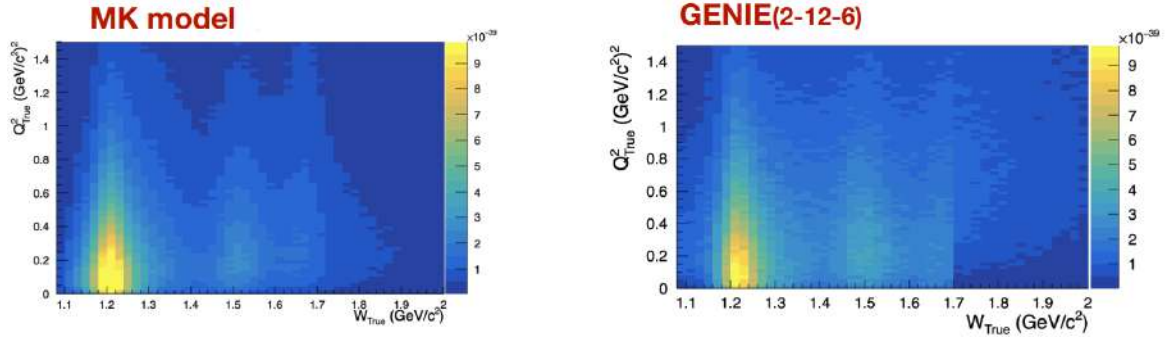


Figure 6.34: The z axis is $d\sigma/dQ_{\text{True}}^2 dW_{\text{True}}$ ($\text{cm}^2/(\text{GeV}/c^2)^2$)/nucleon and corresponds to charge current $\nu_\mu n \rightarrow \mu^- p \pi^0$ channel.

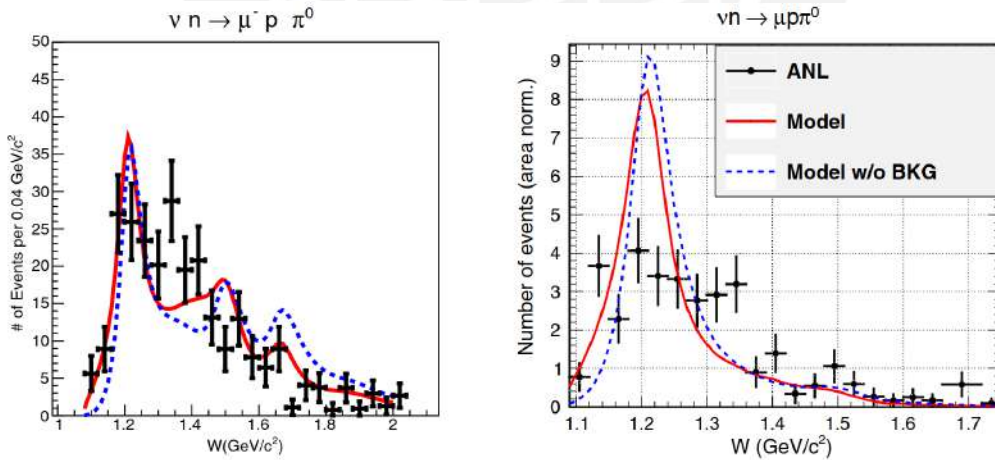


Figure 6.35: Data of BEBC [276] (left) and data of ANL [277] compared against MK-SPP model with (red) / without (dashed blue) background. Plots taken from Figure 10 and 11 from [272] and thesis [278].

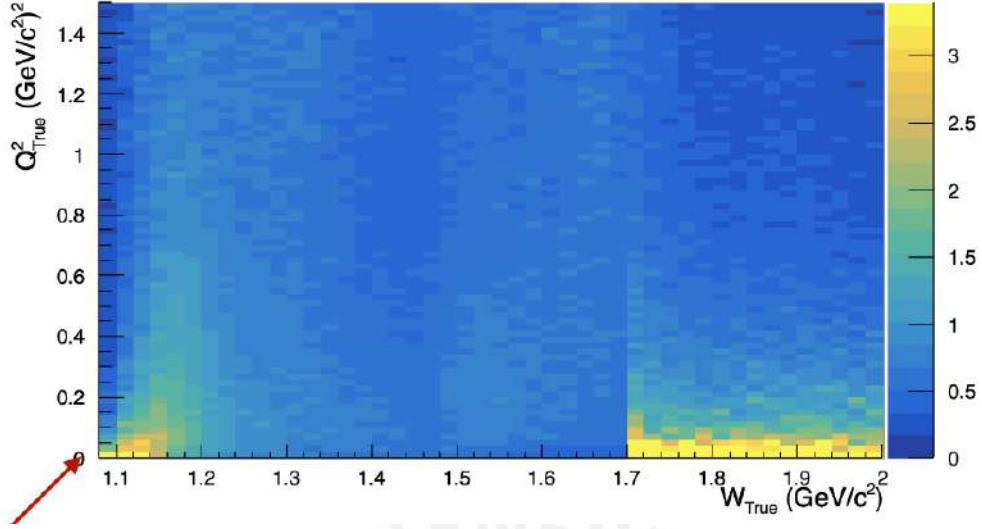


Figure 6.36: Ratio of left (MK model) plot over right plot (GENIE) of Figure 6.34, the region of interest is $1.08 < W < 1.7(\text{GeV}/c^2)$ and $0. < Q^2 < 1.5 (\text{GeV}/c^2)^2$.

CC $\nu_\mu n \rightarrow \mu^- n \pi^+$ Channel

The trend is similar than Δ and $\nu_\mu n \rightarrow \mu^- p \pi^0$ channel (see Figure 6.37, 6.38, and 6.39), for more resonance channels, with same ANL/BEBC 90 data comparison and background effect.

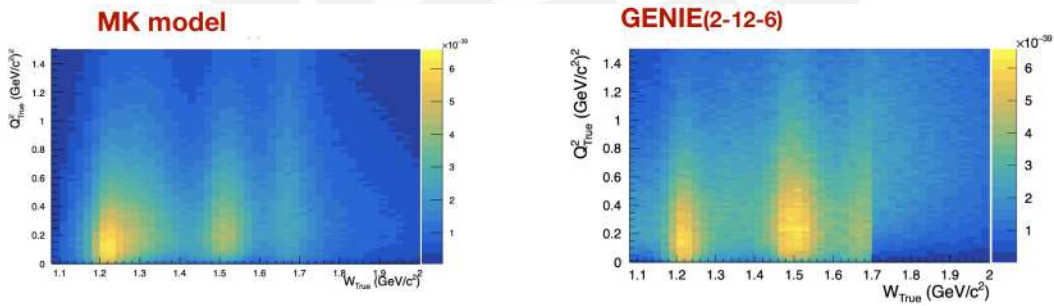


Figure 6.37: The z axis is $d\sigma^2/dQ_{\text{True}}^2 dW_{\text{True}}$ ($\text{cm}^2/(\text{GeV}/c^2)/(\text{GeV}/c^2)^2/\text{nucleon}$) and corresponds to charge current $\nu_\mu n \rightarrow \mu^- n \pi^+$ channel.

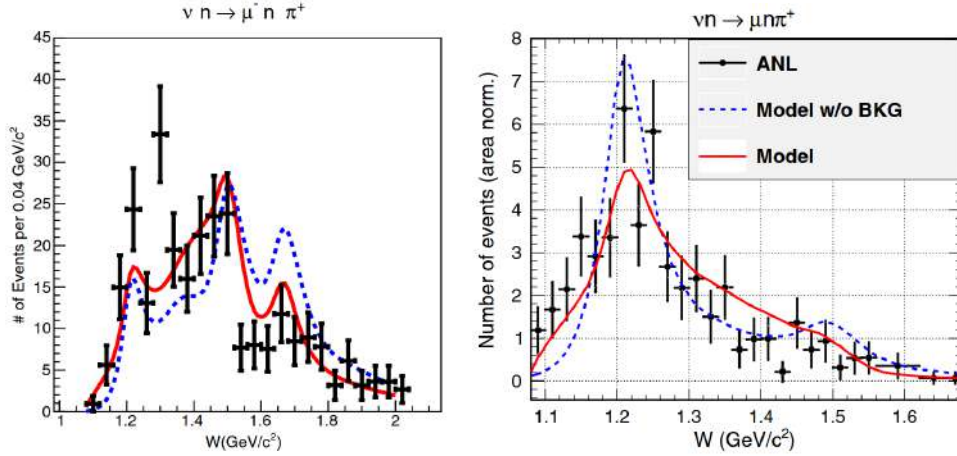


Figure 6.38: Data of BEBC [276] (left) and data of ANL [277] compared against MK-SPP model with (red) / without (dashed blue) background. Plots taken from Figure 10 and 11 from [272] and thesis [278].

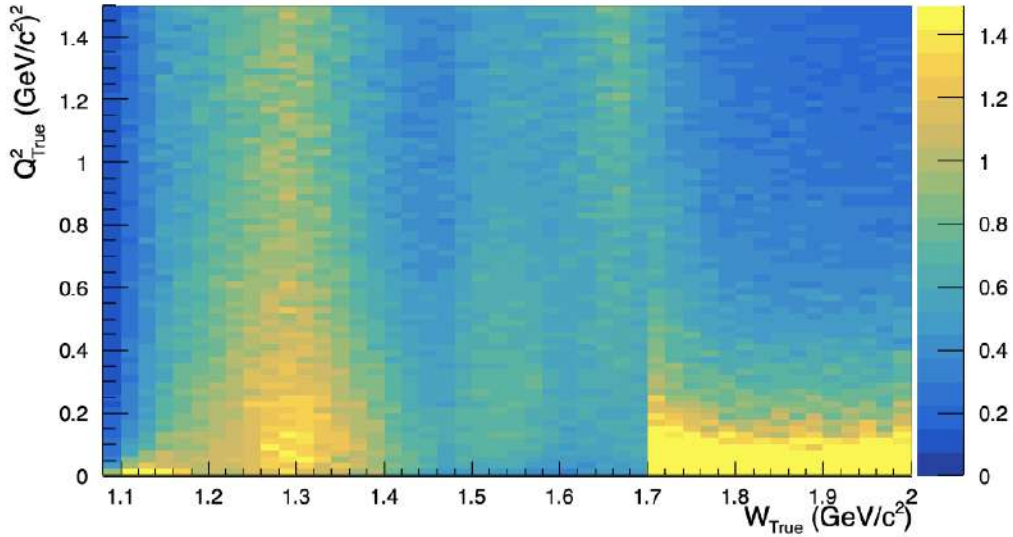


Figure 6.39: Ratio of left (MK model) plot over right plot (GENIE) of Figure 6.37, the region of interest is $1.08 < W < 1.7(\text{GeV}/c^2)$ and $0. < Q^2 < 1.5 (\text{GeV}/c^2)^2$.

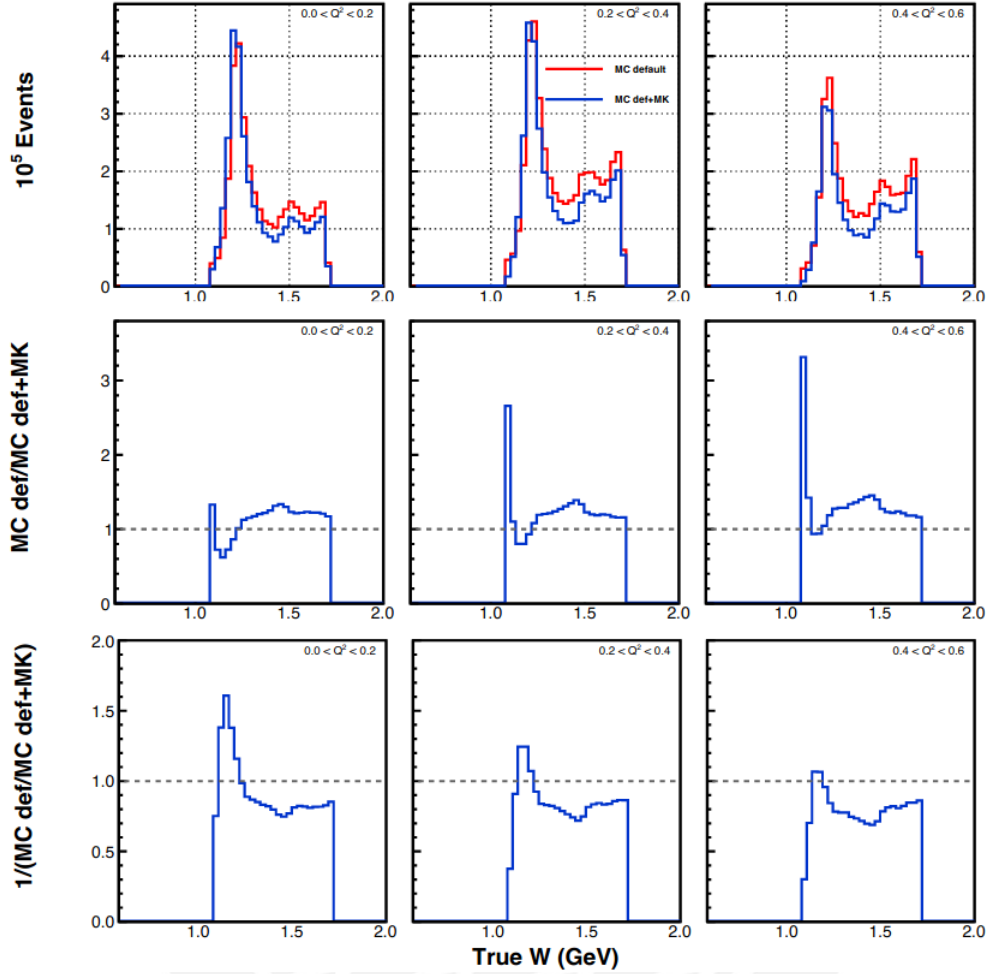


Figure 6.40: True W distributions of low recoil sample, the top plots represent the comparison of overall MK-SPP model against of MnvTune.v1, then the following plots on bottom are the ratio and one over the ratio.

Effect on Low Recoil Sample

In low recoil variable q_3 and E_{avail} the effect follows pretty much like the described in the Figure 6.42 and Figure 6.43. Which is a small shift of the Δ peak to lower W and therefore lower hadron energy, and a suppression of the rate in the region where higher resonances and the non resonant terms overlap.

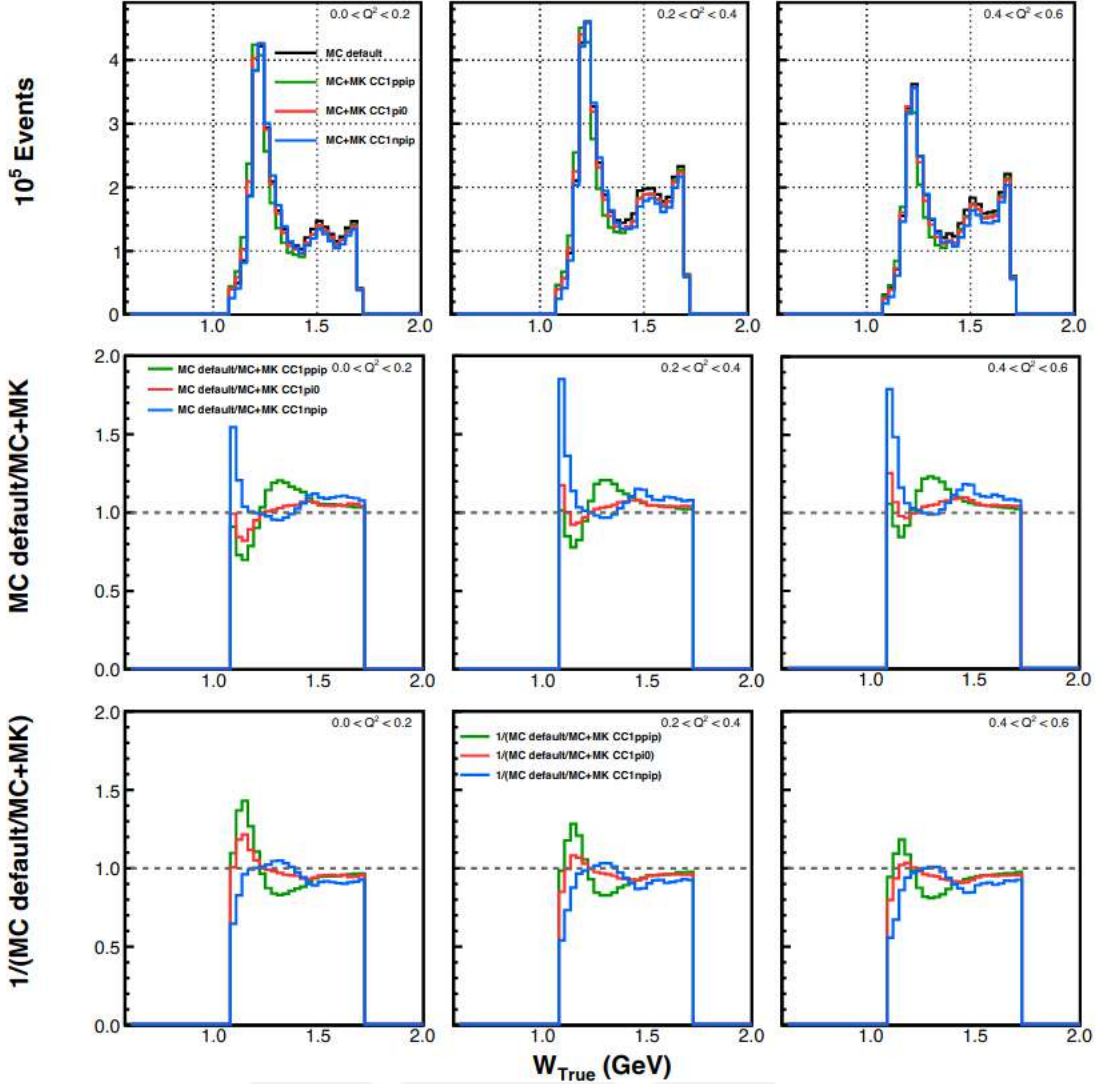


Figure 6.41: True W distributions of low recoil sample, the top plots represent the comparison of channel MK-SPP model against of MnvTune.v1, then the following plots on bottom are the ratio and one over the ratio respect to MnvTune.v1.

That shift and suppression behaviour is conserved partially in the E_{avail} and q_3 variables, see Figure 6.44 and 6.45. This model is similar with less suppression and shift to Low- Q^2 suppression, and resonant removal energy. The improvement is in the medium and higher E_{avail} , with effect in all range of q_3 Figure 6.46.

6.6. MINOO KABIRNEZHAD SINGLE PION PRODUCTION MODEL

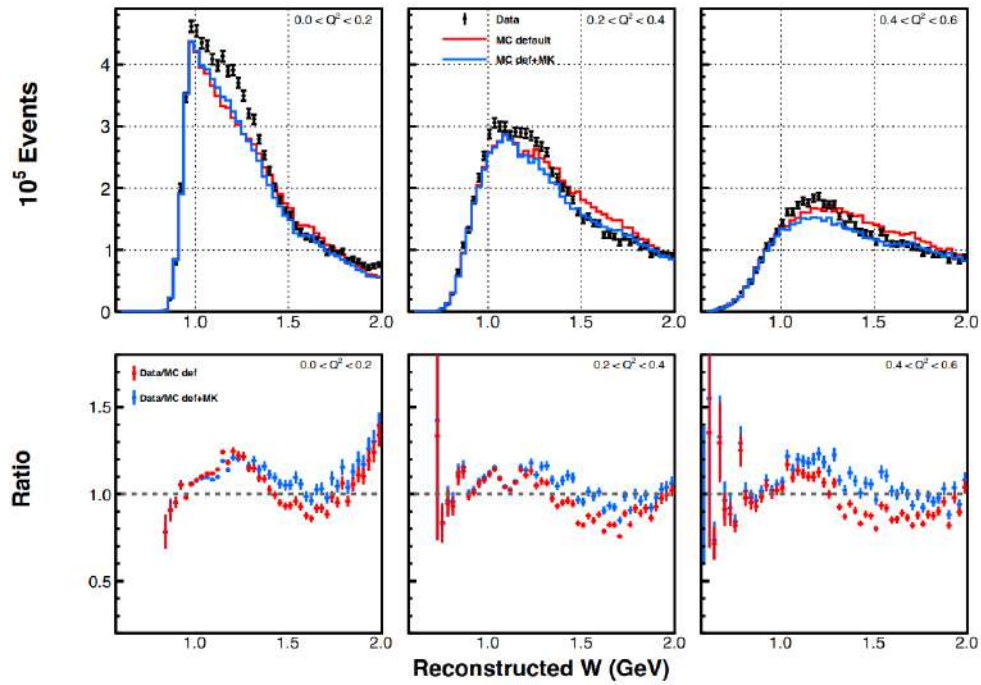


Figure 6.42: Reconstructed W distributions of low recoil sample, overall effect in the total MC compared MC MK-SPP model with MnvTune.v1 (labeled as MC def.). Bottom plots are the ratio between data over MC.

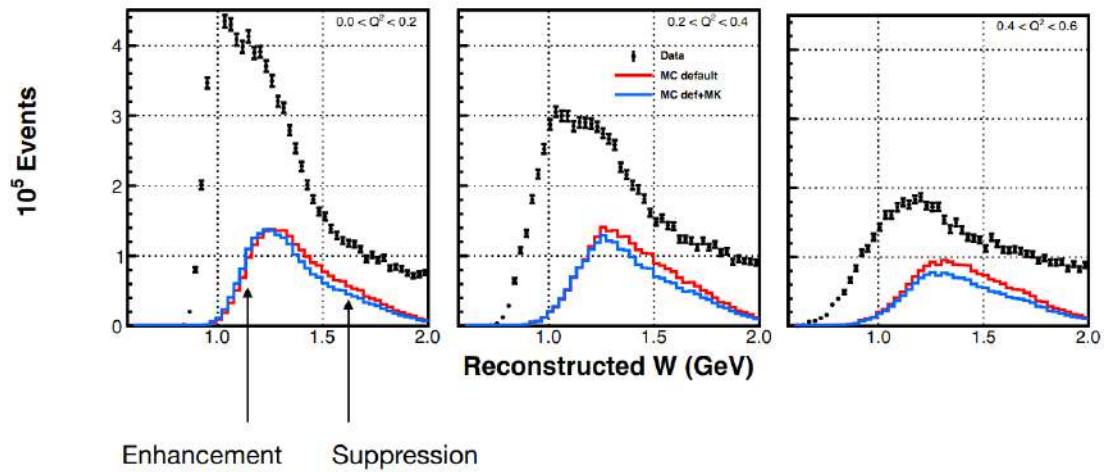


Figure 6.43: Data compared with MC-RES with MnvTune.v1 (default in the label) and MK-SPP.

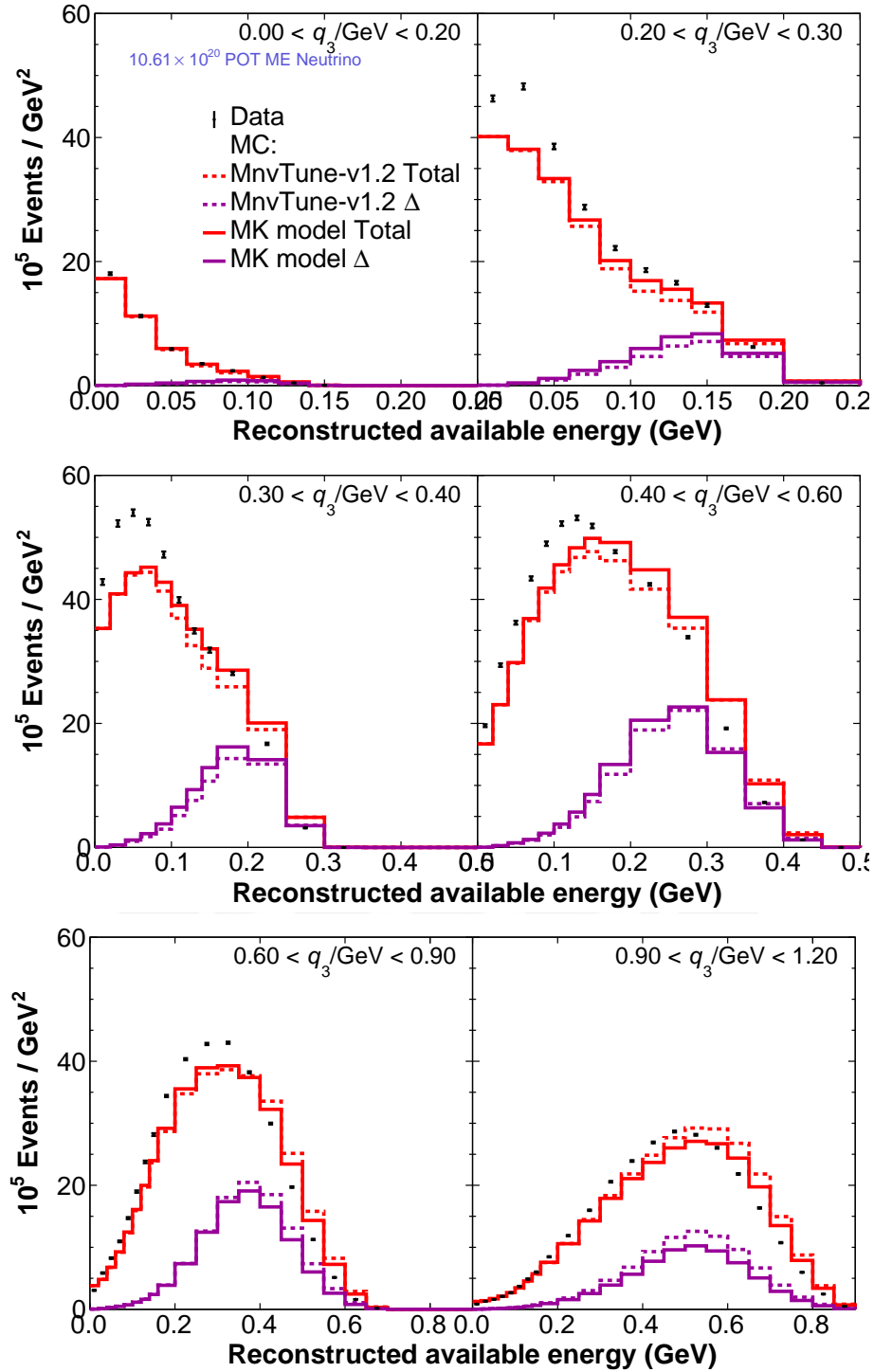


Figure 6.44: Reconstructed E_{avail} in projections of reconstructed q_3 regions, the dashed lines are nominal MC, and continuous lines are the purple MK-SPP effect. In red the Total MC and in purple RES event types.

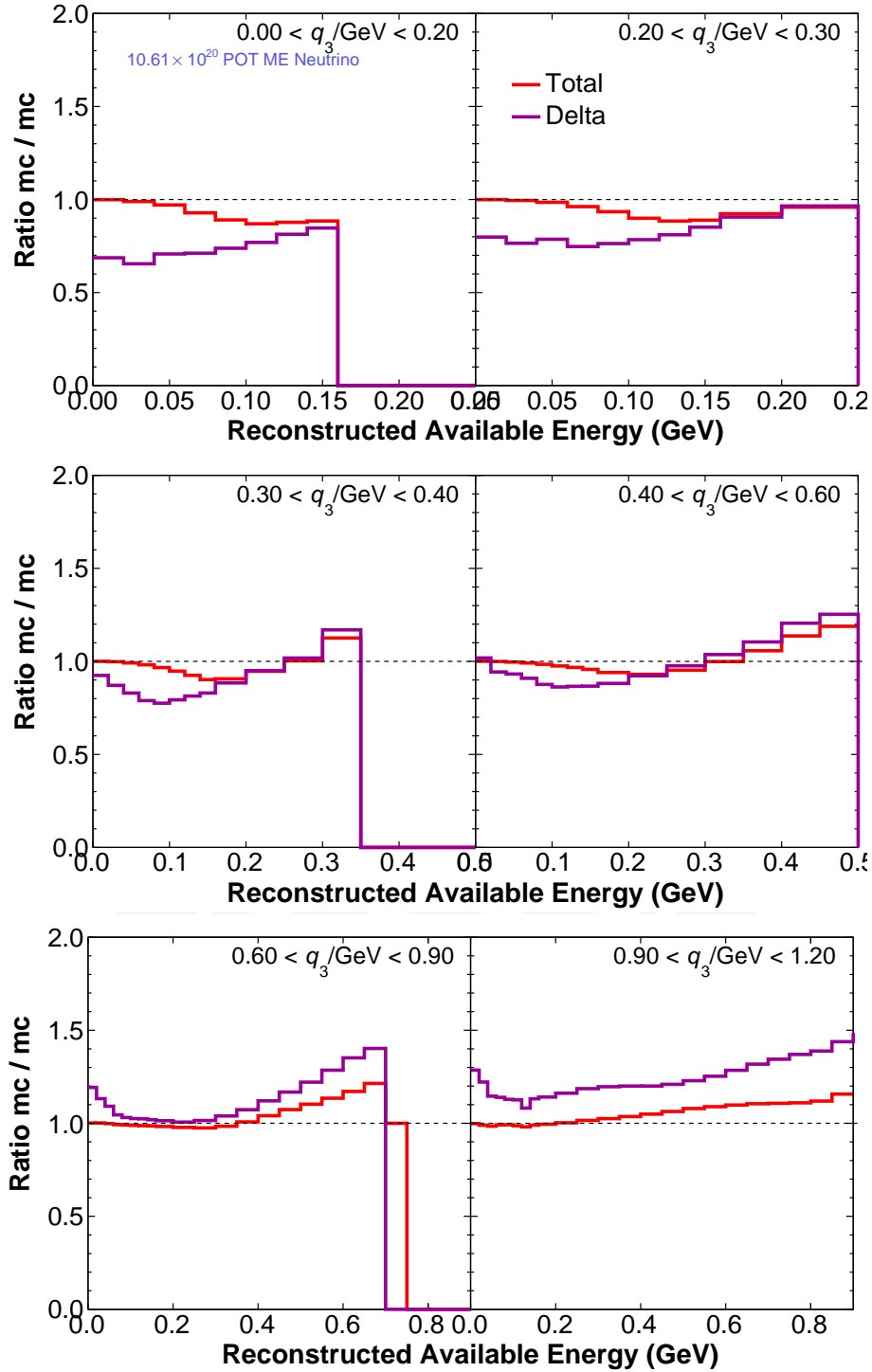


Figure 6.45: Ratio of nominal MC over MC MK for reconstructed E_{avail} in projections of reconstructed q_3 regions, the dashed lines are nominal MC, and continuous lines are the MK-SSP effect. In red the Total MC and in purple RES event types.

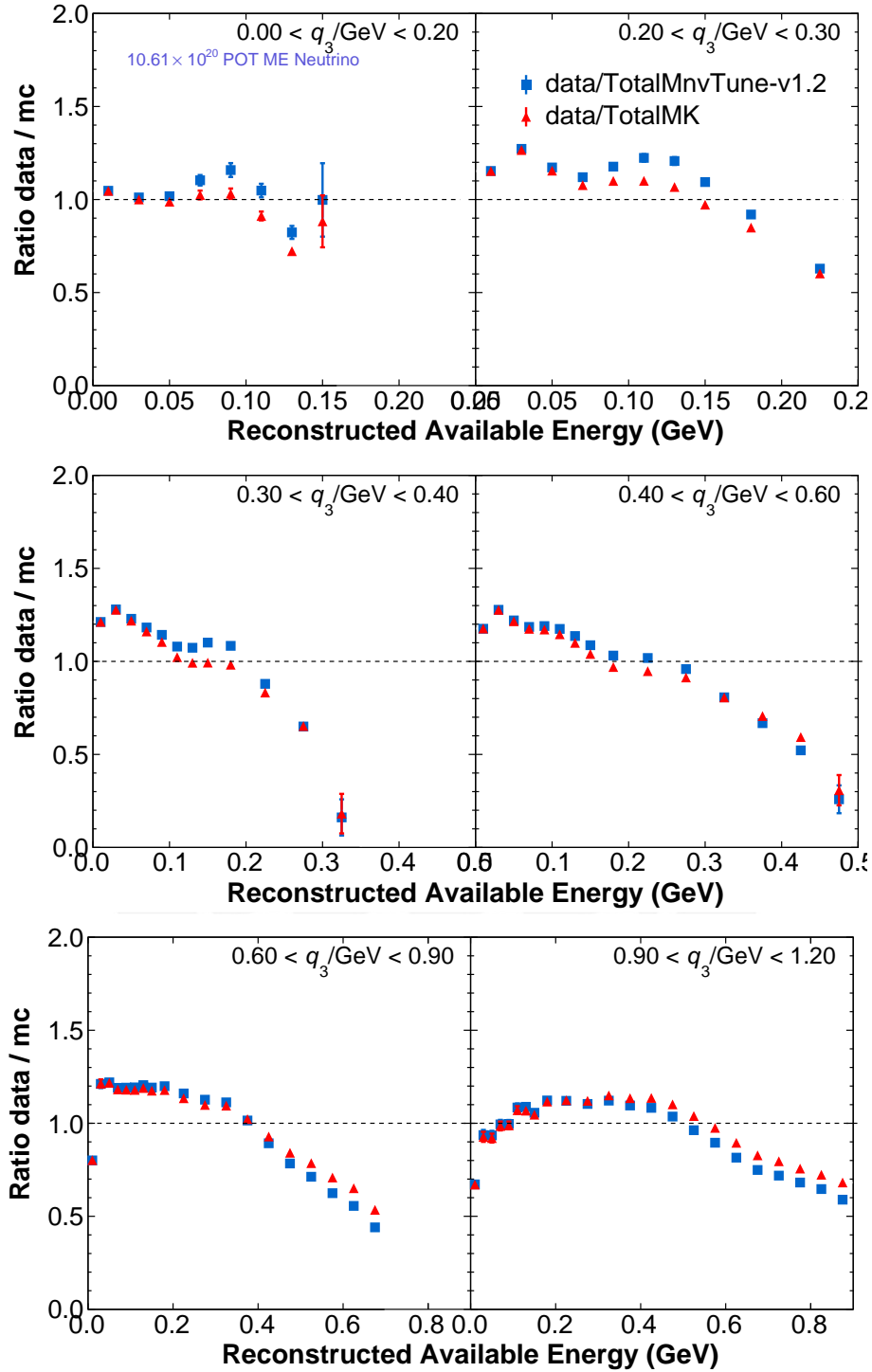


Figure 6.46: Ratio of data over MC MK for reconstructed E_{avail} in projections of reconstructed q_3 regions, the dashed lines are nominal MC, and continuous lines are the MK-SPP effect. In red the Total MC and in purple RES event types.

6.7 QERPA to RES events

In this section, we are going to discuss a re-weight of GENIE with QE-RPA [227] to the resonant region. As we show above, the feature that should have the resonant model is suppressed at low Q^2 . A suppression like QE-RPA does in quasi-elastic. Here we tested moving or applying that weight into a different event type region. The Valencia QE-RPA suppression depends on q_0 and q_3 and with this test we want to see if the screening effect can be in the Δ relative to the minimum energy transfer to produce the resonance. Maybe this effect is similar to the calculated QE form and we can apply it with a shift whose magnitude is mass delta minus mass nucleon.

The effect of this weight in the resonant part kind of BS plus Pauli blocking, but in less intensity (see Figure 6.48). Indeed, there is a suppression which describes better compared the MnvTune.v1 at high available energy and q_3 (see Figure 6.49).

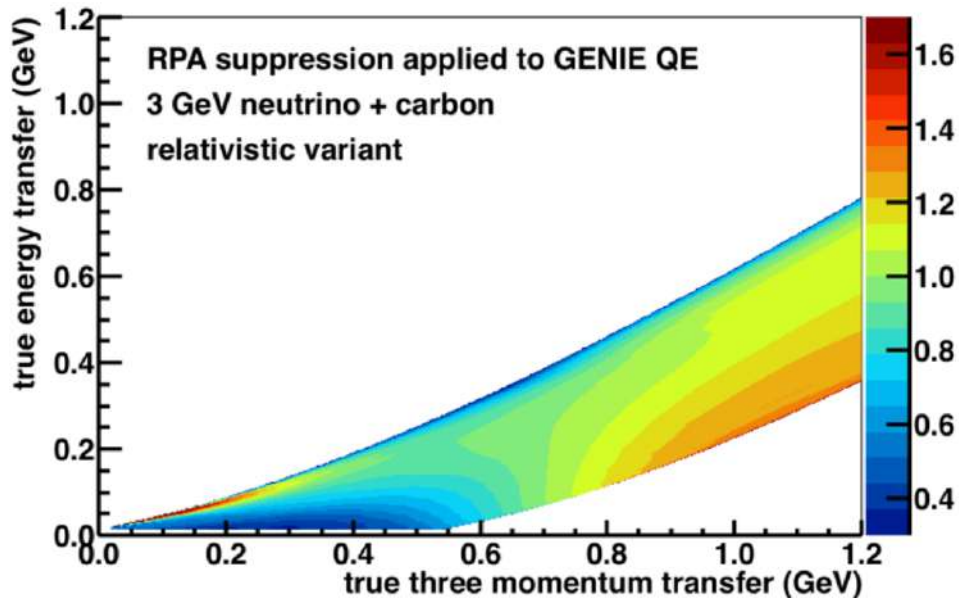


Figure 6.47: Quasi-elastic RPA weight, figure taken from [227].

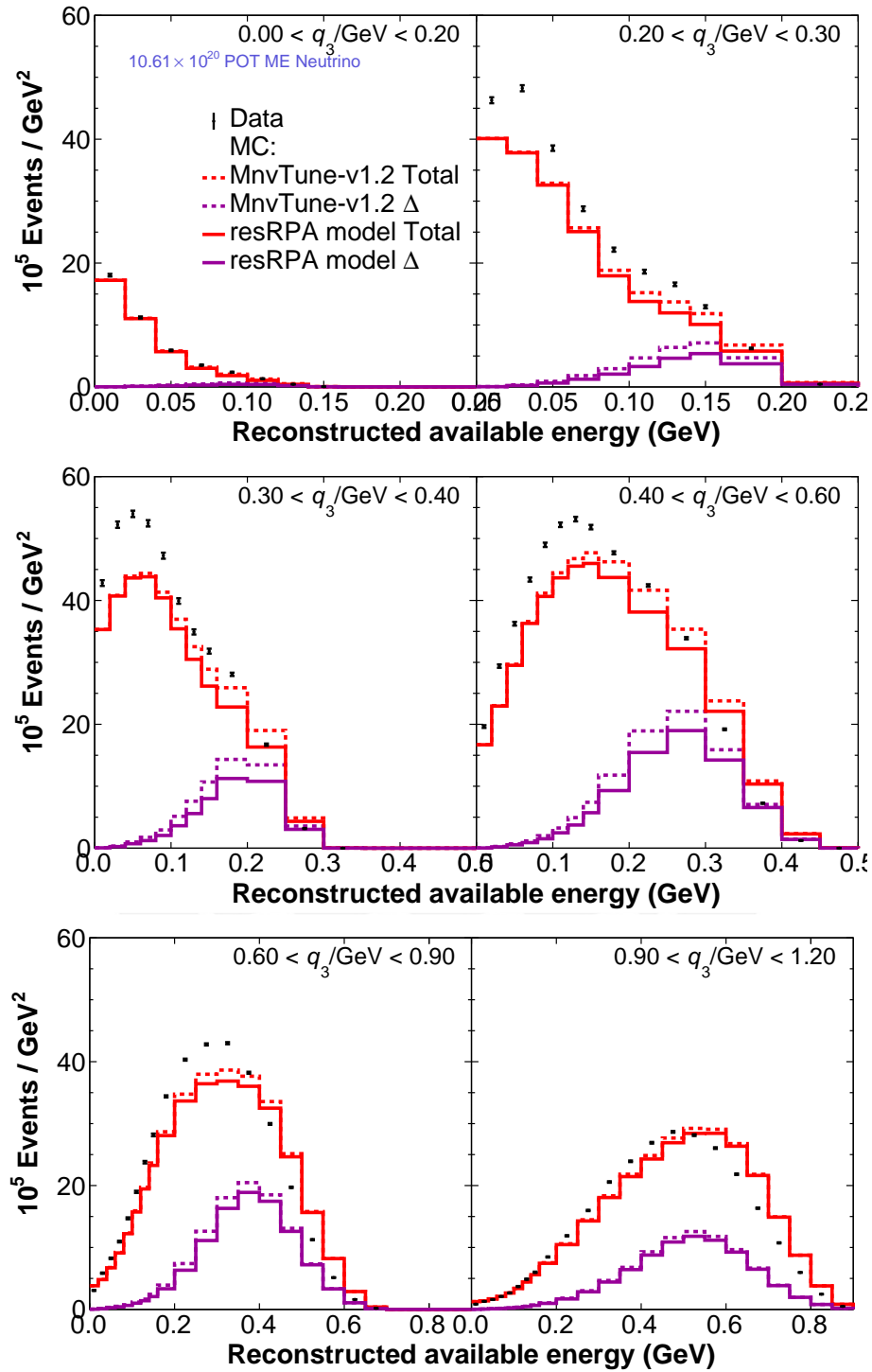


Figure 6.48: Reconstructed E_{avail} in projections of reconstructed q_3 regions, the dashed lines are nominal MC, and continuous lines are the purple QERPA to RES effect. In red the Total MC and in purple RES event types.

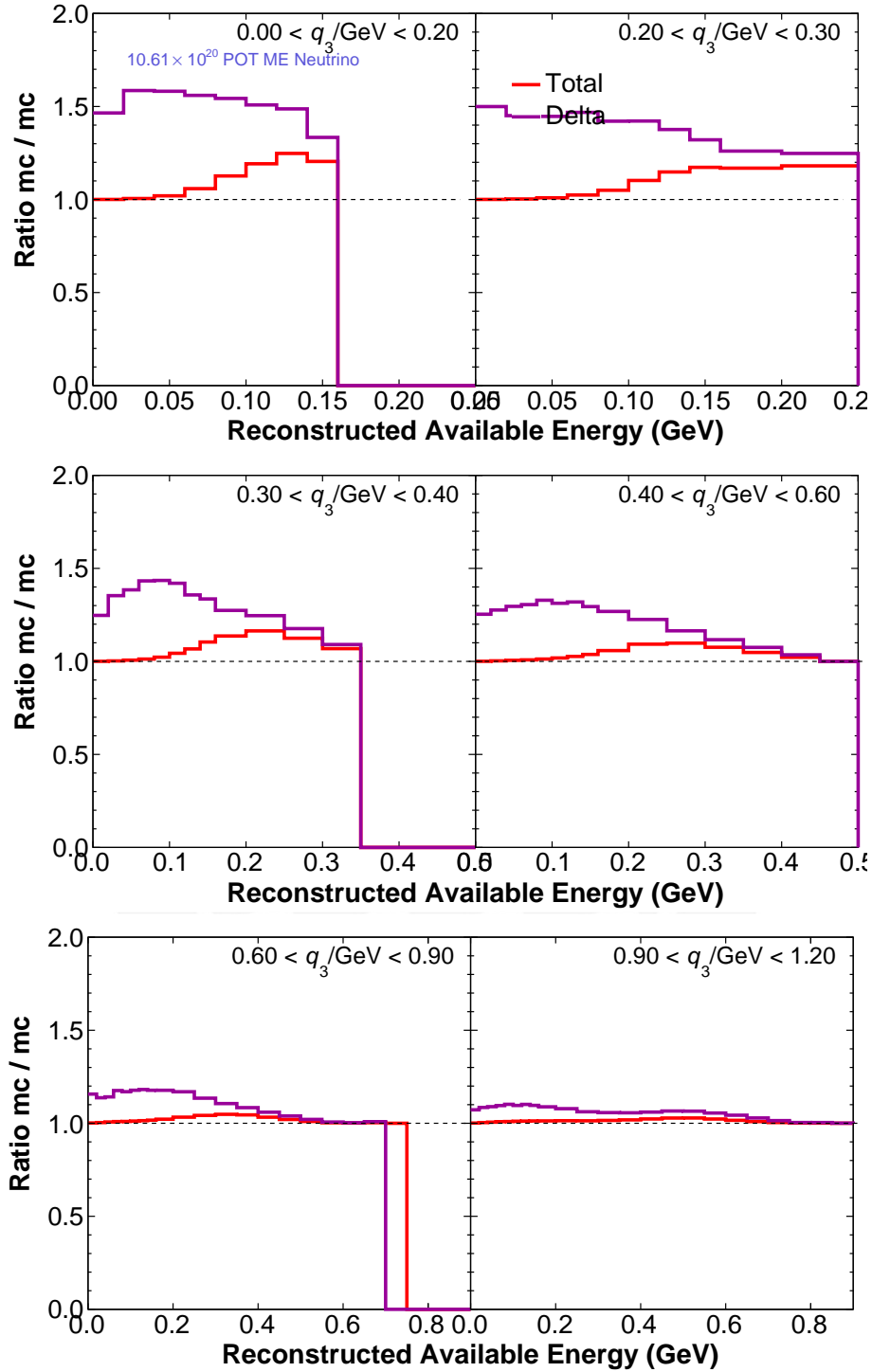


Figure 6.49: Ratio of nominal MC over MC QERPA-RES for reconstructed E_{avail} in projections of reconstructed q_3 regions, the dashed lines are nominal MC, and continuous lines are the QE-RPA to RES effect. In red the Total MC and in purple RES event types.

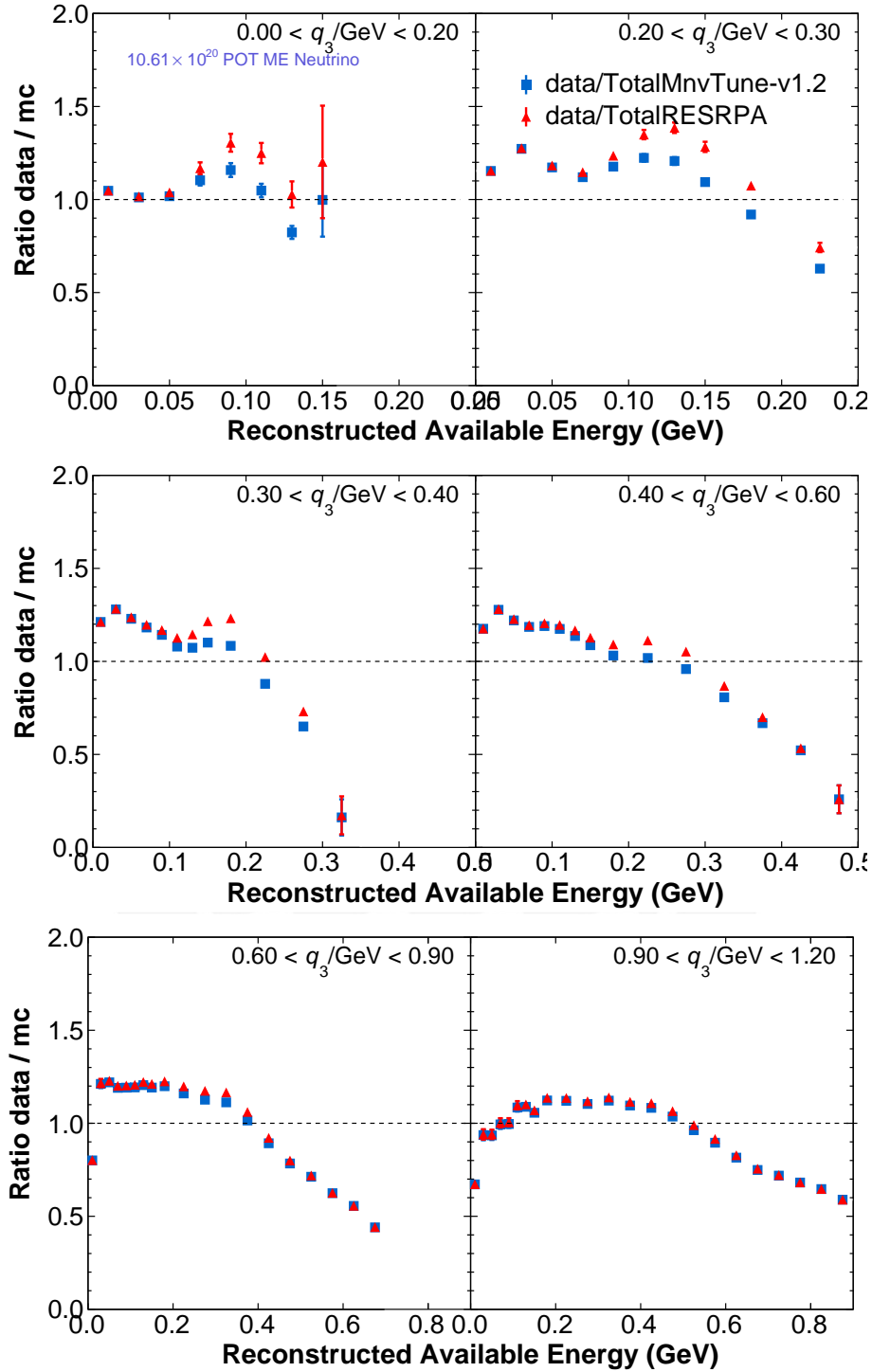


Figure 6.50: Ratio of data over MC QERPA-RES for reconstructed E_{avail} in projections of reconstructed q_3 regions, the dashed lines are nominal MC, and continuous lines are the QE-RPA to RES effect. In red the Total MC and in purple RES event types.

6.8 Summary

Some of the most recent theory-motivated models are added to examine the reconstructed distributions to understand better the model elements that could characterize the medium energy inclusive MINERvA data in Figure 5.1. The MnvTune.v1.2 Monte Carlo simulation⁵ does not describe the MINERvA data. The MnvTune.v1.2 includes a 2p2h model that was empirically tuned to previous MINERvA data [279]. The Low- Q^2 pion suppression (see section 6.4 and [264]) improves the simulation⁶, but it is also another empirical model based on MINERvA data that is similar to the one measured by MINOS using an iron target [265].

The previous sections described the effort in detail of all the models, from QE to RES regions. The summary plots for each region are shown in Figures 6.51 and 6.53. The qualitative description of each model is presented in a single Table 6.1. In addition, the ratio plots of MINERvA ME inclusive data over the simulation of each model are presented in Figures 6.52 and 6.54.

Incorporating the most recent theoretical work into the analysis reveals that a new tuning is required. The result is the so-called MnvTune.v3 (the reconstructed distribution plots are presented in the next chapter). The MnvTune.v3 replaces the Valencia 2p2h model and its enhancement by the SuSA 2p2h model [280, 281, 282], which has more events in the dip region and fewer in the very low Q^2 . In the QE process, the initial nucleon's high momentum tail increases, which raises the QE rate overall, especially outside the QE peak (in this thesis known as Bodek-Ritchie tail enhancement). And the outgoing hadronic system for resonances takes away 25 MeV from events with at least one proton in the final state; this moves Δ events into the dip region and away from very low Q^2 (in this thesis known as resonant removal energy).

⁵Usually used as the CV in MINERvA collaboration.

⁶The simulation with this tune is often called MnvTune.v2 by MINERvA collaboration.

The quantitative difference between the models is presented in terms of χ^2 . The matrix elements of χ^2 is defined by,

$$\chi_{ij\text{model}}^2 = (x_{i,\text{measured}} - x_{i,\text{expected}_{\text{model}}}) \times V_{ij}^{-1} \times (x_{j,\text{measured}} - x_{j,\text{expected}_{\text{model}}}) \quad (6.5)$$

where the V is the measured covariance matrix and x is the cross-section. The equation (6.5) shows the elements of the χ^2 matrix. The χ^2 is the the sum of all the elements of the matrix. At the reconstructed level the data distribution only has statistical uncertainties and the χ^2 only accounts the data covariance matrix. Later, at the background subtracted and unfolded stage the data covariance matrix will play a bigger rule. For the moment the Equation 6.5 is equivalent to $((\text{data} - \text{mc})/\sigma_{\text{data}})^2$.

The Table 6.2 shows the χ^2 values of each q_3 region and the total χ^2 for all the models; this includes the MnvTune.v3. The Figures 6.55 and 6.56 show the scaled bin-by-by χ^2 (E_{avail} and q_3 bins) for QE/2p2h and RES models respectively.

Models	Nuclear Model	QE	2p2h	RES.	Non-RES	DIS
MnvTune.v1.2	RFG+B-R tail	L-S + RPA	IFIC V. model +Enh.	R-S	Scaled B-Y+ non-res π supp.	B-Y
Bodek-Ritchie Tail Enh.	RFG+B-R tail	L-S + RPA + B-R tail Enh.	IFIC V. model+Enh.	R-S	Scaled B-Y+ non-res π supp.	B-Y
SuSA QE	RFG+B-R tail	L-S+SuSAQE	IFIC V. model+Enh.	R-S	Scaled B-Y+ non-res π supp.	B-Y
SuSA 2p2h	RFG+B-R tail	L-S + RPA	SuSA 2p2h	R-S	Scaled B-Y+ non-res π supp.	B-Y
PauliB+BS	RFG+B-R tail	L-S + RPA	IFIC V. model+Enh.	B-S+Pauli B.	Scaled B-Y+ non-res π supp.	B-Y
Rem. Energy	RFG+B-R tail	L-S + RPA	IFIC V. model+Enh.	R-S+R.E.	Scaled B-Y+ non-res π supp.	B-Y
Low Q^2 π Supp	RFG+B-R tail	L-S + RPA	IFIC V. model+Enh.	R-S+low Q^2	Scaled B-Y+ non-res π supp.	B-Y
M.K.	RFG+B-R tail	L-S + RPA	IFIC V. model+Enh.	M.K.	M.K.	B-Y
QERPA to RES	RFG+B-R tail	L-S + RPA	IFIC V. model+Enh.	R-S+RPA	Scaled B-Y+ non-res π supp.	B-Y
MnvTune.v3	RFG+B-R tail	L-S + RPA + B-R tail Enh.	SuSA 2p2h	R-S+R.E.	Scaled B-Y+ non-res π supp.	B-Y

Table 6.1: RFG + B-R tail refers to Relativistic Fermi Gas [263] with default Bodek-Ritchie tail (SRC) [245], L-S+RPA refers to Llewellyn-Smith [73] with Random Phase Approximation [227, 94, 234] (+B-R tail Enh refers to Bodek-Ritchie tail enhancement showed in Section 6.1), IFIC V. model+Enh refers to IFIC Valencia model [233, 234] with low energy analysis low recoil fit [221], R-S refers to Rein-Sehgal [76], B-S+Pauli B, refers to Berger-Sehgal [267, 268, 269, 270] with RES Pauli Blocking showed in Section 6.5, Scaled B-Y + non-res π supp. refers to DIS Bodek-Yang model [283] scaled with [284, 285] implemented in [82] with non-res π 43% reduction [228, 229], M.K. to Minoo Kabirnezhad Single Pion Production Model [272], Low Q^2 refers to Low Q^2 π Suppression tune [266].

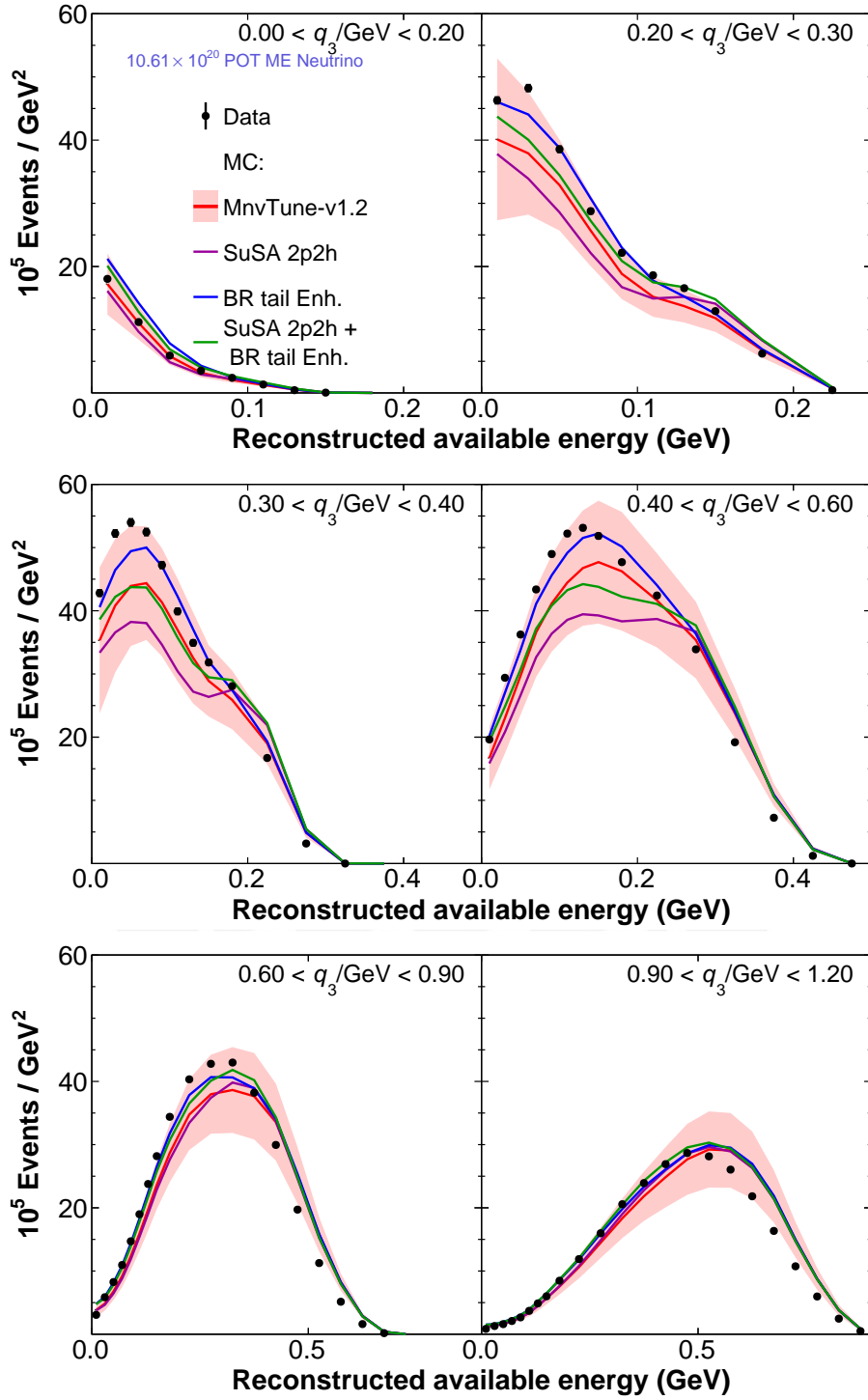


Figure 6.51: Reconstructed E_{avail} in projections of reconstructed q_3 regions, summary plot for the QE and 2p2h models study.

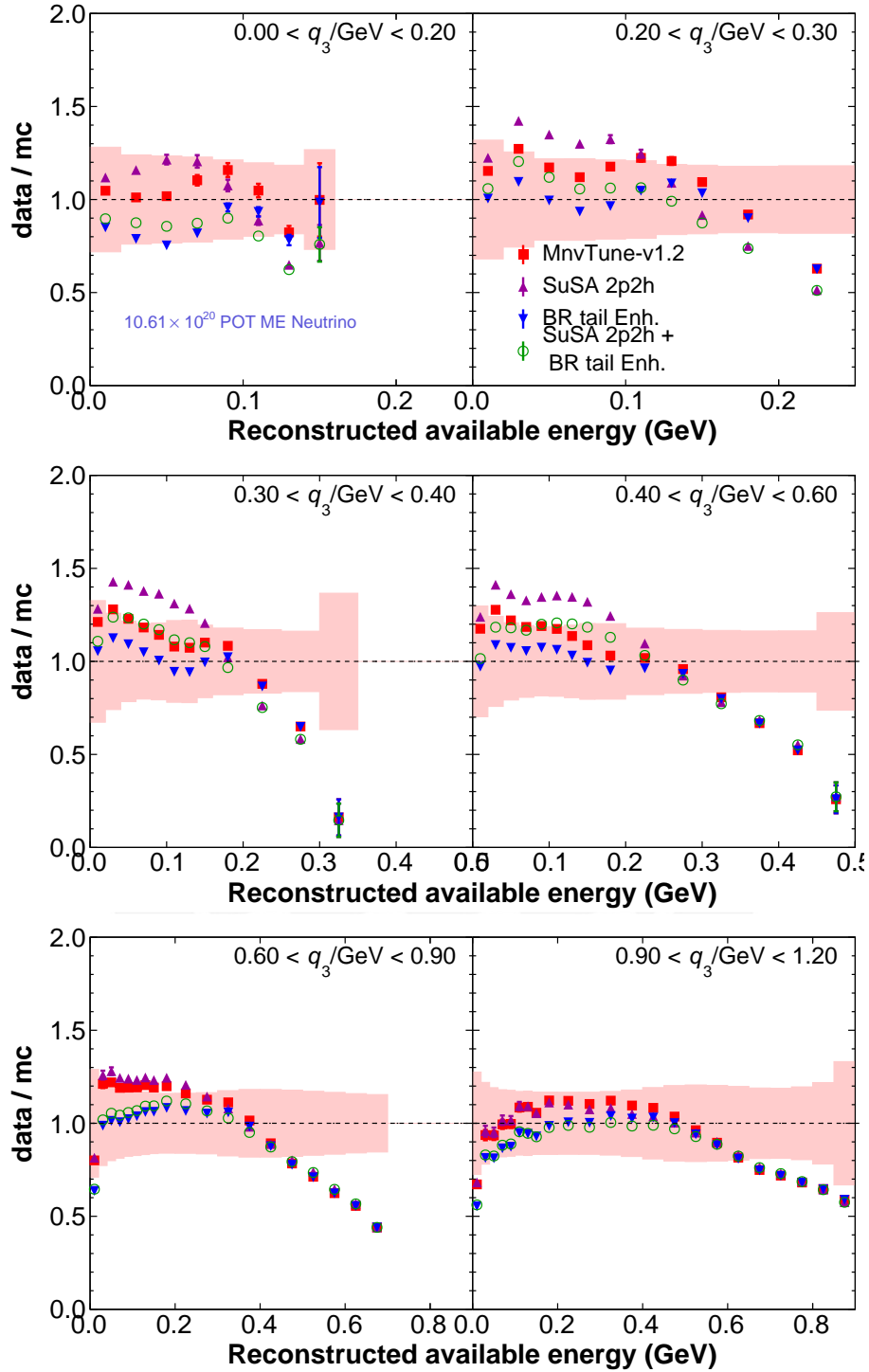


Figure 6.52: Ratio of data over MC RE for reconstructed E_{avail} in projections of reconstructed q_3 regions, the dashed lines are nominal MC, and continuous lines are the QE-RPA to RES effect. In red the Total MC and in purple RES event types.

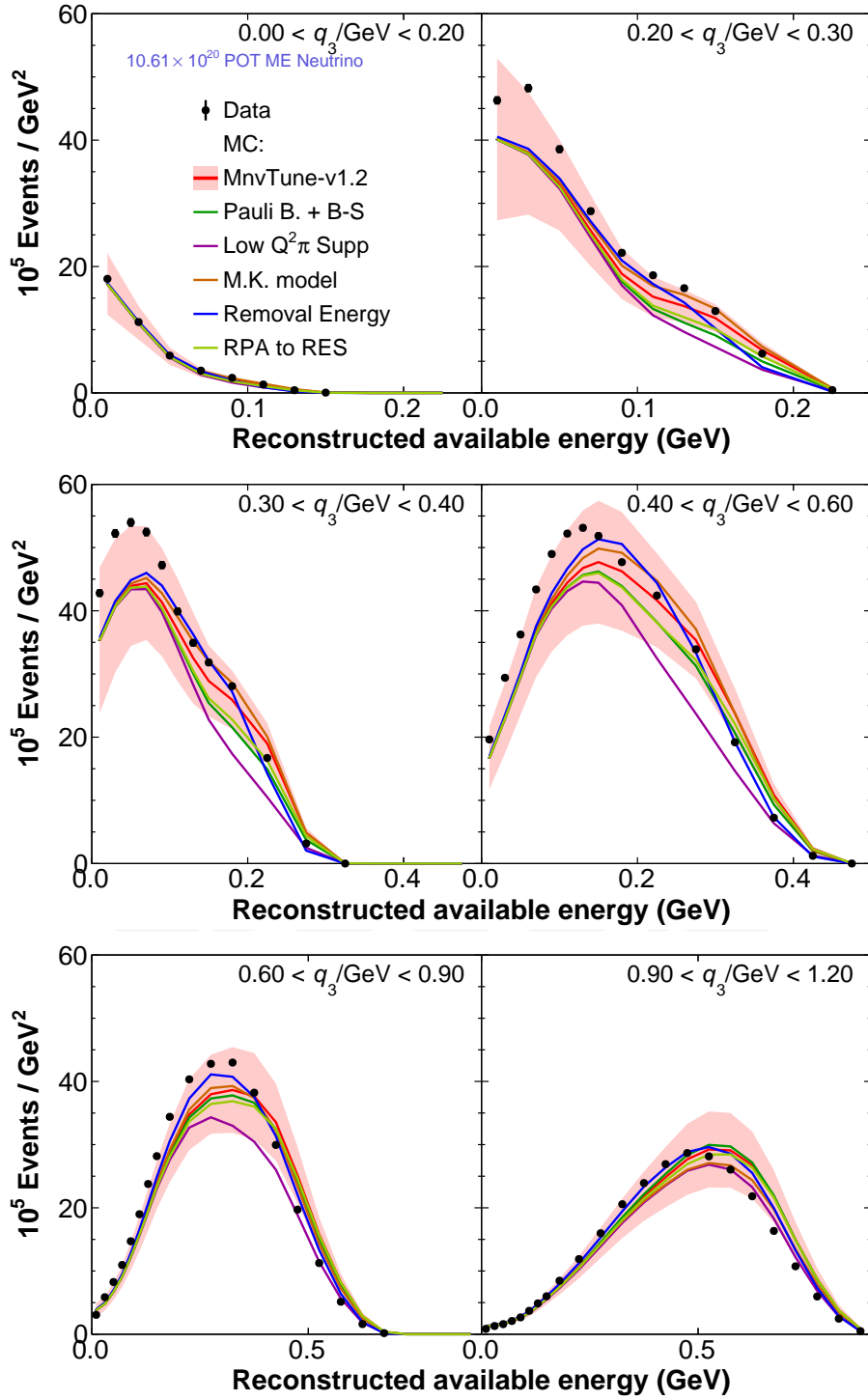


Figure 6.53: Reconstructed E_{avail} in projections of reconstructed q_3 regions, summary plot for resonant models study.

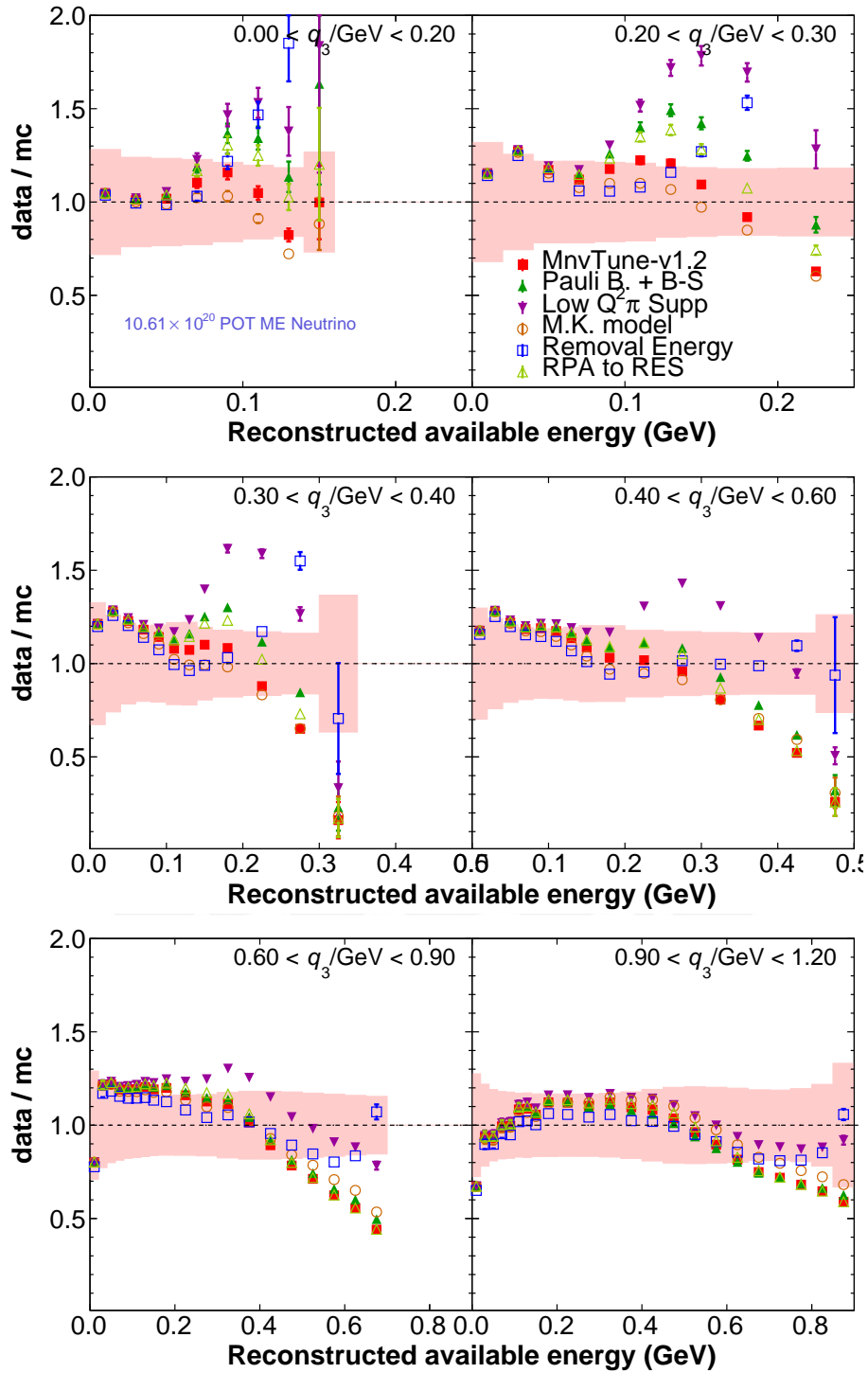


Figure 6.54: Ratio of reconstructed E_{avail} in projections of reconstructed q_3 regions, summary plot for resonant models study.

Model	$0.0 < q_3 < 0.2$	$0.2 < q_3 < 0.3$	$0.3 < q_3 < 0.4$	$0.4 < q_3 < 0.6$	$0.6 < q_3 < 0.9$	$0.9 < q_3 < 1.2$	total q_3
MnvTune-v3	392.055	348.078	1143.55	2150.36	2139.16	4831.46	11004.7
MnvTune-v1.2	55.197	1276.2	2398.66	7111.61	16091.7	12580.2	39513.6
RES Removal En.	138.873	1244.33	1588.71	2213.51	4047.33	4534.58	13767.3
SuSA 2p2h	344.72	2914.46	6405.35	14673.6	16161.3	10755.1	51254.6
SuSA 2p2h + B-R t.	392.573	1011.05	3340.57	8301.42	11645.4	10988.3	35679.3
Pauli B. + B-S.	166.02	2099.61	2943.02	5545.34	14061.8	12635	37450.8
MK model	46.8538	1014.62	2226.67	5977.98	9325.34	7041.15	25632.6
Low $Q^2\pi$ Supp	248.074	3129.47	5531.65	11324.6	15413	4548.34	40195.1
RPA to RES	122.432	1727.42	2724.15	7083.15	17545.2	12373.6	41575.9
Bodek-Ritchie T.	888.343	248.365	1036.13	4867.08	12489.2	12093.5	31622.7

Table 6.2: χ^2 of reconstructed distributions in bins of q_3 (1D) and total (2D). The degree of freedom of q_3 bins are 8, 10, 12, 15, 19, and 24. The total degree of freedom is 88. The $i < q_3 < j$ intervals refers the q_3 binning region limits in GeV.

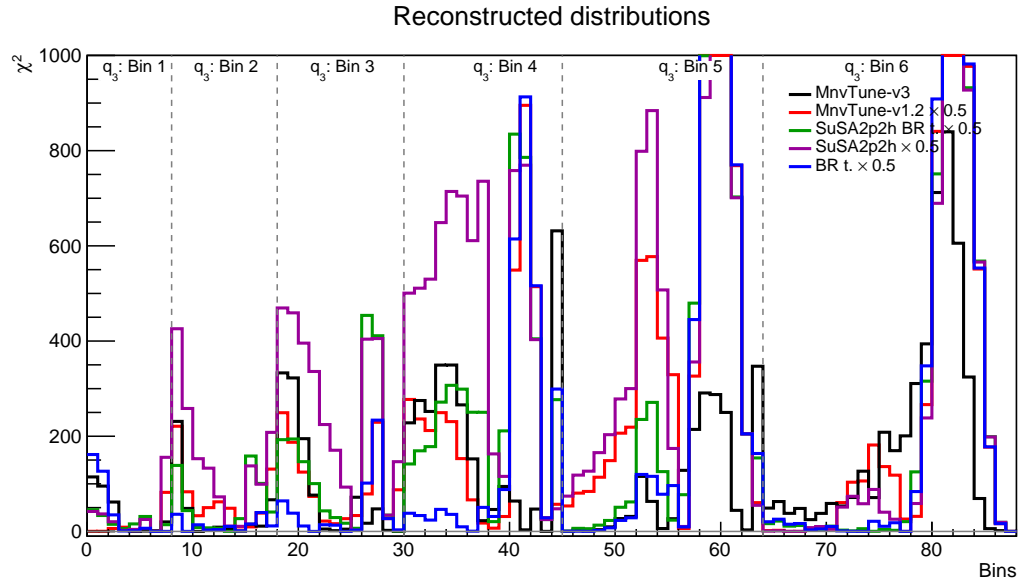


Figure 6.55: χ^2 at reconstructed level for QE and 2p2h models.

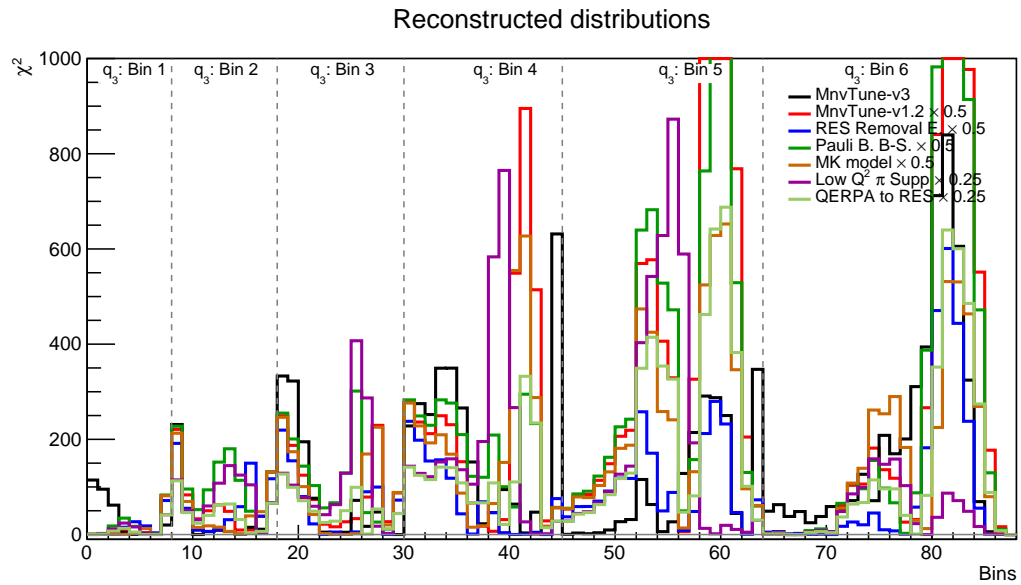


Figure 6.56: χ^2 at reconstructed level for RES models.

CHAPTER 7

MEASUREMENT OF DOUBLE DIFFERENTIAL CROSS-SECTION

In this chapter, we will present the double differential cross-section in q_3 and E_{avail} variables. The binning used here is the second presented in chapter 5 (Binning II). Before presenting the measurement, we will discuss the difference between MnvTune.v1.2 and MnvTune.v3. The event selection with MnvTune.v1.2 was presented in chapter 5. However, those were with small binning, do an apple-to-apple comparison is presented in the following section.

The ingredient needed to get the cross-section is the background-subtracted distribution, the efficiency, the migration matrices to unfold the

background-subtracted distribution, the flux, bin-width, and target normalization. The double differential measurement follows:

$$\left(\frac{d^2\sigma}{dx dy}\right)_{\alpha\beta} = \frac{\sum U_{ij\alpha\beta}(N_{\text{data}, ij} - N_{\text{data}, ij}^{\text{bkgd}})}{A_{\alpha\beta}(\Phi T)(\Delta x \Delta y)}, \quad (7.1)$$

where x and y are any variable, $N_{\text{data}, ij}$ is the reconstructed events, $N_{\text{data}, ij}^{\text{bkgd}}$ is the predicted background events, $U_{ij\alpha\beta}$ is the unfolding matrix which takes into account the two truth (α and β) binning and two reconstructed binning (i and j), Φ is the flux integrated, T is the target, $A_{\alpha\beta}$ is the efficiency and acceptance correction, and $(\Delta x \Delta y)$ are the bin-width.

The last part of this chapter is dedicated to discussing the systematic uncertainty in the reconstructed and cross-section distributions.

7.1 Event distribution

In this section, we will focus on the shape difference between MnvTune.v1.2 and MnvTune.v3. The physics discussions are shown in the previous chapter. In order to do that, we split into three regions of q_3 , as was presented in chapter 5. Besides that, the ratio plots also are included to have a better conclusion.

Low q_3

QE dominates the low q_3 (see Figure 7.1) as we saw previously; the difference between MnvTune.v1.2 and MnvTune.v3 is the Bodek-Ritchie enhancement, which means QE events have risen. We saw that the amount of the enhancement is 25%; that effect, plus the small other component makes the total MC increment. So, compared with the data, the data-MC difference is larger than MnvTune.v1.2 (see first q_3 panel). But, this is not the case in the second panel, in which the data-MC difference is small.

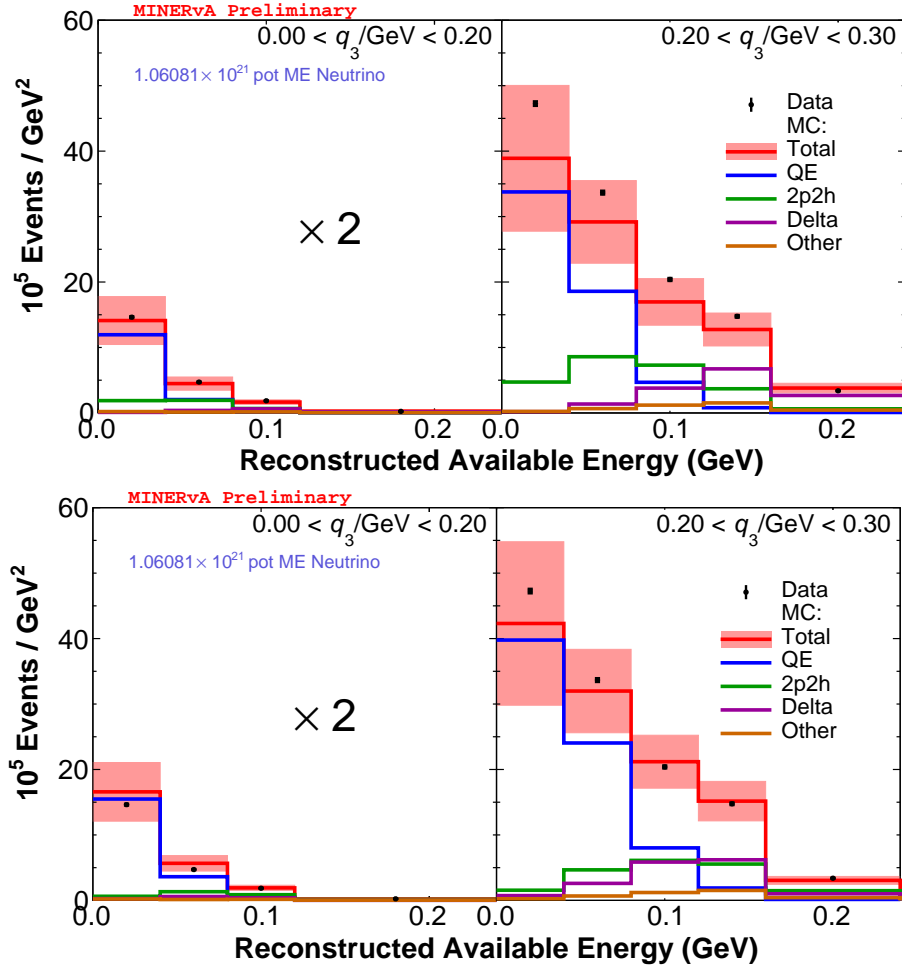


Figure 7.1: Reconstructed E_{avail} in projections of reconstructed q_3 regions. The upper plots represent the MnvTune.v1.2 MC, and the lower plots are MnvTune.v3 MC, in both cases compared against data. These are for the low q_3 region.

Another important observation is that in the same region where the Bodek-Ritchie enhances QE, there is also 2p2h, and it is small. Therefore, making the overall MC is less enhanced than if we use 2p2h without SuSA. This observation is more noticeable in the second panel of Figure 7.1.

One more observation we can make, and it is related to the error band, as we will see in the last part of this chapter, the MnvTune.v1.2 has the low recoil fit uncertainty, which is gone in the MnvTune.v3 case. However, the error band seems large because the RPA uncertainty and the RPA weight

7.1. EVENT DISTRIBUTION

depend on how many QE events we have, so modifying that we change the RPA uncertainty, therefore, the total uncertainty. The data and total MC ratio with the last three comments are shown in Figure 7.2.

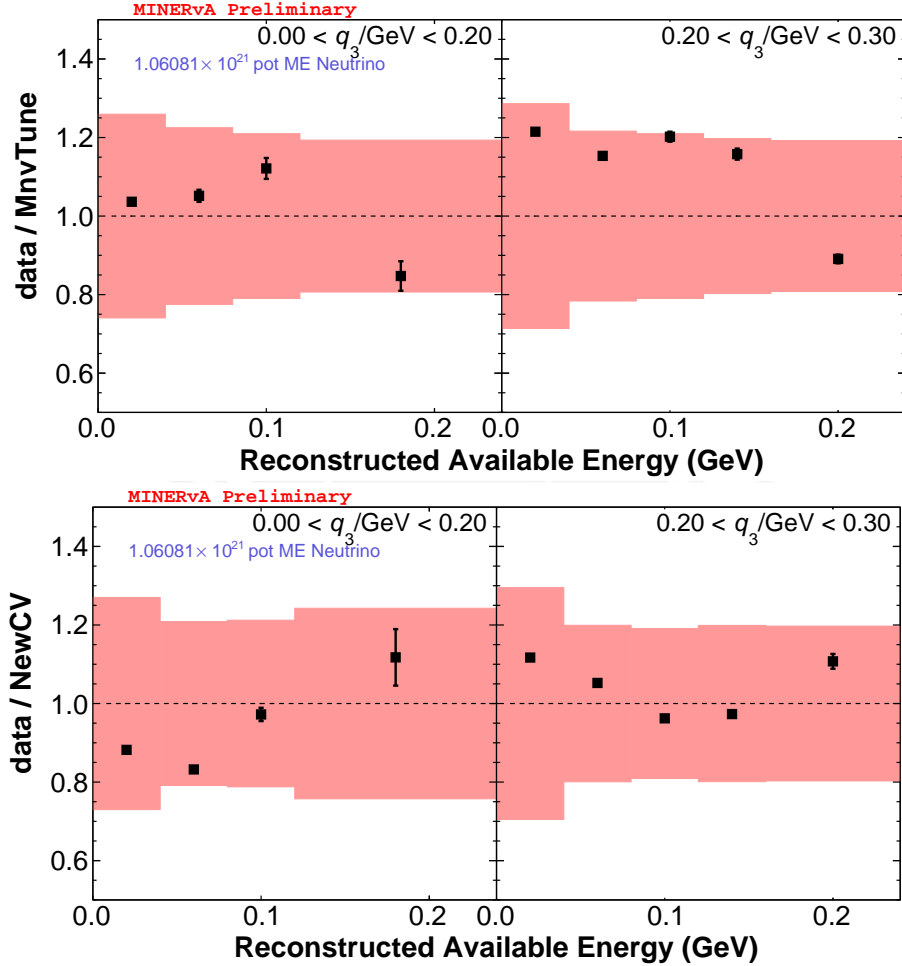


Figure 7.2: Reconstructed E_{avail} in projections of reconstructed q_3 regions ratios. The upper plots represent the data/MnvTune.v1.2 MC, and the lower plots are data/MnvTune.v3 MC. These are for the low q_3 region.

Medium q_3

In this region, we can see the importance of the 2p2h events. The difference between both is the Valencia MEC, low recoil fit, and SuSA 2p2h. As we saw partial in the previous region, the Valencia MEC plus low recoil fit is larger than SuSA 2p2h. However, this difference is compensated with Bodek-Ritchie enhancement. A similar comment that low q_3 is valid for the error band. The

error associate to SuSA is handle in the last stage, at cross-section level.

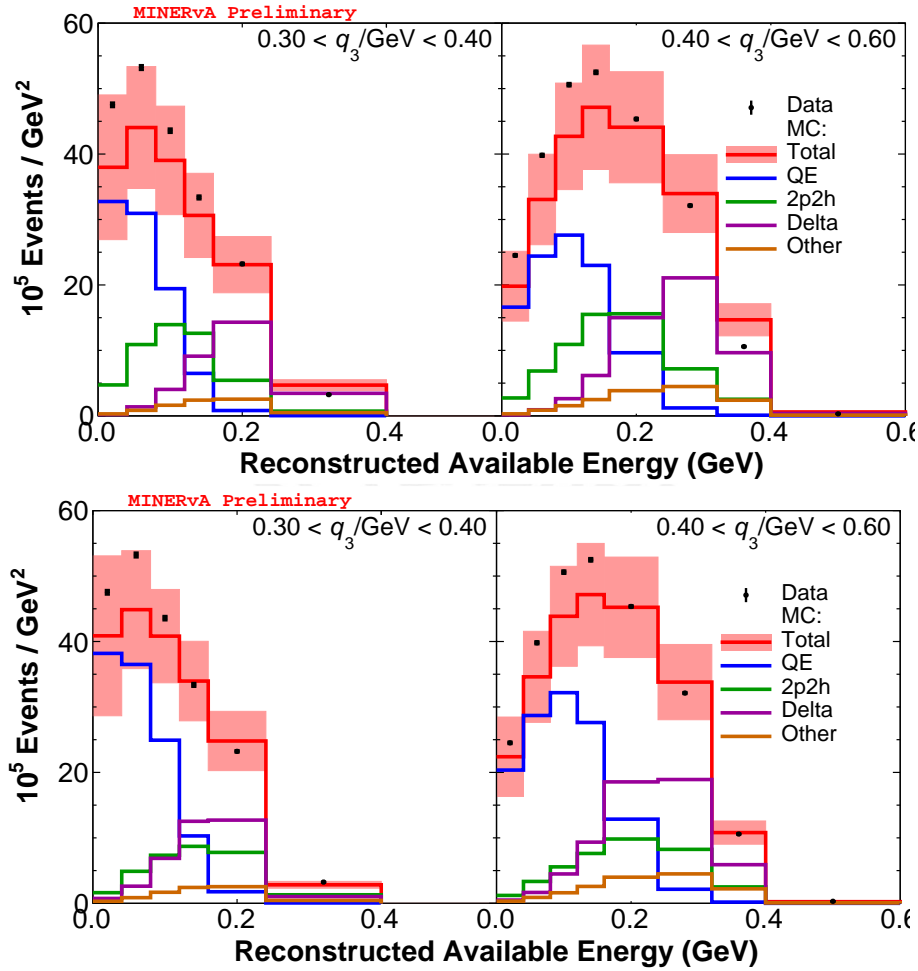


Figure 7.3: Reconstructed E_{avail} in projections of reconstructed q_3 regions. The upper plots represent the MnvTune.v1.2 MC, and the lower plots are MnvTune.v3 MC, in both cases compared against data. These are for the medium q_3 region.

Another observation, which will be valid for the high q_3 is the Resonant events. The difference between both modes regarding interaction type is the RES removal energy applied on MnvTune.v3. The contribution of the addition was also visible in the low q_3 region, at high E_{avail} . The overall effect is the shift in the Delta-peak, enhancing particular regions of low E_{avail} and suppressing others, and compared against data, it does a better description. Similar uncertainty treatment that SuSA is performed in RES removal energy,

7.1. EVENT DISTRIBUTION

which is added as the difference between data cross-sections unfolded with MnvTune.v3 MC minus data cross-sections unfolded with MnvTune.v1.2 MC together with Bodek-Ritchie tail enhancement and SuSA 2p2h, which we will cover in the systematic section.

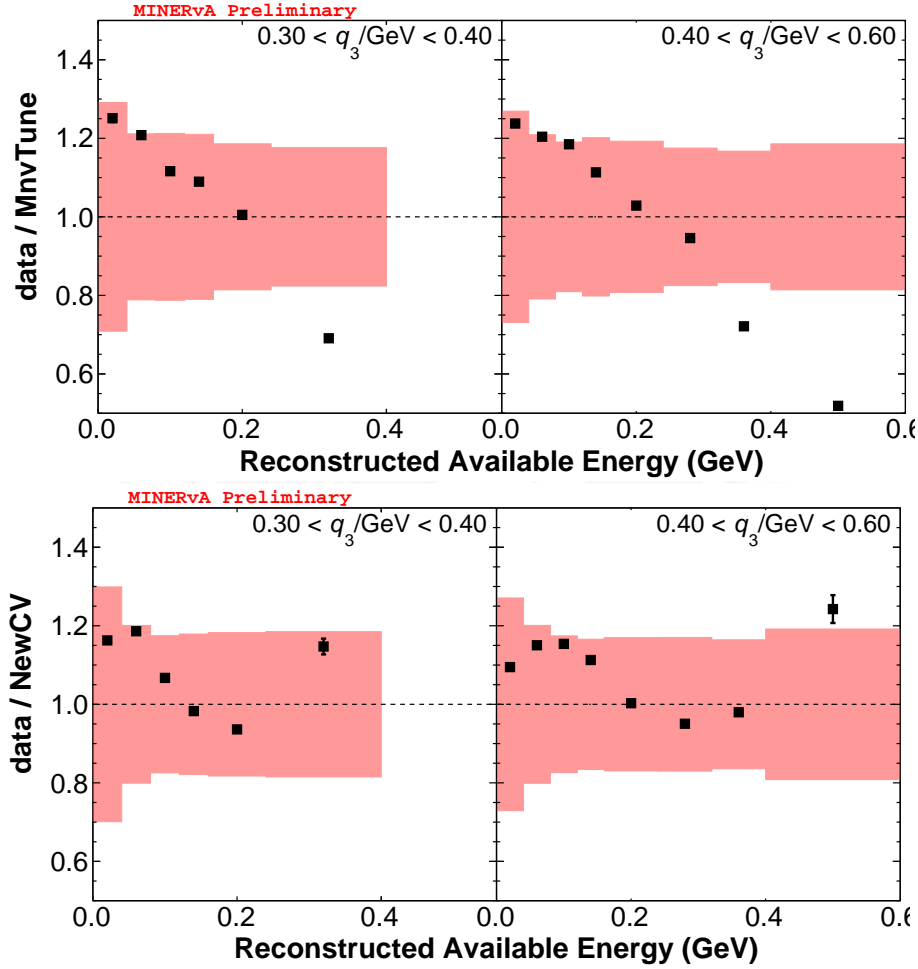


Figure 7.4: Reconstructed E_{avail} in projections of reconstructed q_3 regions ratios. The upper plots represent the data/MnvTune.v1.2 MC, and the lower plots are data/MnvTune.v3 MC. These are for the medium q_3 region.

High q_3

Finally, we have the high q_3 region, in which we have the full effect of the model variation coming from MnvTune.v3, the QE enhancement, the 2p2h suppression compared with MnvTune.v1.2, and the resonant events shift. In this panel, we can see another component growing and labeled as “other”, which

7.1. EVENT DISTRIBUTION

is, as we saw before, the other resonances different from Δ , DIS events, and a small number of coherent events. We can see an almost null difference between MnvTune.v1.2 and MnvTune.v3 in the “other” type component. The reason is that “other” is affected by the RES removal energy from MnvTune.v3.

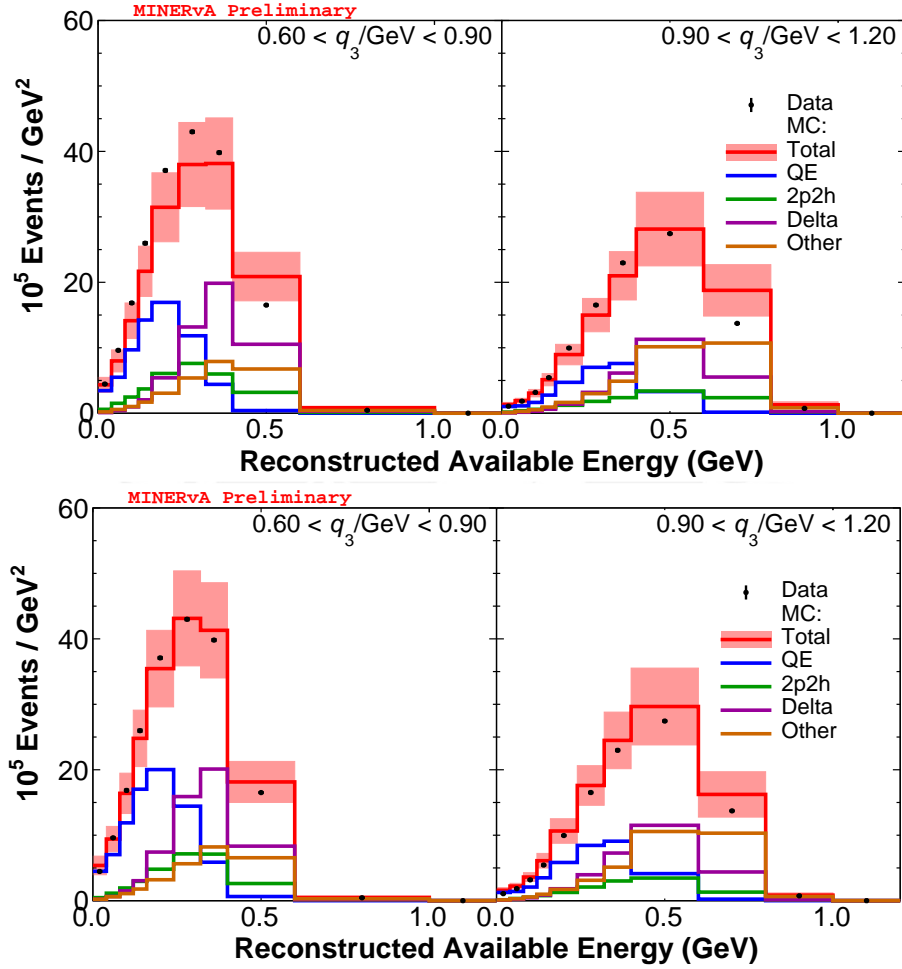


Figure 7.5: Reconstructed E_{avail} in projections of reconstructed q_3 regions. The upper plots represent the MnvTune.v1.2 MC, and the lower plots are MnvTune.v3 MC, in both cases compared against data. These are for the high q_3 region.

The data event only has statistical uncertainty. The data distribution will acquire the systematic uncertainty when we subtract the background, and by the unfolding process, which will be described later in this chapter. In conclusion, we can see that the ratio points are in the error band; only a few

are outside. The double differential cross-section measurement will have the uncertainty coming for the MnvTune.v3 covering those regions.

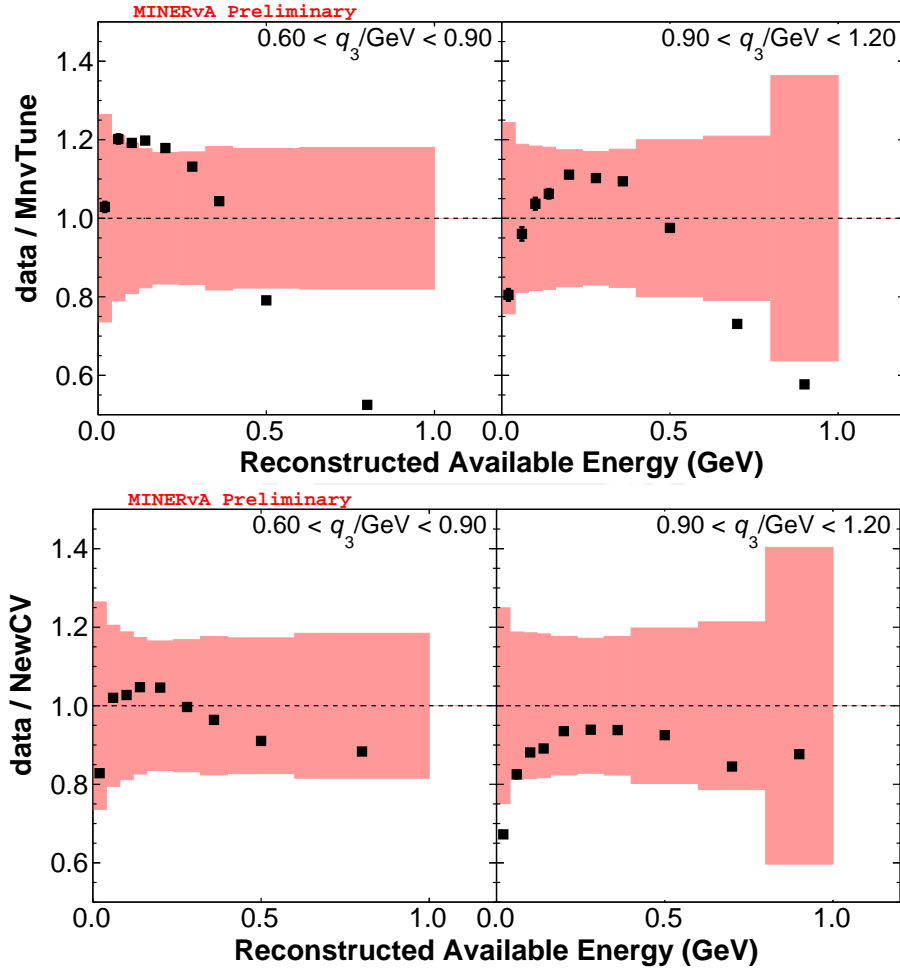


Figure 7.6: Reconstructed E_{avail} in projections of reconstructed q_3 regions ratios. The upper plots represent the data/MnvTune.v1.2 MC, and the lower plots are data/MnvTune.v3 MC. These are for the high q_3 region.

7.2 Background Subtraction

The background is mostly coming from the neutral-current and μ^+ . The overall background is small, and it is 1.42%. Figure 7.7 shows the total MnvTune.v3 MC compared with the scaled background ($\times 10$ in order to see the background). The background subtracted data and MC will be used in the unfolding step.

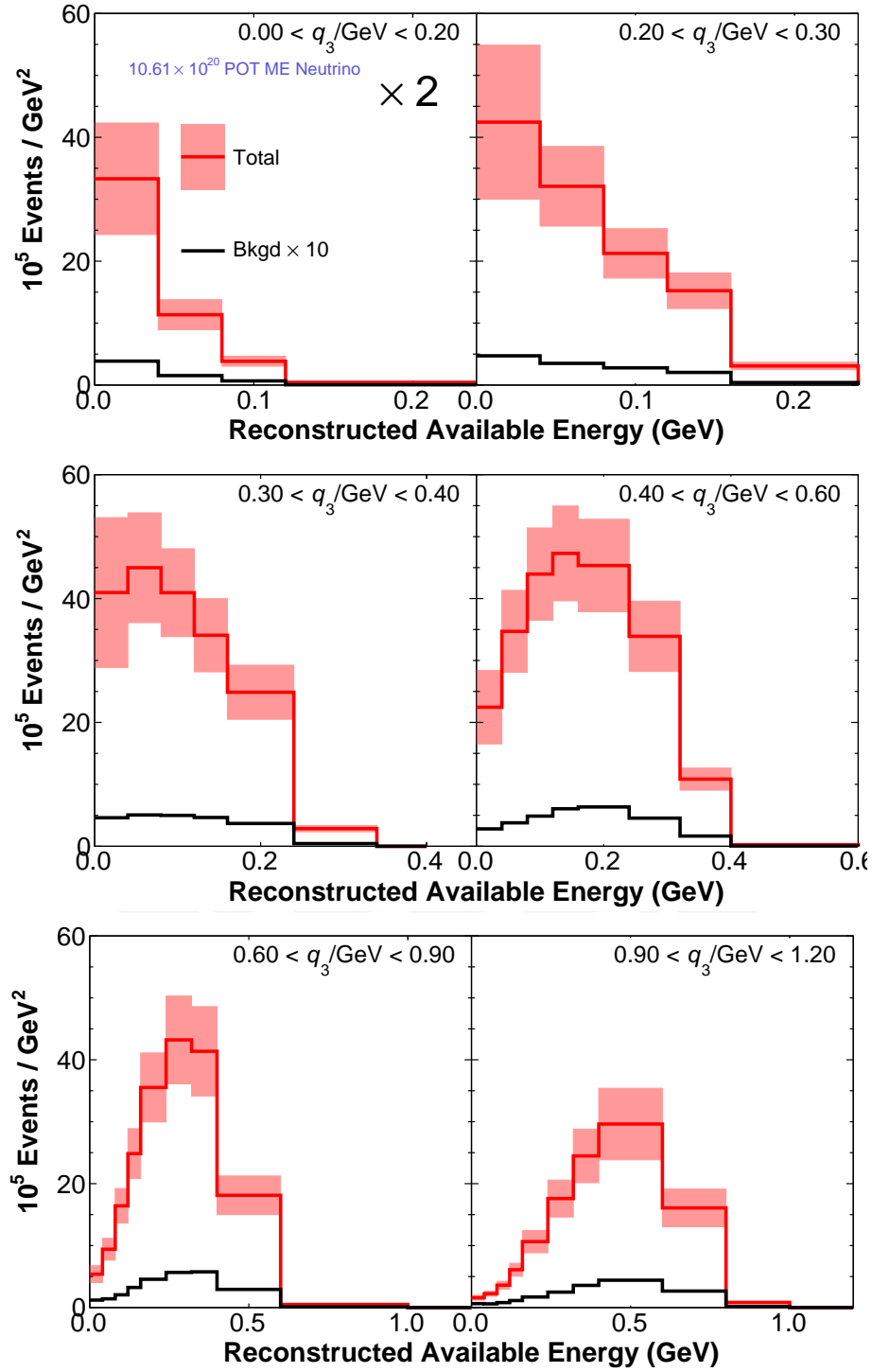


Figure 7.7: Reconstructed E_{avail} in projections of reconstructed q_3 regions. In red the total MC and in black the background scaled by 10 to be visible.

7.3 Efficiency

Another ingredient to get the double-differential cross-section, as we have seen in the equation 7.1 is the efficiency. The definition follows:

$$\text{Efficiency} = \frac{\text{Selected signal events}}{\text{Total signal events}}. \quad (7.2)$$

The efficiency usually depends on selection cuts and kinematic thresholds or geometric acceptance of the MINERvA detector. This is the case here, Figure 7.8 shows higher efficiency at low E_{avail} and poor efficiency at high E_{avail} . The maximum efficiency is of 80% in some bins and minimum of 21% through a combination of muon acceptance and resolution migration across the $q_3 < 1.2$ GeV analysis boundary. The low q_3 region bins have, on average, 77%, medium q_3 region bins, 72%, and high q_3 region bins 53%, where high E_{avail} and q_3 containers have the lower efficiency. The breakdown in interaction component are shown in Figure 7.9.

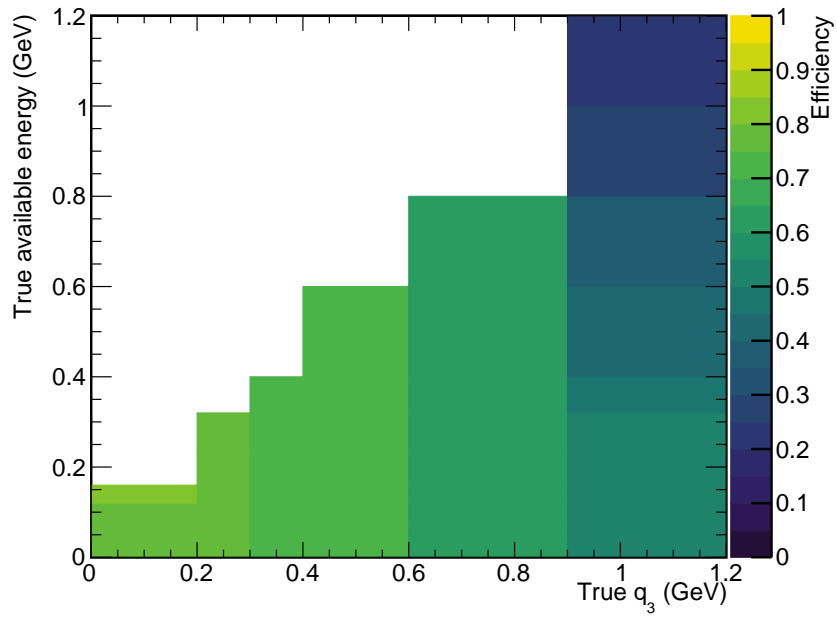


Figure 7.8: 2D efficiency distribution as a function of E_{avail} and q_3 (only illustration, there is a mismatch in the binning).

The last bin of the low q_3 region shows large different efficiency of Δ . That is consistent due to low resonant events in the low q_3 region and large errors due to low MC statistics.

7.3. EFFICIENCY

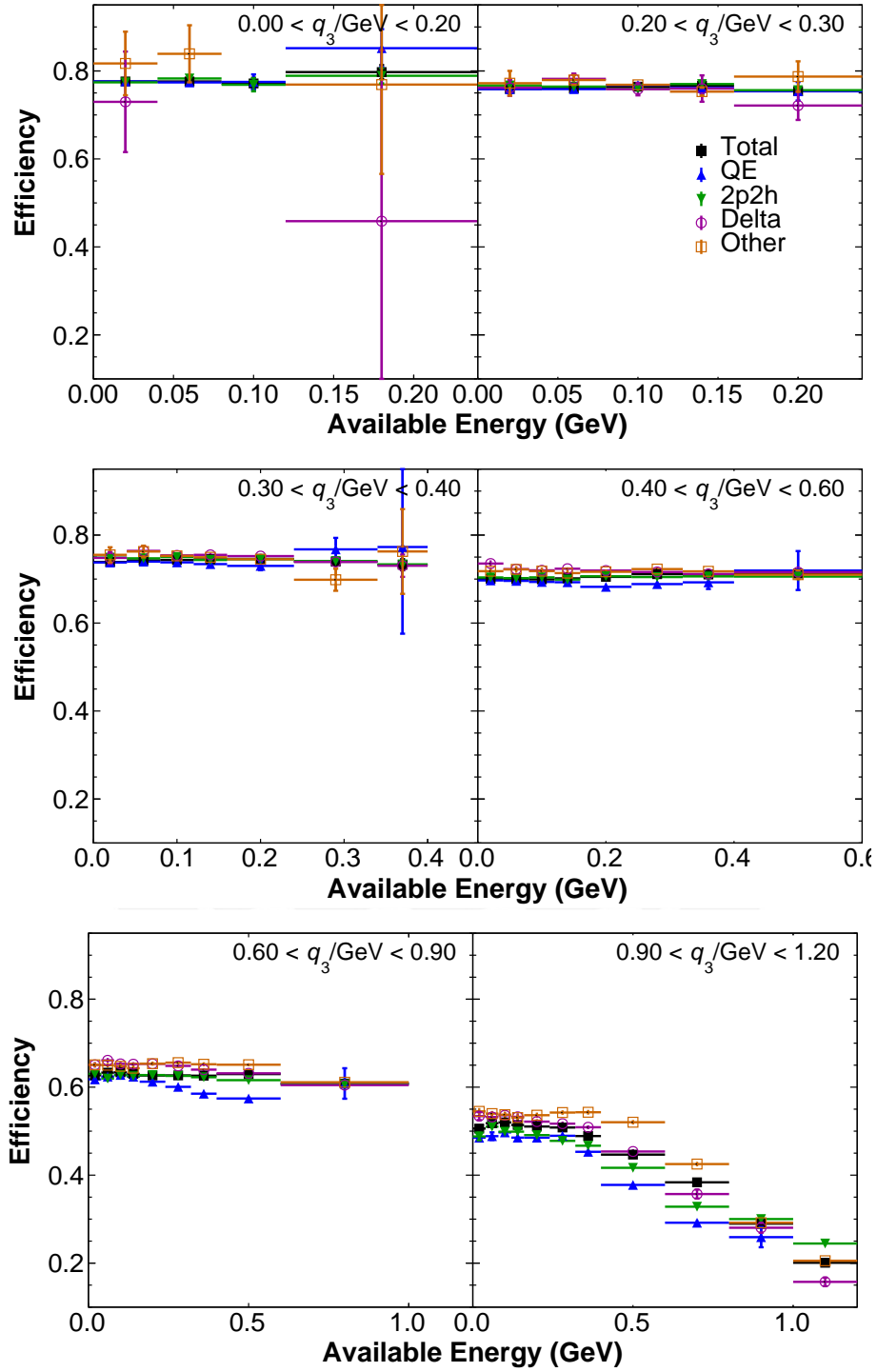


Figure 7.9: Efficiency breakdown in E_{avail} and projections of q_3 regions.

7.4 Migration Matrix

The next component to unfold the data and then get the double differential cross-section is the migration matrix. Figure 7.10 account all reconstructed and truth directions at once. The migration matrix allow as to see the resolution of the analysis. For instance in Figure 7.10 the overall behavior corresponds to E_{avail} (big boxes), in which we can see better resolution at low E_{avail} and poor resolution at high E_{avail} . Similar behaviour is shown in q_3 (small boxes).

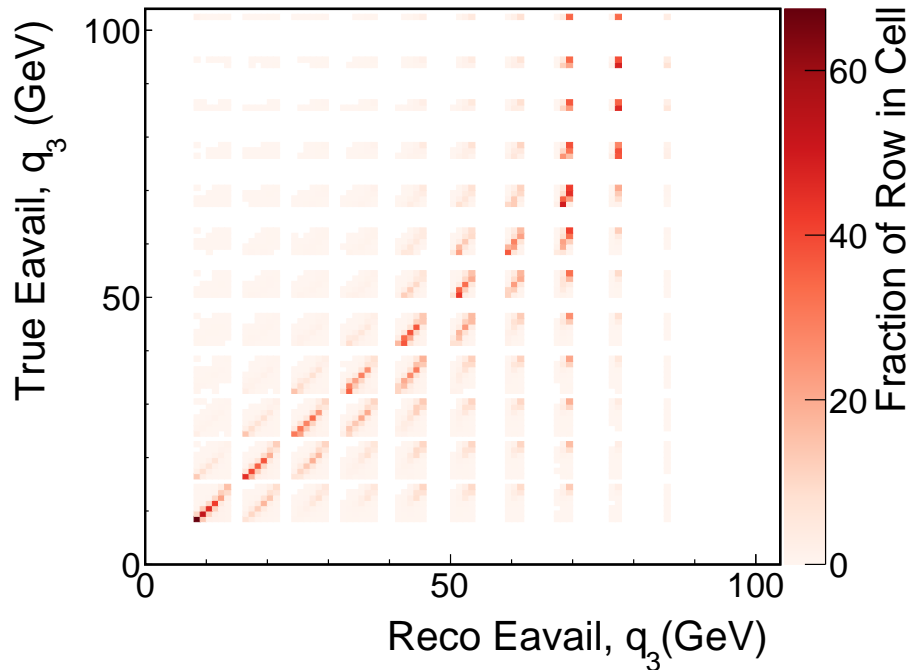


Figure 7.10: Row normalized migration matrix of the 2D distribution. Small boxes are q_3 bins and big boxes are E_{avail} . The matrix also consider the overflow and underflow bins.

The row normalized breakdown of the migration matrices is shown below, where we can observe that at high E_{avail} and high q_3 have poor resolution due to Other contributions mostly (see the unpopulated diagonal bins in almost all bins). The reason for that might be how we are handling the neutrons.

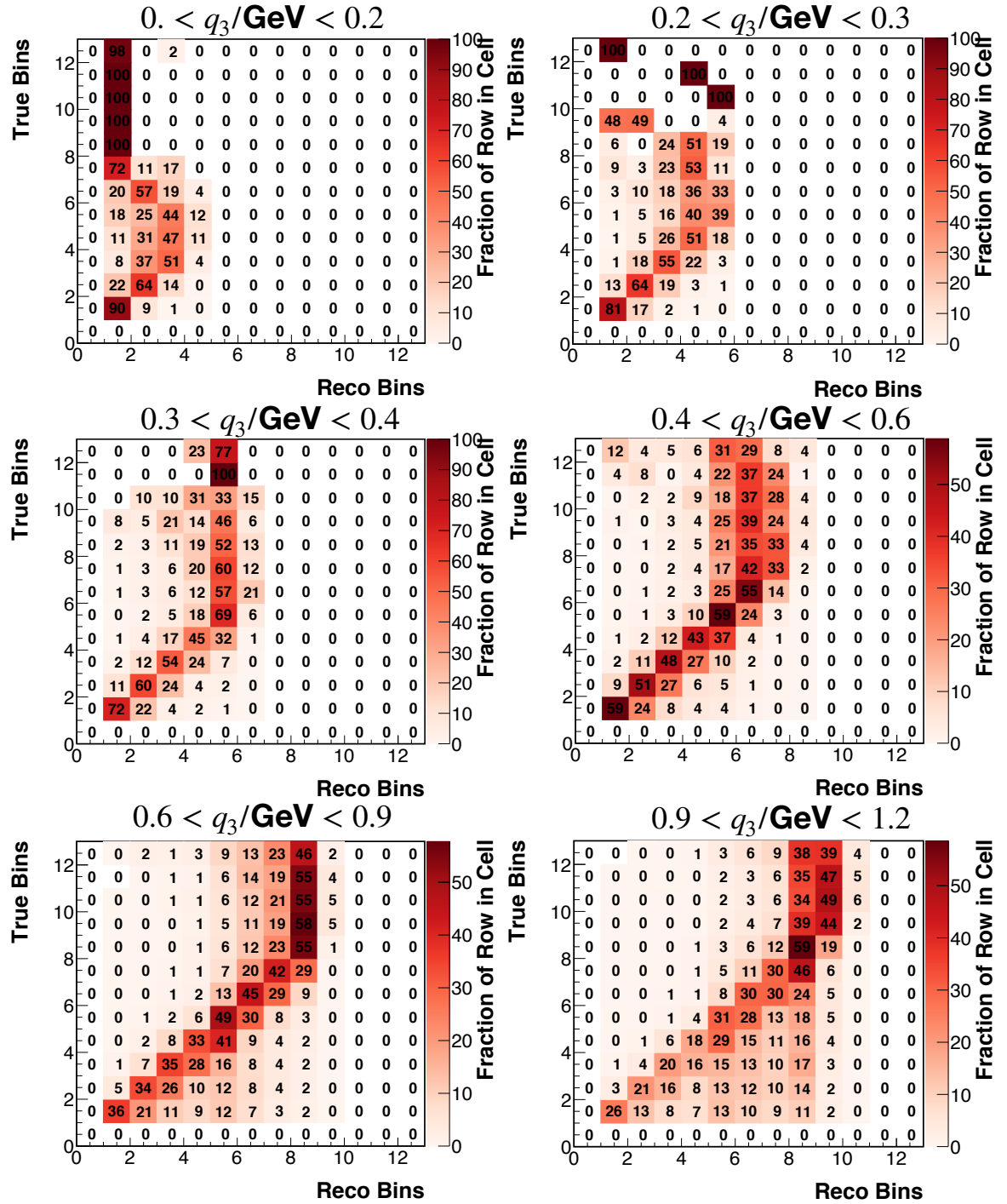


Figure 7.11: Total migration matrices of E_{avail} in panel of reconstructed q_3 , which corresponds to diagonal big boxes of Figure 7.10.

QE

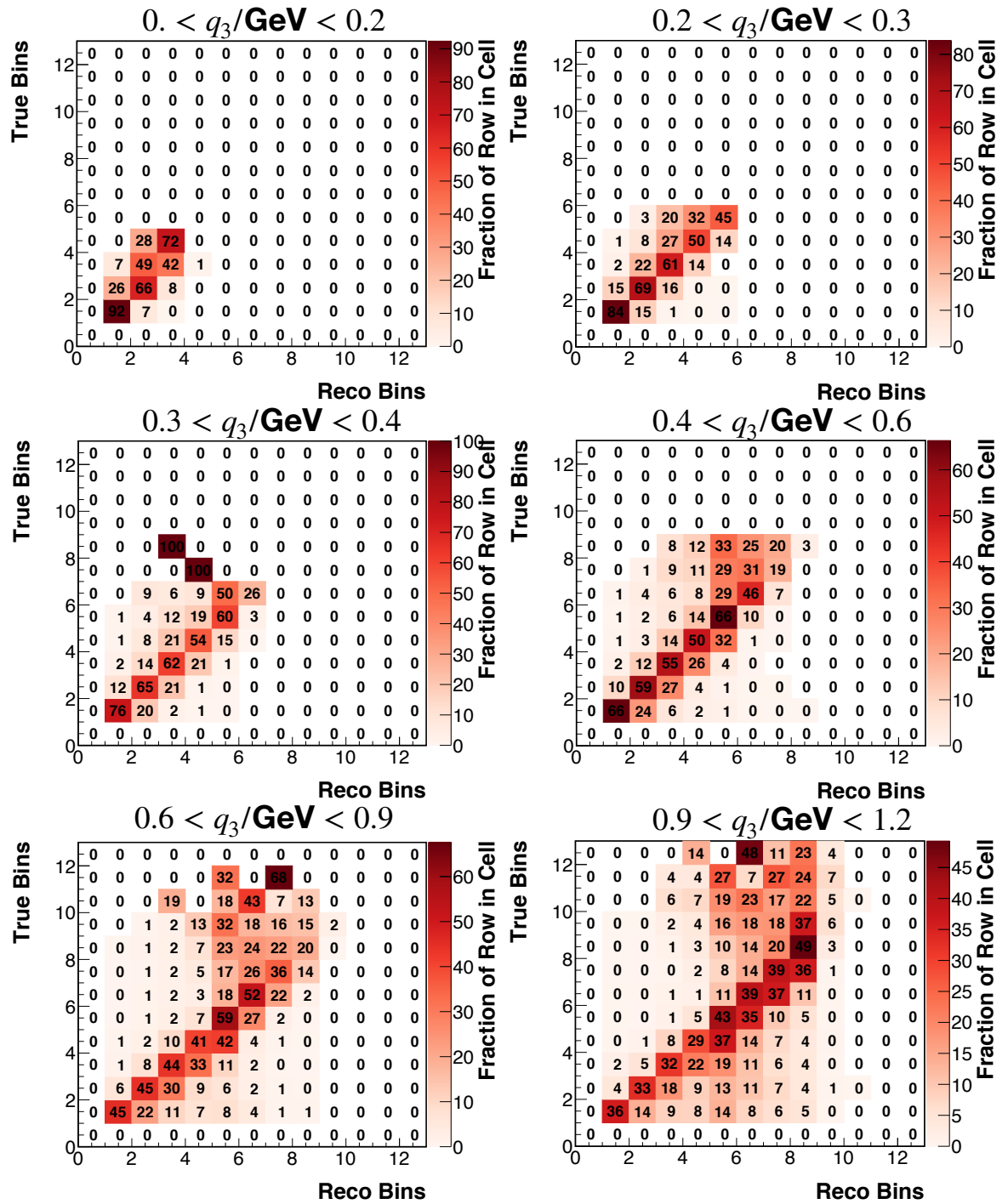


Figure 7.12: QE migration matrices of E_{avail} in panel of reconstructed q_3 , which corresponds to diagonal big boxes of Figure 7.10.

7.4. MIGRATION MATRIX

2p2h

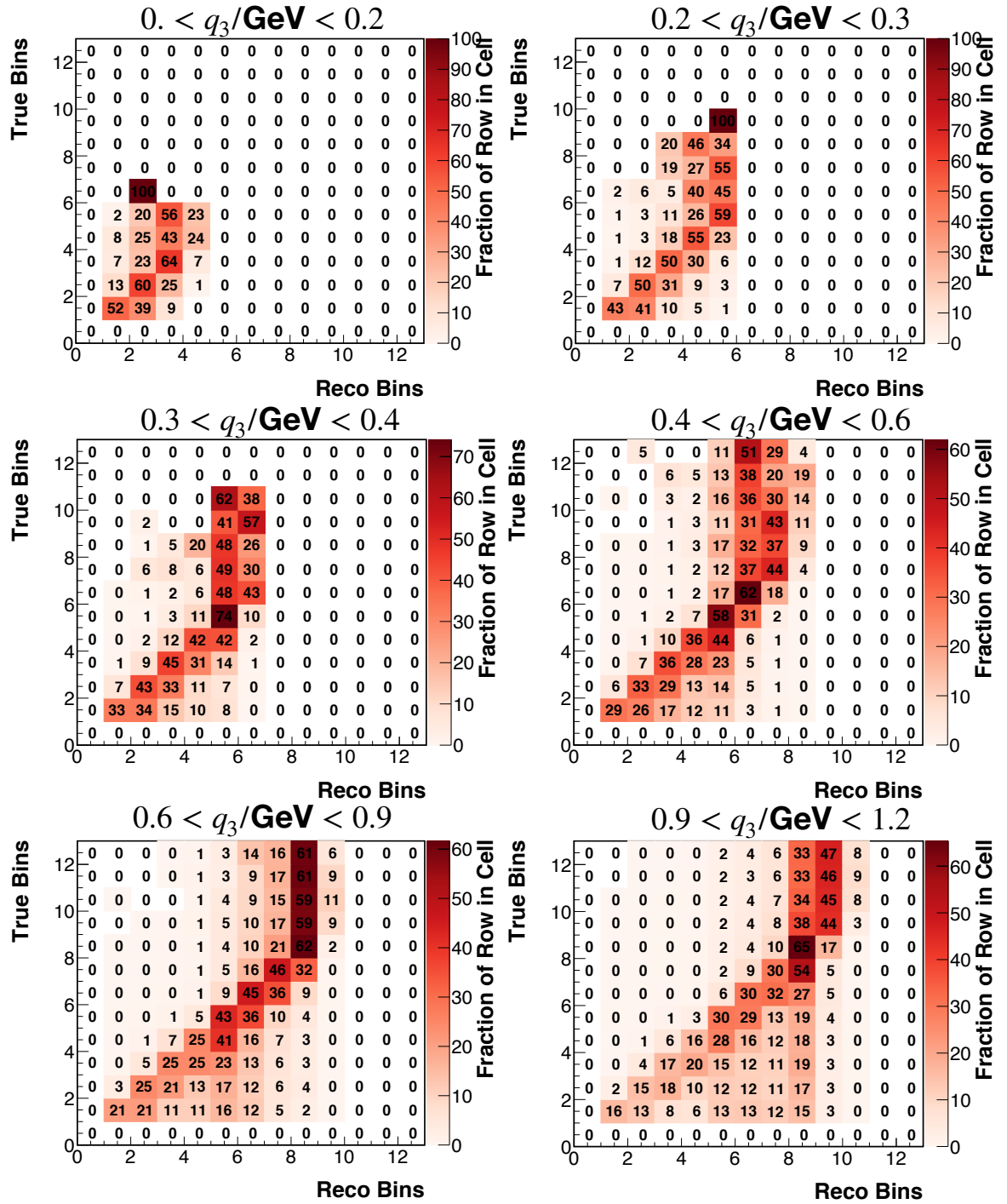


Figure 7.13: 2p2h migration matrices of E_{avail} in panel of reconstructed q_3 , which corresponds to diagonal big boxes of Figure 7.10.

7.4. MIGRATION MATRIX

Delta

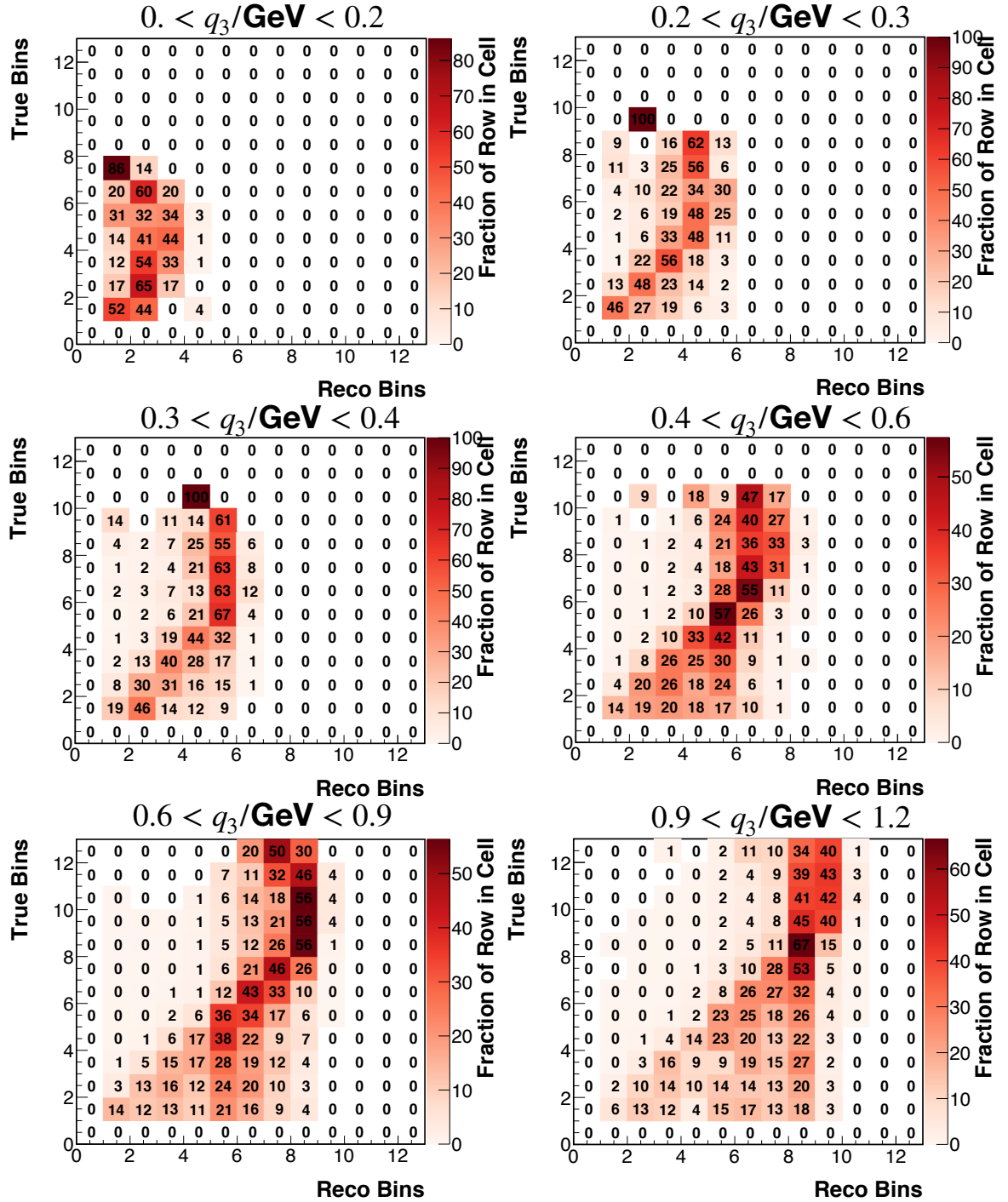


Figure 7.14: Delta migration matrices of E_{avail} in panel of reconstructed q_3 , which corresponds to diagonal big boxes of Figure 7.10.

7.4. MIGRATION MATRIX

Other

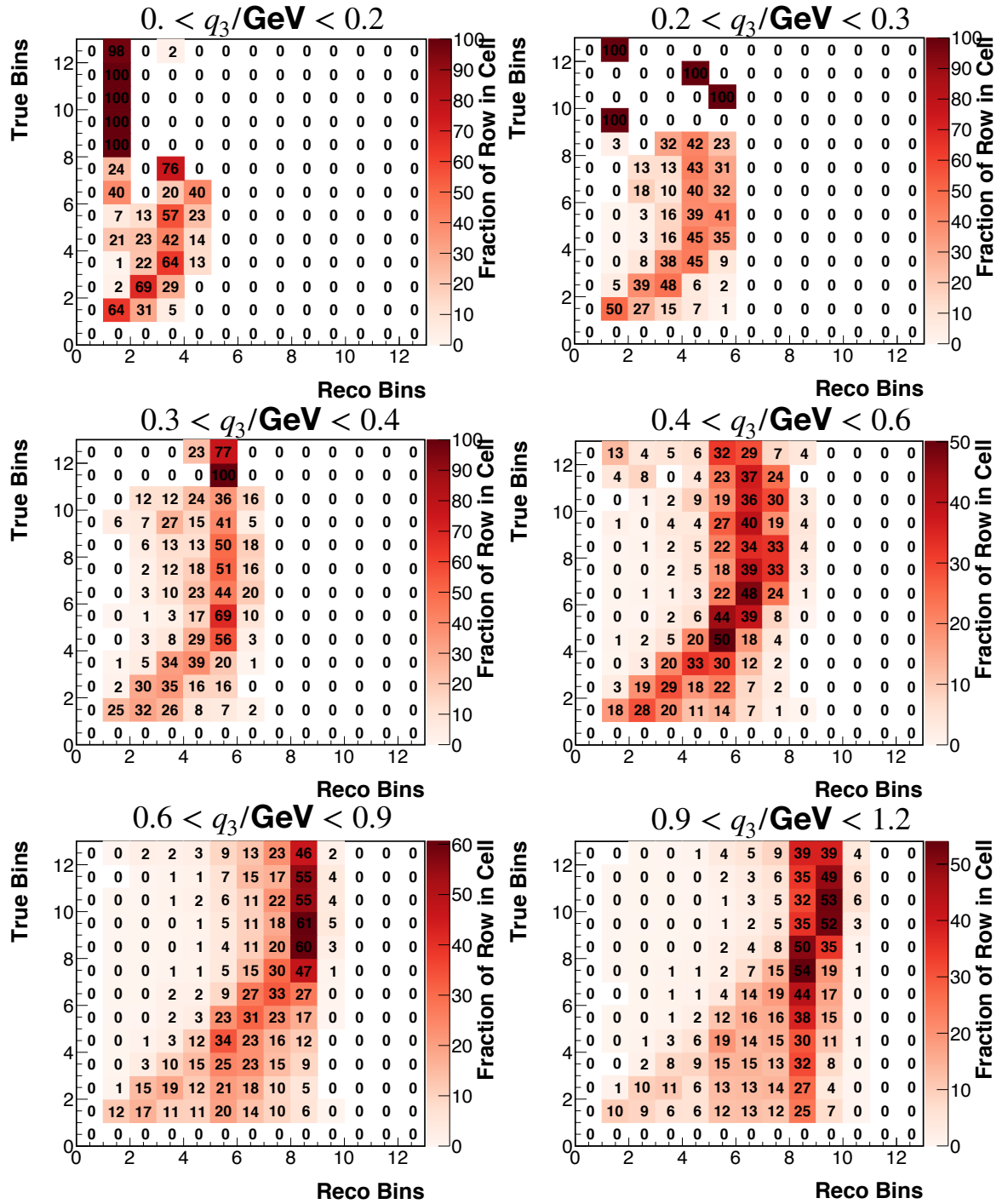


Figure 7.15: Other migration matrices of E_{avail} in panel of reconstructed q_3 , which corresponds to diagonal big boxes of Figure 7.10.

7.5 Unfolding

The unfolding procedure is made because one wants to remove the detector or model effect in some distribution. The place where that is hold is the migration matrix. So, this means it is like an inverse problem that depends on the migration matrix. But, given that the matrix can change, it makes an ill-posed inverse problem due to sensibility to initial condition fluctuation. So, a regularization method is introduced to solve that problem. MINERvA uses D'Agostini iterative regularization method [286] (see more detail of the method in the Appendix A).

To determine the number of iterations in the D'Agostini regularization method, MINERvA uses an approximation of the response of the data (as pseudodata), where Poisson throws¹ were done within the data equivalent statistical uncertainty and unfolded using the MnvTune.v3 model smearing matrix. The pseudodata is obtained by modifying (or warping) the MC CV, we denominate “fake data”.

If both distributions are the same, “fake data” and MC, then the reconstructed MC unfolded distribution compared with the truth fake data distribution should be the same in all iterations and all random universes. However, if the warped MC is different, then the reconstructed MC unfolded compared with truth fake data are different for low iteration, but they become the same at large iteration. The χ^2 versus the number of iterations information is used to quantify the bias.

Another point to consider in the iterative regularization method is that we get large uncertainties at high iterations. That inflation was observed in the study with pseudodata and real data. As we will see in section 7.8, how the uncertainty is assessed in MINERvA makes the inflation propagate to all steps of the cross-section extraction for each systematic source.

¹Random distribution known as random universes.

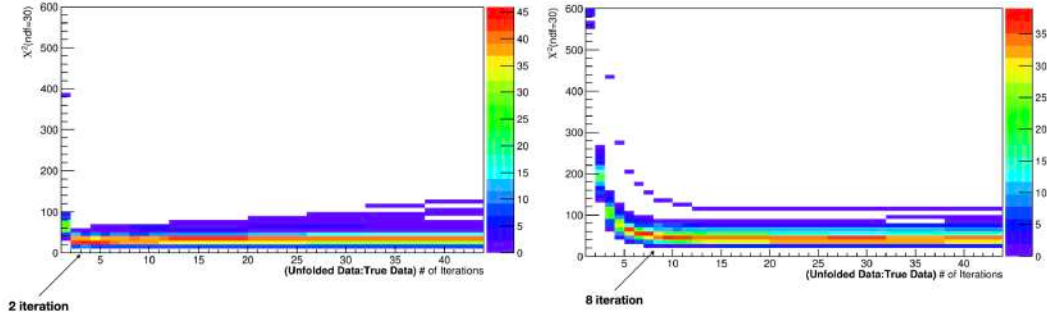


Figure 7.16: Number of iterations vs χ^2 of “truth fake data” and unfolded distribution. Left, reconstructed MC unfolded with 1σ RPA variation. Right, reconstructed mc unfolded with one of the low recoil fit uncertainties. Thrown with 100 Poisson random variations.

The low recoil analysis is sensitive to changes in the 2p2h region, giving large χ^2 no matter how small that warping is. That is not the case; for instance, if we use one sigma shift of RPA to warp the MC (see Figure 7.16). A detailed study was performed to understand the modification in the 2p2h region. We saw, for instance, when we warped the MC with one of the low recoil systematic (nn initial state), even if the χ^2 is large, the unfolding was performing as expected. In that case, the nn initial states move 2p2h strength to higher true q_0 , but because there are so many neutrons in the final state, the same cross-section strength appears at lower E_{avail} (expressed as 15% in truth fake data/truth MC and 5% in reconstructed ratio), that effect was preserved for the first iterations where the unfolded distribution is very close to truth fake data [287].

For models or warping functions’ parameters that change the unfolding matrix ², like in the 2p2h region explained above, can induce large differences between the primary and varied unfolded results. In these cases, MINERvA opts for smaller numbers of iterations. So, we chose two as a number of iterations. In general, the iterative regularization unfolding reduces the

²Can be understood as statistical fluctuations due to large numbers of iterations

bias, but will not completely eliminate it.

The fact that data is affected differently than MC by the unfolding, indicates that the MC model does not describe the data. Because unfolding procedure, in the case of data, modifies the migration matrix to match with the data distribution (matrix represented in Figure 7.17). In the MC case, the migration does not need a modification, so it is not affected by iterative regularization. The background-subtracted data and MC unfolded distributions are shown in Figure 7.18.

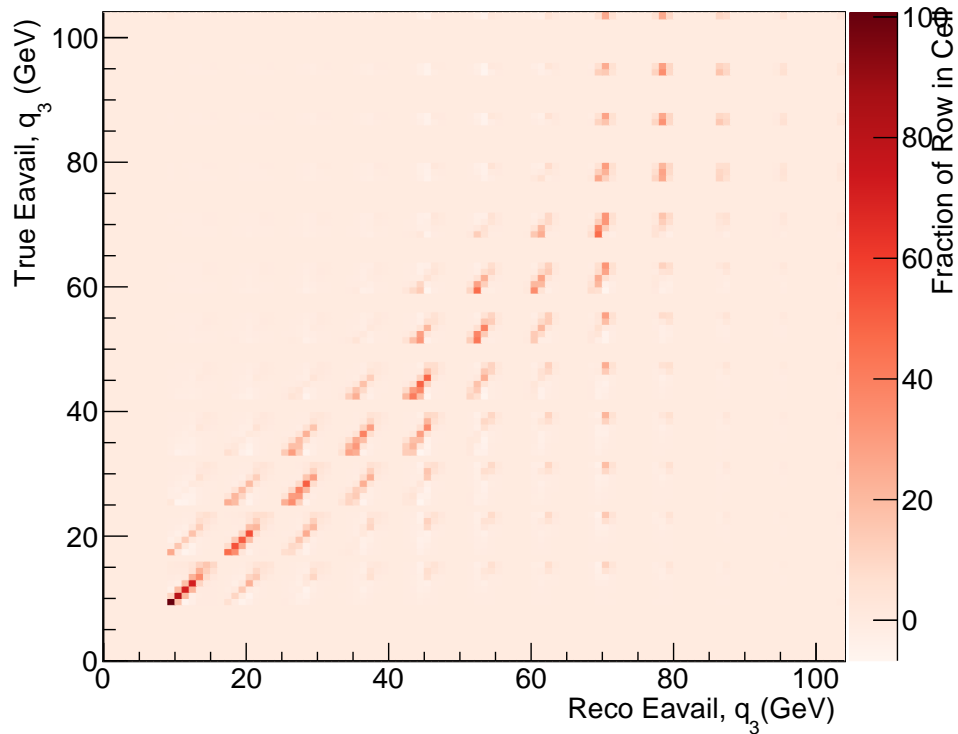


Figure 7.17: Unfolding matrix with row normalized. It following the same structure that the migration matrix (see Figure 7.10), where the big boxes represent the E_{avail} and the small boxes are the q_3 .

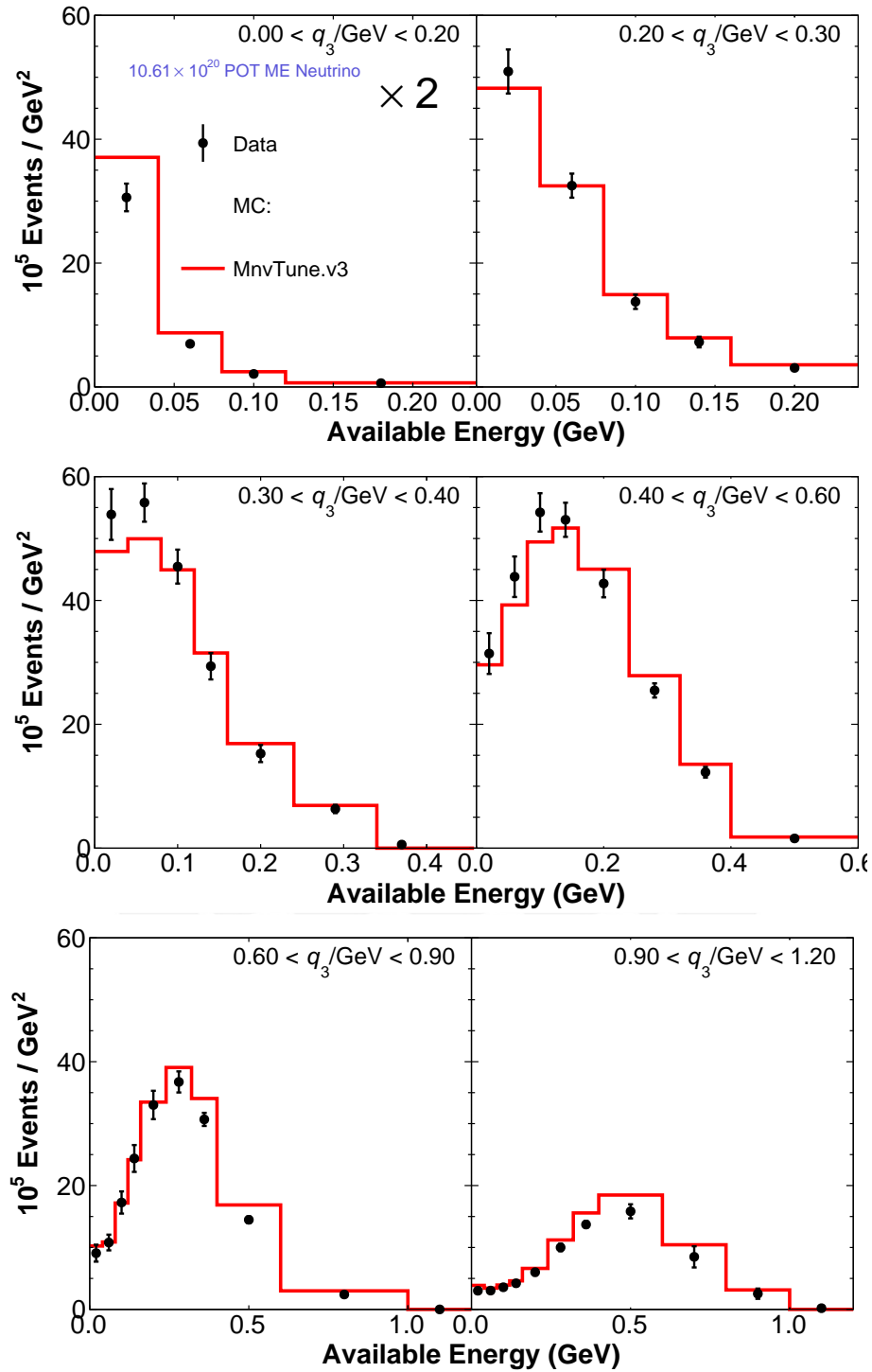


Figure 7.18: Unfolded background subtracted data and MC distributions. The error on data came from the background subtraction and unfolding procedure.

7.6 Flux and Target Normalization

The normalization factor, representing the flux integral from 0 to 100 GeV, 3.115×10^{30} nucleon targets and 1.061×10^{21} proton on target, is used to obtain the double differential cross-section.

7.7 Cross Section Extraction

The double differential cross-section in term of E_{avail} and q_3 ,

$$\frac{d^2\sigma}{dE_{\text{avail}}dq_3} = \frac{\sum U_{ij\alpha\beta}(N_{\text{data},ij} - N_{\text{data},ij}^{\text{bkgd}})}{A_{\alpha\beta}(\Phi T)(\Delta E_{\text{avail}}\Delta q_3)}, \quad (7.3)$$

is calculated, using the unfolded background subtracted event selection, then it is divided by nucleon target and neutrino flux integration factor and efficiency. The measured double differential cross-section is shown in Figure 7.19.

The error bars shown in the data points correspond to total uncertainty (statistical and systematic uncertainties). The breakdown of the systematic uncertainties for fractional and absolute uncertainties are shown in Figures 7.40 and 7.42. The description of individual uncertainties is presented in Section 7.8.

A discussion about cross-section comparison with neutrino generator, GENIE 3, NuWro SF and NuWro LFG (see Figures 7.44 and 7.45) will be discussed in section 7.10. The χ^2 interpretation of the different models (MnvTune.v1.2 and MnvTune.v3) is presented in the section 7.11.

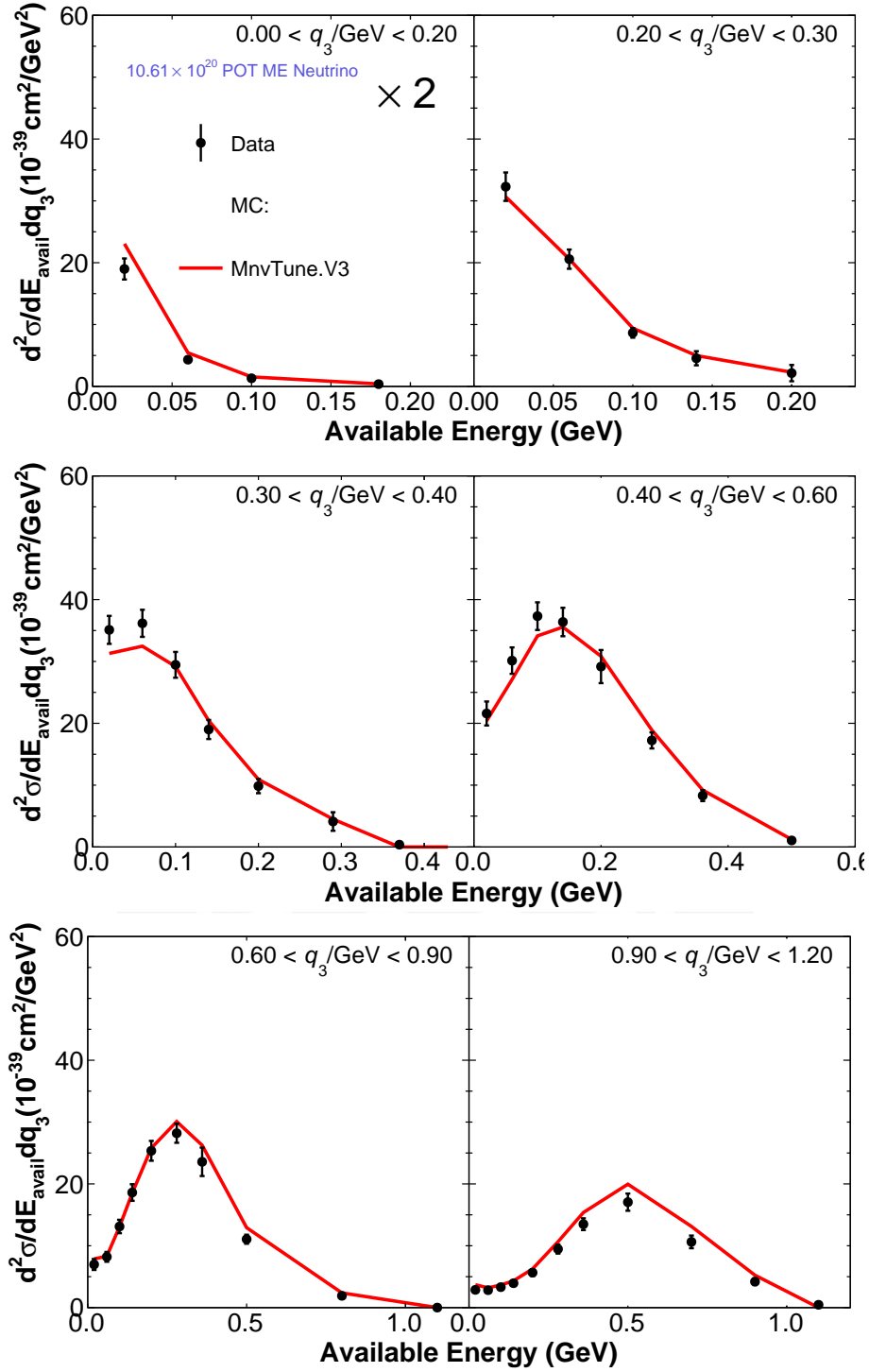


Figure 7.19: Data double differential cross-section as function of E_{avail} and q_3 , compared with MnvTune.v3. The first bin of q_3 is scaled by two.

7.8 Systematic Uncertainty

Imperfect understanding of the flux and detector energy response and the interaction model cause uncertainty in the measured double differential cross-section. The treatment of the uncertainties follows the multi-universes method, a similar method described in Section 3.4. The cross-section is re-extracted in many simulations, where each MC has a shifted parameter that corresponds to the source of each uncertainty. This makes a different systematic "universe" that can be used to make a covariance matrix (see Section 7.9) based on how it differs from the nominal cross-section. The multiverse method is critical because it allows us to propagate the uncertainties in every step until getting the cross-section.

In MINERvA a histogram holder objects (`MnvHnDs`) based on `ROOT THnDs` [288] is used. The (`MnvHnDs`) object stores each systematic histogram universe, the central value as well as a `ROOT TMatrix` for the covariance matrix [289]. We can group the universes to get error bands.

The description of the uncertainties used in the measurement at reconstruction level are in the Tables 7.1 - 7.6. In GENIE there are two types of parameters for intranuclear rescattering: those that control the total rescattering probability, and those that control the fraction of each process (the so-called "fate"), given a total re-scattering probability [290, 291].

Detector Uncertainty

Systematic Uncertainty	Description
Flux	The flux uncertainties has three contributions, the hadronic production (see Table 3.2 and Figures 3.9 and 3.11), the focusing uncertainty (see Figure 3.12) and the neutrino-electron flux constrain (see Section 3.5). All of them were discussed in the Chapter 3.
Hadronic Energy	The input uncertainty is determined from hadron calorimetry data taken with a test beam detector [292].
Muon Energy	Similar that Hadronic Energy it was determine with test beam detector [292]. In addition it has muon scale [225, 201] which it has up 3%.

Table 7.1: Detector uncertainty description.

Final State Interaction Uncertainty

Systematic Uncertainty	Description
FrPiProd N	Represents the nucleon fates-pion production and it is the tweak pion production probability for nucleons, for given total rescattering probability, where 1σ is $\pm 20\%$ [291].
FrPiProd pi	Represents the pion fates-pion production and it is the tweak pion production probability for pions, for given total rescattering probability, where 1σ is $\pm 20\%$ [291].

Table 7.2: FSI uncertainties I. Table taken from [290].

Systematic Uncertainty	Description
MFP N	Represents the nucleon mean free path and it is the tweak where 1σ is $\pm 20\%$. It is fully correlated with nucleon elastic fates cross section [291].
MFP pi	Represent the pion mean free path and it is a tweak, where 1σ is $\pm 20\%$ [291].
FrAbs N	Represents the nucleon fates-absorption and it is the tweak absorption probability for nucleons, for given total rescattering probability, where 1σ is $\pm 20\%$ [291].
FrAbs pi	Represents the pion fates-absorption and it is the tweak absorption probability for pions, for given total rescattering probability, where 1σ is $\pm 30\%$ [291].
FrCEX N	Represents the nucleon fates-charge exchange and it is the tweak charge exchange probability for nucleons, for given total rescattering probability, where 1σ is $\pm 50\%$ [291].
FrCEX pi	Represents the pion fates-charge exchange and it is the tweak charge exchange probability for pions, for given total rescattering probability, where 1σ is $\pm 50\%$ [291].
FrElas N	Represents the nucleon fates-elastic and it is the tweak elastic probability for nucleons, for given total rescattering probability, where 1σ is $\pm 30\%$. It is also fully correlated with nucleon mean free path [291].
FrElas pi	Represents the pion fates-elastic and it is the tweak elastic probability for pions, for given total rescattering probability, where 1σ is $\pm 10\%$ [291].
FrInel N	Represents the nucleon fates-Inelastic and it is the tweak inelastic probability for nucleons, for given total rescattering probability, where 1σ is $\pm 40\%$ [291].
FrInel pi	Represents the pion fates-inelastic and it is the tweak inelastic probability for pions, for given total rescattering probability, where 1σ is $\pm 40\%$ [291].

Table 7.3: FSI uncertainties II. Table taken from [290]

Interaction Uncertainty

Systematic Uncertainty	Description
AGKYxF1π	Represents the AGKY hadronization model – x_F distribution and it is the tweak x_F distribution for low multiplicity (N + pi) DIS final state produced by AGKY, where 1 σ is $\pm 20\%$ [293] (see new update [294]).
AhtBY	Represents the Bodek-Yang parameter A_{HT} and it is the tweak the Bodek-Yang model parameter A_{ht} -incl. both shape and normalization effect, where 1 σ is $\pm 25\%$.
BhtBY	Represents the Bodek-Yang parameter B_{HT} and it is the tweak the Bodek-Yang model parameter B_{ht} -incl. both shape and normalization effect, where 1 σ is $\pm 25\%$.
CV1uBY	Represent the Bodek-Yang parameter $C_{V_{1u}}$ and it is the tweak the Bodek-Yang model parameter $C_{V_{1u}}$ -incl. both shape and normalization effect, where 1 σ is $\pm 30\%$.
CV2uBY	Represent the Bodek-Yang parameter $C_{V_{2u}}$ and it is the tweak the Bodek-Yang model parameter $C_{V_{2u}}$ -incl. both shape and normalization effect, where 1 σ is $\pm 40\%$.
EtaNCEL	Represent the Eta (Elastic scattering) and it adjusts eta in elastic scattering cross section, where 1 σ is $\pm 30\%$.
MaCCQE	Represent the M_A (CCQE Scattering) and it adjusts M_A in Llewellyn-Smith cross section, affecting shape and normalization. Earlier 1 σ were $+25\%$ and -15% [295], now $\pm 9\%$ in this study due to a fit from z-expansion with deuterium data [296].
MaNCEL	Represent the M_A (Elastic Scattering) and it adjusts M_A in elastic scattering cross section, where 1 σ is $\pm 25\%$.
MaRES	Represent the M_A (Resonance Production) and it adjusts M_A in Rein-Sehgal cross section, affecting shape and normalization, where 1 σ is $\pm 20\%$ [295]. In addition GENIE has separate knobs for resonance CC (MaCCRES) and NC (MaNCRES), which we gang together.

Table 7.4: Interaction uncertainties I. Table taken from [290] except the MaCCQE 1 σ uncertainty.

Systematic certainty	Un-	Description
MvRES		Represent the M_V (Resonance Production) and it adjusts M_V in Rein-Sehgal cross section, affecting shape and normalization. One σ is $\pm 10\%$. In addition, GENIE has separate knobs for resonance CC (MvCCRES) and NC (MvNCRES), which we gang together.
NormDISCC		Represent the DIS CC Normalization and it adjusts the overall normalization of the non-resonance inclusive cross section [295].
NormNCRES		Represent the NC Resonance Normalization and it changes the normalization of NC Rein-Sehgal cross section, where 1 σ is $\pm 20\%$.
RDecBR1gamma		Represent the resonance decay branching ratio to photon and it is the tweak resonance $\rightarrow X + \text{gamma}$ branching ratio, eg $\Delta(1232) \rightarrow p \text{ gamma}$. One σ is $\pm 50\%$.
Rvn2pi		Represent the 2pi production from $\nu n/\bar{\nu} p$ non-resonant interactions and affects NC and CC production of two pion final states from non-resonant inelastic (i.e. Bodek-Yang) scattering. $\nu n/\bar{\nu} p$ primary process. One σ is $\pm 50\%$ [295]. On the other hand, GENIE has separate knobs for resonance np and nubar-n which we gang together (isospin symmetry). Also gang together NC and CC channels. Value must be positive states.
Rvp1pi		Represent the 1pi production from $\nu p/\bar{\nu} n$ non-resonant interactions and affects NC and CC production of single pion final states from non-resonant inelastic (i.e. Bodek-Yang) scattering. $\nu p/\bar{\nu} n$ initial states. One σ is $\pm 50\%$ [295].
Rvp2pi		Represent the 2pi production from $\nu p/\bar{\nu} n$ non-resonant interactions and affects NC and CC production of two pion final states from non-resonant inelastic (i.e. Bodek-Yang) scattering. $\nu p/\bar{\nu} n$ initial states. One σ is $\pm 50\%$ [295].
Theta Delta2Npi		Represent the delta decay angular distribution and changes it in ON/OFF. The reweight to more correct angular distribution (i.e. not isotropic).
VecFFCCQEshap		Represent the CCQE Vector Form factor model and changes from BBBA to dipole, affecting shape only.

Table 7.5: Interaction uncertainties II. Table taken from [290].

RPA and low recoil fit Uncertainties

Systematic Uncer- tainty	Description
RPA	The RPA suppression uncertainty depend on Q^2 , to high Q^2 are calculated by changing at once all parameters of the particle-hole potential (see Appendix D) with 1σ which is the sum of the effects in quadrature. The Low Q^2 is using the muon capture constraint (full description in [227]).

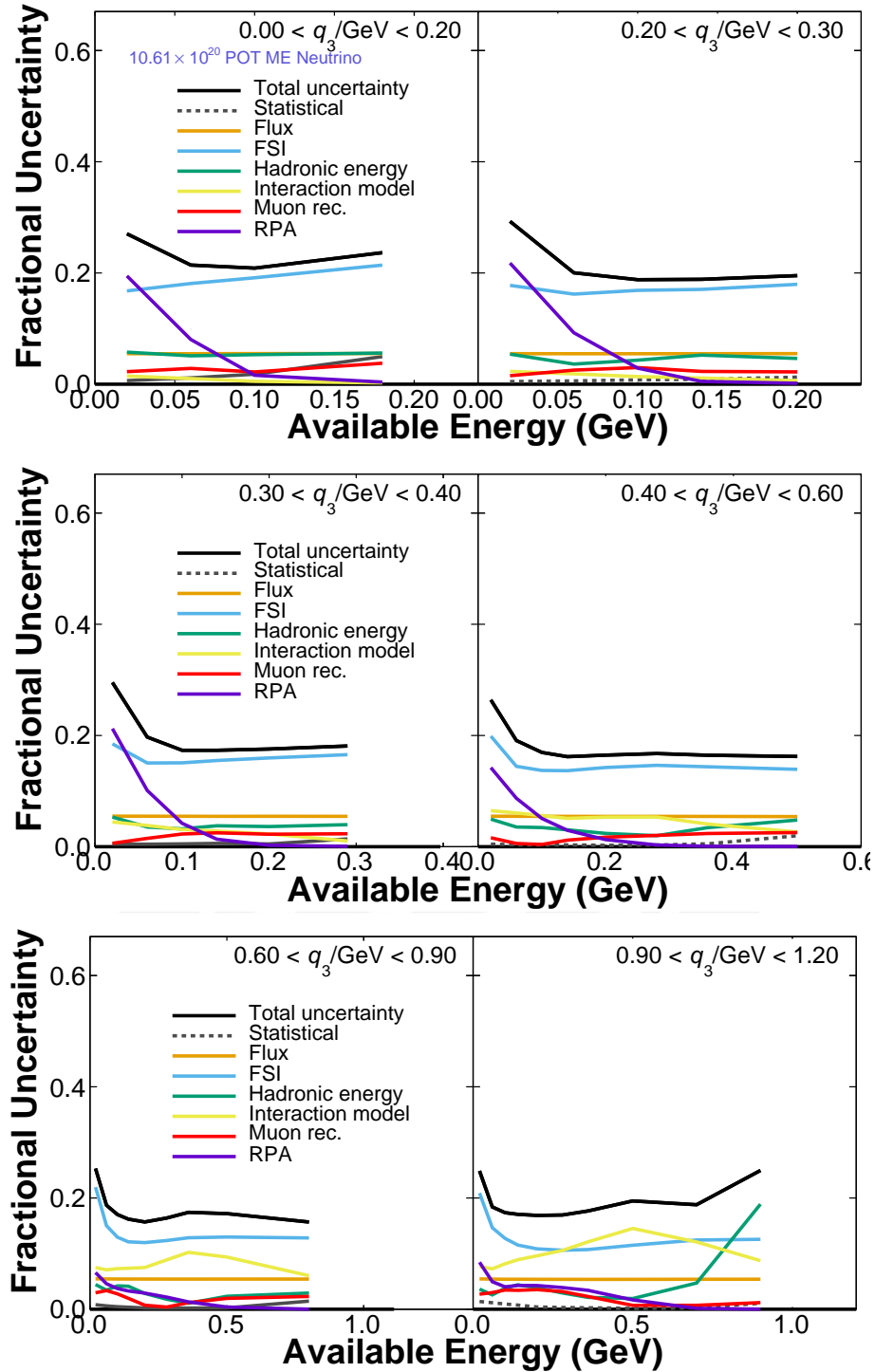
Table 7.6: RPA and Low Recoil Fit uncertainties.

Event Selection Uncertainties (MC reconstructed uncertainties)

The following plots are the fractional uncertainties of the MC reconstructed event selection. The presentation structure follows with a full summary of the grouped main uncertainties (see Figure 7.20). Then the breakdown of the FSI uncertainty (see Figure 7.22), Interaction uncertainty, and RPA uncertainty (see Figure 7.27).

Main Fractional Uncertainties Grouped

The uncertainties can be split into three parts—first, the detector uncertainties are Flux, Muon energy, and Hadronic Energy. Second, the FSI uncertainties, and Finally, the Interaction and RPA uncertainties.

Figure 7.20: Fractional uncertainties in projections of reconstructed q_3 .

The detector uncertainty (FLux, Hadron energy, Muon reconstruction energy, and angle) on average correspond to 10% in the event selection

distribution. The bigger fraction uncertainties are RPA at low q_3 and Hadronic Energy at high q_3 . The dominant uncertainty along all the q_3 and E_{avail} phase space is the FSI.

Fractional FSI Breakdown Uncertainty

The fraction breakdown systematic uncertainties names follow same like Tables 7.2 and 7.3. The Dominant uncertainties are the (Main Free Path) MFP for nucleons and nucleon fates–elastic. At low q_3 and low E_{avail} the nucleon fates–Inelastic also play an important role (QE mostly in those bins), and at high q_3 the important fraction comes from MFP of pions (basically DIS region).

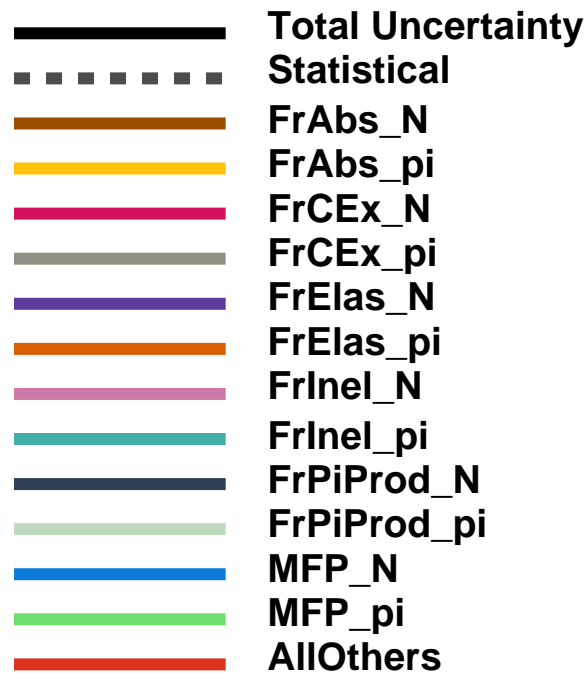


Figure 7.21: Legend used in Figure 7.22.

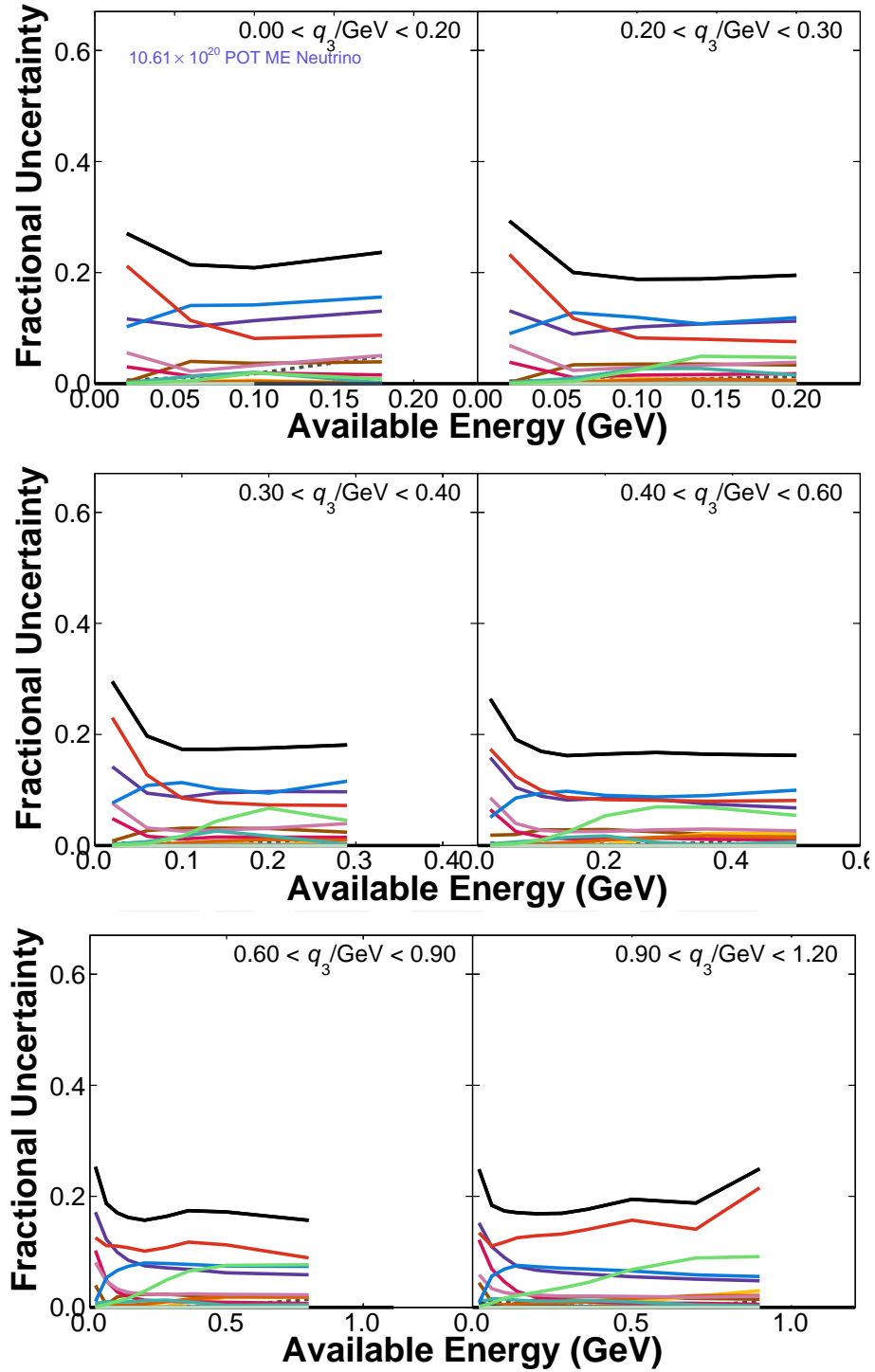


Figure 7.22: Fractional uncertainties of Final State Interaction in projections of reconstructed q_3 .

Interaction Breakdown Uncertainty

The fraction uncertainties of the Interaction model dominate the high q_3 region, where the DIS events are relevant. The large uncertainty is coming from MaRES the Axial Mass in the resonant region (resonances higher than Δ at high q_3) and MvRES the vector part. Another larger uncertainty is coming from MaCCQE, the analogous uncertainty for QE (affecting at low E_{avail} as is expected).

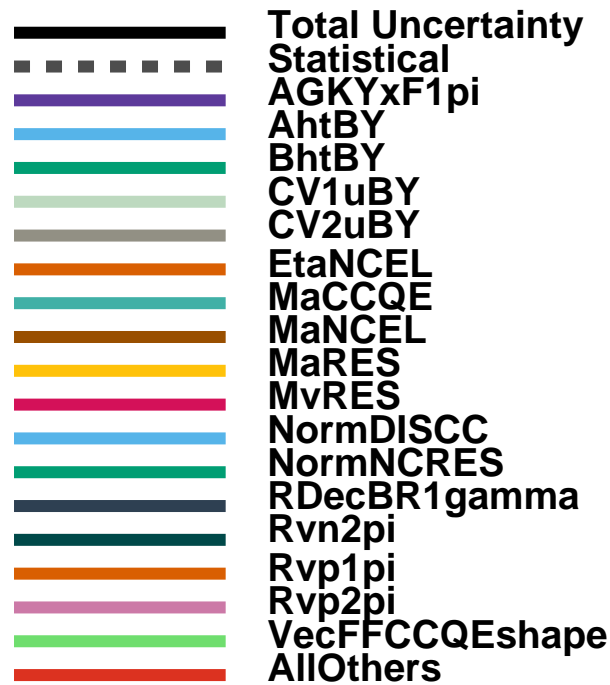


Figure 7.23: Legend of Interaction fractional uncertainty of Figure 7.24.

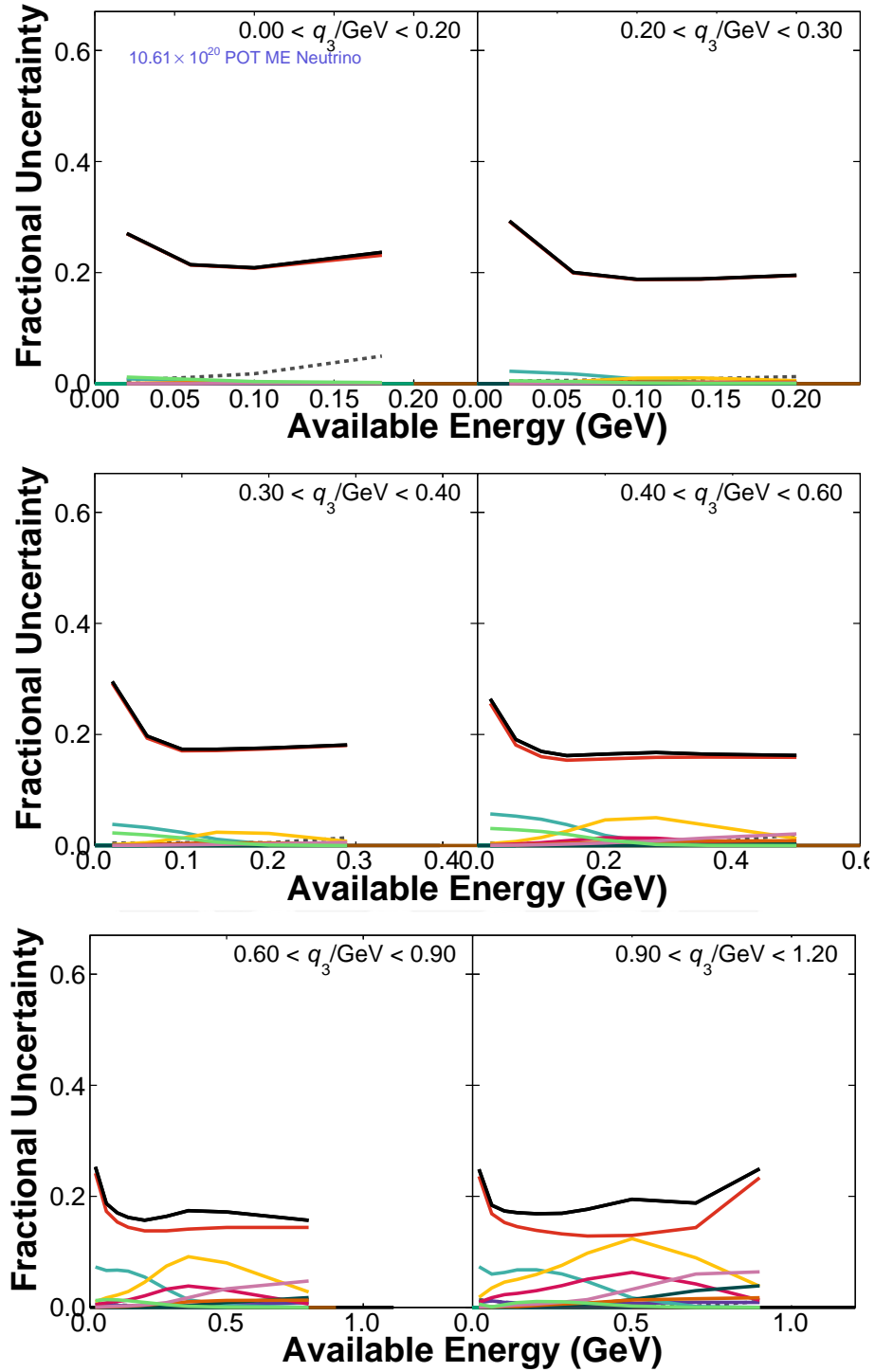


Figure 7.24: Fractional Interaction breakdown uncertainties.

RPA uncertainties

The RPA as it was shown before, has two sources of systematic uncertainty affecting low Q^2 and high Q^2 . On the other hand, we know that RPA is only applied to QE, therefore the only affected region should be low E_{avail} .

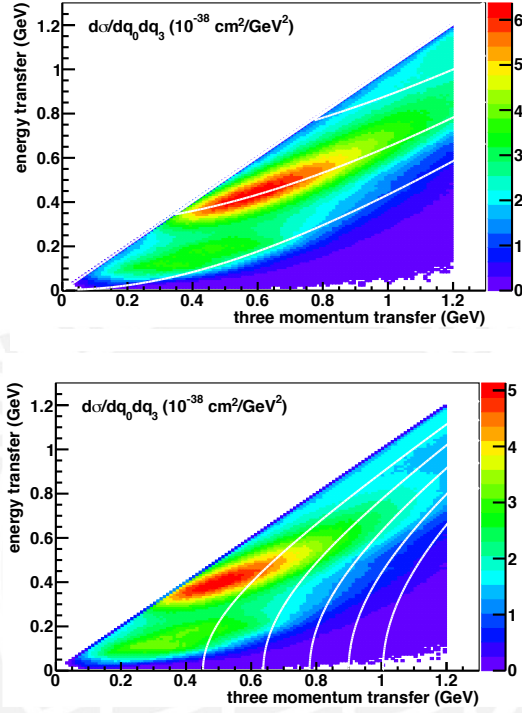


Figure 7.25: Differential cross-section with neutrino energy of 3 GeV. Left plot is neutrino, where the white lines are $W = \{0.938, 1232, 15220\}$ GeV. The right side plot is anti-neutrino, where the white lines represents Q^2 from 0.2 to 1.0 GeV^2 . Figure taken from [235].

Given the lines in Figure 7.25, we can easily see the Q^2 in the q_3 and q_0 (which is close to E_{avail}) to understand the effect of the RPA systematic uncertainty. Let's take for instance the $0.9 > q_3 > 1.2$ region; the low Q^2 component remains, that is because at that high q_3 region we have low Q^2 component.



Figure 7.26: Legend of fractional RPA uncertainty of Figure 7.27.



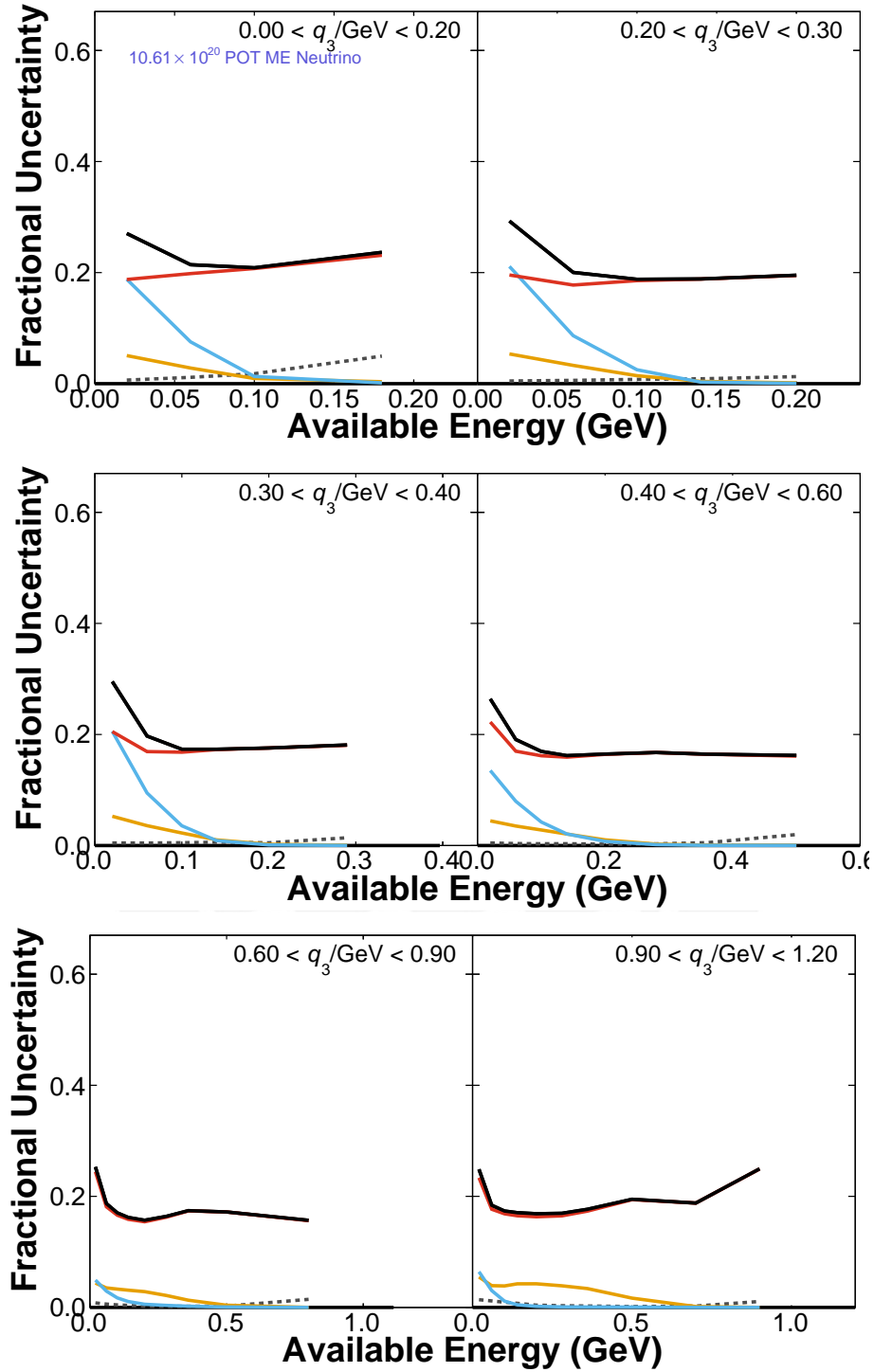


Figure 7.27: Fractional RPA uncertainty.

Detector Uncertainty

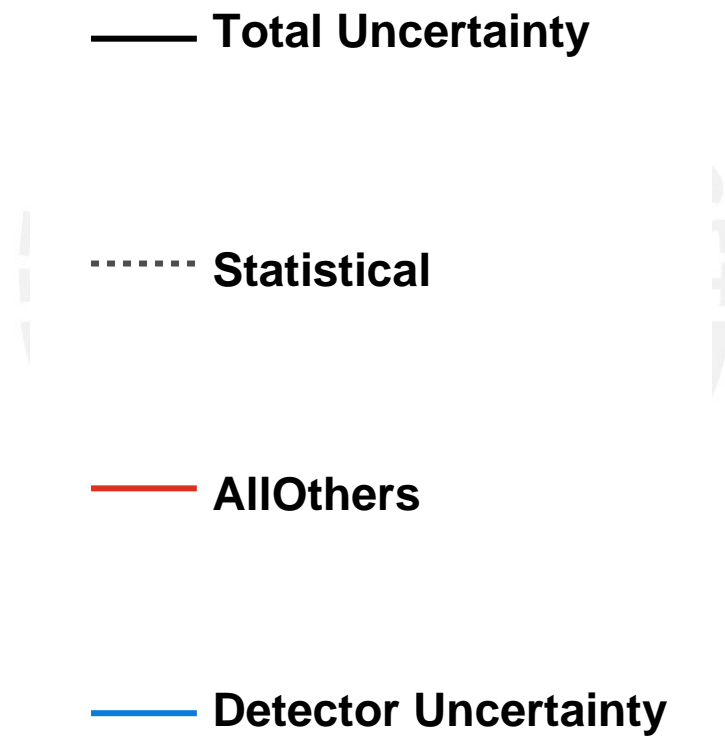


Figure 7.28: Legend of fractional Detector uncertainty of Figure 7.29.

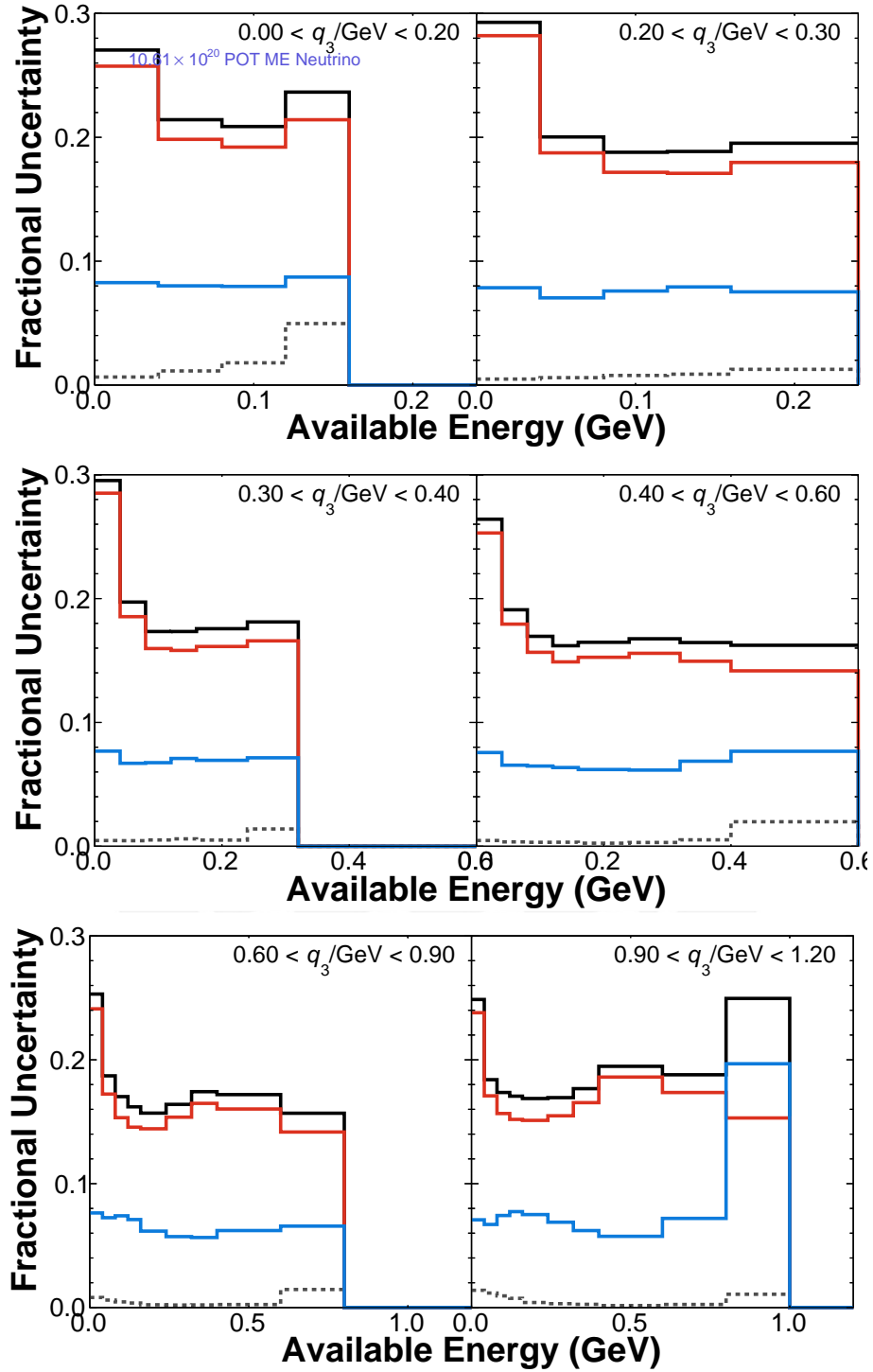


Figure 7.29: Fractional detector uncertainty.

Detector Uncertainty Breakdown

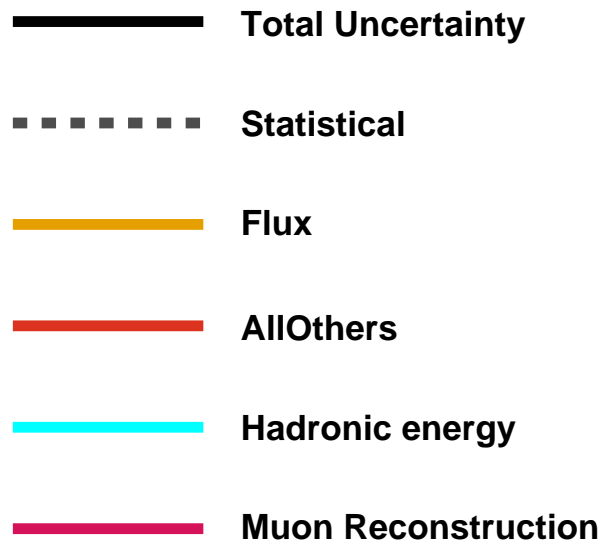
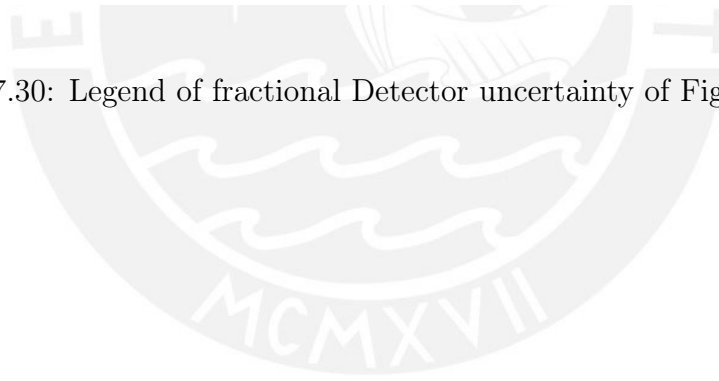


Figure 7.30: Legend of fractional Detector uncertainty of Figure 7.31.



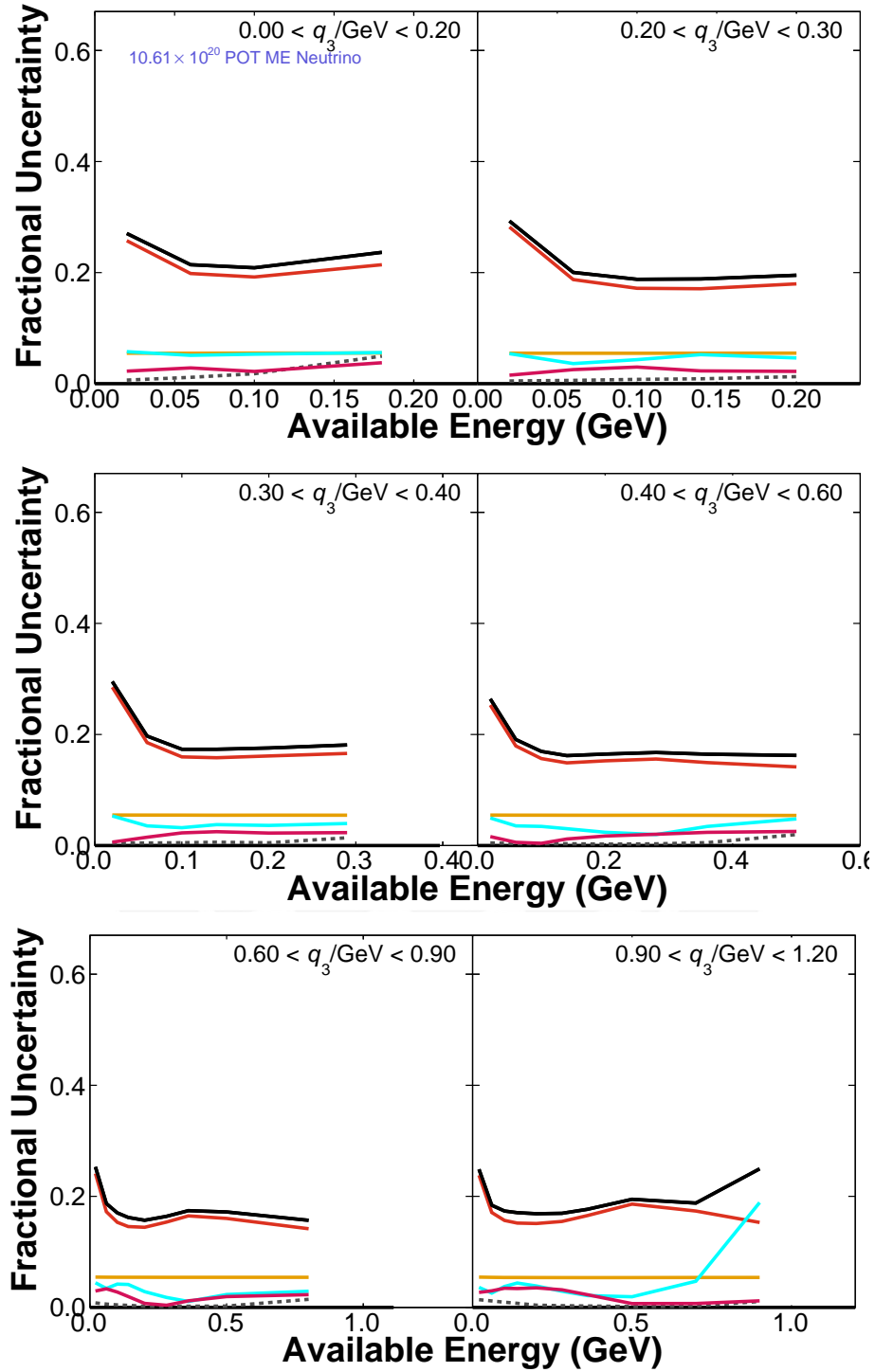


Figure 7.31: Fractional detector (breakdown) uncertainty.

Hadronic Uncertainty

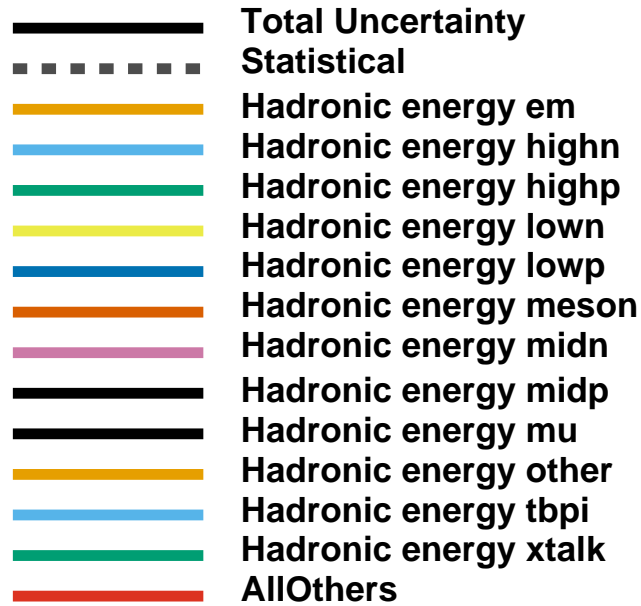


Figure 7.32: Legend of fractional Detector uncertainty of Figure 7.33.

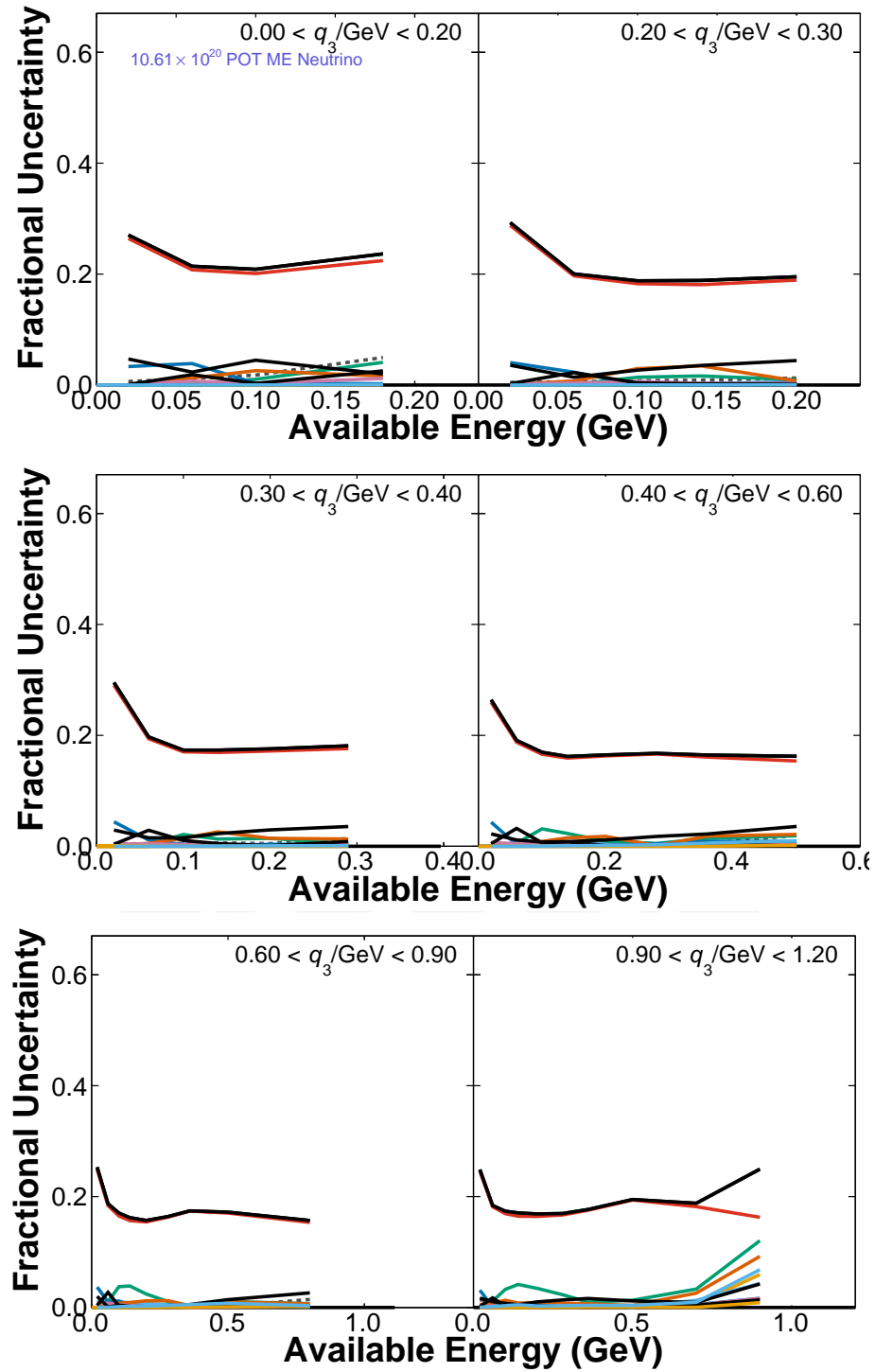


Figure 7.33: Fractional detector (breakdown) uncertainty.

Muon Reconstruction Uncertainty

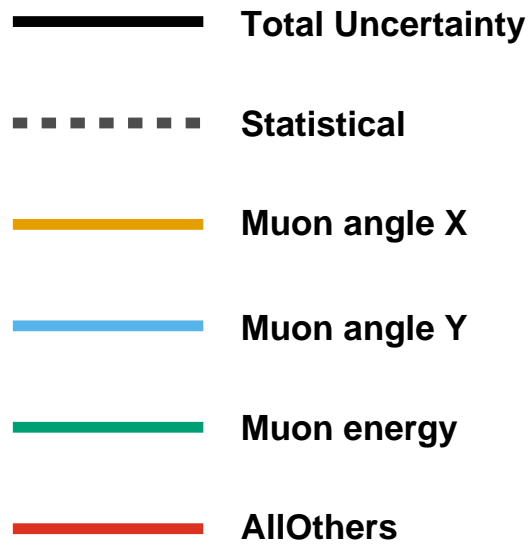


Figure 7.34: Legend of fractional Detector uncertainty of Figure 7.35.

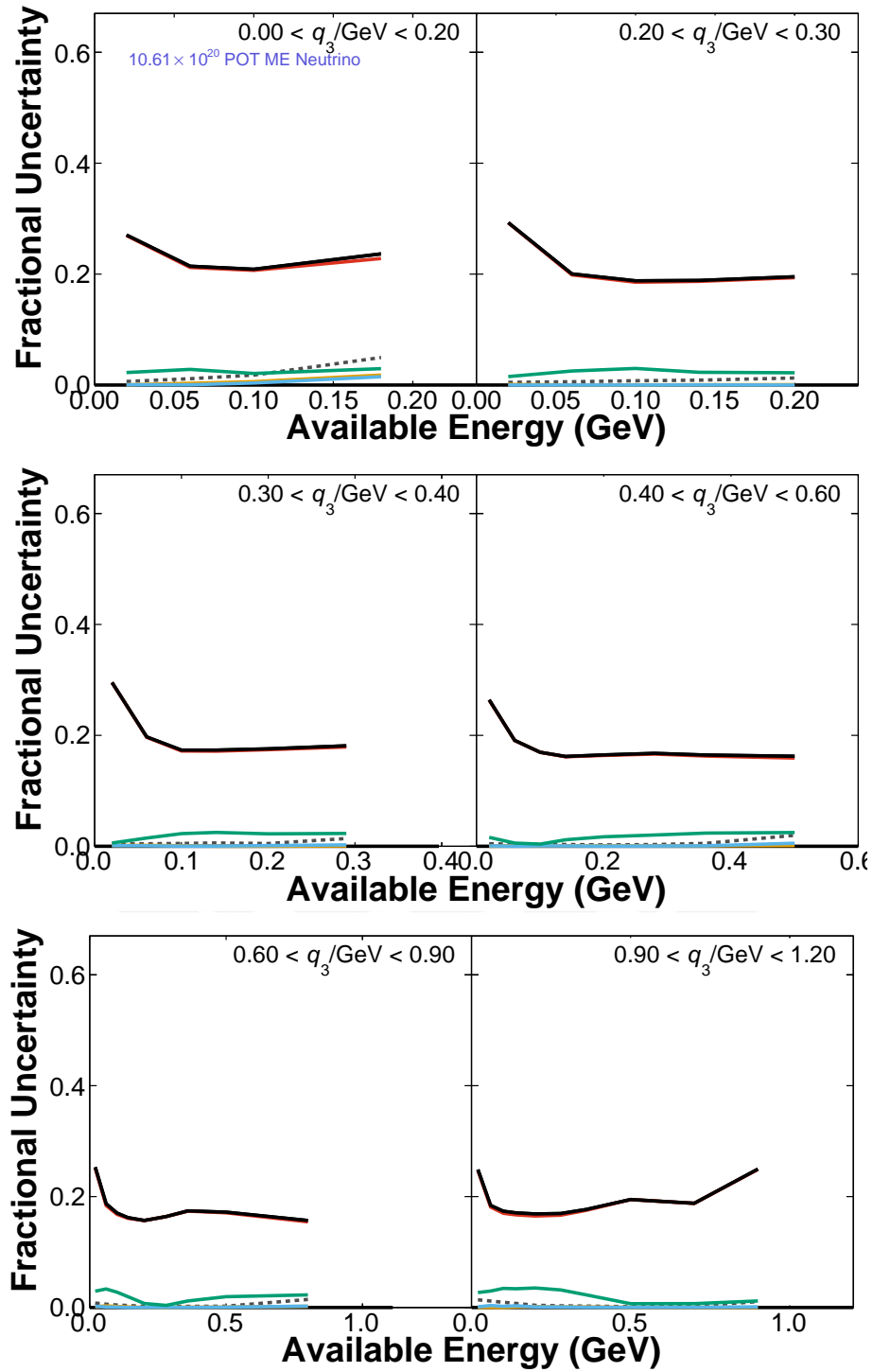


Figure 7.35: Fractional detector (breakdown) uncertainty.

Fractional Uncertainty of Background Subtracted Data

The point of start for data getting systematic uncertainty is at the background-subtracted level. Before that step, the reconstructed data only holds statistical uncertainty. A brief technical description is, that the universes associated with each uncertainty variation must be created as the empty universe for background-subtracted data. After this step, the uncertainty propagation in the universes is straightforward.

As we saw above, the background is so small; therefore, the uncertainty coming from that procedure is small too. Figure 7.37 is zoomed in to see the details of the component of the uncertainties. The main contribution is the statistical uncertainty, especially for a bin in the $0.0 < q_3 < 0.2$ GeV region, followed by the FSI at low Eavail and hadronic energy.

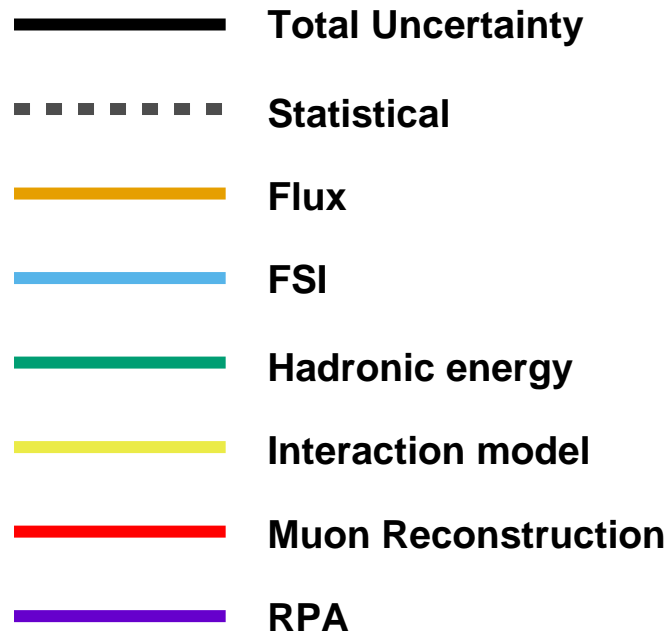


Figure 7.36: Legend of grouped fraction uncertainties background subtracted data (see Figure 7.37).

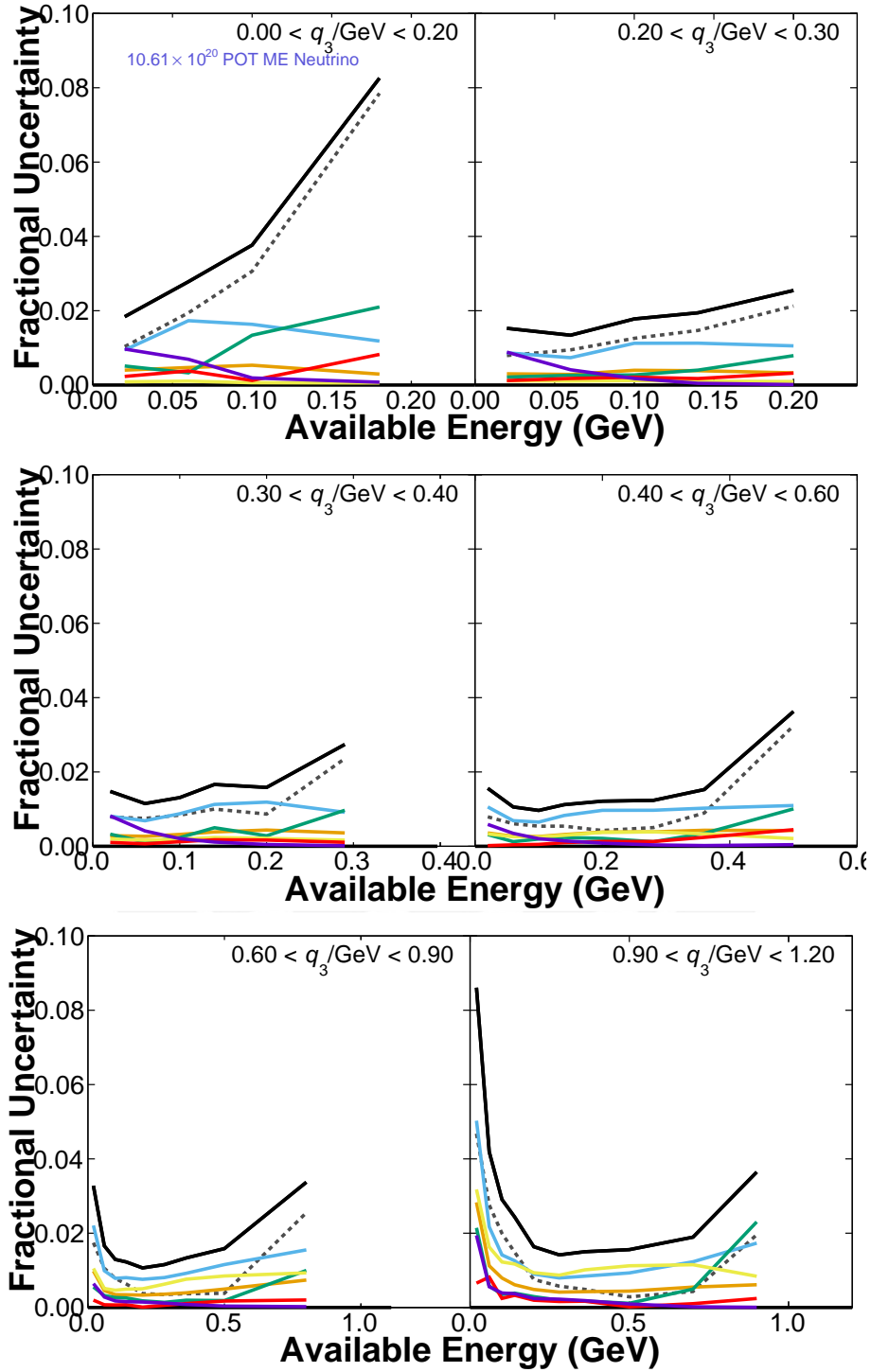


Figure 7.37: Fractional Uncertainty of Background Subtracted Data. Y-axis zoomed.

Fractional Uncertainty of Unfolded Background Subtracted Data

The second way how the data acquire the systematic uncertainty is through the unfolding procedure. Again, every universe is treated just like the central value; D'Agostini's iterative regularization is employed for every systematic universe. This means, for instance, background-subtracted data with a shift given by one of the uncertainties is unfolded, making the end an effect in the uncertainty. At this step one of the uncertainties started to grow; the hadronic energy. To understand why it is necessary to remember. First, the unfolding is applied to remove the detector effects to make comparable the data measured. Second, at this very high q_3 region, the DIS is one important component, and as shown in the migration matrices, the poorest resolution region is high q_3 . So, because the migration matrix is needed to unfold, the hadronic energy is sensitive at that q_3 range.

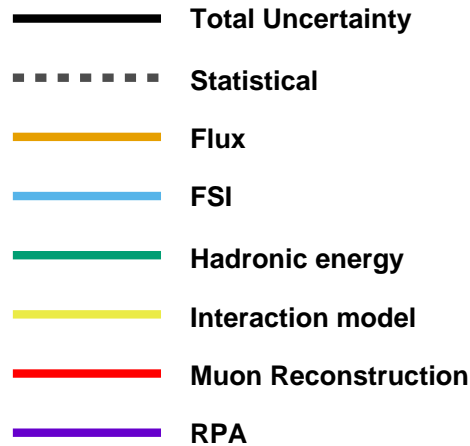


Figure 7.38: Legend of grouped fraction uncertainties background subtracted data (see Figure 7.39).

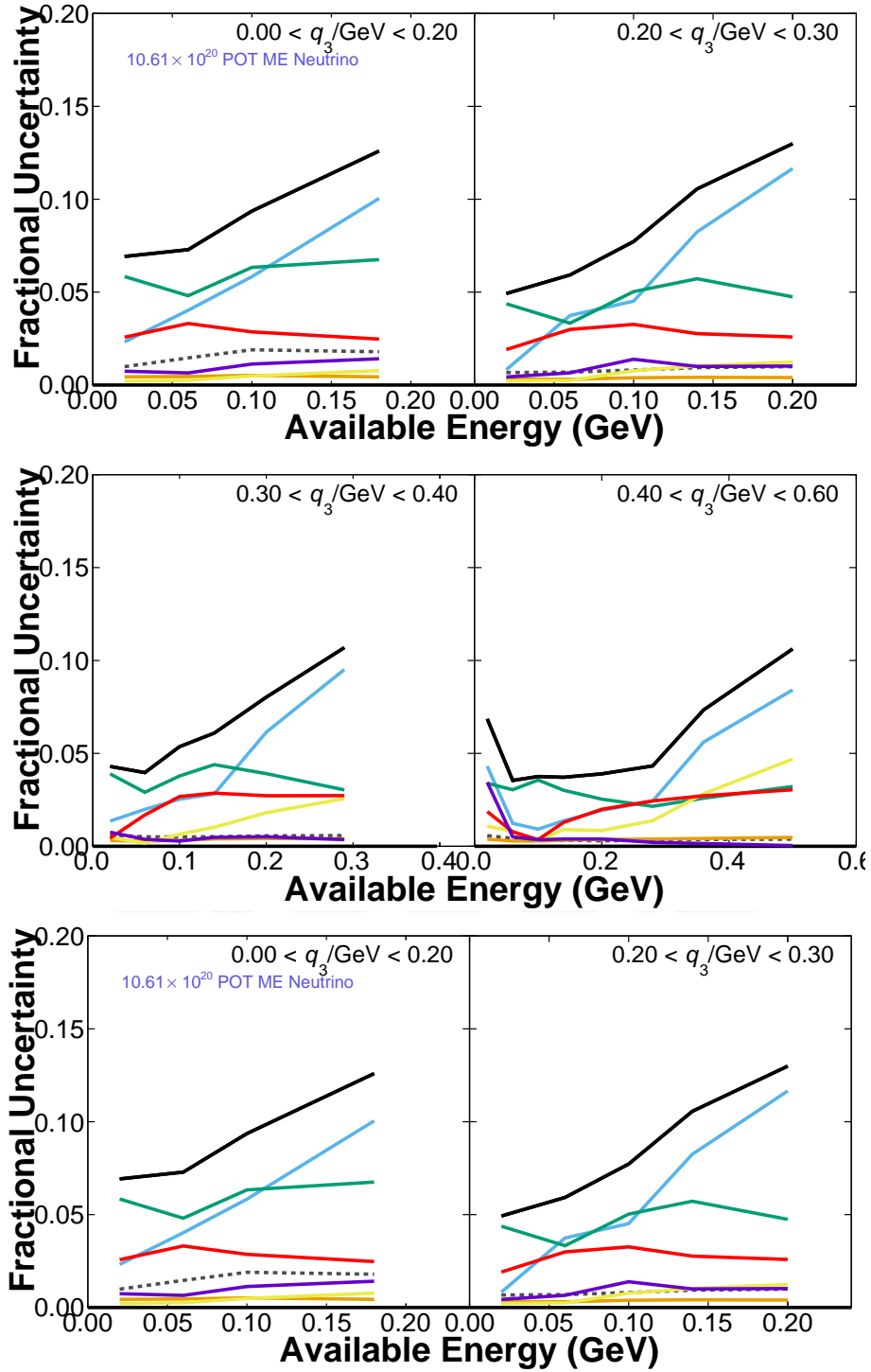


Figure 7.39: Fractional Uncertainty of Unfolded Background Subtracted Data.

Cross-Section Fractional Uncertainties

Finally, the fractional uncertainty of the data double differential cross-section. In this section, the uncertainty like background-subtracted step and unfolding is the propagation of the systematic uncertainty coming from the reconstruction level. All the uncertainties are described in the previous tables except the new ones introduced at this stage, the so-called Signal Models (see Figure 7.40). Unfolding MnvTune.v1.2 uncertainty considers the difference between the data cross-section unfolded with MnvTune.v3 and the data cross-section unfolded with MnvTune.v1.2. With this, we are adding an uncertainty model that is not in GENIE. With the procedure mentioned above, the idea is to introduce an uncertainty due to model changes or improvements that MnvTune.v3 has.

However, there is an important feature to notice, in a few particular bins, the uncertainty coming from the new models is significant. The main component contributing to that uncertainty is SuSA2p2h, with few contributions of removal energy. Careful identification and evaluation of the source of that uncertainty are described in Appendix E. Another important contribution at a very high q_3 region is one of the detector component uncertainty; the Hadronic energy. That uncertainty starts growing at around 4% at the background subtraction step. Then after the unfolding, it becomes large.

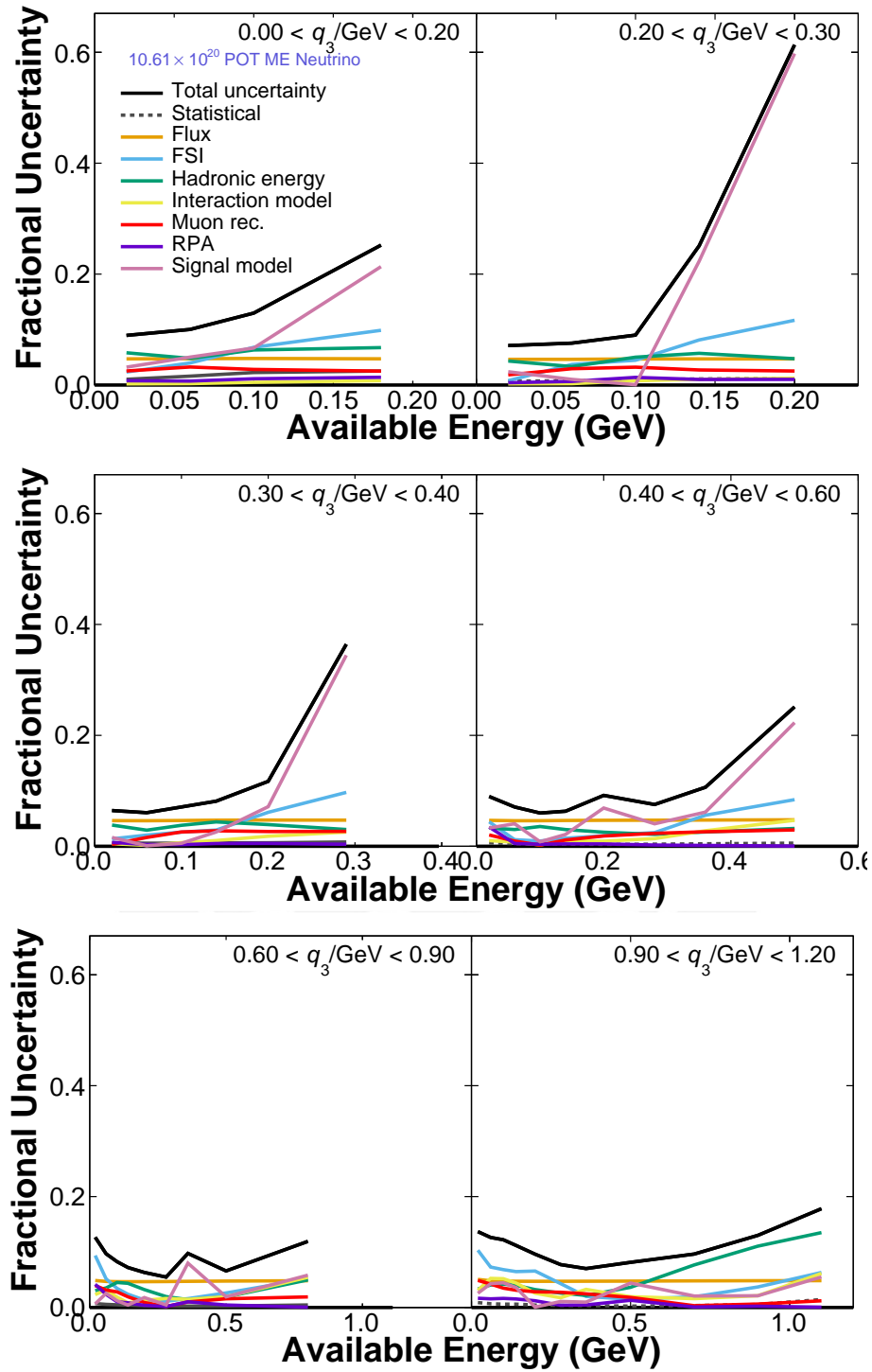


Figure 7.40: Fractional Uncertainty of Data Cross-Section.

Cross-Section Absolute Uncertainties

The Absolute Uncertainties of the data cross-section is showed in Figure 7.42, compared with the fractional partner, this does not show large values.

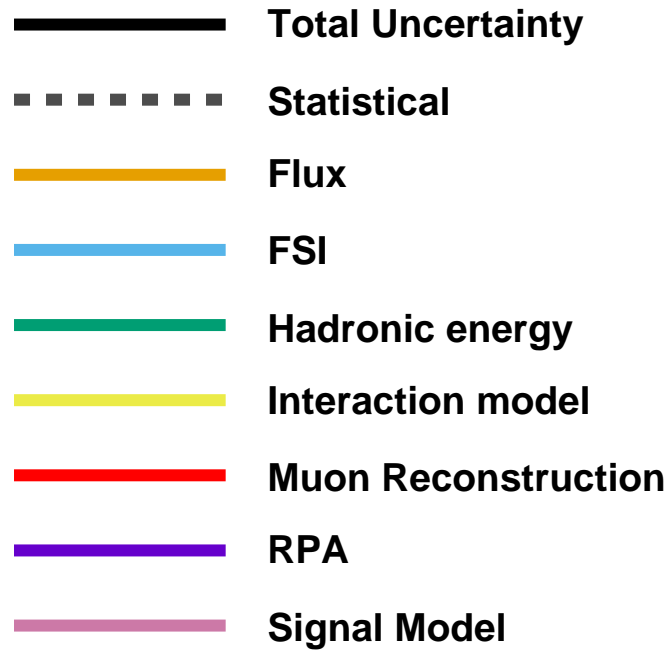


Figure 7.41: Legend of grouped absolute uncertainties background subtracted data (see Figure 7.42).

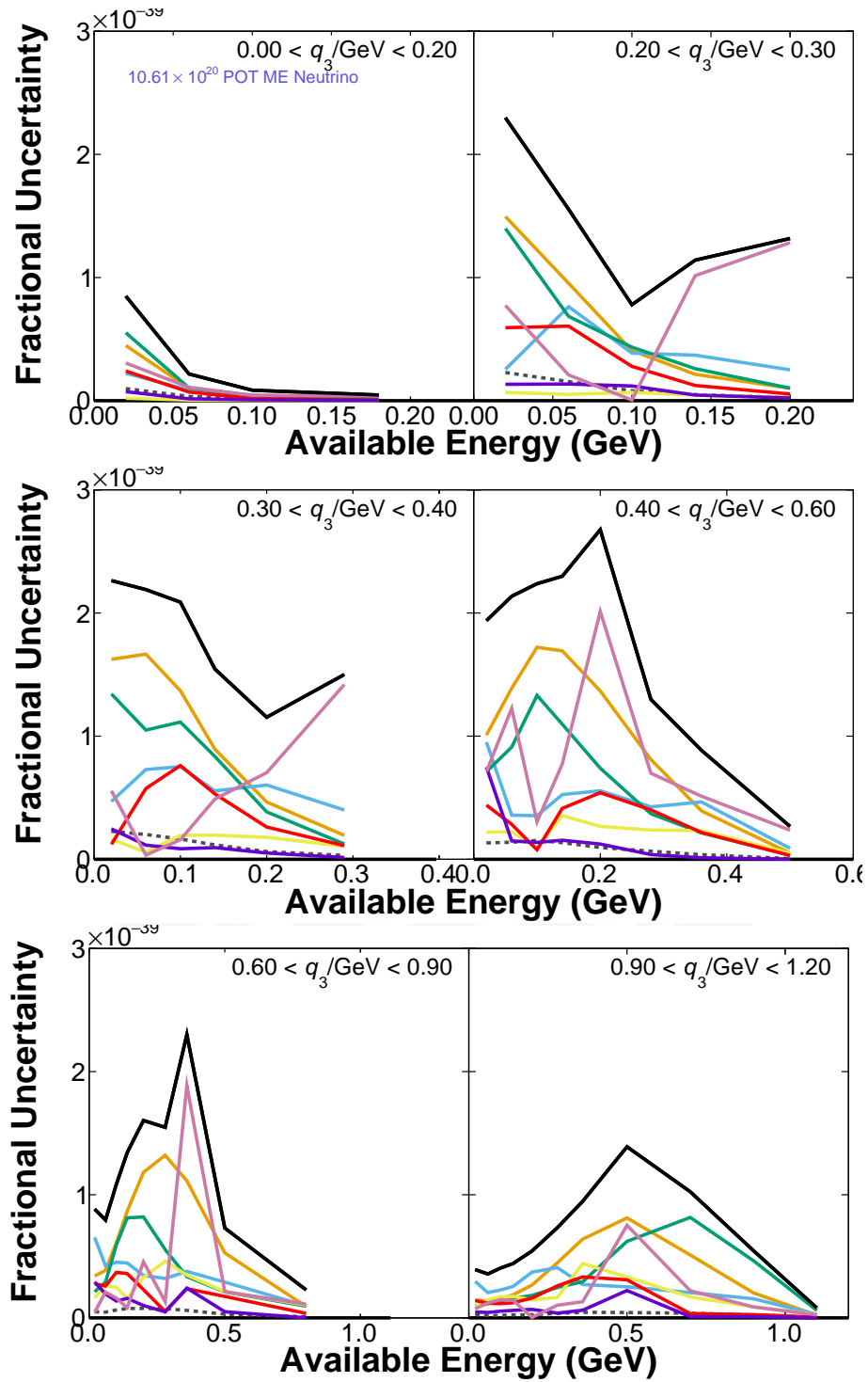


Figure 7.42: Absolute Uncertainty of Data Cross-Section.

7.9 Covariance Matrix

The total covariance matrix showed in Figure 7.43 is formed by adding the covariance matrices for all sources of systematic uncertainty. The diagonal elements of this matrix are represented by the error bars in Figure 7.19 as well as the fractional and absolute uncertainties (see Figures 7.40 and 7.42).

For uncertainties that require more than one variation in the model parameter, for instance, a $\pm 1\sigma$ shift in the energy scale. The covariance matrix of that uncertainty is the average of the covariance matrices. On the other hand, there are uncertainties like flux, which has hundreds of universes. Each universe variation comes from the random variation of its parameters according to their probability distributions and correlations. Therefore, the covariance matrix of that uncertainty is the covariance matrix of the averaged universes.

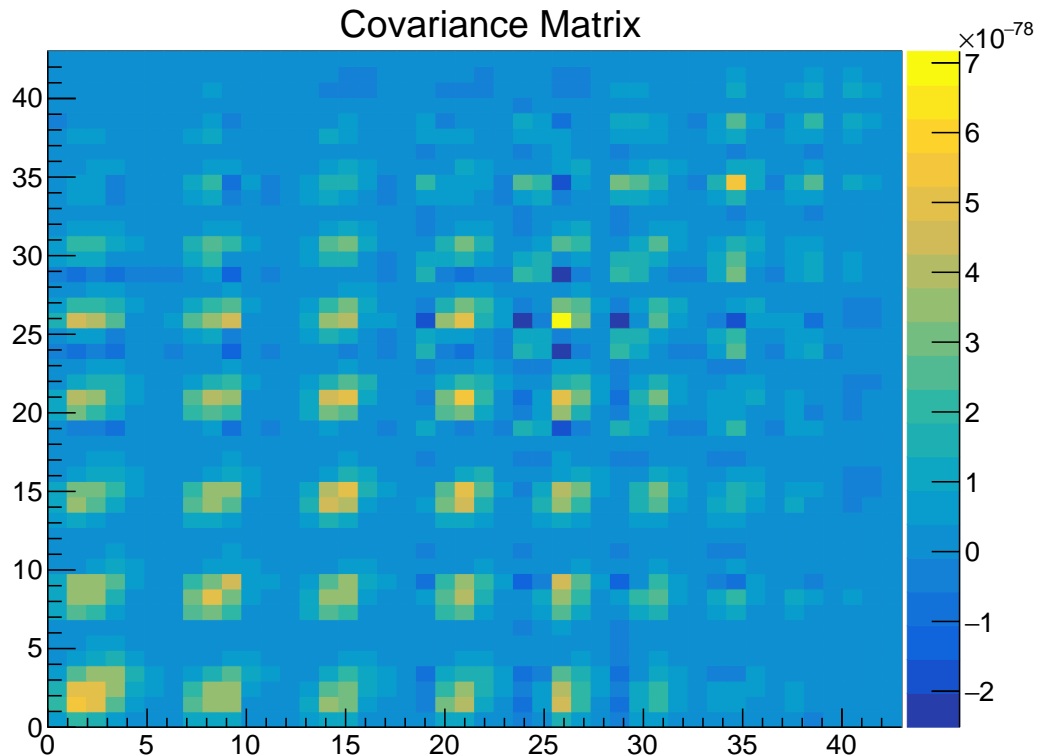


Figure 7.43: Covariance matrix in q_0 and q_3 bin index mapping (V)

7.10 Cross-section compared to neutrino generators

The double differential cross-section shown in Figure 7.19, 7.44, and 7.45 is compared to different neutrino event generator predictions: MnvTune.v3, MnvTune.v1.2, NuWro [297] (Spectral Function (SF) and Local Fermi Gas), and the GENIE v3.0.6. This is similar to the LE data comparison models [298]. The GENIE v3 version uses a (LFG) and the Valencia model for both QE with RPA [226] and 2p2h [233]. In the resonant region, the Berger-Sehgal model replaces Rein-Sehgal [299]. The DIS region used Bodek-Yang model [300], that includes the non-resonant background in the resonance region by scaled the DIS model. The FSI uses the empirical hA FSI model due to the MnvTune.v1.2 and MnvTune.v3 is based on GENIE v2 generator. The GENIE collaboration call to this configuration as “G18_10a_02_11a” [294, 301].

The NuWro configuration for QE in LFG combined one with the RPA effect. The SF configuration uses the GFG with a spectral function initial nucleon state. In the resonant region, NuWro only has Δ resonance, and the non-resonant is the scaled Bodek-Yang DIS model for the rest of the resonance region. In contrast to the empirical hA, NuWro uses Salcedo and Oset’s model for FSI [302].

The model elements chosen for MnvTune.v3 at the reconstructed level make, overall, a better agreement with the extracted cross-section. The NuWro and GENIE v3 models, on the other hand, describe only parts in the kinematic space of the data distribution. The considerable discrepancies are in the QE and 2p2h regions. Both MnvTunes are far better compared with the other generators. However, a comparison between them is challenging in the sense that, in shape, the MnvTune.v3 seems a better model to describe the data, but at the χ^2 level is, by a small amount, the opposite. The interpretation and discussion about that behavior are presented in the next section.

The comparison with the NuWro and GENIE 3 represents another

challenge due to overlapping effects.

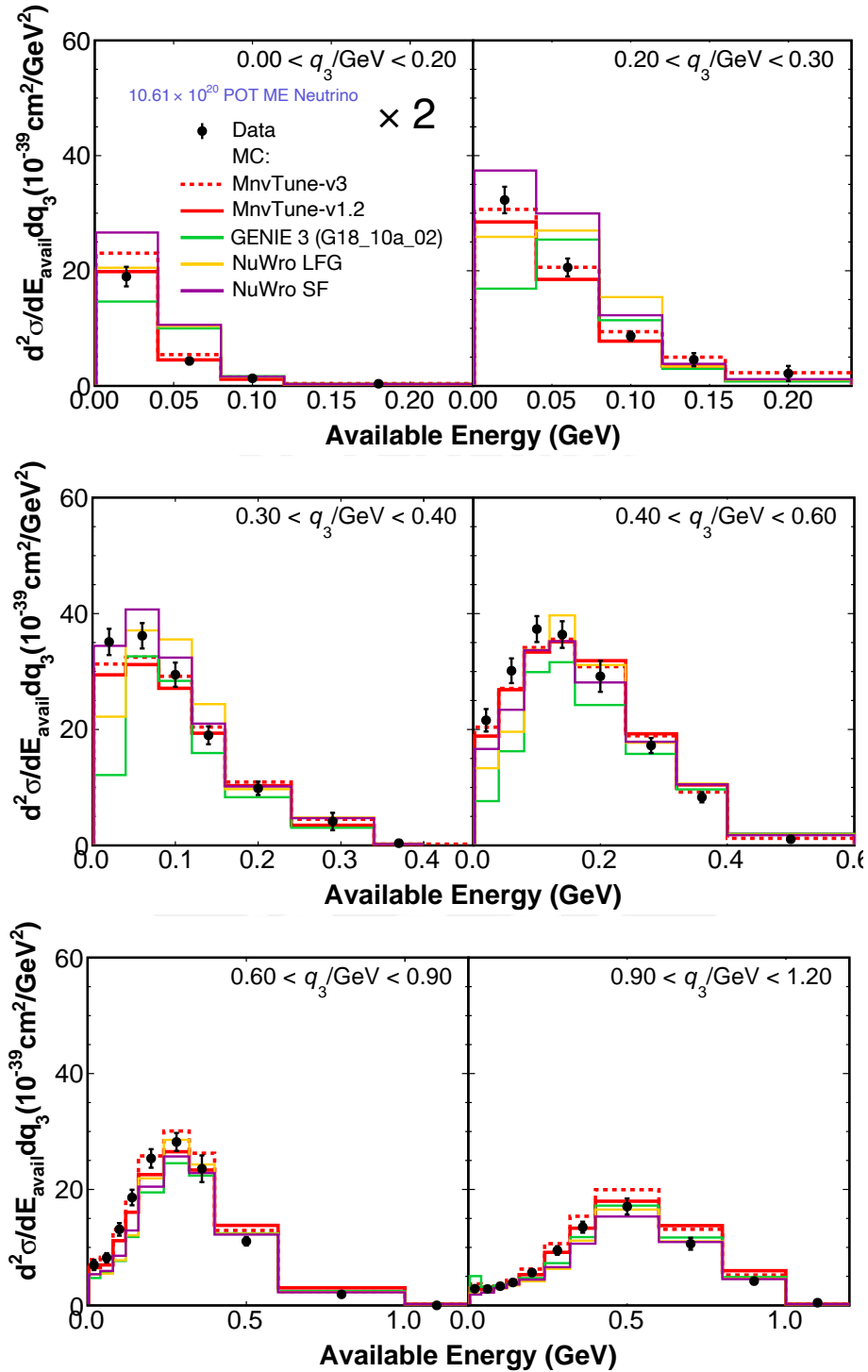


Figure 7.44: Data double differential cross-section as function of E_{avail} and q_3 , compared with MnvTune.v3, MnvTune.v1.2, GENIE3, NuWro SF, and NuWro LFG.

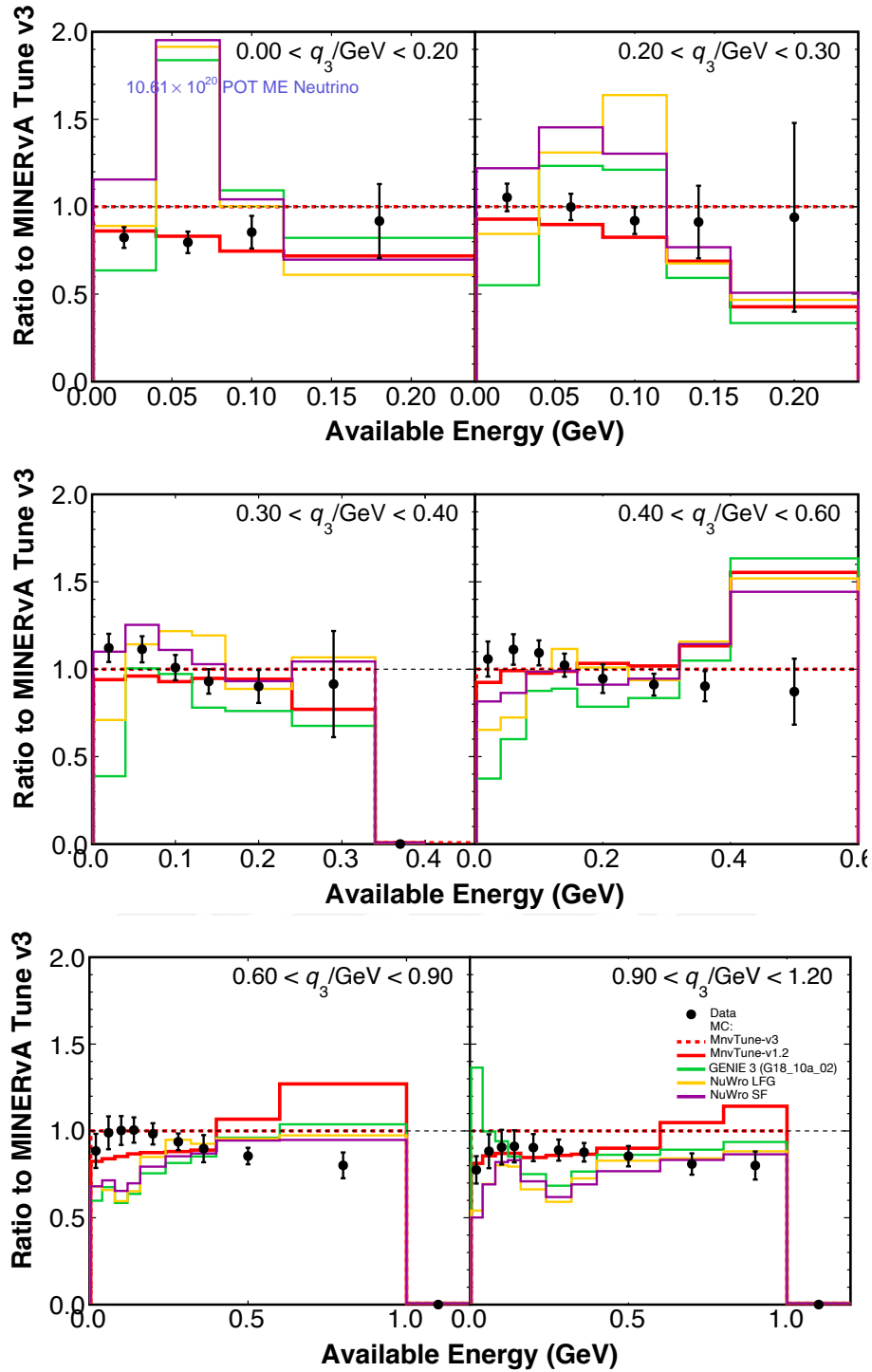


Figure 7.45: Data double differential cross-section as function of E_{avail} and q_3 , compared with MnvTune.v3, MnvTune.v1.2, GENIE3, NuWro SF, and NuWro LFG (Ratio).

The QE process

As indicated previously, the largest differences between models are in the QE region, which comprises nearly half of the provided data in each panel q_3 . The only difference between versions in the NuWro case is the QE process, which can be used to highlight how this aspect of the distribution is affected.

The spectral function model is notably distinct due to the absence of an RPA screening (or empirically version [303, 304]) effect, and not due to the spectral function. In the first one or two bins in panels with $q_3 < 0.4$ GeV, it generates a higher prediction than the data and all other models. The cross-section is integrated into the NuWro spectral function using a two-dimensional distribution of initial state off-shell nucleon momentum and removal energy. Its implementation is substantially distinct from the enhanced Bodek-Ritchie tail in MnvTune.v3, despite the fact that they share the theoretical motivation. Figures 7.44 and 7.45 show two models with 5% to 10% differences in the QE region. In contrast to the NuWro comparison, both models, in this case, have the RPA effect, so only the spectral function and 2p2h changes are active, and the spectral function effect alone has less than a five percent influence.

The data in the lowest bin in all panels is under-predicted by the local Fermi gas version (NuWro LFG), then it resembles the other NuWro model. At low Q^2 , it has an RPA screening effect. Its implementation is independent of the Valencia model [226], although it is designed to generate a comparable prediction. Moreover, it differs from the Valencia model RPA weight applied to the two GENIE v2 tunes, and it underestimates the data in the first bin of all panels. However, in other bins (around the QE peak), this model is higher than the NuWro SF model and significantly higher than the GENIE models, including the identical MnvTune.v1.2 and GENIE v3, and is a poor overall description of the data. The initial nucleon momentum distribution of the namesake LFG does not contain nucleons with high momentum and has, on average, smaller momenta than a standard Fermi gas. This would result in

a more narrow QE peak, but its impacts are harder to determine.

Comparing NuWro and MnvTune tunes relative to the data reveals a second trend: in the following three to five available energy bins, as a function of q_3 , NuWro shifts from overestimating to systematically underestimating the data. In contrast, the two modified GENIE models are close to the data and to one another, with certain data points preferring one model over the other. These bins are a combination of the QE peak, 2p2h, and a small amount of *Delta* resonance. The NuWro behavior could be explained by incorrectly estimating the relative strength of these three processes. Even a simple form factor impact (such as M_A^{QE}) for QE could explain a portion of these variances in total rate and q_3 trends for the generators.

The lowest available energy bins

Most of the difference between the predictions is in the lowest energy bins in each panel. In addition to the RPA effect, there are three other effects. Two come from how strong the FSI processes are that lead to neutrons and low-energy nucleons in the final state. One is related to the removal of energy applied to the hadronic system for the QE process.

The transformation of a QE proton into a neutron prior to its exit from the nucleus is a unique component of these bins. The GENIE v2 tunes predict that 20% of the events in the first E_{avail} bin of the lowest $q_3 < 0.6$ GeV panels are QE events with energy transfers above 100 MeV and feed down via an FSI process, 10% are 2p2h events, and 2% are resonance events with the same kinematics. In the most extreme scenario, 10% of the events have only neutrons as the final state, resulting in zero E_{avail} . These happen when the generator's FSI model produces either the $p \rightarrow pn$ knockout process, the $p \rightarrow n$ charge exchange process, or pion absorption followed by ejection of two or more nucleons. The empirically tuned hA FSI model is nearly identical for all three genie versions, but distinct from the Oset model utilized by NuWro[302] . A

study of the hA vs. hN models in genie 3 (see Appendix G) indicates that this choice alone accounts for 10% of the variance in these bins.

The FSI in GENIE hA and NuWro models produce a similar prediction as does the INCL++ but, hN model and NEUT behaved differently (see reaction cross-section in [305]). Therefore, that is significantly translated to the lowest E_{avail} bin.

The change in the nucleon removal energy for QE is translated an underprediction in GENIE v3. In GENIE v2 (as well as the two MnvTunes), 25 MeV is explicitly subtracted from the proton. This 25 MeV is also subtracted from the hadron state in resonance modification (RES Removal Energy). In GENIE v3, this subtraction is not made. To reiterate the design, in the classic (e,e') nuclear effect paper [306], the QE peak is higher by 25 MeV. In GENIE, this is accomplished by using the deForest prescription [307]. With Pauli-blocking and the final 25 MeV subtraction, the resulting protons in GENIE v2 are produced down to zero kinetic energy. In GENIE v3 start the same, but the Pauli-blocking step is not followed by a 25 MeV subtraction, so very few protons are produced below 20 MeV. Additional ways to treat these effects were described in section 6.3 for resonances and can be found in [308, 262] and has been implemented for QE in MINERvA previous publication [309]. Overall this creates $\pm 20\%$ differences in the QE-rich first bin in each q_3 panel.

The low Q^2 resonances

All generators in 7.44, and 7.45 describe the low- Q^2 resonances better than MnvTune.v1.2 and the Rein Sehgal model. The MnvTune.v3 uses a new prescription to apply removal energy to resonances similar to what GENIE v2 does for the QE process (see Section 6.3). It preserves the event rate but shifts it to lower E_{avail} . The pion production models in NuWro are within a few percent of the MnvTune-v3 in the bins where this effect is significant. The Δ model is from Lalakulich and Paschos [310] with deuterium-data based axial

and vector form factors [311] and Pauli blocking. It would be similar to the Berger-Sehgal with Pauli Blocking (see Section 6.5). On the other hand, the higher resonances are treated very differently in NuWro, preventing firm conclusions. Instead of simulating the non- Δ resonances and their decay like other generators, the NuWro event rate is entirely provided by the DIS model using only the quark-hadron duality principle to reproduce the resonance interaction rate on average.

Comparison to the previous measurement

Compared with the previous MINERvA result in Low Energy analysis [279], this result has several improvements. All these changes cause the reconstructed distributions to differ even with a consistent MC configuration like MnvTune.v1.2. The important changes are in flux. In ME we applied the 12% $\nu + e$ scattering constrain [205]. However, the 8% LE adjustment [312] was not yet available for the first analysis. The +3.6% muon energy scale correction that is applied to the ME data [201] has complex effects on this sample and is also significant. There are numerous improvements of 2% or less including the detector mass model and efficiency corrections. And the sophistication of the uncertainty budget is improved.

On the unfolding side, the distributions use different central values MC. The most prominent change is that the original analysis did not have any addition to the 2p2h or QE rate in the dip region, that aspect of MnvTune.v1.2 was added afterward. Of equal significance, the original analysis used neither a low- Q^2 resonance suppression nor a Δ hadronic energy shift to account for that poorly predicted region of the sample.

A third effect comes from the unfolding technique, which introduces shifts in the data/MC ratio compared to the ratio in the reconstructed distributions. Some of these shifts are from features encoded in the migration matrix. Other shifts arise from the iterative unfolding method. When the

input model is far from the data, iterations can lessen the gap, removing some of the bias from an imperfect starting model. In this analysis, iterations move the ratio by 0.08 in the QE region compared to the ratio after the first unfolding and the reconstructed distributions, closing the gap. The discrepancy started at 25% and was reduced to 17% for MnvTune-v1.2, and went from 16% to 9% for MnvTune.v3. In the QE region of the previous measurement, the reconstructed distribution was already well described, so iterations had a negligible effect. Because of these changes, combining the published unfolded LE result with the new ME result is not a viable analysis. Future analysis to bring the LE cross-sections on the same footing or a joint analysis with the reconstructed data using the data preservation packages [313] may shed more light on the neutrino energy dependence.

7.11 Interpretation of the chi-square and conclusions

In the previous section, we discussed the distinctions between the various model components in MnvTune and the neutrino generators. This section discusses the chi-square metric at the cross-section level. Similar to the one presented at the reconstructed level, this covariance matrix contains only the diagonal elements, followed by the full covariance. Finally, a $\Delta\chi^2$ Metric is presented to comprehend the numbers' underlying significance.

The χ^2 is defined in Equation 6.5, each value for each bin is presented in Figure 7.46 for the models presented in Figures 7.44, and 7.45. The summary in each q_3 region is presented in Table 7.7. Finally the all χ^2 with diagonal only covariance matrix is presented in Table 7.8. In contrast to the χ^2 presented in Table 6.2 the diagonal elements of the covariance matrix do have systematic uncertainties.

Similarly, the χ^2 with full covariance matrix is presented, for each bin (see Figure 7.47), in bins of q_3 (see Table 7.9), and total χ^2 (see Table 7.10).

The bin-by-bin $\Delta\chi^2$ in each q_3 and E_{avial} bin is defined as:

$$\Delta\chi_i^2 = \sum_j \left(\chi_{i,j,\text{model}}^2 - \chi_{i,j,\text{MINERvA Tune v3}}^2 \right), \quad (7.4)$$

where $\chi_{i,j,\text{model}}^2$ comes from Equation 6.5. The $\Delta\chi^2$ for diagonal and full covariance matrices is shown in Figure 7.48, the metric in all other models are shown in Figure 7.49, and the Signal model uncertainty effect is illustrated in Figure 7.50. The metric was used in previous MINERvA analysis [314]. A negative $\Delta\chi^2$ represents a bin where MnvTune-v1.2 predicts the data better than MnvTune-v3 while a positive value means MnvTune-v3 predicts the data better.

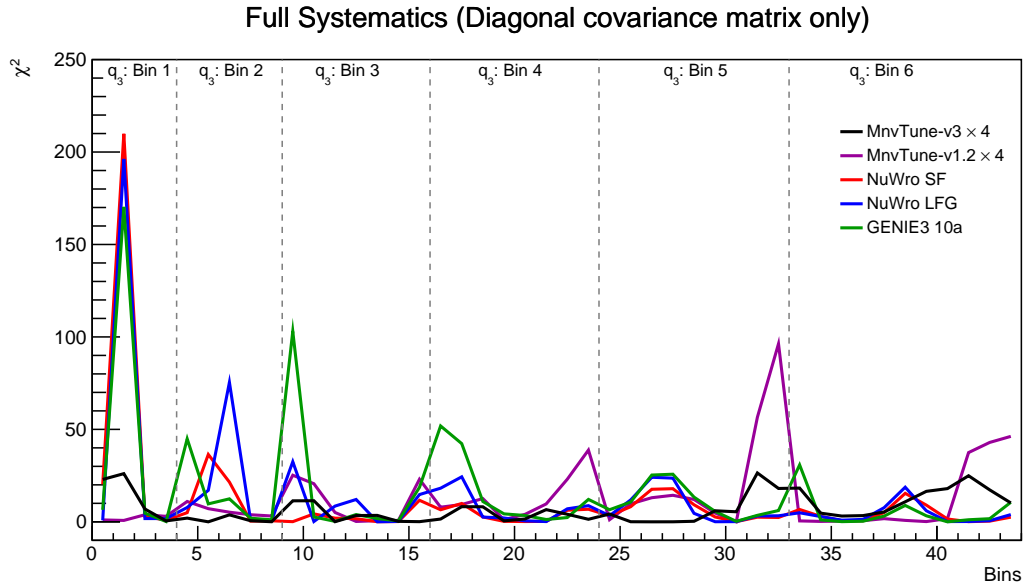


Figure 7.46: χ^2 calculated with only the diagonal elements of the covariance matrix V

7.11. INTERPRETATION OF THE CHI-SQUARE AND CONCLUSIONS

Table 7.7: χ^2 of the data with MC at cross section level. Here the NDF is 44. Only Diagonal elements of covariance matrix.

MC/Generators	q_31	q_32	q_33	q_34	q_35	q_36
MnvTune-V3	14.101	1.603	7.515	7.985	15.119	33.113
MnvTune-V1.2	2.147	7.582	18.872	26.654	52.008	33.187
NuWro SF	233.941	63.824	19.961	32.843	63.823	44.794
NuWro LFG	200.621	101.953	68.258	63.62	74.05	47.142
GENIE 3 (G18_10a_02)	181.701	70.072	130.798	128.573	97.159	60.865

Table 7.8: χ^2 of the data with MC at cross section level. Here the NDF is 44. Only diagonal elements of the covariance matrix

MC/Generators	χ^2	χ^2/NDF
MnvTune-V3	79.4	1.8
MnvTune-V1.2	140.5	3.2
NuWro SF	459.2	10.4
NuWro LFG	555.6	12.6
GENIE 3 (G18_10a_02)	669.2	15.2

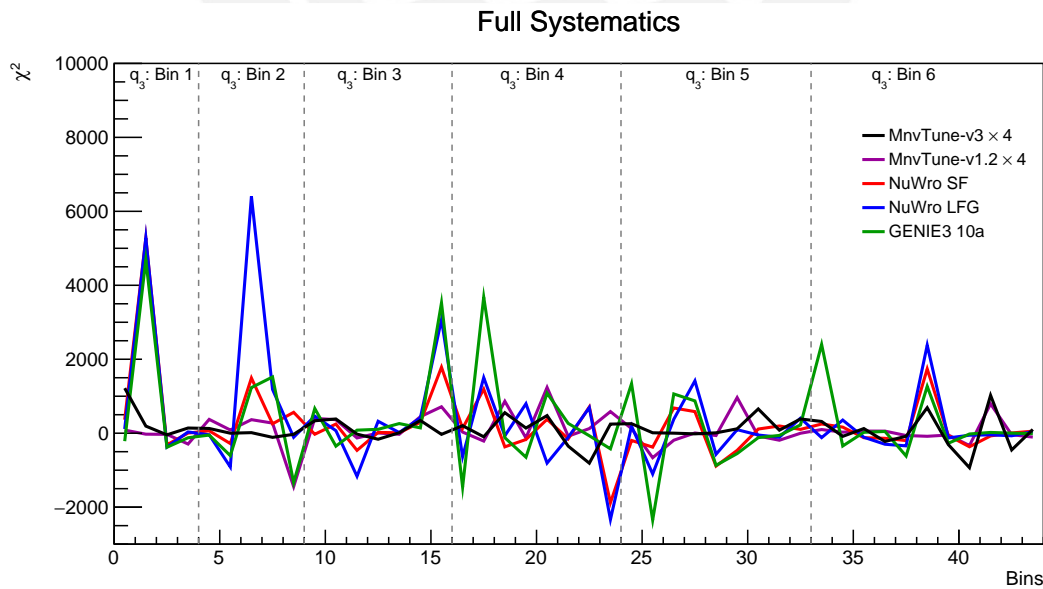


Figure 7.47: χ^2 calculated with full elements of the covariance matrix V

7.11. INTERPRETATION OF THE CHI-SQUARE AND CONCLUSIONS

Table 7.9: χ^2 of the data with MC at cross section level. Here the NDF is 44. Full covariance matrix

MC/Generators	q_31	q_32	q_33	q_34	q_35	q_36
MnvTune-V3	376.333	0.004	214.505	90.979	375.73	43.198
MnvTune-V1.2	-66.576	-86.212	443.791	604.878	-22.448	89.721
NuWro SF	5325.64	2095.72	1866.02	-163.935	-250.224	1249.7
NuWro LFG	5054.29	6522.03	3196.81	-965.231	654.536	1610.43
GENIE 3 (G18_10a_02)	3972.51	763.282	4433.98	2309.32	-448.594	2491.57

Table 7.10: χ^2 of the data with MC at cross section level. Here the NDF is 44. Full covariance matrix

MC/Generators	χ^2	χ^2/NDF
MnvTune-V3	1100.8	25.
MnvTune-V1.2	963.2	21.9
NuWro SF	9981.8	226.9
NuWro LFG	16363.8	371.9
GENIE 3 (G18_10a_02)	14148.9	321.6

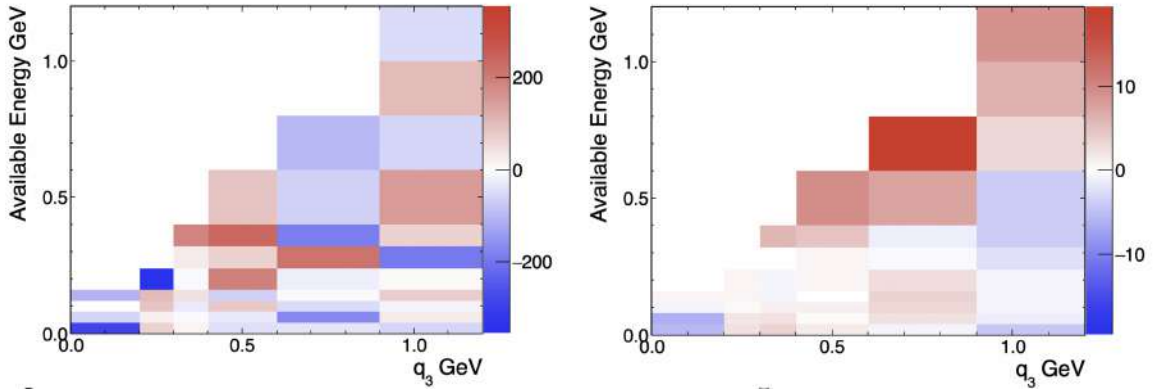


Figure 7.48: $\Delta\chi^2$ for with all cross-section models. Left plot corresponds to calculation with full covariance matrix, and right plot corresponds to diagonal only covariance matrix.

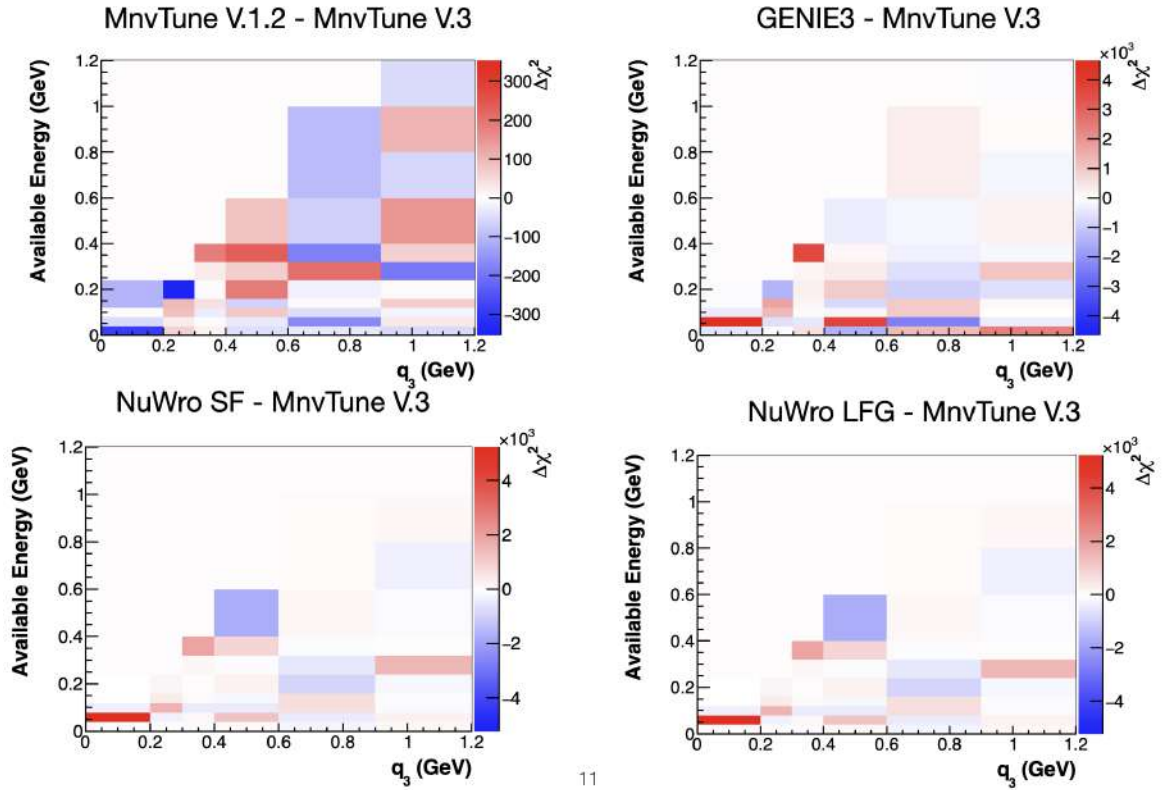


Figure 7.49: $\Delta\chi^2$ comparison with full (left plots) and diagonal only (right plots) covariance and matrix. Z-axis is the $\Delta\chi^2$.

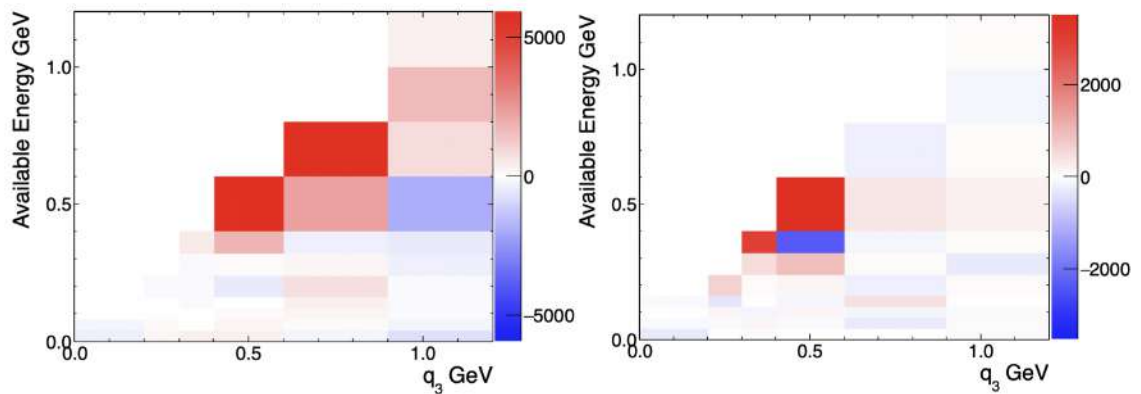


Figure 7.50: $\Delta\chi^2$ with full covariance matrix. With (only systematic in left plots) and without (the systematic is excluded right plot) the Signal Models uncertainty. Z-axis is the $\Delta\chi^2$.

Although it seems intuitive to assert that a lower chi-square indicates a superior model, this is not the case. For instance, this is true in cases where a single variable is tested, such as parameter fitting. At a first quick look, the χ^2 with the full covariance matrix appears to indicate that MnvTune.v1.2 is superior to MnvTune.v3 by approximately 137. The other models' χ^2 shows way worst values. On the other hand in the diagonal-only covariance matrix case, the behavior is the opposite which follows the known lines of physics models.

In order to understand the results, Equation 7.4 was introduced. Blue means MnvTune.v1.2 is better, and red means MnvTune.v3 is better in each bin. That description matches with the Figures 7.44 and 7.45 in diagonal covariance matrix case, but not in the full covariance matrix case. That happens mostly at high E_{avail} and high q_3 regions. Consequently, the "three" model changes between the two MnvTunes (MnvTune.v1.2 and MnvTune.v3) do not produce a unique solution. Another observation is the size of the $\Delta\chi^2$ in the full covariance in bin-by-bin is on the same scale of full difference. In contrast, the calculation of the χ^2 with the diagonal only elements shows less of this behavior; we can see more positive values than negative ones. In conclusion, the observation of the case of the full elements suggests that the full covariance χ^2 sum is not significant, and it can be thought of as fluctuations of some kind.

A detailed study of the effect of each systematic uncertainty in $\Delta\chi^2$ was performed in [315]. When a model uncertainty has the same shape as a discrepancy, this can influence the ordering of chi-square. For instance, a significant amount of χ^2 in MnvTune.v1.2 could originate from the low Q2 resonance region addressed in MnvTune.v3. Therefore, MnvTune.v1.2 would have a small χ^2 at the end. The largest effect was observed in the Signal model uncertainty (see Figure 7.50).

On the other hand, negative values in Figure 7.47 are due to large anti-correlations in the E_{avail} and q_3 bins, such as the one observed due to hadronic energy (see Section H.2). Removing the Signal model in the χ^2 calculation is 14053.4 for MnvTune.v3 and 30064 for MnvTune.v1.2.

In conclusion, this analysis describes the inclusive charged-current neutrino interactions on a hydrocarbon (polystyrene) target at low three-momentum transfer, as well as several model variants for these interactions. The measured double-differential cross-section as a function of three-momentum transfer and available energy is compared to three variants of genie and two NuWro event generator configurations. The QE, 2p2h, and resonance processes are inadequately described by these generators, despite the fact that the most recent model elements represent a substantial advance.

Using an analysis of reconstructed data distributions with multiple model elements, a new central value (MnvTune.v3) is generated for unfolding and evaluating systematic uncertainties. The SuSA prediction for the 2p2h model, an enhancement of the high momentum tail of the struck nucleon momentum for QE, and a deduction of 25 MeV removal energy from the resonance final state replace empirical tunes to MINERvA data. The choice of that theory-motivated models certainly makes MnvTune-v3 superior overall, but there is still a disagreement between the model and the data in different regions suggesting better modeling is needed.

CHAPTER 8

SUMMARY AND CONCLUSIONS

The thesis has two main topics. The phenomenology study of the light neutrino decay at future long-baseline neutrino oscillation experiments and the experimental study of the neutrino-nucleus interaction by measuring the double differential cross-section.

The neutrino decay in the presence of matter was examined in the first topic. Two upcoming oscillation experiments — Deep Underground Neutrino Experiment (DUNE) [148] and Agua Negra Deep Experiment Site (ANDES) [154] — were considered. A hypothetical beam from the Neutrino of Main Injector (NuMI) was assumed for ANDES. The differences between them are the baseline ($L_{DUNE}=1300$ km and $L_{ANDES}=7650$ km) and the density ($\rho_{DUNE} = 2.96$ g/cm³ and $\rho_{ANDES} = 4.7$ g/cm³).

The phenomenological study of the light neutrino decay examines the matter effect (for DUNE and ANDES), the sensitivity to the decay parameter (only for DUNE), and the influence of the neutrino decay in determining the θ_{23} and δ_{CP} (only for DUNE). For these studies, the ν_μ and ν_e disappearance and appearance channels were considered for both Forward Horn Current (FHC) and Reverse Horn Current (RHC) flux modes. In this work, the decay is due to the coupling of the neutrinos with a massless scalar, denominated Majoron. The coupling can be scalar (S) or pseudoscalar (PS). In addition, the normal mass ordering with the stable lightest neutrino was assumed. When the ν_1 mass is zero ($m_{lightest} = 0$ eV) the couplings are indistinguishable and it is tagged as $x_{31} \rightarrow \infty$. On the other hand, when the ν_1 mass is different from zero ($m_{lightest} = 0.07$ eV [147]) is tagged as $x_{31} \rightarrow 1$. On the other hand, when the decay products are not detectable, it is referred to as invisible decay (ID), and if they are detectable, it is called visible decay (VD). The sum of ID and VD give us full decay (FD), and the absence of any decay is the standard oscillations (SO).

To investigate the effect of matter on neutrino decay, the quantity $\Phi \times \sigma$ was defined. This value is proportional to the product of the flux and cross-section. Also, the neutrino mass difference and mixing parameters were fixed as follow [158]: $\Delta_{21}^2 = 7.5 \times 10^{-5}$ eV², $\Delta_{31}^2 = 2.524 \times 10^{-3}$ eV² (for normal ordering), $s_{12}^2 = 0.306$, $s_{23}^2 = 0.441$, $s_{13}^2 = 0.02166$, and $\delta_{CP} = -\pi/2$. The decay parameters tested were $\alpha_3 = 4 \times 10^{-5}$ eV² and $\alpha_3 = 8 \times 10^{-6}$ eV². Those decay parameters represent the 10% of $\langle E \rangle / L$ for DUNE and ANDES, respectively.

In DUNE, the Matter effect in ID or VD for the ν_μ disappearance channel is negligible for both flux modes. In this channel, however, the difference between ID and VD is more significant in FHC than in RHC. Due to the pseudoscalar coupling, in the case of FHC, the decay product's neutrinos become antineutrinos (the opposite for RHC). Since the antineutrino cross-

section is smaller than the neutrino, the final result leads to a large difference in FHC mode. In general, the VD component is dependent on the coupling. In the ν_e appearance, however, the VD component is relevant at low energies and dominant in some cases like RHC. Similar to the ν_μ disappearance channel, the slight difference between VD and ID for FHC is attributed to the helicity-flipping decay. In contrast to ν_μ disappearance, the matter effect in the ν_e appearance becomes relevant, but that is consistent with the vacuum-matter difference in SO. Because the decay parameter tested is smaller, the result is in the order of ID.

In ANDES, the matter effects are much more relevant due to the larger baseline and matter density. However, the more remarkable result, by far, is the suppression of ID contribution in the ν_e appearance channel at low energy, leaving VD as the main component. At high energies, the difference between VD and ID is smaller vacuum and larger in matter due to the enhancement of ID to the matter. The $x_{31} \rightarrow \infty$ contributes more in the lower energy on contrast to $x_{31} \rightarrow 1$.

The number of events was employed to determine the sensitivity of DUNE to the decay parameter (in FD). In addition, only θ_{23} and δ_{CP} were taken into account because the θ_{13} is fixed by reactor measurements [163]. The sensitivity to α_3 is obtained by marginalizing the chi-square over the defined truth values of θ_{23} and δ_{CP} combining ν_μ and ν_e disappearance and appearance respectively. At $3\sigma(5\sigma)$ the sensitivity of α_3 for $x_{31} \rightarrow 1$ and the pseudo-scalar coupling is, $\alpha_3 = 3.8 \times 10^{-6} \text{ eV}^2$ ($6.4 \times 10^{-6} \text{ eV}^2$), in the scalar case is, $\alpha_3 = 5.2 \times 10^{-6} \text{ eV}^2$ ($8.8 \times 10^{-6} \text{ eV}^2$). On the other hand, the sensitivity to α_3 for $x_{31} \rightarrow \infty$ is, $\alpha_3 = 6.1 \times 10^{-6} \text{ eV}^2$ ($1.0 \times 10^{-5} \text{ eV}^2$). The best sensitivity found at 90% of C.L. is $\alpha_3 = 2.0 \times 10^{-6} \text{ eV}^2$, which is comparable to the limits get from atmospheric neutrinos $\alpha_3 = 2.2 \times 10^{-6} \text{ eV}^2$ [316]. Finally, with the phenomenological study, the impact of the SO, ID and FD was compared in the determination of θ_{23} and δ_{CP} . The results show a small difference between

SO and ID (for $\alpha_3 \sim 10\%$ of $\langle E \rangle/L$ for DUNE) and for FD the allowed regions would shift towards larger values of θ_{23} .

The experimental study of neutrino-nucleus interaction is an additional contribution to this thesis. The research was conducted within the context of the Main Injector Neutrino Experiment to study ν -A interactions (MINERvA) experiment[212]. MINERvA is an experiment on-axis in the NuMI beamline [174]. Its active region consists of scintillation planes. The detector is divided into a nuclear target, active scintillator, tracker region, electromagnetic and hadronic calorimeters[213], and MINOS Near Detector (ND) [214] as a spectrometer. The neutrino flux has an exposure of 10.61×10^{20} protons on target with a neutrino energy peak of 6 GeV. The final measurement reports the double differential cross-section for ν -carbon in two variables, three-momentum transfer ($q_3 = |\vec{q}|$), and available energy. The second variable corresponds to the kinetic energy of protons and charged pions, plus the total energy of any other final state particles except neutrons.

A inclusive charge-current ν_μ interactions events were selected, with the following requirements: $\theta_\mu < 20^\circ$ and $1.5 < p_\mu < 20.0$ GeV. The selected sample yielded 3,390,718 events with 98.64% purity. The measurement region has a limit in momentum transfer ($q_3 < 1.2$ GeV). The nominal Monte Carlo (Mnvtune-v.1.2) employed is a GENIE v.2.12.6 [224] modified with Valencia Random Phase Approximation (RPA) suppression applied to Quasi-elastic (QE) interaction[226, 227], 43% of suppression on the non-resonant pion production base on bubble chamber data[228, 229], suppression on coherent production of pion with kinetic energy lower than 450 MeV based on Low Energy (LE) MINERvA data [317], and an enhancement of Valencia 2p2h based a two-dimensional Gaussian fit on LE MINERvA data [279]. On the other hand, the flux has an improvement using the neutrino-electron scattering MINERvA data [318], and finally, the muon energy from MINOS ND has a scaling of 3.6%.[201]

Despite the tunes employed in MnvTune-v.1.2, the disagreement between data and MC remains mostly along the QE to the resonant (RES) region. Motivated by the discrepancy, several studies were conducted at the reconstructed level. The region between QE and RES denominated “dip” region has the contribution of Meson Exchange Current (MEC) or 2p2h. The first study conducted was on the QE; by modifying the nuclear model. In GENIE, the nuclear model is a relativistic Fermi-gas RFG. The nucleon momentum distribution in RFG has a component attributed to the Short Range Correlation (SRC) from 221 MeV to 500 MeV[239, 245]. The SRC represents the correlation of pair nucleons, denominated Bodek-Ritchie (BR) tail. The modification was applied to the BR tail. The change enhances the QE contributions by around 25%. The second study was in the 2p2h region, where the Valencia 2p2h and its tune were replaced by Super-Scaling Approximation (SuSA) 2p2h model [280, 281, 282]. Both BR tail enhancement and SuSA 2p2h are about the size nominal MC. The third component that contributes to the dip region is the RES events. A major number of studies were performed on RES, from new models to new data-based tunes. Instead of GENIE’s Rein-Sehgal (RS) model, the Minoos Kabirnezhad (MK) model was applied[272, 278]. The relevant difference between MK and RS is the non-resonant pion production and interference terms. The next variation was the addition of Pauli blocking in RES with the Berger-Sehgal (BS) model[299], which, compared to the default model, the new one includes the lepton mass and pion pole term. Another update to the RS is the re-weight of a non-linear suppression function based on exclusive analysis MINERvA data. The function depends on Q^2 , and the suppression happens at low Q^2 . Similar suppression was observed in MINOS iron data. Another test was the application of RPA to RES since RPA in the QE has the suppression behavior at low Q^2 . Finally, a RES peak shift (mostly Δ peak) in E_{avail} was added. Similar to QE removal energy from nuclear potential, a 25 MeV was removed from the available energy (RES-RE).

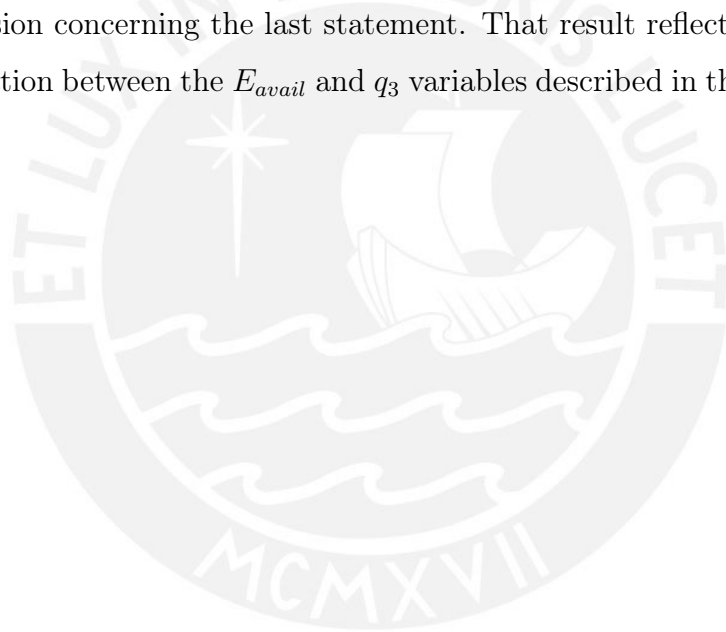
Based on all the studies on the reconstructed level, a new central value (CV) was built, denominated MnvTune.v3, which corresponds to BR tail Enhancement, SuSA 2p2h, and RES-RE.

The selected data events and later background subtracted. The background represents 1.42 % of the entire sample. The distribution was then unfolded with the D'Agostini regularization [286]. The unfolded events were then divided by the efficiency and scaled by normalization factors, which include 3.115×10^{30} nucleon target, flux integral, and the total exposure. The final result represents the double differential cross-section $d^2\sigma/dE_{avail}dq_3$.

The measurement uncertainty arises from the detector energy response, the neutrino flux, the interaction model, the FSI, and MINERvA's modified interaction model. Evaluating each uncertainty source requires a re-extraction of the cross-section, using a modified simulation with shifted parameters of its uncertainty. Then, the difference between each re-extracted cross-section with the nominal cross-section is used to build the covariance matrix.

Finally, the double-differential cross-section data were compared with different neutrino generators. Two versions of NuWro[297], and GENIE 3[294, 301]. the main difference between GENIE 3 and MnvTune.v3 are the Local Fermi Gas (LFG) instead of RFG, Valencia RPA to QE, Valencia 2p2h, and BS instead RS. The FSI is similar to the one used in MnvTune.v3. On the other hand, both NuWro models have different QE implementations than MnvTune.v3, and for the initial nucleon state, one is LFG, and the other is RFG with Spectral Function (SF). The RES region only accounts for the Δ resonance with a model different from RS. NuWro uses the Lalakulich-Paschos [310] with deuterium-data-based axial and vector form factors and Pauli Blocking model. Similarly, the FSI differs from GENIE, using a Salcedo-Oset FSI hadron res-catering model[302].

The generators describe the data in some regions. The significant difference is at low available energy, where the QE interaction dominates the distribution. The different QE treatments in NuWro explain the difference at low available energy. Similarly, the under-prediction of GENIE 3 is explained due to the systematic shift of the QE peak to higher available energy distribution. The reason is the lack of the 25 MeV QE removal energy. With the exploration of the RES available energy shift, still, a suppression at low Q^2 may also be needed to describe the data. Overall, a single model can not explain discrepancies in all the phase space, but the chosen models (MnvTune.v3) perform better. On the other hand, the comparison shown at the chi-square level creates tension concerning the last statement. That result reflects the significant correlation between the E_{avail} and q_3 variables described in the covariance matrix.



APPENDIX A

MULTI-UNIVERSE METHOD

This appendix will describe the multi-universe method mathematically using the multivariate normal distribution and random variable definitions. The first definition needed is the symmetric positive definite matrix.

Definition A.1 *Let G a symmetric positive definite matrix if*

$$G \in \mathbb{R}^{n \times n} : G = G^T \text{ and } Gv^T G > 0 \quad \forall v \in \mathbb{R}^n / v \neq 0. \quad (\text{A.1})$$

Using the previous definition we can define the multivariate normal distribution, like

Definition A.2 *Let R a continuous random vector in \mathbb{R}^n , μ a vector in \mathbb{R}^n , and V a matrix $V \in G$. The multivariate normal distribution of R with mean*

μ and covariance V if its probability density function is

$$f_R(\mu, V) = \frac{1}{\sqrt{2\pi^n \det(V)}} e^{-\frac{1}{2}(R-\mu)^T V^{-1}(R-\mu)}. \quad (\text{A.2})$$

Proposition A.1 *Let R a vector in \mathbb{R}^n with multivariate distribution, mean μ , and covariance matrix V . Then,*

$$R = \mu + SU, \quad (\text{A.3})$$

where U is random vector in \mathbb{R}^n and S an invertible matrix in $\mathbb{R}^{n \times n}$.

The vector U has $E[U] = 0$ and $\text{Var}[U] = I$. While the S matrix comes from $V = SS^T = S^T S$ where it follows the Cholesky decomposition (see proof in [319])

The proof of the proposition uses the linear density function proved in [320] and probability density function 1D. The step-by-step proof of the proposition A.3 is in the reference [321].

On the other hand, from equation A.2, we can say that the expected value of R is given by $E[R] = \mu$, and the covariance matrix by $\text{Var}[R] = V$, therefore,

$$V = E[(R - \mu)(R - \mu)^T] = E[RR^T] - \mu\mu^T, \quad (\text{A.4})$$

the proof uses the previous proposition A.3 and the mean and variance of U (see also [321]).

APPENDIX B

DERIVATION OF ITERATIVE REGULARIZATION: D'AGOSTINI METHOD

In this appendix we will revisit the D'Agostini iterative regularization, using the following references: [286, 322, 323, 324, 325, 326, 327, 328].

The unfolding techniques, in general, answer the question of how to extract a true spectrum from an observed smeared one. That means that it does not have a unique solution due to sensibility to initial condition fluctuation [326] . In the discrete case, the unfolding problem corresponds to:

$$y \sim \text{Poisson}(U\lambda), \tag{B.1}$$

where y is the observed (smeared) data, λ is the truth distribution that we want

to measure, and the U_{ij} is responsible for the *bin migration* from the original histogram to the observed histogram,

$$U_{ij} = P(\text{smearred in bin } i | \text{truth in bin } j). \quad (\text{B.2})$$

Bayes' theorem and iterative regularization

Let's begin with the Bayes' theorem as follow:

$$P(C_j|E) = \frac{P(E|C_j)P(C_j)}{\sum_{l=1}^p P(E|C_l)P(C_l)} \quad (\text{B.3})$$

Where C_j are the independent *causes* ($C_j, j = 1, 2, \dots, c_n$) which produce a single *effect* E . The $P(C_j)$ is the initial probability of the causes and $P(E|C_j)$ is the conditional probability of the j th cause to produce the effect.

If we consider many events $n(E)$ with one effect, the expected number of events assignable to each cause is [286]:

$$\hat{n}(C_j) = n(E)P(C_j|E) \quad (\text{B.4})$$

Now, if we have many effects E_i ($i = 1, 2, \dots, n_E$) for a given cause C_j , the Bayes formula (equation B.3) becomes,

$$P(C_j|E_i) = \frac{P(E_i|C_j)P_0(C_j)}{\sum_{l=1}^p P(E_i|C_l)P_0(C_l)}. \quad (\text{B.5})$$

In the equation B.5 C_j corresponds to true values in bin j and the E_i corresponds to an event reconstructed in bin i . Considering the equation B.2 and conditional probability from equation B.3, we have,

$$U_{ij} = P(E_i|C_j), \quad (\text{B.6})$$

Which plays the rule of the response matrix. For n^{obs} experimental observations, the distribution of frequencies is,

$$n(E) = \{n(E_1), n(E_2), \dots, n(E_{n_E})\} \quad (\text{B.7})$$

And the expected number which will be assigned to each of the causes and get it only due the observed events is,

$$\hat{n}(C_j)^{obs} = \sum_{i=1}^{n_E} n(E_i)P(C_j|E_i) \quad (\text{B.8})$$

The $P_0(C_j)$ is the λ_j^0 over the total observed, as follow, From the previous equation, $P_0(C_j)$ the from equation B.5 is:

$$P_0(C_j) = \frac{\lambda_j^0}{\sum_{i=1}^{n_E} n(E_i)} \quad (\text{B.9})$$

Therefore we can rewrite the equation B.5, using equation B.6 and B.9

$$P(C_j|E_i) = \frac{U_{ij}\lambda_j^0}{\sum_{l=1}^p U_{il}\lambda_l^0} \quad (\text{B.10})$$

Finally the expected number of events $\lambda_j^{(1)} = \hat{n}(C_j)$ assigned to each cause C_j is, taking into an account a term due to finite efficiency or inefficiency $\sum_{i=1}^{n_E} P(E_i|C_j) = \epsilon_j$, and lets call $n(E_i) = y_i$,

$$\lambda_j^{(1)} = \sum_{i=1}^{n_E} n(E_i) \frac{P(C_j|E_i)}{\epsilon_j} = \frac{\lambda_j^0}{\sum_{i=1}^{n_E} U_{ij}} \sum_{i=1}^{n_E} \frac{U_{ij}y_i}{\sum_{l=1}^p U_{il}\lambda_l^0} \quad (\text{B.11})$$

Expectation-Maximization(EM) algorithm in iterative regularization

The Expectation-Maximization(EM) is a technique discovered by Dempster, Laird, and Rubin in 1977. Let's assume that we have observed the random variable y , and we know that its distribution depends on some parameters θ . The goal of the ME algorithm is to find the Maximum Likelihood Estimator(MLE) of θ by the maximum likelihood $L(\theta; y) = P(y|\theta)$ when some of the data is missing.

Suppose we have an estimation problem in which we have a set $\{y^{(1)}, \dots, y^{(m)}\}$ consisting of m independent examples. We want to fit the pa-

rameters of a model $P(y, z)$ to the data. The likelihood is:

$$l(\theta; y) = \sum_{i=1}^m \log \sum_z p(y, z|\theta), \quad (\text{B.12})$$

where $z^{(i)}$ is a random variables, that is solved by two steps so called E-step and M-step until convergence happen.

- E-step– For each i , set

$$Q_i^{(t)}(z^{(i)}) := p(z^{(i)}|y^{(i)}; \theta^{(t)}) \quad (\text{B.13})$$

- M-step– Set

$$\theta^{(t)} := \arg \max_{\theta} \sum_i \sum_{z^{(i)}} Q_i^{(t)}(z^{(i)}) \log \frac{p(y^{(i)}|z^{(i)}; \theta^{(t)})}{Q_i^{(t)}(z^{(i)})} \quad (\text{B.14})$$

But using the Jensen's inequality ($l(\theta^{(t+1)}) \geq l(\theta^{(t)})$) we can have

$$l(\theta^{(t+1)}) \geq \sum_i \sum_{z^{(i)}} Q_i^{(t)}(z^{(i)}) \log \frac{p(y^{(i)}|z^{(i)}; \theta^{(t)})}{Q_i^{(t)}(z^{(i)})} \quad (\text{B.15})$$

For the case of iterative D'agostini iteration, we have to find the log-maximum likelihood $l(\lambda; y)$, the random variable, in this case, let's say z . As we mentioned before, the EM algorithm finds the MLE when some data is missing. In this case, the incomplete data is y and is related to the complete data $Z = z_{ij}$ by [325, 327]

$$y = [y_1, \dots, y_p]^T = g(Z) = \left[\sum_j z_{1j}, \dots, \sum_j z_{pj} \right]^T \quad (\text{B.16})$$

Form equation B.1, we have,

$$y_j = \sum_{i=1}^n \lambda_i U_{ij}. \quad (\text{B.17})$$

For the another hand the random variable z_{ij} are Poisson distributed and conditionally independent,

$$z_{ij} | \lambda_j \sim \text{Poisson}(U_{ij} \lambda_j) \quad (\text{B.18})$$

Then the the complete-data log-maximum likelihood $l(\lambda; Z)$ is as follows,

$$l(\lambda; Z) = \sum_{ij} (z_{ij} \log(U_{ij} \lambda_j) - \log z_{ij}! - U_{ij} \lambda_j) \quad (\text{B.19})$$

Hence the E-step need $p(z_{ij}|y_i, \lambda^{(k)})$ of z_{ij} given y and $\lambda^{(k)}$ is binomial with sample size parameter or the number of successes y_i and probability parameter

$$U_{ij} \lambda_j^{(k)} / \sum_{l=1}^n U_{il} \lambda_l^{(k)} \quad (\text{B.20})$$

On the other hand, in the E-step of the EM algorithm, the conditional expectation of complete data log-maximum likelihood $l(\lambda; Z)$ given y the observation and the value $\lambda^{(k)}$ of parameter λ is:

$$Q(\lambda; \lambda^{(k)}) = E[l(\lambda; Z)|y, \lambda^{(k)}] \quad (\text{B.21})$$

considering the probability parameter (equation B.20) we can get for our case,

$$E[z_{ij}|y_i, \lambda^{(k)}] = \frac{U_{ij} \lambda_j^{(k)}}{\sum_{l=1}^n U_{il} \lambda_l^{(k)}} y_i \quad (\text{B.22})$$

Then changing z_{ij} to $z_{ij}^{(k)}$ in equation B.19 and applying M-step on the $(k+1)$ th iteration we have finally have the D'Agostini formula,

$$\lambda_j^{(k+1)} = \frac{1}{\sum_{i=1}^n U_{ij}} \sum_{i=1}^n U_{ij} E[z_{ij}|y_i, \lambda^{(k)}] = \frac{\lambda_j^{(k)}}{\sum_{i=1}^n U_{ij}} \sum_i \frac{U_{ij} y_i}{\sum_{l=1}^n U_{il} \lambda_l^{(k)}}. \quad (\text{B.23})$$

Estimation of the uncertainty

Let's consider a general case, if we have measurement values of parameters β_1, \dots, β_m provided by an inference procedure, the new set of parameters η_1, \dots, η_k , determined as functions of the measured ones. We want the uncertainties on the new parameters. The covariance matrix C_{ij} of the modified parameters may typically be derived from the covariance matrix Θ_{kl} of the original parameters as shown in [324]:

$$C_{ij} = \sum_{p,q} \frac{\partial \eta_i}{\partial \beta_p} \frac{\partial \eta_j}{\partial \beta_q} \Theta_{pq} \quad (\text{B.24})$$

In our case, let's consider the equation B.11 and rewrite it as,

$$\hat{n}(C_j) = \lambda_j^{(1)} = \sum_{i=1}^{n_E} M_{ij} n(E_i) \quad (\text{B.25})$$

where

$$M_{ij} = \frac{1}{\epsilon_j} \frac{P(E_i|C_j)P_0(C_j)}{\sum_{l=1}^p P(E_i|C_l)P_0(C_l)}. \quad (\text{B.26})$$

The covariance matrix V of the unfolded estimates $\hat{n}(C_j)$ is following the equation B.24 [328]

$$V(\hat{n}(C_k), \hat{n}(C_l)) = \sum_{i,j}^{n_E} \frac{\partial \hat{n}(C_k)}{\partial n(E_i)} V(n(E_i), n(E_j)) \frac{\partial \hat{n}(C_l)}{\partial n(E_j)} \quad (\text{B.27})$$

where $\frac{\partial \hat{n}(C_j)}{\partial n(E_i)}$ in general is

$$\frac{\partial \hat{n}(C_j)}{\partial n(E_i)} = M_{ij} + \frac{\hat{n}(C_j)}{P_0(C_j)} \frac{\partial P_0(C_j)}{\partial n(E_i)} - \sum_{k=1}^{n_E} \sum_{l=1}^{C_n} \frac{n(E_k)\epsilon_l}{P_0(C_l)} M_{ik} M_{lk} \frac{\partial P_0(C_l)}{\partial n(E_i)}. \quad (\text{B.28})$$

The covariance $V(n(E_i), n(E_j))$ due to independent Poisson fluctuation, and it is [328],

$$V(n(E_i), n(E_j)) = n(E_j)\delta_{ij}. \quad (\text{B.29})$$

APPENDIX C

HADRONIC TENSOR AND W SELF-ENERGY IN NUCLEAR MATTER IN THE CONTEXT OF NEUTRINO-NUCLEUS SCATTERING

This appendix includes remarks from [94] as well as the material given by [329]. It will be beneficial to have a general understanding of Neutrino-Nucleus Scattering in the Many-Body Framework (MBF). This appendix does not provide a step-by-step deduction.

In the electroweak Charge Current (CC) neutrino-nucleus inclusive

scattering we have, the following reaction,

$$\nu_l(k) + A_Z \rightarrow l^-(k') + X, \quad (\text{C.1})$$

in the laboratory frame. The neutrino (ν_l) with momentum k interacts with nucleus A_z and as a result we get the charged lepton with momentum (k') and the recoil X . One can describe the double differential cross-section in terms, for instance, in terms of the charged lepton kinematics [330, 331, 94, 332],

$$\frac{d^2\sigma}{d\Omega(\hat{k}')dE_l'} = \frac{|\vec{k}'|}{|\vec{k}|} \frac{G^2}{4\pi^2} L_{\mu\sigma} W^{\mu\sigma}, \quad (\text{C.2})$$

where G is the Fermi constant, E_l' is the energy of the charge lepton, L is the leptonic tensor, and W the hadronic tensor. So far, the treatment is a regular procedure. Then, we could decompose the Equation C.2 by writing the the tensors, where we could introduce the structure functions for W and so on. But, we want to do the procedure in the MBF [94].

The hadronic tensor is determined by W -boson self-energy, $\Pi_W^{\mu\sigma}$, perturbative expansion in the nuclear medium. For that purpose, the neutrino self-energy is evaluated for a neutrino moving in an infinite nuclear matter [94]. The process is represented in Figure C.1.

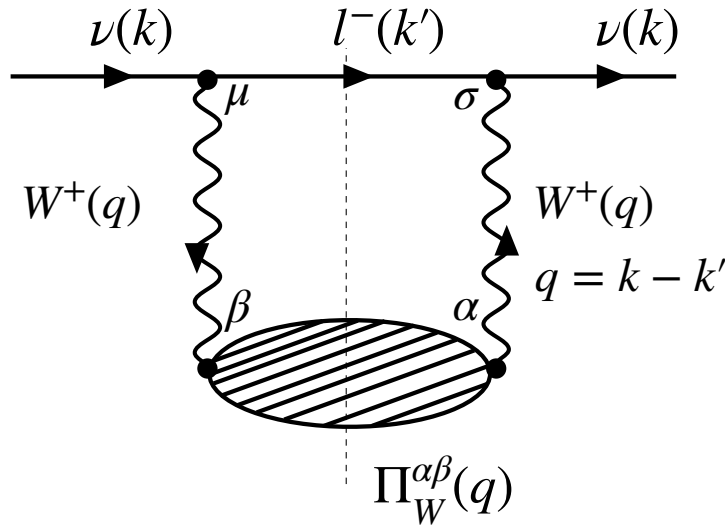


Figure C.1: Diagram of W -boson self-energy in a nuclear matter.

The self-energy for a neutrino (with momentum k) moving in Fermi gas, for instance, with a nuclear matter density ρ is given by [94],

$$\Sigma_\nu^r(k, \rho) = \int \frac{d^4q}{(2\pi)^4} i\bar{\Gamma}_r^\mu(k) D_{\mu\alpha}(q) \Pi_W^{\mu\sigma} D_{\beta\sigma}(q) S(k') \Gamma_r^\sigma(k), \quad (\text{C.3})$$

where $D_{\mu\nu}(q)$ is the propagator, in general has the following structure,

$$D_{\mu\nu}(q) = \frac{-g_{\mu\nu} + q_\mu q_\nu / M_W^2}{q^2 - M_W^2 + i\epsilon}, \quad (\text{C.4})$$

where M_W is the W boson mass and $q = k - k'$. The $\bar{\Gamma}_r^\mu(k)$ and $\Gamma_r^\sigma(k)$ are given by,

$$\bar{\Gamma}_r^\mu(k) = \bar{u}_r(k) \frac{g}{2\sqrt{2}} \gamma^\mu (1 - \gamma_5), \quad (\text{C.5})$$

$$\Gamma_r^\sigma(k) = \frac{g}{2\sqrt{2}} \gamma^\sigma (1 - \gamma_5) u_r(k), \quad (\text{C.6})$$

where r represents the helicity of neutrino, $g = e \sin \theta_W$, e the electron charge, and θ_W is the Weinberg angle. The spinor normalization is $\bar{u}u = 2m$. Finally the lepton propagator $S(k')$ is given by,

$$S(k') = \frac{\not{k}' + m_l}{k'^2 - m_l^2 + i\epsilon}, \quad (\text{C.7})$$

where m_l is the lepton mass. Summing over all neutrino polarization, $\Sigma_\nu = \sum_r \Sigma_\nu^r(k, \rho)$, then using the Cutkosky's rules [333] (split by the dashed line in Figure C.1, details, see [332]) to extract the imaginary part ¹, we can get the cross-section in terms of W -boson self-energy [94],

$$\frac{d^2\sigma}{d\Omega(\hat{k}') dk'^0} = \frac{|\vec{k}'|}{|\vec{k}|} \frac{G^2}{4\pi^2} \left(\frac{2\sqrt{2}}{g} \right)^2 \times \int \frac{d^2r}{2\pi} [L_{\mu\beta}^s \text{Im}(\Pi_W^{\mu\beta} + \Pi_W^{\beta\mu}) - L_{\mu\beta}^a \text{Re}(\Pi_W^{\mu\beta} - \Pi_W^{\beta\mu})] \Theta(q^0), \quad (\text{C.8})$$

where $\Theta(q^0)$ is the Heavyside function, index s and a refers to symmetric and anti-symmetric component of the tensor². That way the hadronic tensor for the Equation C.2 will be in term of W -boson self energy.

¹From optical theorem [334], where the imaginary part is directly proportional to cross-section [329]

²Remember that $W^{\mu\nu} = W_s^{\mu\nu} + iW_a^{\mu\nu}$.

In summary, the neutrino from the flux may disappear by inducing many kinds of processes (introduced in the ‘blob’ of Figure C.1) such as one-particle-one-hole (1p1h), two-particles-two-holes (2p2h), $\Delta(1232)$ -hole (Δh), etc., until it appears again. In the coming Appendices, we will have brief look at these excitations.



APPENDIX D

PARTICLE HOLE: 1P1H, 1P1H π , 2P2H AND RPA

In this example, the setting is neutrino scattering with the nucleus. In Appendix C we saw how the MBF treatment was used to calculate the double differential cross-section by incorporating W-boson self-energy. The purpose of this appendix is to provide a general understanding of how the W-boson self-energy increases. The first expansion term in 1p1h¹ corresponds to the QE process² when the W-boson is absorbed by a nucleon (see left diagram of Figure D.1). The 1p1h1 π process comes next (right diagram of Figure D.1), followed by the 2p2h phase (see Figure D.2). Finally, the linked Random Phase Approximation (RPA) with the 1p1h contributions to W-boson self-energy accounts for the influence of medium polarization (see set of diagrams

¹refers to 1 particle (p) - 1 hole (h) due to one particle going out, leaving a hole in the nucleus.

²The QE process for a neutrino-nucleon scattering within the nucleus.

in Figure D.3).

D.1 1p1h

In order to evaluate the self-energy for 1p1h case, the propagator of the free nucleon is needed (see [332]),

$$S(p; \rho) = (\not{p} + M) \left[\frac{1}{p^2 - M^2 + i\epsilon} + \frac{2\pi i}{2E(\mathbf{p})} \delta(p^0 - E(\mathbf{p})) \Theta(k_F - |\mathbf{p}|) \right], \quad (\text{D.1})$$

, where k_F is the local Fermi momentum, M the nucleon mass, $E(\mathbf{p}) = \sqrt{M^2 + \mathbf{p}^2}$, and ρ the nuclear matter density. Given in equation D.1 we can define $G(p; \rho)$,

$$G(p; \rho) = \frac{1}{p^2 - M^2 + i\epsilon} + \frac{2\pi i}{2E(\mathbf{p})} \delta(p^0 - E(\mathbf{p})) \Theta(k_F - |\mathbf{p}|) \quad (\text{D.2})$$

Considering the nonsymmetric nuclear matter and taking into account the vector and axial nucleon currents, the W-boson self-energy is given by [94],

$$\Pi_W^{\mu\nu} = -i \cos^2 \theta_C \left(\frac{g}{2\sqrt{2}} \right)^2 \int \frac{d^4 p}{(2\pi)^4} A^{\mu\nu}(p, q) G(p; \rho_n) G(p + q; \rho_p), \quad (\text{D.3})$$

where θ_C is the Cabibbo angle, $A^{\mu\nu}(p, q)$ is the nucleon tensor. To get the cross-section the W-boson self-energy should be added in equation C.8.

The nucleon tensor is given by,

$$A^{\mu\nu}(p, q) = \frac{1}{\cos^2 \theta_C} \text{Tr} \left[\bar{\Gamma}^\mu(q) (\not{p} + \not{q} + M) \Gamma^\nu(q) (\not{p} + M) \right], \quad (\text{D.4})$$

where the Γ^μ is the interactions vertex of W-boson, and it has the vector-axial form

$$\Gamma^\mu = V^\mu - A^\mu. \quad (\text{D.5})$$

According to [304, 332, 94] the vertex considers Lorenz invariance, QCD symmetries, conservation vector current, and partial conservation of axial current.

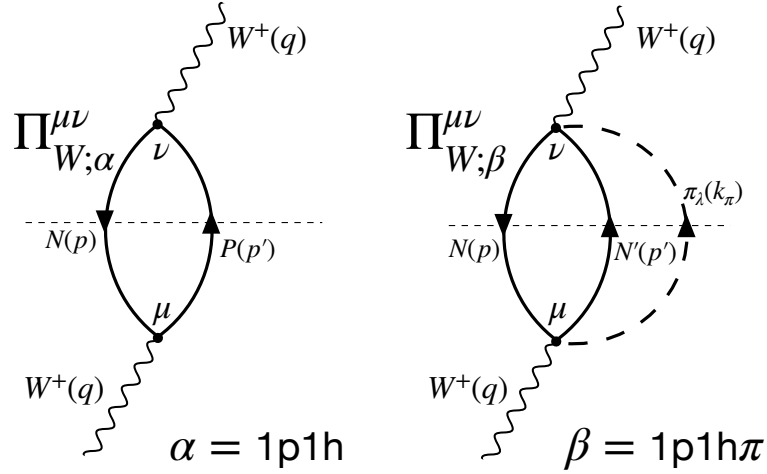


Figure D.1: Diagram of W -boson self-energy in a nuclear matter, 1p1h and 1p1h π .

D.2 1p1h 1 π

The W -boson self-energy of the right diagram in Figure D.1 accounts for the pion production in the intermediate states. In contrast to the previous case, here we have a sum in the vertex which describes the $WN \rightarrow \pi N'$, and the pion propagator needs to be taken into account to have the W -boson self-energy, which is given by [233]

$$\begin{aligned}
\Pi_W^{\mu\nu} = & \left(\frac{g}{2\sqrt{2}} \right)^2 \sum_{N,N',\lambda} \int \frac{d^4 k_\pi}{(2\pi)^4} \int \frac{d^4 p}{(2\pi)^4} G(p; \rho_N) G(p'; \rho_{N'}) D_\pi(k_\pi) \\
& \times \text{Tr} \left((\not{p} + M) \gamma^0 j_A^{\mu\dagger} \gamma^0 (\not{p}' + M) j_A^\nu \right), \tag{D.6}
\end{aligned}$$

where $p' = p + q - k_\pi$, $\sum_{N,N',\lambda}$ is the sum over all possible charge for pion and nucleon, $D_\pi(k_\pi)$ is the pion propagator. J_A^μ account for part of the amplitude of $W^+ N \rightarrow N' \pi^\lambda$ process, where λ is the charge of the pion. The contributions of the amplitudes are coming from the seven Feynman diagrams of Fig. 2 [273]. As the aim of this appendix is to describe superficially the components of the W -boson self energy for 1p1h1 π , the reader can find all the contributions of J_A^μ explicitly in [233, 273].

D.3 2p2h

In this case, the W-boson self-energy starts as the 1p1h1 π (right diagram of Figure D.1). However, the pion is interrupted by a second 1p1h (see Figure D.2). The cut rule does not affect the pion; therefore, their propagators contribute to the cross-section as virtual meson, which is known as meson exchange current (MEC).

The W-boson self-energy for 2p2h follows similar like 1p1h1 π except the propagator part, and is given by [233],

$$\begin{aligned}
 -i\Pi_W^{\mu\nu} = & -i\left(\frac{g}{2\sqrt{2}}\right)^2 \sum_{N,N',\lambda} \int \frac{d^4k_\pi}{(2\pi)^4} \int \frac{d^4p}{(2\pi)^4} (p,q)G(p;\rho_N)G(p';\rho_{N'}) \\
 & \times D_\pi^2(k_\pi)F_\pi^4(k_\pi^2)\frac{f_{\pi NN}^2}{m_\pi^2}\vec{k}_\pi^2 U_\lambda(k_\pi) \\
 & \times \text{Tr}\left((\not{p}+M)\gamma^0 j_A^{\mu\dagger}\gamma^0(\not{p}'+M)j_A^\nu\right), \tag{D.7}
 \end{aligned}$$

where $F_\pi(k_\pi)$ is the pion form factor and it is,

$$F_\pi(k_\pi^2) = \frac{\Lambda_\pi^2 - m_\pi^2}{\Lambda_\pi^2 - k_\pi^2}, \tag{D.8}$$

where $\Lambda_\pi = 1.2$ GeV and $\frac{f_{\pi NN}^2}{4\pi} = 0.08$ [335]. The U_λ in equation D.7 is the Lindhard function³ for a 1p1h by an object of charge λ [233].

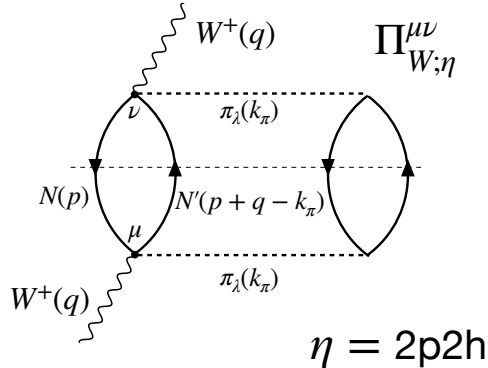


Figure D.2: Diagram of W-boson self-energy in a nuclear matter, 2p2h.

³A recommended book with discussions about the Lindhard functions is [336].

In summary, the double differential cross-section of the inclusive CC neutrino interaction is expressed in terms of the lepton and hadron tensor ($d^2\sigma_{\nu l}/dAdB \sim L_{\mu\alpha}W^{\mu\alpha}$). The hadron tensor is determined by the W-boson self-energy ($\Pi_W^{\mu\rho}(q)$ of Figure C.1) in the Many-Body Framework (MBF) treatment for a given nuclear medium. The important part then becomes on what kind of processes we include in the W-boson self-energy (the ‘shaded’ with the region in Figure C.1). So, by introducing a 1p1h process, for instance, we can get the QE interaction, or by introducing the 1p1h1 π , we can get the pion production, and so on.

The hadronic tensor is not just replaced by the W-self energy, instead, the self-energy of the neutrino is evaluated (represented diagrammatically in Figure C.1). On the other hand, it turns out that the imaginary part of that process is equivalent to the nuclear cross-section due to the so-called optical theorem. The theorem takes advantage of the unitary nature of the S-matrix (it can be understood as a matrix that has the time evolution information of all the initial and final states [337]). Finally, in order to get the imaginary part, a set of rules (Cutkostky’s rules [333]) is needed.

The more complex the process we want to introduce, the more complex the W-boson self-energy becomes. In this appendix, we superficially included 1p1h, 1p1h1 π , and 2p2h, but we can have W-boson self-energy that involves delta particles, and so on.

D.4 RPA

The nuclear environment yields an additional effect, a deviation (usually quenching) on the value of the couplings (axial-vector) [338],

$$g_A^{\text{eff}} = qg_A^{\text{free}}, \quad (\text{D.9})$$

where q is denominated quenching factor, g_A^{free} is the free-nucleon value of the axial-vector coupling. In other words, the strength of the electroweak couplings may vary from their free nucleon values due to the bound nucleons

in the nuclear media. This effect can be interpreted as a long-range correlation due to its medium polarization effect. The method used by [94] to introduce that effect in the neutrino-nucleus is by replacing the 1p1h excitation with a Random Phase Approximation (RPA) response.

The RPA response was initially derived by [339, 340, 96] without the diagrammatic technique, which latter was justified by [341]. The ‘random phase’ name remains more historical than an actual random process.

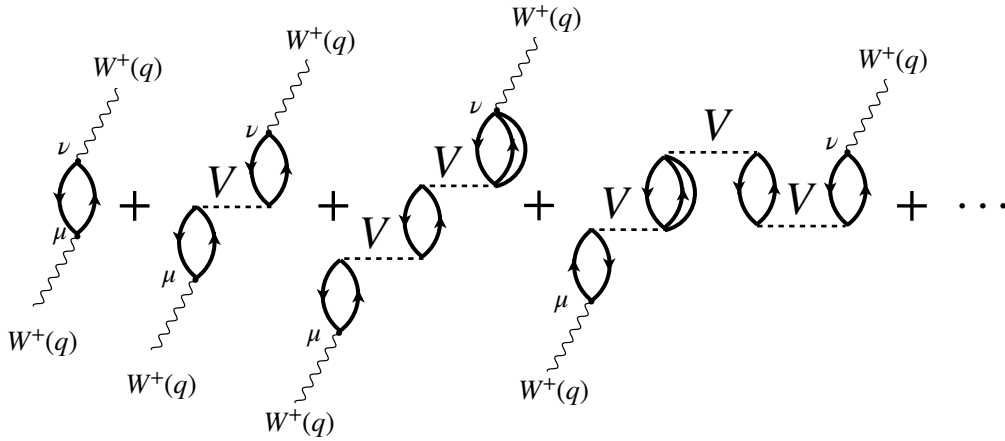


Figure D.3: Diagram of W -boson self-energy in a nuclear matter. Figure based on [94].

The Figure D.3 shows an infinite series of irreducible diagrams to account the RPA in 1p1h process. So, the diagrams can be expressed in general terms as [329],

$$\begin{aligned} \sum(\text{contributions}) &= \bar{U}(q) + \bar{U}(q)V(q)\bar{U}(q) + \bar{U}(q)V(q)\bar{U}(q)V(q)\bar{U}(q) + \dots \\ &= \frac{\bar{U}(q)}{1 - \bar{U}(q)V(q)} \end{aligned} \quad (\text{D.10})$$

where $\bar{U}(q)$ represents the propagator and it can be expressed as a non-relativistic Lindhard function. In the example diagram of Figure D.3, V lines stand for an effective interaction.

So, returning to the discussion about the couplings, only axial couplings are more likely to vary⁴ due to pionic effects changing the nuclear response functions [342]. Because of the link between the partial axial-vector conservation and pion field, or called PCAC relation, in the nuclear environment [343]. So, in a realistic case, the particle-hole is described by mesons π and ρ exchanges. The effective interaction V for the particle-hole, can be [233],

$$V = c_0 \{f_0(\rho) + f'_0(\rho) \vec{\tau}_1 \vec{\tau}_2 + g_0(\rho) \vec{\sigma}_1 \vec{\sigma}_2\} + \vec{\tau}_1 \vec{\tau}_2 \sum_{i,j=1}^3 \sigma_1^i \sigma_2^j V_{ij}^{\sigma\tau}(q) \quad (\text{D.11})$$

V is Landau-Migdal type interaction [233], and the coefficients c_0 , $f_0(\rho)$, $f'_0(\rho)$, $g_0(\rho)$, $g'_0(\rho)$ are determined in [344, 233]. $\vec{\sigma}$ is the Pauli matrix in the spin space and $\vec{\tau}$ in the isospin space [233]. The last part of the equation D.11 is,

$$V_{ij}^{\sigma\tau} = q_i q_j V_l(q) + (\delta_{ij} - q_i q_j) V_t(q), \quad (\text{D.12})$$

where

$$V_l(q) = \frac{f^2}{m_\pi^2} \left[\left(\frac{\Lambda_\pi^2 - m_\pi^2}{\Lambda_\pi^2 - q^2} \right)^2 \frac{q_3^2}{q^2 - m_\pi^2} + g'_l(q) \right] \quad (\text{D.13})$$

$$V_t(q) = \frac{f^2}{m_\pi^2} \left[C_\rho \left(\frac{\Lambda_\rho^2 - m_\rho^2}{\Lambda_\rho^2 - q^2} \right)^2 \frac{q_3^2}{q^2 - m_\rho^2} + g'_t(q) \right] \quad (\text{D.14})$$

where g' is the Landau-Migdal parameter.

⁴Other couplings, like charge couplings, are prohibited by the conservation of vector current.

APPENDIX E

CROSS-SECTION UNCERTAINTY UNDERSTANDING

In this appendix, we are focused on understanding which of the components of the MnvTune.v3 (in this appendix referred to as newCV too) models are affecting the uncertainty in the data cross-section. The plot in question is the upper left in Figure E.1. At high E_{avail} there is a large uncertainty.

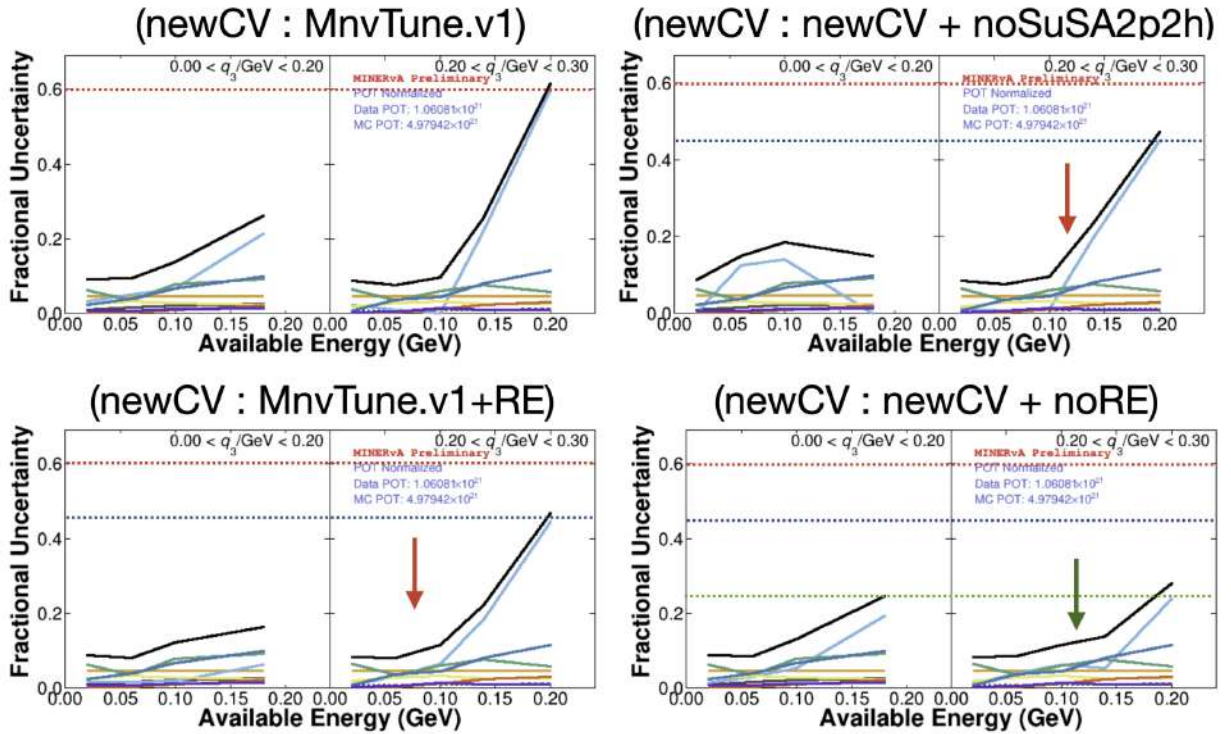


Figure E.1: Low q_3 region fractional uncertainty. Understanding the second q_3 panel, we compare newCV:MnvTune.v1.2, newCV:newCV(no SuSA), newCV:MnvTune.v1.2 with removal energy, newCV:newCV(no removal energy). In this context newCV means MnvTune.v3. The red line represents 60%, back lines represents 45% and green line represents 25% of the fractional uncertainty.

The uncertainty is addressed by counting the difference in data unfolded by different MCs. The upper right side (newCV:MnvTune.v1.2) means both have removal energy and Bodek-Ritchie tail enhancement. But, the only difference is the SuSA2p2h. In other words, it is missing SuSA2p2h in one of the MC, and as a consequence, it is returning large uncertainty. Second, the left plot at the bottom (newCV:MnvTune.v1.2 with removal energy) says that the difference is in low recoil 2p2h enhancement and SuSA2p2h, so, in conclusion, the removal energy contributes but is not that much larger than SuSA2p2h. Finally, the bottom left plot (newCV:newCV(no removal energy)) says that if both have SuSA2p2h, the large uncertainty reduces significantly,

confirming the left-side plot conclusion.

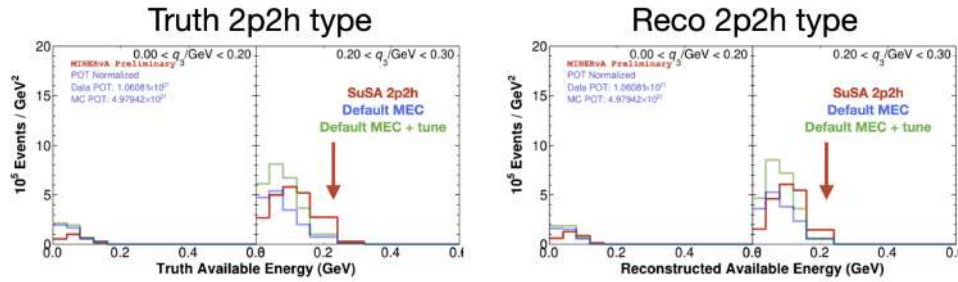


Figure E.2: Reconstructed 2p2h and truth 2p2h for SuSA2p2h, default MEC and default MEC withlow recoil tune.

Previously we identified the largest contribution of the uncertainty; now, let's focus on understanding why that happens. Figure E.2 shows the truth and reconstructed distribution for all the three components of the 2p2h contributions. It turns out that the bin causing the problem is not affected by the low recoil tune (no enhancement at all). In that particular bin, the comparison is direct with what default Valencia MEC gives.

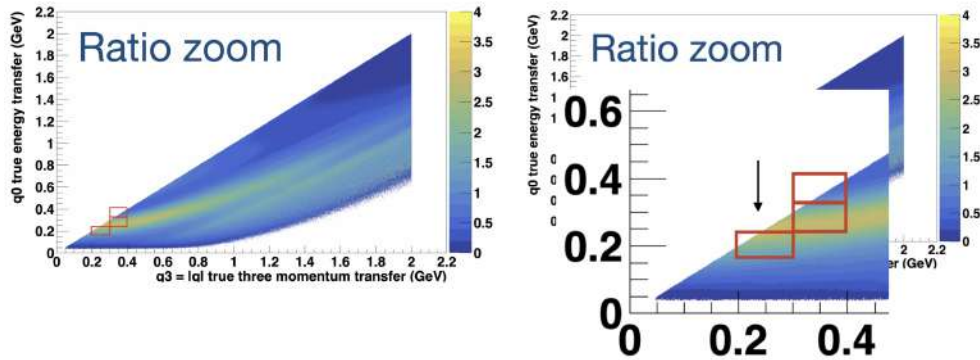


Figure E.3: Ratio of double differential cross-section with SuSA over Valencia default MEC.

In Figure E.3 the ratio of SuSA2p2h over MnvTune.v1.2 is shown, and the plot in question is pointed by the arrow. This particular bin is where there is a large difference between SuSA2p2h and Valencia. The Default MEC enhances the dip region while the SuSA 2p2h enhances the Δ region.

APPENDIX F

REMOVING THE UNPHYSICAL EVENTS OF THE EXTENDED 2P2H SAMPLE

In order to use the SuSA 2p2h prediction the Valencia 2p2h model should be extended to higher q_3 regions ($q_3 < 2.0$ GeV). However, the Valencia model has a non-relativistic component to the calculation (see high q_3 region of Figure F.1), it produces an unphysical prediction especially at high q_3 but low Q^2 .

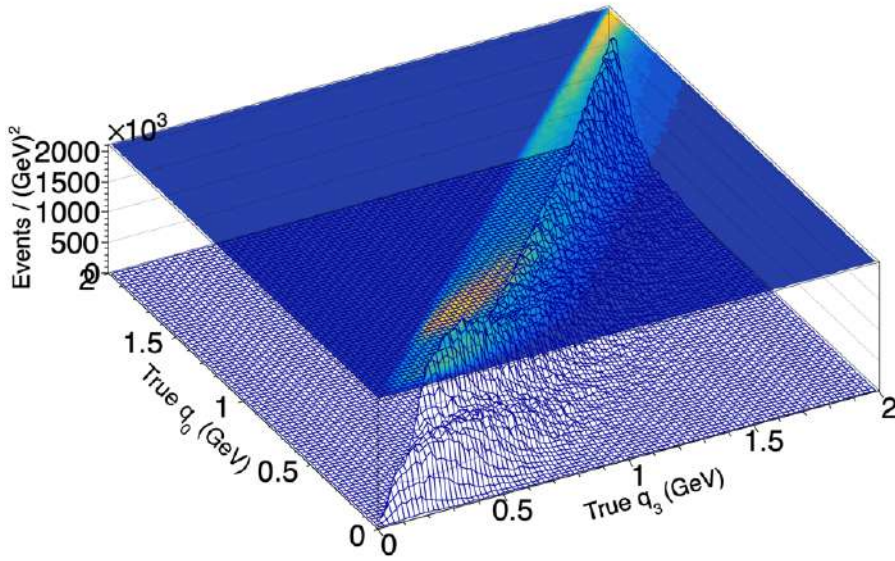


Figure F.1: Extended 2p2h distribution in truth variables (q_3, q_0) with unphysical events at high q_3 region.

To remove the unphysical events an additional weight reduces the prediction to zero in that region, keeping the Valencia prediction at lower energy transfers. The weight has a W and q_0 dependence.

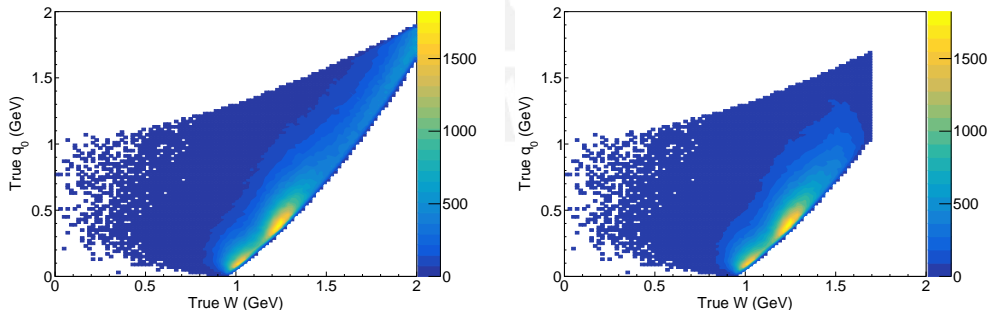


Figure F.2: Right side, truth W and q_0 before weight to remove the unphysical events. Left side, same distribution with the removing weight.

In Figure F.2 the weighting function reduces to zero for events ($W > 1.7$ GeV), and between 1.5 to 1.7 GeV negative linear weight was applied. In addition, the q_0 has the same treatment in the region from 1.8 to 2.0 GeV.

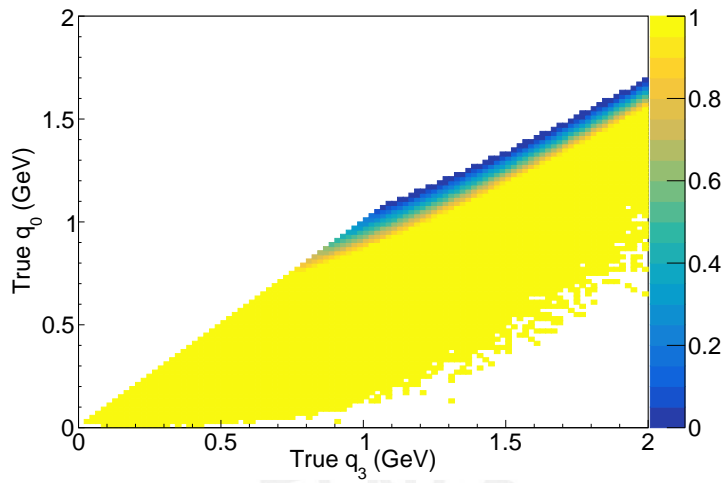


Figure F.3: The weight function in the truth q_0 and q_3 distribution designed by Richard Gran.

After re-weighting the distribution (q_0, q_3) with the function shown in Figure F.3 is illustrated in Figure F.4.

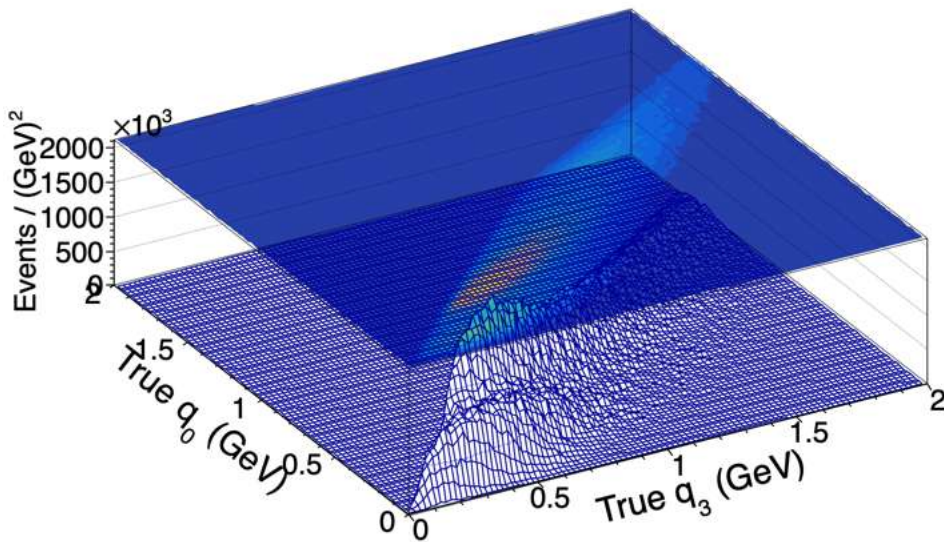


Figure F.4: Extended 2p2h distribution in truth variables (q_3, q_0) without unphysical events at high q_3 region.

APPENDIX G

CROSS SECTION COMPARISON WITH GENIE 3 VARIATIONS

In this appendix, the double differential cross-section is compared with other configurations of GENIE 3. The labels of the configurations represent different variations on the modification on the ground state, interaction types, and (more importantly) in the final state interaction [294, 301].

The comparison are presented in Figure G.1 and the ratios respect to the MnvTune.v3 are presented in Figure G.2.

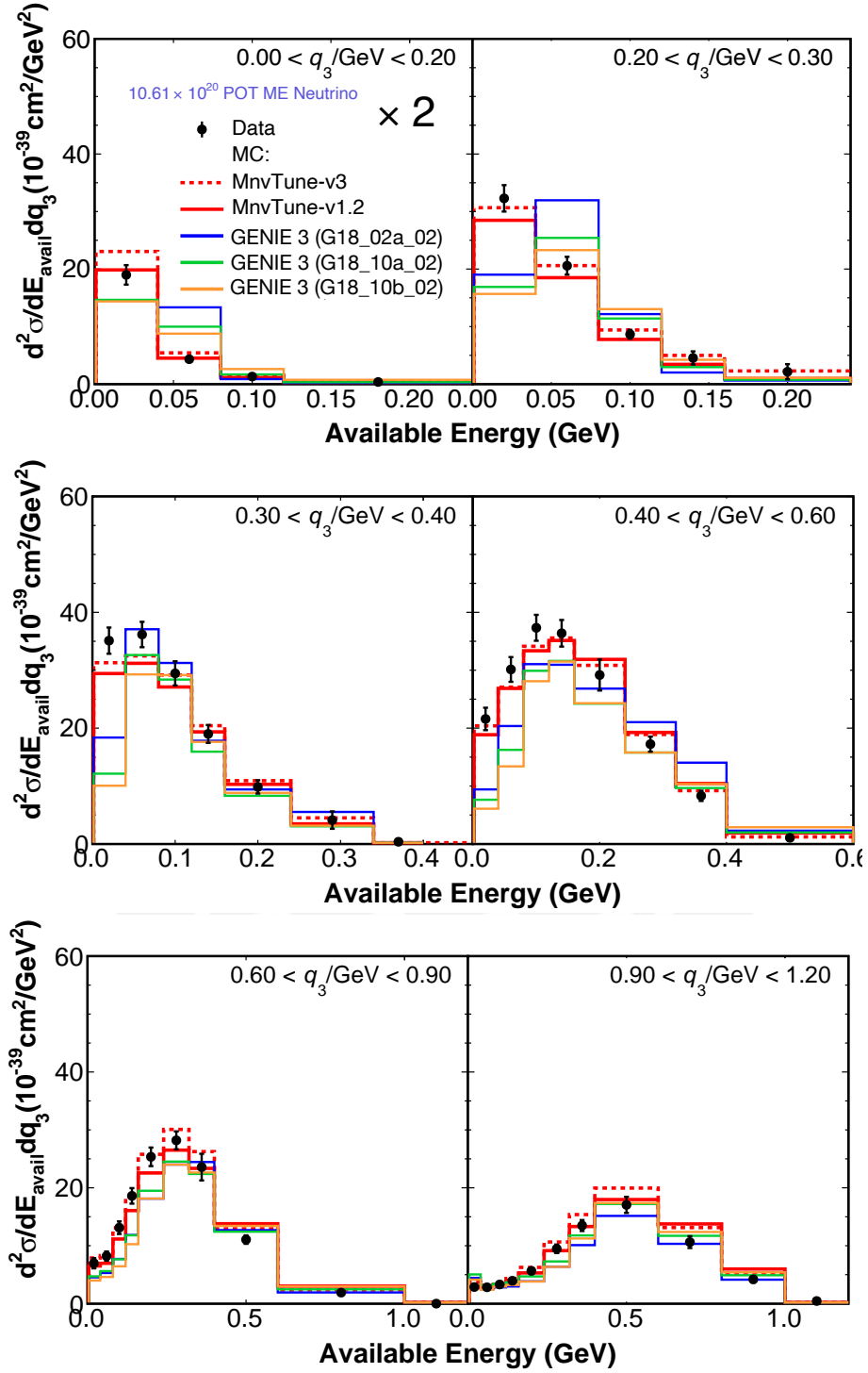


Figure G.1: Data double differential cross-section as function of E_{avail} and q_3 , compared with MnvTune.v3, MnvTune.v1.2, and GENIE3 (variations).

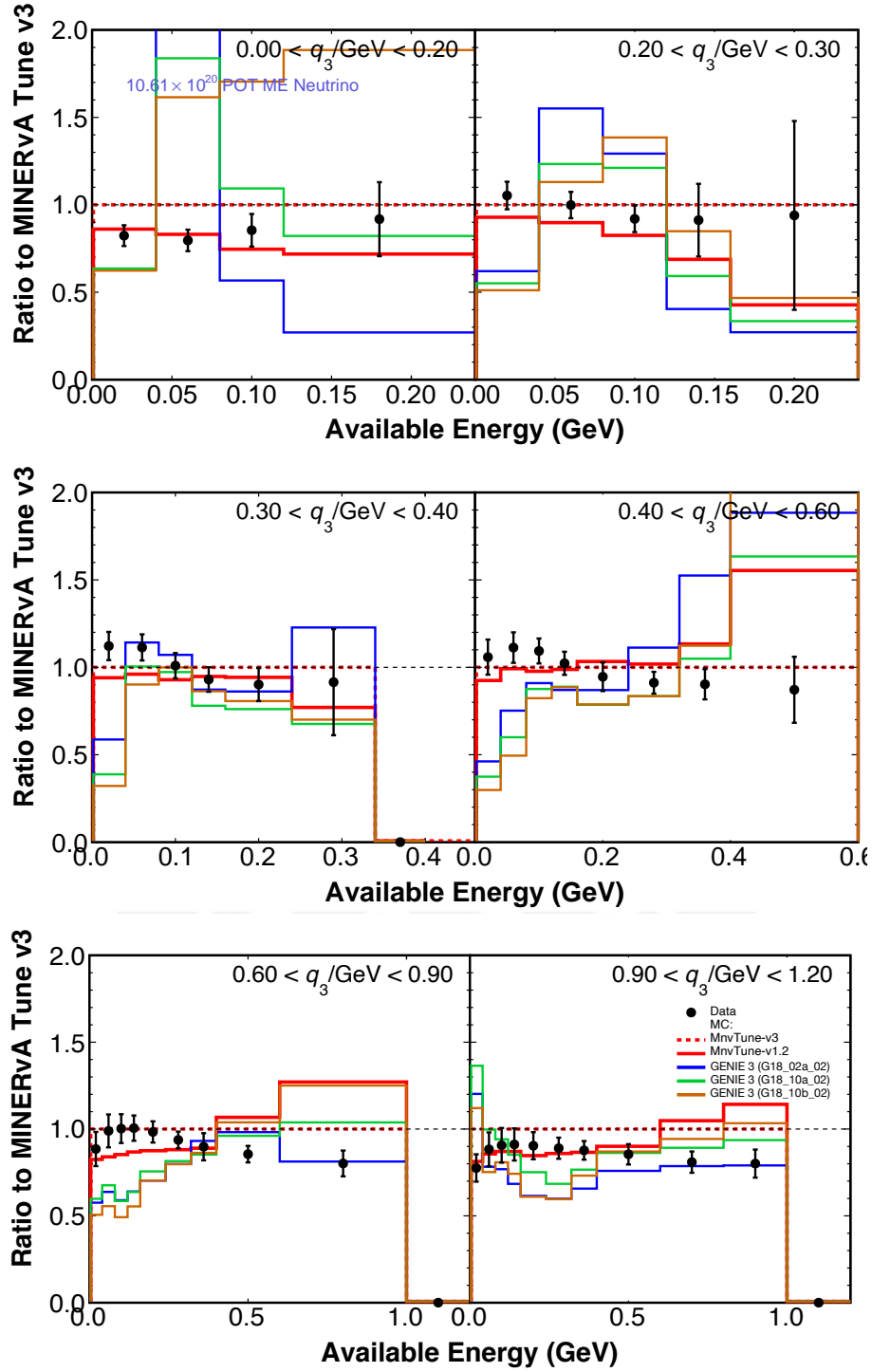


Figure G.2: Data double differential cross-section as function of E_{avail} and q_3 , compared with MnvTune.v3, MnvTune.v1.2, and GENIE3 (variations) Ratios.

APPENDIX H

CROSS SECTION χ^2 AND COVARIANCE MATRIX

In the present appendix, the χ^2 and covariance matrix is presented. For the MnvTune.v3, MnvTune.v1.2, NuWro FS, NuWro LFG, and GENIE 3 (10a). Then, an evaluation of the contributions of each systematic uncertainty (Flux, Hadronic Energy, Muon Reconstruction, RPA, FSI, Interaction Models, and Signal Model) on the χ^2 is displayed. Finally, a combination of the systematic uncertainties (FSI+Interaction Models, Flux + Hadronic Energy, Flux + Hadronic Energy + Muon Reconstruction, and Hadronic Energy + Muon Reconstruction) are presented.

H.1. CROSS-SECTION χ^2 COMPARISON DIAGONAL/FULL COVARIANCE MATRIX

~~H.1 Cross-section χ^2 comparison diagonal/full covariance matrix~~

MnvTune.v3

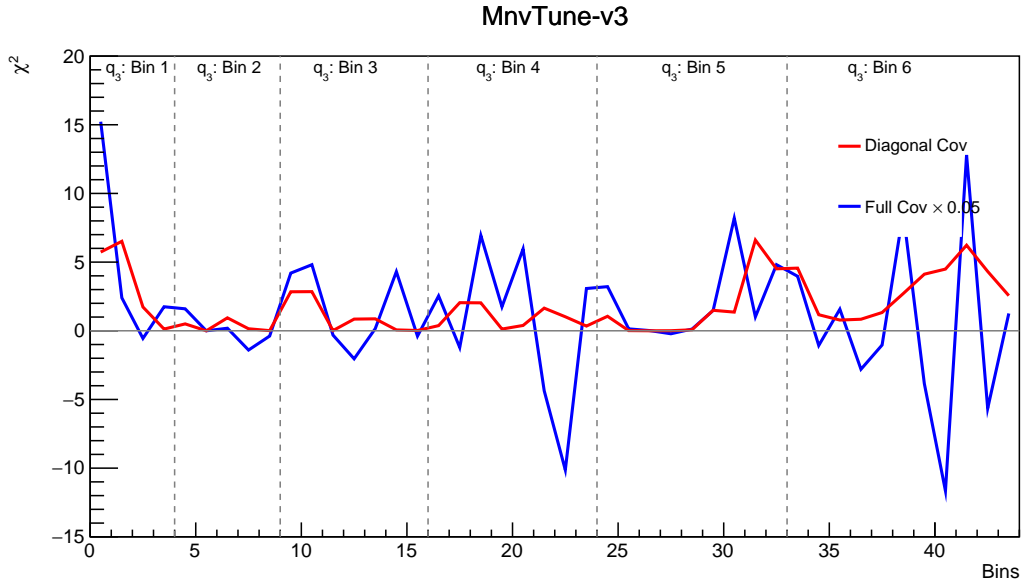


Figure H.1: χ^2 comparison mc:MnvTune-v3

MnvTune.v1.2

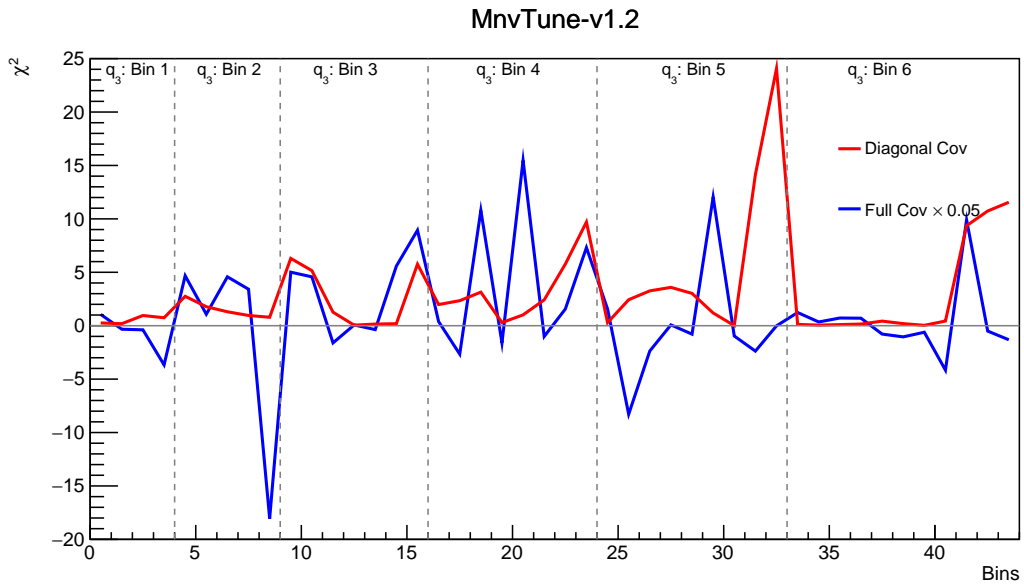


Figure H.2: χ^2 comparison mc:MnvTune-v1.2

H.1. CROSS-SECTION χ^2 COMPARISON DIAGONAL/FULL COVARIANCE MATRIX
NuWro SF

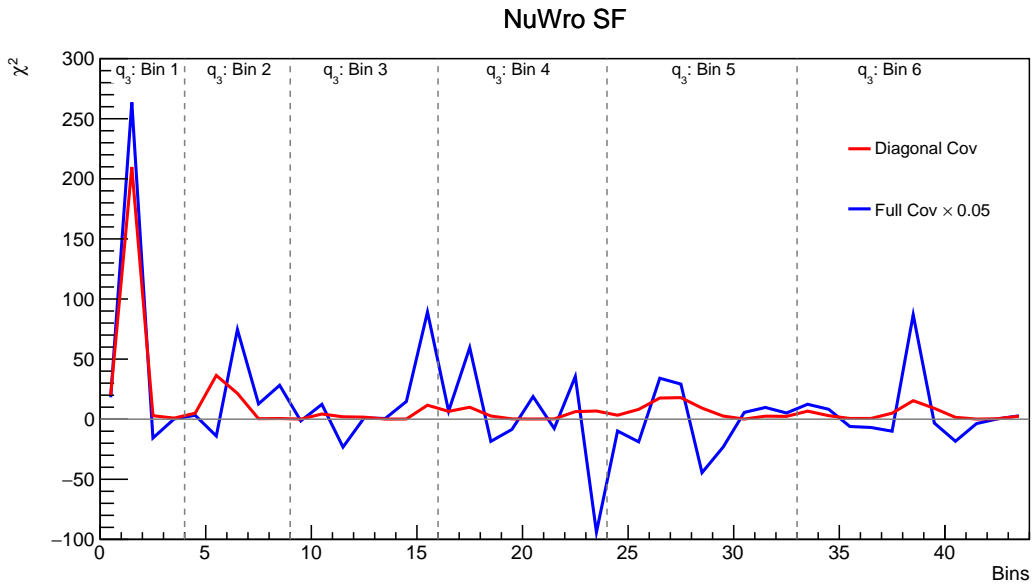


Figure H.3: χ^2 comparison mc:NuWro SF

NuWro LFG

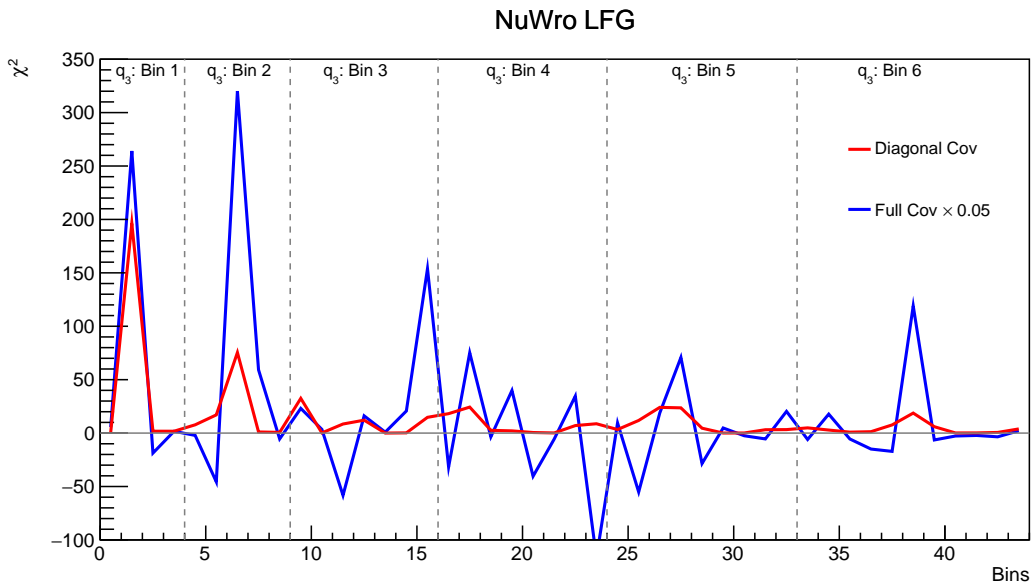


Figure H.4: χ^2 comparison mc:NuWro LFG

H.1. CROSS-SECTION χ^2 COMPARISON DIAGONAL/FULL COVARIANCE MATRIX
GENIE3 10a

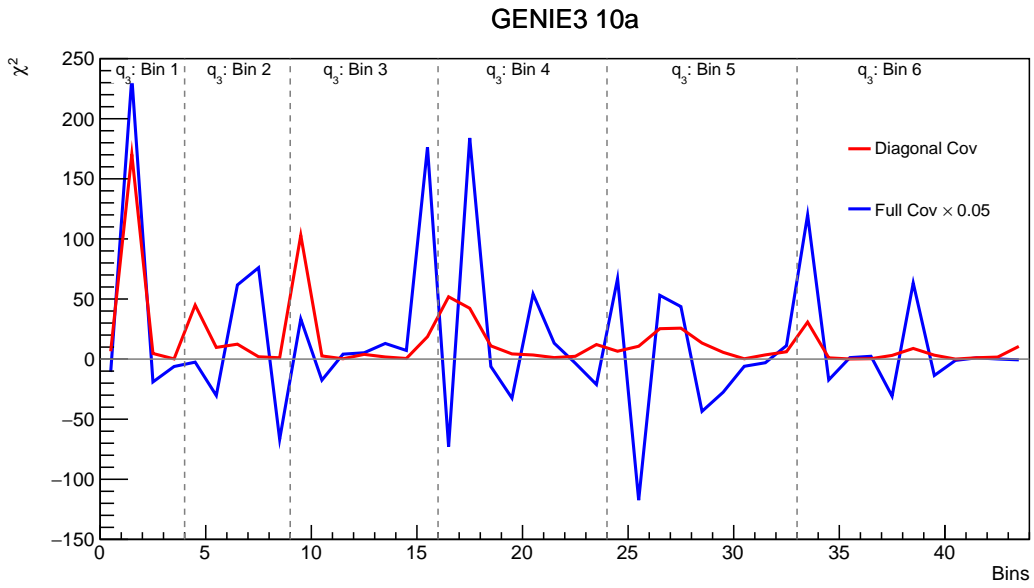
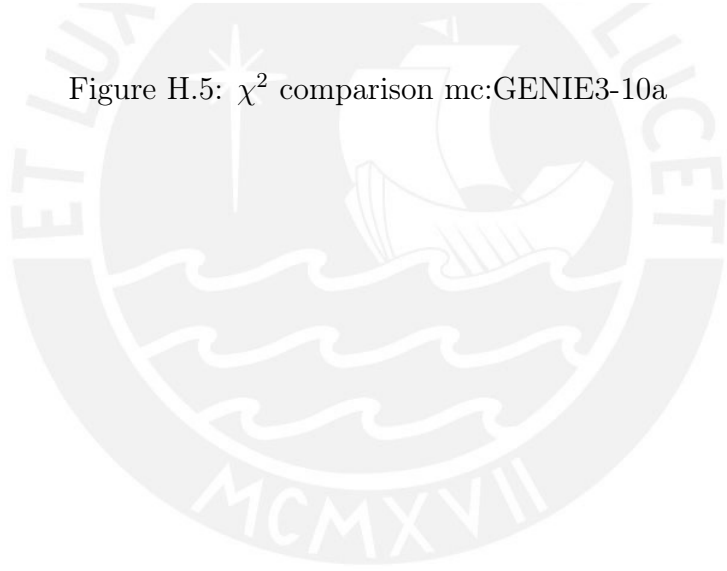


Figure H.5: χ^2 comparison mc:GENIE3-10a



H.2 Cross-section χ^2 and covariance matrix (systematic)

Full Covariance matrix with only Flux uncertainty

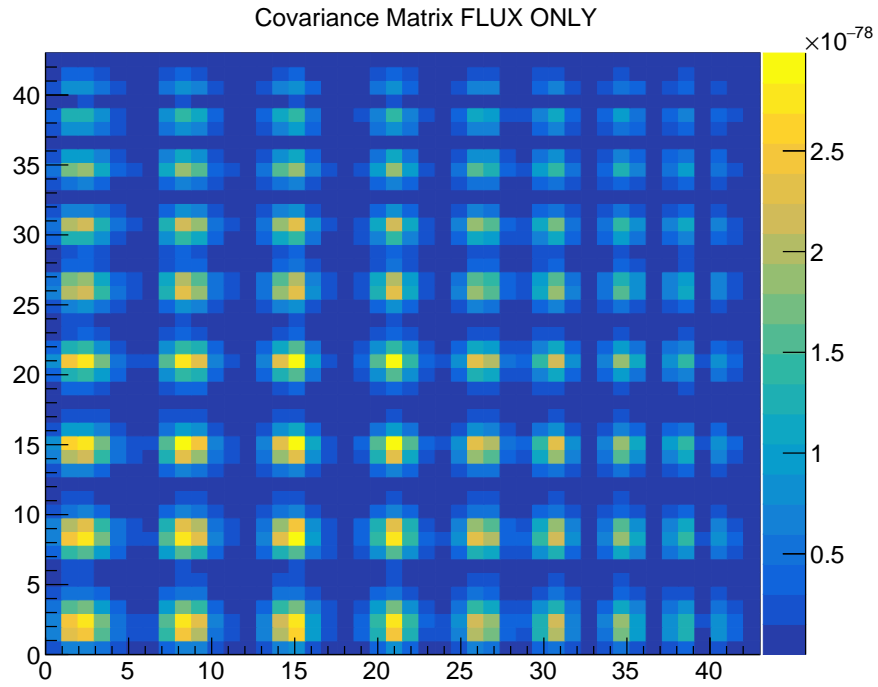


Figure H.6: covarianve matrix with only flux uncertainty

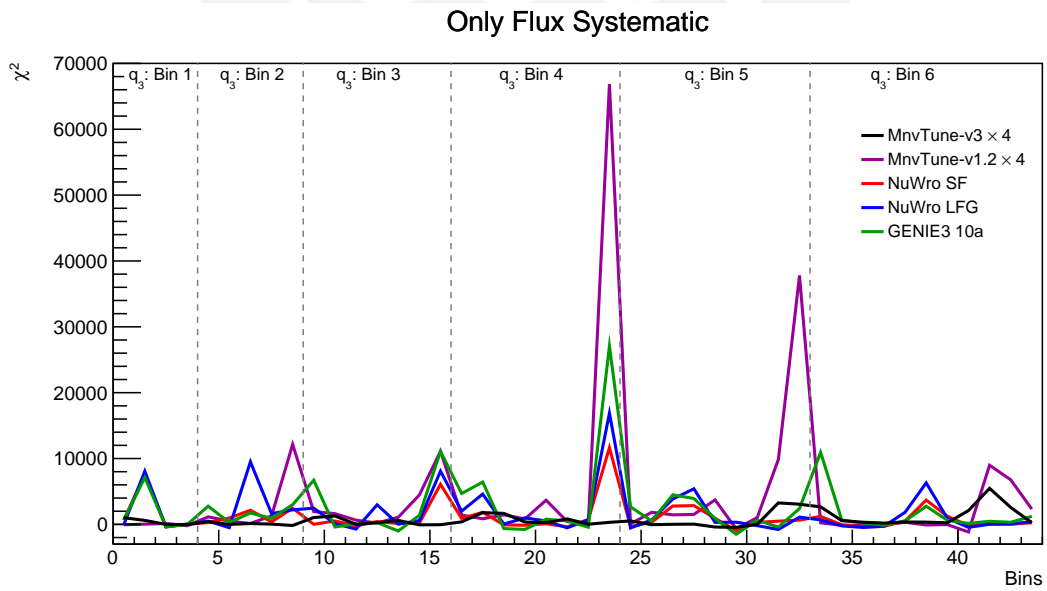


Figure H.7: χ^2 full covarianve matrix with only flux uncertainty

Full Covariance matrix with only Hadronic energy uncertainty

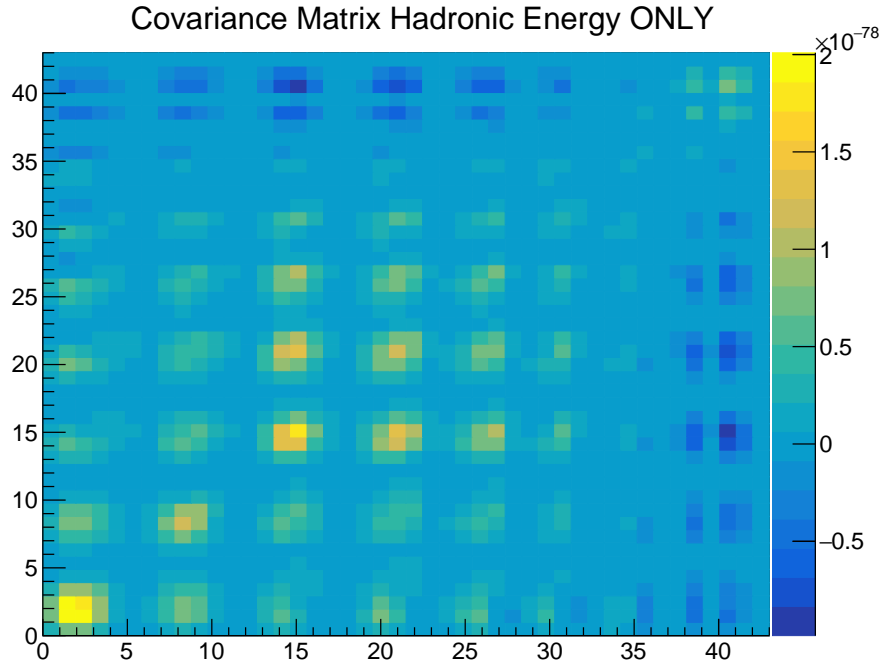


Figure H.8: covarianve matrix with only hadronic energy uncertainty

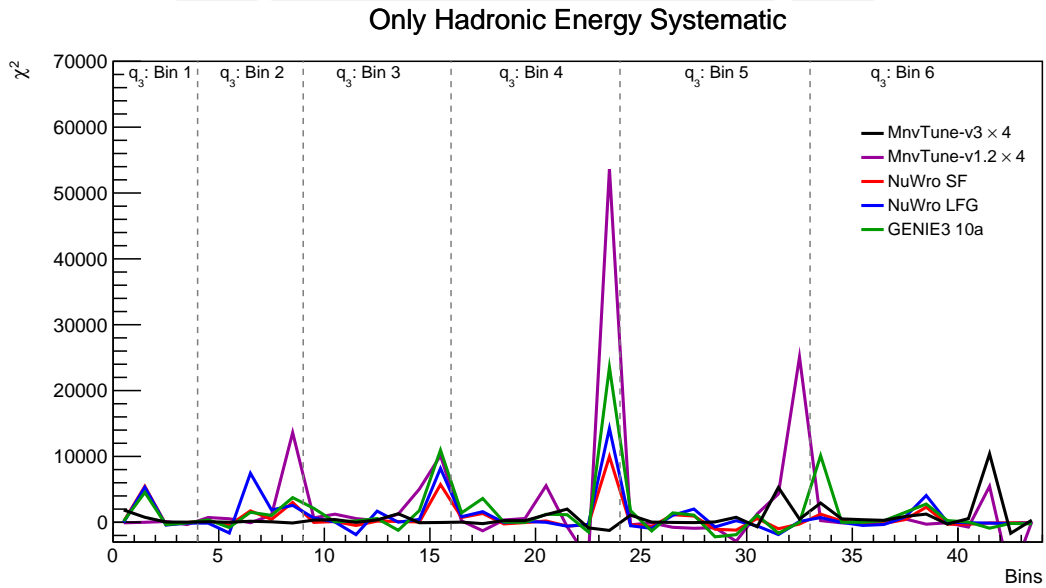


Figure H.9: χ^2 full covarianve matrix with only hadronic energy uncertainty

Full Covariance matrix with only Muon energy and angle uncertainty

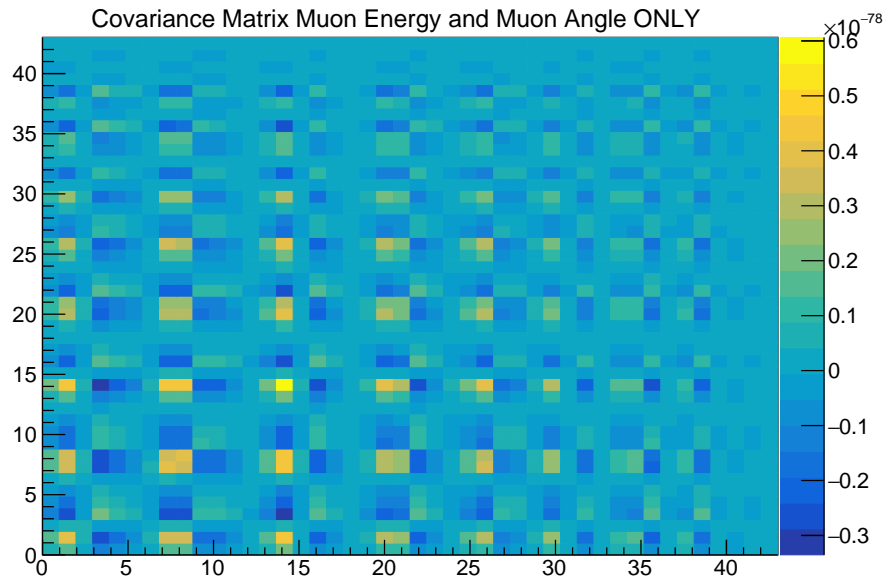


Figure H.10: covarianve matrix with only Muon reconstruction uncertainty

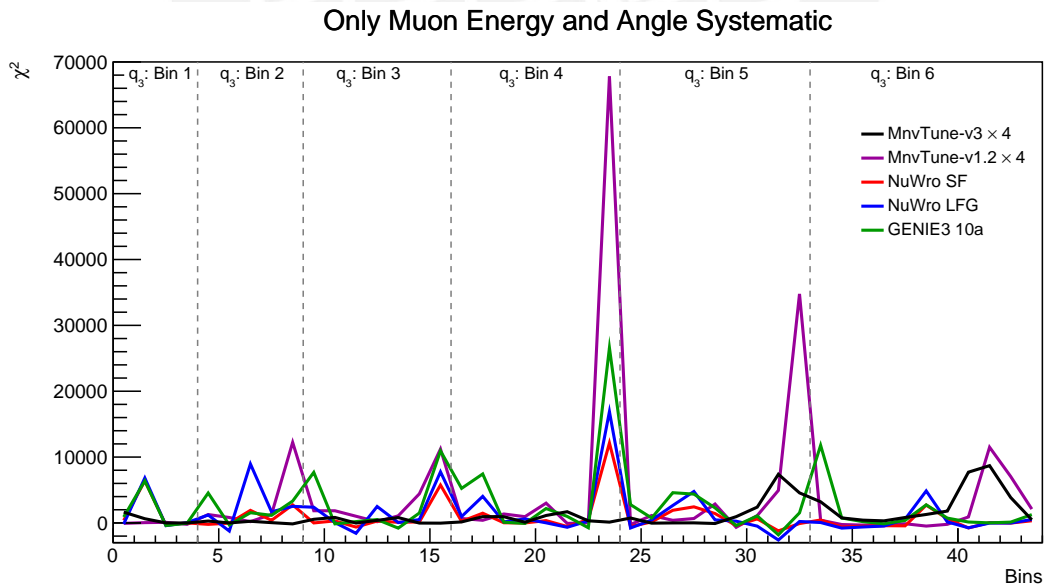


Figure H.11: χ^2 full covarianve matrix with only muon energy and angle uncertainties

Full Covariance matrix with only RPA uncertainty

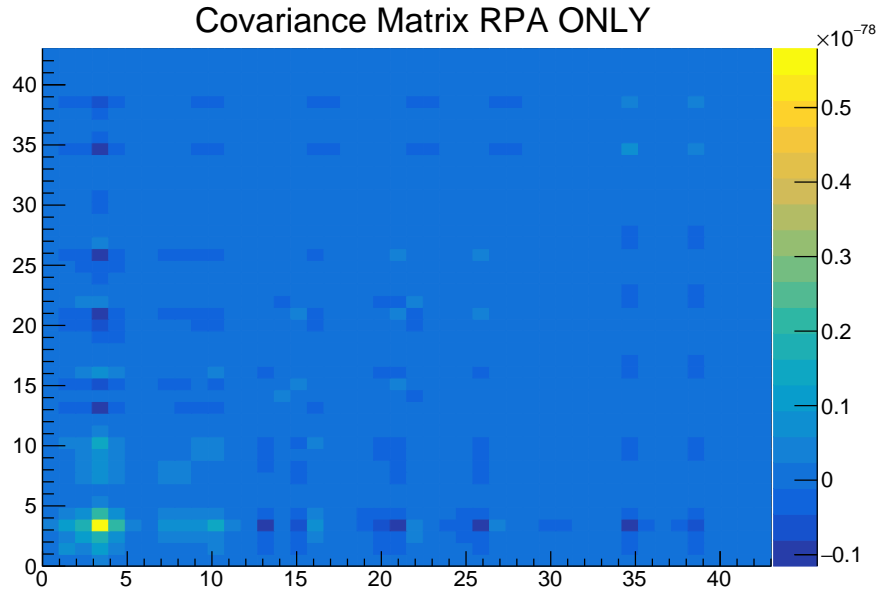


Figure H.12: covarianve matrix with only RPA uncertainty

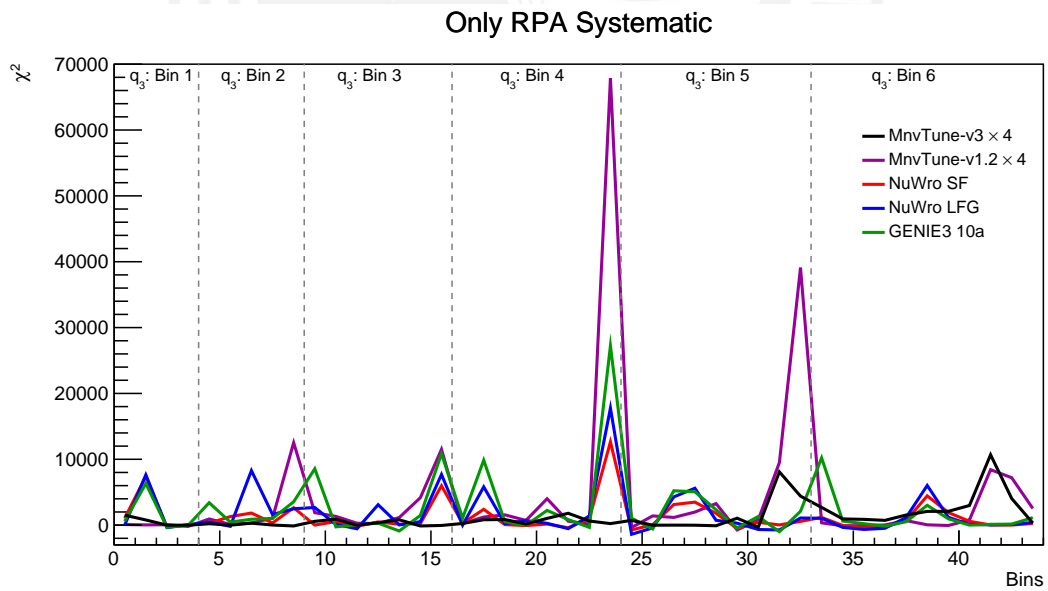


Figure H.13: χ^2 full covarianve matrix with only RPA uncertainty

Full Covariance matrix with only FSI uncertainty

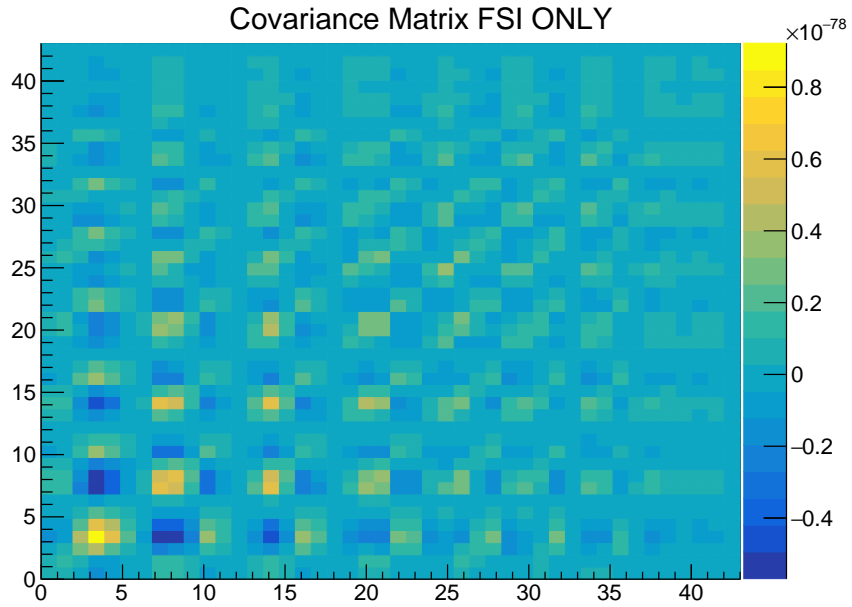


Figure H.14: covarianve matrix with only FSI uncertainty

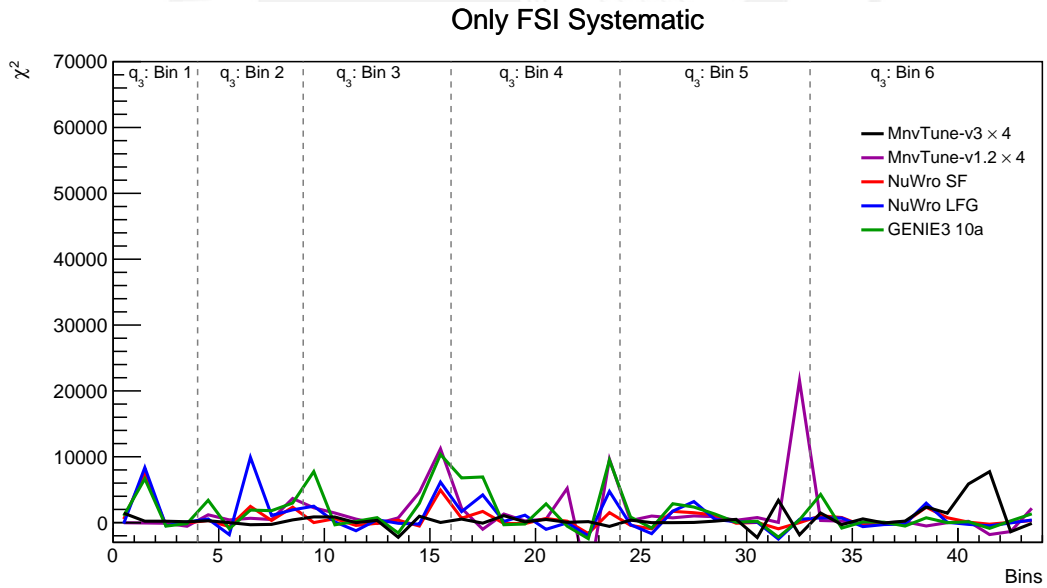


Figure H.15: χ^2 full covarianve matrix with only FSI uncertainties

Full Covariance matrix with only Interaction model uncertainty

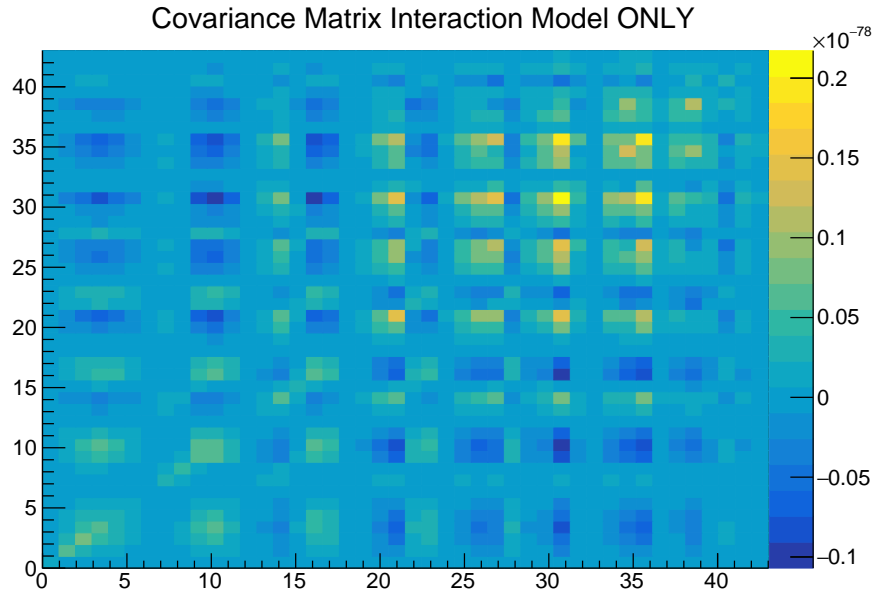


Figure H.16: covarianve matrix with only Interaction model uncertainty

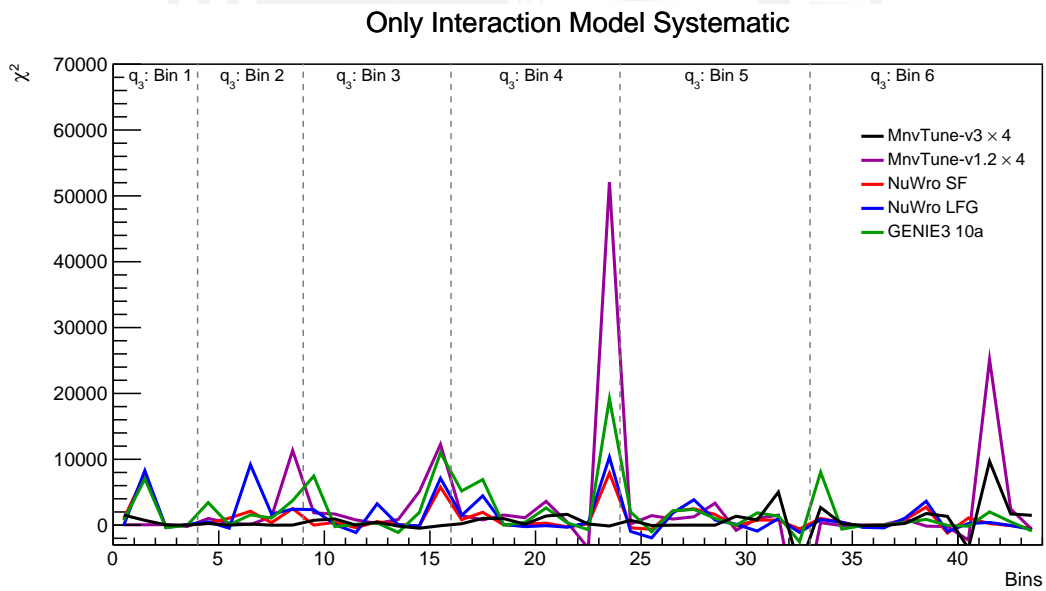


Figure H.17: χ^2 full covarianve matrix with only interaction models uncertainties

Full Covariance matrix with only Signal Model uncertainty

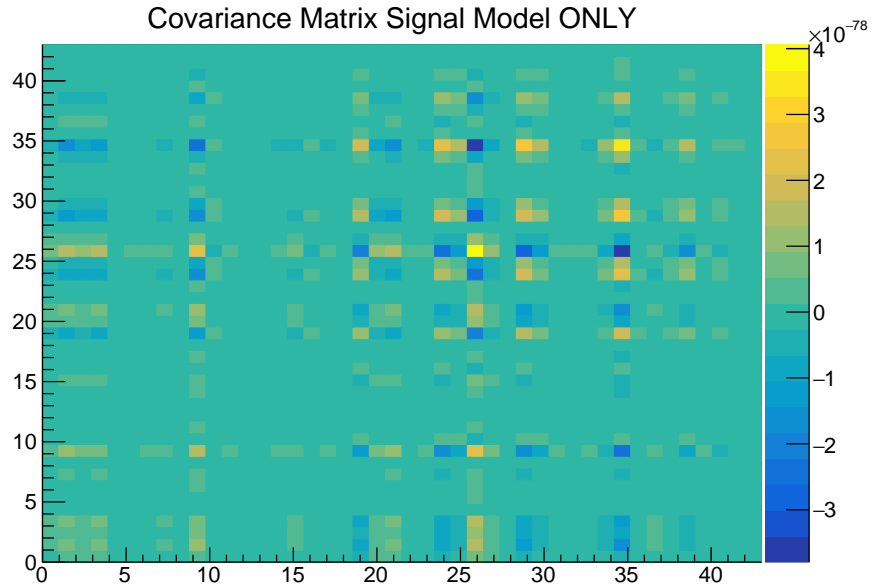


Figure H.18: covarianve matrix with only Signal Model uncertainty

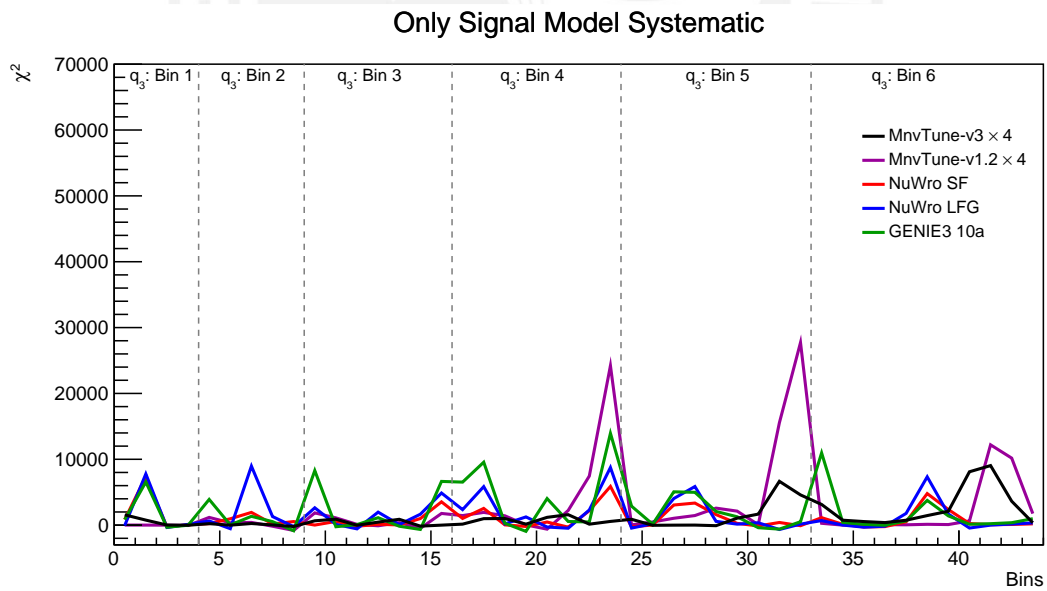


Figure H.19: χ^2 full covarianve matrix with only Signal model uncertainty

H.3 Cross-section χ^2 (systematics Unc. combinations)

Full Covariance matrix with only FSI + Interaction model uncertainties

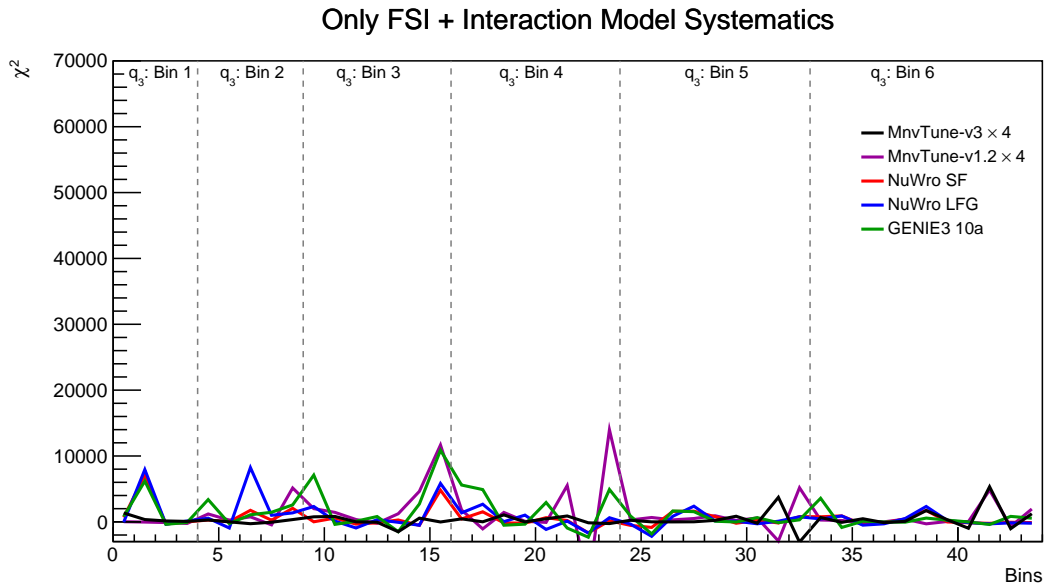


Figure H.20: χ^2 full covariance matrix with only FSI and Interaction model uncertainties

Full Covariance matrix with only Flux + Hadronic energy uncertainty

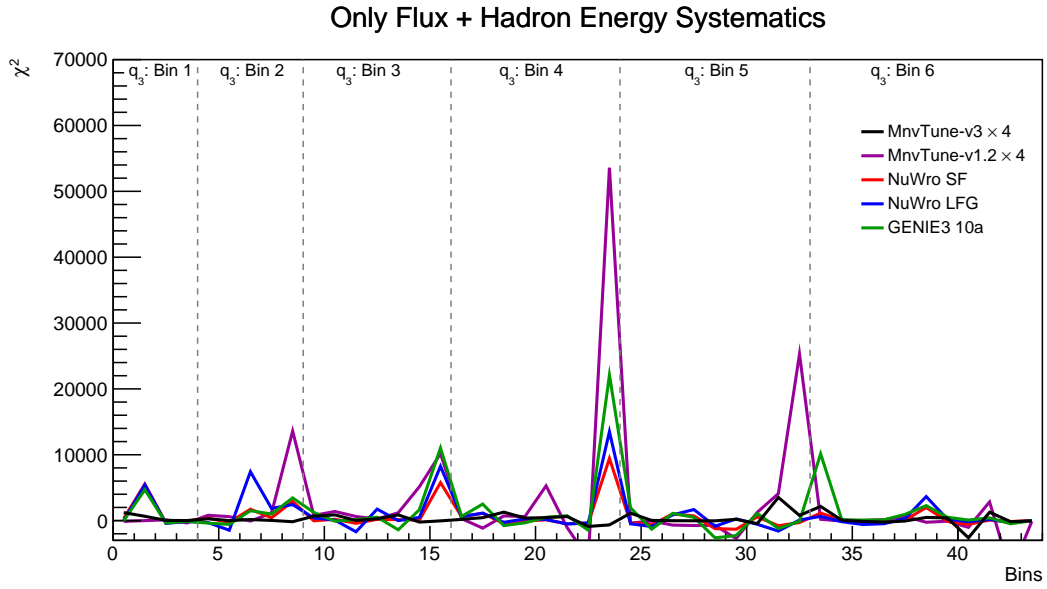
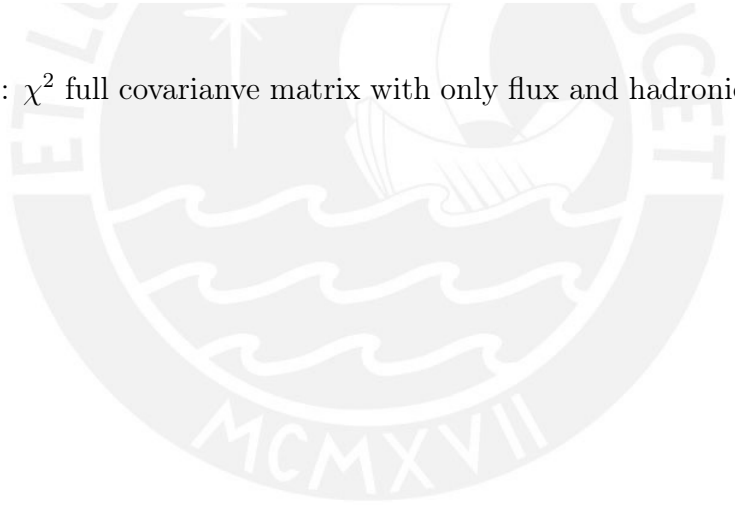


Figure H.21: χ^2 full covariance matrix with only flux and hadronic uncertainties



Full Covariance matrix with only Flux + Hadronic energy + Muon energy and angle uncertainty

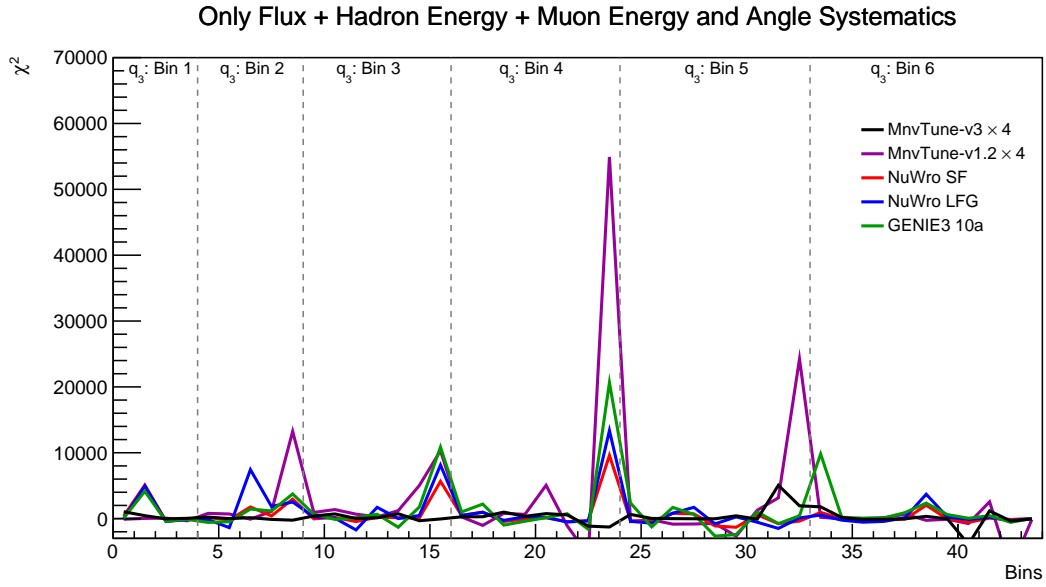


Figure H.22: χ^2 full covariance matrix with only flux, hadronic energy, muon energy+angle uncertainties

Full Covariance matrix with only Hadronic energy + Muon energy and angle uncertainty

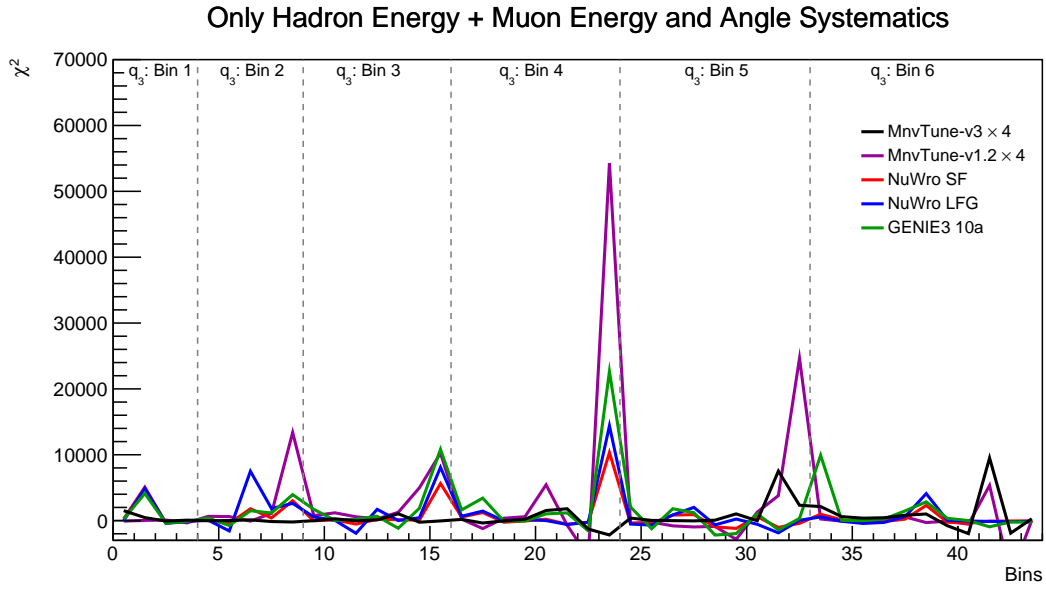


Figure H.23: χ^2 full covariance matrix with only hadronic energy, muon energy+angle uncertainties

APPENDIX I

SUSAV2 QE

Its implementation is a hadron tensor. It pulls one target nucleon from a GENIE Local Fermi Gas and then gives it energy and momentum transfer in the lab frame to send it out in the nucleus to be FSI re-scattered [260]. The general feature of the SuSA QE compared to the GENIE GFG, is that GENIE has a more narrow effect on the QE peak, and SuSA QE extends on the tails, contributing to the dip region between the QE and the Delta (see Figure I.1 and I.2). This feature of putting events in the dip region had the same SRC motivation as the spectral function and the Bodek Ritchie tail and our enhancement of it.

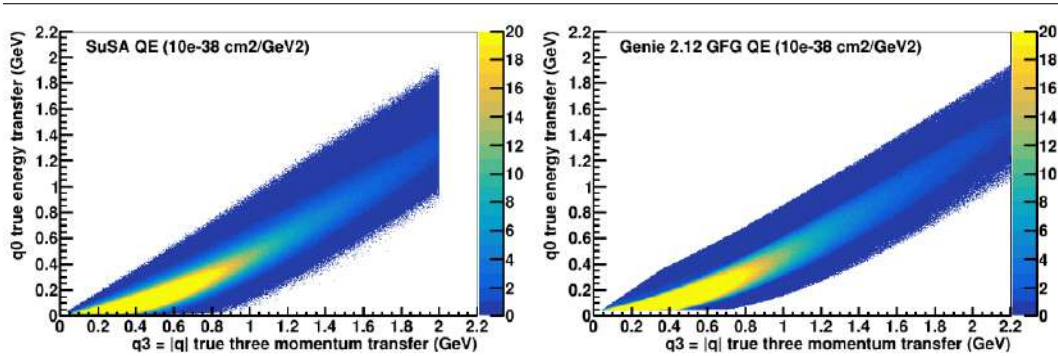


Figure I.1: SuSAv2 QE cross-section in function of q_0 and q_3 on the left, and the right hand side plot GENIE with GFG cross-section in terms of q_0 and q_3 , plots taken from [260]. Z-axis represents the cross-section.

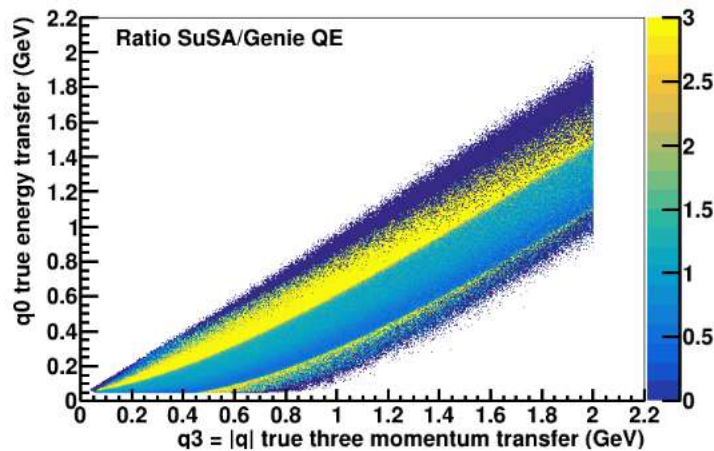


Figure I.2: Ratio plot from SuSAv2 QE cross-section over GENIE with GFG cross-section in terms of q_0 and q_3 . The enhancement on the high energy transfer side is unmistakable, compared to the Global Fermi gas. Plots taken from [260]

Effect of SuSAv2 QE on low recoil sample

For the SuSAv2 QE the RPA effect is turned off. The difference between SuSAv2 QE (RPA turn off) with nominal is around 40% maximum at the low q_3 region. However, the higher contrast in QE events is more than 60% in the tails of QE distribution shadowing from other contributions (Figure I.3), as is expected from the 2D ratio above (Figure I.2). Compared with the data, higher q_3 agrees better and is not the case at low q_3 where the nominal MC works

better (Figure I.4 and I.5). Compared with the previous Bodek-Ritchie tail enhancement, SuSA-QE preserves the quasi-elastic rate. The data prefers the overall increase in quasi-elastic as much as the increase in the dip region. The second observation from [260], the simulation of the resulting ejected nucleon in the SuSA implementation in GENIE is suspicious [345] and anyway can not be reproduced by simple re-weighting. The E_{avail} prediction not only does not describe data, but it also does not describe the SuSA prediction. We will not use this iteration for the newCV (referred to in the thesis also as MnvTune.v3) and hope a better implementation is available in the future.



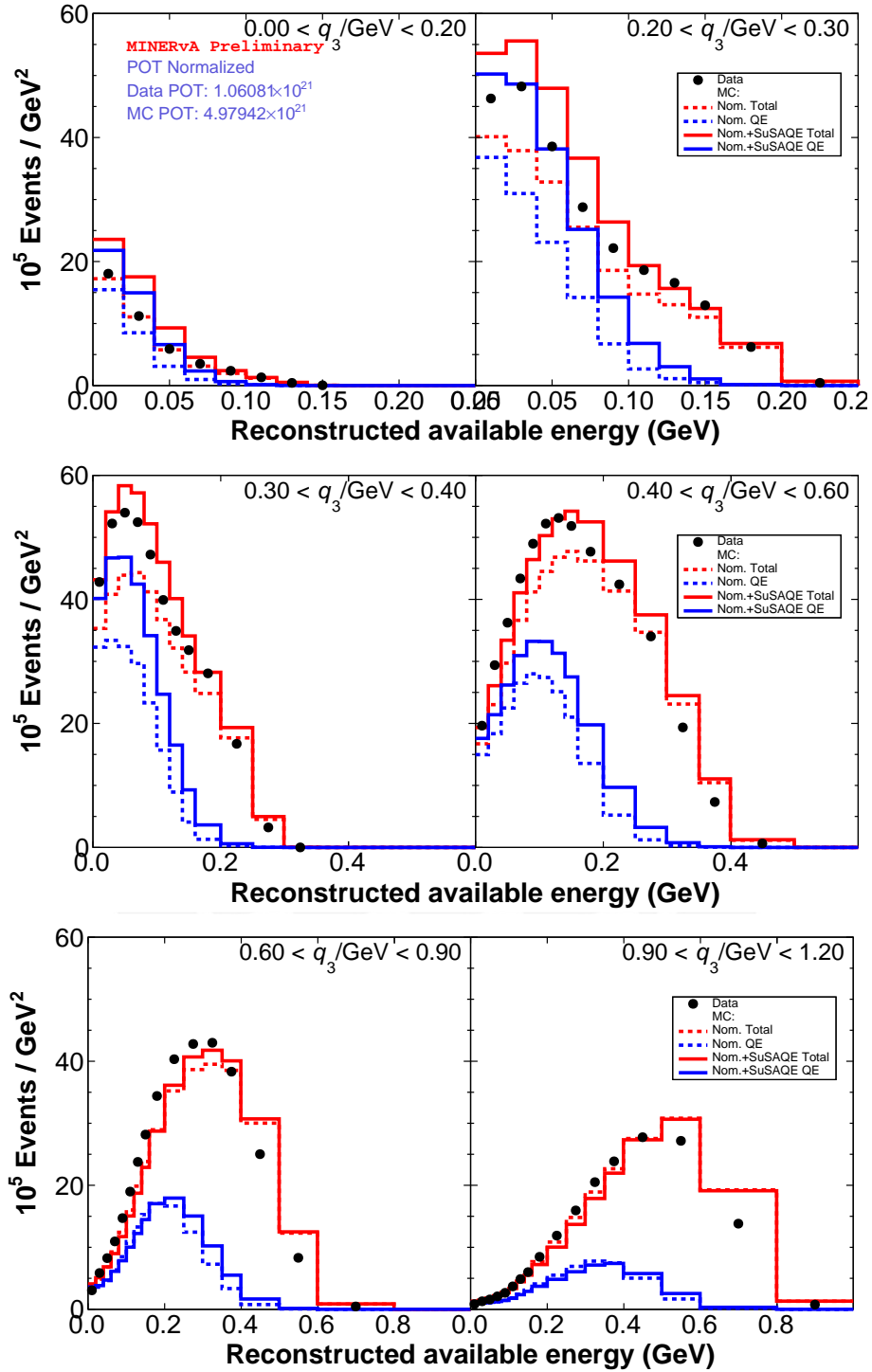


Figure I.3: Reconstructed E_{avail} in projections of reconstructed q_3 regions, the dashed lines are nominal MC, and continuous lines are the SuSAv2 QE effect. In red the Total MC and in blue QE event types.

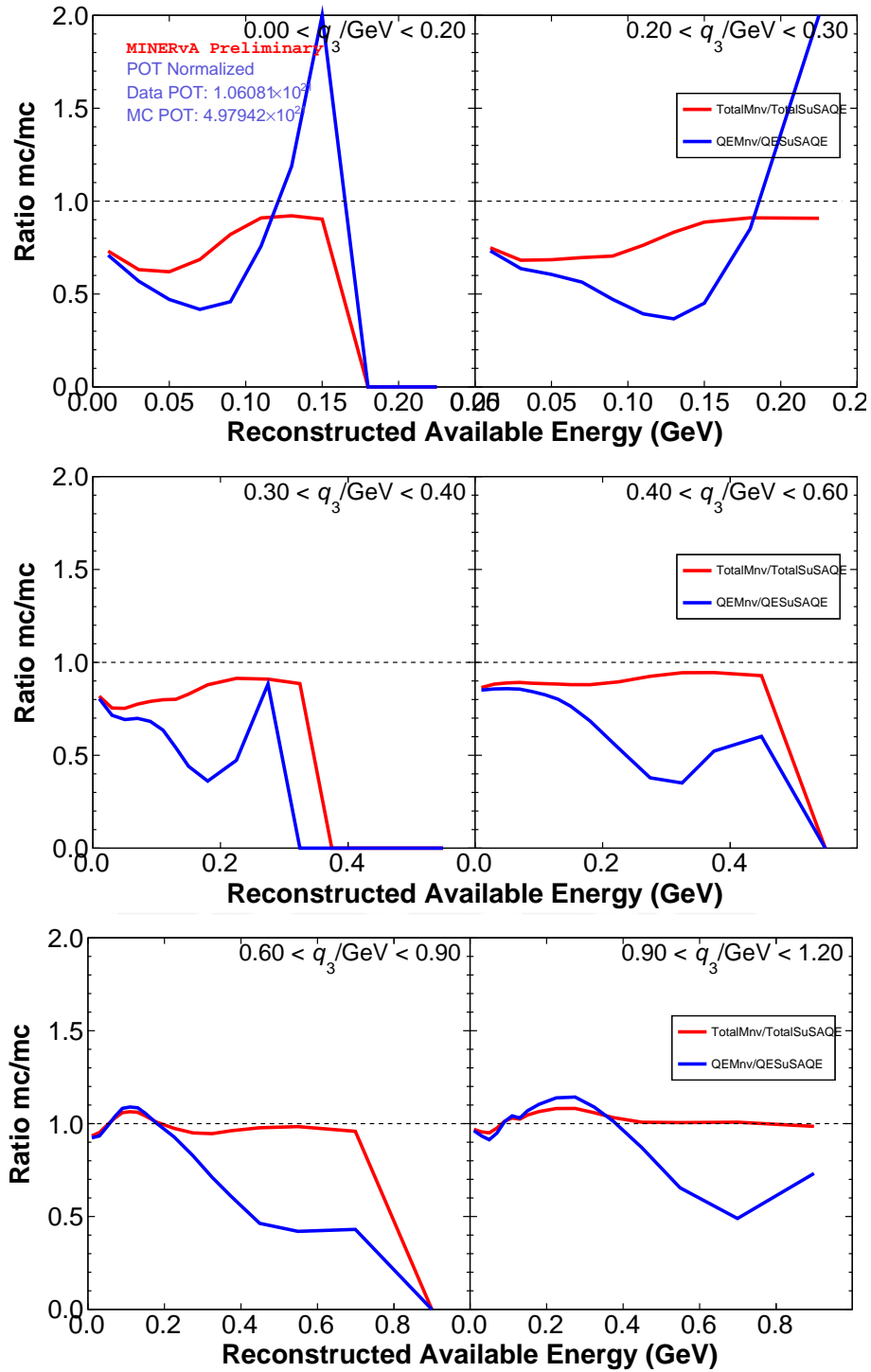


Figure I.4: Ratio of nominal MC over SuSAv2 QE MC for reconstructed E_{avail} in projections of reconstructed q_3 regions, the dashed lines are nominal MC, and continuous lines are the SuSAv2 QE effect. In red the Total MC and in blue QE event types.

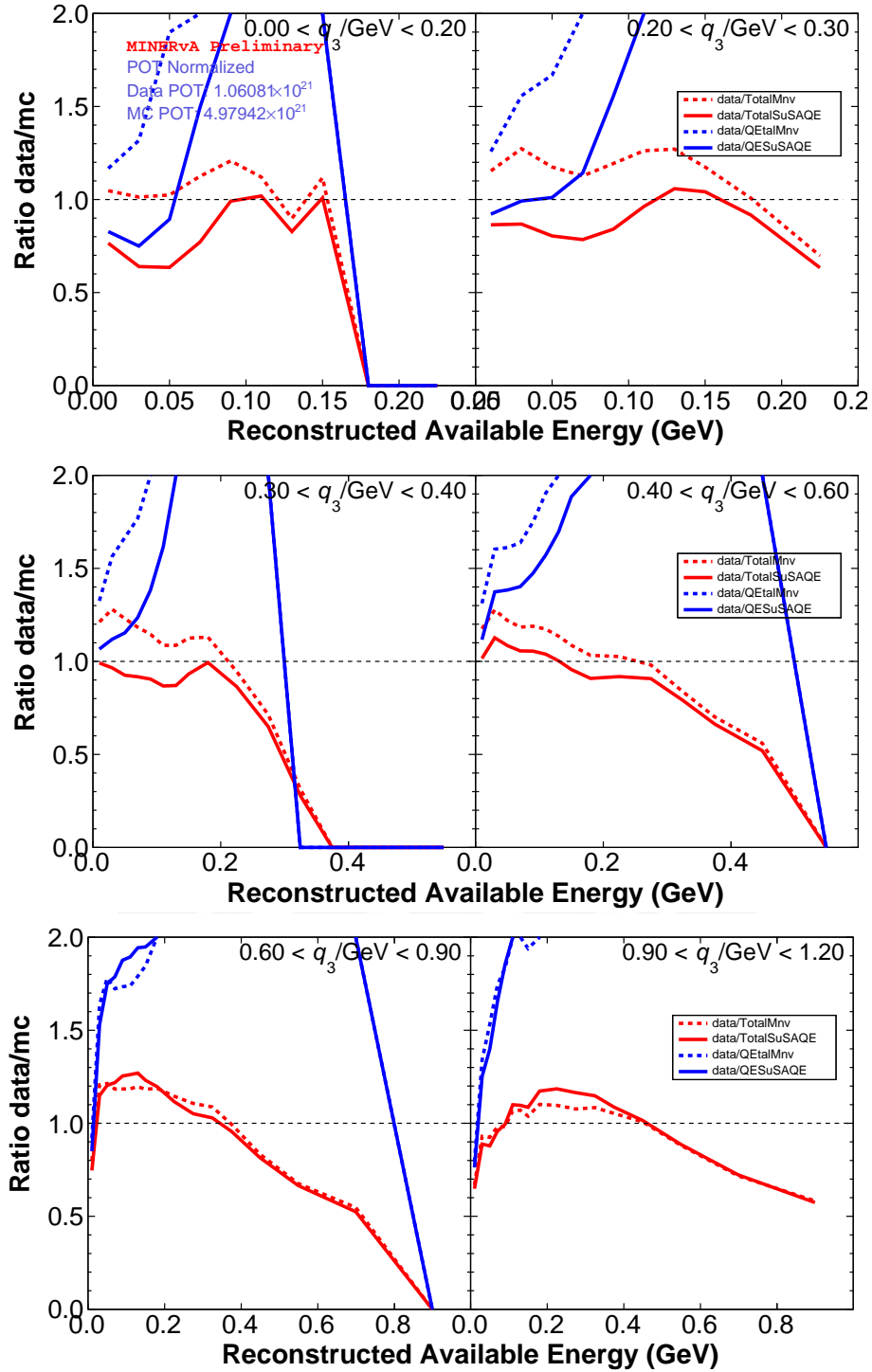


Figure I.5: Ratio of data over SuSAv2 QE MC for reconstructed E_{avail} in projections of reconstructed q_3 regions, the dashed lines are nominal MC, and continuous lines are the SuSAv2 QE effect. In red the Total MC and in blue QE event types.

APPENDIX J

MINER_vA COLLABORATION



Figure J.1: MINER_vA Collaboration meeting Pittsburgh, USA 2019

(The MINERvA collaboration)

Faiza Akbar, Mohammad Sajjad Athar, Huma Haider, Vaniya Ansari,

Prameet Gaur, Sayeed Akhter

Aligarh Muslim University, Aligarh, India

Gian Caceres, Helio da Motta, Adrian Lozano, Gilson Silva

Centro Brasileiro de Pesquisas Físicas, Rio de Janeiro, Brazil

Omar Miranda, Luis Montano, Marco Torres

Centro de Investigación y de Estudios Avanzados del Instituto Politécnico

Nacional, Mexico City, Mexico

Jennica LeClerc, Christian Nguyen, Heather Ray

University of Florida, Gainesville, Florida

Leo Bellantoni, Minerba Betancourt, Robert Hatcher, Deepika Jena, Jorge

Morfin, Gabe Perdue

Fermilab, Batavia, Illinois

Eric Christy

Hampton University, Hampton, Virginia

Alessandro Bravar

University of Geneva, Geneva, Switzerland

Everardo Granados, Diego Andrade, Jose Luis Bonilla, Julian Felix

Universidad de Guanajuato, Guanajuato, Mexico

Anežka Klustová, Abbey Waldron

Imperial College London, London, UK

Nishat Fiza, Satyajit Jena

Indian Institute of Science Education and Research, Mohali, India

Emily Maher

Massachusetts College of Liberal Arts, North Adams, Massachusetts

Laura Fields

University of Notre Dame, Notre Dame, IN

Amit Bashyal, Mateus Carneiro, Sean Gilligan, Maggie Greenwood, Heidi
Schellman, Noah Vaughan

Oregon State University, Corvallis, Oregon

Nathaniel Tagg

Otterbein College, Westerville, Ohio

Komninos-John Plows, David Wark

University of Oxford, Oxford, United Kingdom

Steve Dytman, Ben Messerly, Donna Naples, Vittorio Paolone, Hang Su

University of Pittsburgh, Pittsburgh, Pennsylvania

Marvin Ascencio Sosa, Alberto Gago

Pontificia Universidad Catolica del Peru, Lima, Peru

Arie Bodek, Howard Budd, Tejin Cai, Gonzalo Diaz, Rob Fine, Sarah Henry,
Jeffrey Kleykamp, Steve Manly, Kevin McFarland, Aaron McGowan, Miriam
Moore, Andrew Olivier, Daniel Ruterbories, Mehreen Sultana, Clarence Wret

University of Rochester, Rochester, New York

Ronald Ransome

Rutgers University, New Brunswick, New Jersey

Hugh Gallagher, Trung Le, Tony Mann, Vladyslav Syrotenko

Tufts University, Medford, Massachusetts

Rik Gran, Emily Haase, Kyle Jacobsen, Ishmam Mahbub, Brandon Reed,

Asit Srivastava

University of Minnesota at Duluth, Duluth, Minnesota

Carlos Solano Salinas

Universidad Nacional de Ingeniería, Lima, Peru

Jorge Chaves, Keith Kroma-Wiley, David Last, Christopher Mauger,
Alejandro Ramirez Delgado

University of Pennsylvania, Philadelphia, Pennsylvania

William Brooks, Anushree Ghosh, Jonathan Miller, Barbara Yaeggy
Universidad Técnica Federico Santa María, Valparaiso, Chile

Steve Boyd, Xianguo Lu

University of Warwick

Jan Sobczyk

University of Wrocław

Zubair Ahmad Dar, Amy Filkins, Michael Kordosky, Oscar E Moreno,
Jeffrey Nelson, Edgar Valencia, Luis Zazueta

College of William and Mary, Williamsburg, Virginia

Deborah Harris, Maria Mehmood

University of York, Toronto, Ontario, Canada

BIBLIOGRAPHY

- [1] Wolfgang Pauli. “Pauli letter collection: letter to Lise Meitner”. Typed copy. 1930. URL: <http://cds.cern.ch/record/83282>.
- [2] J. Chadwick. “The intensity distribution in the magnetic spectrum of beta particles from radium (B + C)”. In: *Verh. Phys. Gesell.* 16 (1914), pp. 383–391.
- [3] Charles Drummond Ellis, W. A. Wooster, and Ernest Rutherford. “The average energy of disintegration of radium E”. In: *Proceedings of the Royal Society of London. Series A, Containing Papers of a Mathematical and Physical Character* 117.776 (1927), pp. 109–123. DOI: [10.1098/rspa.1927.0168](https://doi.org/10.1098/rspa.1927.0168). eprint: <https://royalsocietypublishing.org/doi/pdf/10.1098/rspa.1927.0168>. URL: <https://royalsocietypublishing.org/doi/abs/10.1098/rspa.1927.0168>.
- [4] James Chadwick. “The existence of a neutron”. In: *Proceedings of the Royal Society of London. Series A, Containing Papers of a Mathematical and Physical Character* 136.830 (1932), pp. 692–708. DOI: [10.1098/rspa.1932.0112](https://doi.org/10.1098/rspa.1932.0112). eprint: <https://royalsocietypublishing.org/doi/pdf/10.1098/rspa.1932.0112>. URL: <https://royalsocietypublishing.org/doi/abs/10.1098/rspa.1932.0112>.
- [5] Roger H. Stuewer. “The Seventh Solvay Conference: Nuclear Physics at the Crossroads”. In: *No Truth Except in the Details: Essays in Honor of Martin J. Klein*. Ed. by A. J. Kox and Daniel M. Siegel. Dordrecht: Springer Netherlands, 1995, pp. 333–362. ISBN: 978-94-011-0217-9. DOI:

- 10.1007/978-94-011-0217-9_15. URL: https://doi.org/10.1007/978-94-011-0217-9_15.
- [6] E. Fermi. “An attempt of a theory of beta radiation. 1.” In: *Z. Phys.* 88 (1934), pp. 161–177. DOI: [10.1007/BF01351864](https://doi.org/10.1007/BF01351864).
- [7] Francis Perrin. “Possibilité d’émission de particules neutres de masse intrinsèque nulle dans les radioactivités β ”. In: *Comptes Rendus des Séances de l’Académie des Sciences* 197 (1933), p. 1625.
- [8] Enrico Fermi. “Tentativo di una Teoria Dei Raggi β ”. In: *Il Nuovo Cimento (1924-1942)* 11.1 (Sept. 2008), p. 1. ISSN: 1827-6121. DOI: [10.1007/BF02959820](https://doi.org/10.1007/BF02959820). URL: <https://doi.org/10.1007/BF02959820>.
- [9] G. Gamow and E. Teller. “Selection Rules for the β -Disintegration”. In: *Phys. Rev.* 49 (12 Jan. 1936), pp. 895–899. DOI: [10.1103/PhysRev.49.895](https://doi.org/10.1103/PhysRev.49.895). URL: <https://link.aps.org/doi/10.1103/PhysRev.49.895>.
- [10] Frederick Reines and Clyde L. Cowan. “The neutrino”. In: *Nature* 178 (1956), pp. 446–449. DOI: [10.1038/178446a0](https://doi.org/10.1038/178446a0).
- [11] F. Reines et al. “Detection of the Free Antineutrino”. In: *Phys. Rev.* 117 (1 Jan. 1960), pp. 159–173. DOI: [10.1103/PhysRev.117.159](https://doi.org/10.1103/PhysRev.117.159). URL: <https://link.aps.org/doi/10.1103/PhysRev.117.159>.
- [12] Frederick Reines and Clyde L. Cowan. “Free Antineutrino Absorption Cross Section. I. Measurement of the Free Antineutrino Absorption Cross Section by Protons”. In: *Phys. Rev.* 113 (1 Jan. 1959), pp. 273–279. DOI: [10.1103/PhysRev.113.273](https://doi.org/10.1103/PhysRev.113.273). URL: <https://link.aps.org/doi/10.1103/PhysRev.113.273>.
- [13] G. Danby et al. “Observation of High-Energy Neutrino Reactions and the Existence of Two Kinds of Neutrinos”. In: *Phys. Rev. Lett.* 9 (1 July 1962), pp. 36–44. DOI: [10.1103/PhysRevLett.9.36](https://doi.org/10.1103/PhysRevLett.9.36). URL: <https://link.aps.org/doi/10.1103/PhysRevLett.9.36>.
- [14] E. J. Konopinski and H. M. Mahmoud. “The Universal Fermi Interaction”. In: *Phys. Rev.* 92 (4 Nov. 1953), pp. 1045–1049. DOI: [10.1103/PhysRev.92.1045](https://doi.org/10.1103/PhysRev.92.1045). URL: <https://link.aps.org/doi/10.1103/PhysRev.92.1045>.
- [15] B. Pontecorvo. “Electron and Muon Neutrinos”. In: *Zh. Eksp. Teor. Fiz.* 37 (1959), pp. 1751–1757.
- [16] T. D. Lee and C. N. Yang. “Proceedings of International Conference on High Energy Physics, Rochester (New York: Interscience) P. 567, 1960”. In: (1960).

- [17] M. Schwartz. “Feasibility of Using High-Energy Neutrinos to Study the Weak Interactions”. In: *Phys. Rev. Lett.* 4 (6 Mar. 1960), pp. 306–307. DOI: [10.1103/PhysRevLett.4.306](https://doi.org/10.1103/PhysRevLett.4.306). URL: <https://link.aps.org/doi/10.1103/PhysRevLett.4.306>.
- [18] K. Kodama et al. “Final tau-neutrino results from the DONuT experiment”. In: *Phys. Rev. D* 78 (5 Sept. 2008), p. 052002. DOI: [10.1103/PhysRevD.78.052002](https://doi.org/10.1103/PhysRevD.78.052002). URL: <https://link.aps.org/doi/10.1103/PhysRevD.78.052002>.
- [19] S. Schael et al. “Precision electroweak measurements on the Z resonance”. In: *Phys. Rept.* 427 (2006), pp. 257–454. DOI: [10.1016/j.physrep.2005.12.006](https://doi.org/10.1016/j.physrep.2005.12.006). arXiv: [hep-ex/0509008](https://arxiv.org/abs/hep-ex/0509008).
- [20] Bruce T. Cleveland et al. “Measurement of the Solar Electron Neutrino Flux with the Homestake Chlorine Detector”. In: *The Astrophysical Journal* 496.1 (Mar. 1998), pp. 505–526. DOI: [10.1086/305343](https://doi.org/10.1086/305343). URL: <https://doi.org/10.1086/305343>.
- [21] Y. Fukuda et al. “Evidence for Oscillation of Atmospheric Neutrinos”. In: *Phys. Rev. Lett.* 81 (8 Aug. 1998), pp. 1562–1567. DOI: [10.1103/PhysRevLett.81.1562](https://doi.org/10.1103/PhysRevLett.81.1562). URL: <https://link.aps.org/doi/10.1103/PhysRevLett.81.1562>.
- [22] Q. R. Ahmad et al. “Direct Evidence for Neutrino Flavor Transformation from Neutral-Current Interactions in the Sudbury Neutrino Observatory”. In: *Phys. Rev. Lett.* 89 (1 June 2002), p. 011301. DOI: [10.1103/PhysRevLett.89.011301](https://doi.org/10.1103/PhysRevLett.89.011301). URL: <https://link.aps.org/doi/10.1103/PhysRevLett.89.011301>.
- [23] H. A. Bethe. “Energy Production in Stars”. In: *Phys. Rev.* 55 (5 Mar. 1939), pp. 434–456. DOI: [10.1103/PhysRev.55.434](https://doi.org/10.1103/PhysRev.55.434). URL: <https://link.aps.org/doi/10.1103/PhysRev.55.434>.
- [24] J N Bahcall. “Solar Models and Solar Neutrinos”. In: *Physica Scripta* T121 (Jan. 2005), pp. 46–50. DOI: [10.1088/0031-8949/2005/t121/006](https://doi.org/10.1088/0031-8949/2005/t121/006). URL: <https://doi.org/10.1088/0031-8949/2005/t121/006>.
- [25] K.S. Hirata et al. “Experimental study of the atmospheric neutrino flux”. In: *Physics Letters B* 205.2 (1988), pp. 416–420. ISSN: 0370-2693. DOI: [https://doi.org/10.1016/0370-2693\(88\)91690-5](https://doi.org/10.1016/0370-2693(88)91690-5). URL: <https://www.sciencedirect.com/science/article/pii/0370269388916905>.
- [26] K.S. Hirata et al. “Observation of a small atmospheric $\nu_{\mu\mu}/\nu_e$ ratio in Kamiokande”. In: *Physics Letters B* 280.1 (1992), pp. 146–152. ISSN:

- 0370-2693. DOI: [https://doi.org/10.1016/0370-2693\(92\)90788-6](https://doi.org/10.1016/0370-2693(92)90788-6). URL: <https://www.sciencedirect.com/science/article/pii/S0370269392907886>.
- [27] R. Becker-Szendy et al. “The Electron-neutrino and muon-neutrino content of the atmospheric flux”. In: *Phys. Rev. D* 46 (1992), pp. 3720–3724. DOI: [10.1103/PhysRevD.46.3720](https://doi.org/10.1103/PhysRevD.46.3720).
- [28] Christoph Berger et al. “A Study of atmospheric neutrino oscillations in the FREJUS experiment”. In: *Phys. Lett. B* 245 (1990), pp. 305–310. DOI: [10.1016/0370-2693\(90\)90150-5](https://doi.org/10.1016/0370-2693(90)90150-5).
- [29] V. Barger et al. “Neutrino Decay as an Explanation of Atmospheric Neutrino Observations”. In: *Phys. Rev. Lett.* 82 (13 Mar. 1999), pp. 2640–2643. DOI: [10.1103/PhysRevLett.82.2640](https://doi.org/10.1103/PhysRevLett.82.2640). URL: <https://link.aps.org/doi/10.1103/PhysRevLett.82.2640>.
- [30] B. Pontecorvo. “Mesonium and anti-mesonium”. In: *Sov. Phys. JETP* 6 (1957). [*Zh. Eksp. Teor. Fiz.*33,549(1957)], p. 429.
- [31] M. Gell-Mann and A. Pais. “Behavior of Neutral Particles under Charge Conjugation”. In: *Phys. Rev.* 97 (5 Mar. 1955), pp. 1387–1389. DOI: [10.1103/PhysRev.97.1387](https://doi.org/10.1103/PhysRev.97.1387). URL: <https://link.aps.org/doi/10.1103/PhysRev.97.1387>.
- [32] Samoil M. Bilenky and B. Pontecorvo. “Again on Neutrino Oscillations”. In: *Lett. Nuovo Cim.* 17 (1976), p. 569. DOI: [10.1007/BF02746567](https://doi.org/10.1007/BF02746567).
- [33] Samoil M. Bilenky and B. Pontecorvo. “Lepton Mixing and Neutrino Oscillations”. In: *Phys. Rept.* 41 (1978), pp. 225–261. DOI: [10.1016/0370-1573\(78\)90095-9](https://doi.org/10.1016/0370-1573(78)90095-9).
- [34] A. A. Aguilar-Arevalo et al. “Significant Excess of ElectronLike Events in the MiniBooNE Short-Baseline Neutrino Experiment”. In: *Phys. Rev. Lett.* 121.22 (2018), p. 221801. DOI: [10.1103/PhysRevLett.121.221801](https://doi.org/10.1103/PhysRevLett.121.221801). arXiv: [1805.12028](https://arxiv.org/abs/1805.12028) [hep-ex].
- [35] Steven Weinberg. “A Model of Leptons”. In: *Phys. Rev. Lett.* 19 (21 Nov. 1967), pp. 1264–1266. DOI: [10.1103/PhysRevLett.19.1264](https://doi.org/10.1103/PhysRevLett.19.1264). URL: <https://link.aps.org/doi/10.1103/PhysRevLett.19.1264>.
- [36] Abdus Salam. “Weak and Electromagnetic Interactions”. In: *Conf. Proc. C* 680519 (1968), pp. 367–377. DOI: [10.1142/9789812795915_0034](https://doi.org/10.1142/9789812795915_0034).
- [37] S. L. Glashow. “Partial Symmetries of Weak Interactions”. In: *Nucl. Phys.* 22 (1961), pp. 579–588. DOI: [10.1016/0029-5582\(61\)90469-2](https://doi.org/10.1016/0029-5582(61)90469-2).

- [38] Peter W. Higgs. “Broken symmetries, massless particles and gauge fields”. In: *Phys. Lett.* 12 (1964), pp. 132–133. DOI: [10.1016/0031-9163\(64\)91136-9](https://doi.org/10.1016/0031-9163(64)91136-9).
- [39] Peter W. Higgs. “Broken Symmetries and the Masses of Gauge Bosons”. In: *Phys. Rev. Lett.* 13 (16 Oct. 1964), pp. 508–509. DOI: [10.1103/PhysRevLett.13.508](https://doi.org/10.1103/PhysRevLett.13.508). URL: <https://link.aps.org/doi/10.1103/PhysRevLett.13.508>.
- [40] Peter W. Higgs. “Spontaneous Symmetry Breakdown without Massless Bosons”. In: *Phys. Rev.* 145 (4 May 1966), pp. 1156–1163. DOI: [10.1103/PhysRev.145.1156](https://doi.org/10.1103/PhysRev.145.1156). URL: <https://link.aps.org/doi/10.1103/PhysRev.145.1156>.
- [41] T. W. B. Kibble. “Symmetry Breaking in Non-Abelian Gauge Theories”. In: *Phys. Rev.* 155 (5 Mar. 1967), pp. 1554–1561. DOI: [10.1103/PhysRev.155.1554](https://doi.org/10.1103/PhysRev.155.1554). URL: <https://link.aps.org/doi/10.1103/PhysRev.155.1554>.
- [42] G. S. Guralnik, C. R. Hagen, and T. W. B. Kibble. “Global Conservation Laws and Massless Particles”. In: *Phys. Rev. Lett.* 13 (20 Nov. 1964), pp. 585–587. DOI: [10.1103/PhysRevLett.13.585](https://doi.org/10.1103/PhysRevLett.13.585). URL: <https://link.aps.org/doi/10.1103/PhysRevLett.13.585>.
- [43] F. Englert and R. Brout. “Broken Symmetry and the Mass of Gauge Vector Mesons”. In: *Phys. Rev. Lett.* 13 (9 Aug. 1964), pp. 321–323. DOI: [10.1103/PhysRevLett.13.321](https://doi.org/10.1103/PhysRevLett.13.321). URL: <https://link.aps.org/doi/10.1103/PhysRevLett.13.321>.
- [44] V. A. Rubakov. *Classical theory of gauge fields*. Princeton University Press, 2002. ISBN: 9780691059273. URL: <https://press.princeton.edu/books/hardcover/9780691059273/classical-theory-of-gauge-fields>.
- [45] C. S. Wu et al. “Experimental Test of Parity Conservation in Beta Decay”. In: *Phys. Rev.* 105 (4 Feb. 1957), pp. 1413–1415. DOI: [10.1103/PhysRev.105.1413](https://doi.org/10.1103/PhysRev.105.1413). URL: <https://link.aps.org/doi/10.1103/PhysRev.105.1413>.
- [46] Peter Renton. *Electroweak Interactions: An Introduction to the Physics of Quarks and Leptons*. Cambridge University Press, 1990. DOI: [10.1017/CB09780511608148](https://doi.org/10.1017/CB09780511608148).
- [47] E. C. G. Sudarshan and R. E. Marshak. “THE NATURE OF THE FOUR-FERMION INTERACTION”. In: *Current Science* 63.2 (1992),

- pp. 65–75. ISSN: 00113891. URL: <http://www.jstor.org/stable/24095422>.
- [48] E. C. G. Sudarshan and R. E. Marshak. “Chirality Invariance and the Universal Fermi Interaction”. In: *Phys. Rev.* 109 (5 Mar. 1958), pp. 1860–1862. DOI: [10.1103/PhysRev.109.1860.2](https://doi.org/10.1103/PhysRev.109.1860.2). URL: <https://link.aps.org/doi/10.1103/PhysRev.109.1860.2>.
- [49] R. P. Feynman and M. Gell-Mann. “Theory of the Fermi Interaction”. In: *Phys. Rev.* 109 (1 Jan. 1958), pp. 193–198. DOI: [10.1103/PhysRev.109.193](https://doi.org/10.1103/PhysRev.109.193). URL: <https://link.aps.org/doi/10.1103/PhysRev.109.193>.
- [50] J. J. Sakurai. “Mass reversal and weak interactions”. In: *Nuovo Cimento* 7.5 (Mar. 1958). ISSN: 0029-6341. DOI: [10.1007/BF02781569](https://doi.org/10.1007/BF02781569). URL: <https://www.osti.gov/biblio/4324864>.
- [51] Raymond Davis. “Solar Neutrinos. II. Experimental”. In: *Phys. Rev. Lett.* 12 (11 Mar. 1964), pp. 303–305. DOI: [10.1103/PhysRevLett.12.303](https://doi.org/10.1103/PhysRevLett.12.303). URL: <https://link.aps.org/doi/10.1103/PhysRevLett.12.303>.
- [52] Y. Fukuda et al. “Solar Neutrino Data Covering Solar Cycle 22”. In: *Phys. Rev. Lett.* 77 (9 Aug. 1996), pp. 1683–1686. DOI: [10.1103/PhysRevLett.77.1683](https://doi.org/10.1103/PhysRevLett.77.1683). URL: <https://link.aps.org/doi/10.1103/PhysRevLett.77.1683>.
- [53] S. Fukuda et al. “Solar ^8B and hep Neutrino Measurements from 1258 Days of Super-Kamiokande Data”. In: *Phys. Rev. Lett.* 86 (25 Jan. 2001), pp. 5651–5655. DOI: [10.1103/PhysRevLett.86.5651](https://doi.org/10.1103/PhysRevLett.86.5651). URL: <https://link.aps.org/doi/10.1103/PhysRevLett.86.5651>.
- [54] D. Vignaud. “The GALLEX solar neutrino experiment”. In: *Nuclear Physics B - Proceedings Supplements* 60.3 (1998), pp. 20–29. ISSN: 0920-5632. DOI: [https://doi.org/10.1016/S0920-5632\(97\)00498-2](https://doi.org/10.1016/S0920-5632(97)00498-2). URL: <https://www.sciencedirect.com/science/article/pii/S0920563297004982>.
- [55] V.N. Gavrin et al. “Sage: The Soviet-American gallium solar neutrino experiment”. In: *Nuclear Physics B - Proceedings Supplements* 28.1 (1992), pp. 75–81. ISSN: 0920-5632. DOI: [https://doi.org/10.1016/0920-5632\(92\)90149-M](https://doi.org/10.1016/0920-5632(92)90149-M). URL: <https://www.sciencedirect.com/science/article/pii/092056329290149M>.
- [56] Y. Ashie et al. “Measurement of atmospheric neutrino oscillation parameters by Super-Kamiokande I”. In: *Phys. Rev. D* 71 (11 June 2005),

- p. 112005. DOI: [10.1103/PhysRevD.71.112005](https://doi.org/10.1103/PhysRevD.71.112005). URL: <https://link.aps.org/doi/10.1103/PhysRevD.71.112005>.
- [57] M. C. Gonzalez-Garcia et al. “Atmospheric Neutrino Observations and Flavor Changing Interactions”. In: *Phys. Rev. Lett.* 82 (16 Apr. 1999), pp. 3202–3205. DOI: [10.1103/PhysRevLett.82.3202](https://doi.org/10.1103/PhysRevLett.82.3202). URL: <https://link.aps.org/doi/10.1103/PhysRevLett.82.3202>.
- [58] J. C. Romão et al. “Supersymmetric solution to the solar and atmospheric neutrino problems”. In: *Phys. Rev. D* 61 (7 Mar. 2000), p. 071703. DOI: [10.1103/PhysRevD.61.071703](https://doi.org/10.1103/PhysRevD.61.071703). URL: <https://link.aps.org/doi/10.1103/PhysRevD.61.071703>.
- [59] A. M. Gago, H. Nunokawa, and R. Zukanovich Funchal. “Solar Neutrino Problem and Gravitationally Induced Long-Wavelength Neutrino Oscillation”. In: *Phys. Rev. Lett.* 84 (18 May 2000), pp. 4035–4038. DOI: [10.1103/PhysRevLett.84.4035](https://doi.org/10.1103/PhysRevLett.84.4035). URL: <https://link.aps.org/doi/10.1103/PhysRevLett.84.4035>.
- [60] B. Pontecorvo. “Inverse beta processes and nonconservation of lepton charge”. In: *Sov. Phys. JETP* 7 (1958). [*Zh. Eksp. Teor. Fiz.*34,247(1957)], pp. 172–173.
- [61] B. Pontecorvo. “Neutrino Experiments and the Problem of Conservation of Leptonic Charge”. In: *Sov. Phys. JETP* 26 (1968). [*Zh. Eksp. Teor. Fiz.*53,1717(1967)], pp. 984–988.
- [62] V. Gribov and B. Pontecorvo. “Neutrino astronomy and lepton charge”. In: *Physics Letters B* 28.7 (1969), pp. 493–496. ISSN: 0370-2693. DOI: [http://dx.doi.org/10.1016/0370-2693\(69\)90525-5](http://dx.doi.org/10.1016/0370-2693(69)90525-5). URL: <http://www.sciencedirect.com/science/article/pii/0370269369905255>.
- [63] S.M. Bilenky and B. Pontecorvo. “Lepton mixing and neutrino oscillations”. In: *Physics Reports* 41.4 (1978), pp. 225–261. ISSN: 0370-1573. DOI: [http://dx.doi.org/10.1016/0370-1573\(78\)90095-9](http://dx.doi.org/10.1016/0370-1573(78)90095-9). URL: <http://www.sciencedirect.com/science/article/pii/0370157378900959>.
- [64] J. Beringer et al. “Review of Particle Physics”. In: *Phys. Rev. D* 86 (1 July 2012), p. 010001. DOI: [10.1103/PhysRevD.86.010001](https://doi.org/10.1103/PhysRevD.86.010001). URL: <https://link.aps.org/doi/10.1103/PhysRevD.86.010001>.
- [65] C. Jarlskog. “A basis independent formulation of the connection between quark mass matrices, CP violation and experiment”. In: *Zeitschrift für Physik C Particles and Fields* 29.3 (1985), pp. 491–497. ISSN: 1431-

5858. DOI: [10.1007/BF01565198](https://doi.org/10.1007/BF01565198). URL: <http://dx.doi.org/10.1007/BF01565198>.
- [66] X. Qian and P. Vogel. “Neutrino mass hierarchy”. In: *Progress in Particle and Nuclear Physics* 83 (2015), pp. 1–30. ISSN: 0146-6410. DOI: <https://doi.org/10.1016/j.pnpnp.2015.05.002>. URL: <https://www.sciencedirect.com/science/article/pii/S0146641015000307>.
- [67] L. Wolfenstein. “Neutrino oscillations in matter”. In: *Phys. Rev. D* 17 (9 May 1978), pp. 2369–2374. DOI: [10.1103/PhysRevD.17.2369](https://doi.org/10.1103/PhysRevD.17.2369). URL: <https://link.aps.org/doi/10.1103/PhysRevD.17.2369>.
- [68] S. P. Mikheyev and A. Yu. Smirnov. “Resonance Amplification of Oscillations in Matter and Spectroscopy of Solar Neutrinos”. In: *Sov. J. Nucl. Phys.* 42 (1985), pp. 913–917.
- [69] S. P. Mikheev and A. Yu. Smirnov. “Resonant amplification of neutrino oscillations in matter and solar neutrino spectroscopy”. In: *Nuovo Cim. C* 9 (1986), pp. 17–26. DOI: [10.1007/BF02508049](https://doi.org/10.1007/BF02508049).
- [70] Carlo Giunti and Chung W Kim. *Fundamentals of neutrino physics and astrophysics*. Oxford university press, 2007. DOI: [10.1093/acprof:oso/9780198508717.001.0001](https://doi.org/10.1093/acprof:oso/9780198508717.001.0001).
- [71] A. M. Gago Medina. “Solucões de grande comprimento de oscilacao para o problema de neutrinos solares”. PhD thesis. Universidade de Sao Paulo, Mar. 2001. DOI: [10.11606/T.43.2001.tde-04122013-105222](https://doi.org/10.11606/T.43.2001.tde-04122013-105222).
- [72] Ivan Esteban et al. “The fate of hints: updated global analysis of three-flavor neutrino oscillations”. In: *JHEP* 09 (2020), p. 178. DOI: [10.1007/JHEP09\(2020\)178](https://doi.org/10.1007/JHEP09(2020)178). arXiv: [2007.14792](https://arxiv.org/abs/2007.14792) [hep-ph].
- [73] C.H. Llewellyn Smith. “Neutrino reactions at accelerator energies”. In: *Physics Reports* 3.5 (1972), pp. 261–379. ISSN: 0370-1573. DOI: [https://doi.org/10.1016/0370-1573\(72\)90010-5](https://doi.org/10.1016/0370-1573(72)90010-5). URL: <https://www.sciencedirect.com/science/article/pii/0370157372900105>.
- [74] Teppei Katori. “A Measurement of the muon neutrino charged current quasielastic interaction and a test of Lorentz violation with the Mini-BooNE experiment”. PhD dissertation. Indiana University, 2008. DOI: [10.2172/945410](https://doi.org/10.2172/945410). URL: <https://www.osti.gov/biblio/945410>.
- [75] A. Mann. *Calculate like a Llewellyn*. Tech. rep. MINERvA DocBD 18203. Tufts University, 2018. URL: <https://minerva-docdb.fnal.gov/cgi-bin/sso/ShowDocument?docid=18203>.

- [76] Dieter Rein and Lalit M. Sehgal. “Neutrino Excitation of Baryon Resonances and Single Pion Production”. In: *Annals Phys.* 133 (1981), pp. 79–153. DOI: [10.1016/0003-4916\(81\)90242-6](https://doi.org/10.1016/0003-4916(81)90242-6).
- [77] G. Breit and E. Wigner. “Capture of Slow Neutrons”. In: *Phys. Rev.* 49 (7 Mar. 1936), pp. 519–531. DOI: [10.1103/PhysRev.49.519](https://doi.org/10.1103/PhysRev.49.519). URL: <https://link.aps.org/doi/10.1103/PhysRev.49.519>.
- [78] Rabindra N Mohapatra and Palash B Pal. *Massive Neutrinos in Physics and Astrophysics*. 3rd. WORLD SCIENTIFIC, 2004. DOI: [10.1142/5024](https://doi.org/10.1142/5024). eprint: <https://www.worldscientific.com/doi/pdf/10.1142/5024>. URL: <https://www.worldscientific.com/doi/abs/10.1142/5024>.
- [79] J I Friedman and H W Kendall. “Deep Inelastic Electron Scattering”. In: *Annual Review of Nuclear Science* 22.1 (1972), pp. 203–254. DOI: [10.1146/annurev.ns.22.120172.001223](https://doi.org/10.1146/annurev.ns.22.120172.001223). eprint: <https://doi.org/10.1146/annurev.ns.22.120172.001223>. URL: <https://doi.org/10.1146/annurev.ns.22.120172.001223>.
- [80] A. De Roeck and R.S. Thorne. “Structure functions”. In: *Progress in Particle and Nuclear Physics* 66.4 (2011), pp. 727–781. ISSN: 0146-6410. DOI: <https://doi.org/10.1016/j.pnpnp.2011.06.001>. URL: <https://www.sciencedirect.com/science/article/pii/S0146641011000937>.
- [81] R.A. Smith and E.J. Moniz. “Neutrino reactions on nuclear targets”. In: *Nuclear Physics B* 43 (1972), pp. 605–622. ISSN: 0550-3213. DOI: [https://doi.org/10.1016/0550-3213\(72\)90040-5](https://doi.org/10.1016/0550-3213(72)90040-5). URL: <https://www.sciencedirect.com/science/article/pii/0550321372900405>.
- [82] Costas Andreopoulos et al. “The GENIE Neutrino Monte Carlo Generator: Physics and User Manual”. In: (Oct. 2015). arXiv: [1510.05494](https://arxiv.org/abs/1510.05494) [hep-ph].
- [83] W. Kohn and L. J. Sham. “Self-Consistent Equations Including Exchange and Correlation Effects”. In: *Phys. Rev.* 140 (4A Nov. 1965), A1133–A1138. DOI: [10.1103/PhysRev.140.A1133](https://doi.org/10.1103/PhysRev.140.A1133). URL: <https://link.aps.org/doi/10.1103/PhysRev.140.A1133>.
- [84] S. K. Singh and E. Oset. “Inclusive quasielastic neutrino reactions in ^{12}C and ^{16}O at intermediate energies”. In: *Phys. Rev. C* 48 (3 Sept. 1993), pp. 1246–1258. DOI: [10.1103/PhysRevC.48.1246](https://doi.org/10.1103/PhysRevC.48.1246). URL: <https://link.aps.org/doi/10.1103/PhysRevC.48.1246>.

- [85] T. S. Kosmas and E. Oset. “Charged current neutrino-nucleus reaction cross sections at intermediate energies”. In: *Phys. Rev. C* 53 (3 Mar. 1996), pp. 1409–1415. DOI: [10.1103/PhysRevC.53.1409](https://doi.org/10.1103/PhysRevC.53.1409). URL: <https://link.aps.org/doi/10.1103/PhysRevC.53.1409>.
- [86] Tomasz Golan. “Modeling nuclear effects in NuWro Monte Carlo neutrino event generator”. PhD dissertation. University of Wrocław, 2014. URL: http://wng.ift.uni.wroc.pl/files/Golan_PhD.pdf.
- [87] Omar Benhar and Nicola Farina. “Neutrino-nucleus cross section in the impulse approximation regime”. In: *Nucl. Phys. B Proc. Suppl.* 139 (2005). Ed. by F. Cavanna et al., pp. 230–233. DOI: [10.1016/j.nuclphysbps.2004.11.233](https://doi.org/10.1016/j.nuclphysbps.2004.11.233). arXiv: [nucl-th/0407106](https://arxiv.org/abs/nucl-th/0407106).
- [88] Artur M. Ankowski and Jan T. Sobczyk. “Construction of spectral functions for medium-mass nuclei”. In: *Phys. Rev. C* 77 (4 Apr. 2008), p. 044311. DOI: [10.1103/PhysRevC.77.044311](https://doi.org/10.1103/PhysRevC.77.044311). URL: <https://link.aps.org/doi/10.1103/PhysRevC.77.044311>.
- [89] Maria Goeppert Mayer. “The shell model”. In: *Science* 145.3636 (1964), pp. 999–1006.
- [90] O. Benhar et al. “Spectral function of finite nuclei and scattering of GeV electrons”. In: *Nuclear Physics A* 579.3 (1994), pp. 493–517. ISSN: 0375-9474. DOI: [https://doi.org/10.1016/0375-9474\(94\)90920-2](https://doi.org/10.1016/0375-9474(94)90920-2). URL: <https://www.sciencedirect.com/science/article/pii/0375947494909202>.
- [91] P K A de Witt Huberts. “Proton spectral functions and momentum distributions in nuclei from high-resolution (e,e’p) experiments”. In: *Journal of Physics G: Nuclear and Particle Physics* 16.4 (Apr. 1990), pp. 507–544. DOI: [10.1088/0954-3899/16/4/004](https://doi.org/10.1088/0954-3899/16/4/004). URL: <https://doi.org/10.1088/0954-3899/16/4/004>.
- [92] S. Frullani and J. Mougey. “Single Particle Properties of Nuclei Through (e, e’ p) Reactions”. In: *Adv. Nucl. Phys.* 14 (1984), pp. 1–283.
- [93] Artur M. Ankowski. “Efekty jądrowe w oddziaływaniach neutrin”. PhD dissertation. University of Wrocław, 2008. URL: http://wng.ift.uni.wroc.pl/files/Ankowski_PhD.pdf.
- [94] J. Nieves, J. E. Amaro, and M. Valverde. “Inclusive quasielastic charged-current neutrino-nucleus reactions”. In: *Phys. Rev. C* 70 (5 Nov. 2004), p. 055503. DOI: [10.1103/PhysRevC.70.055503](https://doi.org/10.1103/PhysRevC.70.055503). URL: <https://link.aps.org/doi/10.1103/PhysRevC.70.055503>.

- [95] David Pines. “A Collective Description of Electron Interactions: IV. Electron Interaction in Metals”. In: *Phys. Rev.* 92 (3 Nov. 1953), pp. 626–636. DOI: [10.1103/PhysRev.92.626](https://doi.org/10.1103/PhysRev.92.626). URL: <https://link.aps.org/doi/10.1103/PhysRev.92.626>.
- [96] David Bohm and David Pines. “A Collective Description of Electron Interactions: III. Coulomb Interactions in a Degenerate Electron Gas”. In: *Phys. Rev.* 92 (3 Nov. 1953), pp. 609–625. DOI: [10.1103/PhysRev.92.609](https://doi.org/10.1103/PhysRev.92.609). URL: <https://link.aps.org/doi/10.1103/PhysRev.92.609>.
- [97] A. Gil, J. Nieves, and E. Oset. “Many-body approach to the inclusive (e, e') reaction from the quasielastic to the Δ excitation region”. In: *Nuclear Physics A* 627.4 (1997), pp. 543–598. ISSN: 0375-9474. DOI: [https://doi.org/10.1016/S0375-9474\(97\)00513-7](https://doi.org/10.1016/S0375-9474(97)00513-7). URL: <https://www.sciencedirect.com/science/article/pii/S0375947497005137>.
- [98] Robert Jastrow. “Many-Body Problem with Strong Forces”. In: *Phys. Rev.* 98 (5 June 1955), pp. 1479–1484. DOI: [10.1103/PhysRev.98.1479](https://doi.org/10.1103/PhysRev.98.1479). URL: <https://link.aps.org/doi/10.1103/PhysRev.98.1479>.
- [99] Nadia Fomin et al. “New Results on Short-Range Correlations in Nuclei”. In: *Annual Review of Nuclear and Particle Science* 67.1 (2017), pp. 129–159. DOI: [10.1146/annurev-nucl-102115-044939](https://doi.org/10.1146/annurev-nucl-102115-044939). eprint: <https://doi.org/10.1146/annurev-nucl-102115-044939>. URL: <https://doi.org/10.1146/annurev-nucl-102115-044939>.
- [100] M. Duer et al. “Probing high-momentum protons and neutrons in neutron-rich nuclei”. In: *Nature* 560.7720 (2018), pp. 617–621. DOI: [10.1038/s41586-018-0400-z](https://doi.org/10.1038/s41586-018-0400-z). URL: <https://doi.org/10.1038/s41586-018-0400-z>.
- [101] R. Subedi et al. “Probing Cold Dense Nuclear Matter”. In: *Science* 320.5882 (2008), pp. 1476–1478. ISSN: 0036-8075. DOI: [10.1126/science.1156675](https://doi.org/10.1126/science.1156675). URL: <https://science.sciencemag.org/content/320/5882/1476>.
- [102] E. Piassetzky et al. “Evidence for Strong Dominance of Proton-Neutron Correlations in Nuclei”. In: *Phys. Rev. Lett.* 97 (16 Oct. 2006), p. 162504. DOI: [10.1103/PhysRevLett.97.162504](https://doi.org/10.1103/PhysRevLett.97.162504). URL: <https://link.aps.org/doi/10.1103/PhysRevLett.97.162504>.
- [103] R. Schiavilla et al. “Tensor Forces and the Ground-State Structure of Nuclei”. In: *Phys. Rev. Lett.* 98 (13 Mar. 2007), p. 132501. DOI: [10.1103/PhysRevLett.98.132501](https://doi.org/10.1103/PhysRevLett.98.132501). URL: <https://link.aps.org/doi/10.1103/PhysRevLett.98.132501>.

BIBLIOGRAPHY

- [104] M. M. Sargsian et al. “Exclusive electrodisintegration of ^3He at high Q^2 . II. Decay function formalism”. In: *Phys. Rev. C* 71 (4 Apr. 2005), p. 044615. DOI: [10.1103/PhysRevC.71.044615](https://doi.org/10.1103/PhysRevC.71.044615). URL: <https://link.aps.org/doi/10.1103/PhysRevC.71.044615>.
- [105] R. Weiss et al. “The nuclear contacts and short range correlations in nuclei”. In: *Physics Letters B* 780 (2018), pp. 211–215. ISSN: 0370-2693. DOI: <https://doi.org/10.1016/j.physletb.2018.01.061>. URL: <https://www.sciencedirect.com/science/article/pii/S0370269318300777>.
- [106] B. Schmookler et al. “Modified structure of protons and neutrons in correlated pairs”. In: *Nature* 566.7744 (2019), pp. 354–358. DOI: [10.1038/s41586-019-0925-9](https://doi.org/10.1038/s41586-019-0925-9). arXiv: [2004.12065](https://arxiv.org/abs/2004.12065) [nucl-ex].
- [107] P. Barreau et al. “Deep Inelastic electron Scattering from Carbon”. In: *Nucl. Phys. A* 402 (1983), pp. 515–540. DOI: [10.1016/0375-9474\(83\)90217-8](https://doi.org/10.1016/0375-9474(83)90217-8).
- [108] SG Mashnik et al. “CEM03 and LAQGSM03—new modeling tools for nuclear applications”. In: *Journal of Physics: Conference Series*. 1. 2006.
- [109] G. D. Harp. “Extension of the isobar model for intranuclear cascades to 1 GeV”. In: *Phys. Rev. C* 10 (6 Dec. 1974), pp. 2387–2396. DOI: [10.1103/PhysRevC.10.2387](https://doi.org/10.1103/PhysRevC.10.2387). URL: <https://link.aps.org/doi/10.1103/PhysRevC.10.2387>.
- [110] AM Gago et al. “Quantum dissipative effects and neutrinos: Current constraints and future perspectives”. In: *Physical Review D* 63.7 (2001), p. 073001.
- [111] A. M. Gago et al. “A Study on quantum decoherence phenomena with three generations of neutrinos”. In: (Aug. 2002). arXiv: [hep-ph/0208166](https://arxiv.org/abs/hep-ph/0208166).
- [112] GL Fogli et al. “Solar neutrino oscillation parameters after first KamLAND results”. In: *Physical Review D* 67.7 (2003), p. 073002.
- [113] Dean Morgan et al. “Probing quantum decoherence in atmospheric neutrino oscillations with a neutrino telescope”. In: *Astroparticle Physics* 25.5 (2006), pp. 311–327.
- [114] E Lisi, A Marrone, and D Montanino. “Probing possible decoherence effects in atmospheric neutrino oscillations”. In: *Physical Review Letters* 85.6 (2000), p. 1166.

- [115] Dan Hooper, Dean Morgan, and Elizabeth Winstanley. “Probing quantum decoherence with high-energy neutrinos”. In: *Physics Letters B* 609.3-4 (2005), pp. 206–211.
- [116] Yasaman Farzan, Thomas Schwetz, and Alexei Yu Smirnov. “Reconciling results of LSND, MiniBooNE and other experiments with soft decoherence”. In: *JHEP* 07 (2008), p. 067. DOI: [10.1088/1126-6708/2008/07/067](https://doi.org/10.1088/1126-6708/2008/07/067). arXiv: [0805.2098](https://arxiv.org/abs/0805.2098) [hep-ph].
- [117] RLN Oliveira and MM Guzzo. “Quantum dissipation in vacuum neutrino oscillation”. In: *The European Physical Journal C* 69.3 (2010), pp. 493–502.
- [118] Roberto Leandro Neves de Oliveira. “Dissipação quântica em oscilações de neutrinos”. In: (2013).
- [119] RLN Oliveira and MM Guzzo. “Dissipation and θ_{13} in neutrino oscillations”. In: *The European Physical Journal C* 73.5 (2013), pp. 1–10.
- [120] Jeffrey M Berryman et al. “Non-unitary neutrino propagation from neutrino decay”. In: *Physics Letters B* 742 (2015), pp. 74–79.
- [121] Jose Carpio, E. Massoni, and A. M. Gago. “Revisiting quantum decoherence for neutrino oscillations in matter with constant density”. In: *Phys. Rev. D* 97.11 (2018), p. 115017. DOI: [10.1103/PhysRevD.97.115017](https://doi.org/10.1103/PhysRevD.97.115017). arXiv: [1711.03680](https://arxiv.org/abs/1711.03680) [hep-ph].
- [122] Pilar Coloma et al. “Decoherence in Neutrino Propagation Through Matter, and Bounds from IceCube/DeepCore”. In: *Eur. Phys. J. C* 78.8 (2018), p. 614. DOI: [10.1140/epjc/s10052-018-6092-6](https://doi.org/10.1140/epjc/s10052-018-6092-6). arXiv: [1803.04438](https://arxiv.org/abs/1803.04438) [hep-ph].
- [123] Maria Concepcion Gonzalez-Garcia et al. “Atmospheric neutrino observations and flavor changing interactions”. In: *Physical Review Letters* 82.16 (1999), p. 3202.
- [124] S Bergmann et al. “Status of the solution to the solar neutrino problem based on nonstandard neutrino interactions”. In: *Physical Review D* 62.7 (2000), p. 073001.
- [125] MM Guzzo, PC De Holanda, and OLG Peres. “Effects of non-standard neutrino interactions on MSW-LMA solution to the solar neutrino problem”. In: *Physics Letters B* 591.1-2 (2004), pp. 1–6.

BIBLIOGRAPHY

- [126] AM Gago et al. “Global analysis of the post-SNO solar neutrino data for standard and nonstandard oscillation mechanisms”. In: *Physical Review D* 65.7 (2002), p. 073012.
- [127] AM Gago et al. “Probing flavor changing neutrino interactions using neutrino beams from a muon storage ring”. In: *Physical Review D* 64.7 (2001), p. 073003.
- [128] GL Fogli et al. “Probing nonstandard decoherence effects with solar and KamLAND neutrinos”. In: *Physical Review D* 76.3 (2007), p. 033006.
- [129] Tommy Ohlsson. “Status of non-standard neutrino interactions”. In: *Reports on Progress in Physics* 76.4 (2013), p. 044201.
- [130] Arman Esmaili and Alexei Yu. Smirnov. “Probing Non-Standard Interaction of Neutrinos with IceCube and DeepCore”. In: *JHEP* 06 (2013), p. 026. DOI: [10.1007/JHEP06\(2013\)026](https://doi.org/10.1007/JHEP06(2013)026). arXiv: [1304.1042](https://arxiv.org/abs/1304.1042) [hep-ph].
- [131] M. V. Ascencio-Sosa et al. “Matter effects in neutrino visible decay at future long-baseline experiments”. In: *Eur. Phys. J. C* 78.10 (2018), p. 809. DOI: [10.1140/epjc/s10052-018-6276-0](https://doi.org/10.1140/epjc/s10052-018-6276-0). arXiv: [1805.03279](https://arxiv.org/abs/1805.03279) [hep-ph].
- [132] John N. Bahcall, Nicola Cabibbo, and Amos Yahil. “Are Neutrinos Stable Particles?” In: *Phys. Rev. Lett.* 28 (5 Jan. 1972), pp. 316–318. DOI: [10.1103/PhysRevLett.28.316](https://doi.org/10.1103/PhysRevLett.28.316). URL: <https://link.aps.org/doi/10.1103/PhysRevLett.28.316>.
- [133] Y. Chikashige, Rabindra N. Mohapatra, and R. D. Peccei. “Are There Real Goldstone Bosons Associated with Broken Lepton Number?” In: *Phys. Lett. B* 98 (1981), pp. 265–268. DOI: [10.1016/0370-2693\(81\)90011-3](https://doi.org/10.1016/0370-2693(81)90011-3).
- [134] G.B. Gelmini and M. Roncadelli. “Left-handed neutrino mass scale and spontaneously broken lepton number”. In: *Physics Letters B* 99.5 (1981), pp. 411–415. ISSN: 0370-2693. DOI: [https://doi.org/10.1016/0370-2693\(81\)90559-1](https://doi.org/10.1016/0370-2693(81)90559-1). URL: <https://www.sciencedirect.com/science/article/pii/0370269381905591>.
- [135] J. Schechter and J. W. F. Valle. “Neutrino decay and spontaneous violation of lepton number”. In: *Phys. Rev. D* 25 (3 Feb. 1982), pp. 774–783. DOI: [10.1103/PhysRevD.25.774](https://doi.org/10.1103/PhysRevD.25.774). URL: <https://link.aps.org/doi/10.1103/PhysRevD.25.774>.
- [136] David B. Reiss. “Can the family group be a global symmetry?” In: *Physics Letters B* 115.3 (1982), pp. 217–220. ISSN: 0370-2693. DOI:

- [https://doi.org/10.1016/0370-2693\(82\)90647-5](https://doi.org/10.1016/0370-2693(82)90647-5). URL: <https://www.sciencedirect.com/science/article/pii/0370269382906475>.
- [137] L. Dorame, O. G. Miranda, and J. W. F. Valle. “Invisible decays of ultra-high energy neutrinos”. In: *Front. in Phys.* 1 (2013), p. 25. DOI: [10.3389/fphy.2013.00025](https://doi.org/10.3389/fphy.2013.00025). arXiv: [1303.4891](https://arxiv.org/abs/1303.4891) [hep-ph].
- [138] I. Z. Rothstein, K. S. Babu, and D. Seckel. “Planck scale symmetry breaking and majoron physics”. In: *Nucl. Phys. B* 403 (1993), pp. 725–748. DOI: [10.1016/0550-3213\(93\)90368-Y](https://doi.org/10.1016/0550-3213(93)90368-Y). arXiv: [hep-ph/9301213](https://arxiv.org/abs/hep-ph/9301213).
- [139] C. Giunti et al. “Majoron decay of neutrinos in matter”. In: *Phys. Rev. D* 45 (5 Mar. 1992), pp. 1557–1568. DOI: [10.1103/PhysRevD.45.1557](https://doi.org/10.1103/PhysRevD.45.1557). URL: <https://link.aps.org/doi/10.1103/PhysRevD.45.1557>.
- [140] P. Astier et al. “Search for $\nu(\mu) \rightarrow \nu(e)$ oscillations in the NOMAD experiment”. In: *Phys. Lett. B* 570 (2003), pp. 19–31. DOI: [10.1016/j.physletb.2003.07.029](https://doi.org/10.1016/j.physletb.2003.07.029). arXiv: [hep-ex/0306037](https://arxiv.org/abs/hep-ex/0306037).
- [141] Manfred Lindner, Tommy Ohlsson, and Walter Winter. “Decays of supernova neutrinos”. In: *Nucl. Phys. B* 622 (2002), pp. 429–456. DOI: [10.1016/S0550-3213\(01\)00603-4](https://doi.org/10.1016/S0550-3213(01)00603-4). arXiv: [astro-ph/0105309](https://arxiv.org/abs/astro-ph/0105309).
- [142] Manfred Lindner, Tommy Ohlsson, and Walter Winter. “A Combined treatment of neutrino decay and neutrino oscillations”. In: *Nucl. Phys. B* 607 (2001), pp. 326–354. DOI: [10.1016/S0550-3213\(01\)00237-1](https://doi.org/10.1016/S0550-3213(01)00237-1). arXiv: [hep-ph/0103170](https://arxiv.org/abs/hep-ph/0103170).
- [143] Mattias Blennow, Tommy Ohlsson, and Walter Winter. “Damping signatures in future neutrino oscillation experiments”. In: *JHEP* 06 (2005), p. 049. DOI: [10.1088/1126-6708/2005/06/049](https://doi.org/10.1088/1126-6708/2005/06/049). arXiv: [hep-ph/0502147](https://arxiv.org/abs/hep-ph/0502147).
- [144] C. W. Kim and W. P. Lam. “Some remarks on neutrino decay via a Nambu-Goldstone boson”. In: *Mod. Phys. Lett. A* 5 (1990), pp. 297–299. DOI: [10.1142/S0217732390000354](https://doi.org/10.1142/S0217732390000354).
- [145] Alberto M. Gago et al. “Visible neutrino decay in the light of appearance and disappearance long baseline experiments”. In: *JHEP* 11 (2017), p. 022. DOI: [10.1007/JHEP11\(2017\)022](https://doi.org/10.1007/JHEP11(2017)022). arXiv: [1705.03074](https://arxiv.org/abs/1705.03074) [hep-ph].
- [146] Sergio Palomares-Ruiz, Silvia Pascoli, and Thomas Schwetz. “Explaining LSND by a decaying sterile neutrino”. In: *JHEP* 09 (2005), p. 048. DOI: [10.1088/1126-6708/2005/09/048](https://doi.org/10.1088/1126-6708/2005/09/048). arXiv: [hep-ph/0505216](https://arxiv.org/abs/hep-ph/0505216).

- [147] P. A. R. Ade et al. “Planck 2013 results. XVI. Cosmological parameters”. In: *Astron. Astrophys.* 571 (2014), A16. DOI: [10.1051/0004-6361/201321591](https://doi.org/10.1051/0004-6361/201321591). arXiv: [1303.5076](https://arxiv.org/abs/1303.5076) [astro-ph.CO].
- [148] R. Acciarri et al. “Long-Baseline Neutrino Facility (LBNF) and Deep Underground Neutrino Experiment (DUNE): Conceptual Design Report, Volume 2: The Physics Program for DUNE at LBNF”. In: (Dec. 2015). arXiv: [1512.06148](https://arxiv.org/abs/1512.06148) [physics.ins-det].
- [149] B. Abi et al. “The DUNE Far Detector Interim Design Report Volume 1: Physics, Technology and Strategies”. In: (July 2018). arXiv: [1807.10334](https://arxiv.org/abs/1807.10334) [physics.ins-det].
- [150] Adam Abed Abud et al. “Deep Underground Neutrino Experiment (DUNE) Near Detector Conceptual Design Report”. In: (Mar. 2021). arXiv: [2103.13910](https://arxiv.org/abs/2103.13910) [physics.ins-det].
- [151] Babak Abi et al. “Deep Underground Neutrino Experiment (DUNE), Far Detector Technical Design Report, Volume III: DUNE Far Detector Technical Coordination”. In: *JINST* 15.08 (2020), T08009. DOI: [10.1088/1748-0221/15/08/T08009](https://doi.org/10.1088/1748-0221/15/08/T08009). arXiv: [2002.03008](https://arxiv.org/abs/2002.03008) [physics.ins-det].
- [152] Babak Abi et al. “Deep Underground Neutrino Experiment (DUNE), Far Detector Technical Design Report, Volume I Introduction to DUNE”. In: *JINST* 15.08 (2020), T08008. DOI: [10.1088/1748-0221/15/08/T08008](https://doi.org/10.1088/1748-0221/15/08/T08008). arXiv: [2002.02967](https://arxiv.org/abs/2002.02967) [physics.ins-det].
- [153] T. Alion et al. “Experiment Simulation Configurations Used in DUNE CDR”. In: (June 2016). arXiv: [1606.09550](https://arxiv.org/abs/1606.09550) [physics.ins-det].
- [154] X. Bertou. “The ANDES underground laboratory”. In: *Eur. Phys. J. Plus* 127 (2012), p. 104. DOI: [10.1140/epjp/i2012-12104-1](https://doi.org/10.1140/epjp/i2012-12104-1).
- [155] P. A. N. Machado et al. “Potential of a neutrino detector in the ANDES underground laboratory for geophysics and astrophysics of neutrinos”. In: *Phys. Rev. D* 86 (12 Dec. 2012), p. 125001. DOI: [10.1103/PhysRevD.86.125001](https://doi.org/10.1103/PhysRevD.86.125001). URL: <https://link.aps.org/doi/10.1103/PhysRevD.86.125001>.
- [156] Frank D. Stacey and Paul M. Davis. “Earth, Density Distribution”. In: *Encyclopedia of Solid Earth Geophysics*. Ed. by Harsh K. Gupta. Dordrecht: Springer Netherlands, 2011, pp. 133–137. ISBN: 978-90-481-8702-7. DOI: [10.1007/978-90-481-8702-7_100](https://doi.org/10.1007/978-90-481-8702-7_100). URL: https://doi.org/10.1007/978-90-481-8702-7_100.

BIBLIOGRAPHY

- [157] Adam M. Dziewonski and Don L. Anderson. “Preliminary reference Earth model”. In: *Physics of the Earth and Planetary Interiors* 25.4 (1981), pp. 297–356. ISSN: 0031-9201. DOI: [https://doi.org/10.1016/0031-9201\(81\)90046-7](https://doi.org/10.1016/0031-9201(81)90046-7). URL: <https://www.sciencedirect.com/science/article/pii/0031920181900467>.
- [158] Ivan Esteban et al. “Updated fit to three neutrino mixing: exploring the accelerator-reactor complementarity”. In: *JHEP* 01 (2017), p. 087. DOI: [10.1007/JHEP01\(2017\)087](https://doi.org/10.1007/JHEP01(2017)087). arXiv: [1611.01514](https://arxiv.org/abs/1611.01514) [hep-ph].
- [159] Sandhya Choubey, Srubabati Goswami, and Dipyaman Pramanik. “A study of invisible neutrino decay at DUNE and its effects on θ_{23} measurement”. In: *JHEP* 02 (2018), p. 055. DOI: [10.1007/JHEP02\(2018\)055](https://doi.org/10.1007/JHEP02(2018)055). arXiv: [1705.05820](https://arxiv.org/abs/1705.05820) [hep-ph].
- [160] Pilar Coloma and Orlando L. G. Peres. “Visible neutrino decay at DUNE”. In: (May 2017). arXiv: [1705.03599](https://arxiv.org/abs/1705.03599) [hep-ph].
- [161] Patrick Huber et al. “New features in the simulation of neutrino oscillation experiments with GLoBES 3.0: General Long Baseline Experiment Simulator”. In: *Comput. Phys. Commun.* 177 (2007), pp. 432–438. DOI: [10.1016/j.cpc.2007.05.004](https://doi.org/10.1016/j.cpc.2007.05.004). arXiv: [hep-ph/0701187](https://arxiv.org/abs/hep-ph/0701187).
- [162] Patrick Huber, M. Lindner, and W. Winter. “Simulation of long-baseline neutrino oscillation experiments with GLoBES (General Long Baseline Experiment Simulator)”. In: *Comput. Phys. Commun.* 167 (2005), p. 195. DOI: [10.1016/j.cpc.2005.01.003](https://doi.org/10.1016/j.cpc.2005.01.003). arXiv: [hep-ph/0407333](https://arxiv.org/abs/hep-ph/0407333).
- [163] F. P. An et al. “Observation of Electron-Antineutrino Disappearance at Daya Bay”. In: *Phys. Rev. Lett.* 108 (17 Apr. 2012), p. 171803. DOI: [10.1103/PhysRevLett.108.171803](https://doi.org/10.1103/PhysRevLett.108.171803). URL: <https://link.aps.org/doi/10.1103/PhysRevLett.108.171803>.
- [164] Robert Miles Zwaska. “Accelerator systems and instrumentation for the NuMI neutrino beam”. In: (Dec. 2005). DOI: [10.2172/879065](https://doi.org/10.2172/879065). URL: <https://www.osti.gov/biblio/879065>.
- [165] Sacha E. Kopp. “Accelerator-based neutrino beams”. In: *Phys. Rept.* 439 (2007), pp. 101–159. DOI: [10.1016/j.physrep.2006.11.004](https://doi.org/10.1016/j.physrep.2006.11.004). arXiv: [physics/0609129](https://arxiv.org/abs/physics/0609129).
- [166] K. Abe et al. “T2K neutrino flux prediction”. In: *Phys. Rev. D* 87 (1 Jan. 2013), p. 012001. DOI: [10.1103/PhysRevD.87.012001](https://doi.org/10.1103/PhysRevD.87.012001). URL: <https://link.aps.org/doi/10.1103/PhysRevD.87.012001>.

BIBLIOGRAPHY

- [167] P. Adamson et al. “The NuMI Neutrino Beam”. In: *Nucl. Instrum. Meth. A* 806 (2016), pp. 279–306. DOI: [10.1016/j.nima.2015.08.063](https://doi.org/10.1016/j.nima.2015.08.063). arXiv: [1507.06690](https://arxiv.org/abs/1507.06690) [physics.acc-ph].
- [168] Ubaldo Dore, Pier Loverre, and Lucio Ludovici. “History of accelerator neutrino beams”. In: *Eur. Phys. J. H* 44.4-5 (2019), pp. 271–305. DOI: [10.1140/epjh/e2019-90032-x](https://doi.org/10.1140/epjh/e2019-90032-x). arXiv: [1805.01373](https://arxiv.org/abs/1805.01373) [physics.acc-ph].
- [169] S. van der Meer. “A Directive Device for Charged Particles and Its use in an Enhanced Neutrino Beam”. In: (Feb. 1961). DOI: [10.5170/CERN-1961-007](https://doi.org/10.5170/CERN-1961-007).
- [170] K Kleinknecht. “High energy neutrino reactions”. In: *Proceedings of the 1978 CERN School of Physics*, pp.43-87 (1978). DOI: [10.5170/CERN-1978-010.43](https://doi.org/10.5170/CERN-1978-010.43). URL: <http://cds.cern.ch/record/879067>.
- [171] M. H. Ahn et al. “Measurement of neutrino oscillation by the K2K experiment”. In: *Phys. Rev. D* 74 (7 Oct. 2006), p. 072003. DOI: [10.1103/PhysRevD.74.072003](https://doi.org/10.1103/PhysRevD.74.072003). URL: <https://link.aps.org/doi/10.1103/PhysRevD.74.072003>.
- [172] Particle Data Group, P A Zyla, et al. “Review of Particle Physics”. In: *Progress of Theoretical and Experimental Physics* 2020.8 (Aug. 2020). 083C01. ISSN: 2050-3911. DOI: [10.1093/ptep/ptaa104](https://doi.org/10.1093/ptep/ptaa104). eprint: https://academic.oup.com/ptep/article-pdf/2020/8/083C01/34673740/rpp2020-vol2-2015-2092_18.pdf. URL: <https://doi.org/10.1093/ptep/ptaa104>.
- [173] C A Ramm. “Neutrino spectra from the two-body decay of relativistic parents: Lecture 9”. In: (1963). DOI: [10.5170/CERN-1963-037.111](https://doi.org/10.5170/CERN-1963-037.111). URL: <https://cds.cern.ch/record/1242337>.
- [174] K. Anderson et al. “The NuMI Facility Technical Design Report”. In: (Oct. 1998). DOI: [10.2172/1156372](https://doi.org/10.2172/1156372).
- [175] Zarko Pavlovic. “Observation of Disappearance of Muon Neutrinos in the NuMI Beam”. In: (May 2008). DOI: [10.2172/945117](https://doi.org/10.2172/945117). URL: <https://www.osti.gov/biblio/945117>.
- [176] Igor Zheleznykh. “Early Years of High-Energy Neutrino Physics in Cosmic Rays and Neutrino Astronomy (1957-1962)”. In: *International Journal of Modern Physics A* 21.suppl1 (2006), pp. 1–11. DOI: [10.1142/S0217751X06033271](https://doi.org/10.1142/S0217751X06033271). eprint: <https://doi.org/10.1142/S0217751X06033271>. URL: <https://doi.org/10.1142/S0217751X06033271>.

BIBLIOGRAPHY

- [177] D. S. Ayres et al. “The NOvA Technical Design Report”. In: (Oct. 2007). DOI: [10.2172/935497](https://doi.org/10.2172/935497).
- [178] David S. Ayres. “The MINOS long baseline experiment at Fermilab”. In: *Nucl. Phys. B Proc. Suppl.* 59 (1997). Ed. by Y. Kuno and M. M. Nojiri, pp. 297–304. DOI: [10.1016/S0920-5632\(97\)00455-6](https://doi.org/10.1016/S0920-5632(97)00455-6).
- [179] Fermilab. *Fermilab Concepts Rookie Book*. 2020. URL: https://operations.fnal.gov/rookie_books/concepts.pdf (visited on 08/25/2021).
- [180] Fermilab. *Fermilab RIL Rookie Book*. 2015. URL: https://operations.fnal.gov/rookie_books/RIL.pdf (visited on 08/25/2021).
- [181] L. Aliaga. “Neutrino Flux Prediction for the NuMI Beamline”. PhD thesis. College of William and Mary, Mar. 2016.
- [182] C. D. Curtis et al. “The Operation of the First Section of the NAL Linear Accelerator”. In: *Part. Accel.* 1 (1970), pp. 93–109. DOI: [10.2172/1155250](https://doi.org/10.2172/1155250).
- [183] D. E. Young. “Construction Progress and Initial Performance of the NAL 200-MeV Linear Accelerator”. In: *Conf. Proc. C 700928* (1970). Ed. by M. R. Tracy, p. 15.
- [184] Arun Saini. “Design Considerations for the Fermilab PIP-II 800 MeV Superconducting Linac”. In: *2nd North American Particle Accelerator Conference*. Jan. 2017. DOI: [10.18429/JACoW-NAPAC2016-WEPOA60](https://doi.org/10.18429/JACoW-NAPAC2016-WEPOA60).
- [185] Maurizio Vretenar. “The radio-frequency quadrupole”. In: *CERN Accelerator School on High Power Hadron Machines*. Mar. 2013. DOI: [10.5170/CERN-2013-001.207](https://doi.org/10.5170/CERN-2013-001.207). arXiv: [1303.6762](https://arxiv.org/abs/1303.6762) [physics.acc-ph].
- [186] Robert J. Noble. “The Fermilab linac upgrade”. In: *15th International Linear Accelerator Conference*. Feb. 1991. URL: <https://lib-extopc.kek.jp/preprints/PDF/1991/9104/9104234.pdf>.
- [187] Fermilab. *Fermilab Booster Rookie Book*. 2009. URL: https://operations.fnal.gov/rookie_books/Booster_V4.1.pdf (visited on 08/25/2021).
- [188] Fermilab. *Fermilab Main Injector Rookie Book*. 2010. URL: https://operations.fnal.gov/rookie_books/Main_Injector_v1.1.pdf (visited on 08/25/2021).
- [189] Sujit Bidhar et al. “Failure investigation of nuclear grade POCO graphite target in high energy neutrino physics through numerical simulation”. In: *Nuclear Materials and Energy* 24 (2020), p. 100761. ISSN: 2352-1791. DOI: <https://doi.org/10.1016/j.nme.2020.100761>.

URL: <https://www.sciencedirect.com/science/article/pii/S2352179120300375>.

- [190] N. Simos et al. “120 GeV neutrino physics graphite target damage assessment using electron microscopy and high-energy x-ray diffraction”. In: *Phys. Rev. Accel. Beams* 22 (4 Apr. 2019), p. 041001. DOI: [10.1103/PhysRevAccelBeams.22.041001](https://doi.org/10.1103/PhysRevAccelBeams.22.041001). URL: <https://link.aps.org/doi/10.1103/PhysRevAccelBeams.22.041001>.
- [191] A. G. Abramov et al. “Beam optics and target conceptual designs for the NuMI project”. In: *Nucl. Instrum. Meth. A* 485 (2002), pp. 209–227. DOI: [10.1016/S0168-9002\(01\)02112-X](https://doi.org/10.1016/S0168-9002(01)02112-X).
- [192] S. Agostinelli et al. “GEANT4—a simulation toolkit”. In: *Nucl. Instrum. Meth. A* 506 (2003), pp. 250–303. DOI: [10.1016/S0168-9002\(03\)01368-8](https://doi.org/10.1016/S0168-9002(03)01368-8).
- [193] L. Aliaga et al. “Publisher’s Note: Neutrino flux predictions for the NuMI beam [Phys. Rev. D 94, 092005 (2016)]”. In: *Phys. Rev. D* 95 (3 Feb. 2017), p. 039903. DOI: [10.1103/PhysRevD.95.039903](https://doi.org/10.1103/PhysRevD.95.039903). URL: <https://link.aps.org/doi/10.1103/PhysRevD.95.039903>.
- [194] C. Alt et al. “Inclusive production of charged pions in p+C collisions at 158-GeV/c beam momentum”. In: *Eur. Phys. J. C* 49 (2007), pp. 897–917. DOI: [10.1140/epjc/s10052-006-0165-7](https://doi.org/10.1140/epjc/s10052-006-0165-7). arXiv: [hep-ex/0606028](https://arxiv.org/abs/hep-ex/0606028).
- [195] T.T. Böhlen et al. “The FLUKA Code: Developments and Challenges for High Energy and Medical Applications”. In: *Nuclear Data Sheets* 120 (2014), pp. 211–214. ISSN: 0090-3752. DOI: <https://doi.org/10.1016/j.nds.2014.07.049>. URL: <https://www.sciencedirect.com/science/article/pii/S0090375214005018>.
- [196] Alfredo Ferrari et al. “FLUKA: A multi-particle transport code (Program version 2005)”. In: (Oct. 2005). DOI: [10.2172/877507](https://doi.org/10.2172/877507).
- [197] D. S. Barton et al. “Experimental study of the A dependence of inclusive hadron fragmentation”. In: *Phys. Rev. D* 27 (11 June 1983), pp. 2580–2599. DOI: [10.1103/PhysRevD.27.2580](https://doi.org/10.1103/PhysRevD.27.2580). URL: <https://link.aps.org/doi/10.1103/PhysRevD.27.2580>.
- [198] P. Skubic et al. “Neutral-strange-particle production by 300-GeV protons”. In: *Phys. Rev. D* 18 (9 Nov. 1978), pp. 3115–3144. DOI: [10.1103/PhysRevD.18.3115](https://doi.org/10.1103/PhysRevD.18.3115). URL: <https://link.aps.org/doi/10.1103/PhysRevD.18.3115>.

BIBLIOGRAPHY

- [199] L. Aliaga et al. *A brief documentation of the Gen2 flux*. 2015. URL: https://minerva-docdb.fnal.gov/cgi-bin/sso/RetrieveFile?docid=7634&filename=flux_nov_2015.pdf&version=9.
- [200] L. Aliaga, M Kordosky, et al. “Neutrino flux predictions for the NuMI beam”. In: *Phys. Rev. D* 94 (9 Nov. 2016), p. 092005. DOI: [10.1103/PhysRevD.94.092005](https://doi.org/10.1103/PhysRevD.94.092005). URL: <https://link.aps.org/doi/10.1103/PhysRevD.94.092005>.
- [201] A. Bashyal et al. “Use of Neutrino Scattering Events with Low Hadronic Recoil to Inform Neutrino Flux and Detector Energy Scale”. In: (Apr. 2021). arXiv: [2104.05769](https://arxiv.org/abs/2104.05769) [hep-ex].
- [202] Frederick James. *Statistical methods in experimental physics*. World Scientific Publishing Company, 2006. ISBN: 9812705279. DOI: <https://doi.org/10.1142/6096>.
- [203] Louis Lyons. *Statistics for Nuclear and Particle Physicists*. Cambridge University Press, 1986. DOI: [10.1017/CB09781139167710](https://doi.org/10.1017/CB09781139167710).
- [204] M. Kordosky. *Error bands from the many universes method*. 2012. URL: <https://minerva-docdb.fnal.gov/cgi-bin/sso/ShowDocument?docid=7433>.
- [205] E. Valencia et al. “Constraint of the MINER ν A medium energy neutrino flux using neutrino-electron elastic scattering”. In: *Phys. Rev. D* 100 (9 Nov. 2019), p. 092001. DOI: [10.1103/PhysRevD.100.092001](https://doi.org/10.1103/PhysRevD.100.092001). URL: <https://link.aps.org/doi/10.1103/PhysRevD.100.092001>.
- [206] Oleksandr Tomalak and Richard J. Hill. “Theory of elastic neutrino-electron scattering”. In: *Phys. Rev. D* 101 (3 Feb. 2020), p. 033006. DOI: [10.1103/PhysRevD.101.033006](https://doi.org/10.1103/PhysRevD.101.033006). URL: <https://link.aps.org/doi/10.1103/PhysRevD.101.033006>.
- [207] J. Park et al. “Measurement of neutrino flux from neutrino-electron elastic scattering”. In: *Phys. Rev. D* 93 (11 June 2016), p. 112007. DOI: [10.1103/PhysRevD.93.112007](https://doi.org/10.1103/PhysRevD.93.112007). URL: <https://link.aps.org/doi/10.1103/PhysRevD.93.112007>.
- [208] K.A. Olive. “Review of Particle Physics”. In: *Chinese Physics C* 38.9 (Aug. 2014), p. 090001. DOI: [10.1088/1674-1137/38/9/090001](https://doi.org/10.1088/1674-1137/38/9/090001). URL: <https://doi.org/10.1088/1674-1137/38/9/090001>.
- [209] D. Ruterbories et al. “Constraining the NuMI neutrino flux using inverse muon decay reactions in MINER ν A”. In: (July 2021). arXiv: [2107.01059](https://arxiv.org/abs/2107.01059) [hep-ex].

BIBLIOGRAPHY

- [210] J. Devan et al. “Measurements of the inclusive neutrino and antineutrino charged current cross sections in MINERvA using the low- ν flux method”. In: *Phys. Rev. D* 94 (11 Dec. 2016), p. 112007. DOI: [10.1103/PhysRevD.94.112007](https://doi.org/10.1103/PhysRevD.94.112007). URL: <https://link.aps.org/doi/10.1103/PhysRevD.94.112007>.
- [211] Robert Fine. “Measurement of the Medium Energy NuMI Flux Using the Low- ν and High- ν Methods at MINERvA”. In: (Aug. 2020). URL: <https://www.osti.gov/biblio/1682274>.
- [212] “MINERvA Technical Design Report”. In: *FERMILAB-DESIGN-2006-01, MINERVA-DOCUMENT-700* (2006).
- [213] L. Aliaga et al. “Design, calibration, and performance of the MINERvA detector”. In: *Nuclear Instruments and Methods in Physics Research Section A: Accelerators, Spectrometers, Detectors and Associated Equipment* 743 (2014), pp. 130–159. ISSN: 0168-9002. DOI: <https://doi.org/10.1016/j.nima.2013.12.053>. URL: <https://www.sciencedirect.com/science/article/pii/S0168900214000035>.
- [214] D.G. Michael et al. “The magnetized steel and scintillator calorimeters of the MINOS experiment”. In: *Nuclear Instruments and Methods in Physics Research Section A: Accelerators, Spectrometers, Detectors and Associated Equipment* 596.2 (2008), pp. 190–228. ISSN: 0168-9002. DOI: <https://doi.org/10.1016/j.nima.2008.08.003>. URL: <https://www.sciencedirect.com/science/article/pii/S0168900208011613>.
- [215] N. Tagg et al. “Arachne - A web-based event viewer for MINERvA”. In: *Nucl. Instrum. Meth. A* 676 (2012), pp. 44–49. DOI: [10.1016/j.nima.2012.01.059](https://doi.org/10.1016/j.nima.2012.01.059). arXiv: [1111.5315 \[hep-ex\]](https://arxiv.org/abs/1111.5315).
- [216] B. Messerly. “Single Charged Pion Production by Muon Neutrinos in the MINERvA Detector Using the NuMI Beam”. PhD thesis. University of Pittsburgh, 2019. URL: <http://d-scholarship.pitt.edu/38098/>.
- [217] G.N. Perdue et al. “Reducing model bias in a deep learning classifier using domain adversarial neural networks in the MINERvA experiment”. In: *Journal of Instrumentation* 13.11 (Nov. 2018), P11020–P11020. DOI: [10.1088/1748-0221/13/11/p11020](https://doi.org/10.1088/1748-0221/13/11/p11020). URL: <https://doi.org/10.1088/1748-0221/13/11/p11020>.
- [218] K.K Hamamatsu-Photonics. *Photomultiplier Tubes*. 2007. URL: https://www.hamamatsu.com/resources/pdf/etd/PMT_handbook_v3aE.pdf.

- [219] Juan Estrada et al. *MCMII and the Trip Chip*. United States. Department of Energy. Office of Energy Research, 2003. URL: <https://inspirehep.net/files/e6b50166351da3bd942bd3cbe6c95844>.
- [220] P. A. Rodrigues et al. “Identification of Nuclear Effects in Neutrino-Carbon Interactions at Low Three-Momentum Transfer”. In: *Phys. Rev. Lett.* 116 (7 Feb. 2016), p. 071802. DOI: [10.1103/PhysRevLett.116.071802](https://doi.org/10.1103/PhysRevLett.116.071802). URL: <https://link.aps.org/doi/10.1103/PhysRevLett.116.071802>.
- [221] R. Gran et al. “Antineutrino Charged-Current Reactions on Hydrocarbon with Low Momentum Transfer”. In: *Phys. Rev. Lett.* 120 (22 June 2018), p. 221805. DOI: [10.1103/PhysRevLett.120.221805](https://doi.org/10.1103/PhysRevLett.120.221805). URL: <https://link.aps.org/doi/10.1103/PhysRevLett.120.221805>.
- [222] R. Gran et al. “Neutrino-nucleus quasi-elastic and 2p2h interactions up to 10 GeV”. In: *Phys. Rev. D* 88 (11 Dec. 2013), p. 113007. DOI: [10.1103/PhysRevD.88.113007](https://doi.org/10.1103/PhysRevD.88.113007). URL: <https://link.aps.org/doi/10.1103/PhysRevD.88.113007>.
- [223] N. Nuruzzaman. *Intensity Dependence Study with NuE Data and MC*. Tech. rep. MINERvA DocBD 21242. Rutgers, The State University of New Jersey, 2018. URL: <https://minerva-docdb.fnal.gov/cgi-bin/sso/ShowDocument?docid=21242>.
- [224] C. Andreopoulos et al. “The GENIE Neutrino Monte Carlo Generator”. In: *Nucl. Instrum. Meth. A* 614 (2010), pp. 87–104. DOI: [10.1016/j.nima.2009.12.009](https://doi.org/10.1016/j.nima.2009.12.009). arXiv: [0905.2517](https://arxiv.org/abs/0905.2517) [hep-ph].
- [225] M. F. Carneiro, D. Ruterbories, et al. “High-Statistics Measurement of Neutrino Quasielasticlike Scattering at 6 GeV on a Hydrocarbon Target”. In: *Phys. Rev. Lett.* 124.12 (2020), p. 121801. DOI: [10.1103/PhysRevLett.124.121801](https://doi.org/10.1103/PhysRevLett.124.121801). arXiv: [1912.09890](https://arxiv.org/abs/1912.09890) [hep-ex].
- [226] J. Nieves, Jose Enrique Amaro, and M. Valverde. “Inclusive quasi-elastic neutrino reactions”. In: *Phys. Rev. C* 70 (2004). [Erratum: *Phys.Rev.C* 72, 019902 (2005)], p. 055503. DOI: [10.1103/PhysRevC.70.055503](https://doi.org/10.1103/PhysRevC.70.055503). arXiv: [nucl-th/0408005](https://arxiv.org/abs/nuc1-th/0408005).
- [227] Richard Gran. “Model Uncertainties for Valencia RPA Effect for MINERvA”. In: (May 2017). arXiv: [1705.02932](https://arxiv.org/abs/1705.02932) [hep-ex].
- [228] Philip Rodrigues, Callum Wilkinson, and Kevin McFarland. “Constraining the GENIE model of neutrino-induced single pion production using reanalyzed bubble chamber data”. In: *Eur. Phys. J. C* 76.8 (2016),

- p. 474. DOI: [10.1140/epjc/s10052-016-4314-3](https://doi.org/10.1140/epjc/s10052-016-4314-3). arXiv: [1601.01888](https://arxiv.org/abs/1601.01888) [hep-ex].
- [229] Callum Wilkinson et al. “Reanalysis of bubble chamber measurements of muon-neutrino induced single pion production”. In: *Phys. Rev. D* 90.11 (2014), p. 112017. DOI: [10.1103/PhysRevD.90.112017](https://doi.org/10.1103/PhysRevD.90.112017). arXiv: [1411.4482](https://arxiv.org/abs/1411.4482) [hep-ex].
- [230] G. M. Radecky et al. “Study of Single Pion Production by Weak Charged Currents in Low-energy Neutrino d Interactions”. In: *Phys. Rev. D* 25 (1982). [Erratum: *Phys.Rev.D* 26, 3297 (1982)], pp. 1161–1173. DOI: [10.1103/PhysRevD.25.1161](https://doi.org/10.1103/PhysRevD.25.1161).
- [231] T. Kitagaki et al. “Charged Current Exclusive Pion Production in Neutrino Deuterium Interactions”. In: *Phys. Rev. D* 34 (1986), pp. 2554–2565. DOI: [10.1103/PhysRevD.34.2554](https://doi.org/10.1103/PhysRevD.34.2554).
- [232] A. Mislivec et al. “Measurement of total and differential cross sections of neutrino and antineutrino coherent π^\pm production on carbon”. In: *Phys. Rev. D* 97 (3 Feb. 2018), p. 032014. DOI: [10.1103/PhysRevD.97.032014](https://doi.org/10.1103/PhysRevD.97.032014). URL: <https://link.aps.org/doi/10.1103/PhysRevD.97.032014>.
- [233] J. Nieves, I. Ruiz Simo, and M. J. Vicente Vacas. “Inclusive Charged-Current Neutrino-Nucleus Reactions”. In: *Phys. Rev. C* 83 (2011), p. 045501. DOI: [10.1103/PhysRevC.83.045501](https://doi.org/10.1103/PhysRevC.83.045501). arXiv: [1102.2777](https://arxiv.org/abs/1102.2777) [hep-ph].
- [234] R. Gran et al. “Neutrino-nucleus quasi-elastic and 2p2h interactions up to 10 GeV”. In: *Phys. Rev. D* 88.11 (2013), p. 113007. DOI: [10.1103/PhysRevD.88.113007](https://doi.org/10.1103/PhysRevD.88.113007). arXiv: [1307.8105](https://arxiv.org/abs/1307.8105) [hep-ph].
- [235] Jackie Schwehr, Dan Cherdack, and Rik Gran. “GENIE implementation of IFIC Valencia model for QE-like 2p2h neutrino-nucleus cross section”. In: (Jan. 2016). arXiv: [1601.02038](https://arxiv.org/abs/1601.02038) [hep-ph].
- [236] L. A. Harewood and R. Gran. “Elastic hadron-nucleus scattering in neutrino-nucleus reactions and transverse kinematics measurements”. In: - (June 2019). arXiv: [1906.10576](https://arxiv.org/abs/1906.10576) [hep-ex].
- [237] S. Dolan, G. D. Megias, and S. Bolognesi. “Implementation of the SuSAv2-meson exchange current 1p1h and 2p2h models in GENIE and analysis of nuclear effects in T2K measurements”. In: *Phys. Rev. D* 101 (3 Feb. 2020), p. 033003. DOI: [10.1103/PhysRevD.101.033003](https://doi.org/10.1103/PhysRevD.101.033003). URL: <https://link.aps.org/doi/10.1103/PhysRevD.101.033003>.

BIBLIOGRAPHY

- [238] A. Bodek, M. E. Christy, and B. Coopersmith. “Effective spectral function for quasielastic scattering on nuclei from ${}^2_1\text{H}$ to ${}^{208}_{82}\text{Pb}$ ”. In: *AIP Conf. Proc.* 1680.1 (2015). Ed. by Barbara Szczerbinska and Elizabeth Worcester, p. 020003. DOI: [10.1063/1.4931862](https://doi.org/10.1063/1.4931862). arXiv: [1409.8545](https://arxiv.org/abs/1409.8545) [nucl-th].
- [239] A. Bodek and J. L. Ritchie. “Further studies of Fermi-motion effects in lepton scattering from nuclear targets”. In: *Phys. Rev. D* 24 (5 Sept. 1981), pp. 1400–1402. DOI: [10.1103/PhysRevD.24.1400](https://doi.org/10.1103/PhysRevD.24.1400). URL: <https://link.aps.org/doi/10.1103/PhysRevD.24.1400>.
- [240] Omar Benhar, Donal Day, and Ingo Sick. “Inclusive quasielastic electron-nucleus scattering”. In: *Rev. Mod. Phys.* 80 (1 Jan. 2008), pp. 189–224. DOI: [10.1103/RevModPhys.80.189](https://doi.org/10.1103/RevModPhys.80.189). URL: <https://link.aps.org/doi/10.1103/RevModPhys.80.189>.
- [241] O. Benhar, S. Fantoni, and G. I. Lykasov. “Backward hadron production in neutrino nucleus interactions”. In: *Eur. Phys. J. A* 7 (2000), pp. 415–419. DOI: [10.1007/s100500050411](https://doi.org/10.1007/s100500050411). arXiv: [nucl-th/9901053](https://arxiv.org/abs/nucl-th/9901053).
- [242] O. Benhar et al. “Multiple hadron production in electron scattering off nuclear targets”. In: *Phys. Rev. C* 55 (1 Jan. 1997), pp. 244–252. DOI: [10.1103/PhysRevC.55.244](https://doi.org/10.1103/PhysRevC.55.244). URL: <https://link.aps.org/doi/10.1103/PhysRevC.55.244>.
- [243] Omar Benhar et al. “Neutrino–nucleus interactions and the determination of oscillation parameters”. In: *Physics Reports* 700 (2017). Neutrino-nucleus interactions and the determination of oscillation parameters, pp. 1–47. ISSN: 0370-1573. DOI: <https://doi.org/10.1016/j.physrep.2017.07.004>. URL: <https://www.sciencedirect.com/science/article/pii/S0370157317302016>.
- [244] T. Golan, J.T. Sobczyk, and J. Żmuda. “NuWro: the Wrocław Monte Carlo Generator of Neutrino Interactions”. In: *Nuclear Physics B - Proceedings Supplements* 229-232 (2012). Neutrino 2010, p. 499. ISSN: 0920-5632. DOI: <https://doi.org/10.1016/j.nuclphysbps.2012.09.136>. URL: <https://www.sciencedirect.com/science/article/pii/S0920563212003532>.
- [245] A. Bodek and J. L. Ritchie. “Fermi-motion effects in deep-inelastic lepton scattering from nuclear targets”. In: *Phys. Rev. D* 23 (5 Mar. 1981), pp. 1070–1091. DOI: [10.1103/PhysRevD.23.1070](https://doi.org/10.1103/PhysRevD.23.1070). URL: <https://link.aps.org/doi/10.1103/PhysRevD.23.1070>.
- [246] K. S. Egiyan et al. “Measurement of Two- and Three-Nucleon Short-Range Correlation Probabilities in Nuclei”. In: *Phys. Rev. Lett.* 96 (8

- Mar. 2006), p. 082501. DOI: [10.1103/PhysRevLett.96.082501](https://doi.org/10.1103/PhysRevLett.96.082501). URL: <https://link.aps.org/doi/10.1103/PhysRevLett.96.082501>.
- [247] Luis Alvarez-Ruso et al. “Recent highlights from GENIE v3”. In: (June 2021). arXiv: [2106.09381](https://arxiv.org/abs/2106.09381) [hep-ph].
- [248] W. M. Alberico et al. “Scaling in electron scattering from a relativistic Fermi gas”. In: *Phys. Rev. C* 38 (4 Oct. 1988), pp. 1801–1810. DOI: [10.1103/PhysRevC.38.1801](https://doi.org/10.1103/PhysRevC.38.1801). URL: <https://link.aps.org/doi/10.1103/PhysRevC.38.1801>.
- [249] Geoffrey B. West. “Electron scattering from atoms, nuclei and nucleons”. In: *Physics Reports* 18.5 (1975), pp. 263–323. ISSN: 0370-1573. DOI: [https://doi.org/10.1016/0370-1573\(75\)90035-6](https://doi.org/10.1016/0370-1573(75)90035-6). URL: <https://www.sciencedirect.com/science/article/pii/0370157375900356>.
- [250] J. E. Amaro et al. “Neutrino Interactions Importance to Nuclear Physics”. In: *AIP Conference Proceedings* 1189.1 (2009), pp. 24–31. DOI: [10.1063/1.3274166](https://doi.org/10.1063/1.3274166). eprint: <https://aip.scitation.org/doi/pdf/10.1063/1.3274166>. URL: <https://aip.scitation.org/doi/abs/10.1063/1.3274166>.
- [251] J. E. Amaro et al. “Using electron scattering superscaling to predict charge-changing neutrino cross sections in nuclei”. In: *Phys. Rev. C* 71 (1 Jan. 2005), p. 015501. DOI: [10.1103/PhysRevC.71.015501](https://doi.org/10.1103/PhysRevC.71.015501). URL: <https://link.aps.org/doi/10.1103/PhysRevC.71.015501>.
- [252] D B Day et al. “Scaling in Inclusive Electron-Nucleus Scattering”. In: *Annual Review of Nuclear and Particle Science* 40.1 (1990), pp. 357–410. DOI: [10.1146/annurev.ns.40.120190.002041](https://doi.org/10.1146/annurev.ns.40.120190.002041). eprint: <https://doi.org/10.1146/annurev.ns.40.120190.002041>. URL: <https://doi.org/10.1146/annurev.ns.40.120190.002041>.
- [253] T. W. Donnelly and Ingo Sick. “Superscaling in Inclusive Electron-Nucleus Scattering”. In: *Phys. Rev. Lett.* 82 (16 Apr. 1999), pp. 3212–3215. DOI: [10.1103/PhysRevLett.82.3212](https://doi.org/10.1103/PhysRevLett.82.3212). URL: <https://link.aps.org/doi/10.1103/PhysRevLett.82.3212>.
- [254] T. W. Donnelly and Ingo Sick. “Superscaling of inclusive electron scattering from nuclei”. In: *Phys. Rev. C* 60 (6 Nov. 1999), p. 065502. DOI: [10.1103/PhysRevC.60.065502](https://doi.org/10.1103/PhysRevC.60.065502). URL: <https://link.aps.org/doi/10.1103/PhysRevC.60.065502>.
- [255] C. Maieron, T. W. Donnelly, and Ingo Sick. “Extended superscaling of electron scattering from nuclei”. In: *Phys. Rev. C* 65 (2 Jan. 2002),

- p. 025502. DOI: [10.1103/PhysRevC.65.025502](https://doi.org/10.1103/PhysRevC.65.025502). URL: <https://link.aps.org/doi/10.1103/PhysRevC.65.025502>.
- [256] M. B. Barbaro et al. “Inelastic electron-nucleus scattering and scaling at high inelasticity”. In: *Phys. Rev. C* 69 (3 Mar. 2004), p. 035502. DOI: [10.1103/PhysRevC.69.035502](https://doi.org/10.1103/PhysRevC.69.035502). URL: <https://link.aps.org/doi/10.1103/PhysRevC.69.035502>.
- [257] M.B. Barbaro et al. “Relativistic γ -scaling and the Coulomb sum rule in nuclei”. In: *Nuclear Physics A* 643.2 (1998), pp. 137–160. ISSN: 0375-9474. DOI: [https://doi.org/10.1016/S0375-9474\(98\)00443-6](https://doi.org/10.1016/S0375-9474(98)00443-6). URL: <https://www.sciencedirect.com/science/article/pii/S0375947498004436>.
- [258] R. González-Jiménez et al. “Extensions of superscaling from relativistic mean field theory: The SuSAv2 model”. In: *Phys. Rev. C* 90 (3 Sept. 2014), p. 035501. DOI: [10.1103/PhysRevC.90.035501](https://doi.org/10.1103/PhysRevC.90.035501). URL: <https://link.aps.org/doi/10.1103/PhysRevC.90.035501>.
- [259] R. Gran, A. Bashyal, and M. Ascencio. *Implementation of SuSA 2p2h and QE weights for MINERvA*. Tech. rep. MINERvA technical note TN92, DocDB 29414. MINERvA Collaboration, 2022. URL: <https://minerva-docdb.fnal.gov/cgi-bin/sso/ShowDocument?docid=30552>.
- [260] R. Gran. *SuSA 2p2h and QE in more detail*. Tech. rep. MINERvA DocBD 25468. University of Minnesota Duluth, 2020. URL: <https://minerva-docdb.fnal.gov/cgi-bin/sso/ShowDocument?docid=25468>.
- [261] E. J. Moniz et al. “Nuclear Fermi Momenta from Quasielastic Electron Scattering”. In: *Phys. Rev. Lett.* 26 (8 Feb. 1971), pp. 445–448. DOI: [10.1103/PhysRevLett.26.445](https://doi.org/10.1103/PhysRevLett.26.445). URL: <https://link.aps.org/doi/10.1103/PhysRevLett.26.445>.
- [262] Arie Bodek and Tejin Cai. “Removal Energies and Final State Interaction in Lepton Nucleus Scattering”. In: *Eur. Phys. J. C* 79.4 (2019), p. 293. DOI: [10.1140/epjc/s10052-019-6750-3](https://doi.org/10.1140/epjc/s10052-019-6750-3). arXiv: [1801.07975](https://arxiv.org/abs/1801.07975) [nucl-th].
- [263] E. J. Moniz. “Pion Electroproduction from Nuclei”. In: *Phys. Rev.* 184 (4 Aug. 1969), pp. 1154–1161. DOI: [10.1103/PhysRev.184.1154](https://doi.org/10.1103/PhysRev.184.1154). URL: <https://link.aps.org/doi/10.1103/PhysRev.184.1154>.
- [264] P. Adamson et al. “Study of quasielastic scattering using charged-current ν_μ -iron interactions in the MINOS near detector”. In: *Phys. Rev. D* 91

- (1 Jan. 2015), p. 012005. DOI: [10.1103/PhysRevD.91.012005](https://doi.org/10.1103/PhysRevD.91.012005). URL: <https://link.aps.org/doi/10.1103/PhysRevD.91.012005>.
- [265] P. Adamson et al. “Study of quasielastic scattering using charged-current $\nu\mu$ -iron interactions in the MINOS near detector”. In: *Phys. Rev. D* 91.1 (2015), p. 012005. DOI: [10.1103/PhysRevD.91.012005](https://doi.org/10.1103/PhysRevD.91.012005). arXiv: [1410.8613](https://arxiv.org/abs/1410.8613) [hep-ex].
- [266] P. Stowell et al. “Tuning the genie pion production model with MINERvA data”. In: *Phys. Rev. D* 100 (7 Oct. 2019), p. 072005. DOI: [10.1103/PhysRevD.100.072005](https://doi.org/10.1103/PhysRevD.100.072005). URL: <https://link.aps.org/doi/10.1103/PhysRevD.100.072005>.
- [267] Ch. Berger and L. M. Sehgal. “Lepton mass effects in single pion production by neutrinos”. In: *Phys. Rev. D* 76 (11 Dec. 2007), p. 113004. DOI: [10.1103/PhysRevD.76.113004](https://doi.org/10.1103/PhysRevD.76.113004). URL: <https://link.aps.org/doi/10.1103/PhysRevD.76.113004>.
- [268] J. Nowak. “Four momentum transfer discrepancy in the charged current π^+ ; production in the MiniBooNE:data vs. theory”. In: *arXiv: High Energy Physics - Phenomenology* 1189 (2009), pp. 243–248.
- [269] R. Gran, I. Mahbub, and A. Mislivec. *Rein Sehgal and Berger Sehgal Resonances*. Tech. rep. MINERvA DocBD 28974. University of Minnesota Duluth, 2021. URL: <https://minerva-docdb.fnal.gov/cgi-bin/sso/ShowDocument?docid=28974>.
- [270] I. Mahbub. *Resonance Production Models: Lalakulich-Pascos and Berger-Sehgal*. Tech. rep. MINERvA DocBD 28338. University of Minnesota Duluth, 2020. URL: <https://minerva-docdb.fnal.gov/cgi-bin/sso/ShowDocument?docid=28338>.
- [271] D. Rein. “Angular Distribution in Neutrino Induced Single Pion Production Processes”. In: *Z. Phys. C* 35 (1987), pp. 43–64. DOI: [10.1007/BF01561054](https://doi.org/10.1007/BF01561054).
- [272] M. Kabirnezhad. “Single pion production in neutrino-nucleon interactions”. In: *Phys. Rev. D* 97 (1 Jan. 2018), p. 013002. DOI: [10.1103/PhysRevD.97.013002](https://doi.org/10.1103/PhysRevD.97.013002). URL: <https://link.aps.org/doi/10.1103/PhysRevD.97.013002>.
- [273] E. Hernández, J. Nieves, and M. Valverde. “Weak pion production off the nucleon”. In: *Phys. Rev. D* 76 (3 Aug. 2007), p. 033005. DOI: [10.1103/PhysRevD.76.033005](https://doi.org/10.1103/PhysRevD.76.033005). URL: <https://link.aps.org/doi/10.1103/PhysRevD.76.033005>.

- [274] Yoshinari Hayato. “A neutrino interaction simulation program library NEUT”. In: *Acta Phys. Polon. B* 40 (2009). Ed. by Arthur Ankowski and Jan Sobczyk, pp. 2477–2489.
- [275] Teppei Katori et al. “First look at PYTHIA8 hadronization program for neutrino interaction generators”. In: *JPS Conf. Proc.* 12 (2016), p. 010033. DOI: [10.7566/JPSCP.12.010033](https://doi.org/10.7566/JPSCP.12.010033). arXiv: [1602.00083](https://arxiv.org/abs/1602.00083) [hep-ph].
- [276] D. Allasia et al. “Investigation of exclusive channels in $\nu/\bar{\nu}$ -deuteron charged current interactions”. In: *Nuclear Physics B* 343.2 (1990), pp. 285–309. ISSN: 0550-3213. DOI: [https://doi.org/10.1016/0550-3213\(90\)90472-P](https://doi.org/10.1016/0550-3213(90)90472-P). URL: <https://www.sciencedirect.com/science/article/pii/055032139090472P>.
- [277] G. M. Radecky et al. “Study of single-pion production by weak charged currents in low-energy νd interactions”. In: *Phys. Rev. D* 25 (5 Mar. 1982), pp. 1161–1173. DOI: [10.1103/PhysRevD.25.1161](https://doi.org/10.1103/PhysRevD.25.1161). URL: <https://link.aps.org/doi/10.1103/PhysRevD.25.1161>.
- [278] Monireh Kabirnezhad. “Improvement of Single Pion Production for T2K experiment simulation tools”. PhD thesis. Wroclaw U., Oct. 2017. URL: <https://inspirehep.net/files/a29746a5bc5392dda0220c658228916f>.
- [279] P. A. Rodrigues, J. Demgen, E. Miltenberger, et al. “Identification of nuclear effects in neutrino-carbon interactions at low three-momentum transfer”. In: *Phys. Rev. Lett.* 116 (2016). [Addendum: *Phys.Rev.Lett.* 121, 209902 (2018)], p. 071802. DOI: [10.1103/PhysRevLett.116.071802](https://doi.org/10.1103/PhysRevLett.116.071802). arXiv: [1511.05944](https://arxiv.org/abs/1511.05944) [hep-ex].
- [280] I. Ruiz Simo et al. “Relativistic model of 2p-2h meson exchange currents in (anti)neutrino scattering”. In: *J. Phys. G* 44.6 (2017), p. 065105. DOI: [10.1088/1361-6471/aa6a06](https://doi.org/10.1088/1361-6471/aa6a06). arXiv: [1604.08423](https://arxiv.org/abs/1604.08423) [nucl-th].
- [281] G. D. Megias et al. “Charged-current neutrino-nucleus reactions within the superscaling meson-exchange current approach”. In: *Phys. Rev. D* 94.9 (2016), p. 093004. DOI: [10.1103/PhysRevD.94.093004](https://doi.org/10.1103/PhysRevD.94.093004). arXiv: [1607.08565](https://arxiv.org/abs/1607.08565) [nucl-th].
- [282] S. Dolan, G. D. Megias, and S. Bolognesi. “Implementation of the SuSAv2-meson exchange current 1p1h and 2p2h models in GENIE and analysis of nuclear effects in T2K measurements”. In: *Phys. Rev. D* 101.3 (2020), p. 033003. DOI: [10.1103/PhysRevD.101.033003](https://doi.org/10.1103/PhysRevD.101.033003). arXiv: [1905.08556](https://arxiv.org/abs/1905.08556) [hep-ex].

- [283] A Bodek and U K Yang. “Higher twist, $\xi(\omega)$ scaling, and effective LO PDFs for lepton scattering in the few GeV region”. In: *Journal of Physics G: Nuclear and Particle Physics* 29.8 (July 2003), pp. 1899–1905. DOI: [10.1088/0954-3899/29/8/369](https://doi.org/10.1088/0954-3899/29/8/369). URL: <https://doi.org/10.1088/0954-3899/29/8/369>.
- [284] C. Andreopoulos and H. Gallagher. “Tools for Neutrino Interaction Model Validation”. In: *Nuclear Physics B - Proceedings Supplements* 139 (2005). Proceedings of the Third International Workshop on Neutrino-Nucleus Interactions in the Few-GeV Region, pp. 247–252. ISSN: 0920-5632. DOI: <https://doi.org/10.1016/j.nuclphysbps.2004.11.242>. URL: <https://www.sciencedirect.com/science/article/pii/S0920563204009375>.
- [285] M.R. Whalley. “A New Neutrino Cross Section Data Resource”. In: *Nuclear Physics B - Proceedings Supplements* 139 (2005). Proceedings of the Third International Workshop on Neutrino-Nucleus Interactions in the Few-GeV Region, pp. 241–246. ISSN: 0920-5632. DOI: <https://doi.org/10.1016/j.nuclphysbps.2004.11.216>. URL: <https://www.sciencedirect.com/science/article/pii/S0920563204007856>.
- [286] G. D’Agostini. “A multidimensional unfolding method based on Bayes’ theorem”. In: *Nuclear Instruments and Methods in Physics Research Section A: Accelerators, Spectrometers, Detectors and Associated Equipment* 362.2 (1995), pp. 487–498. ISSN: 0168-9002. DOI: [https://doi.org/10.1016/0168-9002\(95\)00274-X](https://doi.org/10.1016/0168-9002(95)00274-X). URL: <http://www.sciencedirect.com/science/article/pii/016890029500274X>.
- [287] M. Ascencio. *Low recoil NuMu analysis(unfolding)*. Tech. rep. MIN-ERvA DocBD 28091. Pontificia Universidad Catolica del Peru, 2020. URL: <https://minerva-docdb.fnal.gov/cgi-bin/sso/ShowDocument?docid=28091>.
- [288] Rene Brun and Fons Rademakers. “ROOT — An object oriented data analysis framework”. In: *Nuclear Instruments and Methods in Physics Research Section A: Accelerators, Spectrometers, Detectors and Associated Equipment* 389.1 (1997). New Computing Techniques in Physics Research V, pp. 81–86. ISSN: 0168-9002. DOI: [https://doi.org/10.1016/S0168-9002\(97\)00048-X](https://doi.org/10.1016/S0168-9002(97)00048-X). URL: <https://www.sciencedirect.com/science/article/pii/S016890029700048X>.
- [289] Ben Messerly et al. “An Error Analysis Toolkit for Binned Counting Experiments”. In: *EPJ Web Conf.* 251 (2021), p. 03046. DOI: [10.1051/epjconf/202125103046](https://doi.org/10.1051/epjconf/202125103046). arXiv: [2103.08677](https://arxiv.org/abs/2103.08677) [hep-ex].

BIBLIOGRAPHY

- [290] H. Gallagher. *Reweightable GENIE Uncertainties*. Tech. rep. MINERvA DocBD 7451. Tufts University, 2012. URL: <https://minerva-docdb.fnal.gov/cgi-bin/sso/ShowDocument?docid=7451>.
- [291] S. Dytman, H. Gallagher, and M. Kordosky. “Hadronic Shower Energy Scale Uncertainty in the MINOS Experiment”. In: (June 2008). arXiv: [0806.2119](https://arxiv.org/abs/0806.2119) [hep-ex].
- [292] L. Aliaga et al. “MINERvA neutrino detector response measured with test beam data”. In: *Nucl. Instrum. Meth. A* 789 (2015), pp. 28–42. DOI: [10.1016/j.nima.2015.04.003](https://doi.org/10.1016/j.nima.2015.04.003). arXiv: [1501.06431](https://arxiv.org/abs/1501.06431) [physics.ins-det].
- [293] T. Yang et al. “A Hadronization Model for Few-GeV Neutrino Interactions”. In: *Eur. Phys. J. C* 63 (2009), pp. 1–10. DOI: [10.1140/epjc/s10052-009-1094-z](https://doi.org/10.1140/epjc/s10052-009-1094-z). arXiv: [0904.4043](https://arxiv.org/abs/0904.4043) [hep-ph].
- [294] Júlia Tena-Vidal et al. “Hadronization model tuning in genie v3”. In: *Phys. Rev. D* 105.1 (2022), p. 012009. DOI: [10.1103/PhysRevD.105.012009](https://doi.org/10.1103/PhysRevD.105.012009). arXiv: [2106.05884](https://arxiv.org/abs/2106.05884) [hep-ph].
- [295] C. Andreopoulos et al. *Updated Cross Section Model Uncertainties for the Charged Current Analysis (minos-doc-2989-v6)*. Tech. rep. MINERvA DocBD 7450. MINOS Collaboration, 2012. URL: <https://minerva-docdb.fnal.gov/cgi-bin/sso/ShowDocument>.
- [296] Aaron S. Meyer et al. “Deuterium target data for precision neutrino-nucleus cross sections”. In: *Phys. Rev. D* 93.11 (2016), p. 113015. DOI: [10.1103/PhysRevD.93.113015](https://doi.org/10.1103/PhysRevD.93.113015). arXiv: [1603.03048](https://arxiv.org/abs/1603.03048) [hep-ph].
- [297] T. Golan, J. T. Sobczyk, and J. Zmuda. “NuWro: the Wroclaw Monte Carlo Generator of Neutrino Interactions”. In: *Nucl. Phys. B Proc. Suppl.* 229-232 (2012). Ed. by George S. Tzanakos, pp. 499–499. DOI: [10.1016/j.nuclphysbps.2012.09.136](https://doi.org/10.1016/j.nuclphysbps.2012.09.136).
- [298] M. Buizza Avanzini et al. *Comparisons and challenges of modern neutrino-scattering experiments (TENSIONS 2019 report)*. 2021. arXiv: [2112.09194](https://arxiv.org/abs/2112.09194) [hep-ex].
- [299] Ch. Berger and L. M. Sehgal. “Lepton mass effects in single pion production by neutrinos”. In: *Phys. Rev. D* 76 (11 Dec. 2007), p. 113004. DOI: [10.1103/PhysRevD.76.113004](https://doi.org/10.1103/PhysRevD.76.113004). URL: <https://link.aps.org/doi/10.1103/PhysRevD.76.113004>.
- [300] A Bodek and U. K. Yang. “Higher twist, xi(omega) scaling, and effective LO PDFs for lepton scattering in the few GeV region”. In: *J. Phys.*

- G* 29 (2003). Ed. by K. Long and R. Edgecock, pp. 1899–1906. DOI: [10.1088/0954-3899/29/8/369](https://doi.org/10.1088/0954-3899/29/8/369). arXiv: [hep-ex/0210024](https://arxiv.org/abs/hep-ex/0210024).
- [301] Júlia Tena-Vidal et al. “Neutrino-nucleon cross-section model tuning in GENIE v3”. In: *Phys. Rev. D* 104.7 (2021), p. 072009. DOI: [10.1103/PhysRevD.104.072009](https://doi.org/10.1103/PhysRevD.104.072009). arXiv: [2104.09179](https://arxiv.org/abs/2104.09179) [hep-ph].
- [302] L. L. Salcedo et al. “Computer Simulation of Inclusive Pion Nuclear Reactions”. In: *Nucl. Phys. A* 484 (1988), pp. 557–592. DOI: [10.1016/0375-9474\(88\)90310-7](https://doi.org/10.1016/0375-9474(88)90310-7).
- [303] M. Martini et al. “Electron-neutrino scattering off nuclei from two different theoretical perspectives”. In: *Phys. Rev. C* 94.1 (2016), p. 015501. DOI: [10.1103/PhysRevC.94.015501](https://doi.org/10.1103/PhysRevC.94.015501). arXiv: [1602.00230](https://arxiv.org/abs/1602.00230) [nucl-th].
- [304] Juan Nieves and Joanna Ewa Sobczyk. “In medium dispersion relation effects in nuclear inclusive reactions at intermediate and low energies”. In: *Annals Phys.* 383 (2017), pp. 455–496. DOI: [10.1016/j.aop.2017.06.002](https://doi.org/10.1016/j.aop.2017.06.002). arXiv: [1701.03628](https://arxiv.org/abs/1701.03628) [nucl-th].
- [305] Steven Dytman et al. “Comparison of Validation Methods of Simulations for Final State Interactions in Hadron Production Experiments”. In: (Mar. 2021). arXiv: [2103.07535](https://arxiv.org/abs/2103.07535) [hep-ph].
- [306] E. J. Moniz et al. “Nuclear Fermi momenta from quasielastic electron scattering”. In: *Phys. Rev. Lett.* 26 (1971), pp. 445–448. DOI: [10.1103/PhysRevLett.26.445](https://doi.org/10.1103/PhysRevLett.26.445).
- [307] T. De Forest. “Off-Shell electron Nucleon Cross-Sections. The Impulse Approximation”. In: *Nucl. Phys. A* 392 (1983), pp. 232–248. DOI: [10.1016/0375-9474\(83\)90124-0](https://doi.org/10.1016/0375-9474(83)90124-0).
- [308] Arie Bodek and Tejin Cai. “Comparison of optical potential for nucleons and Δ resonances: In electron scattering from nuclear targets”. In: *Eur. Phys. J. C* 80.7 (2020), p. 655. DOI: [10.1140/epjc/s10052-020-8236-8](https://doi.org/10.1140/epjc/s10052-020-8236-8). arXiv: [2004.00087](https://arxiv.org/abs/2004.00087) [hep-ph].
- [309] T. Cai et al. “Nucleon binding energy and transverse momentum imbalance in neutrino-nucleus reactions”. In: *Phys. Rev. D* 101.9 (2020), p. 092001. DOI: [10.1103/PhysRevD.101.092001](https://doi.org/10.1103/PhysRevD.101.092001). arXiv: [1910.08658](https://arxiv.org/abs/1910.08658) [hep-ex].
- [310] Olga Lalakulich and Emmanuel A. Paschos. “Resonance production by neutrinos. I. $J = 3/2$ resonances”. In: *Phys. Rev. D* 71 (2005), p. 074003. DOI: [10.1103/PhysRevD.71.074003](https://doi.org/10.1103/PhysRevD.71.074003). arXiv: [hep-ph/0501109](https://arxiv.org/abs/hep-ph/0501109).

- [311] Olga Lalakulich, Emmanuel A. Paschos, and Giorgi Piranishvili. “Resonance production by neutrinos: The Second resonance region”. In: *Phys. Rev. D* 74 (2006), p. 014009. DOI: [10.1103/PhysRevD.74.014009](https://doi.org/10.1103/PhysRevD.74.014009). arXiv: [hep-ph/0602210](https://arxiv.org/abs/hep-ph/0602210).
- [312] J. Park et al. “Measurement of Neutrino Flux from Neutrino-Electron Elastic Scattering”. In: *Phys. Rev. D* 93.11 (2016), p. 112007. DOI: [10.1103/PhysRevD.93.112007](https://doi.org/10.1103/PhysRevD.93.112007). arXiv: [1512.07699](https://arxiv.org/abs/1512.07699) [[physics.ins-det](#)].
- [313] R. Fine, B. Messerly, and K. S. McFarland. “Data Preservation at MINERvA”. In: . (Sept. 2020). arXiv: [2009.04548](https://arxiv.org/abs/2009.04548) [[hep-ex](#)].
- [314] D. Ruterbories, A. Filkins, et al. “Measurement of inclusive charged-current ν_μ cross sections as a function of muon kinematics at $\langle E_\nu \rangle \sim 6$ GeV on hydrocarbon”. In: *Phys. Rev. D* 104 (9 Nov. 2021), p. 092007. DOI: [10.1103/PhysRevD.104.092007](https://doi.org/10.1103/PhysRevD.104.092007). URL: <https://link.aps.org/doi/10.1103/PhysRevD.104.092007>.
- [315] M. Ascencio and R. Gran. *Low recoil NuMu ME analysis update - Chi2*. Tech. rep. MINERvA DocBD 30552-v5. MINERvA Collaboration, 2022. URL: <https://minerva-docdb.fnal.gov/cgi-bin/sso/ShowDocument?docid=30552>.
- [316] M.C. Gonzalez-Garcia and Michele Maltoni. “Status of oscillation plus decay of atmospheric and long-baseline neutrinos”. In: *Physics Letters B* 663.5 (2008), pp. 405–409. ISSN: 0370-2693. DOI: <https://doi.org/10.1016/j.physletb.2008.04.041>. URL: <https://www.sciencedirect.com/science/article/pii/S0370269308004863>.
- [317] A. Mislivec, A. Higuera, et al. “Measurement of total and differential cross sections of neutrino and antineutrino coherent π^\pm production on carbon”. In: *Phys. Rev. D* 97.3 (2018), p. 032014. DOI: [10.1103/PhysRevD.97.032014](https://doi.org/10.1103/PhysRevD.97.032014). arXiv: [1711.01178](https://arxiv.org/abs/1711.01178) [[hep-ex](#)].
- [318] E. Valencia, D. Jena, Nuruzzaman, et al. “Constraint of the MINERvA medium energy neutrino flux using neutrino-electron elastic scattering”. In: *Phys. Rev. D* 100.9 (2019), p. 092001. DOI: [10.1103/PhysRevD.100.092001](https://doi.org/10.1103/PhysRevD.100.092001). arXiv: [1906.00111](https://arxiv.org/abs/1906.00111) [[hep-ex](#)].
- [319] William H. Press et al. *Numerical Recipes 3rd Edition: The Art of Scientific Computing*. 3rd ed. USA: Cambridge University Press, 2007. ISBN: 0521880688.
- [320] Dale J. Poirier. *Intermediate Statistics and Econometrics: A Comparative Approach*. The MIT Press, 1995. ISBN: 0262161494.

- [321] Marco Taboga. *Lectures on Probability Theory and Mathematical Statistics*. 2nd ed. CreateSpace Independent Publishing Platform, 2012. ISBN: 1480215236.
- [322] L. A. Shepp and Y. Vardi. “Maximum Likelihood Reconstruction for Emission Tomography”. In: *IEEE Transactions on Medical Imaging* 1.2 (1982), pp. 113–122.
- [323] H.N. Multhei and B. Schorr. “On an Iterative Method for the Unfolding of Spectra”. In: *Nucl. Instrum. Meth. A* 257 (1987), p. 371. DOI: [10.1016/0168-9002\(87\)90759-5](https://doi.org/10.1016/0168-9002(87)90759-5).
- [324] Luca Lista. *Statistical Methods for Data Analysis in Particle Physics*. Vol. 941. Springer, 2017. DOI: [10.1007/978-3-319-62840-0](https://doi.org/10.1007/978-3-319-62840-0).
- [325] Mikael Kuusela. “Statistical Issues in Unfolding Methods for High Energy Physics”. Master thesis. 2012. URL: <https://core.ac.uk/download/pdf/80704245.pdf> (visited on 08/26/2021).
- [326] K. McFarland. *Unfolding MINERvA Report of discussion at NuINT*. 2017. URL: <https://minerva-docdb.fnal.gov/cgi-bin/sso/ShowDocument?docid=15224> (visited on 08/26/2021).
- [327] G.J. McLachlan and T. Krishnan. *The EM Algorithm and Extensions*. Wiley Series in Probability and Statistics. Wiley, 2007. ISBN: 9780470191606. URL: <https://books.google.com/books?id=NBawzaWoWa8C>.
- [328] T. Adye. *Corrected error calculation for iterative Bayesian unfolding*. 2011. URL: https://hepunix.rl.ac.uk/~adye/software/unfold/bayes_errors.pdf (visited on 08/26/2021).
- [329] A. Mann. *Graphs from another world: Neutrino QE, CC(pi), 2p2h, and RPA a la Valencia*. Tech. rep. MINERvA DocBD 25871. Tufts University, 2020. URL: <https://minerva-docdb.fnal.gov/cgi-bin/sso/ShowDocument?docid=25871>.
- [330] K. Bätzner et al. “Separation of σ_S and σ_T in the region of the Δ (1236) resonance and determination of the magnetic dipole transition form factor”. In: *Physics Letters B* 39.4 (1972), pp. 575–578. ISSN: 0370-2693. DOI: [https://doi.org/10.1016/0370-2693\(72\)90348-6](https://doi.org/10.1016/0370-2693(72)90348-6). URL: <https://www.sciencedirect.com/science/article/pii/0370269372903486>.
- [331] A. Gil, J. Nieves, and E. Oset. “Many body approach to the inclusive (e, e-prime) reaction from the quasielastic to the Delta excitation region”.

- In: *Nucl. Phys. A* 627 (1997), pp. 543–598. DOI: [10.1016/S0375-9474\(97\)00513-7](https://doi.org/10.1016/S0375-9474(97)00513-7). arXiv: [nuc1-th/9711009](https://arxiv.org/abs/nuc1-th/9711009).
- [332] M. Valverde-Hermosilla. “Interacción neutrino-núcleo a energías intermedias”. PhD thesis. Universidad de Granada, May 2007. URL: <https://inspirehep.net/files/64f6db5472dd6c1b81b8effa5f7ac35e>.
- [333] C. Itzykson and J. B. Zuber. *Quantum Field Theory*. International Series In Pure and Applied Physics. New York: McGraw-Hill, 1980. ISBN: 978-0-486-44568-7.
- [334] Michael E. Peskin and Daniel V. Schroeder. *An Introduction to quantum field theory*. Reading, USA: Addison-Wesley, 1995. ISBN: 978-0-201-50397-5.
- [335] K. Holinde. “Two-nucleon forces and nuclear matter”. In: *Physics Reports* 68.3 (1981), pp. 121–188. ISSN: 0370-1573. DOI: [https://doi.org/10.1016/0370-1573\(81\)90188-5](https://doi.org/10.1016/0370-1573(81)90188-5). URL: <https://www.sciencedirect.com/science/article/pii/0370157381901885>.
- [336] Gianluca Stefanucci and Robert Van Leeuwen. *Nonequilibrium many-body theory of quantum systems: a modern introduction*. Cambridge University Press, 2013.
- [337] Matthew D Schwartz. *Quantum field theory and the standard model*. Cambridge University Press, 2014.
- [338] Jouni T. Suhonen. “Value of the Axial-Vector Coupling Strength in β and $\beta\beta$ Decays: A Review”. In: *Front. in Phys.* 5 (2017), p. 55. DOI: [10.3389/fphy.2017.00055](https://doi.org/10.3389/fphy.2017.00055). arXiv: [1712.01565](https://arxiv.org/abs/1712.01565) [nuc1-th].
- [339] David Bohm and David Pines. “A Collective Description of Electron Interactions. I. Magnetic Interactions”. In: *Phys. Rev.* 82 (5 June 1951), pp. 625–634. DOI: [10.1103/PhysRev.82.625](https://doi.org/10.1103/PhysRev.82.625). URL: <https://link.aps.org/doi/10.1103/PhysRev.82.625>.
- [340] David Pines and David Bohm. “A Collective Description of Electron Interactions: II. Collective vs Individual Particle Aspects of the Interactions”. In: *Phys. Rev.* 85 (2 Jan. 1952), pp. 338–353. DOI: [10.1103/PhysRev.85.338](https://doi.org/10.1103/PhysRev.85.338). URL: <https://link.aps.org/doi/10.1103/PhysRev.85.338>.
- [341] Murray Gell-Mann and Keith A. Brueckner. “Correlation Energy of an Electron Gas at High Density”. In: *Phys. Rev.* 106 (2 Apr. 1957), pp. 364–368. DOI: [10.1103/PhysRev.106.364](https://doi.org/10.1103/PhysRev.106.364). URL: <https://link.aps.org/doi/10.1103/PhysRev.106.364>.

BIBLIOGRAPHY

- [342] M. Sajjad Athar and S. K. Singh. *The Physics of Neutrino Interactions*. Cambridge University Press, 2020. DOI: [10.1017/9781108489065](https://doi.org/10.1017/9781108489065).
- [343] D. Horn. “Partial Conservation of Axial-Vector Current and Chiral Representation Mixing”. In: *Phys. Rev. Lett.* 17 (14 Oct. 1966), pp. 778–782. DOI: [10.1103/PhysRevLett.17.778](https://doi.org/10.1103/PhysRevLett.17.778). URL: <https://link.aps.org/doi/10.1103/PhysRevLett.17.778>.
- [344] J. Speth et al. “The influence of the π - and ρ -exchange potential on magnetic properties of nuclei”. In: *Nuclear Physics A* 343 (1980), pp. 382–416. ISSN: 0375-9474. DOI: [https://doi.org/10.1016/0375-9474\(80\)90660-0](https://doi.org/10.1016/0375-9474(80)90660-0). URL: <https://www.sciencedirect.com/science/article/pii/0375947480906600>.
- [345] R. Gran. *Private communication*. 2020.

